Czech Technical University in Prague
Faculty of Mechanical Engineering
Department of Physics

Electron beam characterization of technical surfaces at cryogenic temperatures

Dissertation submitted in fulfilment of the requirements
for the degree 'Doctor of Philosophy' by

Ing. Michal Haubner

Doctoral programme: Mechanical engineering
Field of study: Mathematical and physical engineering

Supervisor at CTU in Prague: doc. Ing. Petr Vlčák, Ph.D.
Supervisor at CTU in Prague, former: doc. Ing. Václav Vacek, CSc.
Supervisor at CERN, Geneva: Dr. Vincent Baglin

Geneva, May 2023

Declaration

I hereby declare that I have written this dissertation independently and quoted all the sources of information used in accordance with methodological instructions on ethical principles for writing an academic thesis. Moreover, I state that this thesis has neither been submitted nor accepted for any other degree.

In Geneva, May 2023

.....
Ing. Michal Haubner

Abstract (EN)

This dissertation presents applied research on the electron irradiation-induced emission of electrons and molecules and thermally controlled gas adsorption and desorption at cryogenic temperatures. Various technical-grade metal surfaces and functional surface coatings and treatments are studied under conditions relevant to many technical applications. A particular focus is on understanding the electron cloud and dynamic vacuum phenomena in CERN's Large Hadron Collider (LHC), which operates at cryogenic temperatures below 20 K. Its electron cloud is characterised by low energies in 0–1 keV range but high doses up to 10 mC.mm^{-2}. Such conditions are controllably reproduced in a newly developed cryogenic laboratory setup designed for collector-based measurements of Secondary electron emission (SEY), electron stimulated desorption (ESD), and temperature programmed desorption (TPD) at high sensitivity, precision, and accuracy. The experimental results are acquired, analysed and systematically discussed in detail. Finally, semiempirical parametric models of the SEY and ESD yields are developed to capture the energy, dose, angle, temperature and composition dependencies, allowing further use in the field. While emphasising the LHC's electron cloud-induced dynamic vacuum effect and related phenomena, the research findings are interpreted in a generalist manner, making them relevant to other accelerators and technical applications.

Keywords:
secondary electron emission, electron stimulated desorption, temperature programmed desorption, cryogenic temperatures, cryosorbed gases, technical-grade metals, coatings and treatments

Abstrakt (CZ)

Tato disertační práce se zabývá aplikovaným výzkumem emise elektronů a molekul vyvolané elektronovým zářením a tepelně řízenou adsorpci a desorpci plynů za kryogenních teplot. Studovány jsou různé technické kovové povrchy a funkční povlaky a povrchové úpravy za podmínek relevantních pro mnoho technických aplikací. Zvláštní pozornost se věnuje jevům elektronového oblaku a dynamického vakua ve Velkém hadronovém urychlovači (LHC), který pracuje za kryogenních teplot pod 20 K, a jehož elektronový oblak má nízké energie v rozmezí 0–1 keV ale vysoké dávky až po 10 mC.mm^{-2}. Takové podmínky lze řízeně reprodukovat v nově vyvinutém kryogenním laboratorním systému určeném pro vysoce citlivé a přesné kolektorové měření sekundární elektronové emise (SEY), elektronově stimulované desorpce (ESD) a teplotně programované desorpce (TPD). Získané experimentální výsledky jsou podrobně analyzovány a systematicky diskutovány. Nakonec jsou vyvinuty semiempirické parametrické modely pro jevy SEY a ESD, které zachycují závislosti na energii, dávce, úhlu, teplotě a složení a umožňují další využití výsledků v této oblasti. Přestože je kladen důraz na efekt dynamického vakua vyvolaný elektronovým mrakem na urychlovači LHC a související jevy, jsou výsledky výzkumu interpretovány obecně, takže jsou relevantní i pro jiné urychlovače a technické aplikace.

Klíčová slova:
sekundární elektronová emise, elektronově stimulovaná desorpce, teplotně programovaná desorpce kryogenní teploty, kryosorbované plyny, technické kovové povrchy, povrchové úpravy

To all those who have
supported me along the way.

Acknowledgements

Above all, I wish to express my deepest gratitude to my broad loving family. For introducing me to the charms of the beautiful world around me, and also for generously supporting me in all ways possible during the course of my lengthy studies.

I also wish to proclaim my warmest thanks to my CERN supervisor, Dr. Vincent Baglin, for his limitless time, efforts, trust, understanding and motivation in helping me pursue this research work. Additionally, I extend my thanks to my supervisor at CTU in Prague, doc. Ing. Petr Vlčák, Ph.D., for his sincere support from the beginning to the end of my doctoral studies.

I am also indebted to the inspiring teachers, mentors, and friends who have kept me grounded and sparked my curiosity along the way, including Bernard Henrist, Mark Heinen, Petr Koubek, and Bohumil Černocký. Their support and motivation have been invaluable throughout my academic journey. I also thank my colleagues from CERN and CTU in Prague for all their help and for creating a great academic environment and a friendly atmosphere.

The presented research was supported by CERN's High Luminosity LHC project and the Czech Technical University in Prague grant number SGS21/149/OHK2/3T/12.

Contents

Abbreviations and Nomenclature

Abbreviations

AES	Auger Electron Spectroscopy
BG	BackGround
BS	Beam-Screen
BSE	BackScattered Electrons
CASINO	monte CArlo SImulation of electroN trajectory in sOlids
CERN	Conseil Européen pour la Recherche Nucléaire, European Council for Nuclear Research
COLDEX	Cold Bore Experiment
DIET	Desorption Induced by Electronic Transitions
DEA	Dissociative Electron Attachment
EBID	Electron Beam Induced Deposition
EC	Electron Cloud
EDS	Energy Dispersive X-ray Spectroscopy
ESD	Electron Stimulated Desorption
ESDIAD	ESD Ion Angular Distribution
FCC	Future Circular Collider
FE-SEM	Field-Emission SEM
FWHM	Full Width at Half Maximum
FODO	Focusing-Defocusing Cell
HTS	High-Temperature Superconductor
HL-LHC	High-Luminosity Large Hadron Collider
HOPG	Highly Oriented Pyrolytic Graphite
IMFP	Inelastic Mean Free Path
IMGR	Ishikawa-Menzel-Gomer-Redhead
ISD	Ion Stimulated Desorption
LE-ESD	Low-Energy Electron Stimulated Desorption
LE-SEY	Low-Energy Secondary Electron Yield
LHC	Large Hadron Collider
LTS	Low-Temperature Superconductor
ML	MonoLayer
OFHC	Oxygen-Free High Conductivity copper
PID	Proportional Integral Derivative controller
PLD	Pulsed Laser Deposition
PSD	Photon Stimulated Desorption
RCE-DR	Reactive Co-Evaporation by Deposition and Reaction
REBCO	Rare-Earth Barium Copper Oxide
RF	Radio Frequency
RGA	Residual Gas Analyser
SEM	Scanning Electron Microscope
SEY	Secondary Electron Yield
SNR	Signal-to-Noise Ratio
SS	Stainless Steel
TSE	True Secondary Electron
TPD	Temperature Programmed Desorption
UHV	Ultra-High Vacuum
XPS	X-ray Photoelectron Spectroscopy

Latin nomenclature

C_j	Conductance for species j	[l.s^{-1}]
D	Electron dose	[C.mm^{-1}]
dN/dE	Electron cloud energy spectrum	[eV^{-1}]
dQ/dE	Energy-resolved gas load	[mbar.l^{-1}.s^{-1}.eV^{-1}]
$d\theta/dt$	rate of change of coverage	[mbar.l^{-1}.s^{-1}.cm^{-2}]
E	Energy	[eV]
E_{ads}	Adsorption energy	[meV.bond^{-1}]
E_{thr}	Threshold energy for ESD	[eV]
E_{max}	Energy at maximum	[eV]
i_j	RGA current of species j	[A]
I_b	Electron beam current	[A]
$I_{S,C}$	Electron current at sample, collector	[A]
k	High-angle cut-off parameter	[°]
k	Interaction coefficient in mixtures	[1]
k_B	Boltzmann constant: 1.380649·10^{-23}	[J.K^{-1}]
k_j	RGA sensitivity for species j	[A.mbar^{-1}]
M_j	Molar mass of species j	[g.mole^{-1}]
n	Exponent	[1]
N_A	Avogadro number: 6.022141·10^{23}	[molecules/mole]
p	Pressure, total	[mbar]
p_j	Partial pressure of component j	[mbar]
q_e	Elementary charge: 1.602177 ·10^{-19}	[C]
Q_j	Gas load of species j	[mbar.l^{-1}.s^{-1}]
R	Universal gas constant: 8.314459	[J.mol^{-1}.K^{-1}]
r	Desorption rate	[mbar.l^{-1}.s^{-1}.cm^{-2}]
S_j	Pumping speed of species j	[l.s^{-1}]
s, p, σ	Skewness parameters	[1]
t	Time	[s]
T	Temperature	[K]
T_{max}	Maximum temperature	[K]
$V_{S,C}$	Voltage bias at sample, collector	[V]
V_{inj}	Injection volume	[l]
x	Molar fraction	[1]
Z	Atomic number	[1]

Greek nomenclature

α	Incidence angle from normal	[°]
β	Heating rate	[K/min]
δ	Secondary Electron Yield, SEY	[e$^-$/e$^-$=1]
δ_{max}	Maximum SEY	[1]
$\delta_{A:B,max}$	Maximum SEY of mixture $A:B$	[1]
η	Electron Stimulated Desorption yield	[molecule/e$^-$]
η_{max}	Maximum ESD yield	[eV]
$\eta_{Dyn.BG}$	Background level of ESD yield	[molecule/e$^-$]
$\eta_{A:B\rightarrow A}$	ESD of component A from mixture $A:B$	[molecule/e$^-$]
θ_j	Surface coverage of species j	[molecule/cm^{-2}]
ν	Frequency factor	[Hz]
σ_{EBID}	Effective dissociation cross-section	[cm^{-2}]
σ	Standard deviation	[-]
τ	Time constant	[s]

Introduction

This vacuum science-oriented dissertation consists of four major parts that aim first to motivate the curious reader, then state the research niche, guide through the applied research work, and ultimately reconnect to the experimental results' applicability within the applied research field. The phenomena of secondary electron emission (SEY), electron stimulated desorption (ESD) and temperature programmed desorption (TPD) are investigated at a range of surfaces and conditions relevant for many technical applications. Yet, a particular focus is placed on understanding the electron cloud-induced dynamic vacuum effect in CERN's Large Hadron Collider, the LHC.

The first two Chapters 1 and 2 outline the context of the problematics arising from electron irradiation of technical-grade metal surfaces, and introduce this research field's state-of-the-art. Careful analysis of the problematics allows for setting experimental goals and methods to study the underlying physical phenomena and correctly interpreting the experimental observations.

The experimental Chapter 4 describes the commissioning of the experimental setup and the methodology developed to study in detail the desired phenomena. The setup is calibrated to deliver quantitative results of SEY, ESD and TPD in the targeted conditions of temperature, pressure and energy range relevant to the LHC operation. The developed laboratory experiment grants an unprecedented research capability in terms of the range of controllable parameters, sensitivity, precision and accuracy. The range of observables provides a synergic view of the electron-induced emission of electrons and molecules, along with thermally controlled gas adsorption and desorption.

The following Chapter 5 presents the acquired experimental results that are immediately discussed from the experimental and physics standpoint, transforming data into knowledge. The SEY is addressed first as the origin of the electron cloud activity and is followed by the ESD that links it to the dynamic vacuum effect, both observed in the LHC. The irradiation and environmental parameters are systematically addressed, allowing to disentangle the influence of the primary electron energy, dose, angle, surface temperature, treatments and cryosorbed gases. The TPD measurements then follow as a means to characterise specific surfaces of treatments and the impact of cryosorbed gases on the SEY and ESD.

Finally, the last Chapter 6 elaborates on the direct applicability of the research results and the knowledge derived from within. Although the relevance to the LHC is imperative, the research results are interpreted in a rather generalist manner and other accelerators and technical applications are also addressed where possible. Ultimately, the state-of-the-art theory-backed understanding can be leveraged to generalise the emergent dependencies for further use, as attempted here.

Altogether, this dissertation aspires to intertwine the engineering perspective on the matter with the theoretical background necessary for a correct data interpretation to deliver comprehensible and applicable research results.

May the reader share the author's joy in the discovery process!

Chapter 1
Motivation and objectives

Contents

1.1 CERN's accelerator complex

CERN's accelerator complex consists of a chain of accelerator rings that circulate and accelerate high-energy proton and ion beams and provide them to various experiments, as schematised in Figure 1.1. At its end lies the Large Hadron Collider (LHC) [1] a proton storage ring built at an industrial scale of 27 km, capable of storing high-intensity proton beams and accelerating them from the injection energy 0.45 TeV to a nominal collision energy of 7 TeV per beam, i.e. 14 TeV in the centre-of-mass of the proton-proton collision.

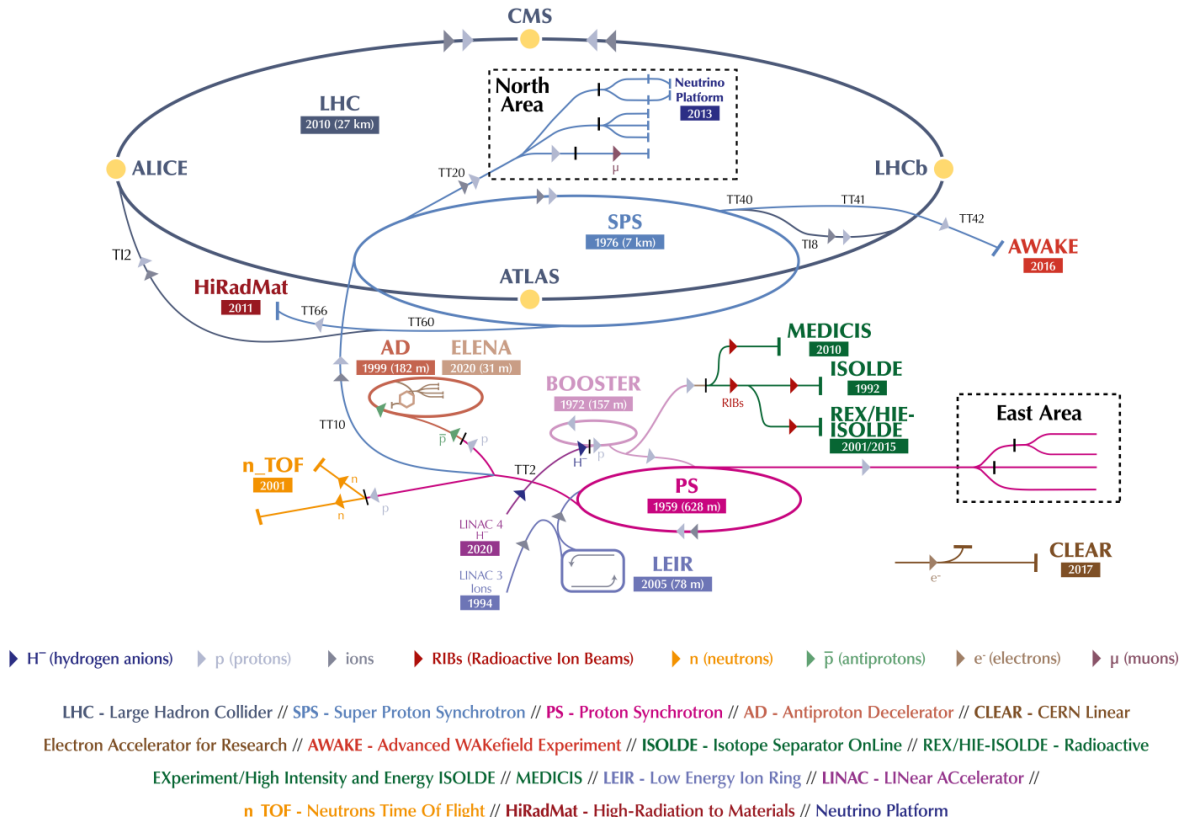

Figure 1.1: Schematic view of CERN's accelerator complex. The accelerator chain starts from linear accelerators, past boosters and through transfer lines continues into the LHC. The PS and SPS provides the proton beam to other experiments when not injecting into the LHC. Image credit: CERN.

The LHC largely consists of superconducting cryomagnets, whose strong magnetic field focuses and circulates the beam on a closed circular trajectory. This is achieved by arranging the cryogenic magnets in a FODO-cell beam optics layout [2], consisting of 3 bending dipoles followed by 1 focusing quadrupole, which repeats all along the cold-arcs, [1]. Their cold bore is held at 1.9 K, being the temperature where the superfluid helium has the largest thermal conductivity, thus effectively thermalising the cold bore and extracting heat. The magnets' cold bore houses a beam tube with a specially designed beam-screen which is cooled to 5-20 K and extracts heat generated by the circulating proton beam before reaching the superconducting magnets' cold mass. The beam-screen has been carefully designed [3] to mitigate the electron cloud and provide vacuum stability in the presence of circulating proton beams, amongst many other design goals reproduced in Fig. 1.5.

1.2 LHC vacuum in the presence of proton beams

The LHC and its upcoming upgrade, the high-luminosity LHC, HL-LHC [4], stands as the next challenge to physicists and engineers in many regards. One of these is the mitigation of the electron cloud and ultra-high vacuum stability while circulating high-intensity bunched proton beams. The negative effect also goes in the opposite direction, as the beam-induced electron cloud acts back on the circulating charged particle beam in a detrimental way [5]. Both of these challenges have been long observed in the accelerator physics community ever since the '60s and, in fact, impose a challenge to this date, also at

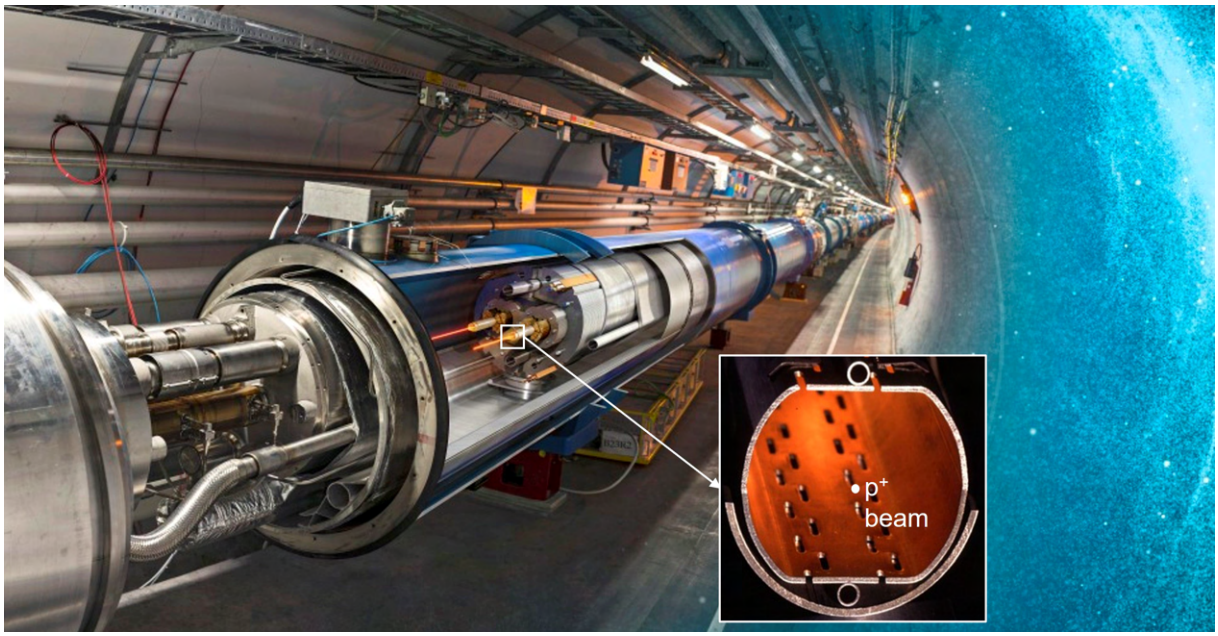

Figure 1.2: Cutaway view of the LHC superconducting dipole magnet and a detailed view of the beam-tube consisting of a vacuum chamber lined with beam-screen. The beam-screen shields the magnets' cold mass from the beam-induced heating via its separate LHe cooling loop and provides vacuum stability, as detailed in the text. Image credit: CERN

other CERN's accelerators such as the Proton Synchrotron (PS) and Super Proton Synchrotron (SPS) [6].

1.2.1 Synchrotron radiation and the electron cloud effect

The circulating relativistic bunched (discontinuous) proton beam emits synchrotron radiation intercepted by the beam-screen (BS). While the synchrotron radiation is harmless at the 0.45 TeV injection energy, the photons' critical reaches 44 eV [7] when the proton beam reaches nominal beam energy of 7 TeV. Hence, the photon energy largely surpasses the ∼4.5 eV work function of the beam-screens copper surface and extracts photoelectrons. Slow photoelectrons are then accelerated by an electric field of passing proton bunches, impinge on the beam-screen surface again, multipact and form an electron cloud (EC). Under certain resonant conditions, the EC can prevail and form a self-sustaining electron population. The EC then induced various beam instabilities, not being of concern in this treatise, and continuously irradiates the beam-screen surface, desorbs gas, and deposits heat into the BS. The closed geometry of a beam tube inherently limits the pumping speed and makes mitigation of gas sources even more important. This non-thermal electron desorption mechanism was identified as the predominant dynamic gas source and needs to be investigated for the efficient operation of the LHC.

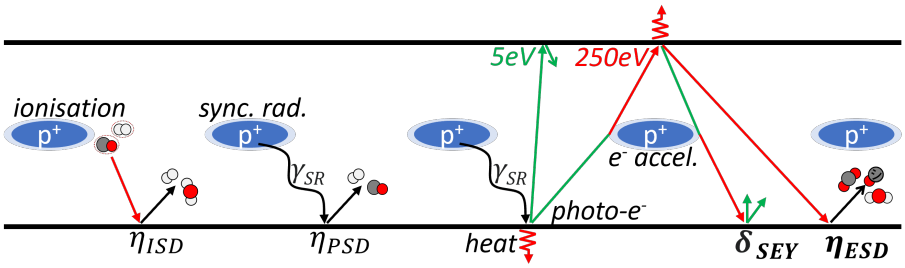

Figure 1.3: Scheme of the main interactions between the proton beam, residual gas and the beam tube surface. Note the ion-, photon-, and electron-stimulated gas desorption mechanisms. Also, note the electron multipacting effect and the heat deposition into the wall.

Available problematics overviews, e.g. [8], including simulations [9] and even recent measurements [10] have shown that energy distribution of EC inside of LHC resides mostly in low-energy range, with a major peak below 10 eV, as visualised in Figure 1.4. When the EC is in a multipacting regime, this major peak is followed by a secondary peak at a few hundred eV. The magnitude and position of the secondary

peak vary with actual beam parameters, the surface state of the beam-screen and geometrical factors. More detailed simulation results are published by Skripka&Iadarola [11], including electron concentration profiles simulated at different conditions in LHC dipoles, quadruples and drift sections. We have therefore designed an experiment for laboratory investigation of samples representative of the copper surface of a beam-screen under the conditions it experiences in LHC's cryogenic magnets. The setup reproduces in a controllable manner the relevant conditions present inside the LHC's beam-screen: temperature under 20 K, ultrahigh vacuum in the 10^{-10} mbar range and low-energy electron irradiation. We focused our present research towards low electron energies in the sub-keV region, focusing on 0-100 eV, which is experimentally very challenging and for which we have developed and commissioned a novel measurement procedure.

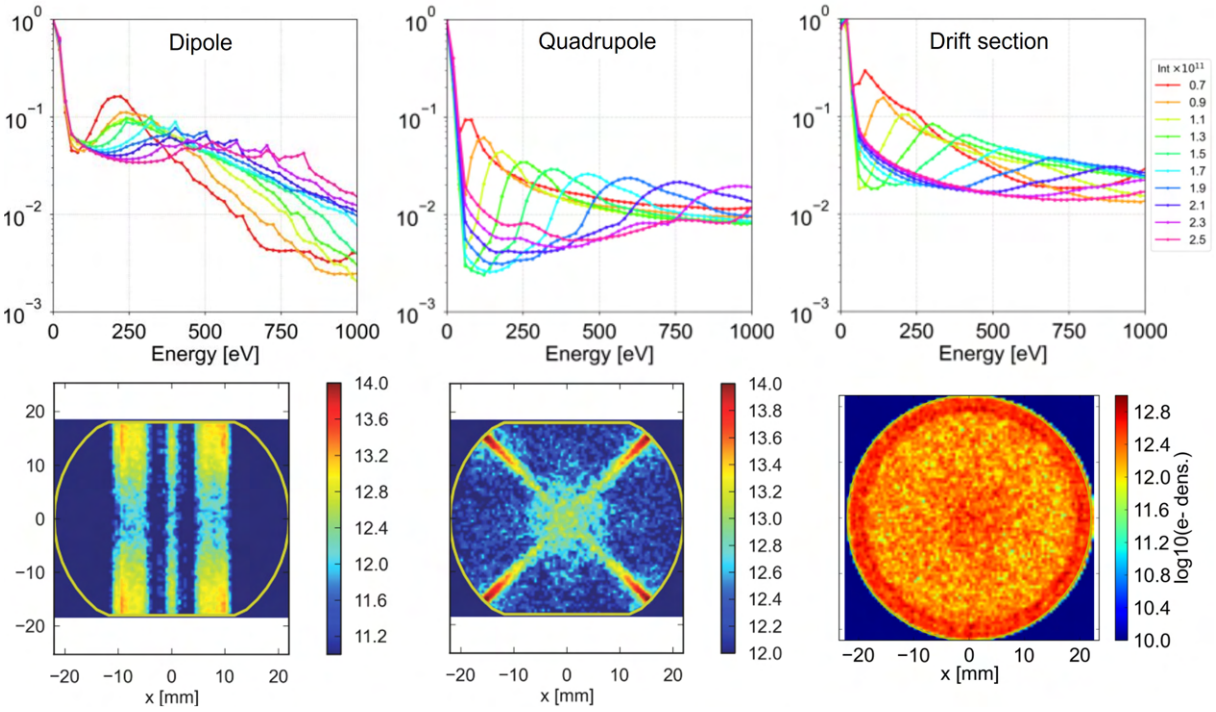

Figure 1.4: Energy distribution of electron cloud electrons as simulated by G. Iadarola [9] for an LHC cryomagnets and field-free regions. Note the primary peak of true secondary electrons at few eV followed by a second peak of beam-accelerated electrons at few hundreds eV, whose amplitude and energy varies with the chamber geometry and beam parameters.

1.2.2 Dynamic vacuum effect in accelerators

The dynamic vacuum effect can be primarily ascribed to non-thermal gas desorption stimulated by particles, such as photons, electrons, ions and beam loss particles impinging on the inner surface of a vacuum vessel where the beam circulates. In particular, the electron stimulated desorption (ESD) phenomenon is important for modern machines exhibiting an electron cloud (EC) and will be addressed here.

Indeed, this problematics is not unique to the CERN's accelerators as similar issues with electron cloud effects and dynamic vacuum phenomena are regularly observed at other machines. In fact, the dynamic pressure rise in accelerators and light sources has been long observed in room temperature machines and, recently, in cryogenic ones. In fact, the dynamic vacuum effect is common to machines circulating bunched charged particles, especially positively charged ones, but not excluding electrons either [12]. As such, the EC activity resulting in a dynamic pressure rise is observed at CERN's Large Hadron Collider (LHC), Fig. 1.6, and other existing machines: RHIC in the USA [13] with its electron-ion variant [14], present and future GSI machines such as SIS100 [15], and SuperKEKB in Japan [16, 17]. This also includes light-sources, which deal with both electron and photon stimulated desorptions, such as [18]. Pressure rise by up to ∼5 orders of magnitude were observed in some cases, which is far beyond acceptable.

For completeness, the electron- and photon-induced dynamic vacuum effect is a mechanism different from the ion-induced pressure instability reported by Calder at CERN's ISR [19], as it lacks a positive

feedback loop, strictly speaking. Conversely, the ion-induced vacuum instability has a closed positive feedback loop [20] that leads to a well-defined stability condition. This feedback can lead to a pressure runaway, which is driven by high beam currents in combination with high ion energy [21] and a high ion stimulated desorption yield [22] from the beam-tube surface.

Future machines are not exempt from these phenomena either. Electron cloud and dynamic vacuum mitigation strategies are already implemented in the beam-screen design phase and represent an important aspect of an accelerator design [23]. This includes CERN's planned FCC-hh variant [24, 25], or Chinese SPPC and CEPC projects [26, 27]. All are designed bearing in mind the electron cloud and resulting dynamic vacuum phenomena, i.e. introducing beam-screen into the design.

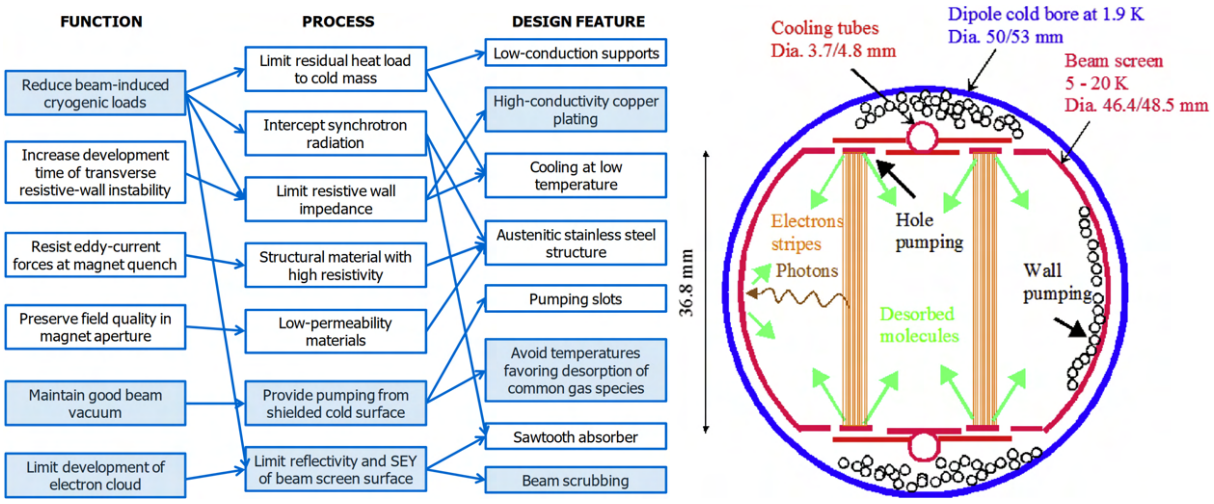

Figure 1.5: Left: Functions and corresponding design features of the LHC beam-screen, adapted from V. Baglin [3]. Right: Schematised cross section of the LHC beam-screen, adapted from V. Baglin [28]. Note the gas sources and sinks in this closed vacuum system, which are discussed in the text.

Beam-screen was designed and introduced into the beam tube as a consequence of these vacuum, and electron cloud-related concerns [29], granting dynamic vacuum stability in the presence of a circulating beam and shielding the magnets' cold bore from beam-induced heat load. Figure 1.5 shows the design map of functions and corresponding design features of the LHC beam-screen. The highlighted ones are linked to the research done in the scope of this dissertation. The scheme on the right side, adapted from V. Baglin [28], schematises the beam-screen cross-section and different dynamic vacuum processes present when circulating the proton beam. Not how the molecules desorbed by ESD and PSD mechanism are pumped through the pumping slots and consequently cryosorbed on the 1.9 K cold bore vacuum tube.

In fact, the beam-screen design has already been iterated upon in some local areas for the HL-LHC upgrade (inner triplet magnets). The design changes are described in a recent paper [30] and mainly consist of a 50 nm thin amorphous carbon coating, stronger supercritical He cooling, higher temperature window at 60-80 K and a tungsten radiation shielding that protects the cryomagnets held at 1.9 K from beam-induced heat loads. Similarly, a full suite of EC mitigation strategies was gradually implemented during SuperKEKB commissioning, and their respective efficacy is now well-analysed [12].

It has also been observed for the LHC machine and others that these unwanted effects diminish with time in operation. The dynamic vacuum effect gradually attenuates with operation time to levels acceptable for nominal operation, as reported by Baglin et al. [28] for the LHC Run 1 and plotted in the adjacent Figure 1.6 for Run 3 supplied by the TE-VSC-BVO section. Each yearly LHC restart is followed by dedicated scrubbing runs performed at the injection energy of 0.45 TeV, during which the electron cloud is intentionally triggered to (re)condition the beam-screen copper surface. This gradual decrease of the pressure rise can be partly assigned to diminishing the electron cloud activity due to the decrease of secondary electron yield (SEY) and surface conditioning under electron bombardment, i.e. decrease of ESD yield.

Figure 1.6 shows the dynamic pressure rise normalised to the proton beam current so as to compensate for the proton beam current changes. The horizontal axis shows the integrated beam time, i.e. the time in operation, as measured by the circulating beam current. The decrease in the normalised pressure rise results from electron-stimulated desorption and its decrease with absorbed electron dose, i.e. conditioning effect. The curve starts with a constant plateau followed by a linear decay (in log-log scaling). After

these dedicated scrubbing runs follows a nominal operation during which the machine further scrubs. Still, this effect remains a concern when pushing up the accelerators' performance in terms of energy and luminosity and/or while trying to optimise its operation.

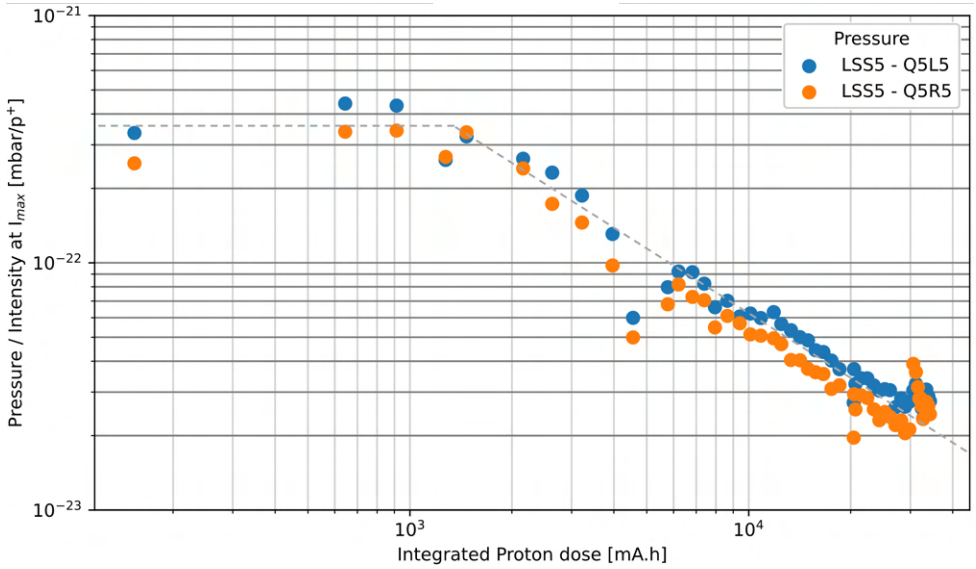

Figure 1.6: Gradual decrease of the dynamic vacuum effect during beam-scrubbing of LHC Run 3, as measured by Penning gauges located around a standalone Q5 quadrupole cryomagnets situated at long-straight-section 5, close to CMS experiment. The dynamic pressure rise is normalised to the proton beam current and plotted against the accumulated beam time, which is an indirect measure of the electron dose imparted onto the beam-screen during the scrubbing run. This plot was kindly provided by CERN's TE-VSC-BVO section.

1.3 Relevance to other technical applications

To deal with the electron cloud and dynamic vacuum effects, one has first to understand the phenomena of electron multipacting and electron stimulated desorption in order to master it. And in the absence of many experimental data taken under the relevant conditions, one must draw inspiration from other fields and the established theoretical background.

Redhead recalls in his memoirs [31] that ESD emerged as an object of concern in various independent technical applications. It was studied in the context of vacuum gauges and mass spectrometry, where it produced a dynamic background signal [32], and in the vacuum tube technology, it manifested as an undesirable *10-Volt effect*. Cross-disciplinary technical interest in the ESD topic gave rise to a theoretical framework of Desorption Induced by Electronic Transitions (DIET) that explains both the ESD and PSD. The explanation was proposed independently around the same time, establishing the now-classical model of Ishikawa-Menzel-Gomer-Redhead (IMGR model) discussed in detail in Chapter 2.5.

The ESD phenomena was later turned into a scientific tool for surface science [33, 34] and biophysics [35] who study the radiation effects on condensed matter, both inorganic and organic. This includes the electron-induced chemistry [36], which was particularly well summarised for low-energy electrons by Arumainayagam et al. [37]. Low-energy electrons are thought to be the main driver of radiation-induced chemistry, because of their shear number [38]. The ESD also manifests in electron microscopy, causing a beam-induced damage that alters and degrades the studied specimen. This effect was even transformed into an imaging technique, say an ESD-mediated scanning electron microscopy by Dylla et al. [39]. Further up, the electron-irradiated surfaces studied in astrophysics [40, 41], are also far from well-defined, though not exactly technical-grade metals, but have been fairly well studied and can provide valuable hints, e.g. on electrodesorption of weakly-bound molecules, fragments and products.

In parallel to the scientific applications, the ESD poses other engineering challenges. The dynamic vacuum effect that systematically haunts numerous particle accelerators was just discussed. A widespread domain that experiences electron multipacting and, therefore also, electrodesorption are radiofrequency (RF) devices [42, 43]. Resonant cavities, including superconducting ones, wave-guides and other components, can also develop an electron cloud once certain resonant conditions are met. The electron cloud not only drastically impairs the RF performance and increases noise in such a system but also desorbs

gas that decreases the breakdown voltage and causes arcing. As a result of the same underlying physical process, the electron cloud energy spectrum of an RF system [44] closely resembles that in accelerators beam-tube, Fig. 1.4, which is indeed an RF device of a kind. The signature behaviour of electron multipacting is a double-peaked spectrum dominated by a low-energy peak of true secondary electrons, the majority of which lies under 20 eV. This is followed by a second peak, typically at few hundreds eV, whose exact position and height depend on the multipacting conditions.

Electrodesorption makes one of the effects in the complex plasma-surface interaction in magnetically-confined fusion devices that produce runaway electrons in the keV-MeV range. These electrons then irradiate the chamber wall and electrodesorb gas that contributes to impurity influx that gradually poisons the plasma and decreases its temperature [45]. A similar electron and ion-driven contaminant influx may compromise the sputter deposition process [46] of coatings, whose properties are known to be altered by unwanted gas molecules present in the plasma discharge. For example, hydrogen present in the process atmosphere degrades the anti-multipacting properties of sputter-deposited carbon-coatings [47] by increasing the SEY. In the aeronautics domain, the spacecraft design and choice of materials also optimise the outgassing [48], including the stimulated one, that can lead to molecular contamination of a spacecraft's instruments. Here the desorbed molecules can impair functional parts of a spacecraft, e.g. re-adsorb on optical instruments or produce false spectrometer readings. The decreased breakdown voltage of insulating components in combination with differential charging effects due to different SEY can lead to electrical discharges across components. However, these application fields are predominantly concerned by other types of irradiation, both thermal and non-thermal, leaving the ESD with a marginal contribution to the total gas desorption.

Indeed, the above-mentioned fields occupy different regions in the parameter space of factors influencing the ESD but can all benefit from developing this research field. Despite its cross-disciplinary technical and scientific importance, the research status of ESD from technical-grade metal surfaces is dismal and lacks behind its well-defined laboratory-grade counterpart. This is partly because the experimental complexity of ESD measurements and partly the complexity of a technical-grade metal surface, which introduces even more dimensions into the already vast parameter space of factors influencing the ESD. Hence the largest drawback is the lack of a systematically populated dataset that spans across large portions of parameter space, in terms of material, environmental and irradiation properties. It is challenging to draw quantitative predictions using the existing theory in well-defined systems and even more so in the case of technical surfaces. Even though there are numerous studies on ESD from technical-grade metal surfaces, the big picture is far from complete and most certainly lacks a predictive capability.

Chapter 2
State of the Art

Contents

This literature survey is subdivided into chapters relevant to each studied phenomena: the secondary electron yield (SEY), electron stimulated desorption (ESD) and temperature programmed desorption (TPD). Each section contains a brief theoretical reminder, a survey of relevant experimental data, and increasingly often, simulation results. The review starts out with the various electron-matter interactions that are a prerequisite for secondary electron emission and gas electrodesorption.

2.1 Electron interactions with a surface

At a macroscopic level, the impact and following interactions of primary electrons with a substrate leads to an emission of secondary particles, such as electrons, photons, and gas. The remainder, and in fact the majority, of the incident primary electron energy, is dissipated as heat, first to electronic shells, then to the atomic movement. This is indeed the source EC-induced heat load in the LHC beam-screen [11]. The desorbed gas species can be atoms or molecules in neutral or charged, excited or ground states. The below-discussed experimental setup used for this research is designed to detect emitted electrons as well as desorbed neutral gas species, as they are predominant. In respect to the LHC, this phenomena is responsible for the dynamic vacuum effect, i.e. EC-induced pressure increase.

As soon as primary electrons reach a target, they electrostatically interact with the electron shells of the target atoms by elastic and non-elastic collisions, as schematised in Fig. 2.1 on the left. This can result in the primary electron re-emission at the original or lower energy. Since this is a direct energy transfer process, it varies with the primary electron beam parameters. Conversely, the true secondary electron generation is an indirect energy transfer process and is, therefore, independent of the primary electron characteristics to a large extent. This is because the incoming electrons scatter in the material, forming an electronically excited volume where the electrons locally thermalize with the Fermi gas. This newly formed short-lived population of hot electrons is the source of true secondary electrons emitted into the vacuum above and is the reason why the secondary electron energy spectrum is invariant with the primary energy.

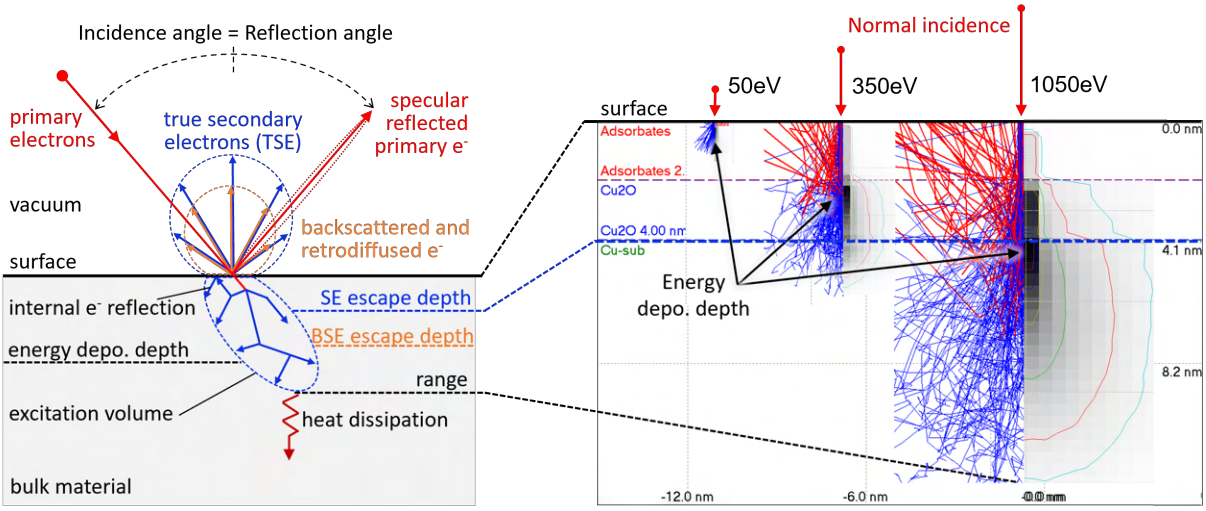

Figure 2.1: Left: Schematised electron interactions with a surface for non-normal irradiation angle. Note the superposition of specular and diffuse electron backscattering. Right: CASINO simulation of 50, 350, 1050 eV electron with a layered surface (2 nm of C, O and H contaminants, 2 nm of Cu_2O on a bulk Cu substrate.) Red trajectories trace backscattered electrons (both elastic and inelastic) and blue traces are the true secondary electrons. Results are only qualitative and details are discussed further in the text. Image and simulation: Author.

Figure 2.1 on the right shows a CASINO Monte-Carlo simulation set for a Cu substrate with a Cu_2O and contaminant overlayers. The normally-incident electrons range from 50 eV to 1050 keV to illustrate the different regimes, ranging from surface-sensitive to bulk-sensitive. The higher energy electrons are more penetrant as visualised by the deposited energy isocontours. Some primary electrons, marked with red trajectories, are reflected, backscattered or rediffused. The reflected portion of electrons follows the specular reflection with the angle of incidence equal to angle of reflection, whilst the backscattered and rediffused follow a diffused pattern, well approximated by a cosine angular distribution. The elastically backscattered electrons have a narrow energy spectrum, with energies about equal to the primary electron energy. It is more likely for low-energy electrons to be elastically reflected away from the surface, while

higher-energy electrons are more likely to be elastically and inelastically backscattered, while producing secondary electrons at the same time.

Many primary electrons penetrate into the bulk without being backscattered and eventually dissipate their kinetic energy, stopping their further advance. A mean penetration depth can be defined as an orthogonal distance from the surface to the location where most electrons end. The electronic scattering process yields an avalanche of secondary electrons, marked as blue, which have lower energy than the primaries. The secondaries were excited enough to leave their electron shells and now travel through the bulk in a Brownian-like motion. If such electronic scattering happens in the close enough vicinity of a surface and the electron energy trespasses the work function, there is a chance of them escaping from the surface into the vacuum, giving arise of secondary electron emission. Such escape depth represents an average depth beneath a surface from which the electrons can still escape. The escape depth is denoted in Figures 2.1 and 2.3.

Inelastic collisions are the driving mechanism for ESD, as they imply an energy exchange with electron shells of atoms and molecules present in the surface layer. The amount of energy lost by electron per unit of length while travelling through a material can be defined via stopping cross-section or conversely by mean free path. Figure 2.2 depicts such dependence for various target materials. Depending on the preferred reference frame, the amount of interaction between an electron and matter can be described either by the free path of an electron between collisions or by stopping cross-sections. In any case, both curves are strongly energy-dependent. This is different, yet correlated to the mean energy deposition depth, which marks the depth at which the primary electrons have deposited most of their energy. Both of these processes depend on the primary electron energy and the bulk properties. For engineering purposes, Fitting [49] gives a good overview of low-energy electron interactions. A solid overview of particle stopping in condensed matter is given in [50], even though no author approaches the low-energy of 0-100 eV with certainty, as illustrated in [51].

Considering electrons in the 0-1 keV range, one can exclude physical phenomena such as radiative stopping and relativistic effects and substrate-related phenomena such as channelling. The process of electron slowing down is the most intense around 100 eV due to the high stopping power [52]. The stopping power is considerably lower for energies under ∼10 eV or higher than ∼200 eV [49]. From an opposite point of view, the IMFP is the shortest for ∼100 eV, as plotted in Fig. 2.2. Not so coincidentally, the de-Broglie wavelength of electrons at these energies is comparable to characteristic dimensions of atoms and molecules, rendering the scattering more probable. The stopping naturally varies with the atomic number of a given material, which determines the number of electrons bound within their atomic orbitals. For example, lighter elements, such as hydrogen molecule, has by about 1 decade lower stopping power than gold [53]. For illustration, an electron with a kinetic energy of 100 eV will lose on average 10 eV within the first layer of gold atoms, but only 2 eV within the first layer of hydrogen atoms. Yet, despite large variations, it is still possible to construct a universal curve for the IMFP [54], which coarsely approximates experimental IMFP values, λ [nm] acquired across a range of energies [eV] and materials (red curve in Fig. 2.2), and is described by the following Eq. 2.1.

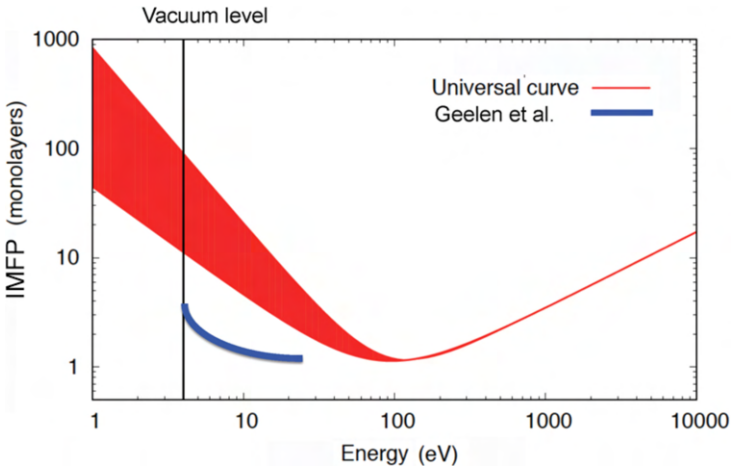

Figure 2.2: *Universal* curve for the inelastic mean free path (IMFP) of electrons in different solids. Not the asymptotic approach to the first and second parts of the equation 2.1 at low and high energy region. Also note the massive uncertainty in the 1-100 eV energy region. Adapted from Werner [51].

$$\lambda(E) = \frac{143}{E^2} + 0.054 \cdot \sqrt{E} \tag{2.1}$$

While this approach gives a reasonably accurate fit for keV and higher energies, the low energy part in 1-100 eV range is massively scattered, as discussed by Werner [51]. Him et al. also present some more precise estimates [55]. Variations by more than an order of magnitude were reported for thin graphene

layers [56]. Hence, the low-energy electron scattering in solids and thin films remains a great challenge, both experimental and theoretical [52].

Ultimately, it is not the energetic primary electrons but the excited secondary electrons that cause electron desorption. The right side of Figure 2.3 schematises the energy transfer from the primary electrons, via secondary electrons, to the surface-bound adsorbates. The energy diagram on the left schematises the energy dissipation cascade. The baseline dependence for the occupancy of energy levels in the electron gas is captured by the Fermi-Dirac distribution marked in blue, which is thermalised to the substrate temperature. Upon its arrival into the bulk, the primary electron deposits its kinetic energy during a collision cascade into a nm-sized volume of electronic excitations. These excitations are created on a fs timescale, resulting in a highly non-thermal electron energy distribution in the local excitation volume, marked as ① in the scheme. These excited *hot* electrons and holes scatter with other electrons in the bulk, following the IMFP curve in Fig. 2.2, which has an energy-dependent scattering probability. By doing so, the hot electrons and holes thermalize with other electrons in the Fermi gas (not yet with the atoms), and attain a Fermi-Dirac distribution marked in red in a 100's fs timescale, marked in ②. During this thermalisation process, the electrons with energy above E_{vac} and E_{des} thresholds (referenced to the Fermi level) *can* result in an electron emission or stimulate molecular desorption, as discussed below. The electrons are now locally thermalised with other electrons in the Fermi gas and gradually also thermalize with the atoms, marked in purple, finally depositing the energy as heat, marked as ③, marked in blue.

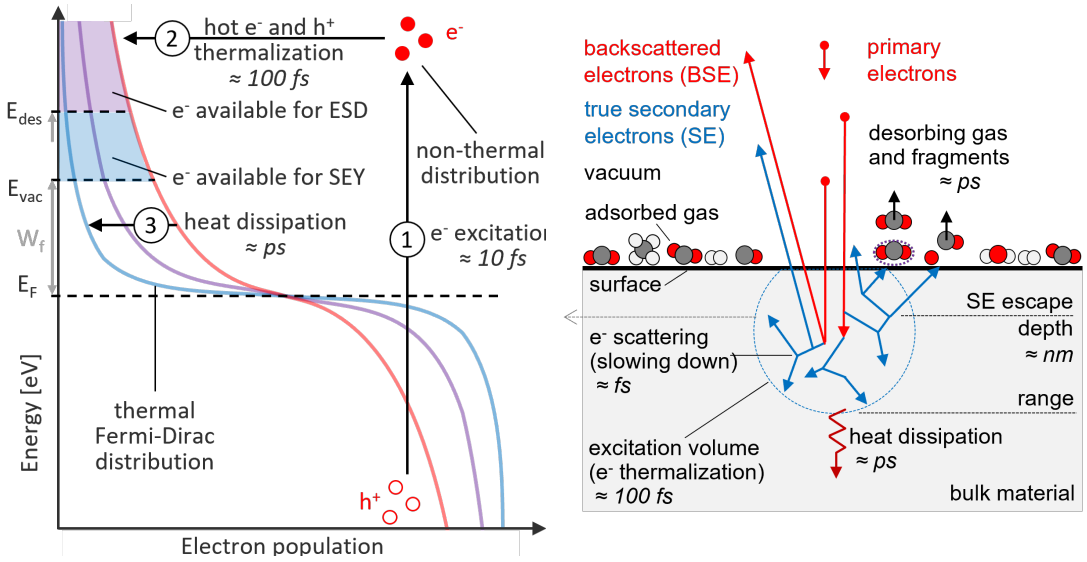

Figure 2.3: Schematised interaction of primary electrons with near-surface electrons and surface-bound molecules. Left: Energetic diagram of primary electron energy dissipation cascade resulting in a population of low-energy electronic excitations. The part of this excited e^- population relevant for SEY and ESD is marked. Right: Simplified sequence of the DIET desorption mechanism. Details are discussed in the text. Image: Author.

2.2 Secondary electron yield

2.2.1 SEY curve origins

The energy spectrum of emitted electrons varies with the primary electron energy, target material, its surface state and angle of incidence of the primary electron. As a consequence, the value of SEY varies as well. It also varies immensely with the surface state of a material, making it a strongly surface-sensitive parameter. Figure 2.4 from [57] shows the secondary electron energy spectrum captured for different primary energies. Note that low-energy primaries are more likely to back-scatter, both elastically and inelastically, whereas higher-energy primaries do not back-scatter nearly that much and generate true secondary electrons instead. Also note the TSE energy spectrum can be approximated by a log-normal distribution, as remarked by Furman&Pivi [58]. The integral of each spectrum would give the total SEY at a given energy, as shown by the black arrows in Figure 2.5.

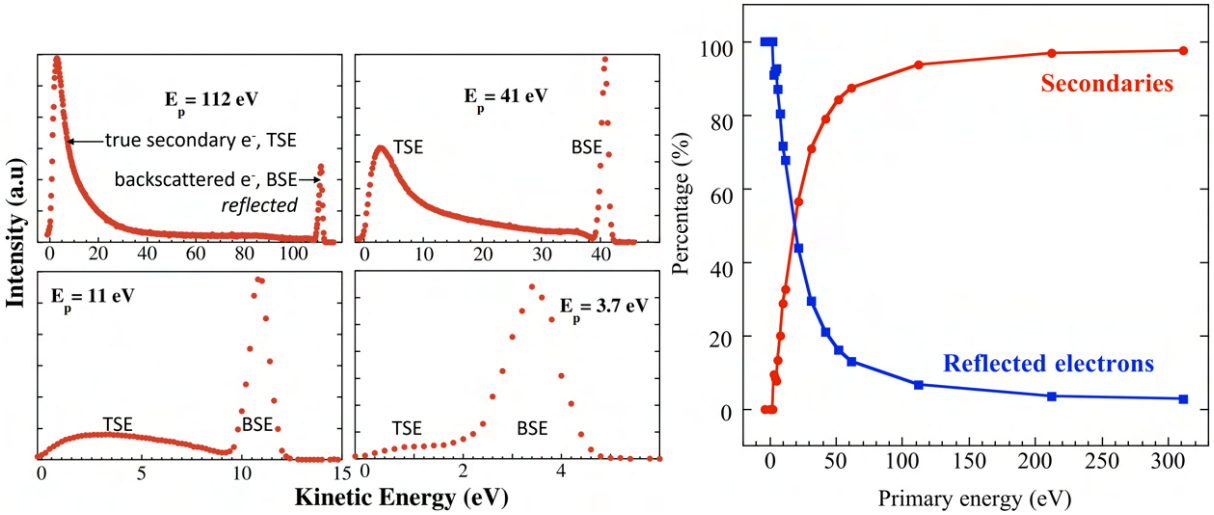

Figure 2.4: Energy spectra of secondary electrons measured by Cimino et al.[57] on a fully scrubbed copper surface held at 10 K, i.e. conditions representative for the LHC beam-screen. The primary electrons impinge at a normal incidence and their energy is varied from 3.7 eV to 112 eV. Note the high reflectivity, i.e. inelastic backscattering of low-energy electrons.

The Secondary Electron Yield (SEY), denoted δ, is defined here as the average number of electrons leaving the surface per impacting primary electron, regardless of their interaction. However, some literature sources consider the Secondary Electron Yield only to form a component of the Total Electron Yield (TEY), which is more appropriate, physically speaking. Though, to align this manuscript with the predominant technical customs, the term SEY will encompass all the electrons leaving a surface regardless of the physical process at their origin. Shall it be necessary to differentiate between true SE and backscattered electrons, it will be brought to attention. Hence, the SEY can be calculated by normalising the secondary electron current by the primary electron current.

$$\delta = I_{Secondary}/I_{Primary} \tag{2.2}$$

Figure 2.5 illustrates the decomposition of SEY into contributions from different processes. Relative contributions of each type of process change with the primary electron energy. For instance, elastically reflected electrons are predominant at very low energies but then decay exponentially as the primary energy increases. Conversely, the number of true secondary electrons increases rapidly as gradually more energy is dissipated in the form of electronic excitations, as deposited in the material by the primary electrons. An energy of about 20 eV demarks the tipping point between the backscattered electron-dominated spectrum and the true secondary electron-dominated spectrum.

Hence, the secondary electrons emitted from a studied surface as a direct result of electron irradiation are a witness of the energy spectrum of electronic excitations in the bulk and as such make for a valuable observable. Hence the energy spectrum provides a clue on what is the number and energy of excitations that can stimulate gas desorption discussed in the following section.

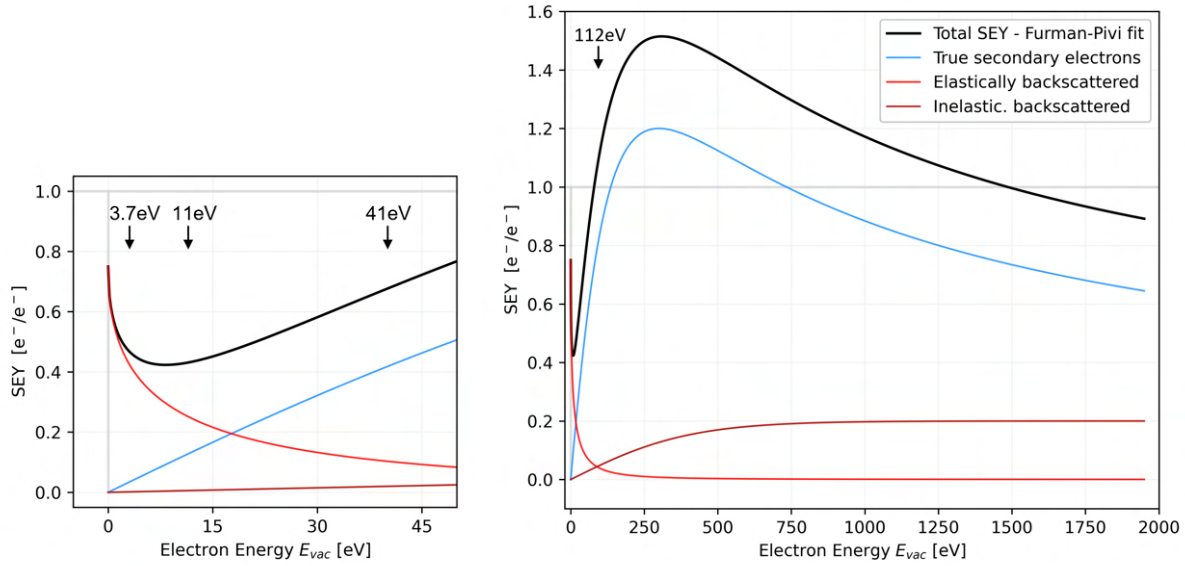

Figure 2.5: SEY energy dependence with a detailed view of the low-energy region decomposed into its constituents according to the Furman-Pivi model [58]. Note how their proportions evolve with energy. The arrow-marked energies correspond to the energy spectra from Figure [57].

2.2.2 SEY curve parametrization

The combination of relatively high measurement uncertainties on the experimental data and the practical need for easy and computationally efficient applicability gave arise to a number of simple semi-empirical models that are a good approximation to commonly measured SEY curves. For a parametrization to be physically meaningful, it typically needs to meet the following boundary conditions.

- Approaches $\delta = 1$ at 0 eV
- Features a maximum at the correct position $\delta_{max}(E_{max})$
- Asymptotically approaches $SEY \propto 1/E^n$ at few keV
- Features the right curvature to approximate the experimental data
- Is smooth, i.e. differentiable with respect to Energy

The challenge is accurately representing the behaviour across a large energy range, from fractions of 0 eV to the keV range. Such requirement is typically met by modelling per-partes the different constituents, whose sum amounts to the total SEY δ_{Total}, as visualised in Figure 2.5 and represented in Eq. 2.3.

$$\delta_{Total} = \delta_{TSE} + \delta_{Inel.BSE} + \delta_{El.BSE} + \delta_{Refl.} \tag{2.3}$$

Each partial contribution represents a particular physical reaction, as schematised in Figure 2.3, leading to an electron emission. As a byproduct of this approach to the SEY curve fitting, one obtains approximate proportions of different electron emission pathways. Note that this energy range is non-relativistic. Electrons only become relativistic in the keV to MeV energy range, which is not of concern here. However, theory and experiment [59] show that the SEY curve departs from the decaying behaviour and starts increasing in the MeV range.

Other models for the SEY do exist, e.g. the Lin&Joy [60] semi-empirical universal SEY model that builds on theoretical analysis of the emission process. Similarly to other authors, such as Cazaux et al. [61], they normalize the SEY curve to its peak value and find a universal fit. Then they compare the model against a Monte-Carlo simulation and experimental data and find that the best-fit parameters periodically follow the atomic shell filling of the studied elements. This observation supports the electronic stopping nature of the slow-down process.

True secondary electrons

The amount of true secondary electrons (TSE) evolves as a function of primary electron energy and has a positively skewed dependence with a long tail towards high energies, as plotted in blue in Figure 2.5. The

number of TSE can be described by the Furman-Pivi model, which is widely implemented in numerical codes, such as the PyECLOUD simulation program [62]. The primary electron energy E is normalized to the peak energy E_{max} and the parameter s changes the sharpness of the curve.

$$\delta_{TSE,F-P} = \delta_{max} \frac{s(E/E_{max})}{s - 1 + (E/E_{max})^s} \tag{2.4}$$

For completeness, Scholtz et al. [63] noted that the log-normal distribution also approximates acceptably well the SEY shape, ranging from metals, and past semiconductors to insulators. The energy E is again normalized to the peak energy E_{max} and the s parameter is the standard deviation as per usual. Hence, the s controls the width and sharpness of the peak, with a typical value of $s \approx 1.6$. Also, this log-normal distribution, albeit shifted, is used later to model the ESD energy dependence in Section 5, Eq. 6.10.

$$\delta_{TSE,L-N} = \exp\left(\frac{-\ln^2(E/E_{max})}{2s^2}\right) \tag{2.5}$$

As a sidenote, the SEY parametrization reviewed in this Section 2.2.2, can serve as an inspiration to also parameterise the ESD energy dependence curve, which is done in Section 6.1.

Elastically backscattered electrons

The elastically backscattered fraction of primary electrons decreases rapidly with increasing energy, as seen in red in Figure 2.5. However, at energies below ∼5 eV, it is the dominant contributor to the SEY curve. Here, the energy E_0 controls the decay rate, being the energy where the elastically backscattered electrons decrease to about 10 % of the initial value R_0 at E=0 eV.

$$\delta_{El.BSE} = R_0 \left(\frac{\sqrt{E_0} - \sqrt{E_0 + E}}{\sqrt{E_0} + \sqrt{E_0 + E}} \right)^2 \tag{2.6}$$

The dominance of reflected electrons can persist until about ∼15 eV in case of a presence of a contaminant overlayer, giving rise to a characteristic 5∼10 eV peak discussed below. This peak is investigated in Chapter 4 and parameterised in Chapter 5 to approximate the experimental data.

Inelastically backscattered electrons

Finally, the contribution from inelastically backscattered electrons is accounted for. As visible on the energy spectra in Figure 2.4, their energy lies in the region in between the true SE peak at ∼3 eV and the elastic peak at the primary beam energy. For the purpose of our fitting, the dependence can be approximated by a logistic s-curve function. This approximation captures the trend sufficiently well when compared to available sources on electron backscattering coefficients, such as Cazaux [64]. For simplicity, the parameter E_0 is chosen to be the same as for $\delta_{Inel.BSE}$ as in $\delta_{El.BSE}$.

$$\delta_{Inel.BSE} = r_{BSE}\left(\frac{2}{1 + \exp(-E/E_0)} - 1\right) \tag{2.7}$$

Low-energy peak of reflected electrons

It was experimentally observed, for example on HOPG [56], that the maxima in reflected electrons correspond to band-gaps in the surface electronic structure. This correspondence is visualised in Figure 4.9. Hence, it is necessary to also model this electron reflection at low energy, which is particularly important with respect to the electron cloud as demonstrated by Iadarola [9]. The low-energy peak of reflected electrons at 5∼10 eV can again be approximated by a log-normal distribution, as elaborated in Section 5.

$$\delta_{Refl.} = \exp\left(\frac{-\ln^2(E/E_{max})}{2s^2}\right) \tag{2.8}$$

2.2.3 Incidence angle dependence

The concept of energy deposition depth being compared to the SE escape depth, which was established for the SEY energy dependence, can also be leveraged to explain the SEY angular dependence. At non-normal incidence angles, the energy deposition depth is geometrically reduced by a factor of $cos\alpha$, with α being the angle measured from the normal. As a result, the energy dissipation cascade happens closer to the surface and electronic excitations created within the SE escape depth are increased by a factor of $1/cos\alpha$. The electrons impinging at shallower angles generate an SEY energy-dependence curve whose linear part extends to higher energies. Not only does the maximum E_{max} offsets higher up but also the δ_{max} increases, since more energy is deposited within the SE escape depth, also at higher energies, which would normally be deposited in the bulk.

Now classical literature on electron emission, such as Bruning [65], Seiler [66], Dekker [67], or Kanaya [53] converges on similar predictions. As foretold by the theoretical exercise, the electron emission generally follows the $cos^{-n}\alpha$ dependence. Other fits also seem to be applicable, as Kirby&King [68], successfully fit their SEY data with an $\exp(1-cos\alpha)$ dependence proposed by Bruining [65]. Henrist et al. [69] summarised the SEY parametric fits for simulation purposes, including its angular dependence. The proposed dependence includes a scaling factor k into the previous relation $\exp(k.(1-cos\alpha))$ to fit the experimental data.

Fitting [49] successfully applies a similar dependence $\exp(k.(1-cos\alpha))$ for the backscattering coefficient, with the parameter k varying with $k \approx -\ln f(\eta, Z, E_0)$.

Liu et al. [70] fit their SEY angular-dependence data with a generic $cos^{-n}\alpha$ with the exponent n varying in a wide range of 0.16 to 0.80. For completeness, it is worth noting that the same SEY angular dependencies are reported for amorphous and glassy materials by Salehi&Finn [71].

Regarding the SEY of cryosorbed gases, Sorensen [72] measured the SEY of condensed H_2 at few keV and reported that it follows the $cos^{-1}\alpha$ dependence. Later, Schou and Sorensen [73] reported the SEY of H_2 and D_2 to follow better the $cos^{-3/2}\alpha$ dependence for energies in 1-3 keV range. They also show that electron reflectivity rises above 30°, meaning fewer electrons penetrate the material. However, the remainder of electrons that do penetrate deposit their energy shallower below the surface. Due to this counter-compensating effect, the SEY of H_2 and D_2 only departs from the $cos^{-3/2}\alpha$ dependence above $\sim 70°$. Remarkably, the D_2 reportedly has double the SEY of H_2, which is surprising since the electronic structure that determines the SEY should be identical.

These SEY measurements converge to the same general behaviour that approximately follows $cos^{-n}\alpha$ dependence until the grazing incidence angle reaches around 70°-80°. At grazing angles, the high electron reflection off the surface effectively decreases the number of electrons that enter the surface, reducing the SE generation and decreasing the SEY. Amongst other authors, Salehi&Flinn [74] measured that the reflected fraction increases with the incidence angle (with respect to the normal).

2.2.4 Electron dose dependence

The decrease of the SEY curve across the full energy range, right side Figure 2.6, as a direct result of electron irradiation is a well-researched topic. For example, it is now known [75, 76] that the SEY curve conditioning happens in two stages, the first of which is dominated by the high-SEY contaminant removal via ESD and the second and final part is dominated by electron-induced graphitization of carbon-containing contaminants. This will also be illustrated here in the Results chapter 5 for both SEY and ESD. Researchers from different institutes confirmed the graphitization of contaminants on the technical-grade copper surface using XPS and AES [77–79] and is now generally accepted as the cause of the low-SEY. Hence, the carbon coatings discussed in the section below 2.3.

Literature is scarce on the energy-dependence efficiency of the conditioning process. However, the SEY and XPS data of Cimino et al. [76], Fig. 2.6, measured on a warm technical-grade copper colaminated onto stainless steel clearly demonstrate that the primary electron energy is crucial to the conditioning process. Moreover, low-energy electrons seem incapable of reaching the same conditioning results, not even at proportionally higher doses. This is an important observation, especially in regard to the low-energy-dominated electron cloud spectrum [8–10].

However, the electron conditioning problematics is more complex, as reported, for instance, by V. Petit at CERN [80]. She correlated the measured SEY curves and XPS data for various surface states of a technical-grade Cu colaminated onto stainless steel held at 300 K, ranging from as-received to conditioned and deconditioned. The XPS analysis uncovered that different initial surface states can lead to different chemical pathways during the electron conditioning process, which are, moreover, temperature-dependent,

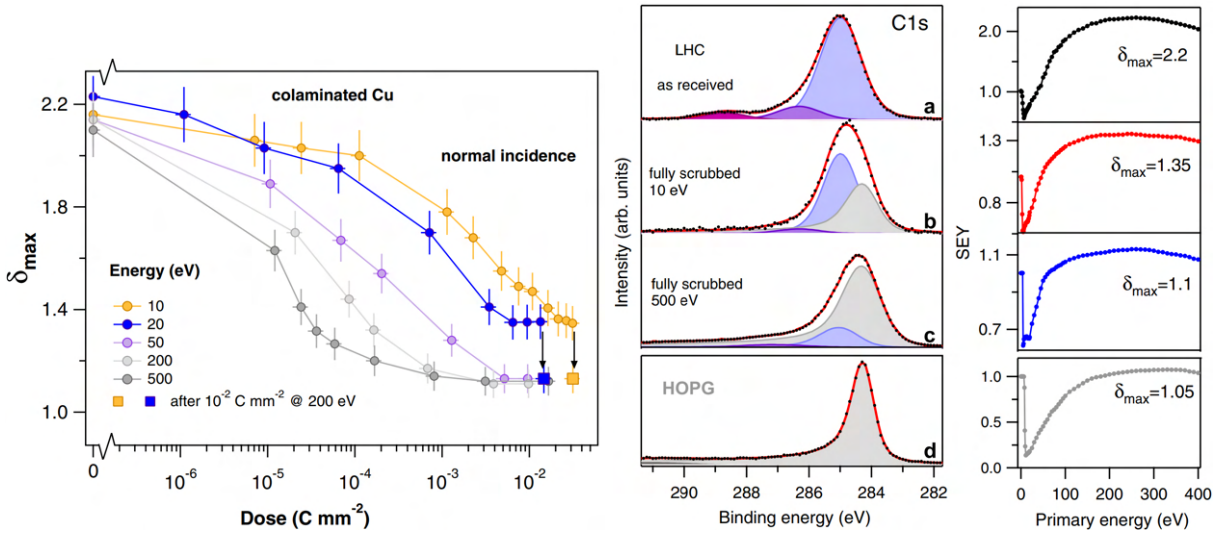

Figure 2.6: Left: SEY conditioning curves measured on an as-received technical-grade copper. Note the monotonic decrease whose rate strongly depends on the primary energy. Center: Carbon peak of XPS spectrum at different surface states. Right: SEY energy dependence curves at different stages before and after conditioning with 10 eV and 500 eV electron. Images adapted from and credited to Cimino et al. [76].

as visualized in Wagner plots. Once again, this is crucial to optimising the SEY in machines like the LHC, which is currently challenged by high SEY in some regions [81, 82].

2.3 SEY of functional coatings and treatments

Various surfaces, coatings and treatments are being developed, tested and applied in technical applications at industrial scales with at least one of the following aims. While one of these aims is always the main motivation, others can not be disregarded either, being a part of a complex interplay of technical requirements and limitations.

- The SEY reduction to prevent electron multipacting and e-cloud formation. By extension, this reduces beam-induced heat-load, the ESD-induced dynamic vacuum effect, and the e-cloud-related beam instabilities.
- Distributed pumping by a gettering effect in conductance-limited geometries. This allows effective pumping of long thin geometries, typical for a beam-tube. As a consequence, lower residual pressure in the beam tube implies less beam-gas scattering, hence lesser background in experimental areas.
- Increased adsorption capacity at cryogenic temperatures by increasing the specific surface area. Offsetting the surface saturation to multiple times higher gas coverages allows a greater margin before the surface becomes saturated with cryosorbed gas. This is inevitably linked to the higher number of binding sites and a wider range of binding energies and also mitigates pressure rises linked to temperature excursions during operation and transient heat loads.
- Mitigating electrical impedance (complex resistance) using superconducting coatings. REBCO-class type-II high-temperature superconductors (HTS) coatings are considered for this purpose, as they feature a higher critical temperature, maintaining its superconducting properties at temperatures as high as that of liquid nitrogen ∼80 K. As a consequence, this relaxes the stringent cryogenic requirements and allows moving the operating temperature window to the 80-100 K region. Higher temperatures are more favourable from the cryogenics standpoint due to a factor ten higher Carnot efficiency than operation at 5-20 K.

2.3.1 Low-SEY coatings and treatments

First and foremost, coatings are employed or considered for application to mitigate the e-cloud by an intrinsically low SEY, without relying on beam-scrubbing. Generally, beam-scrubbing is a very effective means of SEY reduction but was also troublesome under some circumstances [81]. As a side benefit, the low-SEY coatings often feature a high specific surface that increases the adsorption capacity when applied

in a cryogenic environment. Various approaches are available for achieving a low SEY on a surface, which can also be combined [83].

- Electronic surface properties
- Surface composition
- Geometric roughness
- Magnetic roughness
- Electric roughness

The first two are related to physical processes behind primary electron stopping and secondary electron generation at the atomic level. In metals, work function is negatively correlated to secondary electron emission. The work needed to extract an electron acts as a barrier to electron emission. The higher this barrier, the lower the emission probability, as was shown by Cazaux [84] and Schaefer&Hoelzl [85].

Conversely, the last three roughness-related items aim to ensure that secondary electron trajectories are closed back towards the surface. Either by electromagnetically bending the electron trajectories, or by geometrically confining the emitted electrons by restricting the solid angle, making them more likely to hit an opposing facet upon emission. The effect of geometrical parameters of random surface roughness was simulated [86] and yielded an important observation that for certain roughness parameters, the SEY can also increase. Other simulation-based studies [87] converge on the same results for surface grooves with square and trapezoidal profiles, with the latter being more effective. Wang et al. [88] report simulations done for different microgeometries and magnetic fields that also these conclusions of an effective SEY reduction.

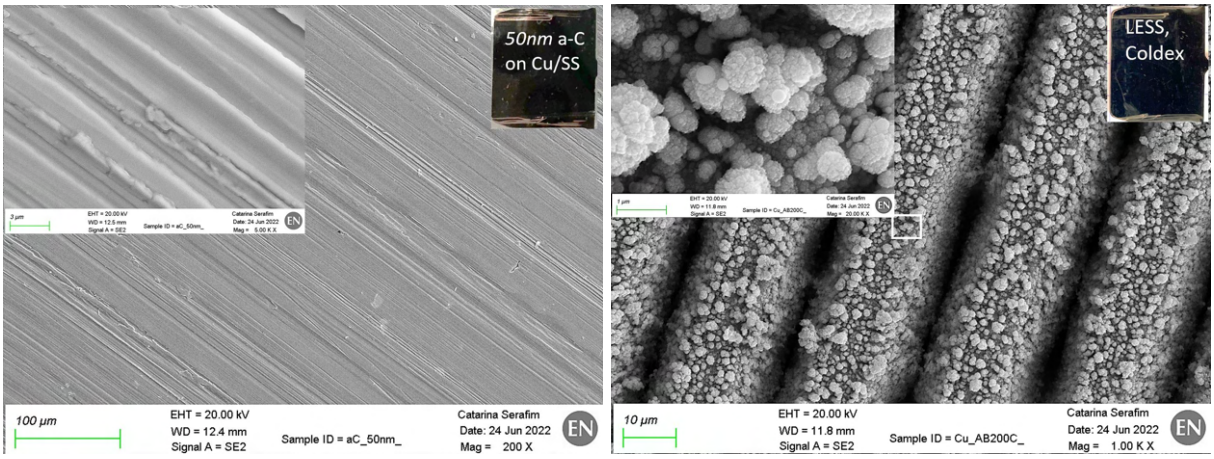

Figure 2.7: Micrographs of the discussed surfaces taken on FE-SEM. Left: 50 nm thin amorphous-carbon coating sputter deposited over a flat surface of a copper colaminated onto stainless steel. Note the copper surface texture still emerging from beneath the thin coating. Right: COLDEX-type laser-treated copper old parameters used to treat the COLDEX experiment [89]. Note the fractal-like microgeometry created by the laser ablation and redeposition in an N_2 atmosphere. Details in the text. The SEM images are taken on FE-SEM Zeiss Sigma and credited to C. Serafim, CERN-TE-VSC-VSM.

Amorphous-carbon coating (a-C) is a typical representative of low SEY achieved by a combination of electronic surface properties, most notably the high work function originating at its graphitic sp2-type bonding. Even though carbon in sp2 bond is not the only determining factor for low SEY and it was shown that sp2 content has in fact a slightly negative correlation with the work function [90].

Carbon also has a low atomic number Z resulting in a lower backscattering coefficient [64, 91–93]. Low-Z materials also feature a better primary electron absorption allowing electrons to penetrate deeper in the bulk and away from the surface. This is due to lower stopping power [94] resulting in a higher IMFP and a longer range [95, 96], as illustratively plotted by Kanaya&Okayama [53]. It is also likely that the SEY suppression is party due to the electron scattering on grain boundaries and other lattice defects that effectively shorten the electrons' IMFP. These properties make graphitic carbon the appropriate element for a low SEY surface.

The amorphous-carbon was proven to lower the SEY below the EC multipacting limit, even at remarkably thin nm-sized coverages [97]. In Section 5, we investigate the same 50 nm thin carbon coating that was recently deployed in one LHC quadrupole magnet during Long Shutdown 2. This is not to be confused with a much thicker version of 400 nm that was tested with LHC-type proton beams at CERN's SPS machine [98, 99] and at cryogenic conditions inside the COLDEX experiment [100–103]. Both thin

and thick carbon coatings are sputter-deposited over a 100 nm thin Ti underlayer that improves carbon adhesion and getter-pumps residual H_2 that would otherwise poison the deposition process.

The samples tested here were created as witness samples when coating the COLDEX beam-screen with a 50 nm carbon prior to installation for future tests in the framework of the HL-LHC upgrade. Both thin and thick carbon coatings were imaged by SEM, as shown in 5.25. In Figure 2.7 here, the 50 nm thin carbon coating is shown for illustration along with the COLDEX-type laser treatment. More SEM images are in the Results section 5.

While the carbon coating effectively absorbs primary electrons and does not produce many secondary electrons at the first place, laser treatments achieve the same goal of low SEY by different means. The copper oxides present on the laser-treated copper do not necessarily have intrinsically low SEY on the microscopic level. Instead, the emitted secondary electrons are immediately confined by a geometric trapping effect in the fractal-like microstructure. That is when appropriately sized, the secondary electrons have a small escape probability due to a geometrically reduced range of angles that can lead to emission. This geometrical entrapment seems to be effective regardless of primary electron energy, at least until 3 keV [104]. The laser settings indeed influence the resulting SEY, as reported [105, 106], and presumably also the ESD. The same laser treatment also generates equally low SEY when applied to stainless-steel and aluminium surfaces, as demonstrated by Valizadeh et al. [107]. Two laser-treated copper samples were investigated here. Regarding the terminology, few somewhat competing abbreviations are often used in the literature: Laser Ablation Surface Engineering (LASE), Laser Engineered Surface Structures (LESS) and Laser-induced periodic surface structures (LIPSS). For simplicity, the generic term 'laser-treatment' will be used in the manuscript and always regarding the following treatments.

The first generation of laser-treatment with the following COLDEX-like parameters: 532 nm wavelength, 5 μJ pulse energy, 10 ps pulse duration, 240 pulses/spot, 200 kHz repetition rate, 12 μm beam width, 24 μm hatch distance, 10 mm/s scanning speed and under N_2 atmosphere. This laser-treated surface was also successfully tested at cryogenic temperatures with LHC-type proton beams in the COLDEX [89, 100] and elsewhere in the SPS accelerator [108].

The second laser treatment that was characterised in terms of its SEY, ESD and TPD was a so-called 'D7' type. The treatment is optimized for faster treatment and done with the following parameters, as extracted from Baudin's dissertation [109]: 532 nm wavelength, 20 μJ pulse energy, 10 ps pulse duration, 693 pulses/spot, 200 kHz repetition rate, 52 μm beam width, 45 μm hatch distance, 15 mm/s scanning speed and under N_2 atmosphere. These parameters result in a significantly faster treatment at the expense of less fractal-like redeposits on the surface and slightly higher SEY as a result. This treatment has presently only been characterised in the lab. Both COLDEX-like and D7 laser-treatments were also imaged by SEM, as shown in 2.7.

For completeness, similar SE trapping was also demonstrated for more of a generalized take on roughness, generated by periodically varying magnetic texture [110, 111], or by periodic electrostatic texture created by sandwiching materials with different surface potentials [112]. Both these periodic structures suppress the SEY to some level.

2.3.2 Non-evaporable getter coating

Non-evaporable getter coating have long been in the scope as a mean to provide distributed pumping in long and thin, conductance-limited geometries that are typical for accelerator beam pipes. Amongst many others, the LHC long-straight sections [113], as well as interaction chambers in detectors, are ex-situ coated with equiproportional Ti-Zr-V NEG coating, which is then in-situ activated and provides outstanding vacuum levels. Aside of their *static* vacuum properties, these NEG coatings are also subjected to irradiation, including electron irradiation of photoelectrons and multipacting electrons from the EC. Hence, aside from suitable vacuum pumping performance, NEG coatings also need to attain modest SEY and ESD properties not to trigger the self-sustaining electron cloud in the first place and not to desorb gas via PSD and ESD mechanism.

The work of Le Pimpec et al. focused mostly on SEY of Ti-Zr-V NEG [114–116] and clearly shows that modest SEY values are attainable under electron irradiation. Meanwhile, Malyshev et al. study various NEG materials in detail, but as it is ESD-oriented, it is discussed in the corresponding section 2.6.

2.3.3 REBCO coated conductors

Ever since their unexpected discovery in 1986 [117], high-temperature superconductors (HTS) [118] are considered for a range of technical applications, including future accelerators [119]. Due to their critical surface being substantially higher than for the classical low-temperature superconductors (LTS), the HTS can operate at higher temperatures, higher fields and higher current densities, or a suitable working point in between, as visualised in Fig. 2.8. This range includes the liquid N_2 (LN2) temperature of 77 K, which is advantageous over the liquid Helium (LHe) temperature of 4.2 K in many regards. This includes higher Carnot efficiency of the cryogenic cooling, higher heat capacity of LN2 and overall higher margin for error resulting in better robustness of this engineering solution.

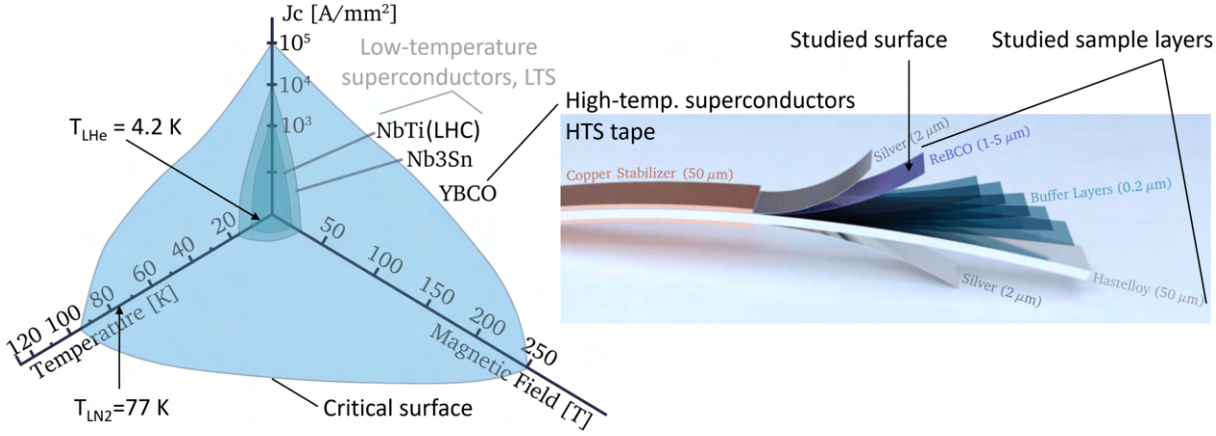

Figure 2.8: Left: Critical surface plotted for classical LTS and new HTS, forming an envelope for the maximum values of temperature, magnetic field and current flux. Right: Scheme of the layered structure of a REBCO HTS-coated conductor tape. Images adapted from and credited to Van Nugteren dissertation[120].

Within the accelerator technology, the HTS is firstly considered for magnets' construction [121], which is not of concern here. Another possible application lies inside the beam-screen (BS) [122] and inside accelerating cavities [123] to decrease its resistive wall surface impedance.

The generic BS design chart shown in Fig. [3] stresses that the BS surface has to be able to grant vacuum stability and provide a low surface impedance in the given temperature range of concern. For the LHC BS, this means lower impedance-induced beam instabilities [124] and lower impedance-induced heat-load to the beam-screen [11]. In other words, more efficient accelerator operation. REBCO surfaces have been shown [125] to provide orders of magnitude gain over a technical-grade copper currently being the standard. Hence, the following measurements aim to characterise surfaces of REBCO (rare-earth barium copper oxide) coated conductors using a variety of electron beam-based methods to infer on their response to conditions representative of an accelerator application, i.e. electron cloud irradiation at cryogenic temperatures. The SEY and ESD yields are equally measured so as to characterise the coatings' capability of mitigating the electron cloud and dynamic vacuum effects.

2.4 Gas desorption induced by electron impact

A range of interactions induced by an electron impact can potentially lead to a gas species emission. Each listed interaction has a distinct signature behaviour that separates the different regimes. Although the theoretical understanding and experimental observations predominantly support the gas desorption induced by electronic transitions, DIET, discussed below, other cases are also listed for completeness. Figure 2.9 schematizes different desorption mechanisms. Note that the origin of electrons is left unspecified: be it true secondary electrons, beam-accelerated electrons, or even photoelectrons (ESD makes one reaction pathway of PSD phenomena).

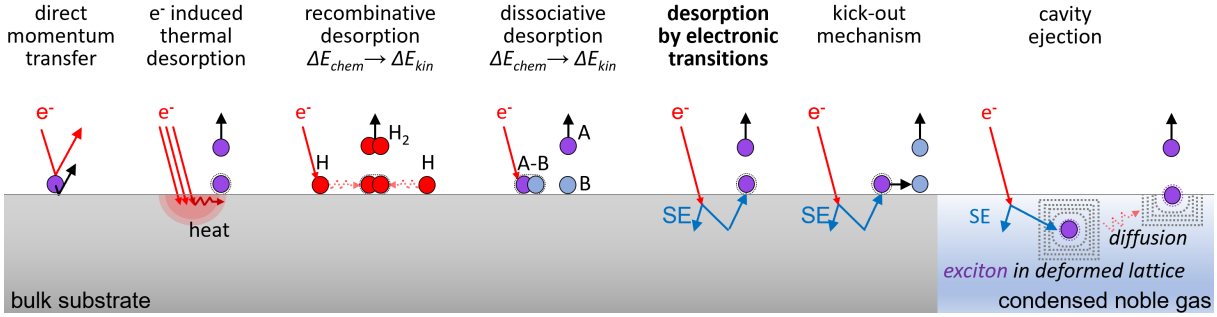

Figure 2.9: Schematic compilation of possible desorption mechanisms induced by electron bombardment of substrate-adsorbate system. Ranging from direct momentum transfer, past thermally and chemically mediated desorption to indirect energy transfer mechanisms - a true DIET. The special case of cavity ejection is added for completeness

The simplest case is gas desorption induced via direct momentum transfer from an inelastically scattered electron. However, the direct momentum transfer mechanism is inefficient for particles of highly dissimilar masses. This is typically illustrated by a 1 keV electron directly impacting H_2 as the lightest molecule. A head-on elastic collision transfers about 0.5 eV, which is sufficient energy to desorb a condensed H_2, but not the chemisorbed one, let alone heavier gas species with higher binding energies. Besides, this process has a very low interaction cross-section and in the case of condensed H_2, the desorption yield would be dominated some 100x by the DIET mechanism discussed below, as demonstrated by data of Tratnik [126].

Another indirect desorption mechanism is electron beam-induced target heating, which results in thermally stimulated desorption, as opposed to the non-thermal ESD. This mechanism is often used in technical applications such as electron beam physical vapour deposition (EB-PVD), where an intense electron beam evaporates material from the target crucible, which immediately recondenses on a substrate. The thermal effect also contributes to a thermally-enhanced desorption yield just under a desorption temperature of common ices, as shown by Schou [127]. This is presumably due to a combined effect of thermal and electron-induced agitation of cryosorbed molecules. In other words, when a gas species has a high thermal energy (residing higher in its potential well) just below its desorption energy, it is more likely to electrodesorb since less energy is necessary to exit the well.

Two more indirect mechanisms can occur, especially with non-thermal desorption of thick adsorbed gas layers. One is a kick-out mechanism, where one electronically excited atom directly transfers momentum in a collision with another gas species, forcing it to desorb instead. This mechanism can potentially lead to an ESD yield enhancement mediated by a more volatile gas species. Andersson&Van Dishoeck [128] report PSD of H_2O and show that can be kicked out by an H atom. Though in very small amounts, due to the large mass difference leading to an inefficient momentum transfer. New data will be presented in the Results section 5 demonstrating the kick-out mechanism in binary ices and a corresponding model will be presented too.

The same article [128] reports a recombinative H_2O desorption, where the desorption energy originates from the excess chemical energy liberated upon H and OH recombination. The recombinative desorption mechanism starts with two precursors that diffuse (thermally or irradiation-driven diffusion) along the surface or through the bulk and form a molecule upon collision. Then, the recombination can liberate excess energy sufficient to overcome the surface binding energy, which leads to species' desorption. For instance, the H_2 desorption originates in a recombination process of two hydrogen atoms, as schematized in Fig. 2.9.

Dissociative desorption, on the other hand, relies on the electron-induced fragmentation of a parent molecule and subsequent desorption of the fragment that carries away the excess energy. This is known

to be the case for more complex molecules, such as CO_2, CH_4 and higher.

To exhaust the list, a cavity ejection mechanism, typical for condensed noble gases, as demonstrated by Runne&Zimmerer [129]. An excited species is created in bulk and forms a small cavity by displacing the lattice atoms. The exciton diffuses towards the surface, where it is ejected into the vacuum, drawing its kinetic energy from the now-relaxed deformation energy of the lattice.

Finally, the most effective desorption mechanism, at least in the sub-keV energy region, is the DIET mechanism driven by an indirect energy transfer from the primary electron to the desorbing species. Here, the gas desorption is caused by a low energy electronic excitations (units to tens of eV) created in the target material by a collision cascade of the incoming primary electron. Such excitations lead to transitions in the substrate-adsorbate system's electronic structure that can result in the desorption of neutrals, excited neutrals, ions and molecular fragments, as discussed below. The ESD phenomena is also often implicitly included in PSD measurements, where an incoming energetic photon causes an internal or external photoelectric effect. The photoelectron can in turn desorb gas via ESD, a photoelectron-induced ESD. Typical photoelectron yield is in units of %, but ESD yields are also 2-3 orders higher than for PSD, which in some cases equalizes the contributions of ESD and PSD mechanisms.

2.5 Desorption induced by electronic transitions

Electron stimulated desorption, hereafter abbreviated as ESD, was eloquently defined by Redhead [31] as: The process of non-thermally induced desorption of ions and neutrals from surfaces as a direct result of electron bombardment. Today's scientific consensus unanimously links the ESD process to originate in electronic transitions in the substrate-adsorbate system. The common shape of an ESD and SEY curve indicates that the SEY process is correlated to that of ESD, as will be readily illustrated.

This well-rounded definition is rather restrictive in the sense that the ESD is a direct consequence of electron impact onto condensed matter, such as surface-bound atoms and molecules. This implicitly differentiates the ESD process from a gas-phase ionization, as illustrated by Redhead [130] in Figure 2.10. The term also encompasses the desorption of both ions and neutrals, as they experience the same desorption sequence, except the very last step. An ionic specie is likely to get neutralized by electron tunnelling. This process is in fact so effective, that neutrals strongly dominate over ions. Feulner reports a 10000:100:1 ratio for neutrals, positive and negative ions [131]. Furthermore, each electron impact onto a surface is an isolated event. A linear relationship between primary electron flux and desorption rate can readily demonstrate this.

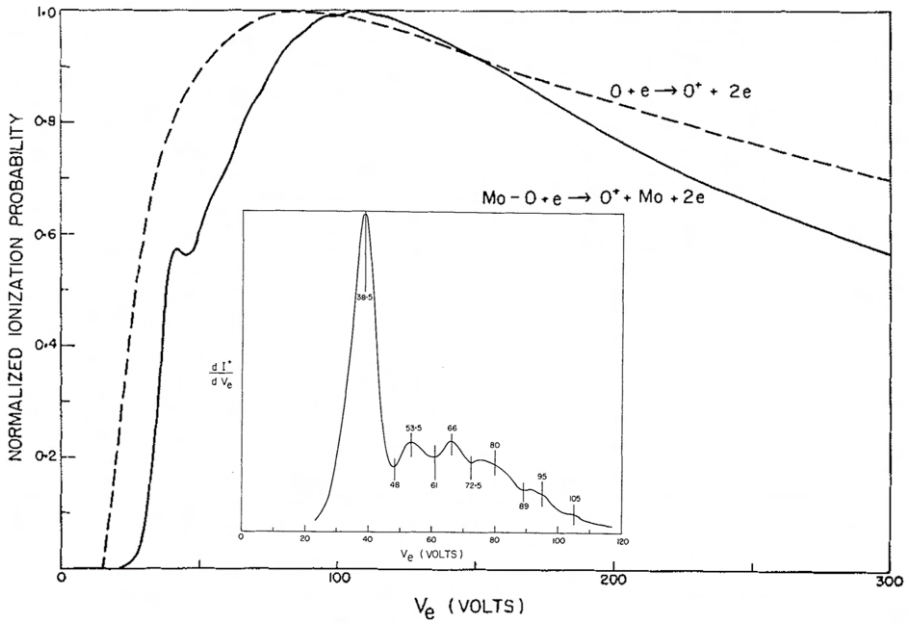

Figure 2.10: Energy dependence of ionization probability of O^+ by an electron impact in gas (dashed line) and solid phase (solid line). The different behaviour points to the different underlying physical mechanisms, as correctly measured and interpreted by Redhead [130]. The inset contains the derivative that exhibits a fine structure, which corresponds to different desorption channels being unlocked with increasing energy. The energy threshold for desorption is also clearly visible.

Already the first experimental observations of ESD behaviour indicated that entirely different processes happen in the condensed matter than in a gas phase. Figure 2.10 shows normalised ionization probability as measured in a pioneering experiment performed by Redhead in 1964. He measured oxygen cations O^+ desorbed from a polycrystalline Molybdenum substrate under electron bombardment of varying energies. The dashed line shows a gas-phase ionization probability for reference and the substantial difference between the two is evident. For completeness, if the gas desorption were caused by knock-on ejection, this dependency would also look very different.

2.5.1 Experimental observations

Fluorescent targets were formerly used to visualise the angular distribution of desorbed species. The first observation was made by Madey [33] of O^+ desorbing from monocrystalline plane W(100) and is reproduced in the left part of Figure 2.11. It has a 4 fold symmetry coming from the geometry of the adsorbate-substrate bond. It became apparent that species desorb preferably in some angles. The immediate and correct conclusion that this corresponds to the direction of the original bond that was broken. Nowadays, a micro-channel plate is often used to digitize the measurement procedure and obtain high-quality data of ESD Ion Angular Distribution (ESDIAD), such as the one on the right. It was measured in a system composed of PF_3 adsorbed on Ni(111) crystalline orientation, so it features a 6-fold symmetry. The shape and intensity of peaks evolve nontrivially with the substrate temperature. Thermal broadening at elevated temperatures flattens the peaks and/or causes some peaks to dim and others to appear.

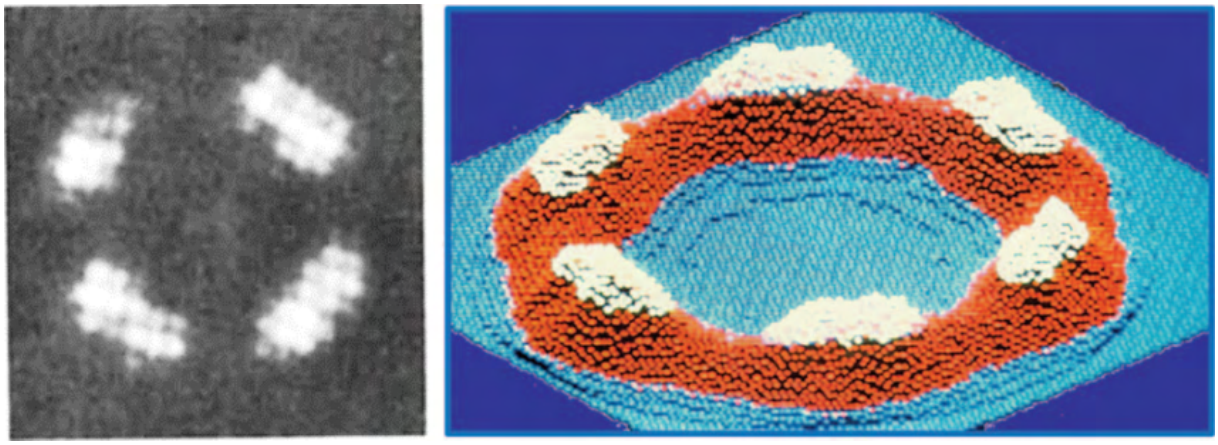

Figure 2.11: ESD ion angular distribution (ESDIAD) patterns with 4-axis and 6-axis symmetry correspond to the symmetry of the monocrystalline substrate used in their experiments. Left: Madey [132] Right: Yates [133, 134].

The first energy spectrum of desorbing ionic species was done using a retarding electrostatic field, see Figure 2.12 by Redhead [130]. Dedicated ion and neutral energy spectrometers were used later and confirmed the following experimental observations. Firstly, desorbed species all have low kinetic energy, which typically has a distinct peak at units of eV, as measured by Feulner [131]. Since the energy distribution of a desorbed species is determined by the given desorption channel(s) and not by a direct energy transfer, the energy spectrum does not evolve drastically either with increasing primary energy, nor with adsorbate coverage, making it largely primary energy- and coverage-invariant. Secondary peaks can possibly appear and correspond to newly accessible desorption channels. This illustrates that primary electron energy has a very limited direct influence on desorbed species with the sole exception that new desorption channels become available as the primary energy increases. This is strong evidence that the desorption process has an intermediate step, which is indeed a generic electronic excitation. In turn, the shape of the energy spectrum is an imprint of the shape of the potential energy curve of the original adsorbate-substrate bond. It also was demonstrated to exhibit thermal broadening.

Experimental measurements of ESD and related effects call for a theoretical explanation of the following observations:

- Distinct energy threshold in units or tens of eV before the onset of desorption
- Fine structure of ESD yield observed under ∼50 eV of primary electron energy
- Similar behaviour for desorption of neutrals and ions

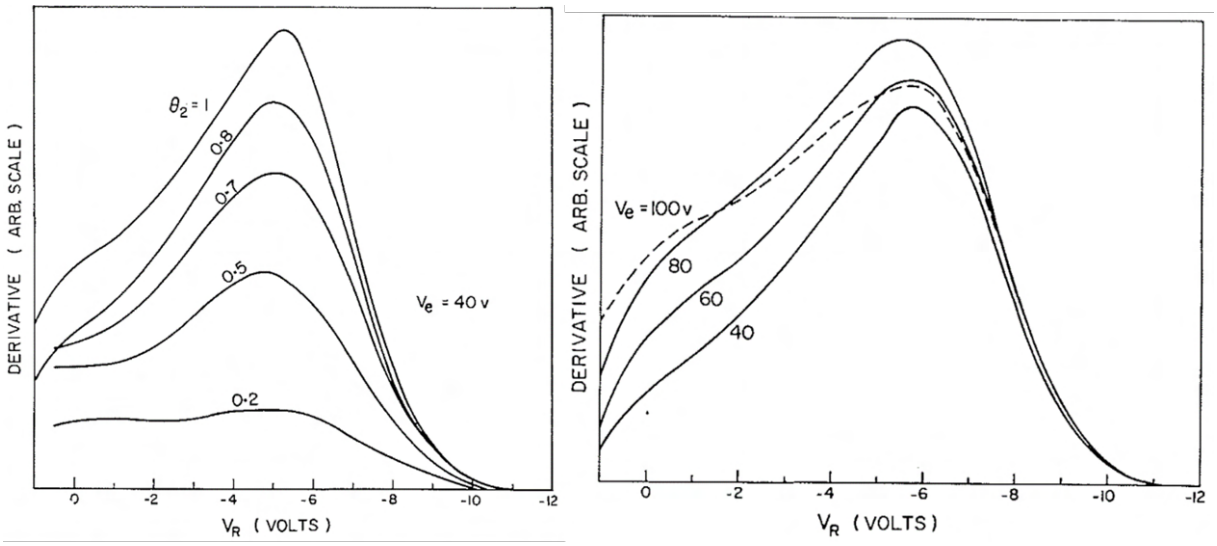

Figure 2.12: Energy distribution spectrum of desorbing oxygen cations O^{1+} as a function of: sub-monolayer oxygen coverage on the left, Primary electron energy on the right. Measured by Redhead [130].

- Large, yet varying predominance of neutrals over anions and cations
- Variation of ESD yield for different surface binding states
- Preferential desorption along the direction of the reaction coordinate

These experimental observations were explained, mostly qualitatively at first, by a number of more or less elaborate models. By the year 1980, a sound understanding of ESD was established, confirmed by numerous measurements in various systems and practically applied in surface science and engineering. Some prominent authors have published summaries of ESD problematics, theoretical treatments, experimental approaches, and coherent data. The simplest models will be covered below to elucidate the nature of processes involved in ESD.

It is worth noting here that the treatment of ESD is from some point onwards identical to that of photon stimulated desorption (PSD), because both desorption processes are ultimately described by the same model: Desorption Induced by Electronic Transitions (DIET). In fact, direct electronic excitation by photons is often used to specifically probe a desired process by bringing an exact excitation energy into a system. The knowledge of precise energy levels needed to excite given electronic states brings clues about the microscopic processes. As a result, many research papers use both ESD and PSD to study a substrate-adsorbate system. However, the similitude between non-thermally induced desorption processes ends here. Desorption induced by ion impact (ISD) is dominated by other mechanisms, such as elastic 'knock-on' ejection and possibly local heating, that are not of concern for ESD and PSD. The case of thermal desorption is already fundamentally different because the kinetic energy required for breaking the bond originates from thermal oscillations of an entire ensemble of molecules and not from a local valence-shell electronic excitation.

2.5.2 Ishikawa-Menzel-Gomer-Redhead model

The first DIET model was proposed independently at 3 different locations. The oldest work that correctly describes ESD as a DIET process was proposed by Ishikawa [135] in Japan in 1942, so the work was unacknowledged for a long time. In 1964, Menzel and Gomer [136] in USA and Redhead [130] in Canada simultaneously developed the same theoretical description. All authors published their work, but in vastly different research fields, different countries and authors unfamiliar with each other. Ishikawa and Ohta unfortunately published during World War 2, so their work remained unacknowledged for decades. Menzel and Gomer specialised in physical chemistry in USA, and Redhead worked in electrical engineering in Canada. This co-invented DIET treatment of ESD phenomena was the first widely accepted theoretical model. The IMGR model qualitatively explains all experimentally observed effects and quickly became a widely accepted baseline model for ESD, serving as a starting point for more elaborate models. The discovery process and what came out of it are captured in detail in the personal memoirs of ESD pioneers. Menzel [137], Redhead [31], Yates[133] and Madey [132] all shed light on the very process of discovery

and first successful attempts to explain the new observations within a newly established field of surface science.

The above-mentioned pioneering research reports include a basic theoretical treatment complemented by supporting experimental evidence. The authors originally conceived the model for systems composed of metal substrates with adsorbed gas molecules. Redhead studied oxygen bound on the molybdenum surface, whereas Menzel and Gomer studied the desorption of hydrogen, oxygen and carbon monoxide from tungsten. Many authors have elaborated and modified this model to match other chemically different systems, be more accurate in terms of quantum physics, or give quantitative predictions. The hereafter mentioned models of Antoniewicz [138] and Knotek-Fiebelman [139]. The primary electrons arriving on a target create a volume of free electrons and electronically excited atoms and ions. This happens in an avalanche-like manner, each primary creating multitude of secondary electrons that diffuse throughout the bulk. Most of the scattered electrons have a low energy under 20 eV. Then comes into play the IMGR model, which presumes that electronic excitations happen and elaborates on top of that, similarly to other DIET models. This electronic excitation is presumed as the initiating step of the entire desorption sequence. The IMGR model then describes the process of conversion of potential energy into kinetic energy.

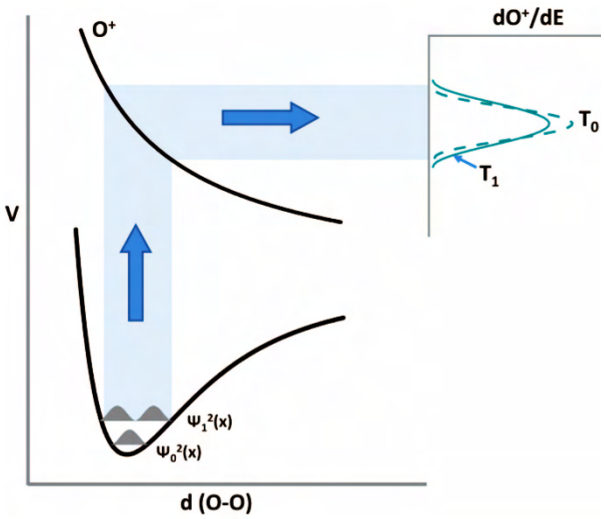

Figure 2.13: Scheme of the IMGR desorption mechanism. Vertical excitation in a Franck-Condon way to an antibonding state and consequent expulsion of specie away from the substrate-adsorbate system along the reaction coordinate. Note how higher temperature broadens the adsorbed and desorbed species' energy distribution. Image: [133]

The principle of IMGR model is schematized on a plot of potential energy as a function of interatomic distance, such as the one in Figure 2.13. The resulting force acting on an atom is proportional to the gradient of that potential energy. It is repulsive when particles are in too close proximity because their electron shells start overlapping and Pauli's exclusion principle yields a strong repulsion force. The force can also be attractive when they are further away because it is energetically advantageous for both atoms to form a bond of some sort. When the two forces are in equilibrium, an atom rests at the bottom of the potential well. An electronic transition excites a surface-bound adsorbate from a bonding state to an excited state via a vertical transition in a Franck-Condon region, if such exists. Provided the excited antibonding state lasts long enough, the resulting electrostatic force repels the ion out of the system. Within the IMGR treatment, the ion is expelled at very low kinetic energy in the general direction of the former bond along the reaction coordinate. This bond-directionality was observed in the first experiments and strongly supports this theoretical description. Chances are high that an ionised gas atom or molecule is neutralised via electron tunnelling while departing from the surface. The neutralisation process is very effective because the expulsion of an ion from a system happens at a much longer timescale than electronic transitions. The desorption process is quenched if the electronically excited state relaxes or is localised before the ion acquires sufficient kinetic energy to leave the system along the reaction coordinate, i.e. the bond direction. The quench is often the case, as the metal substrate readily provides electrons to fill the vacancies in adsorbed gas atoms. Moreover, the metal lattice with a Fermi sea of electrons is also efficient in delocalizing the excitations from the metal-gas bond. The high probability of deexcitation is known as 'bond-healing'. This explains the large difference in cross-sections of gas-phase ionization and desorption. The desorption cross-section is lower than in the gas phase by orders of magnitude. The last important implication of this model is schematized in the inset of Figure 2.13. The energy distribution of desorbed species is a mirror image of their original distribution at the ground state prior to desorption.

The IMGR treatment already explains many experimental observations, such as the following:

- ✓ The measured energy threshold represents the energy needed to excite an electron to an antibonding state and can be actually traced to a specific electronic shell excitation. Shall the energy be lower than this threshold, the electron simply radiatively relaxes back to the original bonding sate.
- ✓ The model explains the observed fine structure of ESD yield as a function of primary electron

energy, as different reaction channels become energetically accessible.

- ✓ Reneutralization of ions via electron tunnelling during the ion expulsion from the system readily explains predominance of neutrals over ions, as well as the change in their ratio for desorbates of different masses and/or isotopic composition.
- ✓ Kinetic energy spectra of desorbed species exhibits thermal broadening.
- ✓ Directionality of the desorbed species is given by the direction of the original bond.

The IMGR model has one shortcoming regarding the longevity of repulsive electronic state. It on average de-excites in a shorter time, than the excited atom needs to acquire sufficient kinetic energy to leave the system. This is especially true for metal substrates, for which it was originally developed. Moreover, a metal substrate can effectively screen the repulsive potential by conduction band electrons. Such situation called for an improvement, which would align qualitative and quantitative prediction. Antoniewicz eventually presented a theory an improvement.

2.5.3 Antoniewicz model

The model proposed by Antoniewicz [138] in 1980 elaborates on the IMGR description of DIET process, but includes one more step to the desorption sequence, which is more accurate from the quantum-mechanics perspective and yields quantitatively more accurate prediction. The differing step from the former IMGR treatment is an attraction phase at the beginning of the desorption sequence when an ion initially moves towards the surface. Figure 2.14 on the left plots two different potential curves; one for a neutral, and one for an ionized adsorbate with an equilibrium closer to the metal substrate. This solves one major theoretical discrepancy regarding the too-short lifetime of electronic excitation in a metal-gas system but renders the same result: neutral-dominated desorption via electronic transition-induced dynamics. The original paper considers an Oxygen atom bound to a Tungsten substrate, which is the same type of system that was used to develop the IMGR model.

The initial phase is again a vertical electronic excitation in the Franck-Condon region: electron ionization forming a cation. The cation formation is followed by a considerable (tens of %) reduction of electron shell diameter due to the charge-screening effect, or a lack thereof. Having one less electron inside the shell, all remaining electrons experience higher effective nuclear charge coming from the positively charged nucleus and, as a result, pack themselves closer around it. Hence, the cation radius is smaller than that of a neutral atom. Conversely, an anion would grow in size compared to a neutral because of the decrease in effective nuclear charge and the Pauli repulsion of electrons. For illustration, a neutral Oxygen atom has atomic radius of 0.66 $\mathring{A}$, but a cation O^{1+} has only 0.22 $\mathring{A}$ while anion O^{2-} has 1.4 $\mathring{A}$ [140]. The now-smaller cation moves towards a new equilibrium position that is much closer to the surface. The positively charged cation induces an image charge within the metal substrate, creating an additional attractive force. The bare presence of a charged ion above the substrate surface deforms electron shells of substrate atoms and induces an equal, but opposite image charge. This virtual charge creates a real attractive force on the ion, pulling it closer to a new equilibrium. The cation-substrate bond is shorter than for neutral, so the vacuum barrier to electron tunnelling shrinks. This increases the reneutralization probability, which inevitably leads to the cation reneutralization. The once-again neutral atom is now closer to the surface then its equilibrium position and finds itself high on a strongly repulsive potential curve. The gradient of potential energy repels the neutral away from the system in the direction of the former bond. The surplus of potential energy is converted into kinetic energy, and a neutral is desorbed, provided that the potential well is not deeper than the available kinetic energy. The same can also be expressed in terms of a reaction coordinate z, marking the metal-gas bond length, which after surpassing a certain distance, inevitably leads to desorption.

Similarly to the original IMGR scheme, the process can be quenched if an ion reneutralizes sooner than it acquires sufficient potential energy to drive the desorption process. The atom can also be ejected in an ionic state if another resonant electron attachment happens via quantum tunnelling while neutral leaves the system. The Antoniewicz explanation solves the theoretical discrepancies of the original IMGR model, mainly the need for long lifetime of excited state before it is relaxed/neutralised, quenching the desorption sequence. This is particularly needed in metal-gas systems, where any excitation is quickly delocalised and electron vacancy quickly refilled. Overall, the model agrees with experimental observations in metal-gas systems for neutrals, ions and different isotopes. Yet, neither of those models can be used to explain desorption from some dielectric compounds, such as maximal-valence metal oxides.

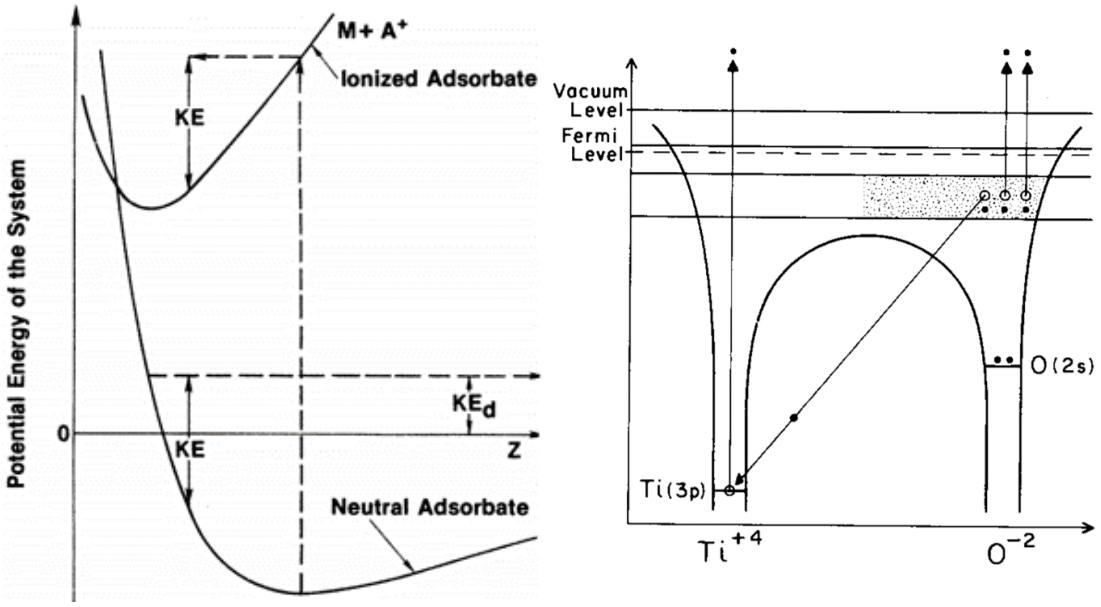

Figure 2.14: Left: Potential energy diagram of ground neutral and ionised states. The dashed line is a vertical Franck-Condon transition between the two states. Antoniewicz model [138] accounts for the ground state of an ionised molecule being closer to the substrate than the neutral one, this being the source of repulsive force after reneutralization. Right: Interatomic Auger process involving two valence electrons excitation following de-excitation of one electron from Oxygen 2s valence level to Ti core-level 3p. This electronic transition explains the experiments of Knotek&Feibelman [139].

2.5.4 Knotek-Fiebelman model

The research paper presented by Knotek and Fiebelman [139] from Sandia Labs in 1978 presents a fundamentally new principle applicable to the desorption of ions from metal oxides. They developed a theory explaining experimental observations on TiO_2, a maximal-valence metal oxide system. They also support their research by surface analysis by low-energy electron-loss spectroscopy. The mechanism involves not only valence-level electronic excitations, but also core-level excitations, which corresponds to higher energy thresholds for desorption. This model explains the 'unexpected' desorption of cations from a solid phase, where they are bound in the form of anions. Such as the transition-metal oxides in a maximal-valence state, that is where the oxygen atom has donated all its valence electrons to the metal atom and therefore is in anionic state O^{2-}.

The working principle of Knotek-Fiebelman ion desorption model is originally illustrated for the case of Titanium dioxide TiO_2 with the help of energy diagram in Fig. 2.14 on the right. Within the TiO_2 molecule, the Titanium atom donated all its valence electrons to Oxygen atoms, thus having no valence electrons left to possibly refill a vacancy within its core orbitals. If an electron is knocked out from the 3p orbital in an electron shell of Ti, it cannot be replaced by another electron descending to its level in a classical Auger process. Instead, an Oxygen atom provides one electron from its valence shell and the excess energy is transmitted to spectator electrons, ejecting them from the system. The oxygen then finds itself in a neutral or even O^{1+} state, which causes its immediate electrostatic expulsion. Despite the primary Ti core-excitation having lower cross-section than valence excitation would have, the channel effectively leads to desorption and renders this process dominant for this class of systems. This is partly due to lower probability of the desorption process being quenched too soon by electron tunnelling.

This model explains desorption of ionised species that, against expectations, have an entirely different charge state than in the former bound state. It is triggered by a core-level electronic excitation followed by an inter-atomic Auger decay, which leads to electrostatic expulsion of an ionised oxygen atom. The model also explains higher energy thresholds in maximal-valence metal-oxides. Similarly to the previous models, energy thresholds can be assigned to different electronic shell excitations when dealing with such a well-defined system.

2.5.5 Dissociative Electron Attachment

The notable exception to the above-discussed energy threshold introduced by the DIET explanation is the Dissociative Electron Attachment (DEA), is another possible type of a process that can lead to desorption

of a parent molecule or its fragment. Here, a resonance, i.e. short-lived and unstable excited molecule is formed by capturing an electron. The relaxation to the ground state potentially leads to desorption of an entire molecule or its fragment. This is typical either for fragments of a parent molecule or noble gases. Some studies and overviews explain this high reactivity of slow electrons by their high capture probability . As a result, the DEA forms a desorption channel that is predominant only at low energies and can lead to desorption even below the energy thresholds for desorption via ionization or excitation.

Figure 2.15, taken from [37], schematises possible dissociation pathways between as an interaction between an electron and diatomic molecule. A simple excitation by an impacting electron into an excited neutral AB* is denoted by (1.) This can be followed by a de-excitation, or dissociation of the diatomic molecule into two neutral species, or form anion and cation. Pathway (2.) shows a temporary electron attachment to the molecule, forming a resonance state AB^{-}*. The electron can then leave the molecule (2.A), form an long-living anion (2.B), or split the molecule into a neutral and anion (2.C). Lastly, the reaction pathway (3.) shows a direct ionization by electron impact, resulting in a loss of valence shell electrons and creation of cation. The cation consequently splits into fragments that can desorb.

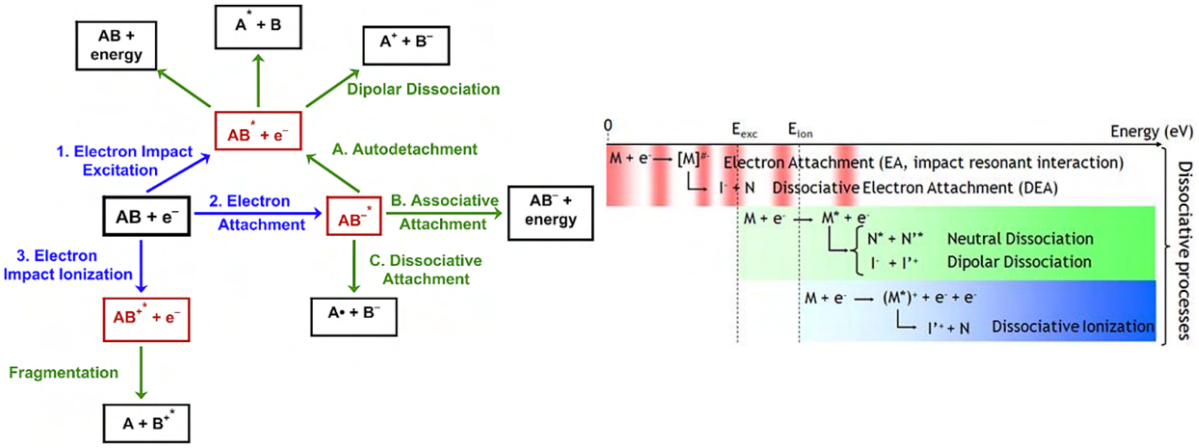

Figure 2.15: Left: Electron-induced dissociation pathways of a diatomic molecule. Image adapted by [37] from [141]. Right: Schematic map of low-energy electron-induced dissociative processes in a diatomic molecule. Note the energy thresholds for different processes and sub-threshold DEA resonances. Image from [142], inspired by [143].

2.5.6 Threshold behaviour and fine structure of ESD yield

Different pathways (channels) yield various reaction products with specific activation energy and probability. New channels may become energetically accessible as the primary electron energy increases. As a result, the branching ratios evolve non-trivially with the primary electron energy. Following the experimental data measured and published by Redhead already in 1964 in his original work [130] a fine structure can be observed in the ESD yield, see Figure 2.10. Taking a derivative of the ESD yield with respect to the primary energy, distinct peaks can be identified where the yield increases more rapidly. These energy thresholds for each of the contributing processes result into a fine structure of ESD yield dependence on energy. As the primary electron energy increases, new desorption pathways become energetically available, so they start contributing to the ESD yield. The structure disappears above 120 eV, where too many processes superpose over each other.

This can be visualised on an energetic diagram of processes, such as Figure 2.15. The horizontal axis represents the increasing energy of primary electrons. Colours stand for various dissociative processes and the colour intensity denotes the intensity. There are multiple energy thresholds, below which a process is not energetically accessible. Red lines depict resonances in the dissociative electron attachment (DEA) process, which happens when a primary electron has just the right energy to interact with a single molecular orbital. All these dissociative reactions can result in particle desorption. As a practical result, a fine structure of desorption yield emerges in the low-energy energy region, around 10 eV, and will be demonstrated later in Section 4. Measurement of such spectra and assignment of energy thresholds and resonances to specific physical processes can provide valuable insight into the physical chemistry of a surface.

Numerous measurements of the threshold behaviour have been done in well-defined systems. Those are notably gases chemisorbed on monocrystalline surfaces, such as the work of Sayyid&Williams [144],

or thick semi-infinite layers of condensed gases on cold substrates. The reviews of Arumainayagam [37] and Bass&Sanche [145] and references therein make a great overview of electron-induced chemistry, both cracking and synthesis, in various condensed gases substrate-adsorbate systems with a focus on organic chemistry, reaction channels and experimental methods to study those.

2.6 ESD from technical surfaces

2.6.1 Engineering perspective on ESD

Classical DIET models describe various ESD scenarios from a generic case, such as the IMGR [130]–[135], to various edge cases, such as the models of Antoniewicz [138] for ionic bonds, or Knotek-Fiebelman [139] for fully-valent oxides.

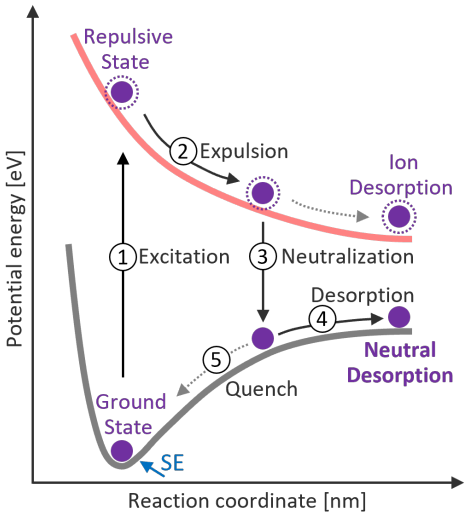

Figure 2.16: Schematised and simplified DIET sequence leading to neutral desorption. Possible alternative routes are also visualised. The scheme is illustrative and not to scale. Credit: Author.

To create a simplified engineering perspective on the ESD process, the above-mentioned models can be somewhat reduced to a more simplistic view, which still gets the important aspects right. The first principles of DIET description must also apply to ESD from technical-grade surfaces, regardless of the ill-defined substrate-adsorbate system. Hence, the DIET framework can be somewhat simplified and leveraged to provide some qualitative predictions regarding the ESD phenomena from technical surfaces. Such educated estimates effectively fill in many blank spaces in this largely uncharted territory. Hence, it suffices for technical surfaces to envision a generic desorption sequence that leads to neutral desorption, such as the one visualised in Figure 2.16. As schematised, the Desorption Induced by Electronic Transitions explains the ESD via the following steps.

1. The first step of the desorption sequence is an incoming electronic excitation in the Franck-Condon region, which happens at a femtosecond timescale. The excitation suddenly puts an adsorbed species on a repulsive potential energy curve. This first step already brings about an important feature of the ESD, which is the threshold behaviour. There is no desorption sequence if the energy initially imparted to the substrate-adsorbate system does not reach the energy required to reach the repulsive curve.

2. Once the to-be-desorbed species, be it an ion or an excited neutral, finds itself on a repulsive potential, it experiences a repulsive force from the substrate. The species gradually gains kinetic energy at the expense of the repulsive potential and starts escaping the system along the reaction coordinate. Once the species accumulates enough kinetic energy to leave the system, it does so at a ps timescale.

3. The second to last and optional step is the neutralisation of the escaping species via electron tunnelling. The neutralisation step is, in fact, so effective that neutrals make for the majority of

desorbed species, typically by 2-3 orders of magnitude. Many experimentalists, including Redhead [130], Figure 2.12, have demonstrated that the leaving species have kinetic energy in the eV range that is largely invariant with the primary energy - a signature of an indirect energy transfer.

4. This step is but the aftermath of Step 3. It captures the desorbing neutral molecule as it leaves the system if it gains sufficient kinetic energy prior to neutralization.

Adopting a rather macroscopic engineering perspective, the key implications of the presented DIET models for desorption are the following:

- The desorption has an energy threshold that can be correlated to specific excitations within the adsorbate-substrate complex. It can serve as a probe to study these.
- From an energetic point of view, the models elucidate the dependence on the primary electron energy and the low-energy spectrum of desorbed species.
- The DIET treatment also explains the predominance of neutrals over ions, which is applicable in the design of desorption experiments and technical applications.
- The desorption probability is lower for stronger bound systems. It will be evidenced later that the ESD yield is inversely proportional to the binding energy, at least in the case of physisorption.
- Desorbed species leave the surface preferably in the general direction of the broken bond. Hence, the angular distribution of desorbed species does not follow the Lambertian cosine distribution but instead has preferred directions.

The following conclusions are equally important for the ESD process, albeit not a direct result of the DIET description:

- The ESD yield is proportional to the amount of energy deposited in the form of electronic excitations that are within the escape depth below the surface.
- The ESD is a strongly surface-sensitive phenomenon, whereas the bulk composition of the substrate is of limited importance.
- The gas desorption and secondary electron emission are strongly linked due to the common origin in electronic excitations. As a resulti, the energy dependence of ESD and SEY often follows a similar profile.
- The physical chemistry of the substrate-adsorbate system determines the composition of desorbed gases and their fragments, as well as their absolute abundance and relative proportions.

The aforementioned DIET models provide a great qualitative prediction necessary to understand the observed ESD processes. However, they struggle to provide quantitative prediction even for well-defined substrate-adsorbate systems. In other words, because of too many unknown parameters, it is impossible to do a predictive ESD yield calculation for a known surface at a given electron energy. Let alone a technical surface.

2.6.2 DIET as a research field

The DIET research field has been blooming field of science ever since its early days. The scientific effort culminated in a series of 5 DIET conferences [146–150] held in 1982–1992. They yielded very complete proceedings that summarised the state of problematics of that time, as explained by the most prominent researchers. These provide a very good DIET source as viewed from the perspective of various scientific fields. Numerous efforts have been made later to integrate the ESD knowledge. This resulted into multiple well-rounded reviews, which extend over both theoretical and experimental aspects.

In 1977, Drinkwine&Lichtman presented a review of ESD which includes the ever-so-important low-energy region and desorption thresholds. Madey&Stockbauer [151] published in 1985 a great review of various experimental methods for electron and photon stimulated desorption research. De Segovia [152] published in 1986 a review focused on ESD measurement problematics, which covers the basic ESD theory to the necessary extent but then focuses on practical aspects and presents various applicable measurement schemes. The author presents an overview of ESD data hand-picked from ESD literature available at that time, which includes desorption cross-sections for various adsorbate-substrate systems and their energy thresholds. He also stresses the importance of ESD as a tool for surface analysis and then pitches its place amongst other related experimental techniques.

In 1990, Ramsier and Yates [153] have conceived the most extensive review so far. At first, they discuss possible mechanisms and applicable models, encompassing the ESD problematics from the surface

science point of view. They briefly present basic experimental arrangements and then support the theoretical treatment with experimental observations and other surface-science techniques, such as energy and angular distribution of ions, temperature programmed desorption and low-energy electron diffraction. They also provide an exhaustive overview of various chemical systems studied by ESD, that were performed in well-defined systems in terms of chemical composition and fixed crystal orientations. Such well-defined systems generally consist of one crystallographic plane with adsorbed gas. Such systems are essential, as they are the simplest of a kind, yet already have immense degrees of freedom and parameters, which complicates analytical description. This, however, is still far from real-life technical surfaces that are miles away from being well-defined. In 1994, Ageev published similarly exhaustive surveys [154, 155] covering the knowledge DIET at that time, which includes both ESD and photon stimulated desorption PSD. This review first discusses basic principles, experimental methods and arrangements, and finally focuses on practical aspects. These include ESD yield variation and threshold energy as influenced by parameters like primary electron energy, current density, substrate composition, temperature, adsorbate coverage, etc.

2.6.3 Desorption from technical surfaces

Unlike ideal systems used to study and elucidate the ESD in laboratories under well-defined conditions, Technical surfaces pose an exceptional engineering challenge. They are typically badly defined and their properties are stochastic. This applies to chemical composition and its depth profile, crystallographic structure, orientation, and texture, likely with various degrees of porosity. Small differences in their manufacturing, cleaning, storage, installation, etc. results into batch-to-batch variation, various degrees of pollution, various air-exposure times. All those nuances effect the surface state of a technical surface, which inevitably manifests as a large variability in SEY and ESD, that are both highly surface-sensitive parameters. The theoretical treatment has demonstrated that ESD comes from electronic transition between different potential energy curves and consequent conversion of the potential to kinetic energy. The DIET theory was derived with the help of data taken in such a well-defined system, where only one type of adsorbed gas desorbs from a single monocrystalline plane of a pure substrate material. Indeed, many experimentalists have wisely chosen a adsorbate-substrate complex in order to infer on theoretical aspects. An applicable solution is already difficult to apply in well-defined systems, as the number of excited states is large. The number of possible electronic transitions is even larger, even though many transitions are not allowed or not likely to occur within the Franck-Condon region. Moreover, the desorption sequence is not always straight forward, as illustrated by the interatomic Auger decay in the Knotek-Fiebelman model. This situation becomes overwhelmingly complex for a system with many atoms, not to mention the influence of surface, lattice defects, different isotopes, and so on. On top of that, technical surfaces have pores of different sizes, the surface layer is often oxidised, contaminated and unrepresentative of the bulk structure and composition. Overall, technical surfaces are often unique with a large variance.

Fortunately enough, many implications of DIET models still hold even when facing the complexity of technical surfaces, as will be later evidenced by selected experimental data. The listed implications are tentative and mostly hold, but exceptions do exist in some special scenarios.

- It is not expected to see a fine structure in ESD yield from technical surfaces, except for the energy threshold, that still needs to be present and possibly a difference between cryosorbed and chemisorbed gases.
- The energy threshold still exists, because the DIET mechanism processes governing desorption still hold the same. It ranges from 5-25 eV, but typically remains around 10 eV or just under.
- The ESD yield is higher for the desorption of light and loosely-bound species, and decreases for heavier and strongly bound species.
- The ESD yield still reaches its maximum at hundreds of eV, which is when the energy brought to the vicinity of a surface is maximum. Lower than that, the energy deposited at a very surface is low. Higher than that, the energy is deposited too deep within the bulk to contribute to DIET. The rare exception are very pure condensed noble gases, where the deposited energy effectively diffuses towards the surface.
- The directionality of the gas desorption is expected to vanish and average out into a Lambertian cosine-type of distribution. This is due to the stochastic nature of the technical surfaces.

The following Figure 2.17 schematises the surface layers a technical-grade OFHC copper that has

undergone an UHV-cleaning process in order to be used to manufacture the beam-screen for LHC's cryogenic magnets. Despite the best efforts and effective removal of the gross contaminants, the surface remains of a technical-grade quality. The UHV-cleaning process is designed to remove all contaminants and the oxide layer, and to form a new compact, fully oxidised Cu_2O surface layer under controlled conditions. Finally, a few nanometer-thin graphitic layer can precipitate on a surface during electron irradiation, i.e. conditioning. The carbon layer typically drives the δ_{MAX} close to 1, which is desirable to prevent electron multipacting and electron cloud formation.

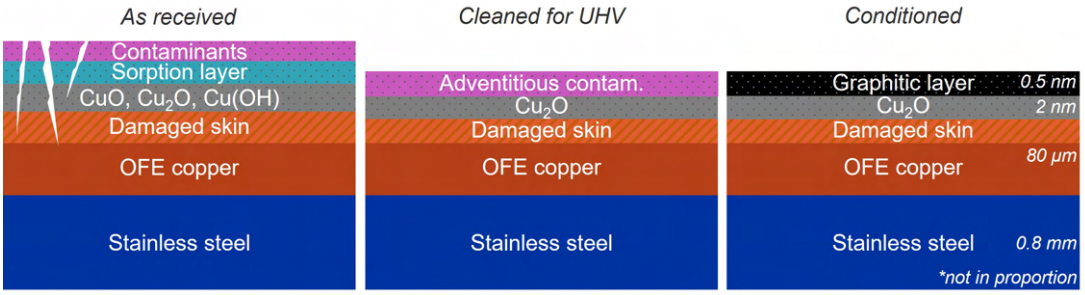

Figure 2.17: Schematised layering on a technical-grade polycrystalline OFHC Copper for the LHC's beam-screen. The UHV-cleaning removes contaminant layers and etches away a generic oxide layer. A compact fully oxidised layer is formed at the end of the UHV cleaning under controlled conditions. The layer of precipitated graphite is later formed during electron conditioning. The scheme is illustrative and not to scale. Image: Author

2.6.4 Material and surface state dependence

The ESD yield of gases from a metal surface is given by the surface chemical composition, the amount of adlayers and their chemical state. It is obvious that a species first needs to be present at the surface if it is to be desorbed. For our technically aimed purpose, Mathewson [156] mentions a definition of a clean surface as one that has less than certain amount of foreign desorbable atoms/molecules atop. The adlayers' surface concentration is indeed determined by the entire history of the material surface, but is particularly influenced by the used cleaning method, various treatments and the method of storage. Different methods can be employed to scrub off surface molecules prone to desorption. The surface can be significantly depleted of contaminants either by chemical agents, via thermal agitation, by sputtering, or a suitable combination of these.

The first essential thermal treatment used in the vacuum technology to reduce adatoms surface concentration is an in-vacuum bakeout, ideally performed in-situ to a few hundred °C. Achard [157] measured a factor of 10 reduction in ESD yield from Cu when baked at 250 °C and another factor of 10 at 600 °C. Air-baking can also be done instead to promote an oxide-layer growth acting as a diffusion barrier, safeguarding the low H_2 surface concentration from being replenished from the metal bulk. Ashraf et al. [158] measured the ESD yield of a technical-grade 304L stainless steel (SS), that was used as a reference before the measurement of 500 nm thick layer of an amorphous carbon sputter-deposited onto the SS substrate. They measured how the H_2, CO, CO_2 and CH_4 yields are influenced by bakeout temperatures and venting-bakeout cycles and the same measurement was performed for as-received state and carbon-coated state. Similarly to Achard, they observed that a 250 °C bakeout reduces ESD yield by a factor of 10 at most. Vallgren et al. [159] made a similar observation when measuring the ESD yield as a function of bakeout temperature for as-received and carbon-coated SS. The bakeout manifested little effect on the ESD yield from SS, whilst that of carbon-coated was dramatically reduced when baked at higher temperatures. This points to the bakeout depleting the adsorbate surface coverage, including the microporous surface of the carbon coating. Vacuum firing on the other hand, done typically to temperatures just under 1000 °C, aims to deplete the subsurface hydrogen concentration. Whilst the high-temperature treatments are necessary to reduce the H_2 thermal outgassing, they do not ensure low ESD and PSD yields by themselves, as shown by Andritschky et al. [160]. Even the highest temperature treatments that are technically achievable, i.e. vacuum firing, only remove molecules with binding energies of few eV, far lower than necessary to desorb chemically bound molecules reaching up to 10 eV. This can be illustrated by performing post-bakeout stimulated desorption, which still desorbs units of gas monolayers.

Second, many researchers, such as Mathewson [156], Malyshev [161] or Kennedy [162] demonstrated that the surface adlayer coverage decreases dramatically after such treatments, and by extension also

the ESD yields decrease. This includes various chemical treatments and sputtering action via glow-discharge, which is particularly effective, as shown by Dean [163], Stori [164] or Malev [165]. These authors not only recollected available datasets, but also added their own theories, experimental data, and compiled comparative analyses. This was often done aiming for an in- and ex-situ applicability to particle accelerator's components. Malyshev underlines the importance of surface cleaning in his book [161], especially when UHV conditions are to be maintained under irradiation. Besides presenting his own results and discussing various experimental methods to acquire those, he also lists ESD and PSD data for various technical-grade metal surfaces, including surface treatments. For instance, Figure 2.18 shows the effect of surface treatments (polishing, firing, both, neither) on water electrodesorption. The initial ESD yields (y-axis) and the amount of desorbable gas (x-axis.) easily vary by order of magnitude, depending on the treatment combination.

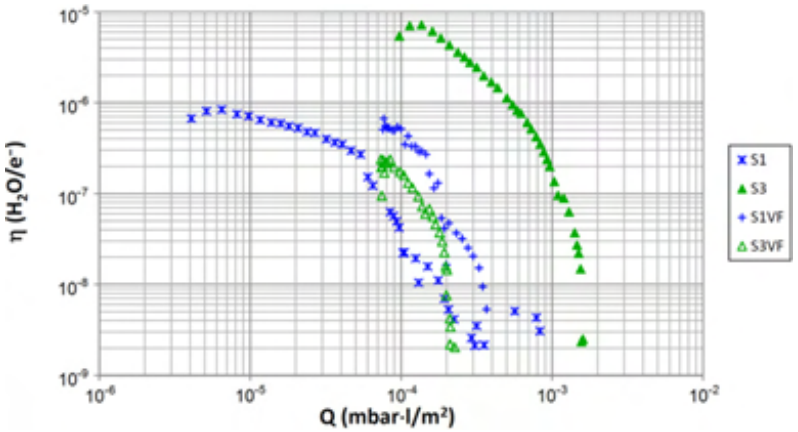

Figure 2.18: ESD yield as a function of total desorbed quantity of H_2O from stainless steel with various surface treatments. The 4 samples have been polished and vacuum fired, both, or neither. The highest is the polished sample, lowest is a combination of both. Image: Malyshev et al. [166].

Lastly, the method of storage determines to what extent does the cleaned surface preserve its state achieved by the prior treatments. The effect of various storage methods was studied via XPS by Scheuerlein&Taborelli [167] as measured by a carbon presence, representative of hydrocarbon surface concentrate on on steel, Al and Cu. They concluded that the best packaging method to preserve UHV-grade cleanliness is by a food-grade wax-free aluminium foil wrapped in multiple winds around a cleaned component. The same conclusion arose from a survey made by Sasaki [168], of cleaning and storage methods used world-wide for UHV-grade cleaning. Furthermore, once the as-received material with adlayers is stored under vacuum, its surface thermally outgasses, which can decrease its initial ESD yield, up to a factor of 10, as noted by Malyshev [161]. The same applies to the SEY, also being a surface state driven property.

To conclude, the importance of cleanings and treatments cannot be stressed enough and, along with storage and bakeout methods, all have a major influence on the amount of desorbable adlayers, hence influencing the ESD yield. Unfortunately, these crucial aspects are often not described in sufficient detail in many publications or even not discussed at all. Authors typically investigate surface treatments applicable in their respective technical applications and/or available at their institution. As a result, an as-received surface state, i.e. state after an UHV-grade cleaning, is in fact ill-defined. Due to this, there is a large variance in the collected data originating simply from different methods of cleaning, in- and ex-situ treatments, storage and possibly bakeout. Further variance then originates in different experimental approaches. This includes the level of vacuum, sample insertion method, but also the experimental arrangement, which influences the dynamic background level present in the measurements. The experimental investigations listed below are usually done for the main technical-grade metal surfaces that received some UHV-grade cleaning and/or treatment, both ex- and in-situ. The baseline temperature for all the measurements is the ambient one, unless said otherwise.

Malyshev characterised the ESD conditioning and energy-dependence very thoroughly under a range of conditions for various NEG compositions ranging from single to quaternary, activation temperatures ranging from 80 °C to 350 °C, including layered NEG coatings. He also demonstrated that NEG activation leads to a significant decrease of ESD yields [169], but heating above ∼200 °C does not lead to a further significant ESD yields reduction, [170, 171] and instead leads to hydrogen diffusion from bulk to subsurface layers and a consequent electrodesorption. Sirvinskaite et al. also did electron-conditioning studies

proving that a single-compound Zr-based NEG activates even at low activation temperatures and features very small ESD yields. Moreover, even a mild-bakeout to 80 °C leads to a factor of 10-100x decrease of ESD yields and corresponding electrodesorbed gas quantities.

2.6.5 Energy dependence

An energy dependence curve of an ESD yield typically contains numerous regions of interest, each of which is dominated by some characteristic phenomena. The energy range spanning from 0 eV to a few keV is particularly interesting in the context of both ESD and SEY, see Fig. 2.19. First, it contains many interesting regions from the physics standpoint, and second, it is in the parameter range of many technical applications, as outlined in the Introduction. Hence, the typical range of electron energies used for irradiation starts at very low energies, say in 0-20 eV range, where the desorption threshold is found. This region is indeed in the scope of the accelerator physics community since the majority of the electron cloud resides here. Then follows a wide region of tens to hundreds of eV, where the multipacting peak of electron-cloud is located [8], and where vacuum gauges and mass analysers operate. Finally, higher energies in the keV range are characteristic for runaway electrons, cosmic radiation, or electron microscopy.

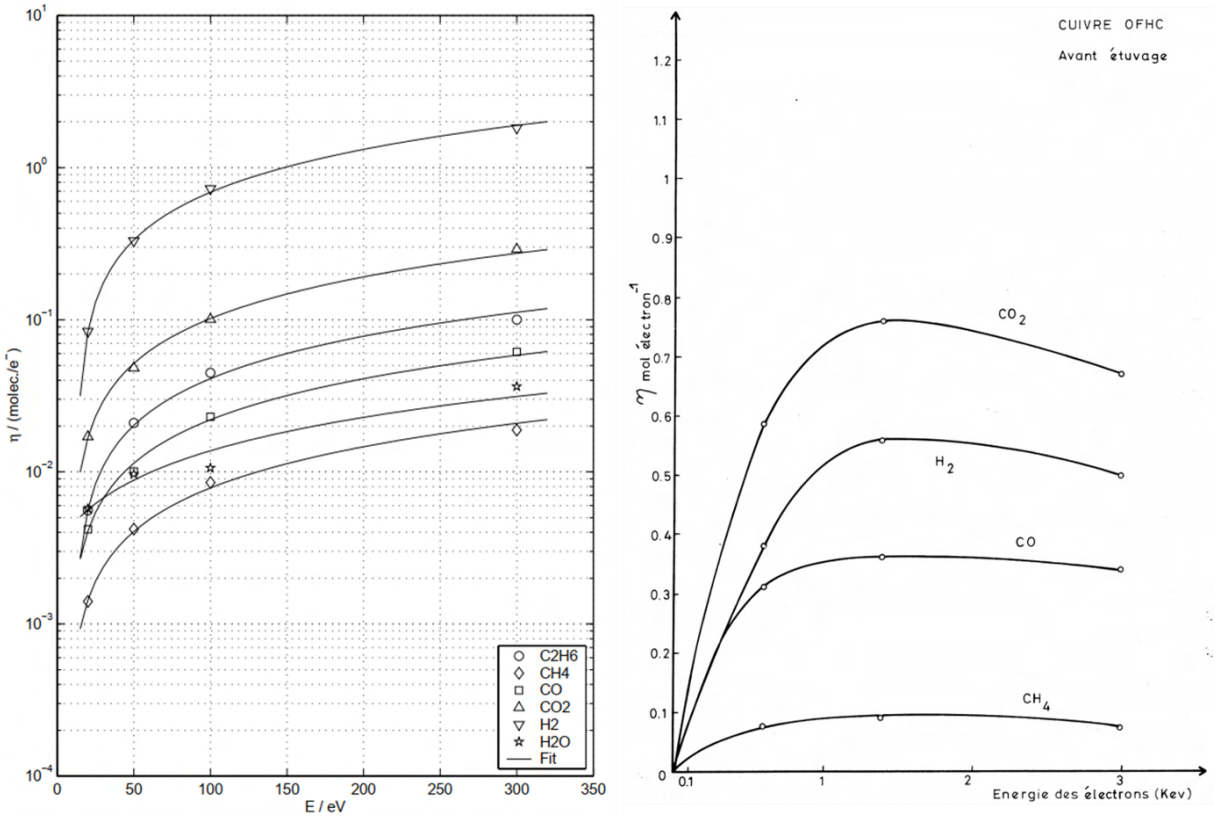

Figure 2.19: ESD yield as a function of energy as measured at CERN on an as-received OFHC by Billard et al. [172], left and by Achard [157], right. Mind the different scaling of axes, logarithmic vs linear.

First, the low-energy region is particularly interesting in the context of both ESD and SEY. As predicted by all DIET models, the ESD process has an inherent threshold behaviour. Below this threshold, the ESD yield is nil because the system does not have enough energy in the form of an electronic excitation that initiates the desorption sequence. Second, above the threshold energy, the ESD yield rises about linearly until a few hundreds of eV, because all the primary electron energy is dissipated in the surface layer and within an escape depth of electronic excitations. This observation in agreement with the concept of the energy deposition depth being compared to the escape depth. When in the low energy region, below about 300 eV, it is the entirety of primary electron energy that is dissipated within the surface layer's escape depth, and therefore potentially available for desorption. This can be readily illustrated by measuring the ESD yield at a oblique (non-normal) incidence angle, which effectively deposits the energy into a shallower depth. As a consequence, the linear part of the ESD yield energy-dependence

extends higher up, offsetting its maximum, and ESD yield is boosted for high energies. Third, at higher energies, the energy deposition depth is to be compared to the diffusion depth of electronic excitations and/or escape depth of molecules. This on the other hand creates a generic $1/E^n$ decay rate typically found at energies in the keV range. The exponent n is reported to vary in range of 1–2 [127]. In between the regions of the linear rise and a power-law decay typically lies a peak, similarly to the SEY curves. The peak position is highly correlated to the stopping power of the target surface and, by extension, to its chemical composition.

Billard et al [172] have done measurements of relatively low energy ESD from OFHC Copper at room temperature. They provide a simple fit to their experimental data applicable in energy range from 20 eV to 300 eV. This fit, upon extrapolation, points to a threshold energy around 10 eV for all typical species except water. Similar threshold at 10 eV was observed in the now-outdated vacuum tube industry, which was mentioned by Redhead in his memoirs [31] as a *'10 Volt effect'*. Such evidence for ESD threshold on technical surfaces is of particular importance, especially with regards to the typical electron cloud energy spectrum. For a more complete perspective, threshold for H^+ desorption from organic materials lies far under 10 eV. By organic materials, one can either mean lubricants used during machining, or organic detergents used for cleaning of technical surfaces, or even amino acids, DNA, and proteins. But these are not of concern here. The energy threshold for desorption also typically resides below 10 eV for gas species cryosorbed onto the cold technical surface.

The fact that the ESD and PSD are both encompassed by the DIET theory can be leveraged to predict one yield from the other, as was pointed out by Collins and Malyshev in [173]. They hypothesise that the ratio between ESD and PSD yield should hold across different experimental conditions, namely between ambient and cryogenic temperatures. Hence, it is possible to use a known PSD yield to somewhat infer on the value of ESD yield, and vice versa.

The ESD yield of water from technical surfaces or water physisorbed onto surfaces, as well as desorption of its fragments is of great technical importance, because moist atmospheric air includes a considerable fraction of it and a long sojourn time of water molecule at room temperature makes it the most abundant residual gas in unbaked UHV systems. Thick water ices are of interest to the astrophysics community, so they made numerous studies on this topic. Rather complex electron induced chemistry can already happen in water molecules, especially in the presence other species, such as CO_2, CH_4, etc. Take for example the study of Noell et al. from Sandia labs [174], with of clear technically-oriented interest. Hydrogen is cracked from the water molecule with an energy threshold of 25 eV and gains some 5 eV of kinetic energy as a result of the desorption process. Such cracking effect was equally observed by Abdulgalil et al. [175] who measured the H_2 yield to be even higher than that of H_2O, as measured by 200-300 eV electrons impinging on 150 ML (assumed 1 ML = 10^{15} molecule.cm^{-2}) of compact amorphous solid water. Same observation was also made in H_2O and D_2O ices by Dupuy [176]. The fact that water residual within a vacuum system can crack into hydrogen is of great technical implications, because H_2 behaves entirely differently within a vacuum system than the parent water molecule. Not only the H_2 has different vacuum dynamics due to the lower molecular mass, but also adsorbs/desorbs at 2 orders lower temperature, has a different interaction cross-section, etc.

As substantiated with water, the dehydrogenation of hydrogen-containing molecules is an efficient reaction channel which can be more effective than the desorption of the parent molecule. Hence, the same case as for water needs to be done for other hydrogen-containing molecules and, more generally, other molecules prone to fragmentation. The energy threshold for dehydrogenation of organic materials, often via DEA, lies far under 10 eV as studied here in the context of radiation-induced damage on DNA. This points towards a very low energy thresholds for the dehydrogenation of carbohydrates that can be present as a residue overlayer on technical-grade metals. This was indeed observed by Rowntree et al. [177] for alkanes, exhibiting a dehydrogenation threshold at 7 eV for both H_2 and H^-. Their measurements also demonstrate that the H_2 increases with increasing stochiometric hydrogen content. Similar dehydrogenation process via neutral H_2 release as for water is also known for hydrocarbons and organic molecules. Such observations also corroborate the reasoning behind electron-induced graphitization originating from carbon-containing contaminants present at the surface, as discussed below.

The following authors investigated the primary electron energy influence for some main technical metals held at ambient temperatures with typical surface cleanings and treatments. Malyshev et al. measured the ESD energy dependence for Al [178] and SS [179] between 10 eV and 6.5 keV. These measurements, taken in a tube-type experimental arrangement, show the ESD yield to monotonically increases in this wide energy range. Ding and Williams measured the ESD yield for Al [180] below 1.5 keV and also observed a monotonic increase of the ESD yield with increasing energy. Achard measured the ESD yield of

CERN-cleaned Al, SS, OFHC and Ti [157] and compared the state before and after bakeout. An exercise that is repeated in this research work, at ambient and cryogenic temperatures. She observed the yield to peak around 600 eV for Al, both before and after bakeout. This observation better follows a typical shape of an SEY curve, which indeed should be the case, at least to some extent. Suzuki et al. [181] measured the ESD yield for Al, Fe, Cu at primary energy in the range of 1–3 keV. Their measurements tend to peak out just below 2 keV.

Parametrization

A good parametric fit should correctly model, with the minimum number of fitting parameters, the key features observed in the energy region of interest, as discussed at the beginning of the section. Those are:

- Energy threshold, below which the ESD yield is nil: $\eta(E < E_{Thr.}) = 0$
- Linear region, corresponding to energy deposition within the escape depth. $\eta(E) \propto E$
- Peak position on the energy scale and its height.
- Decay at higher energies with a proper decay rate. $\eta(E) \propto 1/E^n$

Billard et al. [172] proposed a parametrization that fits their ESD yield energy dependence data in the low energy region of 0-300 eV, as depicted on the left side of Figure 2.19. The $E_{Thr.}$ is indeed the desorption energy threshold, η_0 is the ESD yield of a given species at $E_0 = 300\,eV$ and $\gamma = 0.85$ seems to be an empirical exponent that best fits the data. Whilst this empirical fit models the data well in the considered low energy region and it even captures the threshold energy, it can not by design model the peak at few hundreds eV that is often measured by experimentalists.

$$\eta(E) = \eta_0 \cdot \left(\frac{E - E_{Thr.}}{E_0 - E_{Thr.}} \right)^{\gamma} \tag{2.9}$$

A more suitable parametrization is introduced in the 6.1 and is readily implemented on the newly acquired data in the Results section 5.

2.6.6 Incidence angle dependence

The dependence of ESD yield on the incidence angle is not well-researched at low energies. However, the theoretical understanding and the similarity to the SEY and ESD phenomena can again be cautiously exploited. The PSD was purposely left aside since photons behave vastly differently when compared to electron and ion irradiation.

Building on the concept of energy deposition depth, one can deduce two effects caused by increasing the incidence angle (measured from the normal) of higher energy electrons, i.e. above the peak position. First, shallower incidence angles should lead to a shallower energy deposition and more electronic excitations near the surface. This immediately increases the electron emission and gas desorption yields. Second, higher energy electrons, suppose 1 keV, impacting at shallower angles, still deposit their energy within the escape depth. It takes even higher energy to deposit the energy below the escape depth into the bulk. This offsets the deposition-escape depth balance, also offsets the peak position E_{max} to higher energies, as compared to normal incidence.

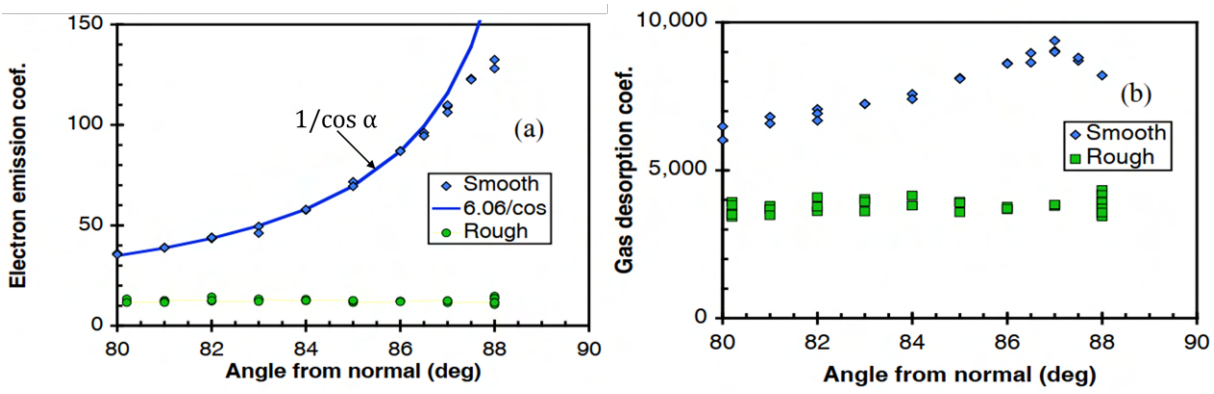

Figure 2.20: Angular dependence of ion-induced electron emission and gas desorption, as measured by Molvik et al. [182]. Note the asymptotic $1/cos\alpha$ behaviour. Also note the incidence angle has a little effect on rough surface.

The angular dependence of ESD yields at energies over ∼100 eV should, in theory, behave similarly to the SEY. Since the SEY asymptotically follows $cos^{-n}\alpha$ behaviour until reaching the grazing incidence angle, where the high electron reflection off the surface effectively decreases the number of electrons that enter the surface.

Molvik et al. [182], reproduced in Fig. 2.20, measured the angular dependence of ISD yields and ion-induced SEY. Angular dependence similar to the SEY is once again visible and the $cos^{-n}\alpha$ fit approximates well the experimental data until about 80°. On the smooth surface, the yields start departing from the $cos^{-n}\alpha$ behaviour once the incidence angle reaches a grazing regime and the reflectivity prevails. Similar angular dependence is also used in the realms of plasma-etching, e.g. [183], which is also an ion-induced process. Rough surfaces do not exhibit such behaviour, and retain constant yields, This is an advantageous behaviour, especially in technical application where low yields are required at non-normal incidence angles.

2.6.7 Electron dose dependence of ESD

Extended electron irradiation is long known to decrease both the SEY and ESD yield. This is a direct cause of scrubbing off surface-bound adsorbates prone to desorption, which results into two effects. Firstly, ESD yield also drops substantially, as the surface concentration of air molecules, contaminants, water and/or hydrocarbon chains is effectively reduced. This is the case for all UHV-typical residual gas molecules, such as physisorbed and chemisorbed gas species like H_2, CO, CO_2, CH_4, etc. The gas depletion directly results into an SEY decrease. For the SEY conditioning, another effect comes in, which is precipitation of a thin graphitic layer, that originate in the adventitious contaminants. This effect has been recently described independently by Cimino et al. [76, 184], Nishiwaki&Kato [185] and Scheuerlein et al. [79]. Note that conditioning curves of both SEY and ESD yield begin with a flat plateau, see Fig. 2.6 and Fig. 2.21. The yield remains constant here, because the surface is not yet significantly depleted of molecules or changed by the incoming electrons at such low doses.

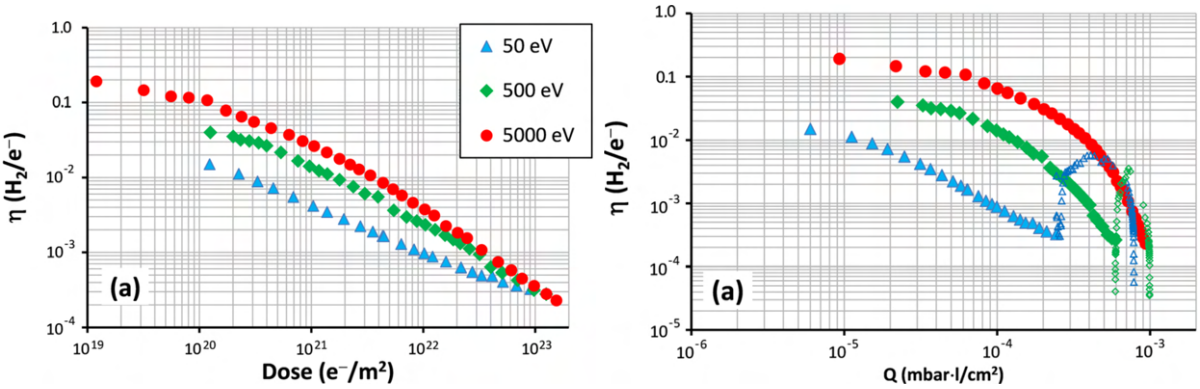

Figure 2.21: ESD conditioning curves measured on an as-received technical-grade 316L stainless steel by Malyshev et al [179]. Left: All curves exhibit a monotonic decrease of the ESD yield with absorbed electron dose, but the rate differs. Right: ESD yield plotted as a function of already desorbed gas. The yield gradually decreases with the dose, but again different primary electron energies release different gas quantities.

The ESD and SEY of OFE copper was measured as a function of dose at room temperature by Henrist et al. [186] and summarised by Baglin et al. [75]. Unfortunately, only the normalised ESD yield is plotted as a function of electron dosed, when conditioned with few hundreds of eV, probably 500 eV. The interesting finding they made is the correlation between the SEY and ESD yield conditioning can be approximated by two linear regions (in log-scale). The first and faster rate corresponds to contaminants removal and the second slower one corresponds to the graphitic layer precipitation and gradual surface depletion. Similar observation is discussed in detail in Section 5.3.2. Hannah et al.[187] made an ESD conditioning study with 500 eV electrons impinging on an OFHC copper held at room temperature. They compared the conditioning curves for an as-received state and laser-treated one of OFHC and stainless steel (SS). The as-received OFHC has initially large H_2, CO and CO_2 yields and conditions more slowly when compared to the laser-treated OFHC and even an untreated SS. Achard [157] and Achard, Calder and Mathewson [188] made another ESD yield measurement from OFHC copper, along with Al, Ti, SS and Inconel. They investigated the impact of primary e^- energy on the ESD yield from as-received and baked state. The bakeout temperature was demonstrated to have a strong conditioning effect on the

ESD yield. Their findings were complemented by AES spectra analysis. Ashraf et al. [158] measured a technical-grade SS, that was used as a reference before a carbon-coated SS measurement. They measured the ESD yield of H_2, CO, CO_2 and CH_4 on as-received 304L SS that was subjected to bakeout to various temperatures. The same measurement was then performed on an SS with a 500 nm thick layer of amorphous carbon sputter-deposited over the SS. Since the ESD is a surface-related property, the chemical state of a surface, its history, depth profile and many other parameters inevitably influence the ESD yield, just like they do the SEY. The question remains to what extent do these parameters influence the ESD yield, as well as the total number of molecules prone to desorption. The measurement of Malyshev [166] clearly illustrates the importance of surface state for the case of SS, which is treated in various ways. The treatment or their absence affects both the initial ESD yield but also the total quantity of desorbed gas. This is visualised in Figure 2.18 for the case of water desorption from vacuum-fired and/or polished steel, as compared to untreated. He also measured the ESD yield of 316LN SS that was polished, vacuum fired and coated with either columnar or dense film of a Ti-Zr-Hf-V getter [171]. The conditioning was done at 500 eV, while varying the NEG activation temperature. The observed conditioning rate exhibits a non-trivial behaviour and even a rise in H_2 yield for samples activated at high temperatures above 180 °C. This is explained by hydrogen diffusion through the thin film, proving that diffusion plays some role in the conditioning process. Besides Malyshev's own results, his book [161] lists the main experimental methods and results regarding the ESD from various technical surfaces and surface treatments.

Dean et al. [163] measured ESD of aluminium at 300 eV in a tube-style setup for the initial surface state and electron-conditioned state. They showed that a glow discharge is an effective means to decrease the ESD, as compared to as-received and baked states. Malyshev [179] observed that the electron energy affects the conditioning rate and the total amount of electrodesorbed gas. It can be seen on the left side of Fig. 2.21 that electrons of different energy condition the ESD at different rates. This can be explained by the amount of energy dissipated in the escape depth. The more of primary e^- energy is dissipated at the surface, the more energy is available for desorption processes and for graphitic layer precipitation. The right chart shows conditioning curves, i.e. the ESD yield of H_2, CO, CO_2, CH_4 measured as a function of adsorbed electron dose. The conditioning rate approaches the slope $\alpha = 1$, i.e. 1 decade yield decrease per 1 decade of extra electron dose, which is characteristic of a surface-limited desorption process. Malev [165] compiled a comparative study of ESD conditioning data from various sources and adds his theoretical considerations regarding surface and bulk diffusion and the resulting trends in the conditioning curves. Kennedy [162] used 1.5 keV electrons to irradiate a number of samples representing candidate materials for beam vacuum chamber. He tracked the ESD yield of common UHV residual gases and commonly observed a gradual decrease with slopes between 0.5 and 1, while the initial yield would vary by 2 magnitudes depending on a surface, coating or a treatment. In his extensive doctoral research, Pivi [189] measured the SEY and ESD of copper colaminated tube, same as type in the LHC, but held at ambient temperature. He stimulated electron multipacting using an RF system coupled to a measurement setup in a tube-style arrangement. This resulted in an electron cloud whose energy distribution he measured with an in-house built energy analyser. He also corroborates his data with SEY measurements. Although his ESD results are only qualitative, he observes the desorption of typical UHV gas species and a conditioning effect.

Electron irradiation can also lead to electron-induced chemistry, particularly visible at higher accumulated e^- doses. Cracking and synthesis of molecules induced by electrons is a well known phenomena, but was only investigated by few authors in the context of ESD from technical-grade metal surfaces. Nishiwaki&Kato [185] observe the H_2O yield induced by 1.5 keV electrons to have a non-monotonic behaviour with absorbed e^- dose. The H_2O yield starts constant at low dose, then increases at medium e^- dose, presumably due to water molecules accumulating on the surface, and only then starts decreasing. Similar effect is also observed for CO_2, though not so profound. Once again, an inspiration can be drawn from PSD measurements and calculations done by Anashin [190] on synchrotron radiation induced photo-cracking of condensed CH_4 and CO_2 molecules. Transient effects are visible on the conditioning curves, owing to an evolving dynamic balance between desorption, synthesis, recycling and pumping of gas molecules and fragments. They argue that in a pumping-limited cryogenic system, the electron-induced molecule cracking favours the production of H_2 and CO at the expense of CO_2 and CH_4.

Parametrization

Similarly to the parametric fit of ESD yield energy dependence, the dose dependence has to satisfy few boundary conditions in order to be physical.

- Asymptotic approach the initial ESD yield for zero dose: $\eta(D \to 0) = \eta_0$
- Asymptotic approach the power-law decrease at high dose $\eta(D \to \infty) = 0$

The ESD yield at high absorbed doses is commonly fitted with a power-law that simply scales the yields with the dose. The immediate shortcoming is that the fit does not work at low electron doses.

$$\eta(D) = \eta_{D=0} \cdot \left(\frac{D}{D_0} \right)^{-\alpha} \tag{2.10}$$

This is impractical firstly because high doses are time-consuming to achieve and because high electron doses imply the low ESD yields high uncertainties, often being at the instrumental sensitivity limit. Finally, a conditioning process starts at $D = 0$, so it needs to be modelled.

Malyshev proposed [161] a modification to the classical fit 2.10 to model the photodesorption dose dependence, that reasonably well approximates the experimental data of PSD in a range of energies and doses. Again, owing to the common origin of ESD and PSD, the formula can equally be considered applicable to the ESD. A modified argument accounts for the boundary conditions, and recreates the initial plateau by pushing the initial as-received yield η_0 at D_0. At high doses, the formula asymptotically approaches the steady decreases modelled by the power law in 2.10.

$$\eta(D) = \eta_{D=0} \cdot \left(\frac{D - D_1}{D_0 - D_1} \right)^{-\alpha} \tag{2.11}$$

The power law exponent typically ranges between from $\alpha = 1$, characteristic for clean flat metal surfaces and a surface-limited desorption. Values of $\alpha = 0.5$, are typical for porous surfaces and coatings and/or for diffusion-limited desorption. Exponents higher than that can signify a dynamic equilibrium between an electron-induced chemical synthesis that is in competition with desorption of a given molecule. Such behaviour is commonly observed in water desorption.

Another parametric fit to the ESD conditioning curves will be presented in the Results section 6.1 below based on the newly available experimental dataset.

2.6.8 Temperature dependence

The temperature dependence of ESD yields seemingly challenges the non-thermal origin of electrodesorption, but indeed the temperature indirectly influences the ESD yield in various ways. First, the substrate temperature determines what kind and quantity of gas species at what binding state can be present at a given temperature on surface characterised by its adsorption site energy distribution. Hence, the temperature possibly limits the surface concentration of an adsorbate, which possibly directly limits the ESD yield.

Second, the temperature has an exponential effect on diffusion rates, both surface and bulk. Lower temperatures will lead to lower ESD yields, if a given desorption sequence is diffusion-limited. Leveraging the relation between ESD and PSD, an argument can be made using PSD data measured by Baglin et al. [191], seen on the left side of Figure 2.22. When approaching cryogenic temperatures, the recombination of molecules prior to their desorption becomes surface diffusion-limited. This is in agreement with the ESD yield of heavier species dropping at lower temperatures. The ratio of ambient and cryogenic ESD yields can indicate to what extent is the desorption sequence diffusion-limited.

Somewhat contradictory is the measurement of Malyshev [192] taken around the ambient temperature. A factor of ∼2 variation on just 40 °C difference is unexpected, especially in comparison with measurements of [193] who observed little to no difference even at 200 °C. The available experimental data are inconclusive and the exact mechanism remains unclear.

The literature survey showed little to no coverage of desorption from technical surfaces held at cryogenic temperatures. Hence the research niche stated above. Few attempts were made to infer the ESD yield indirectly using data from the LHC machine, i.e. correlating the dynamic pressure increase and the electron cloud activity. Though it is hard to decouple the relative contributions of various influencing factors, such as ESD, PSD, ISD, proton-gas interaction, etc. Metals are commonly used as a substrate for ESD measurements of condensed gases, but those are typically high-purity, often monocrystalline,

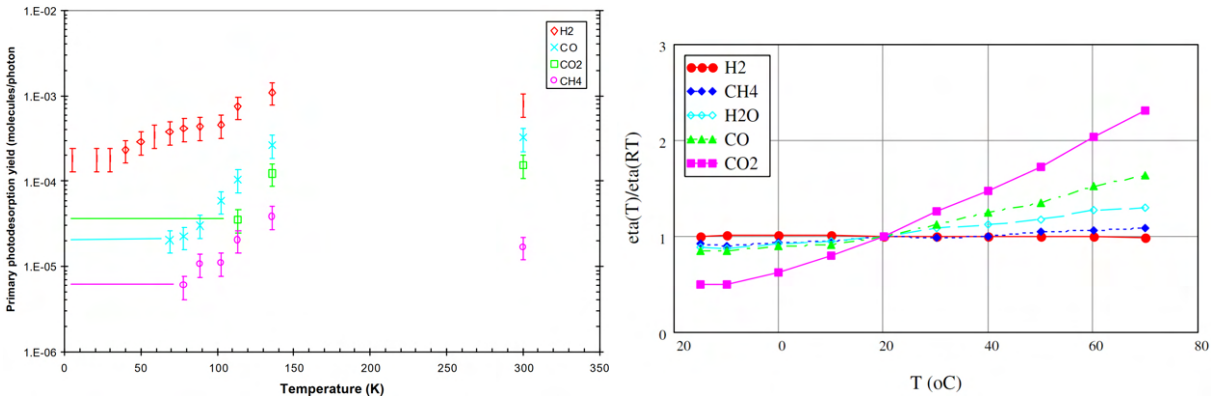

Figure 2.22: Left: PSD temperature dependence measured by Baglin et al. [191] from ambient to cryogenic temperatures. Right: ESD temperature dependence measured by Malyshev&Naran [192] around ambient temperature. The data is normalised to the yield at 20 °C.

sputter-cleaned and generally well-defined. Cryogenic technical grade metal surfaces, on the other hand were not systematically researched except in the following isolated research efforts. The thesis of E. Bez [194] aimed to measure the ESD of Cu and stainless steel held at 4.2 K. The electron-generating array was used as an electron source, which provides a continuous energy spectrum of low-energy electrons. This work provides a rough idea of the ESD yield but struggles to decouple various influencing factors and experimental artefacts clearly. The only other cryogenic ESD measurement known to me was done by Sirvinskaite et al. [195] on a NEG coating held at 90 K. A comparison was done to 300 K and both activated and non-activated state. However, the results are difficult to interpret due to ill-defined experimental procedures and conditions in this brief proceeding, which does not detail the primary electron energy, aside from changing many parameters simultaneously.

2.7 Effect of cryosorbed gases

The cryogenic environment brings about two important factors. First is the drastic decrease of both surface and bulk diffusion caused by the low temperatures, which immediately results in lower ESD yields. The second major effect that differentiates the room temperature SEY and ESD from the cryogenic ones is that the low temperatures implicitly involve the presence of cryosorbed gases that are otherwise not present at ambient temperatures. These physisorbed gas molecules strongly influence SEY and ESD already at submonolayer coverages, as seen in Fig. 2.23 on the right. Moreover, they are, by definition, only weakly bound to the substrate and are more prone to desorption due to that.

Similarly to bare metals, the SEY and ESD yields from condensed gases depend on energy and temperature. Yet the adsorbate also has a certain thickness, morphology, composition and contamination, crystalline or amorphous structure, etc., which considerably complexifies the picture. Once again, for technical purposes, one can focus preferentially on the sub-keV energy range and thin coverages, typically under 1,ML thick. The SEY and ESD of normal and noble gas adsorbates at various energies and coverages were researched at CERN, as detailed in the dissertations of Tratnik [196, 197], Kuzucan [198, 199], Chmielinska [200] and Dupuy [176].

2.7.1 Adsorbate effect on SEY

Beginning with the SEY as the more accessible indicator of electronic processes on a surface. Firstly, the generic shape of a SEY does not change for a range of adsorbate-substrate combinations, as illustrated by Cazaux et al. [61], who normalised different SEY curves by their peak value and position, see the left side of Fig. 2.23. Dekker's phenomenological parametrization [201] can well approximate this shape in the medium to high energy range.

Still, the peak position E_{max} and the δ_{max} value strongly vary with the adsorbate coverage. Taking as an example data measured by Chmielinska [200], and Kuzucan et al. [199] for the SEY evolution with CO_2 coverage on copper at different conditioning states, right side of Fig. 2.23. A clean surface's maximum SEY δ_{max} evolves linearly when increasing coverage until a few monolayers. In this region, the secondary electrons originating from the substrate still penetrate through the thin adsorbate overlayer and exit to the vacuum. This fact substantiates the high inelastic mean free path (IMFP) of low energy electrons and low stopping power of gas adsorbates.

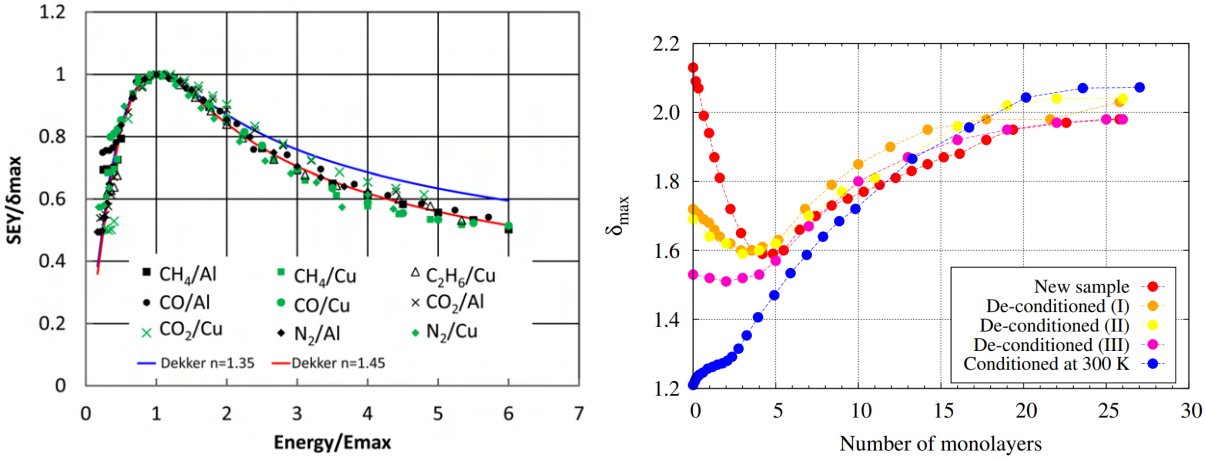

Figure 2.23: Left: SEY energy dependence for gases adsorbed at different substrates, as measured by Kuzucan et al. [199]. The data is normalised on both axes to its peak value and energy fitted using the Dekker fit [201]. Right: SEY dependence on CO_2 coverage, as measured by Chmielinska [200]. The maximum SEY and its energy position both become substrate-independent at about 5 ML coverage and at 20 ML, the SEY resumes that of a bulk adsorbed gas, totally substrate-independent.

The SEY become substrate-independent at about 5 ML coverage, as measured by δ_{max} and E_{max}. The energy of a maximum SEY E_{max} follows the same trend (not shown): at about 5ML it changes from the value influenced by the substrate to that representative of an adsorbate. For higher coverages, the SEY curves asymptotically approach the behaviour of a semi-infinite adsorbate, which is a constant SEY for regular gases and steadily increasing SEY for noble gases [61].

2.7.2 ESD of cryosorbed gases

To an extent, the ESD behaves similarly to the SEY both as a function of energy and coverage. Tratnik researched the ESD yields and sticking coefficients of adsorbed layers of gases quench-condensed over a technical-grade copper held at cryogenic temperatures, investigated in the scope of his dissertation [196], followed by a paper with colleagues Hilleret&Störi [197]. First, they measured typical UHV residual gases, such as H_2, N_2, CO, CO_2 and CH_4, including various quaternary mixtures, and then noble gases: He, Ne, Ar, Kr and Xe. They varied electron energies from 40 eV to 1 keV and adsorbate coverages in the range from submonolayer to multilayer regime. Dupuy [176] further studied the ESD yield of molecules and their fragments and their variation with energy, coverage, temperature and composition. These sources make a great reference for ESD yields of adsorbates in the medium energy range.

The ESD energy dependence is similar to that in bare metal surfaces, with all its features, as illustrated with Tratnik's data [196] in Figure 2.24. The slight difference is a maximum at lower energies, corresponding to lower stopping powers of condensed gases than bulk metals. The sole exception is that the ESD of noble gases, instead of peaking out, only levels off at higher energies around 1 keV.

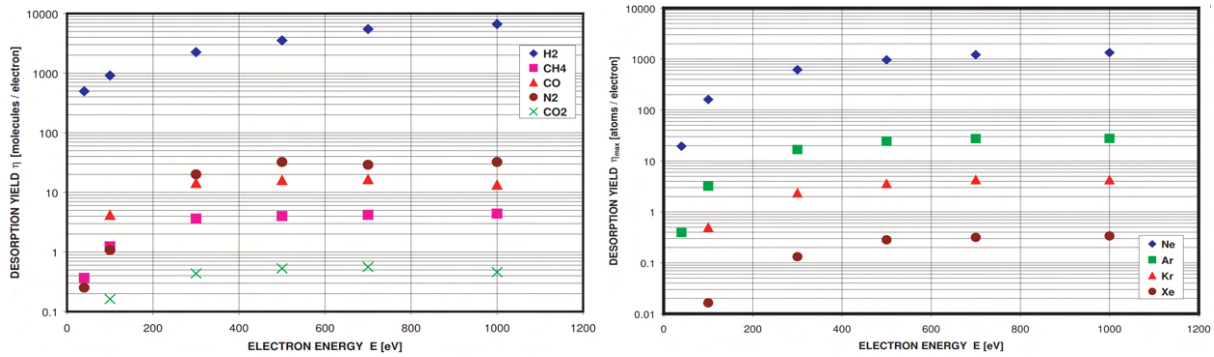

Figure 2.24: ESD yield energy dependence for quench-condensed gases at around 1 ML (100 ML for H_2) precoverage on a technical-grade copper substrate, as measured by Tratnik [196]. Left: regular gases. Right: noble gases.

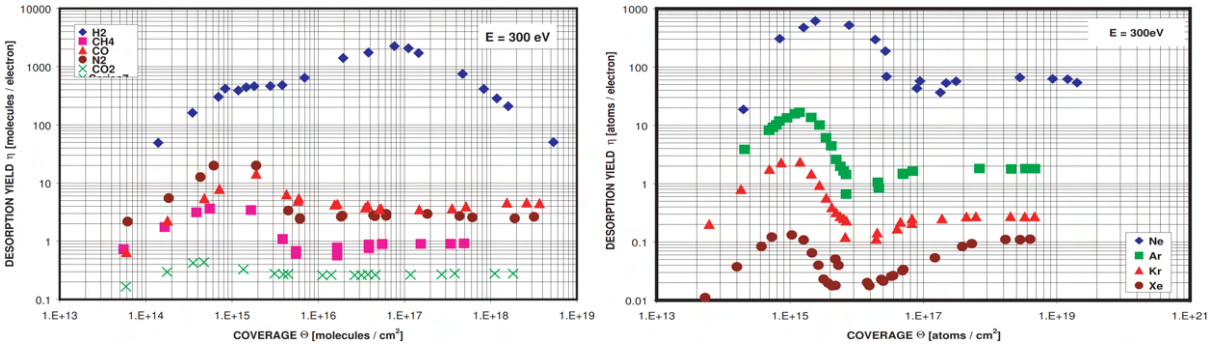

Figure 2.25: Coverage dependence of ESD yields at 300eV for quench-condensed gases on an UHV-cleaned technical-grade copper substrate, as measured by Tratnik [196]. Left: regular gases, Right: noble gases. Mind the ESD yield enhancement at a few monolayers caused by the substrate mirroring the electrons back into the thin overlayer. The dip that follows is discussed also in the text.

Whilst the ESD energy dependence is similar to that in bare metal surfaces, the surface coverage θ of an adsorbate plays a key role in determining the ESD yield. It is reasonable to expect a linear dependence for submonolayer coverages, as the ESD yield simply scales with the coverage and is therefore in a surface concentration-limited regime, see Fig. 2.25 Many authors have observed a boost for thin multilayer coverages that is caused by the substrate mirroring the electrons back towards the surface [202]. This is typically the case from ∼1 ML to an equivalent of about half an electron range in a given adsorbate. At higher coverages, the yield of normal gases tends to assume a dependence θ^{-n}, as demonstrated by Schou et al. for condensed H_2 [126]. This agrees with the concept of energy deposition depth reaching gradually deeper, much below the escape depth. A similar effect is observed in metallic substrates, though at higher energies, because of higher stopping power. In contrast to that, pure noble gases tend to level off without a decrease at very high coverages. Dupuy argued [176] this to be a consequence of a high diffusion distance of electronic excitations and neutrals, allowing them to permeate across thick

adsorbate coverages. All three regimes of ESD yield coverage-dependence: linear, boost and decay, are well illustrated by [197]. Tratnik also observed a dip around 10 ML for both noble and regular gases, but its origin is not discussed. Yet, Kuzucan [198] proposes an explanation for SEY of thin adsorbates, suggesting that secondary electrons produced inside the metal substrate are effectively scattered off the substrate/adsorbate interface and therefore do not reach the adsorbate/vacuum interface. Hence, creating a dip in SEY for thin multilayer coverages. By extension, this seems to apply to ESD yield, as observed by [196].

Another important observation made by Tratnik is a clear correlation between the ESD yield of condensed noble gases and their sublimation energy E_{sub}, which is but a factor away from the adsorption energy E_{ads}. Tratnik derives an empirical exponential relation that fits the experimental ESD yields of noble gases in a multilayer coverage regime, as follows:

$$\eta \propto \exp(\frac{-E_{sub}}{kT}) \tag{2.12}$$

The imminent question is how far does this correlation retain its predictive power when extended to higher binding energies. For instance, is it also applicable to non-noble gases and species in a physisorbed or chemisorbed state? Based on the data shown in 5.68 it seems it could be the case, but with much less precision.

2.7.3 Composition dependence

There is experimental evidence, cross-verified in different laboratories, of a strong impurity effect of ESD yield in noble gases, Reimann&Johnson [147]. Figure 2.26 substantiates the strong influence the gas composition on ESD yield (and luminescence yield) of cryosorbed Ar:O_2 mixture. The nonlinear dependence of ESD yield on adsorbate composition points towards the interaction of the co-adsorbed compounds. In the case of Ar with trace amounts of O_2 impurities, a quenching process caused by trace amounts of O_2 very steeply decreases the Ar yield: a factor of 10x decrease with only 0.5 % O_2 pollution is remarkable. Noble adsorbates allow excitations to diffuse at much larger distances than regular gases. This allows excitations to reach the surface and cause desorption there, even when the deposition depth is high at high energy. Hence high ESD yields at high energies, as compared to other gases. It was argued that the impurities act as sinks for excitations, preventing them from diffusing further towards the surface, hence preventing desorption.

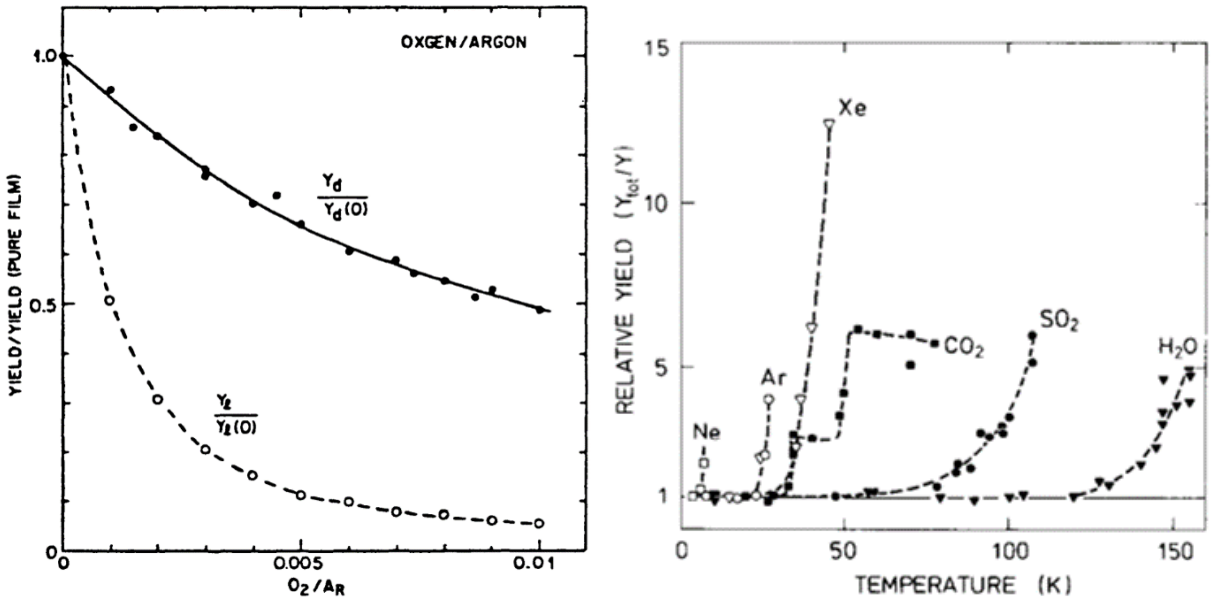

Figure 2.26: Left: Argon ESD yield attenuation with trace amounts of O_2, as measured by Reimann&Johnson [147]. Right: Desorption yields vs temperature and the effect of thermally enhanced desorption closed to the desorption temperature. Recollection of multiple resources by Schou from Riso laboratory. [127].

Tratnik [196] measured the ESD yield of H_2 that was co-adsorbed with other less-volatile species. Even though the fundamental physical process is likely different from the Ar:O_2 system, this end result

is similar: ESD yield of more volatile gases decrease in the presence of other less volatile gases. Tratnik's data also suggests this can work in the opposite direction, i.e. enhancement of low-yielding species by higher-yielding constituents of the same mixed adsorbate. However is to be verified, whether this behaviour comes from a kick-out mechanism or a surface-enrichment. Practical implication of this effect is that mixtures of gases co-adsorbed in multilayer coverages exhibit a strongly nonlinear behaviour than, say, a weighted linear average of the constituents.

2.7.4 Temperature dependence

The temperature dependence of ESD yields seemingly challenges the non-thermal origin of electrodesorption, but the temperature influences the ESD yield in various ways. First, the substrate temperature determines what kind and quantity of gas species at what binding state can be present at a given temperature on a surface characterised by its adsorption site energy distribution. Second, the temperature can dictate the crystallographic structure of thick adsorbates. A step change in CO_2 ESD yield coinciding with the recrystallization temperature substantiates this, Figure 2.26. Last, the deposition temperature (along with deposition rate) determines the orderliness of a grown adsorbate layer. The typical case for thick adsorbate formation in technical applications is a quench condensation on a substrate considerably colder than the desorption temperature of a given gas species. This results in a rather amorphous and porous adsorbate structure, which indeed projects into the ESD characteristics. A parameter range better scouted in the astrophysical realms.

The right side of Figure 2.26 is data compiled by Schou [127] and depicts a large ESD yield boost just under the desorption temperatures of each gas. This is likely due to a combined effect of thermally induced agitation of the substrate-adsorbate system and electron-induced one. It could be argued that plasmons created by impinging electrons are thermalised or delocalised too rapidly, making them negligible at low temperatures, but gain importance when adsorbate is already nearing desorption. Whilst the data is taken for thick multilayer coverages, it is unclear whether this behaviour persists at submonolayer coverages.

2.8 Temperature programmed desorption of cryosorbed gases

With the aim of measuring the ESD and SEY of technical surfaces covered with cryosorbed gases, one needs a way to characterise the substrate-adsorbate system in terms of the adsorbate coverage, regime, binding energy, adsorption site distribution, specific surface, etc. Temperature programmed desorption is a commonly used means to do this quantitatively. This simple and experimentally accessible method essentially measures the gas desorption during a linear temperature ramp-up. The TPD curve shape and its evolution with various parameters reveal much about the nature of the substrate-adsorbate interaction.

The TPD method can also reveal the order of the desorption kinetics [203–207]. As formulated by [208], the *"parameter which characterises that fraction of particles on the surface which participate in the critical step of the desorption."* The TPD curve shape indicates the underlying kinetics and the rate-limiting step of the desorption sequence that determines the kinetics order. This, in turn, is driven by the nature of the interaction between the substrate and the adsorbate. Integer values of desorption kinetics order are common, but non-integer values are also possible for some specific edge-cases [207], both shown in Section 5.5.

Figure 2.27 on the left shows a series of TPD curves for coverages in 0-3 ML range (assumed 1 ML = 10^{15} molecule.cm^{-2}). The first monolayer is bound stronger than additional overlayers, as seen from the peak desorption temperature T_{max} that drops from 55 K to 35 K. The coinciding leading edges are a signature behaviour of zero-order desorption. In the case of blue curves taken in the 0-1 ML coverage range, it is a sign of a 2D evaporation from a CH_4 island formed on the graphene surface. The shared leading edges for higher coverages once again represent zero-order desorption kinetics, this time caused by simple evaporation of a solid adsorbate. The non-zero desorption rate in the window around 45 K is not an experimental artefact but a signature of a compression region where molecules squeeze to form a compressed first monolayer. It is energetically favourable for a molecule to be bound to the surface rather than another adsorbate molecule. A similar case, though less profound, can be made for the second layer of molecules, creating the second peak of the *Tre Cime*. The last peak at the lowest temperature indeed corresponds to the multilayer coverage regime. Finally, integrating the area under a curve gives the total adsorbate coverage. It is common to integrate from the right to determine the amount of gas remaining on the surface at a given temperature.

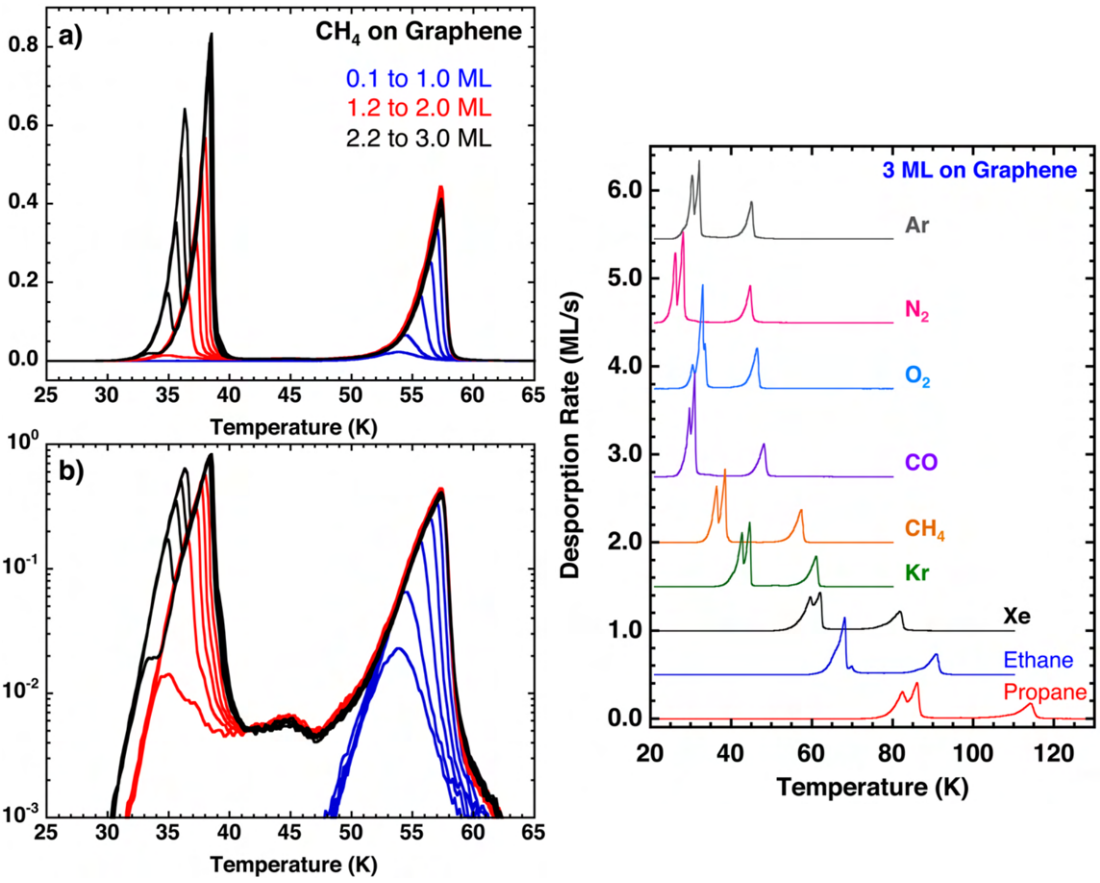

Figure 2.27: Left: Set of TPD curves of CH_4 on graphene for coverages in the 0-3 ML range represented on linear and logarithmic scales (assumed 1 ML = 10^{15} molecule.cm^{-2}). The colour signifies the adsorption regime: blue for sub-monolayer and black for multilayer coverages. The shape and the corresponding binding energies evolve: increasing coverage leads to lower desorption temperatures. Right: TPD of 3 ML coverage of various gases. The TPD curve shape is preserved and only offsets as the desorption temperature varies for each gas. Image source: Smith et al. [209].

Taken from the opposite end, one can use a TPD measurement to determine the specific surface of a material by measuring a series of TPD curves around 1 ML coverage. Knowing how the TPD curve behaviour changes when transitioning from submonolayer (<1 ML) to multilayer (>1 ML) coverage, it is possible to estimate the approximate amount of gas necessary to create a 1 ML coverage behaviour. Finally, the specific surface of coatings and treatments is determined by comparing it to a flat reference surface, as is done in 5.5.3.

2.8.1 Adsorption energy evaluation

The general equation describing thermal desorption was formulated by Polanyi&Wigner[210] as follows and gives the desorption rate r that is proportional to the rate of change of coverage $-d\theta/dt$, which can be expressed comparing the adsorption energy E_{ads}[eV/bond] to the thermal energy $k.T$. The frequency factor ν [Hz] is the oscillation frequency of a molecule in its potential well, and in other words, it is the number of escape attempts per second of a bound molecule. The order of desorption kinetics n determines how, if at all, is the desorption rate r dependent on the coverage.

$$r = -d\theta/dt = \nu\ \theta^n\ \ \exp(\frac{-E_{ads}}{k\ T}) \tag{2.13}$$

The challenge arises because the parameters are cross-related and evolve during desorption. As the coverage decreases, the nature of a bond changes from adsorbate-adsorbate, characteristic of a multilayer regime, to substrate-adsorbate, characteristic of sub-monolayer coverages. Along with the coverage θ changes the adsorption energy E_{ads} and the frequency factor ν. However, It is reasonable to assume that in the first approach, the ν remains constant for a range of coverages for the weakly physisorbed gases studied here. Redhead [211] derived simplified formulas valid for the first-order desorption kinetics $n = 1$ and applicable across a range of parameters. This widely used formula allows calculating the E_{ads} and

ν from a known temperature of peak desorption rate T_{max} [K], heating rate $\beta\,[K.s^{-1}]$ and the frequency factor ν [Hz] and the universal gas constant is R=8.31446 J.mol^{-1}.K^{-1}.

$$E_{ads} = R\ T_{max}\ \ln(\frac{\nu\ T_{max}}{\beta} - 3.46) \tag{2.14}$$

The second equation proposed by Redhead allows determining the frequency factor ν from other known parameters. The equation is valid for $n > 0$ and indeed delivers values very close to the generic value $\nu = 10^{13}[Hz]$.

$$\nu = \frac{E_{ads}\ \beta}{R\ T_{max}^2\ \theta_0^{n-1}} \exp(\frac{E_{ads}}{R\ T_{max}}) \tag{2.15}$$

The resulting E_{ads} comes out in kJ.mol^{-1}. Dividing it by the Avogadro number N_A=6.02214076·10^{23} molecules/mole and the unit charge q_e=1.6021766·10^{-19} [eV/J] converts it to [eV/bond], which is a more meaningful unit for this study.

Given the logarithmic relation, the formula 2.14 for E_{ads} is rather insensitive to variations of the used parameters ν and β and the precise location of the T_{max}. Hence, using a generic value of $\nu = 10^{13}\,[Hz]$ leads to a good estimate of the E_{ads}. A factor of 2 difference in ν leads to a ±5 % variation in E_{ads} [209]. Similarly, a factor of 10 difference in β leads to a ±7 % change in E_{ads}. Even the common mistake of using 3.64, as opposed to 3.46, leads to only 0.5 % error in the adsorption energy E_{ads} calculated in eq. 2.14. The accuracy of this equation is claimed [211] to fall within ± 1.5 % when ν/β remains in the $10^8 - 10^{13}$ range.

Finally, an even more simplistic linear relation exists, serving as a rule-of-thumb to link the peak temperature T_{max} to the binding energy E_{ads} for an 1st order desorption.

$$E_{ads}[meV/bond] \approx 2.5 \cdot T_{max}[K] \tag{2.16}$$

2.8.2 Effect of porosity on TPD

Technical grade metal surfaces, treatments and coatings often have open pores of various types, giving them a large specific surface. Aside from the higher adsorption capacity, the apparent desorption energy also changes, as some adsorbate molecules are geometrically confined inside the pores.

Figure 2.28 by Paldor et al. [212] illustrates the effect of differently sized pores on the TPD curve shape. The SEM image illustrates the high aspect ratio of the open mesopores and a simplified geometry used for model derivation. The TPD curve of a flat surface has only one peak at 60 K corresponding to one type of adsorption site, the ones on the flat surface. For etched silica surfaces, this peak moves towards 65K and, with its slightly higher adsorption energy, represents a contribution from the damaged silica surface outside the pores. The now-emergent secondary peak travels from 70 K to 80 K and increases its width as the increasingly deeper pores trap the adsorbate inside a conductance-limited geometry. The high aspect ratio pores lead to a geometry-limited (∼ pore diameter) desorption, resulting in gas recycling inside the pore before desorption. As a result, the porosity not only increases the specific surface but also offsets part of the TPD curves to higher temperatures. The split of the TPD peak into two separated peaks results from an idealised scenario with single-sized pores. Shall there be a distribution of pore sizes, these peaks should again coalesce into one.

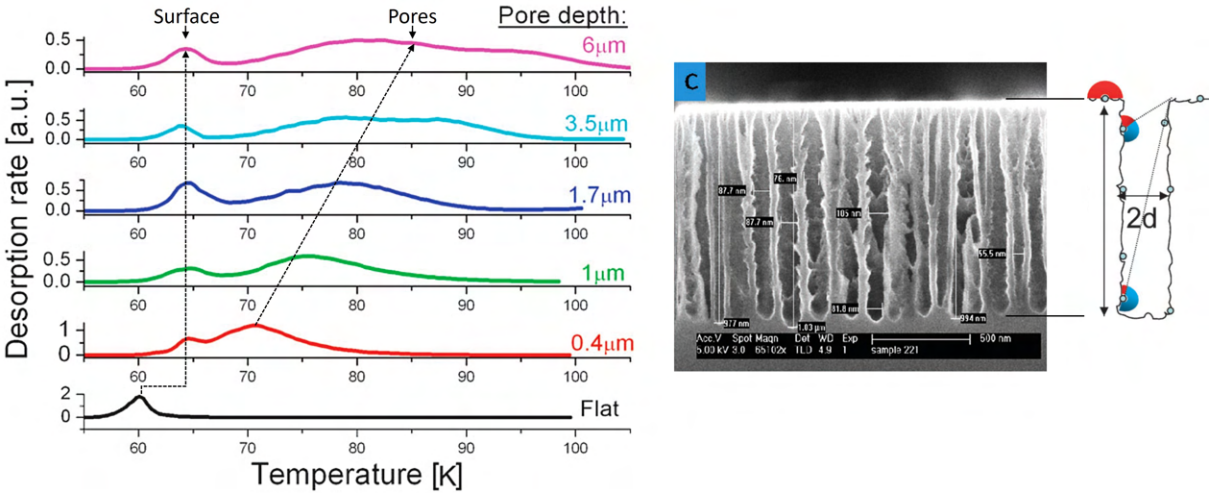

Figure 2.28: Left: TPD of 2.5 ML coverage of Xe on etched silica in a range of pore depths. Right: SEM photograph of the surface cross-section and a corresponding model. The high aspect ratio pores lead to a pore-diameter limited desorption and gas recycling inside the pore. The scheme shows a solid angle leading to desorption (red) and recaptures (blue) inside the pore. Image: Paldor et al. [212].

2.9 Chapter summary

A critical review of state of the art is provided with the following aims. Discuss physical phenomena underlying sub-keV electrons' interaction with technical-grade metal surfaces held at cryogenic temperatures. The literature survey gives an up-to-date overview of the current state of the research field and discusses the effect of various parameters on the ESD, SEY and TPD. This includes material and surface properties, irradiation characteristics and environmental conditions. Numerous examples are used to illustrate the main trends without a particular focus on peculiarities to preserve clarity. However, the research niches are omnipresent, given the number of intervening parameters and the inevitable combinatorial explosion. To tackle this one, can generalise from illustrative examples in the bottom-up direction, which should be facilitated by the presented theoretical understanding.

On one hand, the existing research elucidates many aspects of the wide problematics, and on the other, it substantiates the lack of coverage, solid theoretical understanding and lack of predictability for technical applications. Unfortunately, no literature survey can be exhaustive, as the data is very scarce, scattered across various domains and often not published via standard means.

Finally, this literature survey clearly demonstrates that until now, the vast parameter space of ESD-influencing factors was only probed in a very limited number of isolated points, leaving an extensive blank space for more research. One can amalgamate the presented experimental data and theoretical framework to form a decent understanding of the problematics and bridge numerous blank spaces of this niche field. While many educated guesses can be made for a particular system regarding its ESD yields, thresholds, and conditioning rates, true predictability in an extrapolative manner is still missing.

Chapter 3
Research objectives

Contents

3.1 Research niche identification

The Motivational Chapter 1 underlines the high relevance of the studied problematics to engineers and scientists across disciplines. The survey in Chapter 2 done over commonly accessible literature demonstrates that standard DIET models developed over the past decades provide a coherent view of the underlying ESD problematics. The DIET treatment delivers good qualitative predictions in agreement with experimental observations presented in available ESD literature. However, obtaining precise quantitative predictions using the theoretical approach is challenging, even for well-defined systems. This task is margining the impossible when predicting the ESD properties of technical surfaces. The literature survey also presents numerous data sources spread over various research fields, including vacuum technology, high-energy physics, astrophysics, radiology, etc. However, the accessible data is still very scarce when compared to the vastness of the parameter space of all parameters, possibly influencing the SEY and ESD. Some directions in this parameter space are researched better than others, typically due to some concrete technical or scientific motivation. Be it the electron irradiation of molecular ices that is interesting to the astrophysicist community or the study of technical surfaces that interests the high-energy physics community. And indeed, the field that gave rise to DIET in the first place, the science and engineering behind vacuum tubes and vacuum gauges [31]. Experts in these fields have researched the parameter space important for their particular applications. Yet, the complexity of ESD studies drives the cost high for more systematic experimental research.

The overall scarcity of experimental data is further increased when considering reliability and overall coherence. It is common to see authors struggling to reproduce the work of others and obtaining results that vary greatly from one author, laboratory, or experiment to another. This is partly because of the lack of an exhaustive description of relevant experimental conditions in terms of process parameters, surface characteristics, purity of compounds, etc. Partly it is the lack of coherent and standardised terminology used to describe ESD when approached from different disciplines. These deficiencies mark numerous niche areas within the ESD problematics that are to be developed and filled with experimental evidence and knowledge derived from within.

3.2 Dissertation outline and objectives

3.2.1 Dissertation outline

The general research aim is to study and better understand technical surfaces' response to electron irradiation, especially at low temperatures and low electron energies. The SEY and ESD of technical-grade metals and surface treatments in a range of surface states will be studied in the range of influencing factors that are representative of the LHC beam-screen. This includes ambient to low temperatures (10–300 K), low energies in the 0–1 keV range characteristic for the electron cloud, and in the presence of other influencing factors, such as adsorbed gases. The TPD method will also be leveraged to characterise the surface and the substrate-adsorbate interaction.

3.2.2 Dissertation objectives

The dissertation aims to advance knowledge about secondary electron emission and electron-stimulated desorption phenomena at cryogenic temperatures from technically important materials used, for example, in vacuum apparatuses of particle accelerators, electron microscopes, and radiofrequency or plasma devices. The detailed literature survey revealed the absence of knowledge about the molecular emission from technical materials (e.g. Cu, Al and stainless steel) for low electron energies and cryogenic conditions. In addition, there are no suitable experimental data and predictive models that approximate the dependence of molecular emission (as measured by the ESD yield) as a function of environmental, irradiation and surface parameters. Consequently, this research focuses on the study of electron-stimulated desorption for selected low energies and doses of electrons, substrate and adsorbate compositions and temperatures, as well as its relation to the electronic emission yield (SEY parameter). Hence, the research objectives define as follows:

- Definition, development, commissioning and optimisation of experimental methodology relevant to studying SEY and ESD phenomena and characterising technical surfaces at low electron energies and cryogenic conditions.
- Investigation of electronic and molecular emission (as measured by SEY and ESD yields) from selected materials and treatments in the low-energy range 0–1 keV as a function of electron energy, electron dose and substrate temperature.
- Development of parametric models that approximate the acquired experimental dataset as a function of electron energy and dose, substrate temperature, and adsorbate composition.
- Analysis of applicability of the new experimental evidence, developed models and derived knowledge with regard to representative technical scenarios.

These research objectives are discussed in detail in the below paragraphs and the achievement of these objectives is systematically presented in Chapters 4, 5 and 6, respectively.

Development of the experimental methodology

The ESD research field's status can be deemed unsatisfactory regarding the available datasets for common technical materials, especially at low energies below 100 eV, and at cryogenic temperatures around 10 K. While the SEY is relatively well studied, at least around ambient temperatures, there is a lack of reliable data and predictability of the ESD phenomena. ESD yields of common UHV residual gases and their electron conditioning rates for various substrate-adsorbate systems across different irradiation and environmental conditions are a major unknown. Especially when the ESD yields regularly vary across many orders of magnitude. It was therefore decided to develop an experimental system and corresponding methodology to perform systematic studies of the SEY and ESD phenomena with precise control of measurement conditions. In particular, those representatives of the LHC and other relevant fields of technology, engineering and science.

Acquisition of a systematic dataset

We can define the following circles of parameters that align with the thesis title *Electron beam characterisation of technical surfaces at cryogenic temperatures*. Those are the material, environmental and irradiation properties. The material properties encompass the bulk material, the surface state and possibly the microgeometry. The parameters of electron irradiation come in described by their energy, flux,

total dose and incidence angle. Finally, the environmental factors should be well described by the substrate temperature, which governs the thermal motion, and by the residual gas composition and the cryosorbed gas species. Hence, the parameter space of factors influencing the SEY and ESD can be categorised as follows:

- Material properties
  - Bulk material
    - Bulk composition
    - Concentration profile
  - Surface conditions
    - Surface states
    - Cleaning procedures
    - Contaminants and residues
    - Chemical and thermal treatment
    - Coatings and engineered surfaces
- Irradiation properties
  - Primary electron energy
    - Surface sensitive low energy region
    - Bulk sensitive higher energy region
  - Absorbed electron dose
    - As-received, non-irradiated state
    - Irradiation to high absorbed doses
  - Incidence angle
- Environmental properties
  - Temperature
    - Ambient
    - Cryogenic
    - Intermediate
  - Condensed gases
    - Pure gas adsorbates
    - Binary gas mixtures
    - Adsorbate thickness
    - Substrate effect

Experimental results interpretation, generalisation and application

The research aims to provide a dataset and disentangle the complex interplay of various factors listed in the previous section. The objective is to expand, in a structured manner, the current understanding of ESD problematics into a more coherent and holistic view. The acquired data on ESD can be processed in the following ways. First, the SEY and ESD measurements will be critically analysed and compared to theoretical expectations, simulations results and other authors who performed similar measurements. Second, SEY and ESD yields' conditioning and energy-dependence curves can be fitted with suitable models that will provide some degree of predictive capability. This step is particularly important, as models are crucial for further application in numerical simulations of dynamic vacuum. Electron-induced chemistry and transient dynamics can be investigated for metals, treatments, coatings and adsorbates. Tracing with isotopically labelled molecules could be employed for pure cryosorbed gases and binary mixtures. These can then be compared to the current understanding and other experimental data. The precision and accuracy of our experimental approach can also be evaluated for comparison to other measurement methods used in other laboratories. Lastly, the research findings applicability should be discussed with regards to representative technical scenarios, for instance, linking the electron cloud activity and the dynamic pressure rise.

3.3 Impact of this dissertation

The newly developed and commissioned experimental setup and methodology enables an on-demand electron beam characterisation of technical surfaces, coatings and treatments under the irradiation and environmental conditions that are representative of the LHC cryomagnets. The resulting understanding of SEY and ESD phenomena at cryogenic temperatures should bring the following benefits to the accelerator design, operation and the research community as a whole.

The improved understanding of technical materials' vacuum performance at cryogenic conditions will allow for a well-informed choice of construction materials. Materials used in the LHC, or considered for use, can be studied to understand their vacuum performance under controlled experimental conditions. Newly developed treatments, coatings and engineered surfaces can be tested ex-situ, iterated upon and optimised for a particular set of conditions and requirements, and qualified before their in-situ deployment. The amorphous carbon coating recently deployed in the LHC can also be studied under relevant conditions. Hence, the data can indicate the optimal choice of material with low SEY, ESD yield and a fast conditioning rate, which helps to mitigate the electron cloud activity. Lower EC activity leads to a smaller dynamic vacuum effect, beam instabilities and less heat deposited into the cryogenic system, to name a few imminent benefits.

The dataset will allow a better understanding of the HL-LHC operation and possible optimisation of scrubbing runs. In a scrubbing run, a proton beam in a special scheme is circulated at the injection energy to excite the electron cloud that scrubs the beam-screen surface and conditions both SEY and ESD yield. Indeed, the objective is to scrub the LHC as effectively as possible. Aside from the beam-scrubbing, the luminosity and energy ramp-up can also be optimised, knowing the conditioning rate that can be expected under a given set of conditions. The resulting improvement in beam-vacuum can potentially lead to longer uptime, fewer beam instabilities and less beam-gas scattering that activates the surrounding material, deposits heat into the cryogenics and creates background in experiments.

The developed experimental methodology can equally be used to assess the influence of cryosorbed gases condensed over the bulk technical surfaces. The SEY, ESD yield, energy threshold and conditioning rate can equally be measured under such conditions. This is highly relevant for the LHC's cryogenic beam-screen that cryopumps residual gases. In gas desorption experiments, such as a TPD, the optimal temperature ranges can be investigated so as to ensure that beam-screen temperature excursions will not lead to pressure excursions. Lastly, semi-empirical parametric fits can be developed to model the experimental dataset in order to provide some generalised description allowing predictive capability and serve as an input for numerical simulations of dynamic vacuum.

Aside from this accelerator application, studying electron irradiation of condensed gases, albeit much thicker, is relevant for the astrophysics community.

Chapter 4
Experimental methods and instruments calibration

Contents

4.1 Motivation

In light of the research motivations outlined in Chapter 1 and the lack of systematic and reliable experimental data summarised in Section 2, a new laboratory setup was designed to characterise surface properties of electrically conductive samples of metals, treatments and coatings held at cryogenic temperatures. The scientific aim of this novel setup includes measurements of the Secondary Electron Yield (SEY), Section 2.2, and Electron Stimulated Desorption (ESD) yield, Section 2.5, in the 0-1.5 keV energy region at cryogenic temperatures, Section 3. Obviously, the nickname *Multisystem* arises from the multiple experimental capabilities (cryogenic SEY, ESD, TPD) of this newly conceived laboratory system. These measurements are complemented with Temperature Programmed Desorption (TPD), Section 2.8, as an experimentally accessible method for characterising the substrate-adsorbate interaction of weakly adsorbed gases, corresponding binding energies, as well as a specific surface of the studied sample.

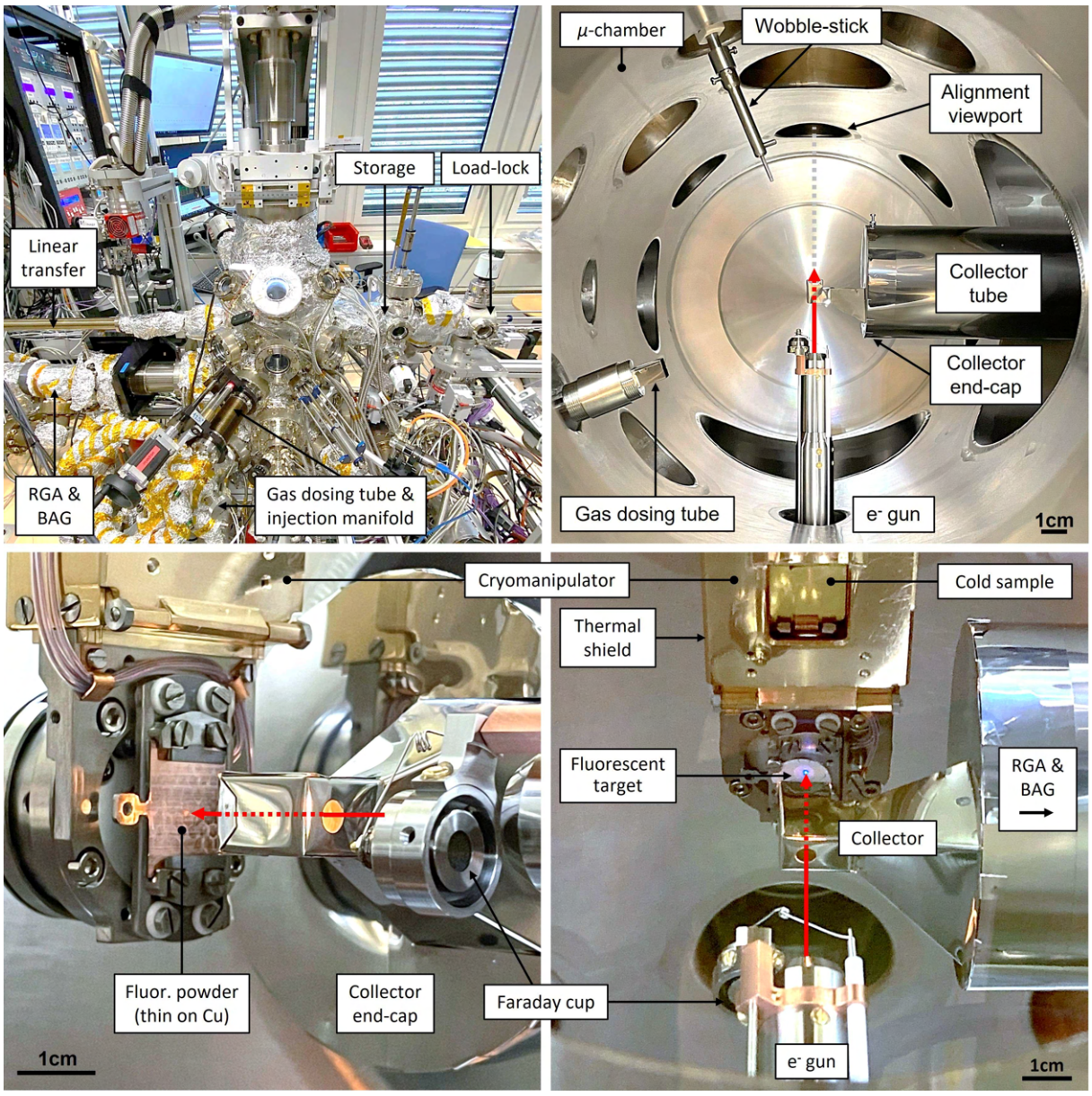

Figure 4.1: Top-left: view on the UHV chamber and ancillaries of the 'Multisystem' laboratory setup. Top-right: Top view on the inside of the UHV μ-metal chamber. The gas dosing tube and the wobble-stick are retracted. Bottom-right: Frontal view on the internal arrangement of the Faraday-cupped electron gun, fluorescent sample-bearing cryomanipulator and a Feulner-cap style collector. This image is published as [A3]. Bottom-left: Side view on the internal arrangement. Note the glowing orange spot on the copper sample with a thin fluorescent powder overlayer, placed in the lower sample-holder. Photo: Author, 2022.

In this chapter, the system is introduced along with its main components. Then, all the hardware

is described in detail, including the operating principle, corresponding calibrations, calculations and simulations used to verify our understanding. Finally, the main experimental methods for measuring SEY, ESD and TPD are elaborated, principles, calculations and calibrations will be presented for these methods. Ultimately, calibration and reference data will be taken to demonstrate the correct commissioning of each experimental method.

4.2 Experimental setup description

As visible in Figure 4.1 and schematised in Figure 4.2, the experimental setup designed to study the ESD and SEY at cryogenic temperatures consists of a μ-metal vacuum chamber, a 4-axis cryomanipulator, a low-energy electron gun and a Residual Gas Analyzer (RGA) fitted inside a collector. The setup is further equipped with a storage chamber and a load-lock chamber to introduce unbaked samples into the baked experimental chamber, allowing to study samples in an as-received unbaked surface state. The chamber and cryomanipulator are custom-built by external manufacturers, whilst the collector and the gas dosing tube are built in-house. Other components are standard, off the shelf.

The SEY and ESD measurement is arranged in the following manner. When the studied flag-type sample is inserted into the sample-holder attached to the cryogenically cooled manipulator, it is covered by a thermal shield with only a square-shaped opening. The cryomanipulator then moves the sample around the chamber to face different instruments and can cool the sample down to 10 K. In the measurement position, the sample faces the electron gun at a short focal distance of ~5 cm and the incoming electrons irradiate the sample at a normal incidence. A hollow collector is placed over the sample and captures secondary electrons and molecules leaving the sample as a result of electron bombardment.

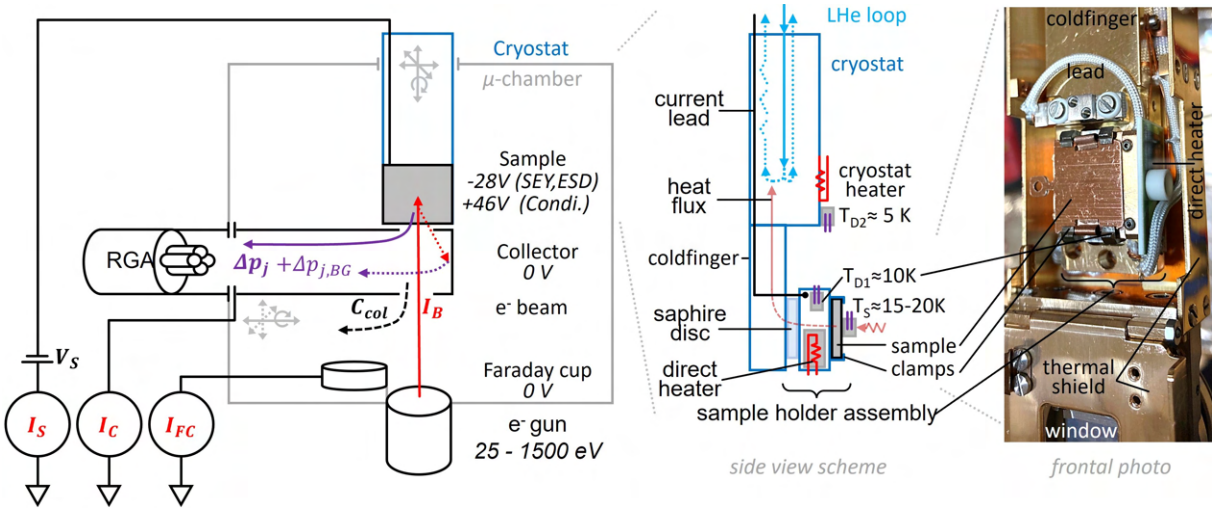

Figure 4.2: Left: Schematised arrangement of the experimental setup specifically designed for SEY and ESD measurements. Right: Schematised and simplified cryomanipulator-sample assembly. Note the temperature gradient resulting from the high thermal impedance path between the LHe loop in the Cryostat and the Sample (here the sample is equipped with a Pt1000 sensor for temperature calibration). The thermal shield, secondary sample holder and Faraday cups were omitted from the scheme for clarity. The thermal shield is visible in the photo.

4.2.1 UHV permalloy chamber

Ultra-high vacuum (UHV) is essential in surface science research to preserve a surface state of a studied specimen and vacuum chambers with base pressures in the 10^{-10} mbar range are therefore necessary. When operating at cryogenic temperatures, it is reasonable to assume a sticking factor σ very close to 1 [213] on the cold surfaces. Hence, the partial pressures of common residual gases need to be in the UHV range to ensure a monolayer formation time of hours. Then the UHV conditions provide a long-enough measurement time before the residual gases cryosorb on the cold sample surface, contaminating it and changing its surface state.

Given the relation 4.1 for a base pressure $p_{ultimate}$ of a vacuum system, a combination of two factors is needed: materials with low outgassing Q_{gas}, achieved by suitable cleaning and bakeout, and high effective pumping speeds S_{eff} achieved by combining momentum transfer vacuum pumps (turbomolecular, TMP),

gas entrapment pumps (non-evaporable getters, NEG, and cryopumping) and a suitable vacuum chamber geometry, i.e. avoiding conductance limitations. An in-situ bakeout is done on the entire system for 3 days to temperatures at least 150 °C (μ-chamber) up to 350 °C (RGA and BAG). Base pressure in the 10^{-10} mbar range is achieved when at room temperature and 10^{-11} mbar range is reached after a cool-down owing to a strong cryopumping. The setup combines a turbomolecular (TMP, measured: $\sim$80 l_{H_2}/s), NEG pump ($\sim$250l_{H_2}/s) and cryopumping on the cryomanipulator ($\sim$3500 l_{H_2}/s). The TMP is conductance-limited to $\sim$50 % by an auto-closing valve that safeguards the UHV in case of power cuts.

$$p_{ultimate}(T) = \frac{Q_{gas}(T)}{S_{eff}}, \tag{4.1}$$

Aside of the UHV requirement, the chamber is made of μ-metal (permalloy, $Ni_{\sim 80}$–$Fe_{\sim 20}$). This alloy shields off stray low-frequency magnetic fields by a factor of $\sim$100, as verified by measurement, so as to not interfere with the low-energy electrons trajectories. This is well illustrated by the fact that the magnetic field of Penning gauges is guided away from the chamber volume and does not interfere with the electron beam, as it is on non-shielding vacuum chambers.

4.2.2 Load-lock and storage chambers

A combination of load-lock and storage chambers decoupled by all-metal CF40 gate valves is used to maintain the UHV in the bakeout-conditioned main chamber, as visualised in Fig. 4.2. The Storage chamber is baked and constantly kept under UHV, firstly to keep calibration reference samples under vacuum and second, to act as a buffer during insertion of an unbaked sample from an unbaked Load-lock chamber.

4.2.3 Cryogenic manipulator

PREVAC cryogenic manipulator with 4 motorised axes (X,Y,Z,R_Z) positioned atop the μ-chamber holds the studied sample and cools it down to 10-15 K using a vibration-free open-cycle liquid He cooling. The lower end of this cryomanipulator is shown in Figure 4.2, schematising the mechanical construction, instrumentation, voltage biasing, heating, etc. The sample-holder is attached to the cold-finger that is cooled to 5 eV. The thermal impedance seems to be mostly driven by the thermal resistance of multiple interfaces and limits the ultimate temperature to about 10 K at the sample holder. Thermal tests were also performed with a Pt1000 temperature sensor instrumented onto Cu and SS samples. These tests point towards a sample surface temperature of $\sim$15 K at best. Since tests with samples of different thermal conductances revealed no tangible difference, the temperature difference is again assigned to the interfacial thermal resistance between the sample and the sample holder.

The sample holder can also be heated using a combination of two resistive heaters. One heater was in-house attached to the sample-holder assembly to promote local heating rather than the warm-up of the whole cryomanipulator. The direct heater at the sample-holder level can be set manually or with a voltage ramp, whilst an inbuilt PID controller drives the thermocoax heater mounted on the cryostat. The combination of these two heaters can generate a stable and controllable temperature ramp $\Delta T/t$, typically at 10 K/min, in the range from 10 K up to 300 K, to perform a TPD measurement.

The thermally-conductive 1.5 mm-thin sapphire disc supports the sample-holder assembly on the cryostat and grants electrical insulation to 100 GΩ (at 500 V_{DC}), allowing for a biasing voltage to 1 kV and a drain current measurement in the sub-nA range.

4.2.4 Absolute pressure measurement

The system houses 3 hot-cathode ionization gauges of Bayard-Alpert type (BAG), designed and manufactured by CERN and SVT company in the 1970ies. These B-A type gauges that are capable of measuring residual gas pressures in the UHV range until reaching their X-ray limit around 2.10^{-12} mbar. All used BAGs have been ex-situ calibrated for a range of gases against a secondary reference BAG. It was then verified in-situ by gas injection that all 3 BAGs read the same pressure. During operation, the emission current of all three gauges was decreased from 4 to 1 mA to prevent gas desorption and fragmentation. This emission current decrease should not alter the gauge sensitivity, at least in the first approximation. However, the lower emission current (and lower filament temperature) yields a tangible decrease in outgassing and gas fragmentation. Using the calibrated BAG and RGA in the collector, their degassing

could be calculated by alternately switching one off and using the other gauge to measure the Δp_{col}. This resulted in 10^{10} mbar.l/s outgassing rate for the RGA and $\sim 10^{-10}$ mbar$_{H2}$.l/s and $\sim$6.10^{-11} mbar$_{H2}$.l/s for the BAG.

It was found out that the BAG massively alters the fragmentation patterns of gases such as CO_2, exhibits a strong memory effect and considerably increases the pressure in the collector p_{col} by increased outgassing. Unlike in the μ-chamber and in the injection system BAGs, decreasing the emission current on the collector's BAG proved insufficient in reducing these detrimental effects to a tolerable level. So, at last, the BAG inside the collector was used solely during an RGA calibration of non-fragmenting gases and was later switched off for data-taking.

Aside of the BAGs, the μ-metal chamber has a cold cathode Penning gauge, that does not operate below 10^9 mbar and is therefore switched off during data-taking. However, it was verified that it does not cause a measurable gas fragmentation when on. It was also verified that the permanent magnet of the Penning gauge does not influence the low-energy electron beam. In spite of its relatively strong magnetic field ($\sim$mT range), and in spite of being in its magnetic axis, the field lines are contained by the surrounding μ-metal chamber.

All ionization gauges present in the setup are positioned in a way to prevent a direct line of sight to each other and to the measurement area. This prevents stray electrons and ions from interfering with the respective readings. The only occasion where this effect remains in the setup is a flux of ions from the RGA hot filament to the inside of the floating collector. This creates a dark current on the I_{col} when pressure is high in the collector, essentially forming a vacuum gauge (with a sensitivity of ~ 0.014 A_{col}.mbar$^{-1}_{N2}$). This effect was leveraged to infer on the total pressure when the pressure was too high for the RGA to be on in the SEM mode, i.e. during a gas injection into the collector.

4.2.5 Partial pressure measurement

The residual gas composition is analysed in this setup using an in-situ calibrated Pfeiffer QMG 700 mass spectrometer with a quadrupolar mass filter and secondary electron multiplier. Since the RGA calibration is essential for partial pressure measurement of individual gas species present in the collector, we performed an in-situ calibration by injecting gases of interest, i.e. dominant residual gases: H_2, CO, CH_4, N_2, $^{15}N_2$, Ar. An ex-situ calibrated BAG served as an absolute pressure reference to determine the absolute sensitivity k_j of the RGA to a partial pressure of a gas species j. A gas injection creates a single gas-dominated atmosphere, that allows us to reference the RGA current reading at the corresponding mass/charge to the pressure read by the BAG, corrected for the relative sensitivity to N_2. The RGA sensitivity k_j is referenced to an ex-situ calibrated BAG (SVT type) that has an estimated 10 % uncertainty on the absolute pressure reading. We calculated a systematic uncertainty of RGA partial pressure p_j measurement of 20 %, induced by long-term variations, but considered constant throughout a run. The noise-induced statistical uncertainty is measured around 10 % for the partial pressure change Δp_j. The calibration procedure is detailed in Section 4.5.1 treating with the gas flux measurement.

4.2.6 Gas injection and deposition system

The gas injection manifold allows the injection of various gas species either directly into the UHV chamber via a known conductance, into the collector, or directly onto the cold sample via a gas deposition tube, as schematised in Fig. 4.3. The gas injection system is designed for pumping speed and conductance measurements by injecting different gas species through a known conductance C_{ref}. This known conductance C_{ref} also serves as a reference for the C_{coll} calibration, as elaborated upon in Section 4.5. Besides this, the cryogenic temperature of the studied sample allows the physisorption of gases using a gas dosing system. In such a case, the gas to be adsorbed is injected using a volume-based injection system. A known injection volume $V_{inj} = 0.0865$ l is equipped with a capacitance absolute pressure gauge that measures the Δp_{cap} in this volume. This method is typically used to dose small amounts of gas directly onto the sample. The injection is limited by the pressure gauge resolution and, at best, is capable of delivering $\sim$0.1 ML coverage over 12.6 mm^2 sample area.

The gas dosing tube is depicted in Fig. 4.3, and it contains a two-stage grid homogenizing the molecular gas flow in such way that their flux is uniform within the cross-section of the 10 mm-wide square profile. This shall ensure that a uniform thickness of the adsorbate layer is made by such injection. The thickness was investigated directly on different spots of the sample by means of electron beam scrubbing and it seems to be uniform up to the measurable precision. However, gas dosing directly via the collector

is preferred and mostly used, out-dating the need for a gas dosing tube that is now used only for very thick coverages.

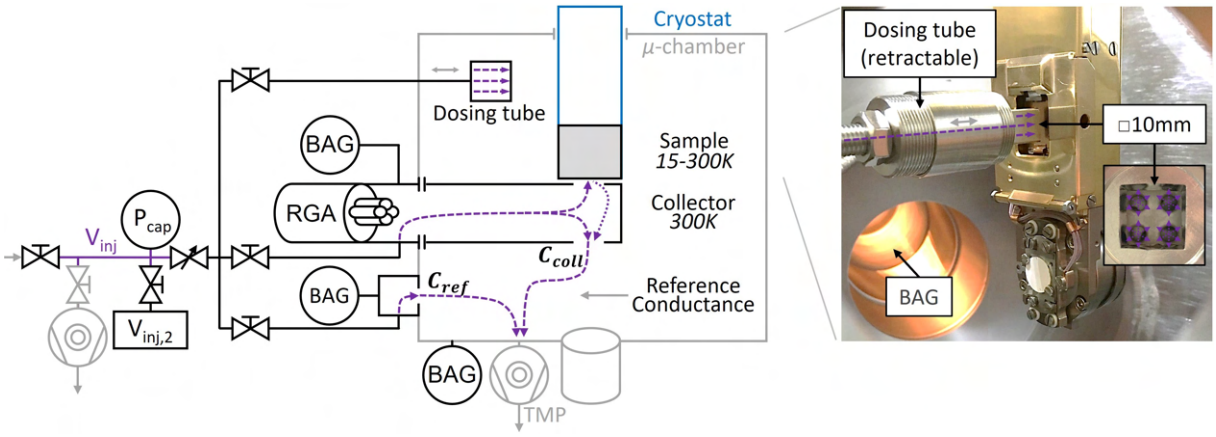

Figure 4.3: Left: Schematics of gas (purple) injections possibilities: reference conductance, collector and gas dosing tube. Right: Detailed view on the gas dosing tube.

The used experimental setup constrains the studied coverage range in the following way. The lower limit of surface coverages is about 0.1 ML, defined by the pressure resolution of the capacitance gauge used in the gas dosing system based on $\Delta p_{cap}.V_{inj}$ injection method. Indeed lower coverages can, in principle, be achieved by monitoring the partial pressure exposure with the RGA in the collector and time-integrating the signal. Although this is not the preferred method, it is feasible if the need arises. The upper limit for the coverages comes from a combination of charging issues, long dosing time (tens of minutes), and the RGA upper-pressure limit (5.10^{-8} mbar with the SEM switched on) that limits the dosing pressure as well as the allowable pressure rise during a TPD or a warm-up. This can also be overcome by switching off the SEM shall the need arise, or by slowing down the ΔT-ramp in a TPD measurement. Hence, coverages from 0.1 ML up to ∼30 ML quench-condensed atop of a sample held at 10-15 K were used and deemed suitable for the SEY and ESD studies. Because of these experimental constraints, particular focus was placed on 10 ML coverages, as this coverage is, to a large extent, fairly independent of the underlying substrate and representative of semi-infinite bulk ice.

4.2.7 Gas mixing and composition measurement

On the experimental note, injecting a pure gas and, by extension, achieving pristine ice is margining the impossible. However, this does not present a major obstacle as long as the gas composition can be monitored. The partial pressures are measured during most of the gas injections using the absolute-calibrated RGA. Single gas purity around ∼99 % was regularly achieved for all gases after multiple injection line purges.

When dealing with gas mixtures with the aim of producing binary ice mixtures of a given composition, an accuracy of ±5 % was achieved during the $\Delta p_{cap}.V_{inj}$-based gas mixing process. Here, gas A is injected into the volume V_{inj} to an absolute pressure p_1 and then a gas B is added to a pressure level p_2. This results in a binary gas mixture with partial pressures of gas A and B are given as $p_A = p_1$ and $p_B = p_2 - p_1$, respectively. Possible second order imperfections due to real-gas expansion dynamics can be neglected under these conditions. Again, this composition is then measured during each injection to measure the exact composition to a sub–% resolution. The RGA analysis of the injected gas allowed us to quantify the ice composition from the known injected gas composition by assuming, for all injected gases, the same sticking factor $\sigma = 1$ and the same adsorption kinetics. This is a reasonable presumption in the first approach for quench-condensing gases heavier than H_2 [213, 214].

However, the H_2 and CO persisted at some 0.1∼1 % concentrations in the gas phase and did cryosorb or cryotrap at an unknown quantity with the other gas being deposited. The H_2 and CO presence was observed e.g. during an ESD energy scan of cryosorbed Argon, as visible in 5.63. This type of impurity is thought to bring a certain scatter into the measured SEY and ESD data.

4.2.8 Electron and molecule collector

The new setup utilises a collector, depicted in Fig. 4.1 and schematised in Fig. 4.2, to capture secondary electrons and molecules emitted from the studied sample, either as a result of electron irradiation via an ESD or thermally induced desorption during a TPD. The collector is constructed from an 75 mm wide and 750 mm long tube equipped with a custom end cap designed to cover the sample. The end cap is positioned at only 0.25 mm away and forms a closed geometry over the studied sample surface. The collector not only effectively forms a Feulner cap, but the sample-collector system forms a Faraday cup that geometrically captures the majority of the incoming electron beam. For SEY measurement, the collector is an advantage but not a must. This is because the SEY can be well measured in a two-stage process using a reverse biasing method, as demonstrated for example by Gonzales [215].

However, given the experimental goal of measuring the ESD yield, the collector was designed and optimised for the ESD measurement. From the vacuum dynamics point of view, the collector functions as a Feulner-cap [216], i.e. maximises the vacuum conductance between the sample and the analyser and restricts the pumping speed towards the vacuum pump. This generates about a 150-fold sensitivity increase, as later illustrated in 4.22, Section 4.7. The ratio is essentially given by relating the collector conductance ($21.8\,l/s_{H2}$) to the vacuum chamber pumping speed ($\sim 3500 l/s_{H2}$).

The collector calibration in terms of its vacuum conductance is detailed in Section 4.5 and makes a crucial part of a high-sensitivity and precision ESD measurement. The collector's contribution to capturing secondary electrons and measuring the electron beam current is detailed in Section 4.3.

4.2.9 Data acquisition system

The used data acquisition system can be somewhat artificially subdivided into two parts. One of a SCADA nature monitoring the functioning of the experimental setup as such in terms of pressures, temperatures, flowrates, etc. and is out of the scope of this work. Another part that directly contributes to the SEY, ESD and TPD measurements will be detailed below.

The sample biasing to either -28 V or +46 V is done by stacking 9 V alkaline battery cells due to their high long-term stability and low intrinsic dark current. To further ensure a low dark current along the current leads, the electrical insulation (to the ground and to other floating parts) is verified to 100 GΩ at 500 V_{DC}, i.e. orders above what is necessary. The only issue occasionally comes with the capacitance along the long wires.

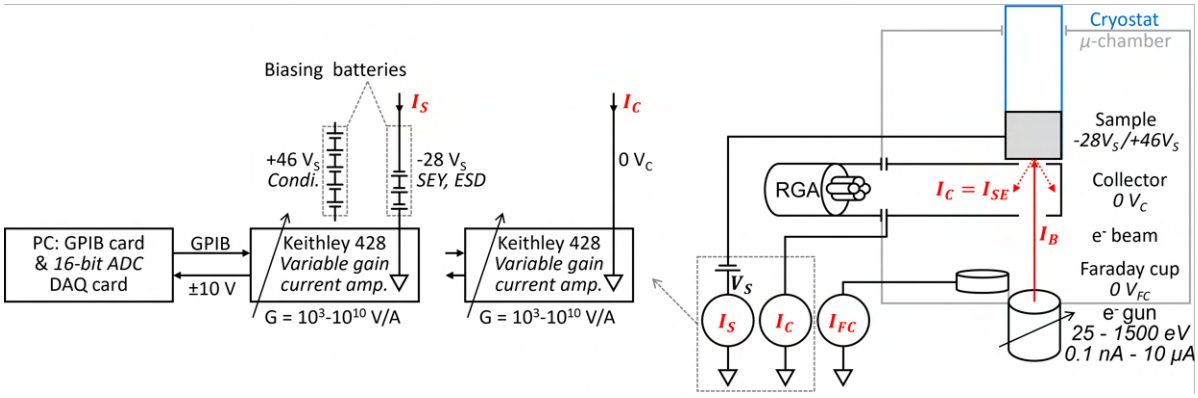

Figure 4.4: DAQ chain for measurement of sample and collector current.

The pair of Keithley 428 ammeters has a variable gain typically set to 10^9 V/A for a SEY measurement and 10^6 V/A for ESD and conditioning measurements. An inbuilt integration time of 100 ms is used to filter the incoming signal before it is amplified to the normalised bipolar ±10 V signal and transmitted to the 16-bit wide A/D converter DAQ card in the supervisory desktop PC. The correct current readout is ensured by a pre-warming and zero-check of the devices prior to measurement. The accuracy is also occasionally verified by plugging in an artificial current supply (battery and resistance in series providing μA-range current) and by interchanging the devices to make sure they read the same current.

As a direct result of this calibration and pre-measurement warm-up routine, both the noise and background level is about a factor of 50 below the signal across all different measurements and conditions. Moreover, the electron beam current is stable during hours-long conditioning measurements to within a few %. Further signal conditioning and processing are either done online in the control LabVIEW

application or in an offline analysis with a highly customised signal post-processing in Python [217]. This typically consists of further low-pass signal filtering and then measuring and subtracting the static background. Finally, the electron beam characterisation can be done with this calibrated DAQ system, as described below in Section 4.3. The LabVIEW applications for general DAQ and control of the electron gun, cryomanipulator and RGA were developed in-house to suit the particular hardware and experimental purposes and meet the user's requirements, with the most credit going to A. Benoit and B. Henrist, CERN-TE-VSC-VSM.

Each component along the entire DAQ chain leading to the ESD and SEY yield measurement was carefully characterised and calibrated with its error contributions quantified. Quantifying the systematic and statistical uncertainties of each contributor, i.e. each measured value allowed to estimate the uncertainty on the calculated results. Hence, the measurement of each quantity, SEY, ESD, Q_{tot}, and electron dose is accompanied by the systematic, statistic and combined uncertainty evaluated for nominal measurement conditions at 1σ. The method for combining the uncertainties into a full uncertainty analysis of the resulting ESD and SEY yields, is elaborated in detail in the Appendix 6.8.

4.2.10 Analytical electron gun

An analytical-type electron gun ELG-2 from Kimball physics is used as an electron source supplying a stable electron beam suitable for surface science experiments, see Fig. 4.5. This particular electron gun model is widely used in surface science research and has a wide customer base. The works of Gonzalez-Gomez [218] and Vincie [219] are a good references, as they well characterise this gun, in particular the low-energy region that is experimentally challenging.

Although the electron gun claims to cover a 2–2000 eV energy range, decent beam tuning was only found for 25–1500 eV in our experimental arrangement, so 25 eV represents the lowest energy used here. The remainder to approach 0 eV, referenced to the sample potential, is realised by imposing a retarding negative -28 V_s bias on the studied sample, as schematised in Fig. 4.2. The pencil beam can be focused into a Gaussian profile using electrostatic optics across most of the working energy range. The electron spectrum is very well monochromatic with a ΔE <1 eV, allowing an excellent energy resolution, owing to the disc cathode design. Two perpendicular pairs of electrostatic deflection plates are mounted at the gun nozzle and use an anti-symmetric biasing about the ground potential to deflect the beam. This represents a sub-optimal engineering solution because it strongly distorts the electron beam, regardless of its energy, but is used nonetheless in a small quantity to compensate for a minor beam-spot drift during an energy scan.

In the used experimental arrangement, the electron beam impinges perpendicularly on the studied sample from a distance of about 5 cm, out of which 1.5 cm is travelled through the hollow collector. This distance presents an improvement from an original 15 cm design that did not allow approaching the low- and high-energy region due to the inability to focus the blown-up beam. The entire drift distance, i.e. beam trajectory between the gun nozzle and the sample, is surrounded by a ground potential and the electron beam is only retarded prior to impact. This preserves the beam quality during the drift towards the sample due to a relatively high rigidity (scales with energy).

Long-term operational experience with two ELG-2 units uncovered a few signature artefacts originating at the gun and manifesting typically in SEY measurements. First is a glitch typically present around 200 eV. After discussion with the manufacturer and other users, it was pinpointed to a resonant condition created between the electron gun and the sample. This results into elastic electrons reflecting in between the sample-gun system, which is thought to increase the transverse beam profile and possibly also increase the electron energy distribution, making the irradiation less monochromatic. Another artefact is the inability to achieve a highly focused beam spot at energies around 1.5 keV and higher, depending on the focal distance. Once again, this causes the transverse beam profile to increase, which results in a subtle SEY increase and a slight, yet reproducible, departure from the $1/E^n$ type of decay in the keV energy range.

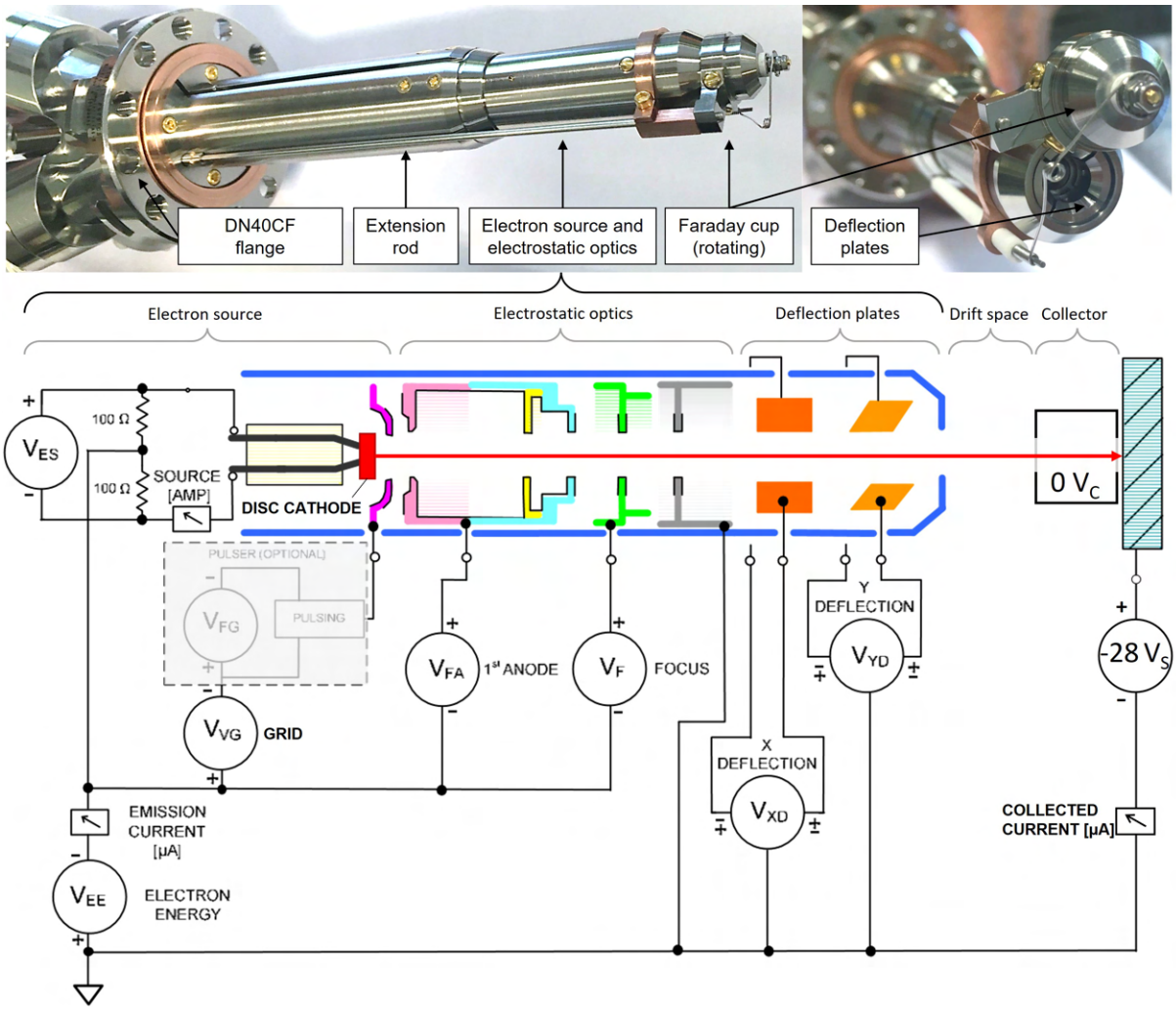

Figure 4.5: Top: E-gun side and front views. Bottom: Schematics and an electrical wiring diagram. Note the electron source is referenced to the accelerating potential, hence the beam-forming optics floats on a common potential above the ground. Note the field-free drift space between the sample-collector system and the e-gun nozzle. The scheme is not to scale.

4.3 Electron beam optimisation and characterisation

The electron source and the electrostatic optics, which extracts the electron beam from the hot cathode and focuses it, are floating at the accelerating potential. Such a method is used in electron microscopy to ensure a stable beam source. Indeed, this approach was deemed the best and utilised in our experimental setup as well. Hence, the beam source became decoupled from the acceleration and focusing, which greatly simplified fine-tuning of the gun. The electron source was therefore operated at a stable setting of V_{grid}=20 V and V_{anode}=200 V. When the accelerating potential V_{ee} was varied in the 25-1500 eV range, only the focus voltage V_f had to be varied accordingly to maintain the beam size in the 2–3 mm range. Finally, the cathode source voltage was varied between V_{es}=0.8 V and 1.2 V depending on the aim of the measurement: low-current SEY measurement, low-current ESD scan and high-current conditioning. The corresponding settings are summarised in the table for each measurement mode. The lowest feasible beam current of I_{beam} ≈0.5 nA was achieved with V_{src}=0.8 V enabling a non-destructive SEY energy scan, whilst a strong electron conditioning beam I_{beam} ≈2 uA was achieved with V_{src}=1.2 V. An even higher source voltage V_{src}=1.4 V resulting in an I_{beam} ≈4 uA was locally used for LE-ESD measurements to generate a measurable ESD signal even in the low-yield region around the threshold. It is important to note that the e-gun and the power supply have to be preheated, typically for a few hours at V_{src}=1.2 V, prior to data-taking in order to stabilise the emission current as well as the beam shape.

The characteristics of the electron gun are regularly verified to ensure its nominal functionality and to monitor possible ageing effects. Insofar, both ELG-2 gun units did not exhibit measurable ageing

effects that would deviate their V_{src}-I_{src}-$I_{emis.}$ characteristics from the factory-generated curve. However, a substantial difference is observed from one unit to another, which is likely caused by the lack of reproducibility in the manufacturing of the cathode disc assembly.

Parameter	**Unit**	**SEY scan**	**ESD scan**	**Conditioning**
e^- current I_{beam}	A	0.5 nA	2	2
Source volt. V_{source}	V	0.8	1.4-1.2	1.2
Spot size D_{beam}	mm	2	2	3
Dose/point	$C.mm^{-2}$	2.10^{-10}	2.10^{-6}	-
Dose/meas.	$C.mm^{-2}$	2.10^{-8}	7.10^{-5}	$\sim$mC.mm^{-2}
Time/point	s	2	4	-
Time/meas.	min	5	5	90
Energy spacing	eV	0.25-50	1-200	
Uncertainties				
Uncertainty systematic		3 %	10 %	
Uncertainty statistical		3 %	28 %	
Uncertainty combined (1σ)		5 %	30 %	13 % at Dose 25 % at $Q_{tot,j}$

Table 4.1: Parameters of different measurements and corresponding electron beam settings optimised for either very low dose (SEY and ESD scan), or high dose (conditioning).

4.3.1 Beam current measurement

Correct beam current measurement is the first essential component for both SEY and ESD measurements. Figure 4.6 on the left shows the same beam current measurement at different arrangements so as to prove that the beam current is well managed and contained where desirable. The beam current collected in a Faraday cup (FC) at the e-gun nozzle matches the one collected in the sample-collector system. According to repeated measurements, this holds true within 95+ % across the entire range of studied energies and beam parameters.

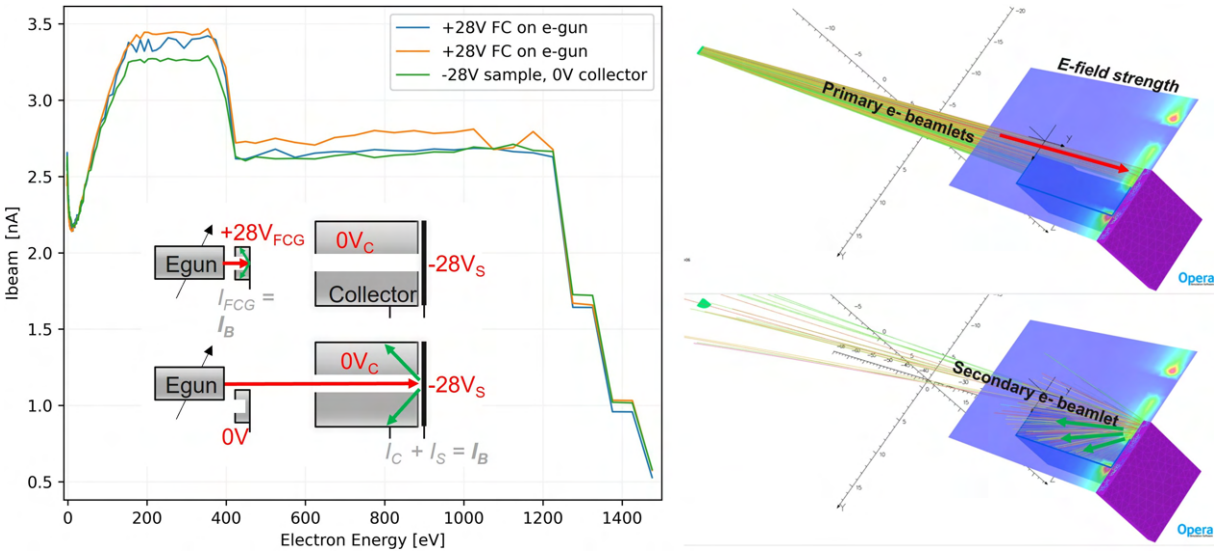

Figure 4.6: Left: Measurement of electron beam recollection efficiency (>95%) using the Faraday cup on the e-gun and the sample-collector system, acting as a Faraday cup that recollects secondary electrons (green). Right: OPERA simulation visualises the electrons in the geometry and electrostatic potential field of the sample-collector system. The symmetry of the arrangement is leveraged to simulate 1/4 of the geometry. The upper image shows the primary electron beamlets (red), the lower image depicts the effective trapping of secondary electron beamlets (green).

The right side of the same Figure 4.6 depicts an OPERA numerical simulation of electron beamlets trajectories moving in the gun-sample-collector system. A beamlet is a possible trajectory solved for a

charged particle moving in an electric field. To avoid misinterpretation, the link to the electron current is not via the density of beamlets, but via their colour code. The geometry was simplified and symmetry was leveraged to solve 1/4 of the problem. Top half shows the primary electron beamlets and the lower half shows the secondary electron beamlets. The simulation suggests that the collector effectively captures the majority of secondary electrons emitted from the irradiated sample. This is in agreement with the experimental observation on the left.

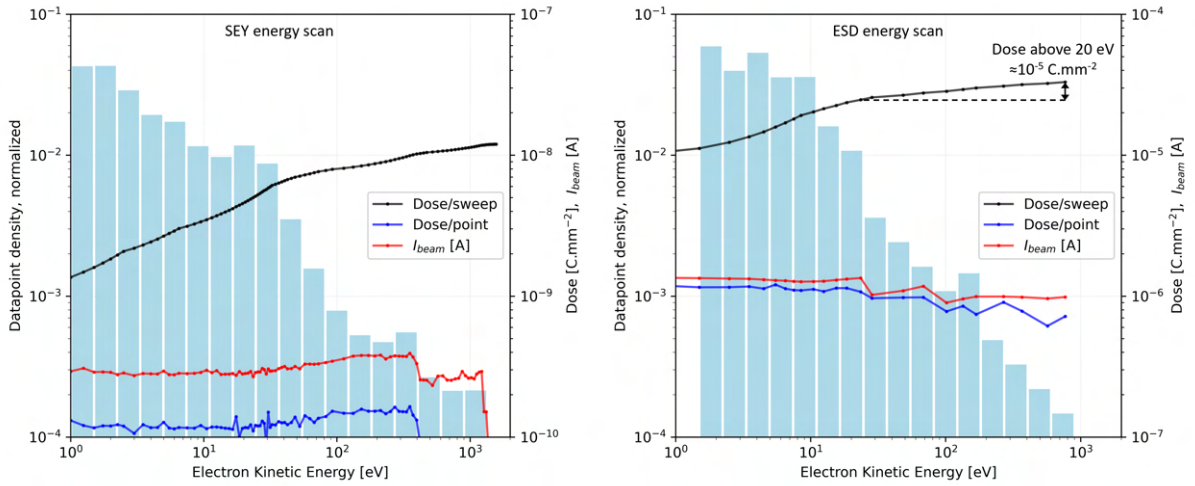

Figure 4.7: Left: Analysis of dose imparted during a SEY energy scan. Left axis shows the density of datapoints vs. primary electron energy. The right axis shows the beam current at a given datapoint, dose per datapoint and integrated dose per scan. Right: Identical analysis was done for an ESD energy scan. Details in the text.

Figure 4.7 shows an analysis of electron dose imparted during an SEY and ESD energy scans as a function of energy. The SEY scan is done with ∼5 nA beam current, which is non-destructive towards the sample and hence the datapoints can be spaced more densely, as visible in the plotted data. Meanwhile, the histogram follows a decreasing trend in the log-log scale, meaning that datapoints are logarithmically scarcer as the energy increases.

Contrary to the SEY measurement, the ESD energy scan represents a compromise between the beam current low enough to avoid the conditioning effect and at the same time high enough to generate a measurable ESD signal with a reasonably high signal-to-noise ratio (SNR). Hence, the beam current is set to $I_b \approx 1\mu$A, as discussed in detail in Section 4.16. The datapoints are also spaced more scarcely to optimise the imparted electron dose as much as reasonably achievable; e.g. compare the 0.25 eV spacing for SEY to the 1 eV spacing for ESD in the 0 eV energy limit.

As a result of this electron beam optimization, the dose imparted during a SEY energy scan remains at $10^{-8}\,C.mm^{-2}$ level, which is well within the initial flat plateau of an ESD conditioning curve, as described and discussed in Section 5.3.2, and annotated in Fig. 4.17. The ESD energy scan is measured at a total dose of a few $10^{-5}\,C.mm^{-2}$, while the dose of electrons with energy above 20 eV is only at $10^{-5}\,C.mm^{-2}$. Such dose only results in a minor conditioning effect, which, however, was tested not to interfere with the experimental results and conclusions.

4.3.2 Beam profile measurement

The Faraday cup duo mounted on the cryomanipulator far side allows for two types of beam profile measurements. Firstly, the current recollected on the e-gun Faraday cup agrees with the current read on the cryomanipulator FCs, amounting to 4.6 μA, as shown by the blue and black curves in Fig. 4.8. A small increase above that, along with the non-zero background, are assigned to the secondary electrons generated at a grounded part and recollected by the positive bias on the FC, an effect that can be disregarded. Further on, the geometrical profile of the two concentric FCs are marked by the black curve, having diameters of 0.5 and 5 mm. The inner FC is at +74 V potential and the outer at +46 V in order to unambiguously determine the flow of secondary electrons in the system.

The knife-edge scan technique, often used in laser technology, consists of traversing the beam across a step edge, essentially convoluting the beam profile with a step function. The beam current (black curve in Fig. 4.8) collected on both Faraday cups I_{FC1+2} increases as the beam gradually enters the 10 mm

wide FC, as marked by A,B,C in the graph and photo alike. Finally, the width of the ramp determines the beam size, which is the same in both X and Z transverse directions, demonstrating the beam profile symmetry.

The second method consists of scanning the beam across a 1 mm wide inner FC, essentially a pin-hole, once again convoluting the beam profile with a square window. When the raw signal (green curve) is deconvoluted by a 1 mm wide square window function, one obtains the pale green curve which should represent the beam profile. Unfortunately, the noise level is high at the input data and even higher at the output, rendering this technique less utile than the knife edge scan. This is only partly due to a non-square beam profile. Instead, the window function of the pinhole seems not to have a square shape.

Finally, by comparing the different measurement methods, the beam profile width converges at approximately 3 mm.

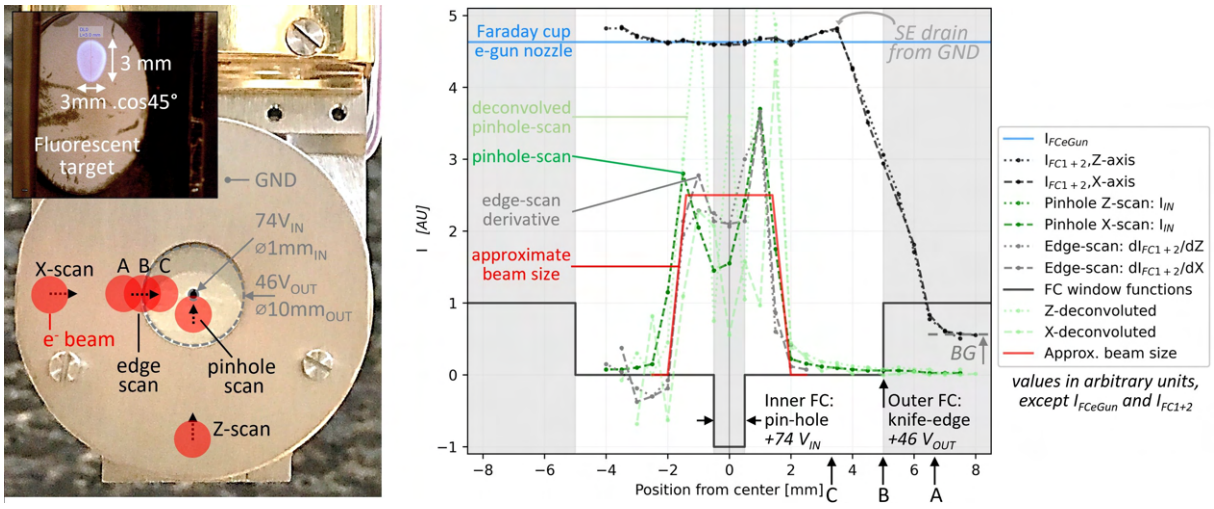

Figure 4.8: An exemplary scan of an electron beam profile (260 eV conditioning beam) in horizontal and vertical directions. The shapes agree in X and Y and also with visualisation on the fluorescent target. The beam profile during an energy scan sequence can be viewed here: video. See text for more detail.

Similar procedure was repeated for various electron beam energies. The resulting profile measurements were verified by visual observation on various fluorescent targets and also post-mortem on a locally discoloured conditioned surface. A combined uncertainty of ±10% can be estimated on the beam diameter. Compared to the uncertainty of ±5% on the beam current measurement, the beam-size uncertainty dominates, translating to some ±15% at 1 σ on the integrated electron dose. The electron flux uniformity, hence the local dose as well, is estimated to be of the same value.

4.4 Secondary electron yield measurement

4.4.1 SEY measurement routine

The SEY measurement in our experimental arrangement builds on two presumptions. First, the entire incoming electron beam current is considered to interact with the sample. Regardless of the chosen biasing scheme, the primary electron current is calculated as a sum of the two measured currents, i.e. $I_b = I_{beam} = I_{Collector} + I_{Sample}$. Second, incoming electron beam current are captured inside the sample-collector system and so are the secondary electrons emitted from the sample. Having the simultaneous measurement of both I_b and I_C allows the acquisition of a full SEY curve during a single routine. This also helps to avoid repeatability-related uncertainties linked to the e^- gun stability when the SEY is acquired in a two-step mode, i.e. by modifying the sample bias or inserting a Faraday cup to measure the primary electron beam. We estimate a combined uncertainty of about 5 % on the SEY value across the studied range.

Given the -28 V potential difference between the sample and collector used for SEY measurement, the secondary electron current direction is unambiguously given from the sample towards the collector. Both of these presumptions were experimentally verified to at least 95 %, as visualised in Figure 4.6. Hence the SEY can be directly calculated as follows.

$$\delta(E) = \frac{I_{Secondary}}{I_{Primary}} = \frac{I_{Collector}}{I_{Beam}} = \frac{I_{Collector}}{I_{Collector} + I_{Sample}} \tag{4.2}$$

When performing an SEY scan to measure the energy dependence, the datapoints are acquired in a discrete manner. The e-gun energy is ramped from 25 eV to some 1400 eV with increments of 0.25 eV around the work function edge, which are geometrically increased to 50 eV at higher energies. The beam current signal is quasi-rectangular with a 4 s periodicity, out of which a 2 s long idle window with no beam is dedicated to e-gun retuning and stabilization. The grid voltage is temporarily decreased from 50 V to 20 V to turn the beam on. A single datapoint is acquired during this 2 s long irradiation before the beam is shut off by increasing the grid voltage again. Such a routine repeats across the entire energy range and lasts about 5 minutes. For completeness, trials with continuous measurement mode also led to identical results. The upcoming ESD energy dependence measurement is done in the same spirit, except for a longer 8 s periodicity: 4 s long idle time to refocus the gun, followed by another 4 s long interval that allows the RGA signal to stabilise.

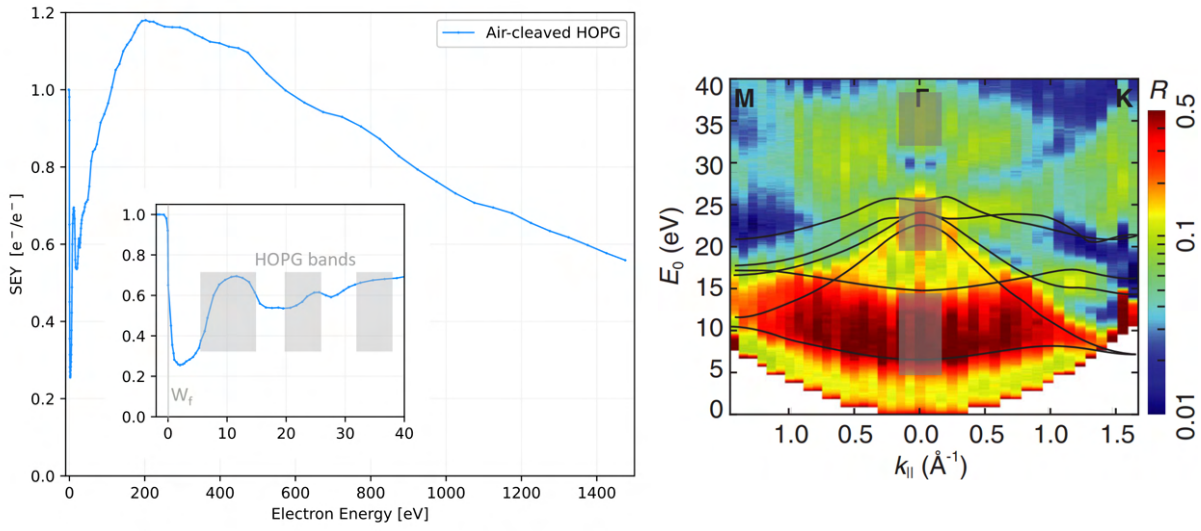

Figure 4.9: Left: SEY curve measured with Multisystem in the 0-1.4 keV range on a HOPG sample held at room temperature. This HOPG sample was exfoliated in air with an adhesive tape [220] and then electron conditioned for contaminant removal. This data is published as [A3]. Right: Band structure of graphene surface, as measured by Geelen et al. [56] and overlaid by calculated bands. Note the correspondence of the HOPG band structure with the peaks and valleys measured in the LE-SEY inset.

The SEY evolves with the primary energy, and so do the amplitudes and relative proportions of reflected, backscattered and secondary electrons. The incoming electrons can either be reflected or elas-

tically backscattered at the original energy, inelastically backscattered at intermediate energy, or create true low-energy secondary electrons. All these contributions have to be accounted for when designing the measurement. The electron energy distribution of secondaries, including the reflected and backscattered part, was measured by Cimino et al. [221] for the same technical-grade polycrystalline copper as in our present investigation. Similar results arise from calculations [222], i.e. reflected electrons and elastically backscattered, are predominant for primary energies below ∼20 eV, and true secondary electrons dominate above. Other materials than copper have indeed qualitatively similar characteristics. This also means that related systematic errors, if any, should be the same for other materials.

Savitzky-Golay (S-G) smoothing filter [223] was used to smoothen the discrete datapoints in a SEY energy scan. Indeed care was taken not to change the underlying signal in any way. These smoothed datapoints are then plotted as continuous lines, forming all the SEY curves. Occasionally, the raw datapoints are plotted too for illustration, such as e.g. in Fig. 5.1.

4.4.2 Low-energy SEY region

In order to reach 0 eV, as referenced to the sample vacuum level E_{vac}, a negative potential is imposed onto the sample via a set of batteries, biasing it to -28 V. This negative potential creates a retarding field for the incoming primary electrons and slows them to 0 eV, referenced to the sample. This experimental method was perfected by Gonzales&Cimino et al. [215]. It is possible to measure the work-function edge with this retarding bias method, see inset in Fig. 4.9. The energy spread of the thermionic electrons (width of the W_f edge), as well as the work-function W_f changes, can be measured using this method, as seen e.g. in Fig. 4.9 and Fig. 5.4. However, it is experimentally very challenging and outside of the research scope of this manuscript which focuses on other aspects of ESD and SEY measurements.

4.4.3 Reference SEY measurement on HOPG

The HOPG used as a SEY reference sample here is B-grade (reported lateral grain size 0.5-1 mm, mosaic spread angle of 0.8°, purity of 10ppm) exfoliated in air and only then inserted via the load-lock. It was scrubbed off contaminants by 300 eV electron irradiation prior to the reference SEY measurements, see Fig. 4.9. The orderly layered structure of HOPG is important because it gives rise to the fine structure in the SEY curve, particularly visible in the low-energy region. Amorphous graphite would not exhibit such behaviour, as was clearly demonstrated by Gonzales et al. [224] who studied SEY evolution while gradually disordering the HOPG by Argon sputtering. The peaks in the LE-SEY zoom, in fact, correspond to electrons reflected off the layered graphitic surface. These maxima of reflected electrons correspond to band gaps of the substrate material. This was readily illustrated by measurements of Geelen et al. [56] who report angle- and energy-resolved secondary electron measurement and show a high reflection peak between 5-15 eV, and around 25 and 35 eV taken on a few-layer graphene. A similar fine structure in the LE-SEY region is also observed in condensed gases, Section 2.23, where it is thought to be an imprint of an electronic structure of the cryosorbed gas, similarly to the HOPG here.

For completeness, vacuum-exfoliated A-grade HOPG exhibited the same fine structure, without needing as much electron conditioning as the air-cleaved HOPG to reveal its fine structure. The ESD energy dependence had a low SNR, but it reached a clear peak even below 200 eV, similarly to the SEY. This low peak position E_{max} is a signature of carbon's low atomic mass, granting the HOPG a low stopping power, as visible in the SEM images, Fig. 4.10. The ESD conditioning of the vacuum-cleaved HOPG, done at 300 eV, also showed very low ESD yields. Also, the amount of electrodesorbed gas (mostly H_2) was practically the same regardless of temperature, within a factor of 2 of a difference at the most. This points to two conclusions: that the hydrogen can freely diffuse across HOPG crystallographic planes, even at cryogenic temperatures. Second, the surface is clean of any other contaminants since the electrodesorbed gas only amounts to a monolayer coverage, excluding H_2. Further conclusions are hard to make given the low SNR of this low-yielding surface.

SEM analysis was performed ex-situ on the used HOPG sample to strengthen the understanding of the used reference substrate. The average surface predominantly present on most parts of the sample is well-defined, as seen in the top-left subfigure, which lacks any features on the flat HOPG surface. As discussed below in Section 4.7, such surface provides an excellent calibration reference for SEY in terms of its electronic properties and also for TPD given its well-defined hexagonal structure.

Though the most interesting features are the defects present around the edges of the sample where the structure is locally damaged, delaminated and plastically deformed. Top-left shows a typical flat well-

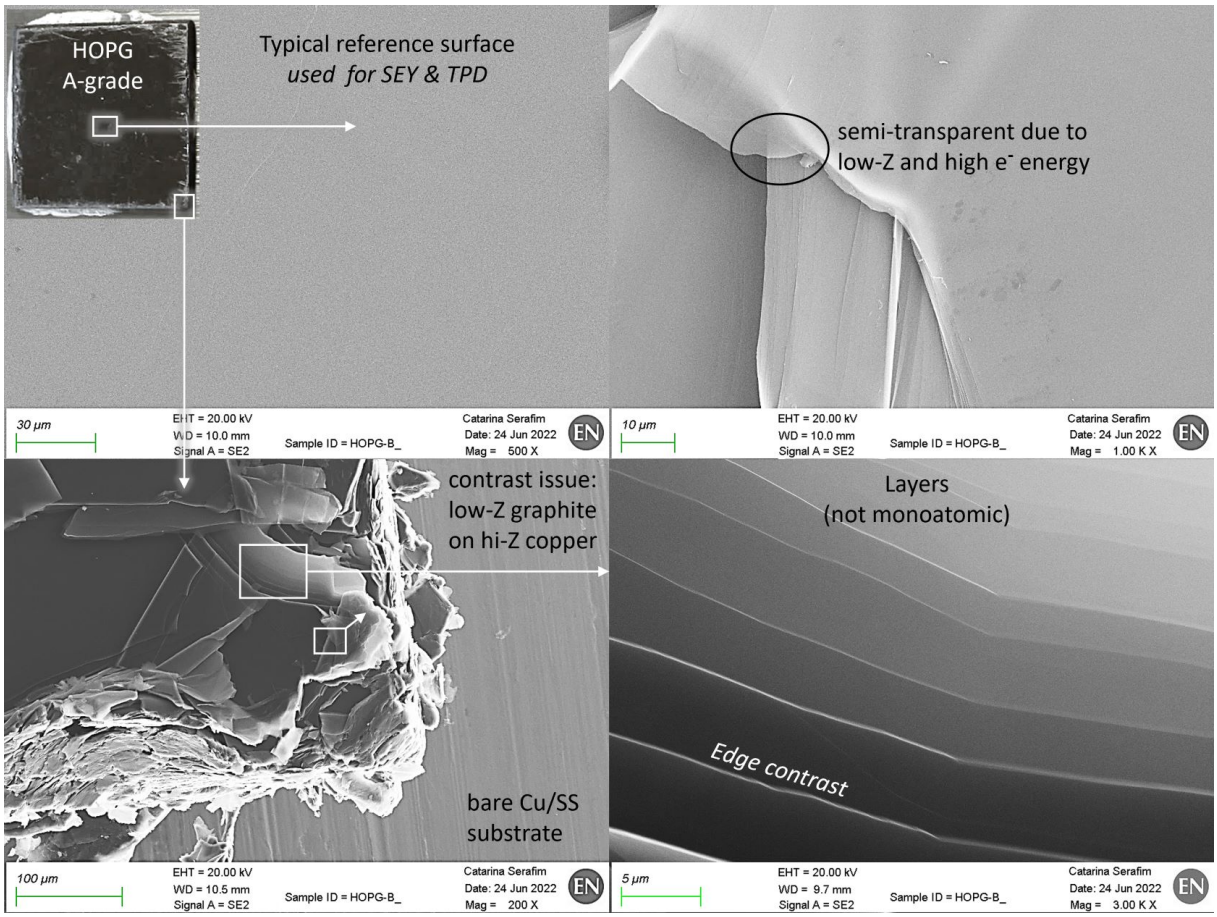

Figure 4.10: SEM images of the 0.1x1x1 cm large A-grade HOPG sample, epoxy-glued to a sample, as used in the experiments. Note the layered structure (lower-right) and the low-Z artefacts, such as partial transparency (top-right) and high contrast against Cu substrate (lower-left). Details are discussed in the text. SEM images were acquired by C.Serafim, CERN-TE-VSC-VSM, on FE-SEM Zeiss Sigma, kindly provided by CERN-EN-MME-MM.

defined surface covering the most of the delaminated sample used as SEY and TPD reference. Achieving a large flat surface typically requires a few delamination trials using a scotch tape, either in-air or in medium vacuum of the load-lock chamber. Top-right image illustrates the transparency of the thin low-Z graphitic layer to the imaging 20 keV electrons. The fact that even features lightly buried under a few graphene layers are visible points to the low scattering of electrons, resulting in high inelastic mean free path (IMFP). Low-left image shows a heavily damaged corner of the HOPG sample. Albeit not monoatomically thin, it demonstrates that the volume of the HOPG sample indeed has highly oriented layers graphitic. Low-right image shows an edge-type contrast created on the delaminated edges.

4.4.4 SEY angular dependence measurement

Despite the inherent design limitations of the experimental setup, a successful attempt was made to measure the incidence angle dependence of the SEY. The measurement was done with the cold-finger retracted away from the collector by about 15 mm and with the thermal screen in opened position, which makes the sample accessible from a 0–60° range.

The collector is maintained at a ground potential such that it electrostatically shields the beam, acting as a field-free guide for the medium energy primary electrons. As a result, the sample repulsive potential of -28 V (imposed to repel secondaries) does not deviate the beam until after it leaves the opposite opening of the collector. Indeed, this imperfect arrangement brings elevated systematic errors, but comparative measurements can still be made and give meaningful results, as shown in Section 5 below.

The beam settings are fixed, and the beam current I_{beam} is measured prior to the angular scan and assumed constant during the measurement. The short-term beam current stability was verified to be better than 95 %. The sample drain current I_{sample} is the second ingredient for SEY calculation, as follows:

$$\delta(\alpha) = \frac{I_{Secondary}(\alpha)}{I_{Primary}} = \frac{I_{beam} - I_{sample}(\alpha)}{I_{beam}} = 1 - \frac{I_{sample}(\alpha)}{I_{beam}} \tag{4.3}$$

The gun is set to 350 eV in this experiment and, given the -28 V sample bias, the primary electron energy is 322 eV at the sample. It is chosen as it is close to the peak SEY value and already represents the bulk-sensitive area of an SEY curve.

Moreover, the electron beam is sufficiently rigid at this energy, making it less prone to deflection and/or deflection. Indeed, the electron beam is expected to deflect when exposed to the asymmetric E-field created by the tilted sample. A rough estimation of this incidence angle error can be made by dividing the retarding/deflecting E-field strength by the electron beam energy: $28/350 = 0.08$. Hence, the incidence angle α differs by less than 10 % in the worst case, i.e. at high incidence angles. The more problematic part of the electron beam deviation due to the asymmetric E-field is that it does not impinge the sample in the original direct line of sight. Instead, it lands considerably off, which makes it difficult to know the exact spot position on the sample. These considerations represent the inherent limitation of this instrumental arrangement.

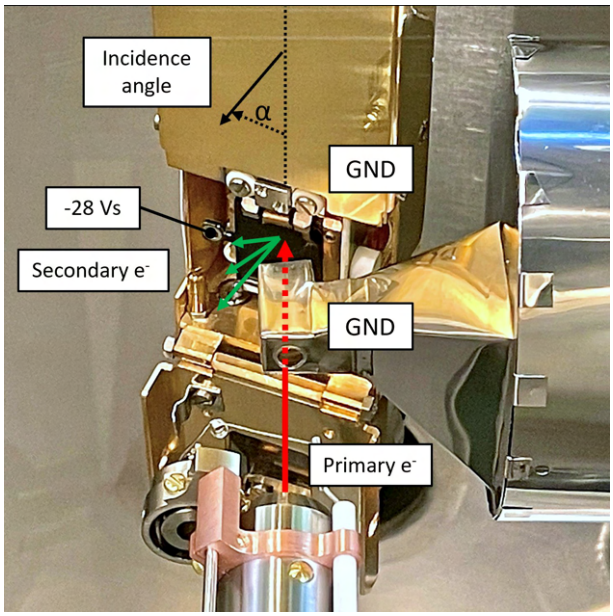

Figure 4.11: Experimental arrangement for angular dependence SEY measure at few hundred eV. The sample is put to -28 V to repel secondaries while all other components are at ground potential. The primary beam is shielded from the sample-generated electrostatic field until the beam reaches the collector's far side.

4.5 Desorbing gas flux measurement

Accurate measurement of the desorbing gas is not only necessary to both ESD and TPD measurements; it is of paramount importance, because the gas flux uncertainty is the main contributor to the uncertainty on the ESD yield. Hence, correct characterisation and calibration are crucial not only to drive down the error bars of the measured ESD yields, but also to increase sensitivity in regions where the signal is just barely over the noisy background. In an effort to increase the measurement precision, care was taken to calibrate the RGA sensitivities $k_{j,abs}$, as well as to carefully measure the pumping speed of the collector $C_j(M_j)$ for a range of masses, as follows.

4.5.1 Mass spectrometer calibration

The absolute calibration of the mass spectrometer is critical for partial pressure calculation and hence for ESD and TPD measurements too, shall they be quantitative. Except for CO_2 and H_2O, the RGA sensitivity k_j was in-situ calibrated for H_2 to be $\sim$0.5 $A_j/mbar_{H2}$ and lower for other gases of interest, N_2, CO, CH_4, C_2H_6 and Ar. Figure 4.12 shows an exemplary set of RGA calibration curves taken in SEM and Faraday modes using direct injection of pure gases into the RGA-housing collector. Note the strictly linear relationships representative of UHV conditions. The slope of the linear fit to the measured datapoints determines the RGA absolute sensitivity to the pressure of a given gas, as measured at a given m/q channel.

The amplification gain of the Secondary Electron Multiplier (SEM) at 1400 V is marked in the graph. The SEM comprises of 17 stages that share the 1400 V feed and divides it by a resistor series forming voltage divider to about 1400/17=82 V per one stage. An average SEM gain of 3200 is measured and when divided equally in between its 17 stages, the average gain per stage is $\sqrt[17]{3200} = 1.6$, being the SEY value at 82 eV of the SEM copper surface in an as-received state. However, the gain of SEM decreases with time in operation due to electron scrubbing of the SEM surface and along with it changes the SEM gain, an effect commonly known as the RGA ageing, [225]. This can be partly compensated by increasing the SEM voltage, which increases the voltage per stage and by doing so offsets the working point higher up on the SEY curve, resulting in higher electron multiplication. The calibration line for the Faraday mode makes an important reference, since it does not change with time, as opposed to SEM mode (presuming the RGA ion source does not age). For completeness, the systematic uncertainty on the RGA sensitivity was guesstimated at a conservative 20 %, which is mostly driven by the imprecision in its measurement, as well as it's day-to-day variation. The SEM ageing per se was not clearly observed during the runs.

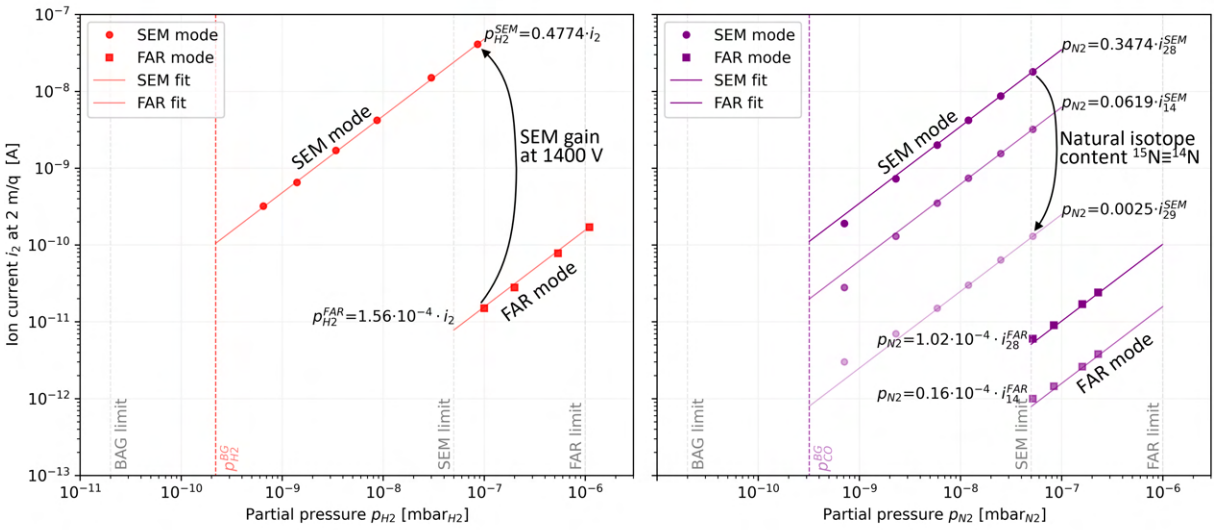

Figure 4.12: RGA calibration curves for H_2 and N_2 molecules. Left: Calibration for the H_2 molecule. Its molar mass of 2 g/mol puts it on the RGA channel 2 m/q in its single ionised state. Right: Calibration for N_2 molecule, molar mass 28 g/mol, in its single and double ionised states N_2^{1+} and N_2^{2+}, found at channels 28 and 14 m/q.

The measurement for N_2 also shows a trace amount of naturally occurring isotope ^{15}N≡^{15}N found at channel 29 m/q, marked by a curved arrow in the graph. Similar measurements were also made

for other gases of interest with the results summarised in Table 4.2 below and in the graph in Figure 4.13. The datapoints are scattered because of two distinct reasons. First, the electron-gas ionization probability differs for each species and generally increases with mass. Second, the RGA transmission factor scales with 1/M, bottlenecking the RGA sensitivity for heavier molecules. As a result, there is a positive mass-to-sensitivity correlation for the BAG, but a negative one for the RGA.

Due to an inherent difficulty, relative sensitivities for CO_2 and H_2O were acquired from multiple other resources in the form of a relative sensitivity and converted to absolute sensitivity using the known ones for H_2, N_2 and CO. The sensitivity values for CO_2 and H_2O obtained in this way were in good agreement with values that were guesstimated from the known ionization probability of other gases by applying a correction for the different ionization probability and 1/M mass-dependent transmission factor. This approximation produces a reasonable estimate of the k_{CO2} from another known absolute sensitivity, take that of CO as an example. The CO sensitivity k_{CO}=0.27, scaled by the ionization probability ratio of 1.05/1.42 (at 100 eV), corrected for the mass difference ratio of 28/44, one obtains k_{CO2}=0.13 - a ballpark figure reasonably close to the what was adopted from ex-situ measurements.

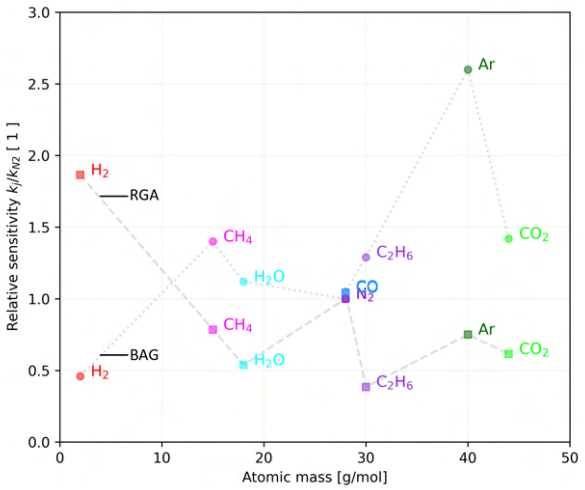

Figure 4.13: Relative sensitivities of RGA and BAG, referenced to N_2 and plotted as a function of mass.

Gas species	Ionic states & fragments	Channel [m/q]	k_{abs} [A_j.mbar$_j$]	$k_{rel,i/N2}$ [1]	*Comment*
H_2	H_2^+	**2**	**0.485**	1.85	
H_2O	H_2O^+	**18**	**0.14**	0.54	*Adopted value*
CH_4	CH_4^+	16	0.236	1.28	*Cross-talk to CO→O^+*
	CH_3^+	**15**	**0.204**	1.09	
CO	CO^+	**28**	**0.27**	1.04	
	O^+	16	0.014		
	C^+	12	0.027		
N_2	N_2^+	**28**	**0.26**	1	**Reference baseline**
	N_2^{++}	14	0.045		
$^{15}N_2$	$^{15}N_2^+$	**30**	**0.26**	1	*Corr. for $^{14}N_2$ content*
	$^{15}N_2^{++}$	15	0.045		
	$^{14}N_2^+$	28	0.001		*Residual $^{14}N_2^+$ content*
C_2H_6	$C_2H_6^+$	**30**	**0.1**	0.38	
	$C_2H_4^+$	28	0.5	1.92	*Cross-talk to CO*
	CH_3^+	15	0.05		
Ar	Ar^+	**40**	**0.195**		
	Ar^{++}	20	0.036		
CO_2	CO_2^+	**44**	**0.16**	0.62	*Adopted value*
	CO^+	28	0.01		*Cross-talk to CO*
$^{13}CO_2$	$^{13}CO_2^+$	**45**	**0.16**	0.62	*Adopted value*
	$^{13}CO^+$	29	0.01		

Table 4.2: RGA calibration data acquired by direct gas injection and analysis of SEM gains and fragmentation patterns used for the gas load calculations. The sensitivity $k_{abs,i}$ is calculated for each fragment of the injected molecule, as referenced to its partial pressure p_i measured by an ex-situ calibrated BAG. Channels and sensitivities used for partial pressure follow-up are marked bold for each gas of interest.

The gas injections allowed us to clearly determine the residual gas composition of this baked UHV system and identify the main contaminants and their corresponding fragmentation patterns. Acquisition of a full mass scan is a matter of tens of seconds with this type of RGA, even at the lowest precision, which makes it impractical for fast time-dependent measurements. This renders it impossible to do a full

analytical spectrum decomposition for the kinds of measurements to be done.

An experimental goal emerged to obtain a seconds-long time resolution of the partial pressure monitoring, either to enable modulating the beam with a few-second periodicity or to measure transient effects. Hence, the necessity for fast sampling in a few Hz range gave rise to the need for this simplistic approach and a single mass-to-species conversion. The calculated absolute sensitivities k_j for each gas species' major peak are directly used to convert the measured RGA current into partial pressures. This simplistic conversion builds upon a presumption of no cross-talk between the measured m/q channels, which is reasonably valid in our experimental conditions. In this light, a selection was made as follows of the RGA channels to follow that are well representative of particular gases and have a little cross-talk, i.e. contribution from fragments of other molecules. Shall this not be the case in some particular measurements, care was taken to modify this selection accordingly. For completeness, trials to remove the small remaining cross-talk between channels did not bring a considerable improvement and instead brought an additional source of noise and uncertainty into the data and were therefore omitted.

- Channel 2 m/q monitors the H_2, presuming that contributions of from H_2O and CH_4 to the H_2 peak are negligible.
- Channel 15 m/q monitors the CH_4 by using its CH_3 fragment, presuming the absence of heavier organic compounds that fractionate into the CH_3
- Channel 18 m/q monitors the H_2O.
- Channel 28 m/q monitors the CO, presuming that contributions from CO_2 and N_2 and the C_2H_6 peak are negligible.
- Channel 30 m/q monitors the C_2H_6. Despite of its molecular mass of 30 g/mol, the peak is predominant at 28 m/q. The same channel is also used to monitor $^{15}N_2$ when necessary. In all other circumstances, this contribution is subliminal.
- Channel 40 m/q monitors the Ar, with no other considerable contributors.
- Channel 44 m/q monitors the CO_2, again with little cross-talk expected.
- Channel 45 m/q monitors the $^{13}CO_2$, along with its ^{13}CO fragment at 29 m/q, are used in certain measurements.

4.5.2 Collector conductance characterisation

By directing the desorbed gas species towards the RGA positioned inside the collector, the gas can be analysed prior to being pumped away from the collector's inner volume. Moreover, the 4 mm hole being the only pumping port, the collector's closed geometry creates a conductance-limited system, with a geometry-restricted pumping speed. This not only decouples the collector's inner volume from the heavily cryopumped chamber but also invariably defines the pumping speed across all experiments and irrespective of possible variations. The differential pumping also rules out possible sample contamination by electron source degassing. Aside from the RGA, the collector houses a Bayard-Alpert Gauge (BAG) that only serves the described calibration purposes and is switched off during regular operation to reduce outgassing and prevent possible gas fragmentation, pumping, and a memory effect, all of which has been observed. A bakeout combined with electron conditioning of the inner surfaces ensures low thermal outgassing [226] and low stimulated gas desorption of the collector [179], further minimising the residual gas background, as detailed in the next section.

For completeness, the collector used here was recently redesigned towards the current Feulner cap style since our last publication [A4]. This upgraded design enhanced the sensitivity of desorption measurements, for both ESD and Temperature Programmed Desorption (TPD). As measured in Fig. 4.22, more than 2 orders of magnitude of gain were achieved by reducing the cryopumping of desorbed molecules onto the cryostat. Finally, given the collector's geometrical proportions, cryopumping on the cold sample can only lead to an underestimation of the measured ESD yield by a factor of 2 in the upper limit. This factor is given by the ratio of pumping to cryopumping speeds, both given by the two 4 mm holes. We indeed observe such transients in the early phase of electron conditioning, which is in agreement with Anashin's [190] and Malyshev's [173] observations and calculations. Besides this, a particle tracing simulation in Molflow+[227], see Appendix 6.25, was performed to support our understanding of the collector vacuum dynamics and the experimentally observed behaviour.

To calculate the gas load Q_j [mbar.l.s^{-1}] of a species j desorbed in the collector, the pumping speed of the collector C_j [l.s^{-1}] is necessary. Also necessary is the change in partial pressure Δp_j, calculated from the known RGA absolute sensitivity k_j [A.mbar^{-1}] and measured change in the RGA current Δi_j

[A] at a channel representative of the given gas species j. Both the conductance and the RGA sensitivity are calibrated in-situ by a gas injection at room temperature, as follows.

$$Q_j = C_j(M_j) \cdot p_j = C_j(M_j) \cdot k_{j,abs} \cdot \Delta i_j \tag{4.4}$$

A known conductance $C_{j,ref}$ is used as a calibration reference to determine the collector conductance C_j, as shown in Fig. 4.3. The calibration is performed for each gas separately for gases across the interesting mass range, i.e. 2-50 m/q. A micro-leak valve is set to deliver a constant flux Q_j of a single gas species in the 10^{-8} mbar.l.s^{-1} range, which is then injected alternately through the collector conductance C_j or through a reference conductance $C_{j,ref}$. This reference conductance is calculated analytically, corrected for the Clausing factor and the result checked against a COMSOL simulation. Since the gas flux Q_j is kept constant during the calibration, the resulting pressure differences Δp_j and $\Delta p_j, ref$ are in the same proportion as the conductances C_j and $C_{j,ref}$. The H_2, CH_4, H_2 and Ar gases were injected to measure the conductance C_j as a function of molar mass M_j, uniformly covering the relevant mass/charge range from 2 m/q to 40 m/q. The measured conductances C_j are then fitted with a scaling factor inversely proportional to the molar mass $(1/M_j)^{1/2}$ to obtain a function of C_j =f(M_j) used further on for the gas load calculation. This calibration procedure for C_j = f(M_j) results into a pumping speed of 21.8 l.s^{-1} for H_2 with a systematic uncertainty of ~20 % across all masses. This approach delivers a more robust estimator for the mass-dependent collector conductance than what could be achieved by simply measuring the H_2 conductance and down-scaling it by $(2/M_j)^{1/2}$ for heavier gases.

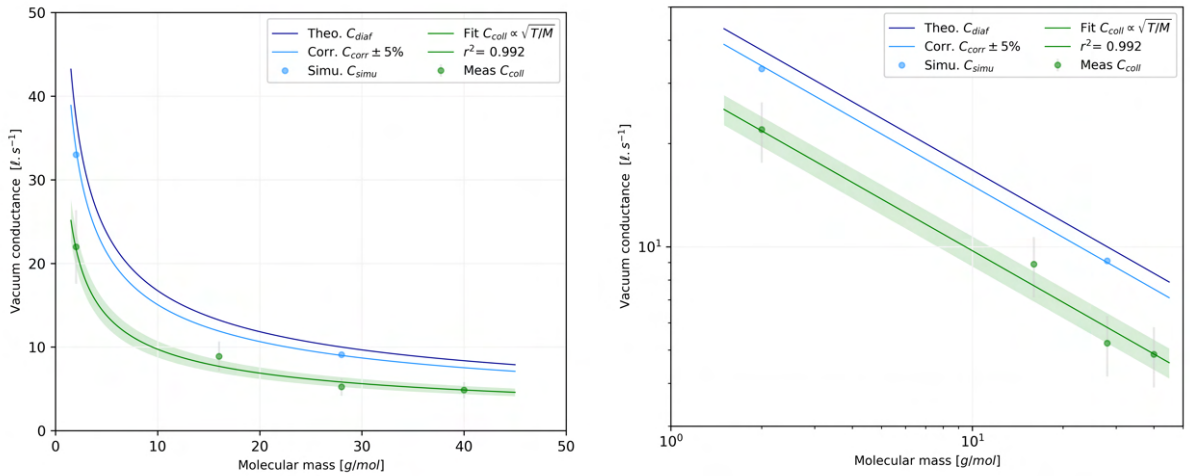

Figure 4.14: Calibration of the collector's vacuum conductance. Four non-sticky (short sojourn time) gases (H_2, CH_4, $^{15}N_2$, Ar) were used to cover the range of molecular weights relevant for the envisioned ESD measurements. The curve fitted through the measured datapoints features a lesser uncertainty than the discrete datapoints alone. Left: Linear scale. Right: Log scaling offering a linear projection.

4.6 Electron stimulated desorption measurement

Molecules desorbed from the sample by incoming electrons are partially contained within the molecule collector and guided to the absolute-calibrated mass spectrometer, which measures partial pressure of desorbed gas species. The sample is negatively biased, so that incoming electron beam is retarded, possibly to 0 eV of kinetic energy. The closed geometry of the molecular collector contains the emitted secondary electrons, which are then measured by a micro-ammeter.

4.6.1 Transient effects in ESD measurement

Figure 4.15 plots a system response to a step change, realised be turning the 300 eV electron beam on (left) and back off (right). In turn, transients of partial pressures are measured by the RGA, as the desorbed gases enter the collector, fill its volume, and build up a signal in the RGA.

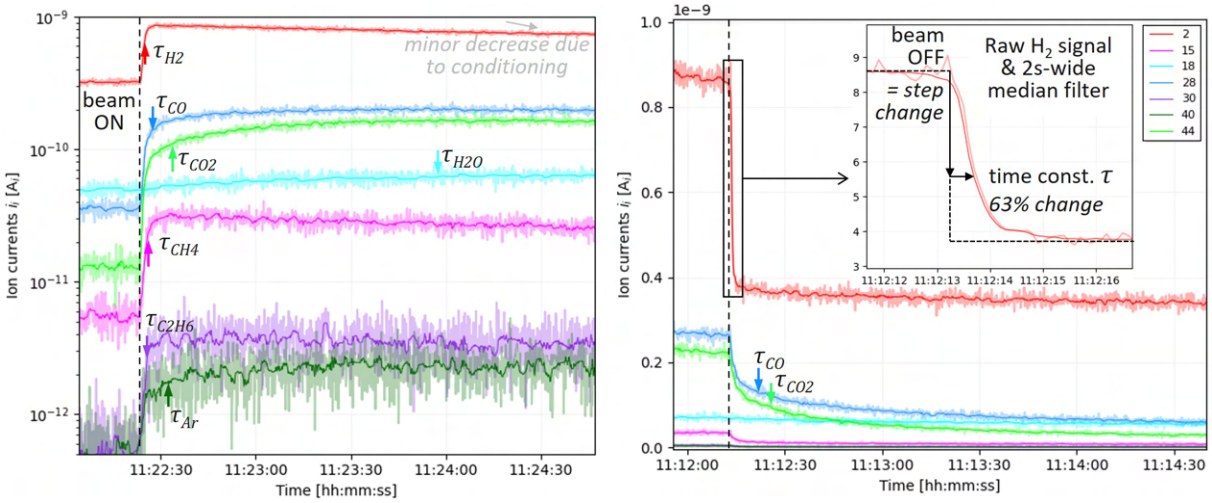

Figure 4.15: Transients of electrodesorbing gases measured by the RGA, as produced from a warm sample by 300 eV irradiation of a semi-conditioned surface. The raw signal was smoothed by a median filter with a 2 s-wide sliding window with. The water signal was granted an additional 3 s-wide filter pass. The approximate time constant locations are marked by arrows for each mass.

This system behaves like a first-order proportional system with no time delay, which can be characterised by a time constant τ and a gain (prop. to ESD yield). Current for each mass exhibit particular time constant τ_j as marked by arrows at approximate time constant locations marked in the Figure. For completeness, both linear and logarithmic representations are shown, and both exhibit the same time constants. The inset shows the time constant identification for H_2 signal. To facilitate the signal interpretation, the raw signal was smoothed by a median filter with a 2 s long sliding window. The filter window was chosen as long as possible, to reduce the noise, but not too high to remove features of the signal (such as peak cut-off). The median filter was chosen as opposed to mean, because it is a more robust estimator for non-Gaussian distributions (and the RGA signal does not exhibit a Gaussian-type of error distribution). The water signal was granted an additional 3 s long filter pass. The general trend visible in the measured transients is that heavier and stickier gases have longer time constants, due to their slower propagation throughout a vacuum system.

Gas species	Mass [g/mol]	Time constant [s]
H_2	2	0.5
CH_4	16	2
H_2O	18	90
CO	28	4
C_2H_6	30	1
Ar	40	2
CO_2	44	6

Table 4.3: Approximate time constants extracted from the above measurements done in a warm system.

The table summarises approximate time constants extracted from the above data for each gas. Taken from the opposite end, the ESD yield measured during a 4 s-long sampling window can only be underestimated by a factor of ∼2 due to the slow signal ramp-up. The most affected are CO, CO_2 and H_2O. Yet, this is a theoretical upper limit and in practice is much smaller due to the signal build-up during the previous pulse and not fully recovered background level. Hence, this effect is quantified but is not corrected for when routinely calculating the ESD yield.

4.6.2 ESD signal linearity

Bearing in mind the theoretical introduction 2.5, the RGA signal of the electrodesorbing gas should be linear with respect to the impinging beam current I_b, which means that the ESD yield η_e is constant (slope of the line) regardless of the beam current. This was verified and illustrated in the left side of Figure 4.16.

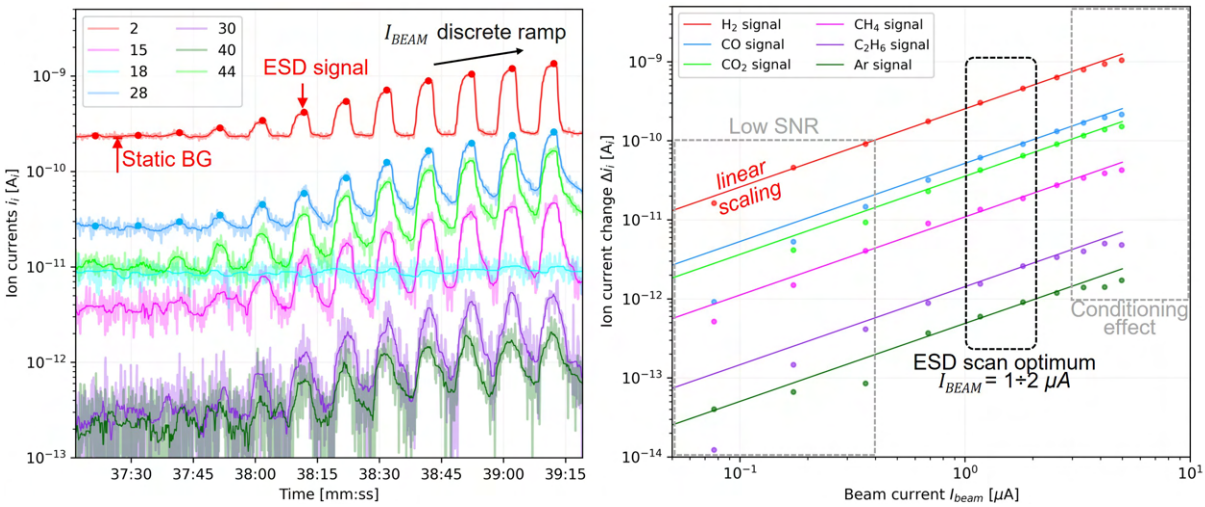

Figure 4.16: Left: RGA signal I_i of electrodesorbing gases produced by 300 eV electrons with a beam current discrete ramp. The raw RGA signal was smoothed by filtering with a 2 s wide sliding window with a median estimator. The water signal was granted an additional 3 s-wide filter pass. Right: Linear dependence of ESD signal and the beam current I_b.

At low I_b currents, the signal-to-noise ratio (SNR) is too low to obtain a precise measurement. The ESD signal measurement is actually limited by signal-to-noise, as opposed to the signal-to-background ratio that can be easily subtracted. On the contrary, this low-beam current region is ideal for a SEY measurement, shall it be non-destructive. A sublinear departure from the linear trend is observed at high I_b currents, which is a sign of the electron conditioning effect. This is a region to avoid in an ESD scan, however, a region to be in during a conditioning measurement. Shall this departure be superlinear, this would either point to beam-induced heating resulting in a combined thermal desorption and electron desorption, with a possible contribution of thermally-enhanced ESD. The superlinear dependence could also points to more than 1 electron excitation contributing to the gas desorption via DIET mechanism, which would contradict the presented theoretical understanding.

4.6.3 ESD yield calculation

The above-described system allows the ESD yield measurement via experimentally accessible values of primary electron beam current I_b and change in RGA current i_j. The remaining terms are also known, such as the ambient temperature of the collector $T = 300$ eV to which the desorbing molecules thermalise, hence no need for thermal transpiration corrections. The calibration process for the collector molecular conductance $C_j(M_j)$, was described and plotted in 4.14 to be 21.8 l/s_{H2} and is scaled with $(T/M)^{1/2}$ for ESD yield calculation of a given species. With this information at hand, one can calculate the fluence of molecules leaving the sample $\dot{N}_j$ as a direct consequence of the incoming number of electrons per unit of time $\dot{\Gamma}_e$, as follows. The beam current is calculated as a sum of sample and collector currents $I_b{=}I_C + I_S$ and divided by the unit charge q_e, the electron flux is obtained: $\Delta(I_b)/q_e = \Delta(I_C + I_S)/q_e = \dot{N}_j$. Similarly, the molecular flux can be calculated from the known $\dot{N}_j = C_j(M_j).(\Delta p_j)/(k_B.T)$, where all values are either directly measured, known or given. The ESD yield for a given gas species is readily

obtained by dividing these two terms. Indeed, all measured values are appropriately low-pass filtered and the static background is corrected before the input.

$$\begin{aligned} \eta_j &= \frac{\dot{N}_j}{\dot{\Gamma}_e} \\ \eta_j &= \frac{C_j(M_j).(\Delta p_j)}{k_B.T} \Big/ \frac{\Delta I_b}{q_e} \\ \eta_j &= \frac{C_j(M_j).(\Delta i_j.k_j)}{k_B.T} \Big/ \frac{\Delta(I_C + I_S)}{q_e} \end{aligned} \tag{4.5}$$

The detailed technical characterisation provides all information necessary for evaluating the ESD yield as a function of various parameters, such as energy, dose and temperature. The experimental details regarding the actual ESD measurement are also presented in a recently published technically-oriented article [A3] and at conferences [A5, A8].

4.6.4 ESD measurement routines

The ESD is typically measured either as a function of energy or dose as described below. The dose-dependent measurement is experimentally simpler in the sense that it requires only one stable and well-defined electron beam setting. The ESD conditioning curves in the following Fig. 4.17 were taken on two copper samples at two experimental settings. The left one is taken with +46 V_S bias, whilst the right one is measured with a -28 V_S bias. The negative bias allows a simultaneous SEY measurement but results in a higher dynamic background that corrupts the measurement of low ESD yields typical for high electron doses and/or low energies, as schematised in Fig. 4.18. Both measurement schemes provide a set of ESD conditioning curves that exhibit the same behaviour, despite different sample biases used. The sole exception is an elevated dynamic background at around 10^{-2} H_2/e^- coming from the secondaries desorbing gases from the collector. The same case can be made for other typical residual gases. The electron gun energy was indeed compensated for the different sample biases. The added advantage of a negative sample bias is the simultaneous SEY measurement, indicative of the immediate surface conditioning state. Further tests were done with variable beam current density by acting on the beam current and on the beam size and revealed no measurable difference in the acquired conditioning curves.

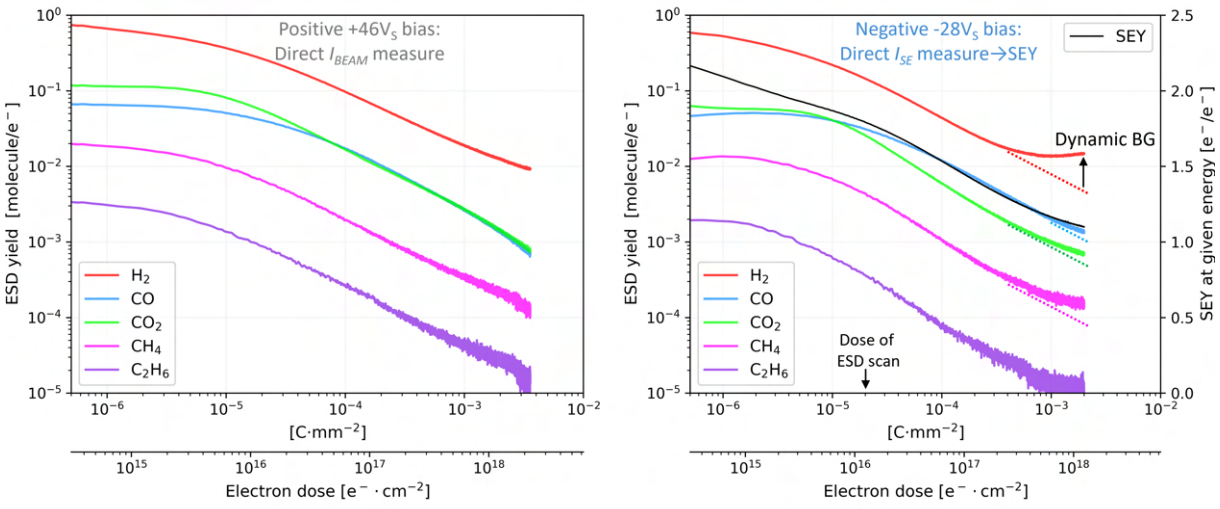

Figure 4.17: ESD conditioning curves measured on two different copper samples held at room temperature and irradiated with 300 eV electrons. One sample is LHC-grade copper colaminate, one is bulk Cu, but both come from an external supplier, were cleaned in isopropanol bath, stored in plastic and have the same 'history'. Left: Data taken with +46 V_S bias. Right: Measured with a -28 V_S bias.

There are two types of ESD measurement routines that were commonly executed. First is the dose-dependent 'electron conditioning' measurement which is experimentally easier and consists simply of an extended sample irradiation at a given energy and monitoring the ever-decreasing desorbing gas. The only

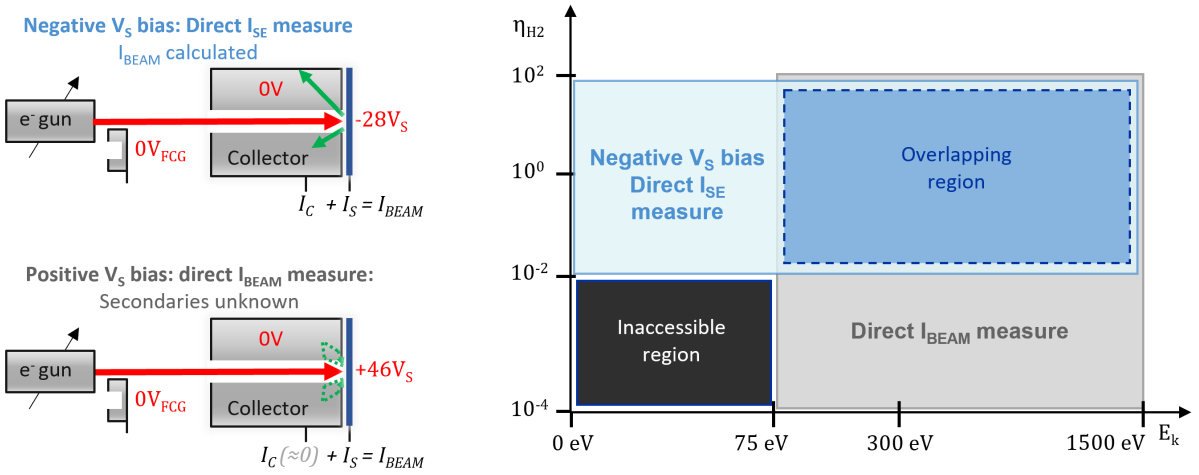

Figure 4.18: Two different biasing schemes for ESD measurements. -28 V_S sample bias allows measuring ESD and SEY simultaneously down to 0 eV at the cost of an elevated background. Biasing at +46 V_S minimises the ESD background but limits the primary energy to about 75 eV and offers not simultaneous SEY measurement.

experimental challenge is to maintain a stable beam and well-defined beam spot to achieve a uniform electron dose. The second is energy-dependent ESD measurement which is done in the same discrete manner as the SEY measurement routine detailed in 4.4. The sole difference from the SEY energy scan is the 8 s long periodicity for the ESD energy scan. This 4 s-long irradiation window (followed by 4 s-long idle time) is required to allow the RGA signal to stabilise in a new dynamic equilibrium before a datapoint can be recorded. Once again, the energy spacing between the datapoints is logarithmically varied from 1 eV at low energy, around the desorption threshold, to 200 eV at high energy. A comparison is made in Figure 4.7 and summarised in 4.1, which shows the typical currents, doses and datapoint densities for SEY and ESD energy scans.

4.6.5 Background signal mitigation

Background mitigation made a considerable portion of the research effort that went into this experimental setup. Various approaches were adopted when dealing with different types of background, with much inspiration drawn from the rigorous experimental work by Peterson et al. [228]. Each potential source of background should be identified, quantified and mitigated. If persistent, it is either accounted for or proven negligible in the final result, hence not worth the effort.

Static background is simply present in every experimental layout. Needs to be minimised by a proper bakeout, in-situ electron preconditioning of surfaces irradiated by stray electrons. The advantage is that the static background can be *simply* accounted for by calibration and/or corrected by subtraction. It can be further differentiated whether the background drifts, or if it is time-invariant.

Dynamic background scales (typically linearly) with the primary electron beam current and as such can not be compensated by increasing the beam current. Instead, the dynamic background should be minimised by optimising the experimental conditions, such as good beam focusing, capturing stray electrons, imposing appropriate biases, preconditioning of surfaces, etc.

Different sources of background were investigated and mitigated by adjustments to the experimental setup. Finally, a conservative approach was adopted such that the static background is measured prior to each measurement and subtracted in the post-mortem data processing. However, the sensitivity for ESD yield measurement is under some scenarios (low yields typical for high electron doses and/or low energies) limited by the dynamic background caused by secondary and backscattered electrons impinging onto the collector's inner surface. For this reason, the collector is spot-welded from a 0.1 mm thin stainless steel sheet, which after proper degassing presents a very limited reservoir of desorbable gases, as shown by Nemanic&Setina[226]. The sheet was cleaned, welded, cleaned again, baked, and electron conditioned at high energies and doses to minimise the gas desorption, both thermal[226] and electron-stimulated one [166]. As a result of this careful commissioning procedure, the ESD yield measurement is only limited by dynamic background at $\sim 10^{-3} H_2/e^-$ when using the -28 V_S bias. This background is in correspondingly lower ranges for other less abundant gases: $\sim 10^{-4}$mol/e^- for CO, CO_2 and H_2O and $\sim 10^{-5}$mol./e^- for CH_4,C_2H_6 and Ar. This background is even lower, by about a factor of 10x, when using the +46 V_S bias

due to lower electron current arriving onto the collector.

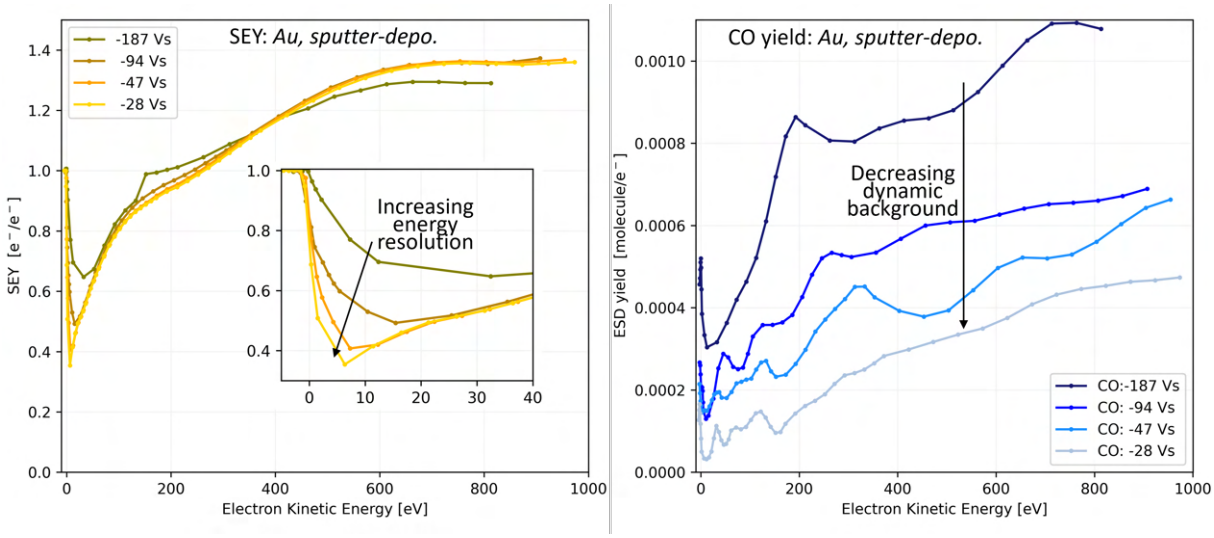

Figure 4.19: Optimization of the sample retarding bias by measuring a series of SEY and ESD curves. Clearly, the optimal results are achieved with the smallest applicable bias of -28 V_S.

To assess the dynamic background in an ESD energy dependence measurement, the same conditioned Au sample was chosen due to its low ESD yield. Hence, the dominant ESD signal originates from the secondary electrons emitted from the sample impinging the collector and desorbing gas. Their energy is given by the potential difference between the sample and collector, with the grounded collector, the V_C= GND. The accelerating potential is therefore given by the sample potential. By minimizing it, one also minimises the dynamic background, as seen in Figure 4.19 for CO yield. Hence, a -28 V_S sample bias and 0 V_C was chosen for SEY measurements, as well as ESD measurements, where SEY needs to be recorded simultaneously.

4.6.6 Low-energy ESD and threshold identification

For the ESD energy-dependence measurement, a procedure was developed to collect discrete datapoints at ever-increasing energies, as visualised in Figure 4.20. The procedure is the same as for the SEY energy dependence detailed in Section 4.4, except the periodicity consists of twice 4 s long interval, one with and one without a beam. The proof-of-concept measurement depicted in Figure 4.20 was done at 5 s time, before the parameters were optimised. Given that an ESD measurement is in principle destructive, the beam current and the datapoint density was minimised. This is to minimise the imparted dose and reduce the conditioning effect as much as reasonably possible without compromising the measurement quality. The top-left plot shows the beam current modulation and the sample and collector current varying in response to the changing energy. The bottom-left plot depicts the RGA currents of monitored masses 2, 28 and 30 that vary in response to the square wave-modulated electron beam. The dynamic background, originating at the collector, not the sample, is visualised and marked in the figure and imposes a detection limit, particularly on H_2 and CO. As shown in Figure 4.19, decreasing the retarding bias also considerably decreased this dynamic background, albeit not entirely, in line with the present understanding. On the contrary, the $^{15}N_2$ exhibits an high SNR when compared to H_2 and CO, being the reason behind employing it at the first place. This is partly due to a high ESD yield (common to cryosorbed gases) and low background at the 30 m/q channel.

The ESD yield on the right side is calculated with the static background subtracted from all measured datapoints, as denoted by the Δi_j in Eq. 4.5. Only the dynamic component is present as it illustrates the detection limit imposed by the dynamic background. Finally, the chart on the right plots the 'uncorrected' ESD yield a function of the primary energy. Savitzky-Golay (S-G) smoothing filter [223] was used to facilitate reading the trend, by effectively removing the noise while preserving detail of the dynamics behind it.

To reproducibly define the desorption thresholds visible in the right figure, one can consider the threshold to be where the first datapoint departs above the noisy background, i.e. above the dynamic background's mean value plus its standard deviation. Hence, the LE-ESD range shows desorption thresh-

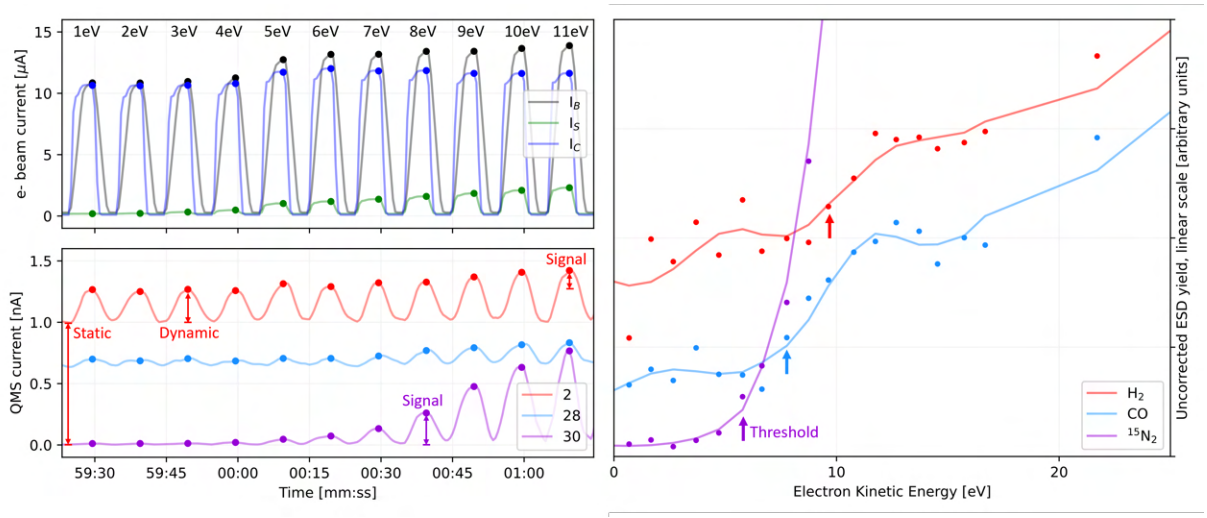

Figure 4.20: Raw data of a low-energy ESD yield measurement of partly conditioned copper surface held at 15 K with a 1 ML precoverage of $^{15}N_2$ used as a tracer. Top-left: Time series of e^- beam, sample and collector currents, all modulated to a square wave by gating via the grid. The kinetic energy is incremented by 1 eV each cycle. Bottom-left: Filtered RGA currents for channels 2, 28 and 30 m/q modulated in response to the Wehnelt cap-gated e^- beam current. Right: Datapoints and trendlines for H_2, CO and $^{15}N_2$ yields as a function of primary e^- kinetic energy. Arrows mark the desorption threshold energies for each gas. Note the noise and dynamic background levels of $^{15}N_2$ compared to H_2 and CO. This data is presented in [A3, A8].

olds of 6 eV for $^{15}N_2$, 9 eV for H_2 and 8 eV for CO, with all energies referenced to the sample vacuum level. This demonstrates the measurement method correctness because various other researchers obtain similar values; Rakhovskaia [229] reports 7 eV for multilayer N_2, and Billard et al. [172] give about 10 eV for H_2 and CO, albeit extrapolated. *Coincidentally*, Redhead's *'10-Volt effect'* is also related to the ESD threshold. The small differences can originate either in the different detection limits, or in a different experimental arrangement bearing different artefacts, or in different substrate-adsorbate systems.

4.6.7 Desorbing gas flux integration

For both the ESD conditioning measurement and TPD alike, the integral quantity of each desorbed gas species at a given relative time can be calculated $Q_j(t)$, Eq. 4.6, as well as its derivative, the desorption rate $dQ_j(t)/dt$.

$$Q_j(t) = C_j \cdot \int_0^t \Delta p_j(t)\, dt = C_j \cdot \int_0^t k_j \Delta i_j(t)\, dt \tag{4.6}$$

To facilitate the data interpretation, the absolute quantity is normalised by the surface area A it concerns. This time-dependent normalised quantity of gas, or its desorption rate, is then used in data visualisation as necessary, either as a function of electron dose $D_e(t)$, or time t. With a direct beam current measurement $I_B(t)$ and a known beam-irradiated area A_{spot}, the $D(t) = I_B(t).A_{spot}$ is known and $\eta_j(t)$ is also experimentally accessible.

In the calculation, the partial pressure signal, represented by the term $k_j \Delta i_j(t)$, is first corrected for the static background, which is presumed constant or sufficiently low during a measurement. A slow background build-up is visible during an ESD conditioning measurement, contributing to the sensitivity limitation at high electron doses and departure from a linear decrease. However, this doesn't contribute significantly to the integral amount, which is much more sensitive to the initial yield value. Finally, to calculate the integral quantity of desorbed gas $Q_j(t)$, the time-dependent partial pressure rise $\Delta p_j(t) = k_j \Delta i_j(t)$ is simply multiplied by the collector conductance for a given species C_j. This makes a more certain estimate of the desorbed gas quantity than integrating the product of ESD yield and the beam current, which unnecessarily brings more uncertainties into the calculation. The correctness of the suite of measurement procedures can be illustrated by the fact that after depositing 10 ML of CO, the same amount is recovered to within ~90 % by integrating the ESD signal during conditioning. Recovering the same amount of gas as dosed strongly indicates the correct RGA calibration, gas dosing, vacuum calculations, desorption signal integration, etc.

The dependence of $\eta_e(t)$ on $Q_j(t)$ is also interesting and is discussed below in Section 5.3 and presents an important insight into the conditioning stages.

The dose of 1 mC.mm^{-2} was selected for comparison for the following reasons. From an experimental standpoint, the ESD signal from the sample still dominates over the dynamic background, and the measurement can therefore be considered accurate and background-independent until this point. Most of the gas available to electrodesorption has already left the surface at this dose, and the ESD conditioning curve has steadily decreased following the power-law decay. From the applicability standpoint, assuming a 300 eV conditioning, the SEY has almost reached its ultimate conditioned value of $\delta_{max}1.1$ at a dose of 1 mC.mm^{-2}. Since at this point the δ_{max} is below the electron multipacting threshold and the EC activity has seized [11], the gas desorbed until this dose is all there will be desorbed.

4.7 Temperature programmed desorption

Given that cryogenic temperatures bring about inevitable residual gas adsorption on the studied surface, a method of characterising the adsorbed gas adlayer is a must. Temperature Programmed Desorption (TPD) is an experimentally accessible quantitative method of choice to do just that, as explained in Section 2.8. When used in combination with an absolute-calibrated Residual Gas Analyser (RGA), a TPD measurement can characterise the amount and adsorption energy of each cryosorbed gas species on a given surface until about 1 eV of adsorption energy (corresponding to 300 K). Coverages ranging from 0.1 ML (resolution limit of the pressure gauge on the gas injection) to about 100 ML (high peak pressure rise) can be studied.

The TPD measurement relies on the sample temperature reading and the desorption rate. Both quantities are easily experimentally accessible but require care in the calibration and data interpretation stage.

4.7.1 Sample temperature calibration

To determine the sample surface temperature $T_{Surface}$, two flag-type samples (Cu and SS) were equipped with Pt1000 temperature sensors. The sensors were glued by silver-filled (electrically conductive) epoxy atop the samples, as schematised in Figure 4.21. One lead of the temperature sensor was wired to the sample itself, while the second lead was positioned to make contact with the collector when carefully positioned atop. This formed an electrical circuit that enabled on-surface temperature measurement. At cold, the contact with the collector had to be brief (~1 s) and subtle not to conduct additional heat that would throw off the temperature measurement

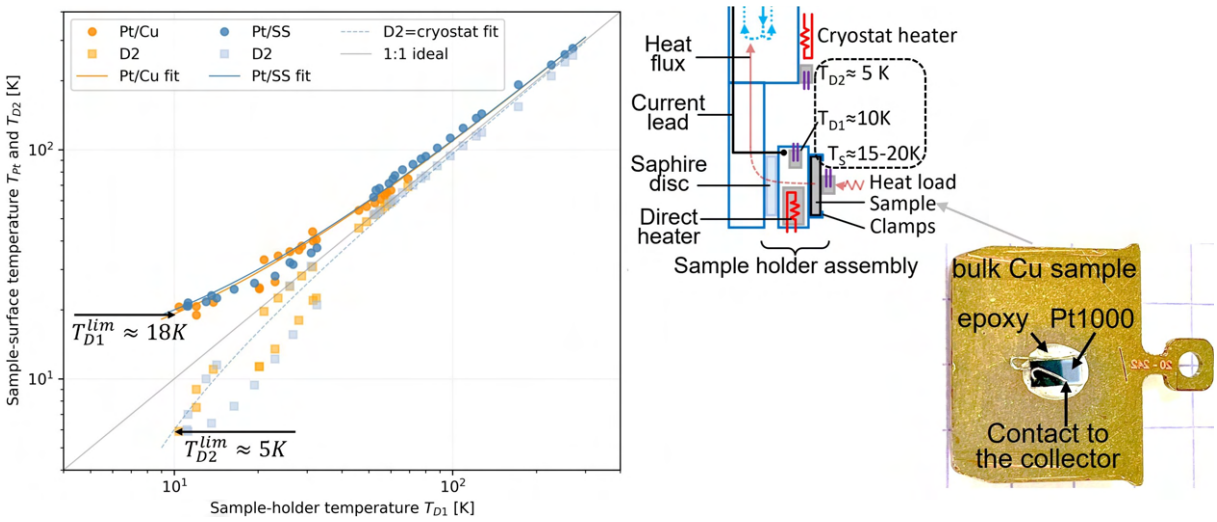

Figure 4.21: Calibration curves relating the sample holder temperature T_{D1} to that on a sample surface $T_{Surface}$ and on the cryostat T_{D2}. Detailed explanation in the text. The calibration curve for a Pt1000 sensor at cryogenic temperature was kindly provided by B. Jenninger, CERN-TE-VSC-VSM.

This investigation demonstrated heat load-induced thermal gradients along the thermal path from the sample to the cryomanipulator. Four different operating scenarios were measured: cool-down, nominal

cooling at T_{D1}=10 K, natural warm-up and forced stepwise heater-induced warm-up. While T_{D2} drops to about ≈5 K, the sample holder only cools to T_{D1} ≈10 K due to thermal gradients. For the same reason, the sample surface only cools to $T_{Surface}$ ≈18 K. All scenarios converged to the sample surface temperature $T_{Surface}$ being 5-10 K warmer than T_{D1}, regardless of the sample material. However, to avoid introducing an ill-defined temperature conversion, we express all the temperature-dependent quantities in terms of the actual measured sample holder-mounted temperature sensor T_{D1}.

Although the above-presented temperature calibration tests did not imply a significant temperature difference between surface temperatures of different materials, here we observe a slight difference in surface temperatures. As a result, the multilayer edge of a TPD curve onsets at a slightly different temperature when taken on a surface with different emissivity. This effect is even more pronounced when measuring TPD curves on samples that had to be glued on the flag-style sample, such as the HOPG, see Fig. 5.43. The additional interfacial thermal impedance added by the epoxy glue between the HOPG and its SS substrate offsets the leading edge of the multilayer desorption peak to ∼17 K, as opposed to ∼19 K for the bare copper sample. To conclude, despite the best efforts, the T_{D1} temperature readout is to be taken with a grain of salt as it tends to underestimate the surface temperature by few degrees K.

4.7.2 Gas injection procedure and calibration

The amount of injected gas can be measured in 2 ways, using the $V.\Delta p_i$ and by integrating the partial pressure rise in the collector $\int_{inj} p_i(t)\,dt$. However, this RGA integration was not used, as the RGA SEM was often switched off to avoid operating at high pressure during gas injection into the collector. Being left with the $V.\Delta p_i$ method, this gas amount is converted into coverage θ by normalizing via the amount of gas it takes to create a 1 monolayer-like TPD curve on a bare copper surface. This is the value in ML shown in the legend. Again, for simplicity, 1 ML is assumed to be 10^{15} molecule.cm^{-2}, irrespective of the surface state; smooth, rough or porous.

Then, the same partial pressure integration $\int p_i(t)\,dt$ is done during a TPD to see what amount of gas is cryosorbed on the sample. This is the amount of ML displayed by each peak. The TPD-integrated value $\int_{tpd} p_i(t)\,dt$ comes out systematically higher, typically by ∼10 %. The reason could be gas readsorption on the cold sample, leading to gas recycling within the collector instead of gas removal from the system. However, other experimental artefacts are also possible.

4.7.3 Collector efficiency assessment

Having developed the TPD method, the efficiency of the molecule collector can be assessed using a series of TPD measurements done at different positioning of the collector with respect to the sample. In this series, the TPD curve is always measured with the same gas amount (4 ML) predeposited over the same cold sample using the gas dosing tube (99+% efficacy) from Figure 4.3.

The default state is characterised by the absence of a direct line of sight from the sample to the collector and no pumping speed reduction between the sample. In other words, the view factor of 0 corresponds to the case of having no molecular collector and the RGA simply being present in the UHV chamber and exposed to the high pumping speeds. In an intermediate state, the collector is centred over the sample but positioned at 15 mm away.

In this slightly retracted position, the collector is in a direct line of sight and centred over the sample, yielding an intermediate view factor. This arrangement covers the peak of Lambertian cosine distribution of the desorbing gas and collects considerably more desorbing gas compared to the baseline.

Finally, the fully approached collector approaches a view factor of 1, effectively capturing the desorbing gas by restricting the pumping speed between the sample and the RGA. This was indeed the design goal and the signal increased by 2 orders of magnitude, compared to no collector. A gain of 150x was determined by numerically integrating the background-corrected TPD signal in 10-60 K temperature range. This signal gain roughly corresponds to the ratio of the main chamber pumping speed S_{eff} and the collector conductance C_{col}, being: 3500 / 21.8 = 160.

4.7.4 Desorbing gas flux integration

The TPD analysis results in a time- and temperature-dependent desorption rate $dQ_j(t)/dt$ which is plotted with respect to (linearly) time-dependent temperature T_{D1}. The integral is calculated in a similar manner as for the ESD measurement discussed around 4.6. The integrated quantity, for some

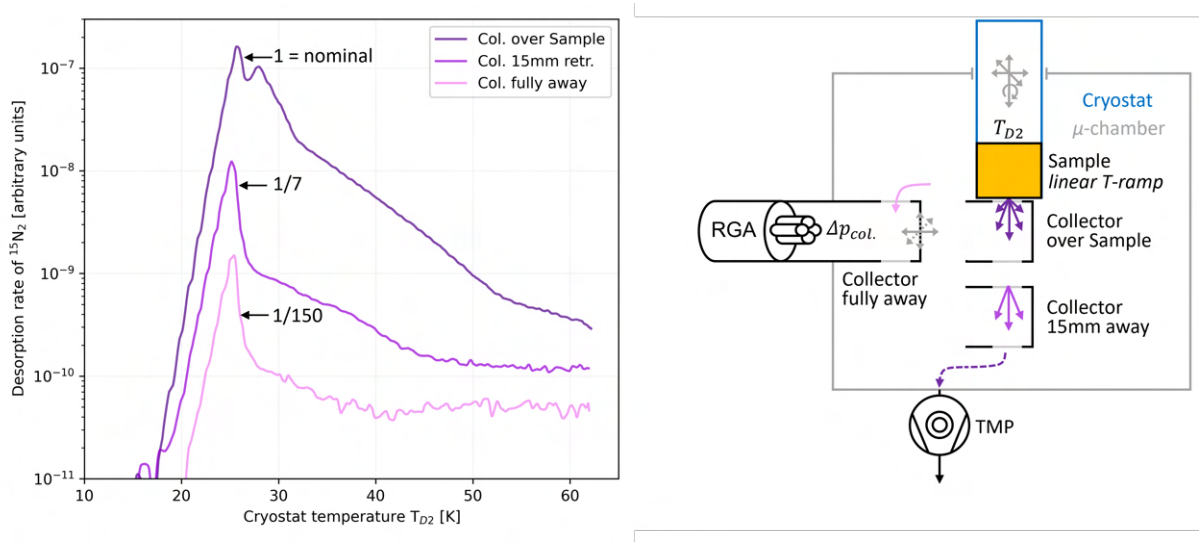

Figure 4.22: Gain assessment of the newly designed collector using a series of TPD measurements always done with the same amount of gas (4 ML) predeposited over the same cold sample using the gas dosing tube. The collector resumed a different position prior to each TPD being either directly over the sample, retracted by 15 mm but still with a high view factor, or entirely displaced away with zero view factor. This study used a temperature sensor T_{D2} mounted on the cryostat due to malfunctioning sample holder-mounted sensor T_{D1}. The double-peaked TPD curve is an experimental artefact caused by an imperfect temperature ramp.

reason, overestimates the amount of dosed pre-condensed gas. This is likely due to gas recycling on the cold sample during later phases of the TPD measurement, which can cause some molecules to be *counted twice*.

We also verified experimentally that the static background indeed remains constant throughout the measurement until about 60 K, at which point the gas desorbing from other parts of the warming-up cryostat dwarfs the signal. This experimental limitation has been battled by installing a direct resistive heater onto the sample holder, see scheme in Fig. 4.2, which successfully pushed this dynamic TPD background to higher temperatures, allowing us to characterise porous surfaces with higher desorption temperatures.

4.7.5 Reference TPD on HOPG

A series of TPD curves of $^{15}N_2$ on HOPG reference sample was acquired to verify that procedures used for gas injection and TPD measurement are correct, i.e. precise, repeatable and well-understood, in terms of the general behaviour, TPD curve shapes and T_{max} peak positions.

The linear and logarithmic plots in Figure 4.23 show TPD curves measured for 1-18 ML quench-condensed $^{15}N_2$ coverages onto a vacuum-cleaved HOPG held at T_{D1}=11 K. The resolution capability is illustrated by observing multiple desorption peaks at similar temperatures, e.g. the bilayer and multilayer adsorption regimes. An optimistic observer could even see a trilayer regime. The coalescent leading edges, representative of surface-agnostic multilayer desorption, demonstrate that the initial warm-up phase of the sample holder is reproducible. On the other hand, the shared trailing edges illustrate two things. First, the system is only pumping speed-limited at high temperatures above 60 K, as identified by the shallower slope. Second, before the system becomes pumping-speed limited, the molecules have high surface mobility prior to desorption, meaning that at a given coverage, the adsorbed molecules fill available binding sites in the same way, regardless of the prior states.

Overall, the measurement temperature (and energy) resolution, reproducibility and high dynamic range are representative of the best TPD measurements presented in the available literature, such as [230, 231], This points to the correct commissioning of TPD (and ESD) experiments.

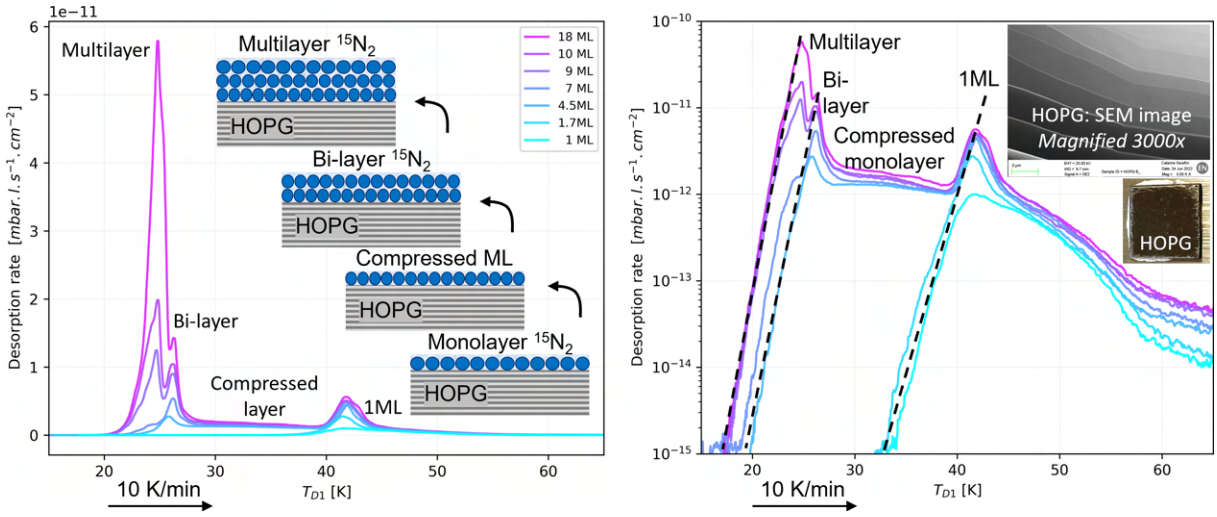

Figure 4.23: TPD curves of $^{15}N_2$ quench-condensed on a HOPG reference sample at 11 K. Linear and logarithmic representations reveal different features. The used A-grade HOPG sample (Reported lateral grain size 3-10 mm, mosaic spread angle of 0.4°, purity of <10ppm) was exfoliated under a medium vacuum of the Load-lock by linear movement with a Kapton tape attached to the HOPG specimen, as described by Hurst et al. [220].

4.8 Measurement procedure

4.8.1 System and sample preparation

Many experimental variations were investigated, but the measurement procedure ultimately settled as follows. A flag-type sample of a material, coating or treatment is shipped into the lab, packaged either in aluminium (preferable), or silk-paper, or plastic packaging (least preferred). The most suitable in terms of surface preservation is a combination of multilayer aluminium foil and a plastic bag.

Typically a day before the measurement is to be taken, the sample is inserted into the Load-lock chamber, which is immediately pumped down. Once a pressure of at least 10^{-6} mbar is reached, the sample can be transferred into the Storage chamber which is baked and maintained in UHV, below 10^{-9} mbar. However, a lower pressure is preferable for the sample transfer to minimise cross-contamination between the chambers.

Then, after about a day of in the storage chamber under UHV, the sample is linear-transferred into the main UHV μ-metal chamber for a measurement run. Sample storage in UHV conditions also implies an inevitable thermal outgassing of the adsorbed gas species, which indeed alters the SEY and ESD yields. Taken to the extreme by a 1 year-long thermal outgassing under UHV (at ambient temperature), the as-received SEY of a laser-treated specimen dropped by 30%, as shown in Fig. 5.32, and the ESD yield and electrodesorbed gas quantity dropped by a factor of 5∼10x.

Before a measurement run can be started, the sample-bearing cryomanipulator positions the sample against the collector, which is pre-aligned with the electron gun. Using the electrical contact between sample and collector, a reproducible distance of 0.25 mm can be achieved. The final sample-collector-gun alignment has to be done on a thermalised system, i.e. either at cold or at ambient temperature. Otherwise, thermal dilatation disrupts the alignment.

In case of a *cold run*, which is the baseline, the system takes about 2 hours to cool down and stabilise around T_{D1}=12 K. The temperature dependence of the ESD yield can be measured during this cool-down ramp. Once the system is cold, a flash desorption to ∼100 K is performed to desorb gases from the sample that cryosorbed from the background during the cool-down. Care is taken during the second and final cool-down from 100 K back to 12 K to ensure that the sample cools down as the last - once again, mitigating the possibility of residual gas cryosorption. The sample is then ready for data-taking.

4.8.2 SEY and ESD measurement

Surface characterisation is typically started by a non-destructive SEY measurement. Multiple SEY curves are acquired at different pristine spots to study variability within the sample itself.

The ESD measurements are only done afterwards as they irreversibly change to the studied spot. The ESD energy dependence is measured first, followed by an ESD yield dose dependence measurement, a

so-called conditioning curve. While the SEY and ESD energy scans take about 5 minutes to finish at the presented resolution, the conditioning measurement takes about 90 minutes.

When the conditioning measurement is done, the SEY and ESD energy scans are made once again to study post-mortem irradiation-induced changes. Typically, 4 distinct, mostly non-overlapping spots are available on each sample, which is usually enough to characterise a sample to the setup's full analytical potential.

4.8.3 TPD measurement procedure

After this electron-related characterisation, a series of TPD curves can be acquired. TPD measurements are, in principle, non-destructive but are acquired as last. Firstly because TPD is anyway insensitive to the conditioning state of the sample. Second, TPD measurement implies dosing gas onto the cold sample, which can change the SEY and ESD yields until a full warm-up to room temperature. More specialised measurements were also performed and are described in the relevant sections.

Once the experimental run is done, the RGA SEM and electron gun are switched off during the natural warm-up ramp to avoid high-pressure operation during pressure transients due to the desorption of cryosorbed residual gases. The sample can be extracted within minutes after the last measurement and sent for a post-mortem analysis at XPS or SEM, as also presented below.

4.9 Chapter summary

In this chapter, the experimental methods and the system instruments were introduced, successfully calibrated or otherwise characterised and put into work with the aim of measuring the SEY, ESD and TPD in the parameter ranges of interest. The used hardware is described in detail, focusing on the major components enabling the target experimental methods, such as the RGA absolute calibration, collector conductance measurement and electron beam characterisation. The operating principles are discussed, including corresponding calculations, calibrations, and simulations used to verify the developed understanding of the used subcomponents, as well as to understand their experimental limitations. The principles and calculations are presented for SEY, ESD and TPD methods as the main experimental methods that are introduced in Sections 4.4, 4.6, 4.7. The uncertainty analysis was also performed and is presented in the Appendix section 6.8 for the ESD yield calculation. Finally, reference data is acquired on a reference/calibration sample to demonstrate the correct commissioning of each experimental method, see Fig. 4.9 for SEY, Fig. 4.17 for ESD and Fig. 4.23 for TPD.

The most novel experimental methodology aspects, i.e. the combined collector-based measurement of electron and molecular emission, was summarised in an instrumentation-oriented publication [A3] and presented at conferences [A7, A8].

Chapter 5
Results and Discussion

Contents

The following sections provide an overview of different effects observed when irradiating a wide range of samples with electrons. The study indeed aims to be coherent but cannot be exhaustive. Partly because of the time-demanding nature of experimental data acquisition, partly due to the bare vastness of the parameters space (energies, doses, temperatures, materials and treatments), essentially resulting in a combinatorial explosion. To tackle this, I systematically investigated one parameter at a time to disentangle their respective influences on SEY and ESD.

First, all used experimental methods were iterated until reaching a sufficient degree of precision, reproducibility, automation, understanding of the acquired data and, ideally, coherence with available literature. This process was described in the previous chapter 4.

Second, each parameter possibly influencing the results was studied separately while having all the other parameters constant. Doing so aided me in decoupling each parameter's influence, allowing me to understand how each input parameter influences the SEY, ESD and TPD at the output. This includes the following most notable directions of research.

- SEY and ESD yield dependence on primary e^- energy and absorbed dose.
- SEY and ESD yield dependence on an absorbed dose at a single given energy.
- Conditioning efficiency of different electron energies.
- Comparative characterisation of different surfaces under the same irradiation conditions.
- Influence of temperatures on electron conditioning and quantity of desorbed gas.
- Influence of residual gas composition on the conditioning process.
- SEY, ESD and TPD characterisation of surface treatments and coatings.
- SEY and ESD yield of cryosorbed gases in thick coverages (substrate-independent).
- TPD studies of specific surface and binding energy for common residual gases.

Finally, the presented results allow one to form an educated estimate in a more generic situation, i.e. data-oriented and theory-based. Moreover, the current theoretical description, datasets and general understanding are expanded towards the cryogenic temperatures, low-energy electrons and high irradiation doses. This renders the work relevant for researchers and engineers, most notably in the aspects discussed in the following application-oriented Chapter 6.

- Availability of experimental data in technically relevant conditions of temperature and energy
- Generalised understanding of main influencing factors to the SEY, ESD and TPD
- Parametric fits to the experimental data on SEY and ESD that are directly and easily applicable to calculations and simulations.

5.1 Studied surfaces

The following dataset, listed in Table 5.1, was acquired using the experimental procedure and methods described above for all the aforementioned techniques: SEY, ESD and TPD. Where possible, the research is supported by SEM imaging and XPS analysis. This paragraph and Table 5.1 describe each studied sample and will only be referenced later.

The research begins with *simple* technical-grade metal surfaces that are in an unbaked, as received, UHV-grade cleaned surface state. Only then, the research gradually builds up towards more complex systems, including non-metallic surfaces, coatings, and laser treatments. Finally, the most technically-relevant surfaces are dosed with gases and probed with the TPD method. The detailed description of functional surface coatings discussed in their respective Section 5.4, whilst their principle was presented in Section 2.3. This includes sputter-deposited coatings (Ti-Zr-V NEG, Ag, Nb), RCE- and PLD-deposited REBCO coatings, and laser-treated Cu.

The surface of a reference is that of the unbaked LHC beam-screen, as currently used in the cold arcs: technical-grade OFE Cu is colaminated by press-rolling onto stainless-steel. This special high-manganese P506 stainless-steel alloy [232] is magnetically transparent and forms the BS mechanical structure, while the OFE Cu overlayer grants high electrical conductivity (high RRR) for impedance mitigation. For the purposes of this research, this sheet material (abbreviated as Cu/SS) was sampled during mid-production: after it was annealed to 950°C under H_2 atmosphere at 1 bar, and before it was bent and welded into the circular BS shape. For clarity, all studied samples were unbaked since this is the baseline. The LHC BS does not need a bakeout for achieving UHV, owing to the effective cryopumping. Stimulated desorption (ESD, PSD, ISD), however, remains a challenge in the presence of circulating beams. Sections 5.8 and

5.23 are exempt because it aimed to study the influence of bakeout temperature and compare the air- and vacuum-bakeout.

Both faces of the Cu/SS samples were investigated, inherently having the same history of cleaning and storage. One batch was cut and cleaned at a supplier from the provided Cu/SS sheet, while another batch was laser-cut and cleaned at CERN. Other investigated Cu, Al, Ti and SS samples were also cleaned ex-situ by the supplier using a warm ultrasonically agitated isopropanol bath, followed by packaging in plastic, unfortunately. As a side note, trials with surface cleaning in an ultrasonic bath with either acetone or isopropanol were deemed uninfluential on the resulting SEY or ESD in as-received or conditioned states.

Sophisticated surface cleaning methods were developed to prevent thermal or stimulated gas desorption. A portion of the studied Cu/SS, SS and Ti samples were cleaned at CERN and are much cleaner, compared to the supplier-cleaned ones, see Fig. 2.21. CERN's proper chemical surface cleaning [233, 234] indeed presented a notable decrease of SEY, ESD and the quantity of gas available for thermal or stimulated desorption. CERN's UHV-grade cleaning consists of a series of ultrasonic baths, first an alkaline bath for gross contaminant removal, followed by degreasing in a detergent (GP 17.40 SUP), and finalised by water and ethanol rinsing and drying. The effect of this cleaning is a slight etching of the contaminated surface oxide and hydroxide layers and the creation of new ones that are better defined - mostly native Cu_2O.

Material	**Specifications**	**References**
Bulk metals		
Cu	cut&clean at supplier	5.5,5.3,5.19
Cu/SS	colam. 80 μm Cu / SS; supplier-cleaned	5.2,5.3,5.13,5.21
Cu/SS	colam. 80 μm Cu / SS; CERN-cleaned	5.2,5.3,5.23
Cu/SS	–/– & ex-situ baked	5.7
SS	bulk, cut&clean at supplier	5.5,5.13
SS	bulk 316L, vac.-fired at CERN	5.42,5.22
Al	bulk, cut&clean at supplier, unknown grade	5.5,5.14
Ti	bulk, clean at CERN, unknown grade	5.5,5.6,6.22
Sputtered metals		
Nb	1250 nm, sput.-depo. at CERN	5.5,5.14,5.37,5.35
Ag	1250 nm, sput.-depo. at CERN	5.6
Non-metals		
Graphite	HOPG, air- & vacuum-cleaved	4.9,4.23,5.42
Silicon	wafer, 100 plane	5.2.2
Epoxy glue	Ag-filled, conductive	5.2.2
Coatings		
a-Carbon/Ti/Cu	50 nm sput.-depo.at CERN	5.4.1
a-Carbon/Ti/Cu	450 nm sput.-depo.at CERN	5.4.1
Ti-Zr-V NEG	1450 nm sput.-depo.at CERN	5.4.3
REBCO, SuNAM	1600 nm, RCE-DR depo.	5.4.4
REBCO, SuperOX	900 nm, PLD depo.	5.4.4
Treatments		
Laser-treat. Cu	C-type, COLDEX witness	5.4.2
Laser-treat. Cu	D7-parameters	5.4.2

Table 5.1: List of acquired data with and corresponding references within this manuscript.

5.2 SEY of technical-grade metal surfaces

A wide range of samples was studied to disentangle the influence of electron irradiation properties and surface characteristics on the SEY in the 0–1.5 keV energy range. A variety of surface and bulk compositions, treatments, coatings and surface states was covered between the ambient and cryogenic temperatures. Conditioning with different primary electron energies was also done to demonstrate the effect of electron energy on the SEY conditioning efficiency (and ESD, as shown below, 5.3).

The following aims were typically pursued. First, to characterise the SEY and ESD under conditions representative of a given sample's technical application, bearing in mind the technical aim of this applied research field. Second, to shed light on intricate dependencies observed in some samples, to improve the understanding and generalise the results. Often to prove a point and support a newly formed hypothesis regarding a specific behaviour - an approach especially useful in Section 5.6 dedicated to SEY and ESD of cryosorbed gases.

5.2.1 Energy dependence

As demonstrated in Section 2, the SEY curve decomposes in constituents whose proportions vary with energy and, as a result, varies the value of SEY. The following Figure 5.1 shows a set of SEY curves across the 0–1.5 keV energy domain of interest. The figure also includes a zoom (left) into the low-energy region, 0–40 eV which is very important in technical applications. Farnsworth studied the low-energy SEY region [235] already in 1925 (!) and is therefore long known ever since, including the fine structure and the contaminant-induced electron reflection around 5 eV. Yet, it only recently gained recognition in the available literature in the past decade or so for its direct application to the electron cloud build-up.

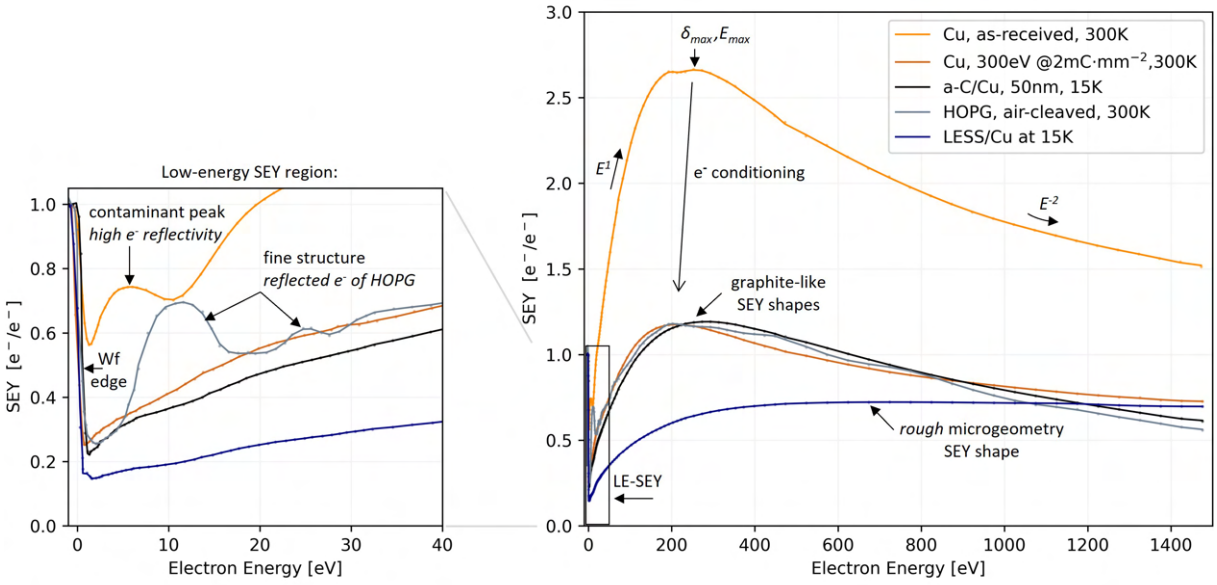

Figure 5.1: Comparison of SEY curves of various surfaces (Cu, Carbon coating, HOPG), surface states (as-received and conditioned Cu) and a laser treatment (rough microgeometry, 5.31). Right: Entire SEY curve in the 0–1450 eV energy region. Left: Zoom into the low-energy region, 0–40 eV.

The most characteristic value is the maximum SEY, δ_{max}, which is a closely followed figure of merit in technical applications dealing with electron irradiation. Rightfully so, but it is often over-optimised for, as it is not the only parameter that characterises an SEY curve. Indeed, more parameters are required for a full description/parametrization from the mathematical standpoint, but also when considering the (typically low-energy) electron spectrum in a given application. E.g. when dealing with an electron cloud, the majority of electrons has $\leq$20 eV, while the secondary peak has hundreds of eV, see Figure 1.4. Under such conditions, the position of δ_{max} on the energy scale E_{max} becomes crucial, and so does the decay rate at energies above $\sim$500 eV, once the SEY curve has peaked off. As outlined in the theoretical Section 2.2, the E_{max} represents a balance between the primary electron energy deposition depth (atomic mass-limited) and the secondary electron escape depth (IMFP- and Wf-limited).

The low-energy SEY (LE-SEY) region becomes crucial with such a strong predominance of low-energy electrons. Here, the energy scale referencing plays a role, so it was decided to put 0 eV at the vacuum level of the studied sample, i.e. where the work function (Wf) edge lies, see the LE-SEY figure. While this approach is commonly used by many experimentalists, referencing to the Fermi energy level is also a possibility, but the work function needs to be known. Hence, while using the Fermi level reference is physically more accurate, it is also experimentally much more challenging. The same figure clearly illustrates that a contaminant overlayer introduces a peak at ∼5 eV that effectively doubles the reflectivity for slow electrons. This effect is addressed and quantified in Chapter 5.6 of this manuscript. Note the low δ_{max} and the low LE-SEY of the carbon coating and laser treatment.

Shifting the focus to the SEY curve of electron conditioned copper surface, an effect is visible across the entire energy range. Not only does electron irradiation scrub off contaminants and decrease the overall SEY, including the maximum δ_{max} and the peak in LE-SEY region. It also graphitizes the surface-bound carbon-bearing contaminants and shifts the entire SEY curve closer to that of pure carbon (here represented by a thin carbon coating and HOPG).

Somewhat aside of the typical SEY curves lies one measured on laser-treated copper. The special shape originates in the geometry-limited secondary electron emission caused by the laser treatment-induced fractal-like structures. Very little energy dependence is visible here (and little angular dependence, Fig. 5.2.5) as the curve almost lacks a peak or decay at high energy.

For completeness, the measurements are typically done below 15 K, unless otherwise specified to 300 K. However, no clearly observable temperature influence on the SEY was measured, as discussed in Section 5.2.3.

5.2.2 Conditioning process

The electron conditioning effect on the SEY was discussed in Section 2.2, i.e. its overall decrease with imparted electron dose, an effect often leveraged in technical applications. It is known that extended exposure of a surface to electron irradiation results into changing the chemical surface state via contaminants removal and reprocessing.

Electrons at 300 eV energy were used systematically throughout all measurements as a comparative baseline, unless specified differently. First, because this value is close to typical SEY peak values δ_{max} and can therefore be used to fairly accurately track the δ_{max} during the conditioning measurement when used with the -28 V sample biasing scheme, as demonstrated in Fig. 5.2. Second, the 300 eV electrons condition very effectively, which reduces the measurement time.

Role of electron energy

To verify these theoretical claims discussed in Section 2.2 and to extend their validity towards the cryogenic conditions down to 12 K, numerous measurements were performed on technical LHC-grade copper colaminate, bulk Cu and many other materials. The conditioning efficiency was investigated for different primary energies of 17 eV (or 20 eV), 300 eV and 1 keV. The same measurements were performed at both at ambient and cryogenic temperatures of 300 K and 12 K.

Figure 5.2 shows SEY curves acquired at different conditioning states at 15 K (right) and 300 K (left). The left side of Figure 5.3 shows SEY at a given energy measured during the electron conditioning process. The right side of the same figure shows SEY conditioning curves are for different grades and surface treatments of copper. The electron irradiation does not alter the SEY until about 10^{-7} C.mm^{-2}. The inflection point typically resides around a few 10^{-5} C.mm^{-2}. The conditioning is mostly done and SEY has almost reached its ultimate value at electron doses above 10^{-3} C.mm^{-2}, or 1 mC.mm^{-2}. The plots of electrodesorbed gas shown below converge to the same conclusion, so a dose of 1 mC.mm^{-2} is typically taken as a comparison baseline.

Firstly, no tangible and direct temperature influence was observed at the cryogenic temperatures. Neither for these measurements nor at any other occasion. Though there are some hints of temperature-dependent conditioning processes ultimately resulting in different SEY [81], this was not observed under the chosen experimental conditions. This measurement also leaves aside the influence of cryosorbed gases that is discussed in detail in Section 5.6.

The first experimental goal was to compare SEY and ESD yield after irradiating the copper surface with identical electron doses but at different primary energies. The most effective conditioning effect is achieved by 300 eV, which includes clear signs of graphitization, i.e. low δ_{max}=1.1 and E_{max}=200 eV.

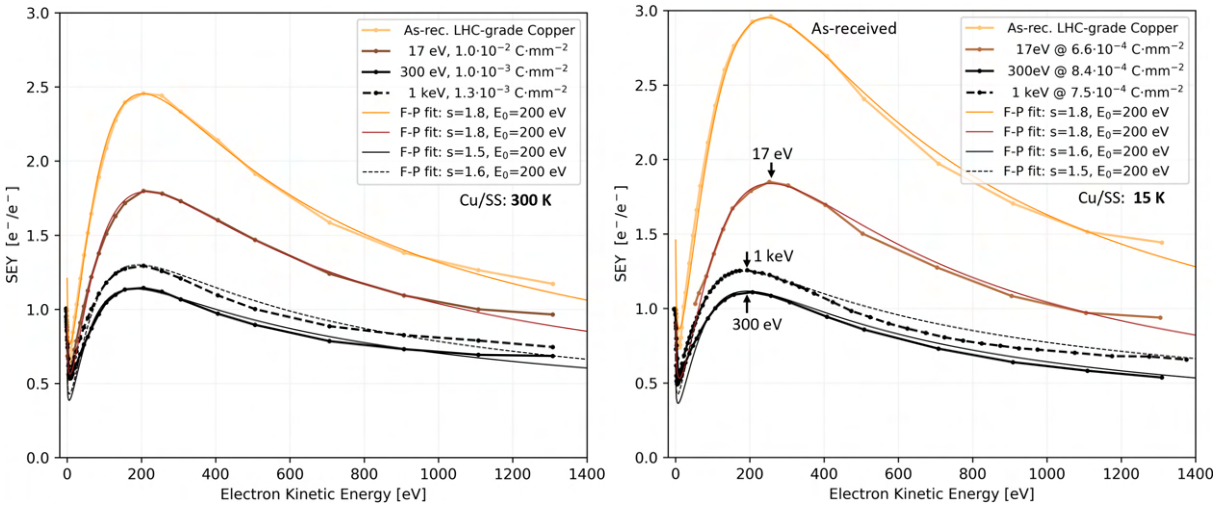

Figure 5.2: SEY curves acquired on a copper colaminate surface held at 300 K (left) and 15 K (right). The curves were measured for different conditioning states achieved by irradiation at 17 eV, 300 eV and 1 keV at medium doses. The corresponding ESD energy scans for the 15 K sample are shown in Fig. 5.21 (performed after SEY measurements). The SEY curves are fitted by Furman-Pivi SEY model [58] with parameters indicated in the legend. The electron energy is referenced to the sample vacuum level. The data for Cu at 15 K is published and presented as [A2, A6, A7]

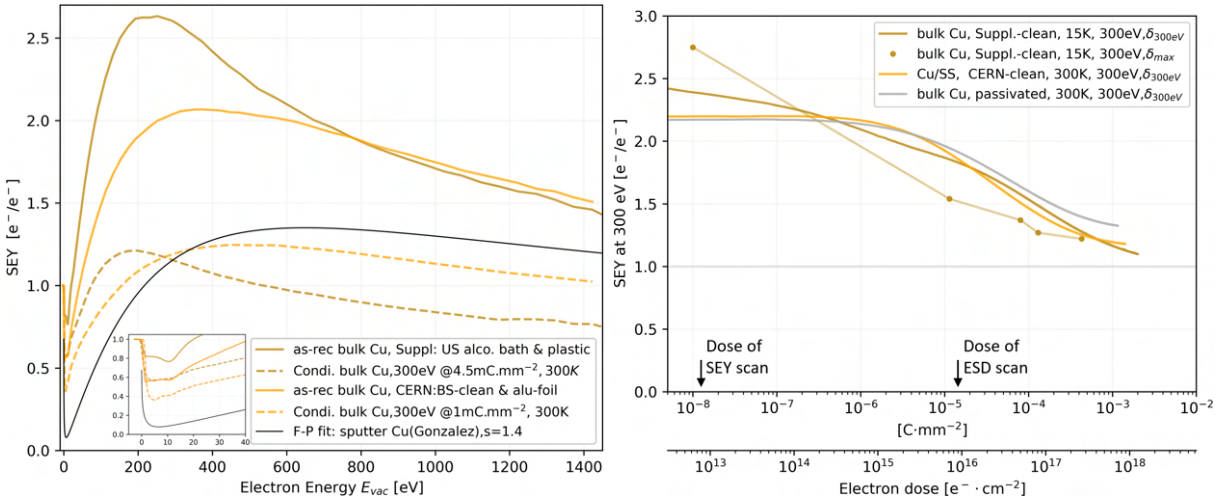

Figure 5.3: SEY curves acquired on Cu samples with different cleaning procedures. The data for sputter-cleaned Cu is adapted from Gonzales [236] using a Furman-Pivi approximation [58]. Right: SEY conditioning measurements done at different grades of copper and different temperatures, 300 K and 15 K. The curves represent continuous measurement, the marks represent δ_{max} sampled from a series of SEY curves taken during interrupted conditioning.

Although this does not affect the end result in any way, the surface state marked as 'as-received' for copper 300 K was in fact mildly conditioned by an unknown but small electron dose.

Another conclusion of this study is that 300 eV provides the fastest conditioning effect and will therefore be systematically used for further studies. An added benefit is that the 300 eV energy is very close to the peak position E_{max} of maximum δ_{max} for many materials. Hence, when measuring with a -28 V sample bias, the SEY at 300 eV δ_{300eV} can be measured simultaneously during electron conditioning, as is shown in Figures 5.3.

The primary electron energy strongly affects the resulting electron-conditioned surface state, as also reported by e.g. by Cimino et al. [76]. Conditioning with 1 keV electrons achieves almost the same result as 300 eV but at a slower pace. This is thought to be due to the fast electrons depositing their energy deeper into the bulk, leaving less near-surface electronic excitations that drive the graphitization process. Somewhat aside is the results of 20 eV irradiation that gave some SEY reduction but no clear signs of graphitization. We verified at much higher electron doses around 1-10 mC.mm^{-2} that 20 eV irradiation is not simply proportionally slower in conditioning, but in fact, seems incapable of graphitising the surface contaminants, at least at the used experimental conditions. The XPS analysis shown below in Fig. 5.9 confirms this.

Numerous authors, however, reported the temperature-dependence of surface chemical pathways. The prime example in this context being the research of Petit et al. [81, 82] done on warm and cold LHC-grade copper. The fact that exposure to moisture and corresponding hydroxide formation atop the copper sample can lead to different electron conditioning pathways is well visualised in a Wagner plot, as measured via in-situ XPS. In the extreme case a CuO phase with a inherently high SEY forms instead of a native Cu_2O. This can lead to insufficient electron conditioning at cryogenic temperatures, when in combination with low carbon surface content.

The observation made here for the SEY curve agrees with research conclusions reached after irradiation of carbon-containing organic compounds with low-energy electrons in 0–100 eV range. First is reported by Neumann et al. [237] who studied electron-induced graphitization of an organic overlayer atop of Au substrate. They quantified the extremely low (yet non-zero) cross-section of sub-10 eV electrons in graphitising the organic overlayer. They report that below 7 eV, the graphitization is induced by dissociative electron attachment (DEA). Above that, the electron-induced ionization dominates the C-H bond scission, which is by orders of magnitude more effective.

The same result was simultaneously reported by [238] showed a threshold behaviour around 6 eV and extremely low C-H bond scission cross-section below ∼20 eV. Similarly to Neumann's work, the cross-section plot can be subdivided into 2-3 different regions that are presumably dominated by different underlying physical mechanisms.

Interestingly enough, a graphitization threshold just below 10 eV was reported by Pokorna in her dissertation [239] using LE-SEM, when studying a beam-induced damage to a hydrocarbon-contaminated Al_{111} specimen. This observation does challenge the lack of graphitization observed in the presented experiments using 20 eV electron irradiation. It is therefore plausible that 10–20 eV electrons are graphitization-capable but with an extremely small cross-section and/or only on some precursor molecules.

Additional conditioning studies were done to better characterise the conditioning process of LE-SEY by tracing the evolution of the contaminant peak in the LE-SEY region, i.e. at 5 eV, see left side of Fig. 5.4. The conditioning measurement was done at ambient temperature on a Cu sample, that was known not to graphitize (as seen in Fig. 5.4) under electron irradiation, possibly due to a surface passivation, contamination or an unknown reasons. Hence, the SEY decrease could be mainly attributed to scrubbing off some surface contaminants and exposing the oxidised Cu, but not graphitizing the surface. Leaving the final δ_{max} aside as unimportant here, the attention should focus on the common trend shared by all dose-dependent curves, right side of Fig. 5.4. Note how the dose-dependent datapoints follow a trend that closely resembles a logistic S-curve. Moreover, the S-curve to best-fit the δ_{max} dose-dependence also seems to fit the δ_{5eV} dependence, i.e. inflection point around $D_0 \approx 1\,\mathrm{C.mm^{-5}}$ and similar steepness p≈2.5. Hence, a sigmoid function in combination with Furman-Pivi fit will be used in Section 6.1 to approximate the dose-dependent amplitude and shape of the LE-SEY peak at 5 eV.

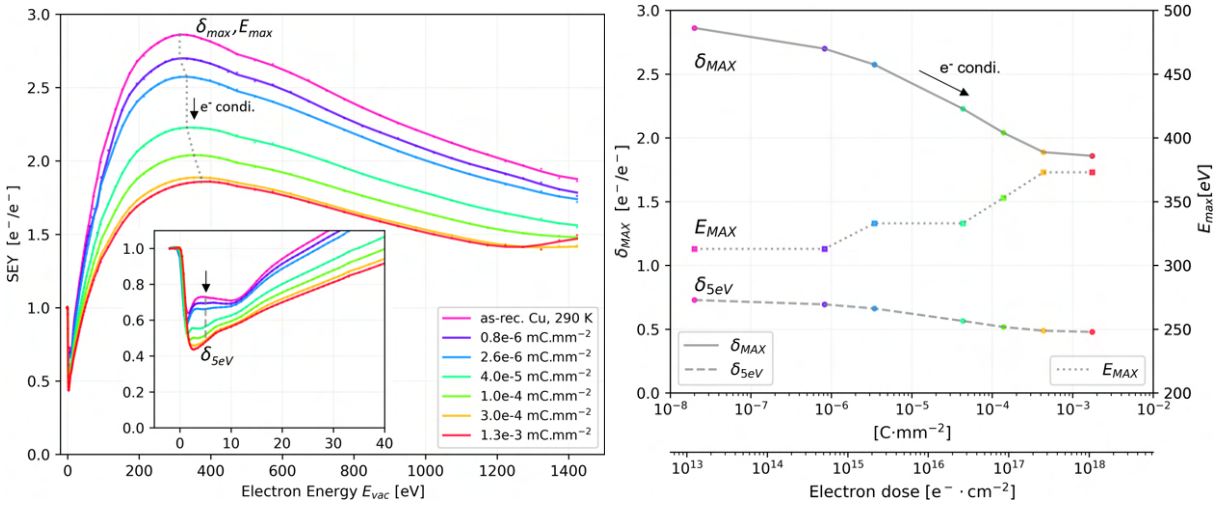

Figure 5.4: Left: SEY curves acquired on a passivated Cu sample held at 300 K (left) during an interrupted conditioning with 300 eV electrons. Right: Values of δ_{max}, δ_{5eV} and E_{max} plotted against absorbed electron dose. Note the common S-curve-like trend shared by all dose-dependent curves. The electron energy is referenced to the sample vacuum level.

Role of surface composition

A similar experimental procedure was also applied to other typical construction materials aside Cu, such as bulk Al, SS and Ti were studied, all in their technical-grade form and cleaned for use in UHV. The SEY curve for technical-grade Cu was adapted from the previous graphs. The SEY curves acquired on other metals, such as Al, Ti and stainless-steel (SS) are compared in Fig. 5.5. Both as-received and electron-conditioned states achieved by 300 eV irradiation at few $\mathrm{mC.mm^{-2}}$, as further precised in the corresponding legends. The selected metal samples were mostly studied at cryogenic temperatures. Technically-relevant metal coatings like Ti-Zr-V NEG, Ag, or REBCO were also studied for comparison against the bulk metals and are discussed in Section 5.4.

It is not a coincidence that the SEY curves are fairly similar, given that the two sides of one sample have exactly the same history of cutting, cleaning, packaging and storage. Indeed, this similarity also extends to ESD yields shown below in Fig. 5.13.

The Al sample (unknown grade) also has exactly the same history; from the cutting onwards, it has been cleaned, packaged and stored in the same way as Cu and SS. However, unlike them, its yield is significantly over δ_{max} >3 and, when conditioned, does not reach δ_{max} values below 1.5. In fact, at very high doses, its SEY starts increasing again, as shown in 5.5 and also observed at SLAC [240] and by Cimino et al. [241]. This is thought to be due to the full contaminant removal and consequent exposure of the underlying aluminium oxide with intrinsically high SEY, much like other dielectrics. For comparison, an anticorrodal version of Al decreased the δ_{max} from 5.5 to 3.4 values during the same 300 eV conditioning. This is twice as high as the previous base-grade aluminium, supporting the hypothesis of a thick oxide layer leads to a high SEY. The depth profiling of an oxidised technical-grade Al surface [242] also showed an unusually thick oxide layer.

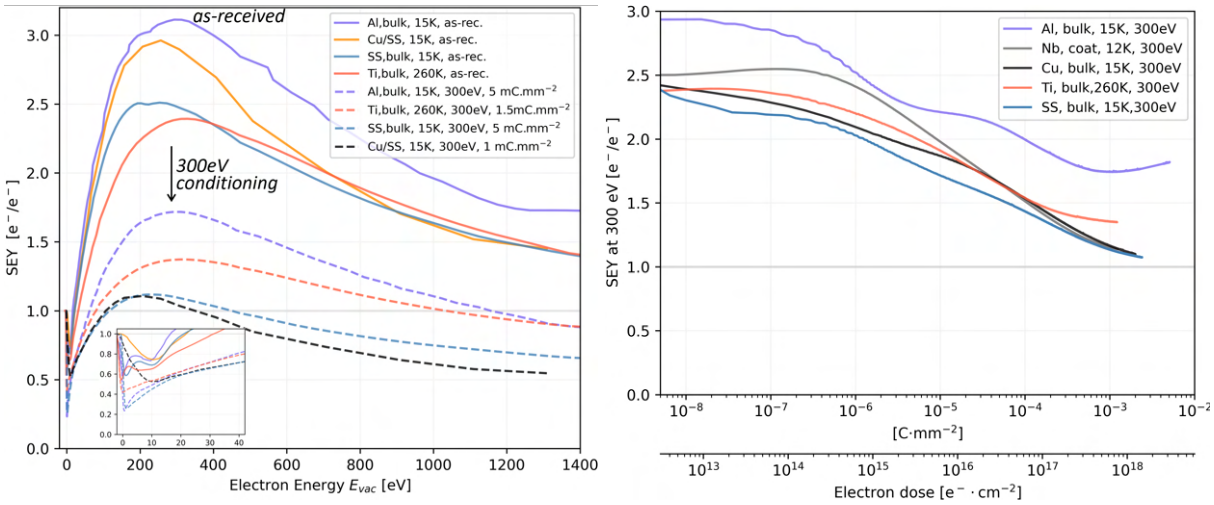

Figure 5.5: Left: SEY curves acquired on typical technical-grade bulk metals were measured for different conditioning states: starting from as-received and after a 300 eV electron irradiation at a dose of few $\mathrm{mC.mm^{-2}}$, as indicated in the legends. Right: Continuously acquired SEY conditioning curves measured at 300 eV, typically at cold, for the same samples. Note the approximate logistic S-curve shape visible in all metals except Al.

Another important observation can be made regarding the E_{max} value, which tends to remain the same before and after conditioning. Unlike the δ_{max}, which decreases during conditioning. This indicates that the material properties mostly dictate the E_{max} position. The composition, atomic mass and corresponding stopping powers determine the balance between the energy deposition depth and SE escape depth. This in turn defines the E_{max} at which the balance tips over. Conversely, the magnitude of δ_{max} is defined by the electronic properties of the surface, mostly the work function that represents a certain barrier (∼4.5 eV) for the escaping secondary electrons. Given the energy spectrum of electronic excitations that is highly skewed towards low energies with a peak around 3 eV, even a small decrease of the work function barrier can lead to a large increase in secondary electrons. As is observed.

To further substantiate the effect of surface composition, Figure 5.6 shows a correlation between the atomic mass of selected substrates and the values of δ_{max} and E_{max}. The surfaces were selected such that they have the least amount of surface contaminants and oxides feasible in a system without a sputtering option. For higher masses, values for sputter-cleaned Cu, Au and Ag were adopted from Gonzalez et al. [236], although the results obtained in this setup converge towards the same values. To probe lower

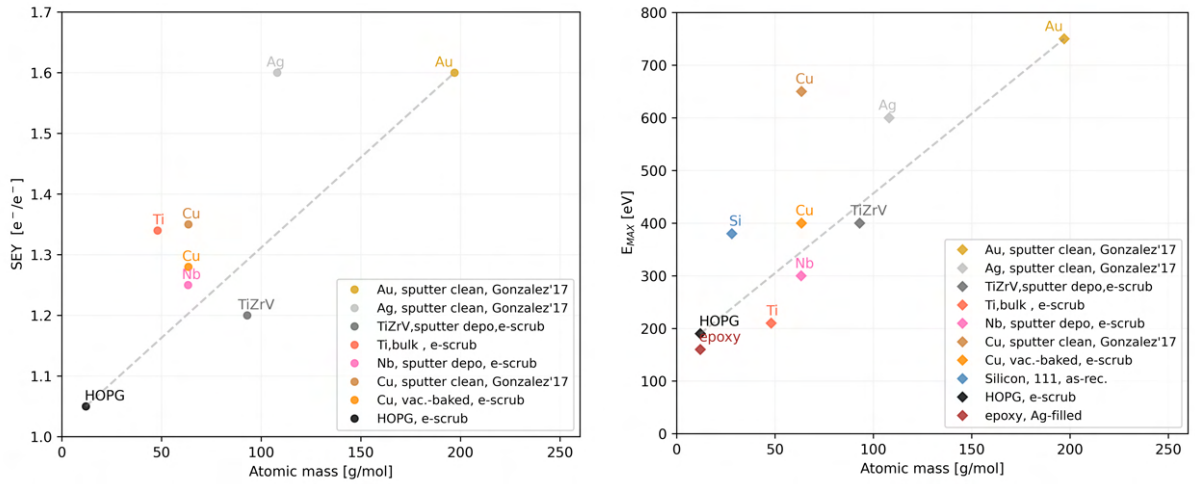

Figure 5.6: Correlation plots between the atomic mass of surfaces and the values of δ_{max} and E_{max}. The SEY values for sputter-cleaned Cu, Au and Ag were adopted from Gonzalez et al. [236]. More details in the text.

masses, lightweight materials were selected, such as Ti, Al, HOPG and epoxy.

A clear positive correlation exists for both δ_{max} and E_{max}. There are two reasons for this, as was argued in the theoretical section 2.3. First, the higher the atomic mass of the metal substrate, the higher the stopping power for impinging electrons, resulting in an energy deposition closer to the surface, inevitably increasing the observed SEY. The positive correlation between the substrate density and maximum SEY value and position is long known ever since Bruining's renowned SEY meta-analysis [65]. It also means that to reach a peak value δ_{max}, the energy must be much higher for the primaries to deposit their energy below the escape depth. Second, the backscattering coefficient is higher for high-Z materials, meaning that more electrons get reflected, both elastically and inelastically. These two trends are believed to explain the higher SEY and its position on the energy scale that rises with the substrate atomic mass.

To conclude, the measurements illustrate that the SEY decrease happens similarly for many technical-grade metals, to a large extent, regardless of the substrate unless the native oxide has a too high SEY, such as Al, the SEY conditions to an acceptable level around δ_{300eV} ≈1.2, as it is the case for Cu, SS, Nb, Au and Ti-Zr-V NEG.

Role of surface state and morphology

We showed in the previous paragraph that higher energy electrons are essential for the graphitization of the surface-bound carbon contaminants. Here, we aim to demonstrate that the carbon precursors must first be present on a surface before being graphitized. From another point of view, this data also shows how air-baking and vacuum-baking influences the SEY in both as-baked and electron-conditioned surface states.

The studied samples came from the same production batch, hence had the same history, and were air-baked to temperatures from 100 °C. to 300 °C. Vacuum-baking to 200 °C was also done for comparison. Figure 5.7 shows photos of the baked samples used for this investigation, including SEM images of the 200 °C air-baked sample. Note how the Cu surface gradually darkens due to oxidation at progressively higher air-bake temperatures. This was not the case for a vacuum-baked sample due to the lack of O_2 that drives the in-air oxidation. Also, note the uniformly sized oxide crystals grown on the surface during the air-baking. This points to self-limited crystal growth of sorts. Despite the obviously highly oxidised dark-tinted and rough surface, the sample preserves its copper look and texture to some extent, unlike a similar sample baked at 300 °C.

The left side of Figure 5.8 shows how the bakeout temperature influences the SEY curves in both as-baked and conditioned states. The right side plots their values of δ_{max} and E_{max} with respect to the bakeout temperature. The comparison is made for an as-received surface state and an electron-conditioned one at 1 mC.mm^{-2} dose of by 300 eV imparted at ambient temperature. There is a clear trend showing that the higher the bakeout temperature the lower yield to begin with, but also the higher yield to end with after conditioning. A similar trend is visible for the E_{max} and, as the bakeout

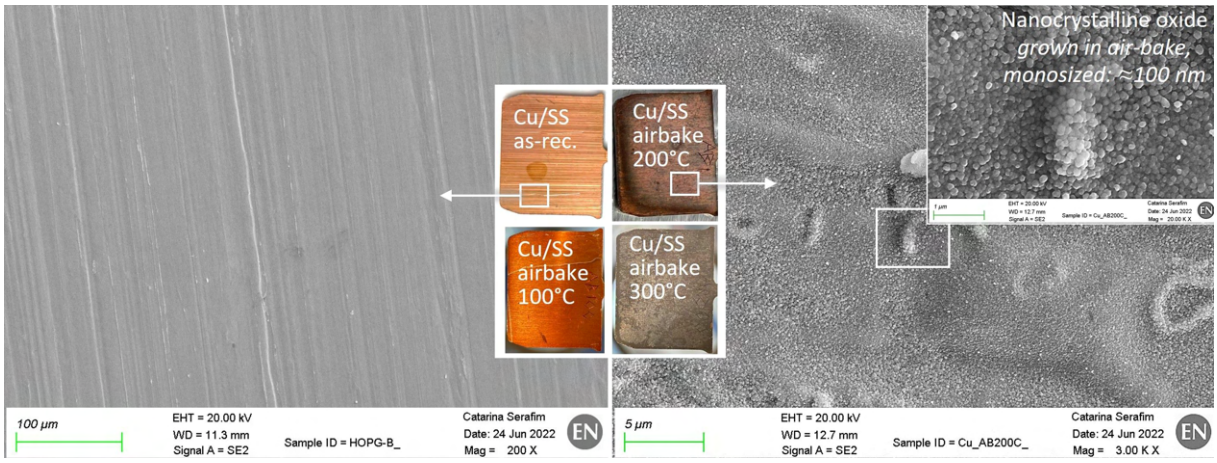

Figure 5.7: SEM images of a copper colaminate surface air-baked at 200°C for 1 day and the unbaked reference, with parallel grooves visible after a press-rolling. Details in the text. The SEM images are taken on FE-SEM Zeiss Sigma, kindly provided by EN-MME-MM, and acquired by C. Serafim, TE-VSC-VSM, at CERN.

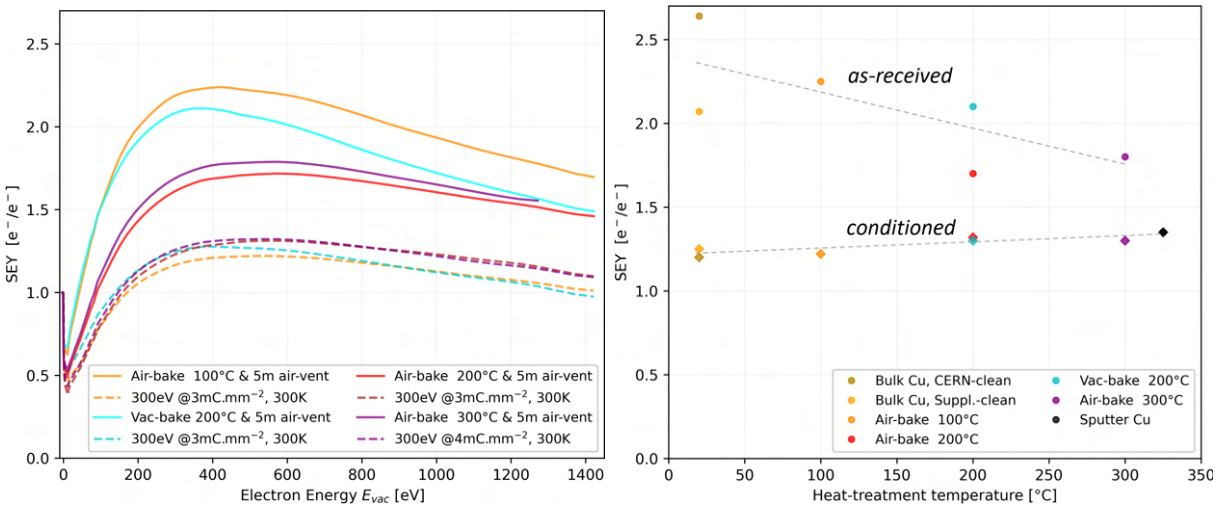

Figure 5.8: SEY curves measured on an as-received and conditioned a Cu/SS held at 300 K, in a range of heat-treatments. The right plot traces E_{max} with respect to the heat-treatment temperature for as-received and conditioned states.

temperature increases, the behaviour approaches that of a sputter-cleaned (unbaked) Cu, data adopted from Gonzalez et al. [236]. Although this trend can only partly be assigned to the surface cleaning, because the air-baked copper surface is heavily oxidised, as visible in the SEM image 5.7.

Hence, an identical SEY (and ESD) measurements were done on a sample baked in vacuum to 200°C, aiming to decouple the influence of in-air oxidation from that of contaminant removal due to baking. The ex-situ bakeout followed by some 5 min air-exposure resulted in a fairly clean surface without many contaminants as visible on both SEY and ESD measurements.

The same trends in SEY behaviour, including surface morphology changes induced by air- and vacuum-bakeout was observed by Bojko et al. [243] on a technical-grade copper. The new data presented here expands the SEY dataset towards the low-energy region and adds complementary ESD measurements.

Although the opposite is generally also possible, the SEY normally increases with increases the coverage of physisorbed or chemisorbed species. Many experimentalists demonstrate this trend by removing adsorbates by different means, leading to decreased SEY. Brown et al. [244] chose the opposite approach and demonstrated experimentally that chemisorbing CO on atomically clean Cu, Ag and Au surfaces increases the SEY. The SEY measurements of cryosorbed gases presented in Section 5.6 also substantiate this trend, albeit only for surfaces with low-enough SEY.

To conclude, this measurement illustrates how a bakeout procedure leads to a decrease in the as-received SEY by thermally removing contaminants, and stimulates surface oxidation when done in the air. However, the SEY also does not electron-condition to as low values as an unbaked Cu does since the surface lacks the graphitizable contaminants that are responsible for driving the SEY curve to low δ_{max} and E_{max} values.

XPS analysis of conditioned copper

The following Figure 5.9 represents an XPS analysis performed on a copper colaminate sample was laser-cut and degreased at CERN and stored in an aluminium foil after cleaning. The as-received Cu sample was sectioned into 4 distinct spots and each was separately conditioned with 20 eV and 300 eV at 1.5 mC.cm^{-2} dose at temperatures of 300 K and 12 K. For clarity, each conditioning was done on a previously intact pristine spot on the same sample and the full combinatorial matrix was investigated: 300 eV & 300 K, 20 eV & 300 K, 300 eV & 12 K and 20 eV & 12 K. Following the electron conditioning, the sample was nitrogen-vented, wrapped in an Al foil, transported into the XPS setup, and put back under UHV in about 30 min.

The former research of Petit et al. [80, 81, 245] and Bilgen [246] are used to draw inspiration for interpreting the XPS spectra taken on similar technical-grade copper surfaces exposed to electron irradiation. The four plots zoom on distinct peaks in an XPS spectrum that well represent the sample surface state by the content of Cu, O and C. The XPS curves are measured at the distinct electron-conditioned spots of the same sample and altogether are a tell-tale of electron irradiation-induced surface-state changes. The as-received state is also depicted for reference and shows the original surface state, mainly consisting of copper hydroxides, oxides, suboxides (not fully-valent oxides) and non-graphitic carbon.

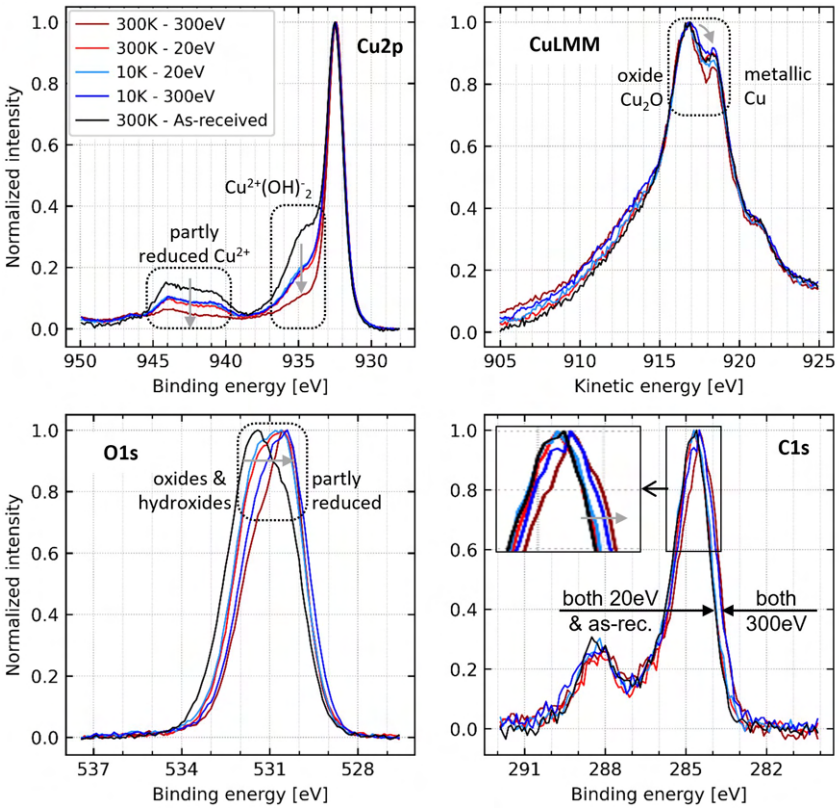

Figure 5.9: XPS analysis done on an CERN-cut&cleaned copper colaminate sample previously electron-conditioned at different energies, 20 eV and 300 eV, and temperatures, 300 K and 12 K. The sample was vented following the electron conditioning in the Multisystem setup and transported to warm XPS in ∼30 min. Data is taken at SPECS setup and interpretation is credited to V. Petit, CERN-TE-VSC-SCC.

The acquired SEY and ESD data helped to form a hypothesis that electron conditioning is a two-stage process. First is the reduction and removal of metal-bound oxides and hydroxides. Second, is the graphitization of surface-bound carbon-containing contaminants. Hence, the Cu_{2p}, Cu_{LMM}, O_{1s} and C_{1s} peaks in the acquired XPS spectra are selected for closer examination to support the hypothesis. These reduction processes consist of the following changes in the XPS spectra that are highlighted in the graph by a dotted frame and a grey arrow that signifies the evolution during electron conditioning. The reduction of Cu^{2+} satellite of the Cu_{2p} line signifies scrubbing the surface of its hydroxide coverage. This reduction is accompanied by shifting of Cu_{LMM} and O_{1s} peaks, also characteristic of the reduction of Cu oxides and hydroxides into a metallic Cu. Meanwhile, the shift of the C_{1s} peak by 0.3 eV is assigned to the graphitization of carbon contaminants.

The 300 eV electrons efficiently condition the Cu regardless of the temperature, albeit the 300 K conditioning is slightly more effective than at 10 K. Conversely, this is not the case for 20 eV conditioning, whose effect consists of a partial surface reduction but not carbon graphitization, regardless of cryogenic or ambient temperatures. What would achieve extremely high doses of 20 eV electron remains questionable because some studies report graphitization down to 10 eV, though with an extremely small cross-section. In any case, the reduction of hydroxides and oxides is responsible for the SEY decrease in the early phases of electron conditioning, i.e. at low doses, regardless of energy and temperature. Meanwhile, this electron-induced chemical reduction is necessary, as the graphitized carbon overlayer on the reduced surface reduces the SEY even lower, with its final value depending on the original carbon contaminant precoverage. This perfectly aligns with the SEY curves previously presented in Fig. 5.2. For instance, Cimino et al. [97] demonstrated an effective SEY suppression by sputter-depositing graphite over a previously sputter-cleaned Cu, with naturally high δ_{max} and E_{max}. Already a nm-thin graphite coverage suffices to decrease the SEY effectively, i.e. few monolayers of carbon in sp2 binding state decrease δ_{max} close to 1 (and E_{max} too). This illustrates the high surface sensitivity of SEY.

The measurements presented here are taken at cryogenic temperatures, but the results correspond to studies available in literature taken at ambient temperatures. However, studies were insofar typically done at ambient temperature. We observe the same graphitization effect as Nishiwaki [77], or Scheuerlein [79], linking the SEY decrease to graphitization and Cimino et al. [76, 78, 184, 247] who also demonstrated the limited conditioning effect of low-energy electrons. The experimental results agree with the general understanding of SEY conditioning developed at ambient temperatures and seen as well at cryogenic conditions by Cimino et al. [221].

In summary, combining the experimental data, simple simulations and theoretical understanding allows for reaching certain conclusions about the electron conditioning process. Firstly, the resulting effect of electron conditioning is strongly energy-dependent, with higher energies being generally preferable for good (low SEY and ESD) conditioning. The paragraphs dealing with surface state composition illustrate that the underlying surface (typically a metal oxide) has to have a sufficiently low native SEY, as is the case for Cu, SS, Nb and NEG, but not for Al. Moreover, the presence of surface-bound carbon-containing contaminants is a precondition for graphitization, which is in fact responsible for the final SEY decrease at the high dose limit, see Fig. 5.18 or ref. [76]. Shall the contaminants be cleaned, as it was done by a bakeout in Fig. 5.7, it cannot be expected to attain a low-SEY graphitic overlayer on an irradiated surface. Regardless of a used electron energy and dose, the graphitization, characterised by a low δ_{max} ≈1.1 and E_{max} ≈200 eV, is not reached unless the carbon is introduced. A possible remedy to an inherently large SEY (e.g. Al) is laser treatment to compensate for this inherently high SEY by a geometrical entrapment of SE, as evidenced [107].

5.2.3 Temperature dependence - Role of cryogenic conditions

The measurements of SEY energy-dependence performed between ambient and cryogenic temperatures did not result in any measurable difference, as far as can be concluded with the precision and repeatability of the given measurement arrangement and the methodology used. This is somewhat expected since SEY is a property strictly related to substrate electronic structure and thermal effects can hardly be expected to play a direct first-order role in the 12-300 K temperature range. This line of argumentation indeed excludes the possibility of cryosorbed gases being present atop of the coating, often being the case at cold, as shown below in Section 5.6.

However, the ESD yields, both initial and after conditioning, were observed to vary greatly with temperature, which is discussed in detail in Section 2.22. The above-discussed measurements of Petit et al. [81, 82] however, evidence a different chemical pathway for electron conditioning at cold and warm. Under special circumstances created by the presence of a hydroxide-terminated copper surface, the cold electron conditioning can lead to preferential CuO formation and simultaneous graphite depletion.

5.2.4 Role of residual gas in conditioning at cryogenic temperature

The experiments did not show a considerable influence of cryogenic temperatures on the SEY conditioning process under the used experimental conditions. However, it was tested by gas injection during electron

conditioning that the residual gas composition influences the electron conditioning under certain extreme circumstances.

A particular type of Cu/SS sample was chosen for this experiment because it previously did not graphitize under electron irradiation, presumably because of being too clean of carbon contaminants and/or being chemically passivated. These measurements are compared to a reference SEY curve, Fig. 5.4, acquired on a different sample from the same batch, also conditioned at 10 K with 300 eV to a 1.3 mC.mm^{-2} dose, but in UHV conditions, i.e. H_2-dominated residual gas at 5.10^{-10} mbar$_{H2}$. Inferring from the high location of E_{max}=450 eV, the reference sample exhibits no noticeable graphitization and does not condition to low δ_{max} and E_{max}.

Knowing this allowed us to test whether a carbon-rich residual gas atmosphere can induce surface graphitization at cryogenic temperatures. To test this, injection directly into the collector inner volume was used to create a CO and CH_4 dominated residual gas atmosphere over the cold copper sample during electron conditioning. The CO and CH_4 gases were selected because of their predominance in the UHV residual gas spectrum. Less abundant residual gases, aside of lower concentrations, have either lower scattering cross-sections ($\sigma_{CH4} > \sigma_{C2H4}$) and/or they decompose into the hereafter studied gases ($CO_2 \rightarrow$CO).

Figure 5.10 shows SEY curves measured before and after electron conditioning with CO and CH_4 co-injection. The as-received spot represents the original pristine state, while the three other spots on the sample were irradiated with the listed combinations of energies and residual gas compositions. The presence of CO and CH_4 gases up till few 10^{-8} mbar did not have clearly interpretable influence, neither facilitate, nor inhibit the electron conditioning process of copper at doses of 1.5 mC.mm^{-2}. It took 10^{-6} mbar of CH_4 partial pressure and a 300 eV dose of 0.5 mC.mm^{-2} to deposit a thin graphitic overlayer that is noticeable; by the naked eye and by XPS. The graphitized surface was visually discoloured and the SEY shape also pointed towards the same conclusion with the E_{max} ≈200 eV.

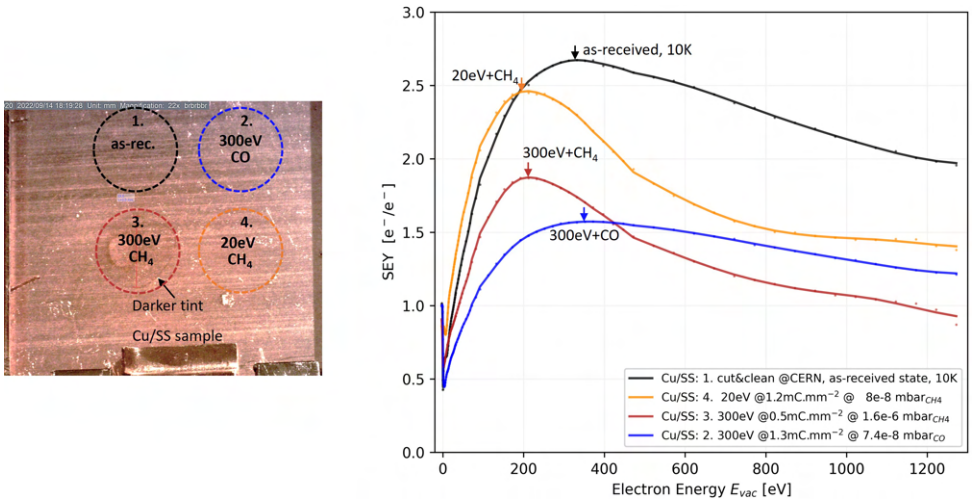

Figure 5.10: Right: SEY curves measured after 300 eV or 20 eV electron conditioning of a Cu/SS sample held at 10 K while co-injecting CO and CH_4 gases. Left: The sample conditioning at 300 eV with CH_4 coinjections shows a discolouration. Details in the text.

An XPS spectrum was taken ex-situ to inspect the post-mortem changes in surface composition due to conditioning under carbon-rich atmosphere. The same peaks as in Fig. 5.9 were used to infer the changes in surface chemistry, as captured by the histogram. The relative atomic concentrations are presumed proportional to the areas under the curves on the right, that characteristic for each element or compound. The CO co-injection during 300 eV conditioning (blue curve) can be deemed uninfluential since all four peaks followed in the XPS spectrum exhibit little change from the original as-received state (black curve). Contrary to that, the CH_4 co-injection during both 20 eV (red) and 300 eV (brown) conditioning leads not only to a partial but significant reduction of oxides and hydroxides but also to carbon deposition, as clearly visible on the C_{1s} peak. Hence, the XPS study proves the electron-beam induced deposition (EBID) of carbon from gas phase precursors is feasible at cryogenic temperatures, although with a very small deposition rate, as calculated below using eq.5.1. The study also suggests that more graphite could be deposited by increasing the irradiation time (feasible), increasing the pressure (not feasible), or the energy in case of 20 eV irradiation. A sweet spot likely exists in this wide parameter space that could

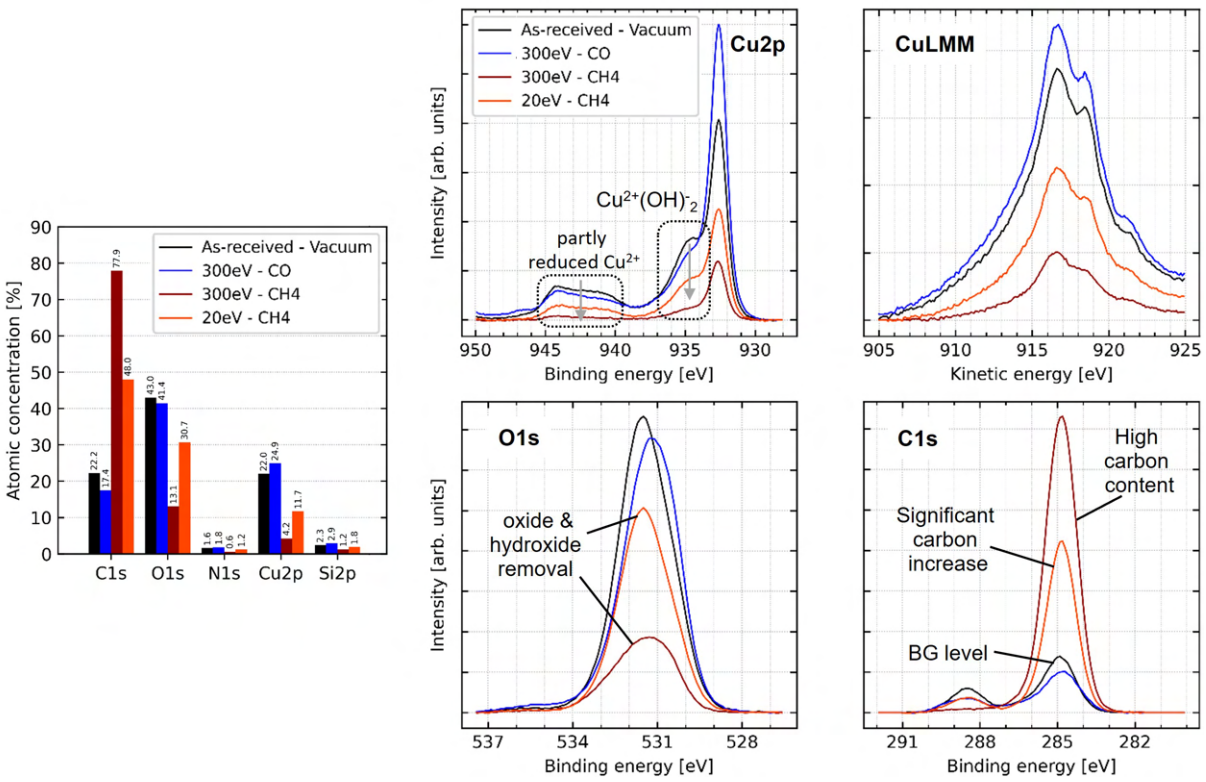

Figure 5.11: XPS analysis done on an CERN-cut&cleaned copper colaminate sample. The sample was electron-conditioned at 20 eV and 300 eV, at 15 K while co-injecting CO and CH_4 gases. The sample was vented following the conditioning in the Multisystem setup and transported to warm XPS in ∼30 min. Data is taken at SPECS setup and interpretation is credited to V. Petit, CERN-TE-VSC-SCC.

be exploited to reach more effective EBID rates, also considering a suitable carbon-rich precursor gas, possibly with carbon in sp2 already present.

Scheuerlein&Taborelli did similar measurements [248] at CERN, where they studied at ambient temperatures the same technical-grade UHV-cleaned copper surface. The AES analysis they performed (sensitivity limited to a coverage of about 0.1 ML ≈ 10^{14} molecule.cm^{-2}) showed no tangible influence of the residual gas composition on the copper conditioning, meaning that dissociation cross-sections are low for this process, at least at ambient temperatures. An approximate value for the EBID deposition rate can be obtained following Scheuerlein&Taborelli's [248] derivation. The EBID deposition rate dN_{EBID}/dT is proportional to the surface coverage θ_i of cryosorbed precursor molecules, electron fluence j_{e-} and the effective dissociation cross-section of cryosorbed molecule σ, as follows:

$$\frac{dN_{EBID}}{dt} = \theta_i \cdot j_{e-} \cdot \sigma_{EBID} \tag{5.1}$$

An equilibrium between adsorption and electrodesorption is quickly established during a 300 eV electron irradiation for both CO and CH_4. Knowing the approximately linear ESD yield dependence on surface coverage, one can deduce the equilibrium coverage θ_{eq} from the equilibrium ESD yield η_{eq}. From other data acquired in this system, this is about 0.1 ML for both CO and CH_4. For simplicity, one monolayer is again presumed to be 1 ML ≈ 10^{15} molecule.cm^{-2}. The dissociation cross-section is adapted from [248] to be σ=10^{-17} cm^{-2}. Plugging these approximative values into the 5.1, an estimate is reached of dN_{EBID}/dt=10^{11} molecule.cm^{-2}.s^{-1}. This corresponds to about 1 ML of carbon formation every 3 hours, presuming the given carbon-rich residual gas pressure of few 10^{-8} mbar, which is unreasonably high for typical UHV conditions. Combining their result with the presented measurement taken at 10 K, not even the high partial pressure resulting in an increased surface concentration of CO and CH_4 gases on the cold and sticky sample, does not compensate for the low efficiency of electron-induced dissociation of carbon-containing molecules cryosorbed on the surface. This is an unexpected result, since the electron-induced graphitization of carbon-containing surface-bound contaminants is believed to be the underlying mechanism of SEY conditioning. Moreover, the electron-induced dissociation of molecules is commonly observed in thick cryosorbed gases with yields orders of magnitude higher than in the gas-

phase counterpart. An argument could be made that the precipitated graphite is hydrogen-terminated, which is known to result in a high δ_{max}, as shown by Shih et al. [249]. The E_{max}=200 eV point to a low-Z surface (graphitic overlayer), but still, the slightly higher δ_{max}=1.3 allows us to hypothesise the hydrogen termination of this graphite layer.

The thickness of the precipitated graphite overlayer can be estimated by comparing it to the work of Inguimbert, Angelucci et al., who simulated [250] and measured [97] the copper SEY with thin carbon overlayers. The SEY curve measured after EBID deposition in CH_4 atmosphere best compares ($E_{max} \approx$ 200 eV followed by a rapid decay) to ∼2 nm coverage, i.e. ∼10 atoms thick overlayer.

It was also verified in another measurement done on a more polluted copper sample held at 10 K that CO coinjection does not inhibit the electron-induced graphitization of surface-bound contaminants. H_2 coinjection was not specifically tested, but the H_2-dominated residual gas composition ($p_{res,H2} \approx 10^{-10} \sim 10^{-9}$ mbar) never seemed to be an issue for electron conditioning. The conclusion of this study done at ∼12 K is that the electron conditioning process is rather agnostic regarding the residual gas composition under typical UHV scenarios unless some extreme edge cases lying strictly outside UHV domain are intentionally created.

5.2.5 Angular dependence

Aside of the primary energy that was discussed above, the incidence angle presents another means to act on the energy deposition depth. The method for incidence angle dependence of SEY was discussed in Section 4.4.4 and gives the following results. The primary electron energy of 320 eV was selected because it lies close to SEY maxima, so the δ_{320eV} is reasonably representative of the peak value. Besides, the e-beam has high-enough rigidity at this energy, so it does not strongly deviate under the non-symmetric electric field induced by the tilted sample that is biased to -28 V. Unfortunately, it was impossible, in this experimental setting, to verify the beam spot shape with the fluorescent target or Faraday cups.

First, bare metal surfaces, i.e. flat, were found to have a strong angular dependence, as investigated in the 0–60° range measured from the normal. This is a known behaviour, as discussed in the theoretical section 2.2.3. The angle-enhanced SEY owes to a shallower energy deposition depth.

Contrary to flat metal surfaces, rough surfaces, such as the laser-treated copper, Fig. 5.31, do not exhibit such a strong angular dependence if any at all. This points to very effective geometrical confinement of SE, even at high incidence angles, as previously discussed in Sections 2.2.3 and 2.6.6. Monte-Carlo simulations were done for a periodically rough Aluminium surface leading to similar results [251].

The carbon-coated surfaces are somewhat in between the two extreme cases. The sputter-deposition coating process gives the amorphous carbon overlayer an inherent roughness resulting into a lesser angular sensitivity.

Given the level of experimental uncertainties and the scatter in the data, it is difficult to conclude on the exact scaling with angle. Both studied dependencies $cos^{-n}\alpha$ and $\exp(k.(1-cos\alpha))$ do approximate the experimental data acceptably well. The question remains regarding the behaviour at grazing incidence angles. Theoretical understanding predicts a growing fraction of reflected electrons at high angles. If all electrons incoming at a grazing incidence are reflected away, this would force the angle-enhanced SEY back towards 1, as $\alpha \rightarrow 90°$. This is elaborated in the Results application Section 6.1.

The CASINO simulation aims for a qualitative illustration of the energy deposition depth concept and how it is influenced by incidence angle and energy. This particular customised simulation is done for a contaminated and oxidised copper surface irradiated by 320 eV electrons at angles 0°, 30° and 60° from normal. Based on various literature resources [80] [246], a 2 nm thin Cu_2O layer was placed over the bulk Cu substrate. An additional 2 nm thin overlayer of adsorbates (H,C,O) was added atop of the oxide layer to simulate the weakly bound physisorbed low-Z hydrocarbon contaminants. The proportion of H:C:O was estimated to be in tens of ML coverage and in 80:10:10% proportion, as deduced from integrating the electrodesorbed gas during 300 eV electron conditioning at 300 K. This gas quantity amounts to about 2 nm thin adsorbates overlayer.

Note that as the primary energy increases, the beam becomes more penetrant and the energy deposition depth increases. This leads to a lesser near-surface concentration of electronic excitation in the SE escape depth and, consequently, to a lower SEY. The 20 eV irradiation seems angle-agnostic, as all the energy is, in any case, deposited within the SE escape depth and can lead to emission. Conversely, as the incidence angle of higher energy electrons increases, the energy deposition depth becomes shallower, and the fraction of backscattered primary electrons (red trajectories) progressively increases.

However, the simulation results are only semi-quantitative at best because of the following reasons.

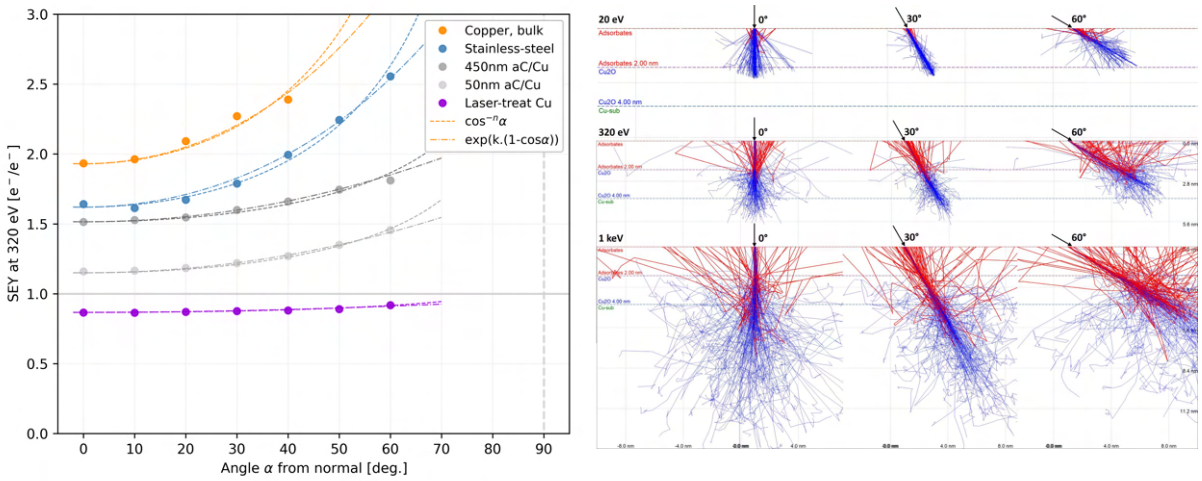

Figure 5.12: Left: SEY at 320 eV of as-received Cu, SS, thick and thin carbon coatings and a Coldex-type laser-treated Cu measured as a function of incidence angle α measured from the normal. The fits $cos^{-n}\alpha$ and $\exp(k.(1-cos\alpha))$ used to approximate the SEY angle-dependence are discussed in Section 2.2.3 and 2.6.6. Right: Illustrative CASINO particle tracing Monte-Carlo simulation for 20 eV, 320 eV and 1 keV primary electrons impinging on an adsorbate-covered oxidised copper surface at 0°, 30° and 60° from normal. Note that increasing energy drives the energy deposition depth progressively deeper. Conversely, the depth gets shallower by increasing the incidence angle. The simulation results were partly presented at [A5, A7].

First, the technical-grade metal target chemical composition and microstructure approximation are hugely simplified. Second, the used input parameters, i.e. low-energy, are margining the applicability range of the CASINO simulation package because the continuous slowing-down approximation (CSDA) fails ($\Delta E_{collision} \approx E_{particle}$) and data on stopping powers are hugely scattered in this low-energy range anyways, see Fig. 2.2 [51]. Moreover, the results also do not show electrons scattering at interfaces. This is again unphysical because it is known from the data presented here 5.50 as well as studied elsewhere [252] that electrons do scatter at interfaces.

5.3 ESD of technical-grade metal surfaces

This chapter's subdivision aims to decouple various factors that influence the ESD yield, always one at a time. Starting with the primary electron energy and dose, continuing with the surface state and composition, and finishing with environmental conditions, i.e. temperature. The mutual interplay of SEY, ESD yield and electrodesorbed gas is also presented to complete the picture started in the previous chapter on SEY.

5.3.1 Energy dependence

Section 2.6 discussed the whereabouts of the ESD yield energy-dependence and its utmost importance, shall the ESD be optimised (minimised or maximised) in a given technical application. According to the theoretical understanding, the energy dependence of ESD yield has the following areas of interest. The low energy part around and under 10 eV contains an energy threshold E_{thr} for desorption, below which the ESD yield $\eta(E)$ is either nil, or below the background (BG) level for detection η_{BG}. This is followed by an approximately linear increase up to 100–200 eV where $\eta \propto E^1$ because all the energy deposited by the primary electron falls into the SE escape depth. The ESD yield peaks out at E_{max} as the energy deposition depth becomes comparable to the escape depth. Above this peak, an asymptotic behaviour leaning towards $\eta \propto E^{-2}$ is gradually attained.

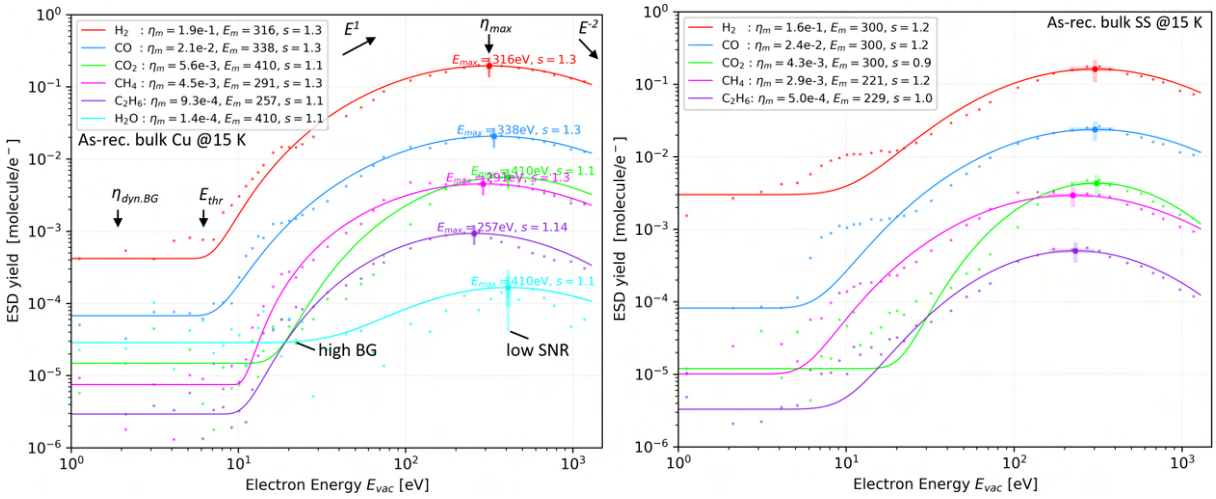

Figure 5.13: ESD yield energy-dependence measured on two sides of one LHC-grade copper (left) colaminated on P506 stainless-steel (right) held at 15 K, in an as-received supplier-cleaned state. The electron energy is referenced to the sample vacuum level. Datapoints are fitted with offset log-normal distribution with best-fit parameters listed in the legend. Combined uncertainty intervals at 1σ are ∼30 % as shown at the peak values. On the left, the systematic and stochastic components are also plotted. The high uncertainty on water is due to a high background (BG) and low signal-to-noise ratio (SNR). The data for Cu were presented in [A2, A3, A6]

Figure 5.13 shows an ESD yield energy dependence measured on an as-received LHC-grade copper colaminate surface held at 15 K. Once again, data for SS and Al shown in 5.13 and the left side of 5.14 is taken on samples with identical cleaning and storage history as the Cu/SS sample. Conversely, the Nb sample is a metal coating sputter-deposited at CERN and packaged in aluminium foil for transport. Hence, the Nb coating has fewer desorbable molecules and, as a result, has comparatively lower ESD yields than more technical-grade bulk metals. Contrary to the lower ESD yields, the general behaviour holds in terms of E_{thr}, E_{max} and decay at high energies.

Similarly to the SEY, the ESD energy-dependence curve can also be conveniently parameterised by a few important parameters. Here it is the desorption threshold and peak values E_{thr}, E_{max} and η_{max}, along with one fitting parameter s. A suitable function that connects these parameters can either be a log-normal distribution used here for metal surfaces or a modified (threshold-offset) Furman&Pivi fit [58], used in Section 5.6 to fit the ESD energy dependence of cryosorbed gases. Both of these are discussed in the Parametrization section 6.1, including the practical aspects of fitting the semi-empirical models to the experimental data. The uncertainty analysis of the single-point measurements and parametric fits to the energy scans are discussed in Appendix 6.8.

The absolute yields agree reasonably well with values found in literature [172, 181]. The energy

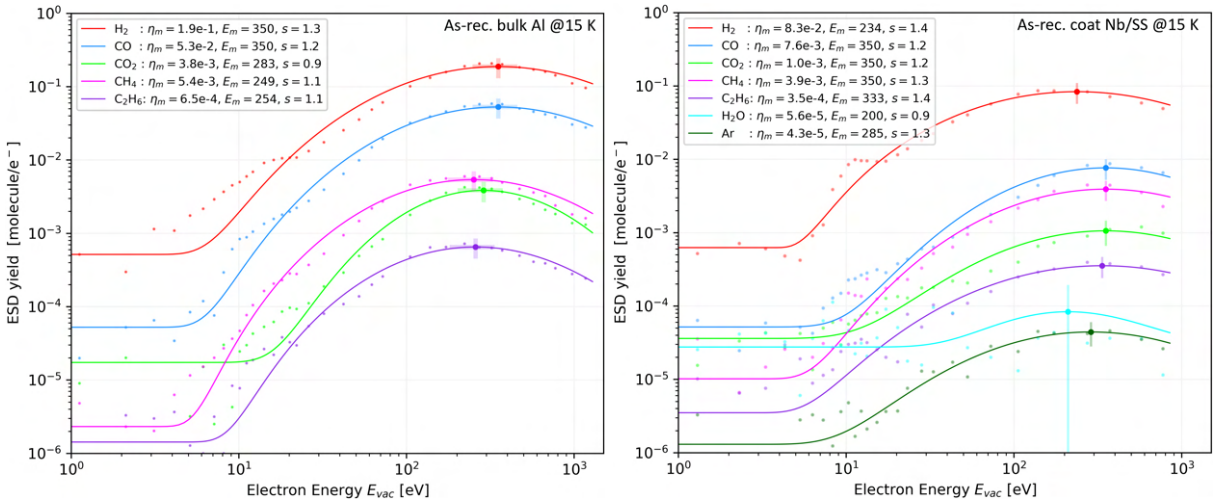

Figure 5.14: ESD yield energy dependence curves measured on as-received metal samples of Al (left) and Nb (right) acquired at 15 K. The electron energy is referenced to the sample vacuum level. Datapoints are fitted with offset log-normal distribution with best-fit parameters listed in the legend. Combined uncertainty intervals at 1σ are ∼30 % as shown at the peak values. Uncertainties on best-fit parameters are 10–20 %. The high uncertainty on water is due to a high BG and low SNR.

dependencies qualitatively agree with Achard's data [157] and Billard [172], including the threshold values (as extrapolated for a warm OFHC-grade UHV-cleaned copper). Coincidentally, the *'10–Volt effect'* brought to attention in Redhead memoirs [31] also agrees with the measured thresholds. The data shown here also agrees with those of Malyshev [179] until about 300 eV, where the dependencies depart, presumably as an artefact of a different experimental arrangement. Auslender&Minchenkov [253] report ESD yields from technical-grade Cu much lower than those measured here, but the energy-dependence they measure is very much alike and has a peak η_{max} at few hundred eV.

5.3.2 Conditioning process

Extended exposure of a surface to electron irradiation, referred to as electron conditioning, changes the irradiated surface state by removing or reprocessing surface-bound contaminants and inducing diffusion.

Shifting fully to the ESD investigation, the following data are mostly taken in an arrangement with +46 V_S bias to minimise the dynamic background visible at high doses around 1 mC, resulting in no simultaneous SEY measurement. The electron energy of 300 eV (compensated for sample bias) and a dose of 1 mC.mm^{-2} is taken systematically for further comparisons of other metals, coatings and treatments.

The ESD yield conditioning curves have two distinct regions of interest. The initial ESD yields η_0 are dose-invariant at very low electron doses around 10^{-6} C.mm^{-2} before a sufficient amount of gas is scrubbed off the surface to make a negative difference. This region is limited by the efficiency of the electrodesorption sequence and it is temperature dependent as shown below in 5.3.3. A transition to a surface concentration-limited region of a steady ESD yield decrease happens at around $D_0 \approx 10^{-5}$ C.mm^{-2}. A steady decrease is attained around and above 10^{-4} C.mm^{-2}, where the conditioning curves asymptotically approaches a power-law decrease (a straight line in log-log plot), as typically fitted by eq. 2.10.

The comparison of bulk Cu conditioning done with 300 eV electrons at 265 K and 15 K shows similar conditioning rates but much lower initial ESD yields at cold, especially for η_{CO2} and η_{H2O}. Conditioning curves for Al and SS that follow in Fig. 5.16 have an identical cleaning and storage history as the supplier-cut&cleaned Cu samples above. Remarkably, the overall behaviour is very similar for all the examined surfaces, which is undeniably a result of similar surface contamination.

Comparing the experimental data with values found across the literature, typically obtained around ambient temperature, shows that the initial yields agree reasonably well with Suzuki et al.[181], Billard et al. [172] and Achard's data [157]. So does the inflection point value D_0 agrees with Kennedy [162], Gomez-Goni&Mathewson[193] or data summarised by Malyshev [161]. The discrepancy, however, lies in the conditioning rates, i.e. the exponent α of the power-law decay. Here, values in a wide range of α≈0.7∼0.9 are typical, while other authors often attain the rate of α ≈1. Once again, the difference can originate as an artefact of different experimental arrangements rather than a physical reason. This discussion is further developed in Section 5.4.5 once the data on coatings and treatments are presented.

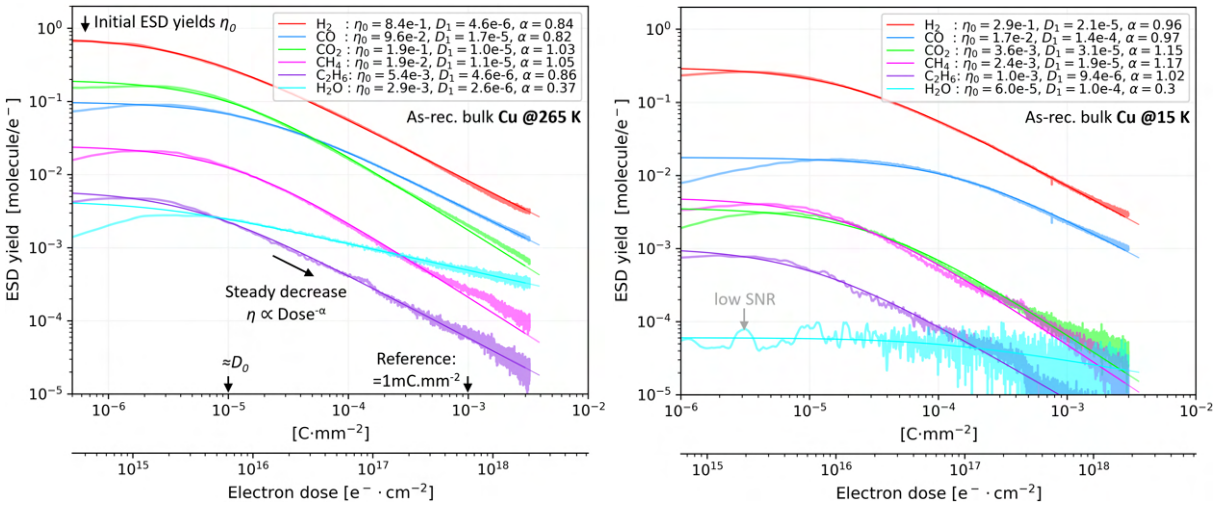

Figure 5.15: ESD yield dose-dependence of an as-received copper (left) measured with 300 eV electrons at 265 K and 15 K. Samples were cleaned at a supplier. Datapoints are median-smoothed and fitted with a modified power-law dose-dependence with best-fit parameters listed in the legend. The data were published in [A2].

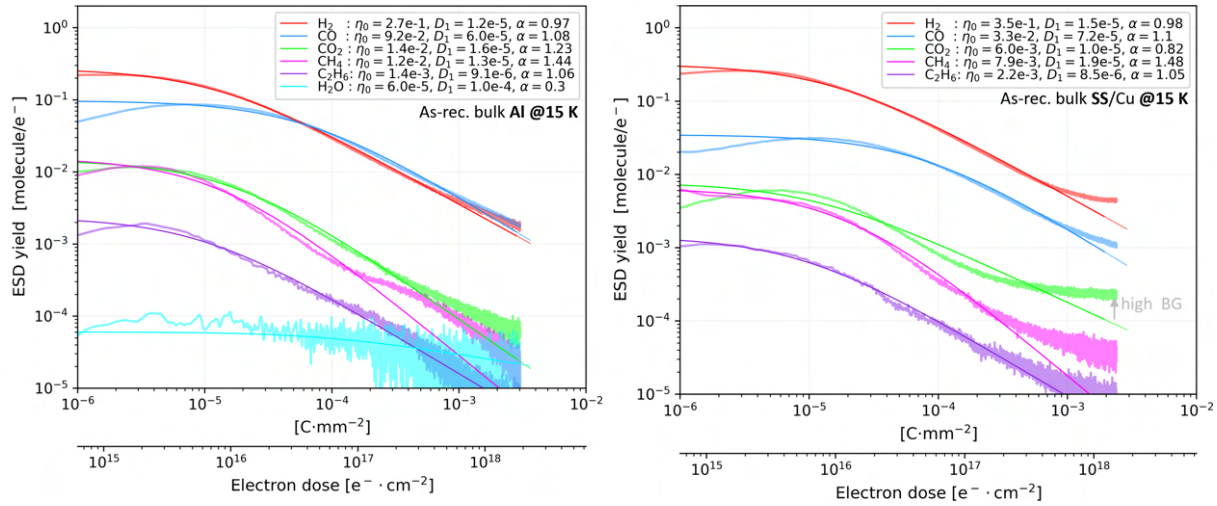

Figure 5.16: ESD yield dose-dependence of an as-received aluminium (left) stainless-steel (right) measured with 300 eV electrons at 15 K. Samples were cleaned at a supplier. Datapoints are median-smoothed and fitted with a modified power-law dose-dependence with best-fit parameters listed in the legend. The curves for P506 SS (right) flatten out around 1 mC.mm^{-2} due to a high dynamic background in the -28 V sample biasing. Other curves are acquired with +46 V sample bias leading to much lower dyn. background.

Electrodesorbed gas quantity

The electrodesorbed gas quantity provides another viewpoint on the ESD conditioning process. Following the ESD yield reduction presented in the previous section, the total quantity of electrodesorbed gas also changes when comparing ambient and cryogenic temperatures.

The quantity of each gas species released during an electron conditioning measurement at any energy can be calculated by integrating the background-corrected gas flux $p_j(t) = k_j.\Delta i_j(t)$, as explained in the Experimental Chapter 4. Hence, the time can be eliminated from the equation and express the ESD yield $\eta_j(t)$ dependence on a desorbed gas load either on the absorbed electron dose D, Fig. 5.15, or on the quantity of already desorbed gas $Q_j(D)$ at a dose D, Fig. 5.17.

The following Figure 5.17 compares the desorbed gases $Q_{tot,j}$ from as-received copper irradiated with 300 eV electrons at 1 mC.mm^{-2} dose. The quantity of desorbed H_2, the $Q_{tot,H2}$ is hardly affected by the low temperature and amounts to $\sim 20 \cdot 10^{15}$ molecule.cm^{-2}, both for cryogenic and ambient conditioning. On the contrary, heavier gases are heavily affected by cryogenic temperatures. At cold, the desorbed CO, $Q_{tot,CO}$ is reduced to about 50 % of its ambient temperature counterpart. The hydrocarbons CH_4 and C_2H_6 are reduced to $\sim$20 % and $\sim$10 % respectively. Finally, the electrodesorption of CO_2 and H_2O is particularly well inhibited by the cryogenic environment with $Q_{tot,CO2}$ and $Q_{tot,H2O}$ reduced to $\sim$5 % of

the ambient temperature value.

This measurement shows a clear trend of lower desorption yields and consequently lower $Q_{tot,j}$ values at cold for molecules that are heavier and/or have higher assembly numbers (number of atoms in a molecule, in this context). Indeed, one should argue that the desorption yields of molecules is only partly diffusion-limited and that other limitations come in at other desorption sequence steps. Take Argon as a counterargument (not displayed), the atomic yield η_{Ar} and desorbed quantity $Q_{tot,Ar}$ changes only slightly with temperature, at least within the experimental precision. This illustrates that other parts of the desorption sequence, such as diffusion of electronic excitations or quenching during ejection, are also somewhat temperature-dependent.

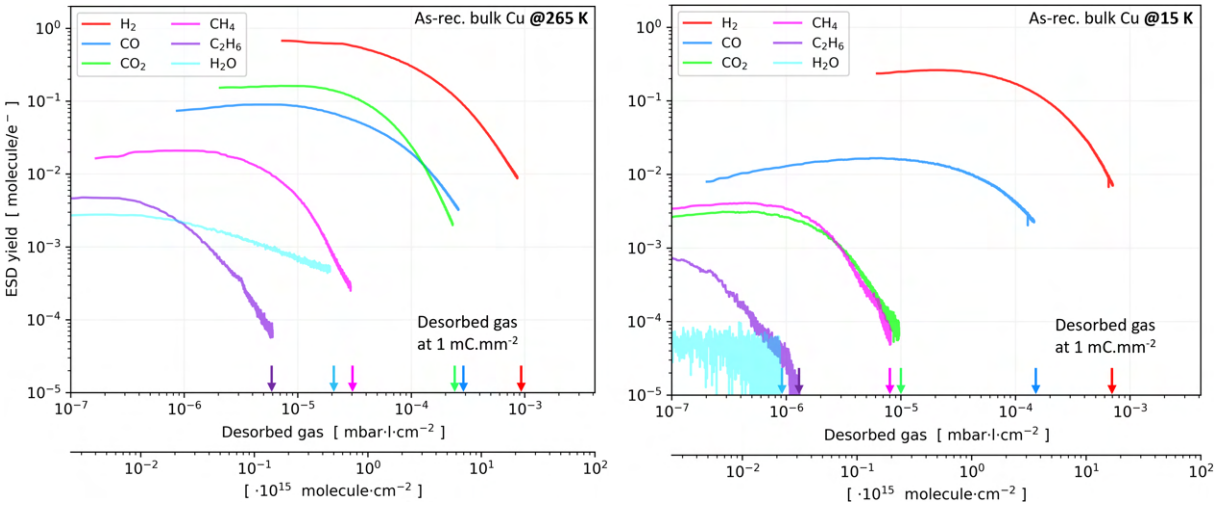

Figure 5.17: ESD yield conditioning at 300 eV of as-received unbaked Cu samples, cut&cleaned at a supplier, measured around ambient (265 K), left, and cryogenic temperatures (15 K), right. Note the difference in initial ESD yields and the electrodesorbed gas quantity at 1 mC.mm^{-2} is used for comparisons in Figs. 5.22 and 5.23.

Despite the cryogenic temperatures, the measured $Q_{tot,H2}$ non-reduction suggests that the hydrogen surface mobility is not a limiting factor for the H_2 desorption sequence.

For comparison, Minissale et al. [254] measured and calculated the oxygen diffusion rate and concluded that thanks to diffusion via quantum tunnelling, the diffusion rate is not zero even when approaching 0 K. In fact, it dominates the diffusion process at cryogenic temperatures and becomes comparable to the classical, thermally-enabled diffusion at 20 K and higher. Indeed, despite having a non-zero diffusion rate, it is considerably slower at cold, in turn lowering the recombination rate. Moreover, as the surface concentration of precursors decreases at high electron doses, the desorption becomes surface concentration-limited. Both these facts are crucial for low desorption yields observed at low temperatures and high doses.

For completeness, a similar conditioning experiment was also performed at 100 K and 200 K, resulting in an ambient-like behaviour for the 200 K conditioning and a cryogenic-like behaviour for conditioning at 100 K. This agrees with the general temperature-dependent behaviour of ESD yield, as measured in Figure 5.24, Section 5.3.3.

Interplay of ESD, SEY and electrodesorbed gas

Here, an ESD conditioning measurement is done on warm Cu with 300 eV electrons, similar to that on the right of Fig. 5.19. The data can be plotted in such a way to capture the mutual evolution of ESD, SEY and the electrodesorbed gas. The left plot of Fig. 5.18 captures the SEY and ESD yield decrease with the electrodesorbed gas quantity. The ESD yield starts with a constant plateau where the ESD yield is limited by the desorption efficiency, and the SEY decreases slowly. As the surface is scrubbed off contaminants, the ESD process now enters heavily coverage-limited desorption and the SEY decreases as a direct result of the surface being depleted of contaminants. Past this knee, the SEY approaches its ultimate value around δ_{300eV}=1.1 in the graphitization-dominated region of the conditioning process. Meanwhile, the ESD yields go to zero because the surface coverage of desorbable molecules goes to zero.

The right plot eliminates the dose from the graph and only captures the SEY dependence on electrodesorbed gas. Once again, two distinct regions are visible in the plot. The same knee as on the left corresponds to the δ_{300eV}=1.8, where about half of the electro-desorbable gas has left the surface. Before this point, the major contributor to the SEY decrease was removing the adsorbed gas from the surface.

Past this point, the SEY decrease is attributed to the electron-induced chemical changes to the surface composition - most notably graphitization of carbon-containing residues, as verified by an XPS analysis, Fig. 5.9.

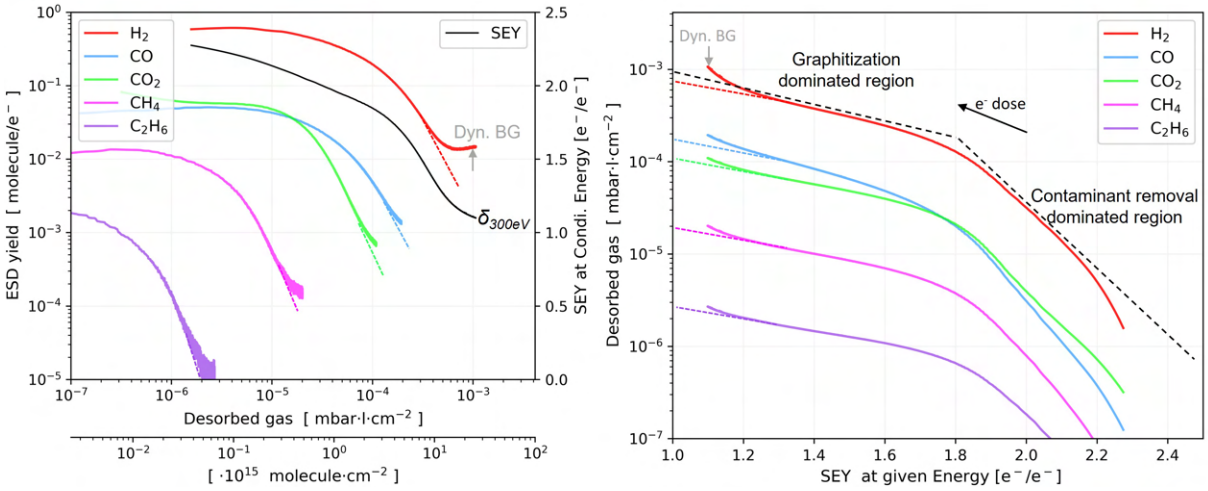

Figure 5.18: ESD yield conditioning at 300 eV of as-received unbaked copper samples taken around ambient temperature. Different projections of the conditioning process are discussed in the text. The electrodesorbed gas is plotted against the ESD yield (left) and the SEY (right). Note the knee at $\sim 2.10^{-4}$ mbar.l.cm^{-2} ($\sim 5{\cdot}10^{15}$ molecule.cm^{-2}) that happens at a $\sim 10^{17}$ e$^-$.cm^{-2} dose of 300 eV electrons.

These two plots become useful if one knows the SEY and needs to approximate the ESD yields and a quantity of gas already desorbed. For instance, when the δ_{300eV} reaches a value of 1.3, being the multipacting threshold in the LHC dipoles, the electron multipacting vanishes and so does the electron conditioning, for the most part. By then, the ESD yields have decreased by a factor of ~10x and about 20 ML of gas has electrodesorbed, mostly being H_2, CO and CO_2. Knowing this strong link between SEY and ESD conditioning, it remains unclear why the SEY conditions very similarly at cryogenic temperatures, while the ESD conditioning at cold removes by a factor of ~10 fewer molecules heavier than H_2 than at 300 K, Fig. 5.17.

Henrist&Baglin et al. [75, 186] reported observations identical to the ones presented here, also done on a LHC-type technical-grade copper held at ambient temperature. Cimino et al. [76] studied the same system and concluded that SEY conditioning can be simplified into a two-step process as described here.

Role of electron energy

The energy indeed has a major impact on the resulting electron-conditioned state, with higher energy electrons being generally favourable to scrub foreign molecule off the surface, consequently decreasing the η. To visualise the link to the SEY conditioning, let us take the SEY and ESD yields plotted as a function of electron dose at two different electron energies: 20 eV and 300 eV, see Figure 5.19.

The left side shows how 20 eV electrons have only a limited conditioning effect on the η of a Cu surface, as already illustrated for the case of SEY, Fig. 5.2. Both measurements are done in -28 V mode, so the SEY is also accessible (at a given energy) and plotted on the secondary axes; mind the different ranges. Note the sudden end of δ_{20eV} conditioning induced by 20 eV around ~ 0.1 mC.mm^{-2} and no significant decrease above ~ 0.3 mC.mm^{-2}. This also projects to no significant gas removal, albeit this ESD measurement has higher uncertainties due to being so low above the dynamic background level (marked on the right plot). The right side shows a full conditioning curve done at 300 eV primary energy, which includes the δ_{300eV} conditioning down to 1.1 and η decrease by about two orders observed for all gas species except H_2O, as discussed in Section 5.4.5. A similar study was done for 1 keV electrons, resulting in a similarly fast ESD conditioning rate for 300 eV. The 1 keV irradiation, despite having slightly lower as-received ESD yields than at 300 eV, electrodesorbs slightly more gas molecules than 300 eV, see Figure 5.20 below. Presumably due to a more effective diffusion of gas (or its precursors) from subsurface layers.

Figure 5.20 summarises the ESD yields of bulk technical-grade Cu measured at 20 eV, 300 eV and 1 keV at 15 K for as-received state and conditioned to 0.3 mC.mm^{-2}. As already foreseen from the SEY and ESD data, the 20 eV electrons do not desorb nearly as much gas as 300 eV and 1 keV, regardless of an electron dose or temperature. While the 20 eV electrons desorb about 1-2 ML of gas, this amount

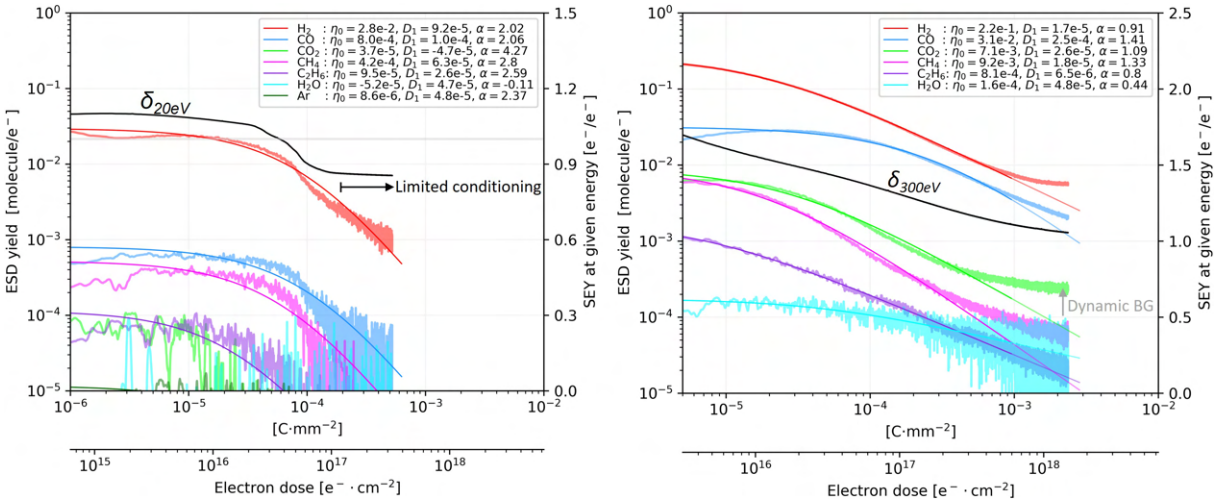

Figure 5.19: ESD and SEY conditioning curves measured at 15 K on Cu samples; Cu/SS (left) and bulk Cu (right) received the same cleaning and storage. Conditioning was done with 20 eV and 300 eV electrons to ∼0.5 mC.mm^{-2} and ∼2.3 mC.mm^{-2}, respectively. The measurement was done in -28 V mode, so the SEY is accessible (at a given energy) and plotted on the secondary axes. Note the sudden end of conditioning induced by 20 eV around ∼0.1 mC.mm^{-2} where about 1 ML of H_2 is desorbed.

increases by a factor of ∼10x for the higher energies. Presumably due to an electron-induced gas diffusion from subsurface layers or pores. If the electron penetration depth scales proportionally to energy, the 300 eV electrons penetrate about 10–15x deeper than 20 eV ones, accessing proportionally more absorbed gas. This approximately agrees with the ESD yield cut-off when about 1 ML of H_2 gets desorbed by 20 eV electrons. For comparison, the ESD yield at 300 eV cuts off after about 10 ML of H_2 gets electrodesorbed.

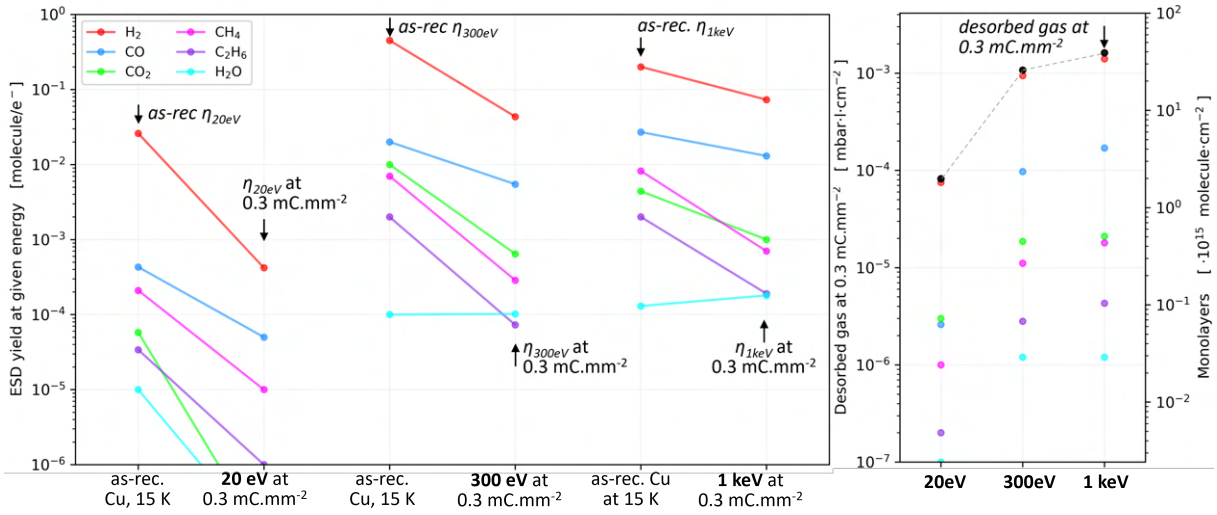

Figure 5.20: Summarised ESD yields of bulk technical-grade Cu measured at 20 eV, 300 eV and 1 keV at 15 K for as-received state and conditioned to 0.3 mC.mm^{-2}. All measurements come from pristine spots of the same supplier-cleaned sample.

The ESD curves shown here were taken directly after the SEY curves shown in Fig. 5.2, i.e. in a semi-conditioned state achieved by irradiation at dose of 17 eV, 300 eV and 1 keV electrons. The threshold around 10 eV and peak around 300 eV are clearly visible and seem to be mostly invariant with the conditioning state, unlike the absolute yield. The ESD yield of a semi-conditioned Cu, taken at its maximum η_{max}, is highly dependent on the conditioning energy. While 300 eV and 1 keV irradiation resulted in a decreased η by around a factor ∼10 across the studied energy range, 17 eV irradiation did not. Further conditioning with 17 eV electrons led to a measurable ESD yield reduction across the studied energy range, but without ultimately reaching the same low ESD yields as irradiation at 300 eV and 1 keV would. This is generally in agreement with the SEY curves measured just prior to these ESD energy-dependent curves and the electrodesorbed gas quantities in Fig. 5.20. This observation aligns with the theoretical understanding because the yield should scale with the (decreasing) surface coverage of to-be-desorbed species. Contrary to this, and regardless of the surface coverage, the nature of the

adsorbate binding and the physical desorption processes remain the same. Since the electrodesorption sequence remains unchanged, about the same energy thresholds and peak values of η_{max} are observed regardless of the conditioning state.

Figure 5.21 shows ESD yield energy-dependence measured for different conditioning states achieved by conditioning with different electron energies but at a comparable dose. Indeed, each energy was measured on a pristine spot of the same sample. This paragraph closely follows the cold SEY conditioning as a function of energy, as sampled at a given dose of $\sim$0.8 mC.mm^{-2}. In fact, this medium dose was chosen to still have a significant ESD signal during the measurement.

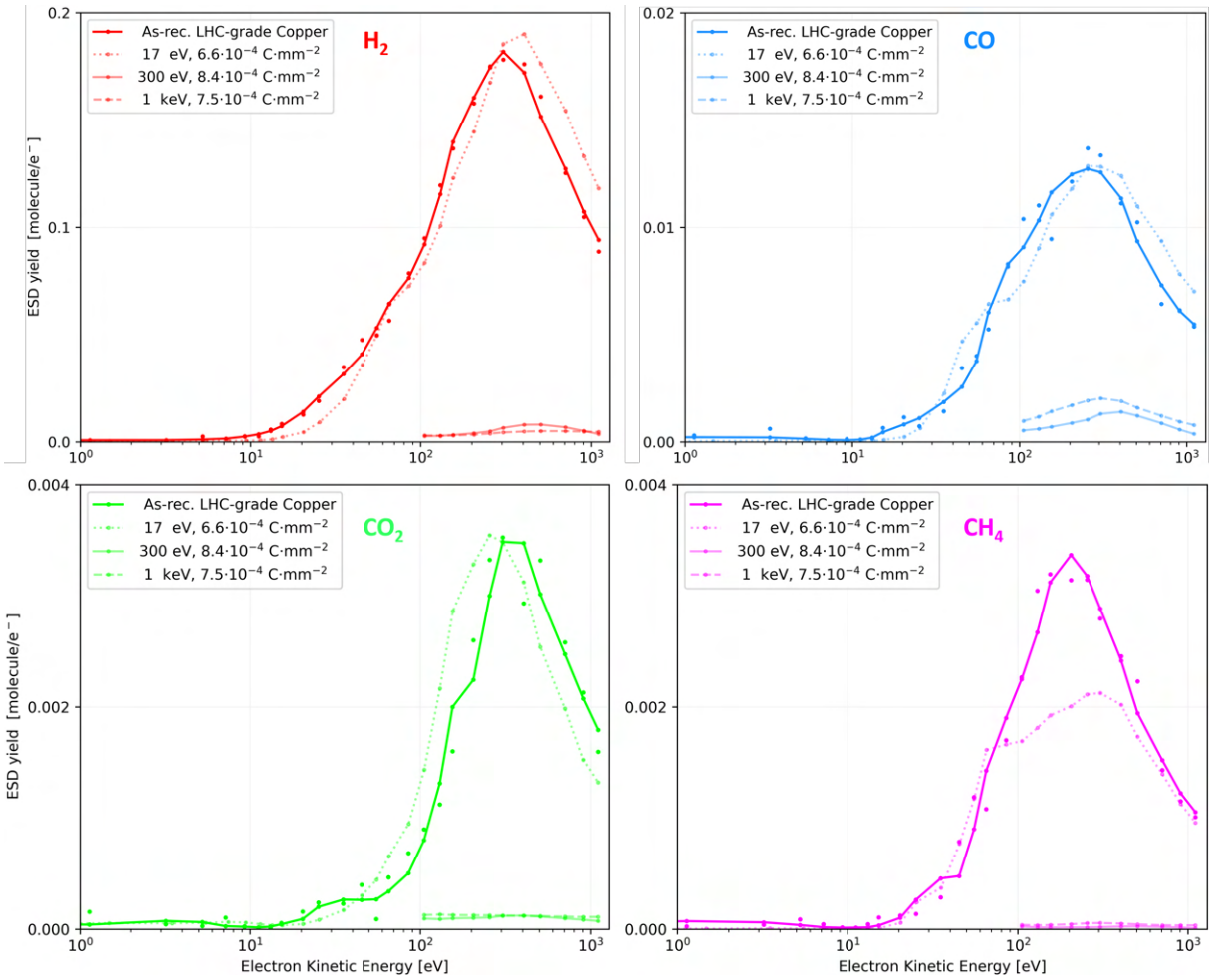

Figure 5.21: ESD yield energy-dependence measured on LHC-grade copper measured after 17 eV, 300 eV and 1 keV conditioning at comparable dose. Mind the log-linear projection used to capture detail across all energies. The corresponding SEY curves for the 15 K and 300 K sample (performed before ESD measurements) are shown in 5.2. At bottom-right plot, the CH_4 yield after 20 eV conditioning is off due to bad signal sampling and high background, but should follow the same trend as others. The electron energy is referenced to the sample vacuum level. Savitzky-Golay filter[223] is used to smoothen the scattered datapoints and guide the eye. Unfiltered datapoints are shown for the as-received state to illustrate the scatter. This data is partly presented in [A3, A7].

The experimental data presented here for initial and conditioned ESD yields, as well as electrodesorbed gas quantities, are in agreement with Kennedy [162], Gomez-Goni&Mathewson[193] and Malyshev [161]. The results reported by Malyshev measured for technical-grade surfaces held at ambient temperatures also show that higher energy electrons desorb larger amounts of gas. As argued, the tentative explanation is that the deeper penetration depth of higher electron energies renders more subsurface gas (or its precursors) accessible to desorption.

Role of surface composition

Figure 5.22 shows that other metals, notably Al and SS have ESD yields, desorption thresholds and electron conditioning curves that are notably similar for different technical-grade metals with the same cleaning and storage method. This is a strong sign of the surface chemistry being the key governing factor

determining the ESD yield, rather than the bulk composition. Aside of bulk metals, metal coatings were also characterised for comparison, with a focus placed on technically-important coatings and their baseline application. The results for treatments and coatings have a dedicated Section 5.4. The measured ESD yield energy and dose dependencies of metals coatings closely resemble those of bulk metals in terms of the threshold and peak positions, but have overall lower yields and are more strongly dominated by H_2 desorption.

An experiment was also done to assess the effect of vacuum firing of stainless steel on the ESD yields. The H_2 yield is particularly interesting since vacuum firing aims to deplete the atomic hydrogen subsurface concentration. The firing led to some limited decrease of H_2 yield, but the difference is comparable to baseline chemical cleanings. This observation points towards the H_2 depth profile having only a limited importance on the ESD yield.

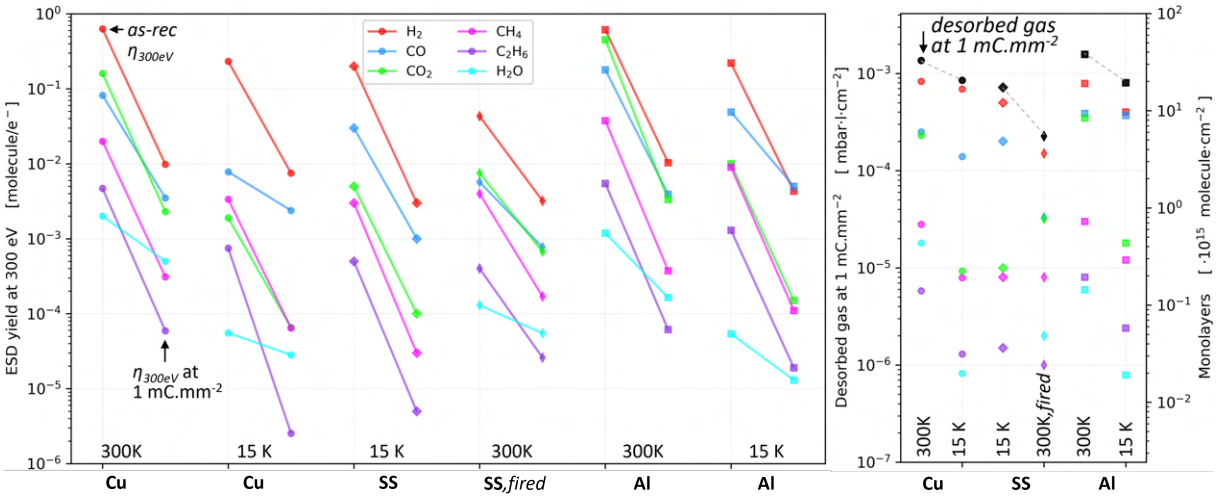

Figure 5.22: ESD of technical-grade samples of Cu, stainless steel and aluminium measured at 300 eV at 15 K and 300 K for as-received state and conditioned at 1 mC.mm^{-2}. Warm and cold measurements are done on pristine spots of the same sample.

The experimental data presented here for Cu in various states show initial and conditioned ESD yields, as well as electrodesorbed gas quantities, that are in general agreement with measurements of Kennedy [162], Gomez-Goni&Mathewson[193] and Malyshev [161].

Role of surface state

Ex-situ chemical and thermal treatments to the copper colaminate samples created different surface states. This in turn manifested in different ESD yields, both as-received and conditioned, as sampled at 1 mC.mm^{-2}. In this case, the ESD was measured at ambient temperatures, as also done for the SEY measured on the same specimen and presented in Figure 5.8.

The quantity of electrodesorbed gas also varies, substantiating how different treatments affect the amount of electron-desorbable gas and the corresponding properties. As the (ex-situ) bakeout temperature increases, the surface is progressively cleaned off contaminants. Owing to the memory effect, the cleaning effect of a bakeout persists throughout a ∼5 min-long sample transfer and is well measurable. The 300 °C bakeout, last sample in Fig. 5.23, does not seem to bring any tangible decrease of ESD yields over the 200 °C bakeout. Also note that both the 100 °C in-air bakeout and the 200 °C in-vacuum bakeout only offer a marginal decrease of ESD yield when compared to the original chemical cleaning. Achard et al. measured a similar trend of ESD decreasing with bakeout temperature, although done in situ, but without levelling yields above 200 °C. It is, therefore, possible that some information was lost due to the ∼5 min long in-air sample transfer.

It is known that a suitable chemical cleaning can reduce the ESD yields by up to an order of magnitude and, by extension, the electrodesorbed gas quantities too. This is readily illustrated by comparing the ESD yield of the supplier-cleaned Cu that was only rinsed in a warm isopropanol ultrasonic bath and that of a Cu chemically cleaned at CERN. Comparative studies were done at CERN to assess surface cleanliness by measuring the ESD yields of copper cleaned with different detergents [156, 255]. Edwards seconds such observations [256], as well as Nishiwaki&Kato [185] who tested different approaches to

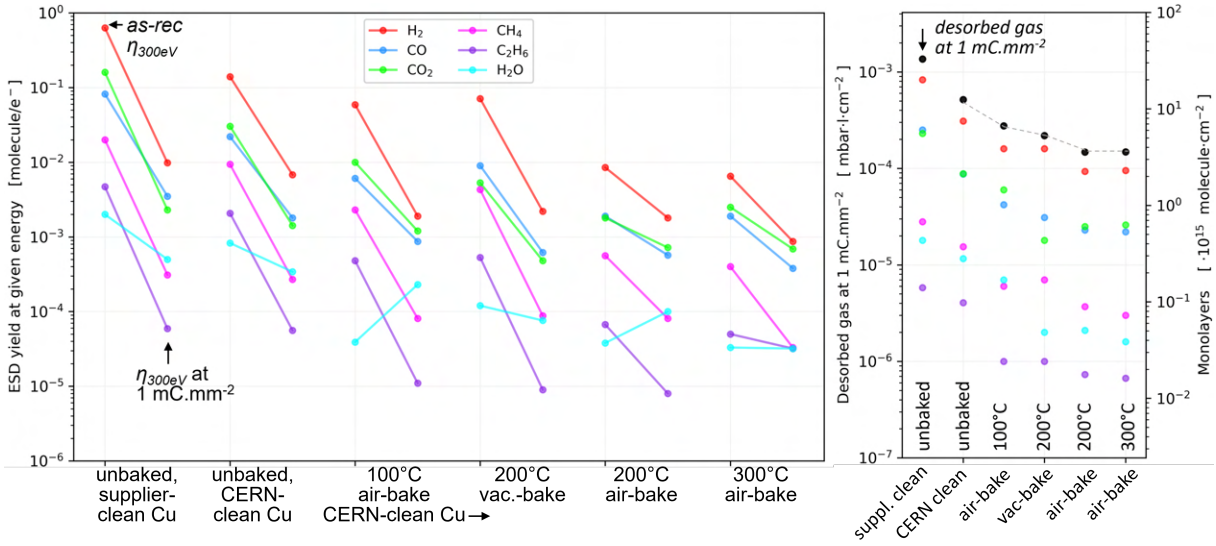

Figure 5.23: ESD of copper colaminate measured at 300 eV for a range of surface states achieved by ex-situ chemical and thermal treatments. Always starting with an as-received state followed by a conditioned state at 1 mC.mm^{-2}.

UHV-grade cleaning and degreasing of different technical-grade metals, such as 304 SS and OFC Cu, respectively.

While chemical and thermal cleanings are a must for achieving UHV-compatible surfaces with low stimulated yields, by far the most effective is a glow discharge. This plasma-based method effectively ion-sputters away the surface-absorbed contaminants that are subsequently pumped away. Unfortunately, this could not be tested with the current experimental capabilities, but ESD yields were reported to decrease by more than 6 orders of magnitude due to an in-situ Argon glow discharge cleaning, as reported by Mathewson&Kouptsidis [257].

5.3.3 Temperature dependence - Role of cryogenic conditions

The initial (as-received) ESD yields were systematically measured at 300 eV for a range of unbaked samples, coatings and treatments. The temperature varied from ambient to cryogenic, i.e. from around 300 K to around T_{D1}=10∼15 K. The measurement was preferably done during a cool-down of the system to prevent cryosorbed gas from influencing the measurement (which was observed in measurements done during a warm-up phase). The CERN-cleaned sample apparently has much less surface-bound contaminant, which resulted in much lower ESD yields and not as dramatic reductions at cryogenic temperature.

The ESD yield reduction factor η_{300K}/η_{15K} is the smallest for H_2, as the lightest molecule, up to 200x for CO_2 as the heaviest molecule.

It would be tempting to assign the η_{300eV} decrease at low-temperature to a slower recombination rate, but note that Ar yield in the right side of Fig. 5.24, which exhibits the same temperature dependence as other regular multi-atomic gases. The fact that the Ar desorption sequence is also temperature-dependent can be explained either by the pre-desorption electron dynamics being temperature-dependent or by a thermally-enabled pore diffusion bottlenecking the Ar atom desorption. Though neither of these hypotheses is very likely, some physical process has to be accountable for these trends.

The ESD yield reduction factor η_{300K}/η_{15K} gradually increases with the molecular mass. Moreover, the position of the inflection point T_p also increases with the atomic mass. The observation that the ESD yield reduction is mass-dependent points to a diffusion-limited desorption sequence. One could also argue that recombination-limited desorption is very limited at cryogenic temperatures. This would leave the cryogenic ESD yield dominated only by molecules already present on the surface, as opposed to the freshly recombined ones. Shall this be the case, the mass-dependence of T_p and the yield reduction factor would also support this interpretation.

It is worth noting that Baglin&Jenninger[191, 258] measured the same reduction of PSD yield between ambient and cryogenic temperatures. They also observed the PSD yield to reduce around the same temperature range of 100–150 K, as reproduced in Section 2.22. This is no coincidence, as part of the PSD can be assigned to photoelectron-induced ESD. This can be readily illustrated by comparing X-ray PSD and ESD yields and cracking patterns of methanol [259], which happen to match very closely and

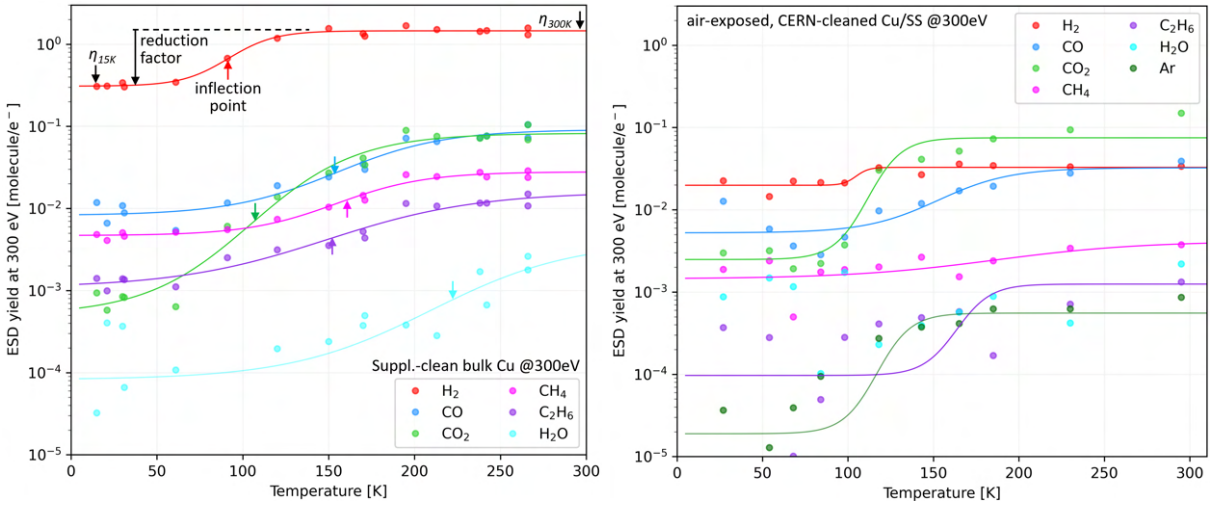

Figure 5.24: ESD yield at 300 eV of as-received unbaked OFE Cu samples measured between ambient and cryogenic temperatures. The datapoints are fitted by a modified sigmoid function discussed in Section 6.2. Left: Sample cut&cleaned by a supplier and long-term stored in plastic. This data is presented at [A3, A5, A6]. Right: Sample cut&cleaned at CERN according to cleaning procedure for LHC beam-screen Cu.

prove that internal photoelectrons have a major contribution to the desorption yields.

For completeness, one could argue that the reduction at cold is due to an experimental artefact: gas sticking in the cold system, which could reduce the signal and hence the measured ESD yield as well. This can be readily disapproved by the fact that the ESD yield drops around 100–150 K for most gases, whereas the cryosorption temperatures are in the tens of K range. Besides, the signal reduction due to gas recycling is a factor of 2x at most in the used experimental arrangement, so it cannot possibly explain a factor of 5-150x observed here in Fig. 5.24. Therefore, the yield reduction comes at a temperature range that has nothing to do with temperatures relevant to the vacuum gas dynamics, decoupling the two phenomena.

5.4 SEY and ESD of functional coatings and treatments

Modification and functionalisation of technical surface properties is often required to suit a particular use case scenario. The surface can be modified electrochemically or via a particle beam (ion, electron or photon). Here, a low-SEY laser-treated Cu surface is characterised in terms of its electronic and molecular emission. Then, technical surfaces can also be coated with suitable materials to deliver a low-SEY (carbon coating), pumping effect (NEG coating), or superconductive properties (Nb, REBCO). Such coated technical surfaces equally emit electrons and molecules upon irradiation, which is critical under some technical applications and is researched in the following paragraphs. SEY, ESD, TPD and SEM investigations presented here were done at ambient and cryogenic conditions, always reflecting the representative use-case scenario of a given technical application of each studied coating and surface treatment. Some research results presented in this Section were published in [A1, A2, A7].

First, low-SEY treatments were investigated, as they have the highest priority. The necessity arises from the electron cloud mitigation strategy for the HL-LHC and the corresponding need for a qualification for an in-situ deployment of an antimultipacting beam-screen treatment. The two approaches that were conceived for an in-LHC application are carbon coating and laser treatment. CERN's in-house produced thick and thin carbon coatings were investigated between 12 K and 300 K. Two types of amorphous carbon coatings were investigated at both ambient and cryogenic temperatures because the baseline use-case applications encompass both cases. The 450 nm thick carbon coating is applied in CERN's SPS machine, whose regular-conducting magnets operate at ambient temperatures. Meanwhile, the 50 nm thin version is being deployed in the cryogenically cooled LHC beam-screen in the framework of the HL-LHC upgrade. The 50 nm thin carbon coating was ex-situ deposited on a beam-screen and is now installed in the inner triplet magnets [30]. laser treatment represents a second approach to antimultipacting surface treatment of the BS, resulting in an efficient EC suppression. Laser-treated technical-grade copper samples were produced externally (Dundee University) with different laser parameters and under a nitrogen atmosphere, as detailed by Baudin [109]. The characterisation was done between 12 K and 300 K to cover the entire relevant range.

To recall, the carbon and Ag coatings were sputter-deposited in the Argon process atmosphere at ∼1 mbar, while the NEG and Nb coatings are done in Krypton due to its higher sputtering efficiency for heavier molecules (similar masses favour knock-on energy transfer that drives the sputtering process). Argon was used to vent all coated parts, although storage and transport were done in air. In either case, Argon remains the highest-yielding electrodesorbing gas, as visible in Figs. below, such as 5.36. This observation points to the airborne Argon entering the metal surface from the atmosphere in the post-production phase instead of being incorporated during the sputtering process.

Next up is CERN's in-house Ti-Zr-V NEG coating method. The sample was analysed between 12 K and 300 K, despite the baseline operation around ambient temperatures, e.g. as applied at the long-straight sections of the LHC.

Finally, REBCO-type HTS were studied to provide relevant input in terms of vacuum design and impedance-mitigation strategies for studies of future machines operating at cryogenic temperatures, such as FCC-hh [25]. Two REBCO samples were acquired from external manufacturers SuNAM and SuperOx and were characterised at 12 K, although higher temperatures, say around the liquid nitrogen boiling point, are the most relevant for real-life applications.

5.4.1 Amorphous carbon coating

The amorphous carbon coatings were sputter-deposited onto UHV-grade cleaned, degreased metal surfaces (SS or copper colaminate onto SS) at 50 nm (thin) and 450 nm (thick) thicknesses. Both coatings have a 110 nm Ti underlayer that enhances adhesion and captures the H_2 during the sputter deposition process which is otherwise detrimental [47].

This thicker version was tested with LHC-type proton beams at CERN's SPS machine [98, 99] and at cryogenic conditions inside the COLDEX experiment [100–103]. Since carbon-coating of few nm only has proved to be sufficient antimultipactor [97], the 50 nm is currently the baseline for the LHC deployment [30].

Figure 5.25 shows an SEM image of the coated copper colaminate. Note that the 50 nm thin version is barely noticeable and the underlying surface features are well visible (parallel grooves after press-rolling). Contrary to that, the 450 nm thick version mostly covers the surface features and creates a

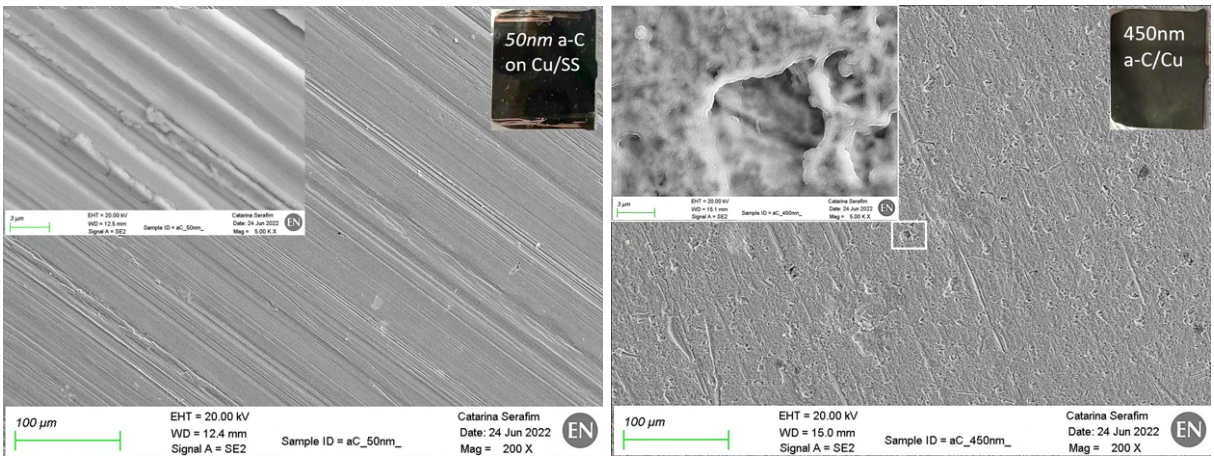

Figure 5.25: SEM images of amorphous-carbon coating on a copper-colaminated surface. Left: 50 nm thin coating. Right: 450 nm thick coating mostly covers the substrate microstructure, unlike the thin one. Details in the text. The SEM images are taken on FE-SEM Zeiss Sigma, kindly provided by EN-MME-MM, and acquired by C. Serafim, TE-VSC-VSM, CERN.

porous overlayer. Indeed, the below-presented TPD measurements show about a 10x (thin) and 50x (thick) higher specific surface than a bare flat copper colaminate.

SEY energy and dose dependence

As discussed in the theoretical Section 2.3, amorphous carbon has a distinct E_{max} position at 200 eV which is caused by the low atomic mass (Z) and consequently low stopping power. As argued in the theoretical Chapter 2.3, the low δ_{max} is caused by a synergy between the low-Z and correspondingly low stopping power and low backscattering coefficient, resulting in a deep electron penetration and a high work function, acting as a barrier to the secondary electron emission. The surface roughness added by the coating also seems to contribute, as visible in the angle-dependent SEY measurements shown in 5.2.5. It is worth noting that the amorphous state of the carbon coating seems to have little effect on the SEY curve shape because the HOPG results in a practically identical SEY curve. This supports the above argument that the substrate density drives the SEY curve shape, which is similar for both amorphous graphite and HOPG, both being different crystalographic of sp2-type carbon.

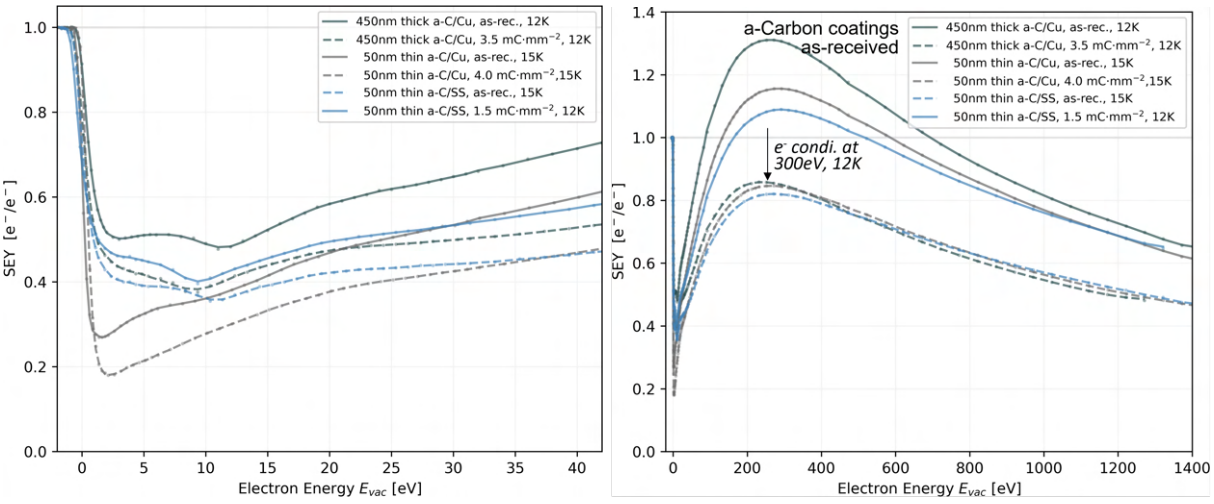

Figure 5.26: SEY energy dependence curves measured for 50 nm thin and 450 nm thick versions in their as-received and electron conditioned states. Electrons at 300 eV were used at a dose indicated in the legend. The electron energy is referenced to the sample vacuum level.

The SEY curves measured on both thick and thin versions illustrate the effect of these phenomena. The low δ_{max} gets even lower once the surface is scrubbed off contaminants by the 300 eV electron irradiation. The E_{max} position remains at 200 eV before and after the conditioning, which again supports the interpretation from Section 5.2, assigning the E_{max} position to the bulk-defined energy deposition profile, rather than the surface-defined work function. In other words, the subsurface layers do not

change during electron conditioning, contrary to the electronic properties of the surface, whose chemical composition changes during irradiation.

The low-energy SEY region shown in the inset shows a very low SEY. Even for the as-received state, the 5 eV peak characteristic for surface-bound contaminants is almost absent. This is a sign of a rather contaminant-free surface, but contrasts with the high ESD yields of the thick coating. It is plausible that the gas is bound in the pores (roughness factor ≈25, see Section 5.2), rather than on the surface, and therefore does not drive the SEY high, but still causes high ESD yields. For completeness, the SEY of amorphous carbon coating was also observed to be temperature-independent.

ESD energy and dose dependence

To a large extent, the ESD energy dependence follows that of SEY. The peak ESD yield η_{max} often copies that of δ_{max} due to the common origin in electronic excitations, as outlined in the theoretical chapter. However, this relation fails here, as illustrated on the 300 K measurement visible in the left of Fig. 5.27, where the η_{max} peaks out at 2-3x higher energy than the δ_{max}. Conversely, an identical measurement done at 12 K on an intact spot of the same sample places the η_{max} only 1-2x higher than the δ_{max} peak. Such observation substantiates that temperature-dependent thermal diffusion of gas (or its precursor) happens prior to its desorption, and can influence the ESD yield at higher energies. In the warm system, the thermally-driven diffusion carries the gas towards the surface. Contrary to that, thermal diffusion is partly quenched at cryogenic temperatures, leaving the gas cryotrapped in the pores and effectively preventing it from electrodesorbing. Though, this hypothesis is somewhat challenged by the temperature-dependence measured at 300 eV, see left side of Fig. 5.30, which is not as profound as one would expect for such a strongly thermally-enabled diffusion-limited ESD that was just theorised.

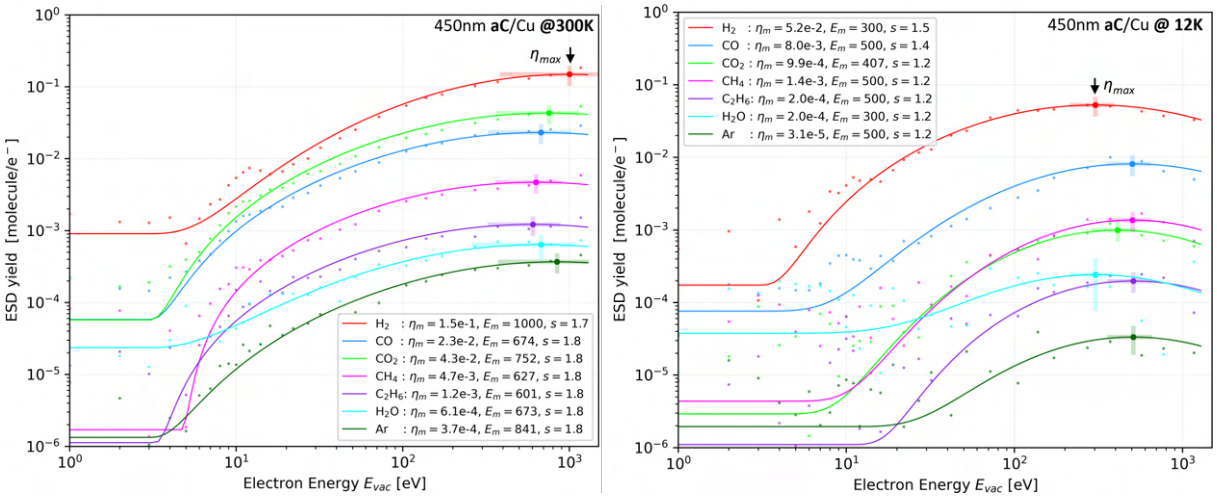

Figure 5.27: ESD energy dependence curves for 450 nm thick amorphous-carbon coating on a copper-colaminated surface taken at 300 K (left) and 12 K (right). Details are discussed in the text.The high uncertainty on water due to a high BG and low SNR. The electron energy is referenced to the sample vacuum level. Combined uncertainty intervals at 1σ are ∼30 % as shown at the peak values. Uncertainties on best-fit parameters are 10–20 %.

To conclude on this, the observation of ESD energy sweep being temperature-dependent is also a direct evidence of subsurface diffusion processes taking an active part in the desorption sequence. This also explains why higher-energy electrons desorb more gas than low-energy ones. Similarly, less gas gets electrodesorbed if low temperatures limit the diffusion. The fact that Argon, as a non-interacting noble gas, follows the behaviour only supports this interpretation.

The ESD yield conditioning was measured at 300 eV for both thick and thin carbon coatings at ambient and cryogenic temperatures. The dose dependence differs from bare technical-grade metals, and exhibits lower initial ESD yields, but also a lower conditioning rate resulting in a flatter dose dependence. The slow conditioning rate $\alpha \approx$ 0.5-0.6 points towards being a result of porosity, as it is higher for the thick coating. This also is in accordance with the TPD surface analysis discussed below in Section 5.5.

Electrodesorbed gas quantity

Similarly to flat metals, the plot in Fig. 5.29 summarises the integral quantity of gas electrodesorbed during 300 eV electron conditioning measurements, as sampled at a dose of 1 mC.mm^{-2}. The amount

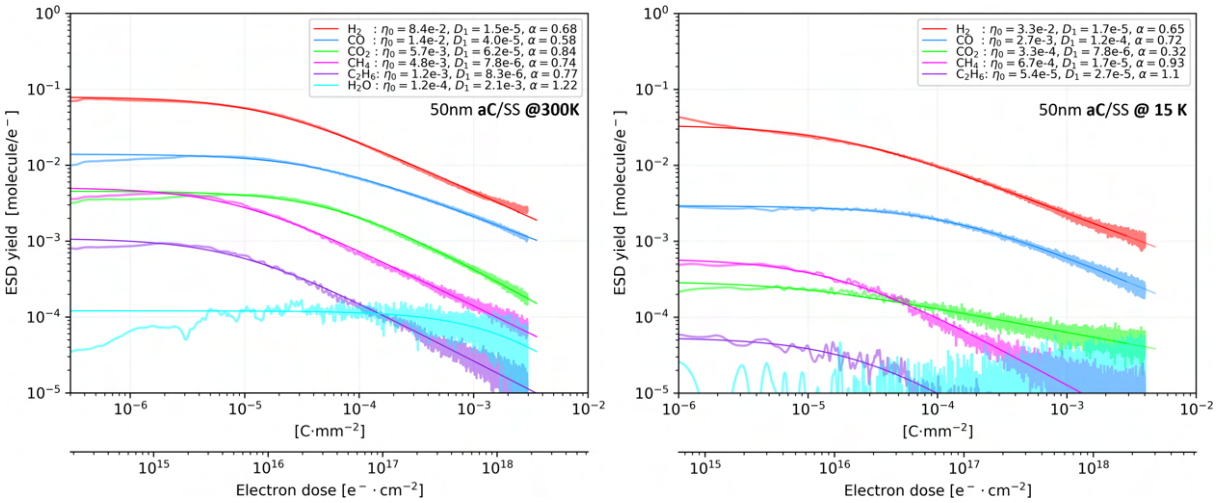

Figure 5.28: Right: ESD conditioning curves for 50 nm thin carbon coating held at 15 K, representative of LHC application Left: Conditioning of a 450 nm thick carbon coating held at 300 K, representative of SPS application. Uncertainties on the best-fit parameters listed in the legend are 10–20 %. Details are discussed in the text. Data for 12 K are presented in [A2, A7].

of gas remains comparable to typical technical-grade metal surfaces that were cleaned for use in UHV. Moreover, the difference between the thick and thin coating is minimal, while cryogenic temperatures can lead to into much lower yields and integrals than at ambient conditions.

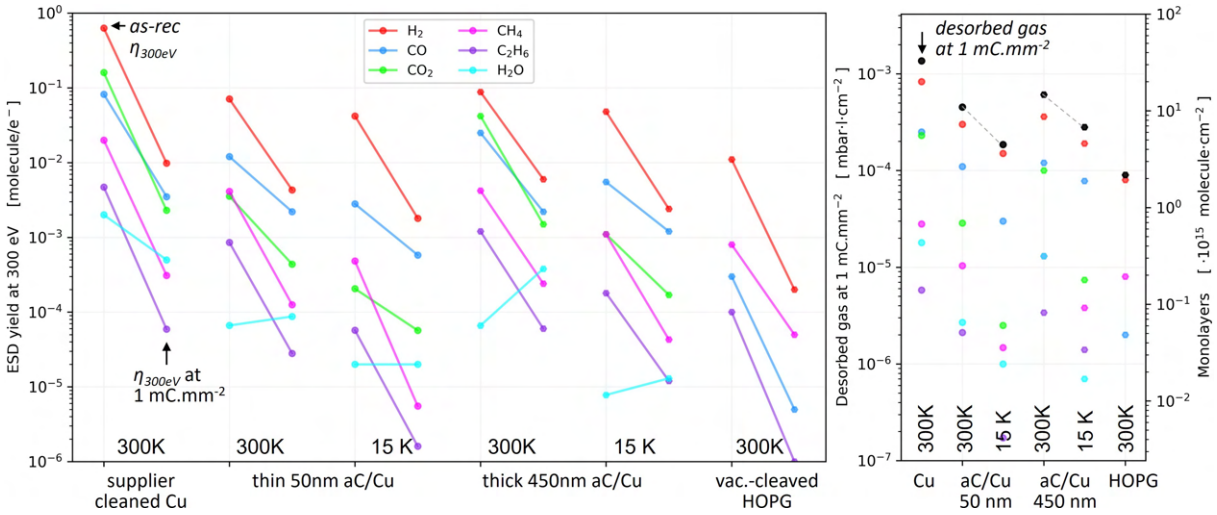

Figure 5.29: ESD of carbon-coated technical-grade Cu measured at 300 eV for as-received state and conditioned at 1 mC.mm^{-2}. All measurements are done on a pristine spot at 15 K and 300 K. Cu surface is shown for reference.

ESD temperature dependence

The left side of Figure 5.30 plots the ESD yield temperature dependence measured at 300 eV for an as-received 50 nm thin amorphous carbon coating atop UHV-grade degreased stainless steel. As far as can be concluded with the experimental precision, the temperature dependence follows a similar trend as other technical-grade metals. However, the proportions differ, as the yields are overall even lower than those seen for bare metals UHV-grade cleaned at CERN, such as the Cu/SS sample on the left side of Figure 5.24. The inflection point is also slightly closer towards 0 K. Still, the exact reason for this and the yield decrease at low temperatures remain unknown, as suitable experimental techniques to explain this trend are lacking in this experimental setup.

Building atop of conclusions reached when studying bare Cu surfaces, the cleaner the surface, the smaller the difference between warm and cold ESD yields. Though, the proportions differ from bare metals. When cold, the large ESD yield reduction for gases heavier than H_2 points to a large content of physisorbed gases, similar to the supplier-cleaned Cu surface. However, the H_2 yield reduces little when

cold and is small to begin with and by extension, also its surface concentration. The carbon coating is typically deposited over a 100 nm thin Ti underlayer that captures H_2 released during the coating process to prevent it from crippling the low-SEY properties of the carbon coating. It could be that the low H_2 yield is due to it being depleted from the surfaces via sub-surface diffusion towards the intermediate Ti layer.

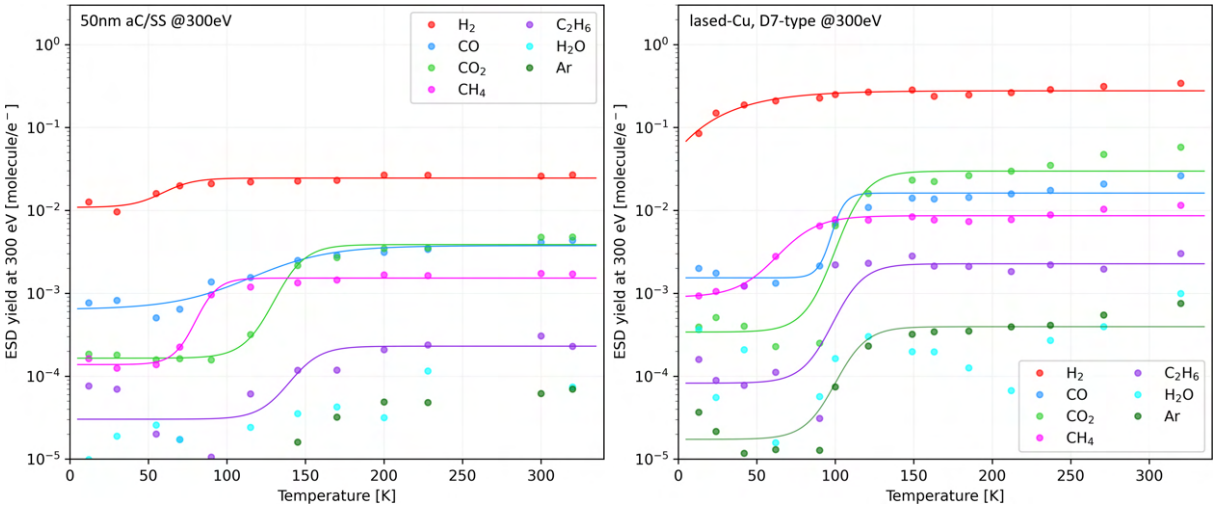

Figure 5.30: Left: ESD yield at 300 eV measured between ambient and cryogenic temperatures for an as-received unbaked sample of 50 nm thin amorphous carbon coating deposited atop of degreased stainless steel. Right: The same for an as-received unbaked D7-type laser-treated copper sample.

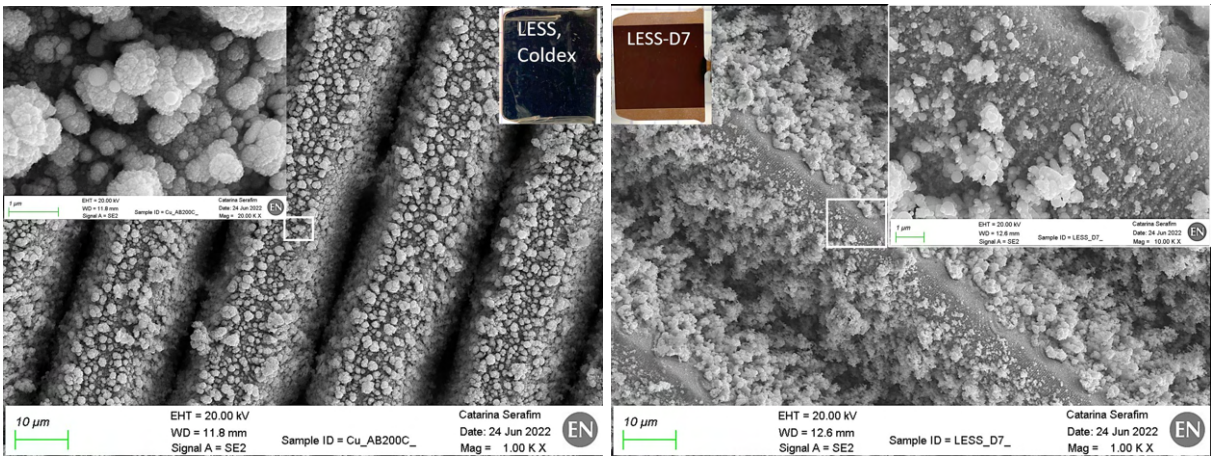

Figure 5.31: SEM images of laser-treated copper. Left: old parameters used for the COLDEX experiment treatment [89]. Right: New parameters 'D7', according to Baudin [109]. Details in the text. The SEM images are taken on FE-SEM Zeiss Sigma, kindly provided by EN-MME-MM, and acquired by C. Serafim, TE-VSC-VSM, CERN.

5.4.2 Laser-treated copper surface

Following the detailed explanation in Section 2.3, the two types of laser-treated copper were characterised in terms of the SEY and ESD yield dependencies on energy, dose and temperature. The copper laser treatment evolved from A-type to D-type, continuously improving on the parameters. Here, the baseline is the C-type laser-treated Cu, parameters listed in Section2.3. This type is applied in the COLDEX experiment, which produced some experimental data with LHC-type beams that can serve as an application reference [89]. This study characterises the treatment in the same 5-20 K temperature range as used by the LHC beam-screen and where the COLDEX operates. A second, D7-type treatment is also characterised. The bulk copper sample was laser-treated at Dundee University using the 'D7' specifications, as described by L. Baudin's [109], and stored in aluminium foil prior to measurement. At the time of writing, it represents the last optimisation iteration with reduced treatment time. Consequently, the D7-type has much fewer fractal-like microstructures and a greater proportion of bare Cu exposed on

the surface, unlike the COLDEX-like treatment with a surface entirely covered by the SEY-suppressing fractal-like microstructures. The advantage is less dust and microparticles produced that can hamper the machine's operation, at the expense of a limited low-SEY capability [260]

SEY energy and dose dependence

The SEY curves visible on the left side of Fig. 5.32 support this visual observation from SEM images 5.31. While the COLDEX-like treatment has a flat SEY energy dependence with barely any peak as well as no decay above 1 keV, the D7-type treatment has the SEY curve shaped half-way between a flat metal surface and a microstructured one. Either way, all these low-SEY treatments start with low SEY and condition even lower, as seen in Fig 5.32 on the right. The added benefit of microstructured surfaces also is the more flat angular dependence, when compared to bare metals, as seen in Fig. 5.2.5. This potentially makes a strong impact on the EC suppression capabilities, since magnetic field-confined electrons hardly impinge the BS at a normal incidence. For comparison, one of the COLDEX-type samples was left in UHV for 1 year prior to this measurement. This long outgassing cleans the surface of some contaminants and leads to a lower as-received SEY, while the conditioned SEY is almost identical.

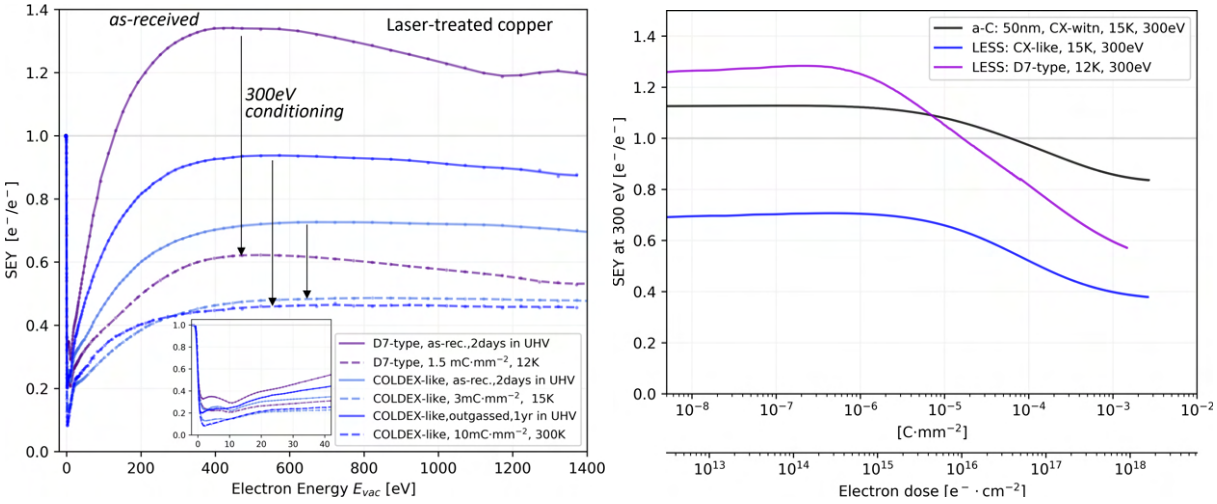

Figure 5.32: ESD conditioning curves measured for as-received COLDEX-type and D7-type of laser-treated Cu. One sample was in a vacuum for 1 year prior to this measurement. Left: SEY curves taken before and after 300 eV conditioning at 15 K. Right: SEY at 300 eV measured during conditioning.

ESD dose dependence

The ESD conditioning curves shown in Fig. 5.33 measured on the COLDEX-like laser-treated copper exhibit vastly different behaviour than flat metals. As a consequence of the high porosity, the conditioning rates are around $\alpha \approx 0.6$ at 15 K, and around $\alpha \approx 0.5$ at ambient temperature, for all monitored gases except water. As typical, water conditions much slower, signifying a fine balance between electron-induced synthesis and electrodesorption. While the initial ESD yields are much lower than those of bare metals, the conditioning process is about 50 % slower.

Electrodesorbed gas quantity

The plot summarises the quantity of gas desorbed during 300 eV electron conditioning measurements, as sampled at 1 mC.mm^{-2} dose of 300 eV electrons, both at 12 K and 300 K. It is noteworthy that the amount of electrodesorbed gas remains comparable to typical UHV-cleaned technical-grade metal surfaces, despite of having a roughness factor 10∼100x larger than flat technical-grade Cu, see the Table 5.2 below.

ESD temperature dependence

The right side of Fig. 5.30 above shows the ESD temperature dependence for the D7-type of laser-treated Cu that exhibits a similar trend as for other surfaces. Yet the characteristic points differ: when cold, the large ESD yield reduces for gases heavier than H_2. The inflection point is at 100 K, making it one of the lowest measurements, along with that of NEG shown in Fig. 5.36. Remarkably, the Ar yield

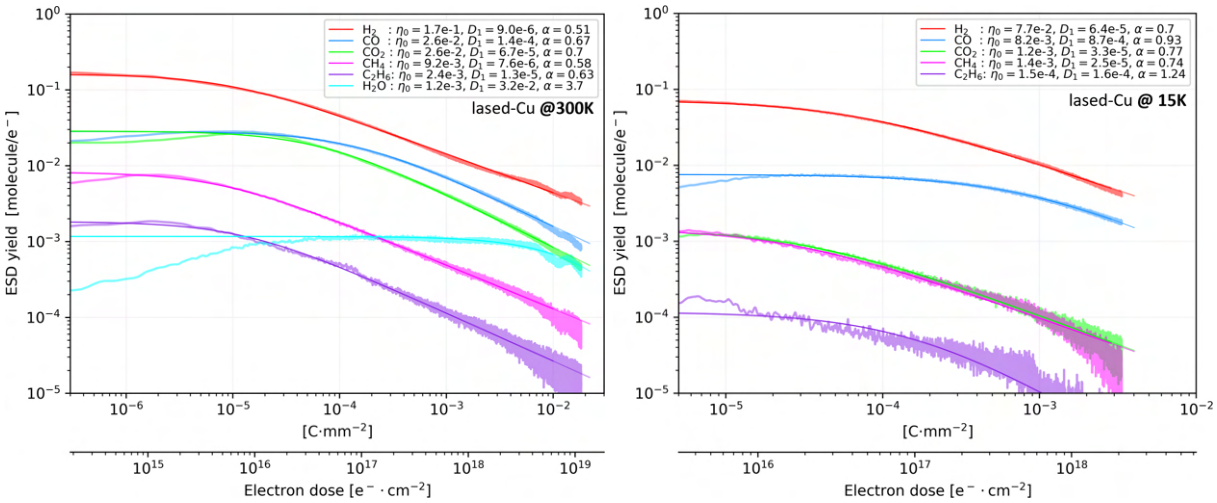

Figure 5.33: ESD conditioning curves measured at 300 eV for as-received COLDEX-type laser-treated Cu, done at 300 K (left) and 15 K (right) . Conditioning was done on different pristine spots of the same sample. Uncertainties on the best-fit parameters listed in the legend are 10–20 %. Data for 15 K are presented in [A2, A7].

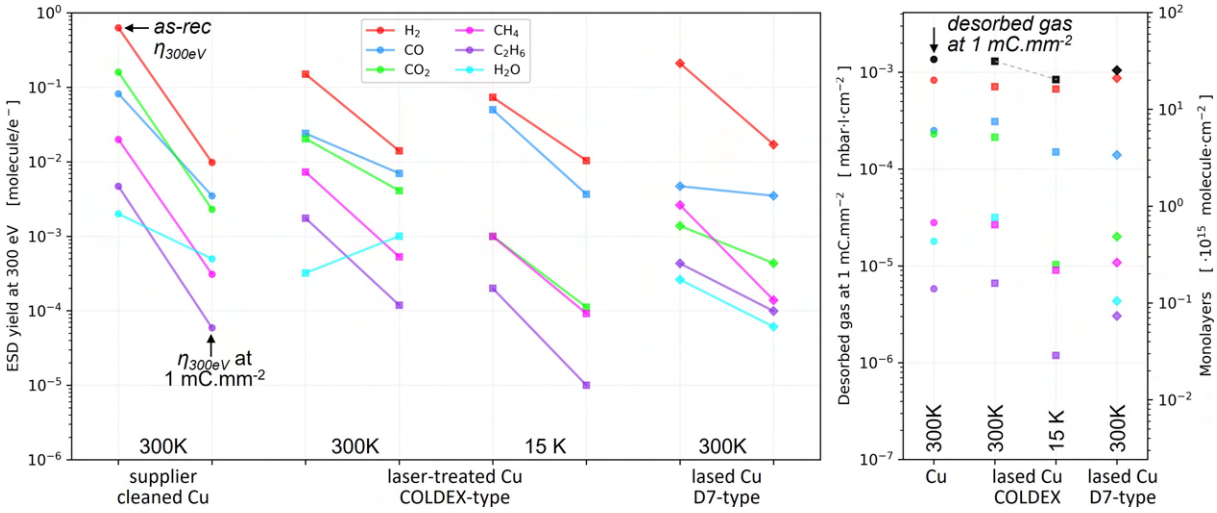

Figure 5.34: ESD of laser treated technical-grade Cu measured at 300 eV for as-received state and conditioned at 1 mC.mm^{-2}. All measurements come from pristine spots of the same sample. COLDEX-type laser-treated copper is measured at 15 K and 300 K and the D7-type is only characterised at 300 K.

follows the same trend as other reactive gases, which strongly supports the hypothesis regarding its pore diffusion-limited ESD efficiency. The Ar was likely used as an inert atmosphere adsorbed during the laser-treatment. The H_2 yield itself is fairly high and reduces little when at cold. Its inflection point is around 15 K, which is about 2∼3x higher then its desorption temperature. In fact, other gases also have an inflection point at about 2∼3x their desorption temperatures. This is noteworthy as it also supports the argument about the pore diffusion-limited desorption process.

5.4.3 Ti-Zr-V non-evaporable getter coating

The Ti-Zr-V NEG coating was characterised similarly to the previous surface treatments in terms of its SEY, ESD and their electron dose dependence. Other sputter-deposited metal coatings were also studied for comparison with NEG and with bulk metals, Fig. 5.5. Nb and Ag were also deposited at CERN in ∼1500 nm thick compact coverages using a magnetron sputter deposition. The details of the Ti-Zr-V NEG deposition at CERN are discussed in detail by Chiggiato&Costa Pinto [113]. AC magnetron sputtering method was used, as it produces more compact layers than its DC counterpart, but indeed, the method changes according to the use case. While porosity benefits the sorption capacity of NEG and carbon coatings, it may not be the goal for other coatings' applications. The Ti-Zr-V NEG should be sputter-deposited in roughly equiproportional composition, but significant departures from this ideal composition were observed. A significant Titanium depletion on the Ti-Zr-V NEG surface was reported

by Sutara et al. [261]. They also report that this is only a surface-related effect, as depth profiling by Ar-sputtering combined with XPS showed a more balanced in-depth composition. Albeit, the surface composition is what matters here. The NEG sputtering was done using Krypton as a process gas at ∼1 mbar. After deposition, the sample was vented with Ar and stored in an aluminium foil in a plastic bag. Despite this, the airborne Argon dominates and traces of Krypton, as the process gas, are practically invisible on the RGA spectrum.

SEM images were taken to correlate the surface morphology to the measured SEY and ESD data, see Fig. 5.35. At this magnification, the Ti-Zr-V NEG surface seems rough but shows no open porosity. Despite 1000 nm thick NEG-coated overlayer, the SEM image unravels that the substrate texture and features of the underlying degreased technical-grade bulk Cu are still partly visible, probably highly influenced by the underlying Cu properties.

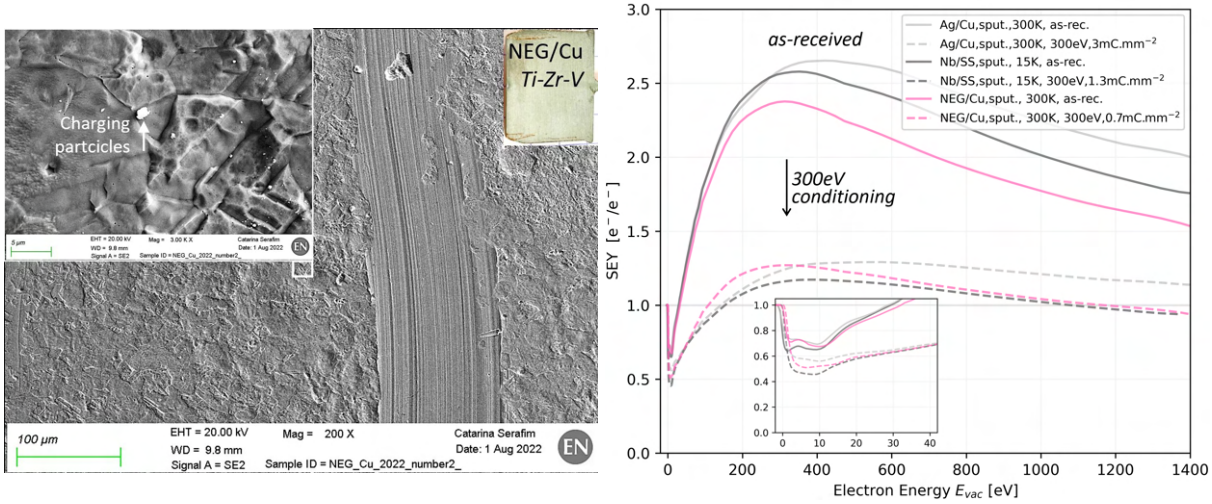

Figure 5.35: Left: SEM images of a Cu surface coated with a 1500 nm thick Ti-Zr-V NEG. The SEM images are taken on FE-SEM Zeiss Sigma, kindly provided by EN-MME-MM, and acquired by C. Serafim, TE-VSC-VSM, CERN. Right: SEY curves were measured on as-received surface and after a 300 eV conditioning at of few mC.mm^{-2} dose, as indicated in the legends. Sputter-deposited metals exhibit the same SEY characteristics as bulk metals. The Ag coating is 1250 nm thick and Nb is 1450 nm tick

SEY energy and dose dependence

The SEY curves shown in Fig. 5.35 above and substantiate the similarity to sputter-deposited Ag and Nb and also to other bulk metals, e.g. Fig. 5.5. Although the baseline temperature for NEG applications is around ambient, the characterisation was done between ambient and cryogenic temperatures. The SEY was measured on an as-received NEG coating before and after conditioning with 300 eV and showed no measurable temperature-induced difference in SEY. From the applicability perspective, the NEG coating conditions to low SEY values of δ_{max}= 1.25 at 0.7 mC.mm^{-2} and would likely continue lower.

ESD dose and temperature dependences

The ESD yield temperature dependence was measured on an as-received NEG surface at 300 eV energy during a cool-down from 300 K to 12 K. The behaviour is very similar to a CERN-cleaned technical-grade Cu shown in Fig. 5.24. When comparing the absolute yields at warm and cold and the inflection point around 100 K. Similarly to Cu, the absence of any remarkable H_2 yield reduction is remarkable, especially in the light of a factor of ∼10x reduction of all other gases. This points to a different desorption mechanism for H_2 than for other desorbed UHV-typical gases.

As a side note regarding the surface-bound gases prone to ESD; Despite using Krypton as a process gas to sputter-deposit the Ti-Zr-V NEG coating, little-to-no Kr ESD yield was observed. Instead, Ar was always the highest-yielding noble gas; see left side of Figure 5.36. This points to the airborne Argon entering the metal surface from the atmosphere in the post-production phase as opposed to being incorporated during the sputtering process.

The conditioning was done with 300 eV electrons at ambient and cryogenic temperatures and the ESD exhibits the same behaviour as other bulk and sputter-deposited metal surfaces. This ESD behaviour is

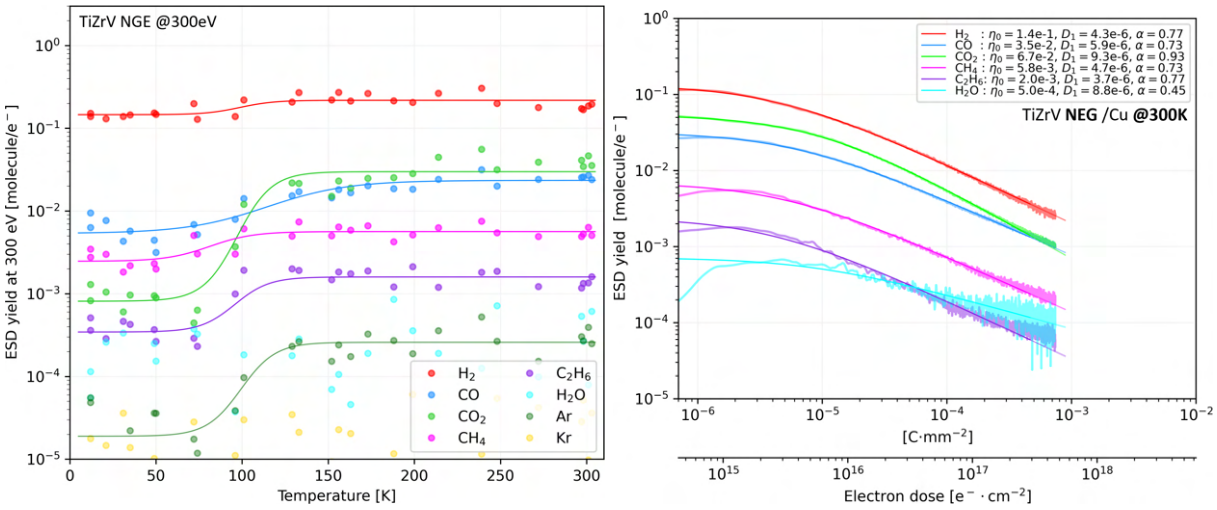

Figure 5.36: Left: ESD yield at 300 eV of unbaked (=non-activated) sample of Ti-Zr-V NEG measured between ambient and cryogenic temperatures. The 1500 nm thick coating was done using Krypton as a process gas at ∼1 mbar at CERN on a degreased bulk Cu. Right: ESD conditioning at 300 eV done at 12 K starting from an as-received state. Best-fit parameters are listed in the legend. More detail in the text.

expected, given the NEG surface is not activated, i.e. saturated by adsorbed gases. The comparative chart in Figure 5.37 captures the comparison to other coatings. The slope of the conditioning curve approaches 0.6 for hydrogen, which points to a diffusion limitation of the desorption process, which can be caused either by bulk or pore-diffusion. Because other gases exhibit steeper conditioning slopes, the surface porosity is probably not limiting the H_2 desorption process and its origin in the bulk-diffused atomic hydrogen.

The data presented here agree with measurements of Malyshev et al.[262] also done on Ti-Zr-V NEG coatings, but activated ones. Their 1 μm thick sample mild-baked to 80 C° compares well to the NEG sample studied here, both in terms of the initial ESD yields and the conditioning rates at high electron doses. Measurements of LePimpec [114], done on a St-707 NEG from SAES Getters company, show similar yields, e.g. initial yield at 0.1 H_2/e^-. Though, his conditing rates are faster, approaching 1 for all gases. The source of this dissimilarity can either originate in the different NEG coating composition, different surface structure or an experimental artefact due to a different setup arrangement.

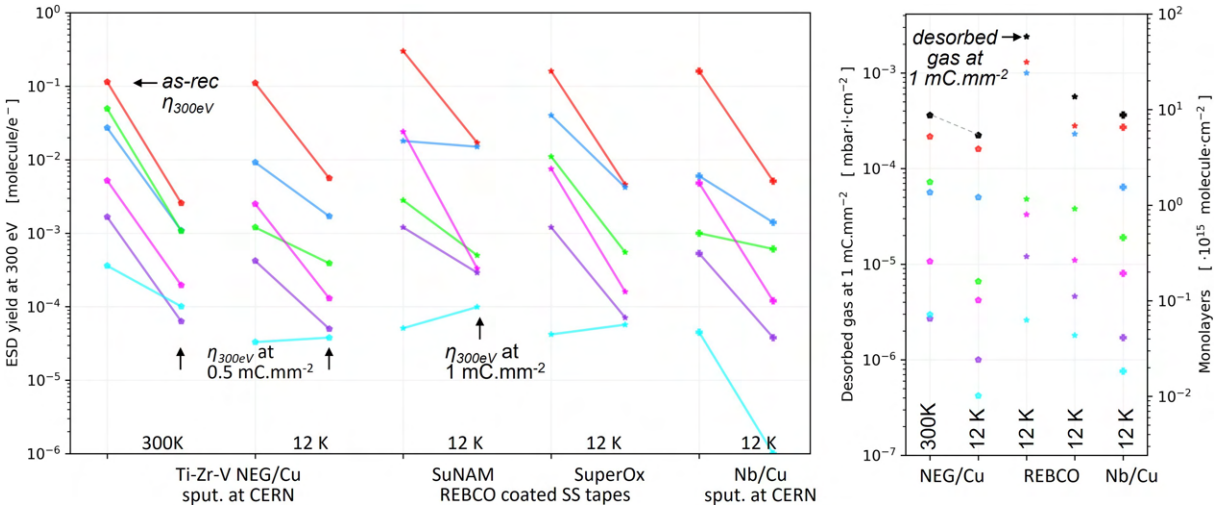

Figure 5.37: ESD measured at 300 eV for as-received state and conditioned at 1 mC.mm^{-2} of: REBCO-coated tapes, and Nb sputter-coated Cu. Ti-Zr-V NEG-coated Cu is sampled at 0.5 mC.mm^{-2}.

Electrodesorbed gas quantity

Figure 5.37 summarises the integrated electrodesorbed gas quantity for the Ti-Zr-V NEG-coated Cu, sputter-deposited Nb coating, both done at CERN, and finally the REBCO samples from the below

Section 5.4.4. The gas is integrated till 1 mC.mm^{-2} dose 300 eV electrons as usual, except for the NEG sampled at 0.5 mC.mm^{-2}. All measurements are done on pristine spots of the same sample and are done at 12 K, since cryogenic conditions are essential for superconducting coatings. The NEG sample is also measured at ambient temperature, being the baseline for NEG application, for instance, at LHC's long-straight sections.

5.4.4 Superconducting REBCO-coated conductors

As outlined in Chapter 2.3, the two investigated REBCO-coated conductors came from two different manufacturers: SuNAM and SuperOx samples were kindly provided by S. Calatroni, CERN-TE-VSC-VSM, as prepared for measurements by A. Romanov. This research direction was eventually expanded into a collaborative publication [A1], which presents the data shown here, ESD models from Section 6, and also XPS and EDS analyses.

The samples were stored in a plastic box filled with air dehumidified by silica beads. Prior to measurements, the REBCO tapes were scissor-cut into 1 cm^2 large pieces, glued to flag-style copper samples with a silver-filled epoxy and cured to 80°C under high vacuum.

The hereafter investigated REBCO-coated tapes have a layered structure deposited over a Hastelloy C276 used as a substrate, as visualised in Fig. 2.8 on the right. The REBCO layer itself, i.e. the Gd-Ba-Cu-O is deposited over a buffer interlayer in a 1600 nm and 900 nm thickness for SuNAM and SuperOx, respectively. The deposition method varies, as SuNAM uses RCE-DR (Reactive Co-Evaporation by Deposition and Reaction) while SuperOx uses PLD (pulsed laser deposition). Moreover, these studied samples are not the typical off-the-shelf REBCO tapes, because they lack the protective overlayers that are typically present on industry-grade tapes. SuNAM samples were delivered without the usual Ag/Cu stabilising overlayer, whereas the protective Ag overlayer had to be etched away from the SuperOx sample. Solution of NH_3:H_2O_2:CH_3OH mixed in 1:1:5 proportions was used to remove the Ag overlayer, as detailed in [122].

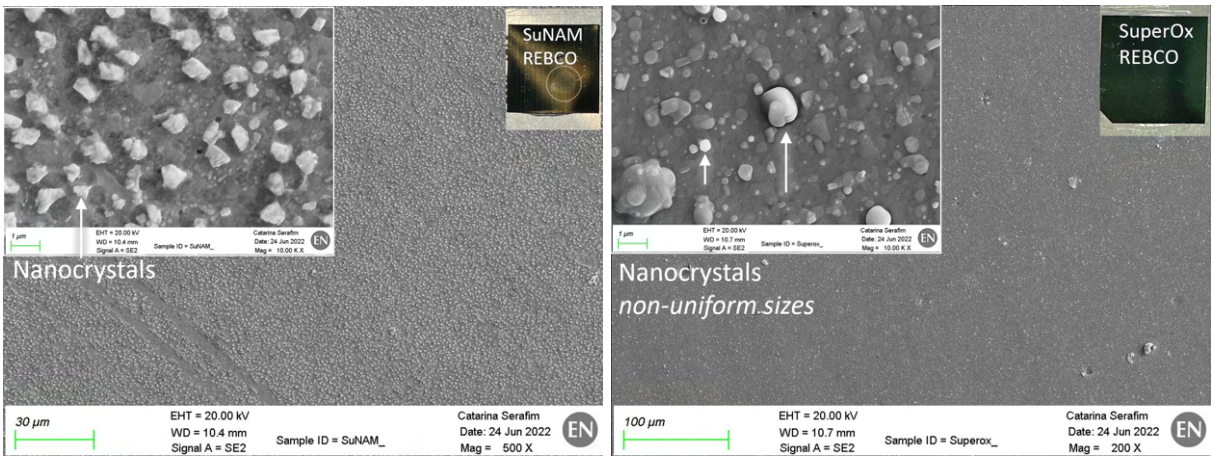

Figure 5.38: SEM images of REBCO samples. The nanocrystalline structure is well visible. Left: SuNAM coating, uniformly sized crystals. Right: SuperOx, a wide range of crystal sizes. Details in the text. The SEM images are taken on FE-SEM Zeiss Sigma, kindly provided by EN-MME-MM, and acquired by C. Serafim, TE-VSC-VSM, CERN. Images are part of [A1].

Figure 5.38 presents the SEM images obtained post-mortem on the two different REBCO tape samples. The obvious surface texture and morphology difference can be attributed to the abovementioned deposition methods. Nanocrystals uniformly cover the entire surface on both samples, most likely Ba-Cu-O, which did not react to form Gd-Ba-Cu-O. The SuNAM coating process produces sharp, uniformly sized and spaced nanocrystals, while the SuperOx coating process gives a wide range of oval-shaped nanocrystal sizes and spacing. The deposition process seems to be Ba-rich and it could be argued that the Ba oxide precipitated from the SuperOx is responsible for higher SEY. However, the SEM images indicate the Ba-Cu-O nanocrystal surface density to be higher and more uniform on the SuNAM sample. Hence, the dissimilarity in electron-conditioned SEY cannot be attributed uniquely to the somewhat higher Ba content.

However, the observed nanocrystals are not likely to form the pinning centers so crucial for superconductors, since they are still too large. As argued by Horvat [263] and shown by Antonick et al. [264], the

ideal size of pinning centers is in the same order as Cooper pair coherence length, i.e. nm-range. since they are still too large. The deposition methods, however, produce such nano-sized defects that result in no shortage of pinning centres in the deposited REBCO overlayer.

Post-mortem XPS analysis of both samples, kindly acquired by V. Petit, CERN-TE-VSC-SCC, showed Gd and Ba content, as expected for gadolinium and barium copper oxides. Traces of Ag residues are visible in the XPS spectra as a residue of the Ag overlayer that was mostly etched away. The XPS spectra also show a lower carbon contamination on the SuperOx sample, which likely results from the etching process, and is possibly responsible for worse SEY conditioning. Other contaminants, like N, P, F, and Cl are also present in trace amounts, with the Cl likely originating from the epoxy-gluing process despite curing in a high vacuum.

SEY energy and dose dependence

Firstly, all SEY and ESD measurements are done on previously pristine spots of the same sample. Data is taken at 12 K, as cryogenic temperatures are representative of the use-case conditions. Regarding the secondary electron emission; there are no charging effects despite the rare earth oxide layer, which is essential for technical applications. The SEY conditions under 300 eV electron irradiation similarly to any other metal under, also at ∼12 K. However, the SuperOx sample only conditions to around δ_{max}=2, which is likely a sign of a thick oxide layer, much like it is the case for a natural aluminium oxide having a high SEY. This value is clearly too high for technical applications and needs further SEY-suppressing treatment. Conversely, the SuNAM conditions to acceptable value of δ_{max}=1.2 . High as-received SEY values were also reported by Puig&Krkotic et al. [265] and by Leveratto et al. [266], measured at ambient temperature.

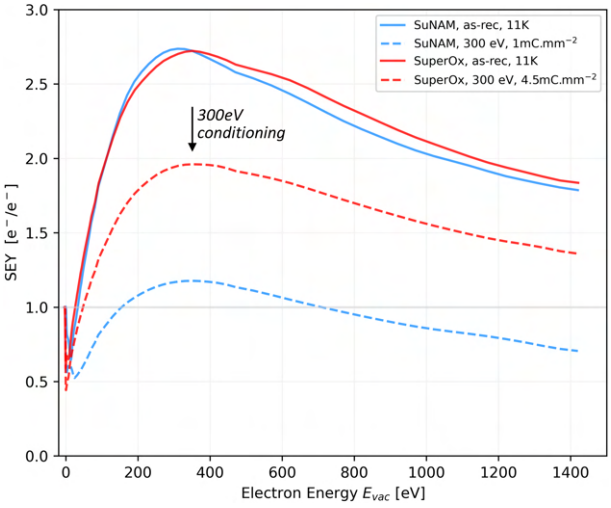

Figure 5.39: Left: SEY measured on REBCO samples in as-received and electron conditioned state at 11 K. Electrons at 300 eV were used for conditioning at doses indicated in the legend. The electron energy is referenced to the sample vacuum level. Data are presented in [A1].

The SEY is found to be temperature-invariant within the experimental precision, similar to all other surfaces studied in the 12–300 K range. Hence, the secondary electron emission seems to be agnostic to cryogenic temperatures, including around the superconducting transition around 90 K. This is indeed explained by comparing the electronic excitations energy of few eV against the Cooper electron pairs' binding energy that is in the order of meV. Although the superconductive properties do not affect the SEY, the opposite could be the case under certain circumstances. During electron irradiation, a higher density of excited electron-hole pairs, i.e. hot electrons, is created in the top tens of nm, which could locally impair the superconducting performance in this near-surface layer.

Recent measurements done by Krkotic et al. [122] at cryogenic temperatures and further reasoning in [125] show that high energy synchrotron radiation does not impair in any way the superconducting properties. Knowing that synchrotron radiation can produce intrinsic electronic excitations in bulk, is a strong indicator that electron irradiation (also decaying into electronic excitations) would not impair the HTS performance either. By extension, the SEY can also be expected to remain agnostic to the conducting state of the HTS.

Contrary to these observations, it was also reported [267] that high-energy electrons at 1 MeV create displacement-type of damage in HTS material that slightly impairs the superconducting properties, e.g. decreases the critical temperature. However, under technically-relevant circumstances, for example considering the electron cloud with ∼keV electrons, the penetration depth is in nm range. The skin depth of the HTS for electromagnetic radiation is in μm range, so the two phenomena happen at largely dissimilar scales, which effectively decouples them. It takes much higher electron energy irradiation to generate displacement type of damage, that in turn detrimentally affects the critical surface, as shown by Ishikawa et al. [267] and Weaver et al. [268], or Sahakyan et al. [269] at high doses of MeV electrons. In contrast to the radiation-induced damage to the HTS, it was even reported [270, 271] that Cu atoms implanted into

the HTS material can, under special conditions, introduce vortex-pinning centres and improve the HTS properties. To conclude, the electron energy range dealt with here is far from being capable of creating displacement-type of damage in bulk and can therefore be considered harmless to the superconducting properties.

ESD energy and dose dependence

Measurements performed on both investigated samples at 12 K, give a few important findings. Aside from the SEY curves, the ESD yields, thresholds and conditioning rates also do not differ from regular metal surfaces, as visible in Figure 5.40.

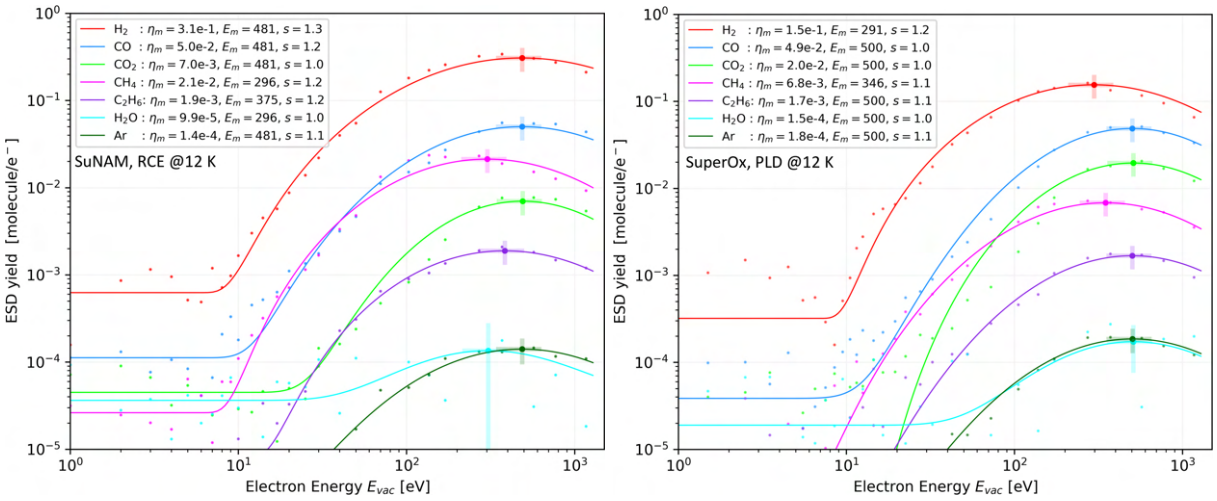

Figure 5.40: ESD energy dependence of as-received REBCO samples. SuNAM sample (left) is characterised at 11 K and SuperOx at 19 K (right). Best-fit parameters are listed in the legend. More detail in the text. Uncertainty for water is off the charts, due to the low SNR and high BG. The electron energy is referenced to the sample vacuum level. Combined uncertainty intervals at 1σ are ∼30 % as shown at the peak values. Uncertainties on best-fit parameters are 10–20 %. Data are presented in [A1].

The energy thresholds for desorption are in the typical 5-10 eV region, characteristic of technical-grade metals. The energy E_{max} of the peak desorption yield η_{max} is in the 300–500 eV region that is typical for flat metal surfaces. Hydrogen has the maximum yield and is followed by CO, CO_2, CH_4 and other UHV-typical but less abundant species. The overall shape of the ESD energy dependence and SEY also resembles that of flat metal surfaces. This is somewhat unexpected, given the roughness observed in the SEM images. The measured energy-dependent ESD datapoints are fitted with log-normal distribution, see Section 6.1. The legend lists the best-fit s parameters for each gas and E_{thr}, η_{max} and E_{max} can be read directly from the chart and plugged in the parametric fits from Section 6.1. The errorbars on η_{max} depict the combined uncertainty of 30 % at 1 σ, similarly for the E_{max}.

ESD yield conditioning curves acquired during a 300 eV electron irradiation done at 12 K also revealed no difference from other technical-grade metals. The initial yield η_0 is characteristic of a UHV-clean surface. The conditioning rates α around 0.7-0.9 represent gas desorption is not limited by the surface porosity. Values for η_0, D_0 and α can be read directly from the chart and plugged in the parametric fits from Section 6.1.

Following the 300 eV electron conditioning at 12 K, the irradiated SuNAM surface showed discolouration, going from dark to light shade, which is the opposite of what happens to metals due to electron-induced surface graphitization. Instead, this bleaching effect could indicate a reduction of surface oxides and hydroxides.

Additional research of these HTS samples led to a collaborative publication [A1], adjoined in the Appendix 6.8, that elaborates on the electron-beam characterisation (SEY, ESD, SEM, EDS, XPS) of REBCO-coated conductor tapes.

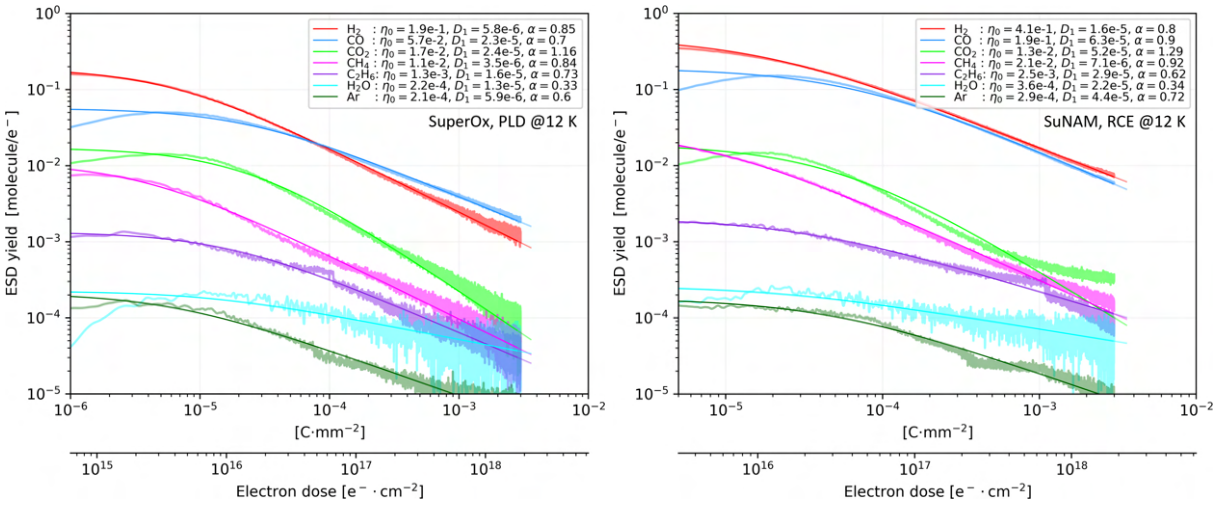

Figure 5.41: ESD conditioning at 300 eV of SuperOx (left) and SuNAM (right) REBCO samples held at 12 K starting from an as-received state. Best-fit parameters are listed in the legend. More detail in the text. Data are presented in [A1].

5.4.5 Role of surface morphology in SEY and ESD

SEY and ESD of low-SEY coatings and treatments

Different means of achieving low SEY were discussed in Section 2.3. As discussed, the amorphous carbon-coated surface achieves a low SEY via suitable electronic properties, which are determined by the sp2 graphitic bonds in the sputter-deposited amorphous carbon layer and its low atomic number. Hence, the combination of a low stopping power owing to the low-Z and a relatively high work function seems to favour low SEY, despite of relatively flat surface microgeometry. Conversely, laser treatment relies on a geometrical entrapment of emitted electrons inside the fractal-like structures. The corresponding surface microstructures are well visible in SEM images of carbon-coated, Fig. 5.25, and laser-treated copper, Fig. 5.31. Figure 5.1 shows that the SEY curves of the two treatments vary greatly as a result of the different surface structures.

The laser-treated copper and the 450 nm thick amorphous-Carbon have an approximately similar specific surfaces, factors of ten larger than the geometrical surface of bare copper. However, the surface roughness (meaning the open geometry one) differs greatly between the two. The studied sputter-deposited amorphous carbon has pores with high aspect ratio and closed geometry. Otherwise, the amorphous carbon-coated surface is rather flat, which results into an *classical* SEY curve of a characteristic shape with a distinct 200 eV peak and a fast decay towards higher energies.

Conversely, the SEY curve of laser-treated samples has an entirely different shape, which is flat even at few keV [104], owing to the highly rough microgeometry and the semi-open low-aspect ratio porosity. It also hardly has any distinct peak; if there is any, it likely corresponds to a flat portion of the surface, such as a crest with little to no fractal-like structures. This flat profile is characteristic of rough surfaces that capture their SE electrons, as opposed to not generating them in the first place. The flatter SEY profile is not to be confused with rather flat SEY curves of sputter-cleaned metal surfaces. The clean metal surfaces in fact only have the peak moved to higher energies, but a $1/E^n$ type of decay still follows in the keV energy range.

Electrodesorbed gas quantity

Similarly to flat metals, the integrated electrodesorbed gas quantity was calculated for the studied coatings and taken at 1 mC.mm^{-2} dose of 300 eV electrons, both at 12 K and 300 K.

The comparative graphs of electrodesorbed gas from carbon coating 5.29, laser treatments 5.34 and REBCO, NEG and Nb coatings 5.37 shows that electron conditioning (at the same dose of 1 mC.mm^{-2}) of all studied coatings and treatments removes a similar amount of gas as in the case of bare technical-grade metals. This would not be remarkable if only the TPD measurements presented below 5.5 did not clearly demonstrate the high specific surface of the studied coatings and treatments. The TPD curve analysis yielded an increase of 10–50x of the specific surface compared to bare metals. Either the entire surface is not covered with adsorbed contaminants, which is very unlikely, or part is not accessible to

electrodesorption, which seems to be the case.

One could suspect the geometrical entrapment of molecules desorbing in a semi-closed pore geometry, but the observation holds at ambient temperatures where this is not a concern. Hence, the following explanation is put forward, considering the short penetration depth of primary electrons, which is in the order of units to tens of nm. The electrons irradiate and create excitations only on surface facets visible from the top projection, i.e., in a direct line of sight of the electron beam. Hence, only the adsorbate molecules visible from the top projection are accessible to the electrodesorption process. Indeed the hypothesis has its limits, such as applicability to non-bulk-penetrating primary electrons, but it seems to explain the presented experimental observations. The SEY and ESD data presented for cryosorbed gases on porous surfaces in Section 5.60 also confess to the same effect. More experiments were performed with precondensed gases to support this hypothesis further. A certain amount of gas precoverage was cryosorbed over the studied surface. If the surface is microscopically flat, the same gas amount is recovered when integrating the electrodesorbed gas during a conditioning measurement. For porous surfaces, however, only a part of the gas precoverage is recovered during conditioning, and the rest does not seem not accessible to electrodesorption (the ESD yield plummets to zero, so higher electron doses would not compensate). Subsequently, this remaining part of the gas precoverage, inaccessible to electrodesorption, was recovered during a TPD. This observation is seconded by the SEY measurements done on carbon coatings and laser treatments with cryosorbed gases in Section 5.6: it takes units of monolayers to observe a change in the SEY curve, including the LE-SEY region. To conclude these experiments, gas can be trapped so deep in high-aspect-ratio pores that it is not accessible to particle-induced desorption and only desorbs thermally.

Similarly to the bare metals, the quantity of electrodesorbed gas from coatings and treatments also generally corresponds well to measurements reported by other authors, such as ones presented Malyshev's book [161], Gomez-Goni&Mathewson[193], or Kennedy [162].

ESD conditioning rate

The ESD conditioning is essentially characterised by the initial yield η and the power law exponent α, which determines its conditioning rate in the log-log plot. The power-law fit modified by Malyshev [161] is used here to approximate the ESD yield dose dependence, eq. 5.2. This fit was introduced in the theoretical Section 2.5 and is further discussed in Section 6.1. The added advantage is a more robust and faster convergence (at lower electron doses) of this fit to the experimental data than its classical version. The value D_0 is a dose imparted at the lowest measurable datapoint, and D_1 positions the end of the initial constant plateau. It must be noted that for usual D_0 of $\approx 5{\cdot}10^{15}\,\mathrm{e^-.cm^{-2}}$, α becomes invariant after $\approx 10^{17}\,\mathrm{e^-.cm^{-2}}$ and the classical form prevails, eq. 2.10.

$$\eta(D) = \eta_0 \cdot \left(\frac{D + D_1}{D_0 + D_1} \right)^{-\alpha} \tag{5.2}$$

The loose similitude to thermally-induced gas desorption can be leveraged here to better interpret the measured ESD conditioning rates. A review article on materials outgassing by Grinham [272] lists values for outgassing decay rates in the 0.5∼1 range. For porous materials, the $\alpha \approx 0.5$, while a value of $\alpha \approx 1$ is characteristic for flat metal surfaces. Even values of α slightly higher than 1 are possible, especially when a surface was UHV-cleaned or otherwise conditioned before the desorption measurement.

Similarly to the ESD conditioning, the decay rate, i.e. the slope α, depends on the rate-limiting step of the desorption mechanism. Hence, the varies α depending on the physical subprocess that bottlenecks the desorption sequence efficiency. This effect can be readily illustrated using various systems with gases sorbed in different chemical states; Starting from the simple case of cryosorbed CH_4, CO and $^{15}N_2$ gases, past UHV-stereotypical weakly adsorbed gases, ending with bulk-absorbed hydrogen in a vacuum-cleaved HOPG.

The conditioning rates obtained here for flat technical-grade metals are in the 0.7-1 range, which corresponds to values reported by Gomez-Goni [193], Malyshev [161], Kennedy [162] and many others.

Starting from the simplest case; a cryosorbed gas quench-condensed over a flat surface in a multilayer coverage. Here, the interaction between the gas and substrate is very weak and most gas molecules are bound to other gas molecules, as opposed to the substrate. Then, considering the initial stage of a conditioning curve where the adsorbates' surface coverage is plentiful, the desorption process only includes the gas molecules and is limited by the quantum efficiency of the desorption process of a given gas species. Such initial conditions result in a flat plateau. Later, when the adsorbate surface coverage is scrubbed

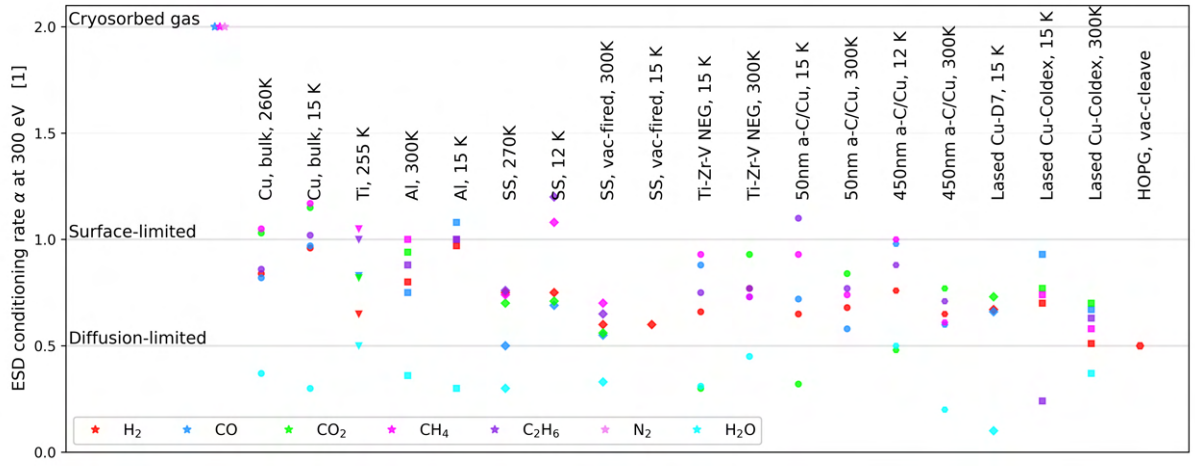

Figure 5.42: ESD conditioning rates of technical-grade metals, coatings and treatments. All are measured at 300 eV at temperatures close to 300 K, and 15 K. All measurements are done on pristine spots. Condensed gases and vacuum-cleaved HOPG illustrate the edge cases.

off, the desorption yield is no longer limited by the desorption sequence efficiency but becomes limited by the (lack of) surface coverage. With no other limitations to the desorption process (such as the necessity of diffusion or recombination), the conditioning rate α transitions from 0 to ~2. This effect was observed experimentally in CH_4, CO and $^{15}N_2$ when transitioning from multilayer coverages to zero.

The vacuum-cleaved HOPG exhibits an extremely low initial ESD yield, dominated by a bulk-diffused hydrogen. When conditioned with 300 eV electrons, the ESD yield decreases with a conditioning rate of α=0.5. This rate represents a bulk diffusion-limited desorption, often observed in thermal outgassing, where the solution to the Fickian diffusion equation has a slope of 0.5. In HOGP, the same effect is observed regardless of temperatures, i.e. at 300 K and 15 K, which point towards electron-induced hydrogen diffusion instead of thermally-induced one. Measurements of Ishida et al. [273] showed that electron desorption is an efficient way to deplete previously ion-implanted hydrogen from graphite, with the recovery yield approaching 50 %. Andritschky et al. [160] developed a simple mathematical model that assumes a uniform semi-infinite hydrogen concentration, leading to a α=0.5 for both ESD and PSD data, in agreement with the results presented here.

Meanwhile, water electrodesorption represents a special case by demonstrating that electron-induced molecule synthesis and surface build-up during irradiation is not to be discarded. In light of the above-discussed simplistic reasoning regarding conditioning rates, the low rate for water seems unphysical. However, the apparently slow water conditioning rate can, in fact, be a manifestation of a fine balance between synthesis and desorption.

To interpret the above data in Fig. 5.42, an explanation can be attempted by assuming that *(electron-induced?)* surface mobility of precursors is the limiting step for water electrodesorption. The precursor hopping rate can be approximated by an Arrhenius-type rate relation for an energy-activated process (here it is electronic excitations, instead of thermal energy), which scales the rate exponentially with available energy and $r \propto exp(\Delta E_{barrier}/E_{available})$. Therefore, a higher diffusion barrier leads to a slower water formation rate, leading to a slower surface coverage depletion and a slower conditioning rate. The fact that higher temperature leads to slightly faster conditioning rates also supports this: higher temperature leads to higher surface mobility and, in conjunction with the electron-induced surface diffusion, leads to faster conditioning rates. The low amount of gas electrodesorbed by slow (~20 eV) electrons also supports this. Contrary to this reasoning, Auslender&Minchenkov [253] studied already in 1966 the influence of temperature between -196~400 °C on the ESD yields of Cu and observed that the conditioning rate at 600 eV is much slower at 400 °C than at -196 °C. It could be argued that lower temperatures quench molecules' thermal diffusion from subsurface layers, which prevents the surface concentration from being replenished, making the conditioning rate faster at cold. But with conflicting evidence, it is challenging to reach a conclusive explanation.

Extending this reasoning to other molecules, it can be argued that flat surfaces can be presumed to have a lower diffusion barrier and allow surface coverage depletion faster. In other words, the balance between synthesis and desorption shifts in favour of desorption for surfaces that have a low diffusion

barrier, low porosity, high temperature, and gases that have a low adsorption energy. Conversely, rough surfaces, such as 450 nm thick carbon coating and laser treatment exhibit α=0.2-0.4, have a higher surface diffusion barrier that generally decreases the recombination rate. The conditioning rate also decreases as the recombination rate bottlenecks the desorption sequence.

Surface porosity brings yet another concern regarding desorption is to be added on top of the diffusion-related limiting step. In light of the thermal desorption-related theory presented in Section 2.8, a desorption process can indeed be geometry-limited by a gas diffusion through high aspect ratio pores. The offset of η_{max} observed in energy-dependent ESD yield measured on thick carbon coating aligns with this interpretation. Besides, the TPD results shown in Fig. 6.14 taken with $^{15}N_2$ demonstrate higher binding energies on carbon coatings than for laser treatments. The microporosity also comes with a higher specific surface, which dilutes the gas surface coverage and lowers the odds of precursor recombination. With this evidence, the SEM images can be misleading and should not be taken quantitatively. To challenge this interpretation, the quantity of electrodesorbed gas from porous surfaces does not surpass that of flat surfaces, as shown in the paragraph below, which greatly diminishes the pore's influence.

To summarise, different substrate-adsorbate systems lead to a strong variation in ESD yields and conditioning rates. The reality of technical-grade surfaces lies among the edge cases discussed here. Clean surfaces tend towards a slope α=1, typical for a surface-limited desorption process. Meanwhile, porous and structured surfaces tend towards the slope α=0.5, typical for a diffusion-limited process. Moreover, the large difference in conditioning rate α further substantiates the importance of both electronically- and thermally-induced physical chemistry on the surface and the effect of surface porosity via geometry-limited gas desorption. This was clearly illustrated on the ESD energy-dependence of cold and warm carbon coating, Section 5.4.

The measurements cover the thick and thin carbon coatings in Fig. 5.29, laser-treated Cu in Fig. 5.34, and NEG, REBCO and Nb coatings in Fig. 5.37. Most notably, the amount of electrodesorbed gas remains comparable to typical UHV-cleaned technical-grade metal surfaces. This is despite having a roughness factor 10∼100x larger than flat technical-grade Cu, as measured via TPD and listed below in Table 5.2.

5.5 TPD of cryosorbed gases from technical surfaces

Closely following the above-discussed theoretical aspects discussed in Section 2.8 and the TPD method commissioning, discussed in the Experimental Section 4.7, a large series of TPD curves were measured for different gases cryosorbed on surfaces of interest. First, the desorption temperature allows determining the binding energies of specific gas-surface combinations. Second, this allows us to determine the specific surfaces of porous samples as compared to the bare flat copper surfaces. Finally, potential temperature windows granting vacuum stability can be identified for various adsorbate-substrate combinations to avoid unwanted gas desorption during the operation of a cryogenic accelerator [161, 274]. This is discussed in the Applications section 6.

For completeness, SEY curves were measured for each gas coverage on each surface. ESD measurements were typically done in separate runs not to throw off the TPDs by electrodesorbing or annealing the cryosorbed gas coverage. This data is then used in the following chapter treating the SEY and ESD of cryosorbed gases.

At first, different coverages of $^{15}N_2$ quench-condensed over microscopically flat surfaces, such as the HOPG, and the technical-grade as-received Cu/SS surface shown in Fig. 5.43 and used as a reference. The isotopically labelled $^{15}N_2$ was once again chosen as a useful tracer gas with a little natural background. Moreover, it has fast vacuum dynamics, i.e. has fast transients, and does not fragment much due to its chemical inertness. These properties translate into a higher time resolution, which implies a higher temperature and energy resolution when concerning TPD measurements.

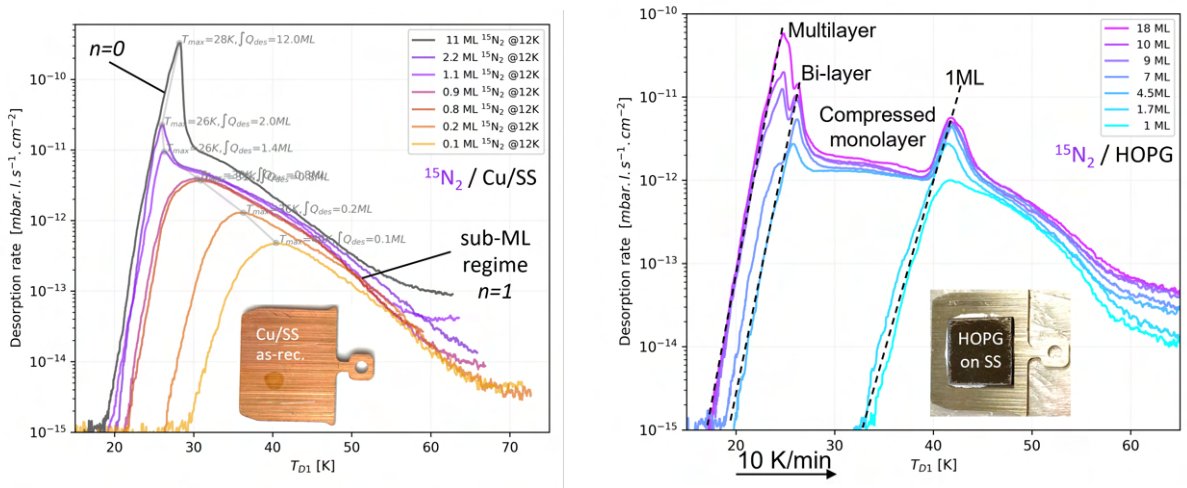

Figure 5.43: Left: Series of TPD curves acquired on copper colaminate Cu/SS surface in an unbaked, as-received state. Right: TPD curves measured on HOPG serve as a commissioning reference. Note the HOPG sample is epoxy-glued to a SS flag-style sample, so temperatures are likely off by few K due to higher thermal impedance. Temperature ramps of 10 K/min were used where possible. Slower ramps were used at very high coverages not to surpass the pressure limit on the RGA's SEM. Assumed 1 ML = 10^{15} molecule.cm^{-2}.

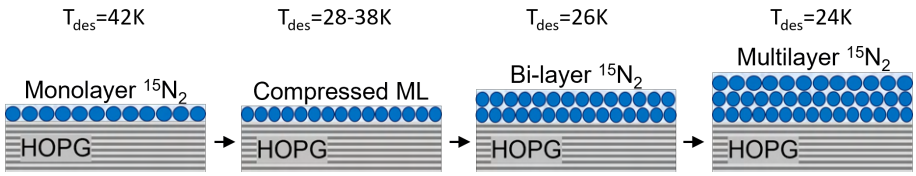

Figure 5.44: Schematised arrangement of $^{15}N_2$ molecules on top of a vacuum-cleaved HOPG at different coverages. Note that a compressed first monolayer forms before the second layer starts growing atop.

The $^{15}N_2$/HOPG was used for TPD method commissioning discussed in the Experimental section 4.7. The $^{15}N_2$ was quench-condensed over a vacuum-cleaved HOPG held at T_{D1}=11 K in multilayer coverages 1-18 ML. This TPD series features a characteristic three-peak pattern also reported by other researchers [209, 230, 231] for multilayer coverages of various gases. These desorption peaks correspond to a monolayer, bilayer and multilayer regime, see Fig. 5.44, each of which has a characteristic binding energy resulting in a distinct peak in Fig. 5.43. An unusual plateau is visible between the monolayer and bilayer coverage, which corresponds to a compressed monolayer coverage. Here, it is still energetically

advantageous for $^{15}N_2$ molecules to bind to the surface, even at the expense of deforming their shape. By comparing the area under the TPD curve, the compression seems to squeeze another ∼0.5 ML before a second layer starts to form. As a result of this compression, the binding energy to the surface is slightly weaker, resulting in a lower desorption temperature, up to 10 K lower from the original 1 ML peak.

5.5.1 Surface microstructure dependence

This study effort aims to infer the surface microstructure by analysing a series of TPD curves. Measurements are typically acquired starting from 0.1 ML coverage and building higher up, until reaching a multilayer-shaped TPD curve. A temperature ramp of 10 K/min is systematically used where possible. When working with too high coverages, such as multilayer-shaped TPDs taken on highly porous surfaces, the heating ramp was decreased to 5 K/min or even 3 K/min to control the peak desorption rate and keep it below the RGA's SEM pressure limit at 5.10^{-8} mbar. The desorption rate was then multiplied accordingly to bring it to the 10 K/min equivalent, hence making it comparable with the rest of the data. On occasions, the PID controller did not manage to maintain the 10 K/min temperature ramp, which results in a few ill-shaped TPD curves, especially around 20 K. The usage of $^{15}N_2$ still could not prevent the gas recycling elsewhere on the cryostat, which introduced a background into the TPD curves above 60–70 K, particularly to the higher coverage ones.

Each series of TPD curves has two distinct regions. First is the low-coverage sub-monolayer region. Here the gas molecules preferentially occupy the higher binding energy sites, as it is energetically favourable in order to decrease the overall energy of the system. In this sub-ML region, the dominant interaction is between the adsorbate and substrate, which determines the TPD curve shape and desorption order $n = 1$. As the coverage increases, progressively more binding sites are occupied at the lower end of their distribution. This offsets the T_{max} to lower temperatures, as lower thermal energy is required to desorb more weakly-bound gas. Ultimately, the entire specific surface is covered by gas molecules and a second layer starts to form. Here, the adsorbate-adsorbate interaction becomes dominant and the adsorbate-substrate effect disappears until the overlayers get desorbed. This leads to a differently shaped TPD curve, characterised by a substrate-agnostic shape following the zero desorption order $n = 0$ kinetics. As a result of this change, the T_{max} starts drifting to higher temperatures.

The transition from sub-monolayer to multilayer regimes observed in all the acquired TPD curve series marks the change in the dominant interaction from adsorbate-substrate to adsorbate-adsorbate. In turn, this is the point when the entire specific surface is covered by a monolayer coverage, presuming the surface mobility of the gas on the given surface at a given temperature. The tell-tale signals of this transition is most notably the emergence of a sharp T_{max} peak. What's more, while the leading edges coalesce for the substrate-independent multilayer regime, it is the trailing edges that merge for the submonolayer regime; see $n = 0$ and $n = 1$ marked in all TPD Figures.

The following values were extracted from each TPD curves series for further comparison in Figure 6.14 of the Application chapter 6: temperature of the peak desorption rate T_{max}, total desorbed gas quantity $\int Q_{des}$ evaluated from a background-corrected TPD curve integral.

A simple relation can be used to coarsely approximate the binding energy of gas adsorption using E_{ads} from the peak desorption temperature T_{max}, as follows:

$$E_{ads}[meV/bond] = 2.5 \cdot T_{max} \qquad [K] \tag{5.3}$$

Or using a more advanced Redhead's [211] relation valid for the first-order desorption kinetics $n = 1$. This widely used formula allows calculating the E_{ads} and ν from a known peak position T_{max}. The heating rate β [K.s^{-1}] is known, the universal gas constant as well R=8.31446 [J.mol^{-1}.K^{-1}] and a generic frequency factor ν=10^{13}Hz is used. The result is converted from [kJ/mole] into [eV/bond] by dividing by the Avogadro number N_A=$6.022{\cdot}10^{23}$ molecules/mole and the unit charge q_e=$1.6022{\cdot}10^{-19}$ [J/eV]. Redhead also derived a formula for estimating ν, listed in eq. 2.15, which renders values of ν very close to the the generic 10^{13}Hz for the used experimental conditions.

$$E_{ads}[kJ/mole] = R\ T_{max}\ \ln(\frac{\nu\ T_{max}}{\beta} - 3.46) \tag{5.4}$$

Comparing the TPD curves taken on the thin and thick carbon coatings immediately shows that the carbon coating creates a large amount of higher energy adsorption sites that effectively bind the cryosorbed gas at much higher temperatures than the bare Cu surface. This results into two consequences, the peak

desorption rate shifts towards higher temperatures, and the surface has a much higher adsorption capacity. The estimate is a factor ∼10x and ∼25x, respectively, for thin and thick. Though, it is challenging to deliver a more exact estimate, even when taking into account all the characteristic behaviours.

It is remarkable that Salemme et al. [275] measured systematically 2∼3x higher desorption temperatures for H_2,N_2 and CO cryosorbed in ∼1 ML coverages on the 400 nm-thick carbon coating in the COLDEX experiment. The reason for this large dissimilarity is unclear.

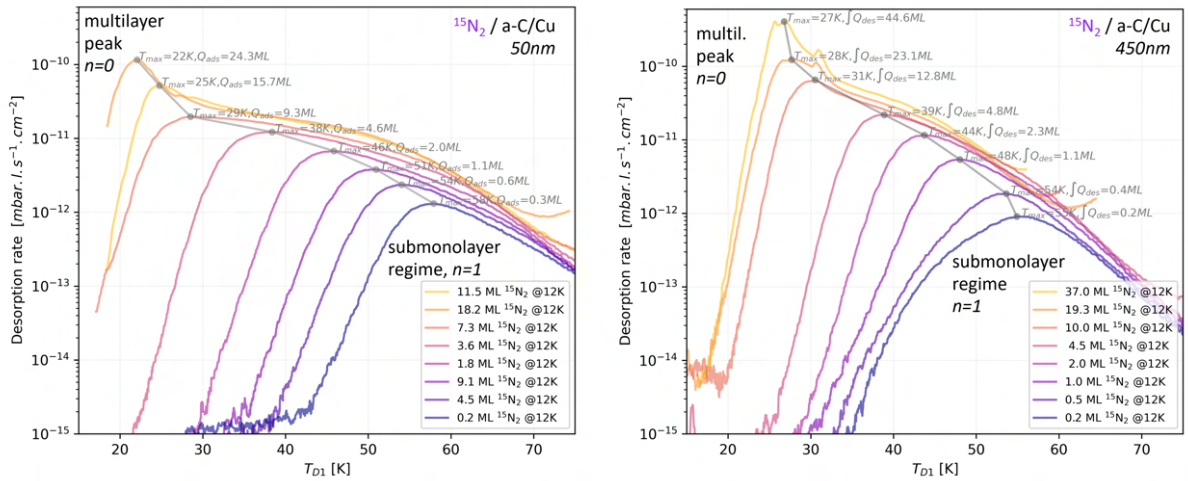

Figure 5.45: Left: TPD curves acquired 50nm thin (left) and 450nm thick (right) carbon-coated copper surface in an unbaked, as-received state. Both sets of TPD were acquired in the same run. Gas was always quench-condensed at sub-15K temperatures. Temperature ramps of 10 K/min were used where possible. Slower ramps were used at very high coverages. Assumed 1 ML = 10^{15} molecule.cm^{-2}, for simplicity and comparison purposes only, despite being unphysical on a rough surface.

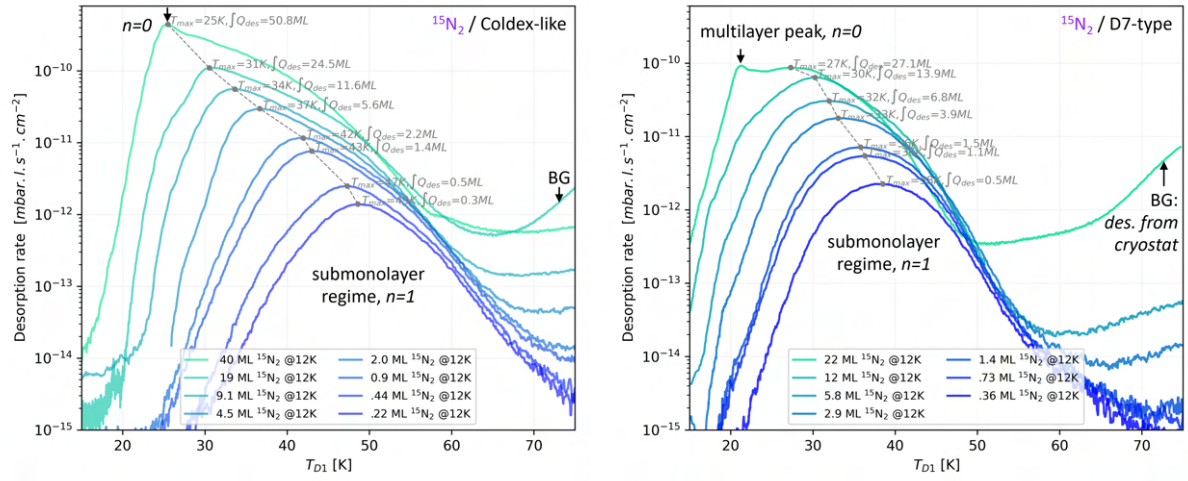

Figure 5.46: Left: TPD curves acquired COLDEX-type (left) and a D7-type (right) laser-treated copper surface in an unbaked, as-received state. Treatment details are listed in Section 2.3. Both sets of TPD were acquired in the same run. Gas was always quench-condensed at sub-15K temperatures. Temperature ramps of 10 K/min were used where possible. Slower ramps were used at very high coverages. Assumed 1 ML = 10^{15} molecule.cm^{-2}, for simplicity and comparison purposes only, despite being unphysical on a rough surface.

The TPD curves' behaviour of the laser-treated copper is different from the amorphous carbon coatings discussed above. Similarly, peak desorption rate points to similarly high porosity. However, the lower desorption temperatures point either to lower adsorption energies or to more open pores, when compared to the carbon coating. Indeed the SEM images point to the latter, as the laser treatment exhibits semi-open low-aspect ratio pores, while the carbon coating has much smaller pores of presumably high-aspect-ratio (pore depth vs. width).

Spallino et al. [276, 277] reported similar TPD measurements taken at cryogenic temperatures on a laser-treated copper, albeit a different type. They obtained a coherent behaviour across multiple

gases which they studied in highly multilayer coverages, and compared them against a technical-grade Cu. Unfortunately, multilayer coverages on highly porous surfaces are just out of practical reach of this experimental setup due to high pressure transients and/or long measurement times. However, it is remarkable that a different type of laser-treated copper has a very differently shaped TPD profile. Most notably it is the presence of a double peak they observed which points to further complexity and calls for further research and explanation, as it is not observed in any of the measurements presented here.

5.5.2 Gas composition dependence

Other gases were also studied aside of $^{15}N_2$. The H_2 can just barely be cryosorbed on the carbon coating in deeply submonolayer coverages at the temperatures that are experimentally achievable here. Hence, the focus was shifted towards other UHV-relevant gases: CO and CO_2. Which both exhibit a somewhat special behaviour, previously not observed with $^{15}N_2$ studies that were more focused on studying the surfaces, rather than the gas-surface interaction.

Figure 5.47 shows that CO *potentially* exhibits an unusual fractional kinetics order of $n = 1/2$ on both carbon and Cu substrates, although much more profound on Cu. The CO clustering was observed before on Ag(111) [278] and can be assigned to a non-uniform charge distribution around the CO molecule. Clustering is commonly observed in molecules with a non-uniform charge distribution of the molecular orbitals, such as H_2O, or $^{13}CO_2$ [279–281], creating a side with a slightly positive charge and a negative side too. This allows a weak electrostatic interaction between adsorbed molecules, which can in fact be stronger than the substrate-adsorbate binding energy. As a result, it is energetically favourable for the molecules to form clusters. These formed clusters can coalesce and form islands.

During a TPD, the first step is the sublimation of molecules from the 2D islands (molecules stationary on the surface) into 2D gas (molecules move freely over the 2D surface) which is followed by desorption into the vacuum. The kinetics order then varies depending on the limiting step of the thermal desorption sequence [207]. If the 2D gas and 2D island establish a thermal equilibrium, the desorption order is $n = 0$ and represents sublimation, albeit in 2D. If the thermal equilibrium is not reached in the 2D binary system, the circumference of the 2D islands limits the desorption. This gives rise to a $n = 1/2$ behaviour since the island's circumference scales with the square root of coverage $\theta^{1/2}$. This is indeed in line with the theoretical introduction presented in Section 2.8.

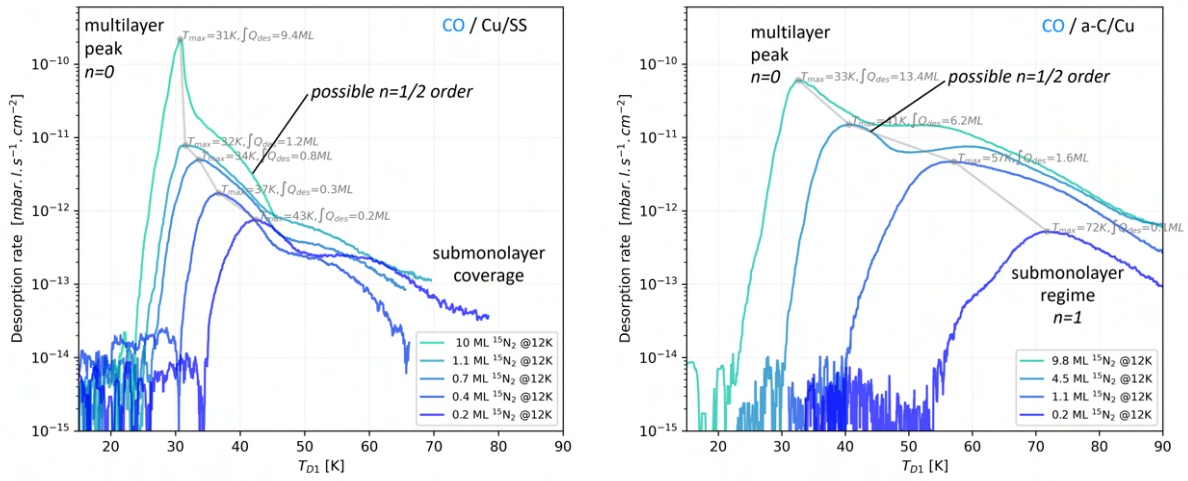

Figure 5.47: TPD curves acquired for CO quench-condensed onto copper on 50 nm thin carbon-coated copper substrates at coverages ranging from 0.1 ML to 10 ML. Left: CO TPDs on LHC-grade copper colaminate onto stainless steel. Right: CO TPDs on a 50 nm thin amorphous carbon-coated copper colaminate. Assumed 1 ML = 10^{15} molecule.cm^{-2}, for simplicity and comparison purposes only, despite being unphysical on a rough surface.

In the case of $^{13}CO_2$, the clustering effect results in a zero-order $n = 0$ desorption kinetics even at sub-monolayer coverages. This effect, however, is only observed on the technical copper surface. The 50 nm thin carbon-coated copper does not allow this clustering effect and the desorption proceeds with a classical first-order kinetics in the sub-monolayer coverage regime like other gases do. This can be either due to a higher diffusion barrier on the amorphous carbon, or due to stronger adsorption energy. Either way, from the vacuum dynamics point of view, this effect alone offsets the $^{13}CO_2$ peak desorption

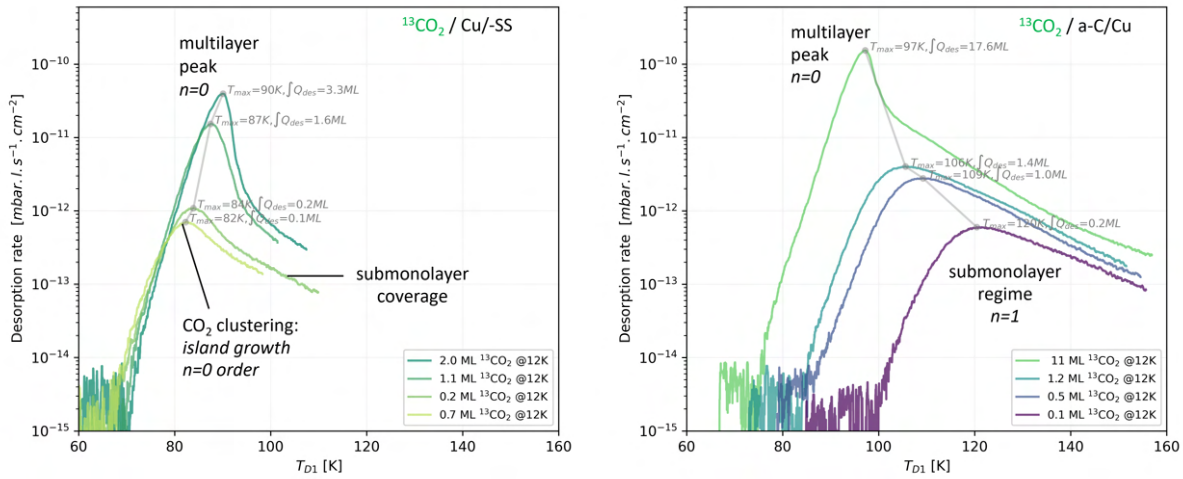

Figure 5.48: TPD curves acquired for $^{13}CO_2$ quench-condensed onto copper on 50 nm thin carbon-coated copper substrates at coverages ranging from 0.1 ML to 11 ML. Left: CO TPDs on LHC-grade copper colaminate onto stainless steel. Right: CO TPDs on a 50 nm thin amorphous carbon-coated copper colaminate. Assumed 1 ML = 10^{15} molecule.cm^{-2}, for simplicity and comparison purposes only, despite being unphysical on a rough surface.

temperature. Measured at a 0.1 ML submonolayer coverage, the peak desorption temperature increase from $T_{max} \approx 82$ K for bare LHC-grade copper to $T_{max} \approx 109$ K for 50 nm thin carbon coating. In other words, this means a higher temperature is necessary to fully desorb submonolayer coverages of CO_2 from amorphous carbon coating than from a Cu surface. Moreover, the CO_2 clustering on copper promotes molecular desorption already at a temperature of 70 K, as opposed to 90 K for aC.

Using the above-listed equations 5.4, the binding energy can be evaluated, for example at 1 ML coverage. The cluster of gases desorbing around T_{max} ≈30 K have are bound with E_{ads} ≈80 meV, while the CO_2 has T_{max} ≈90 K corresponding to E_{ads} ≈260 meV.

The substrate-adsorbate interaction dominates at low coverages. As a result, the TPD curves for porous surfaces clearly show a higher T_{max}, resulting from rough surfaces generally having higher binding energies E_{ads} than bare metals. Partly due to a rough surface, that represents an abundance of high-energy adsorption sites. Partly due to open pores that trap gas and delay desorption, as was well illustrated in Section 2.8. As the surface coverage of adsorbed gas increases all surfaces eventually reach their T_{max} the value of ∼26 K that corresponds to $^{15}N_2$ cryosorbed onto another $^{15}N_2$ molecule, rendering the substrate irrelevant. This sudden change in behaviour is assigned to a transition from substrate-adsorbate to the adsorbate-adsorbate binding regime. Indeed, this transition can be used to identify the amount of gas necessary to create a one monolayer coverage over the entire surface microgeometry, i.e. at the microscopic level, including the pores. The monolayer transition from n =1 to n =0 (at whatever coverage this happens for a given surface) is important, as both the SEY and ESD behaviours tend to flatten out at this point. Also the peak desorption temperature changes a little past this point. A comparative overlay of the TPD results of all gases and surfaces is further elaborated upon in the Applications section 6.

5.5.3 Roughness factor evaluation

Copper colaminated on stainless steel served as a reference for the gas surface coverage measurements since it is the baseline surface due to its large-scale application in the LHC beam-screen. A series of TPD curves was acquired with $^{15}N_2$ and the gradually evolving shape of the TPD curves were used to deduce a 1 monolayer equivalent coverage for all studied coatings and treatments. Surface coverage of 1 monolayer (ML) coverage is assumed to be 10^{15}.molecule.cm^{-2} - a simplistic presumption, which is in fact not far from the truth and in any case it is sufficiently precise given the uncertainty intervals we are dealing with here. In this work, this *1 ML* nomenclature is used regardless of the surface concerned.

The monolayer coverage used in the data evaluation below will always be referenced to the geometrical, macroscopic surface of the copper colaminate sample that serves here as a baseline. The reference copper surface is thought to have no significant porosity in this estimation, hence the macroscopic geometrical surface is taken as equal to its specific surface. Conversely, the studied samples (carbon-coated and laser-treated copper) are porous, and hence the specific surface is r-time higher than the geometric surface,

see eq. 5.5 and Table 5.2. The SEM images presented above clearly illustrate the high surface roughness. Yet, the question remains: by how much is the specific surface higher than the geometric?

The amount of gas dosed onto the sample to just reach a multilayer TPD curve behaviour is known from visually analysing the data. The roughness factor r can be calculated by dividing this amount of gas necessary to create a *monolayer-like* TPD curve on an unknown studied porous surface, $Q_{1ML-like}$, by the amount of gas necessary to form a monolayer-like TPD curve on a flat reference surface, $Q_{1ML,ref.}$. Hence the 1 ML equivalent gas dose $Q_{1ML-like}$ has little physical basis and only serves this comparison. Finally, this ratio r equals the ratio of the two specific surfaces: the studied one $A_{specific}$ and the reference one $A_{geometric}$. This definition follows the IUPAC nomenclature [282], which defines the roughness factor as a ratio between the interface, i.e. specific surface, and the concerned macroscopic geometrical area.

$$r = \frac{Q_{1ML-like}}{Q_{1ML,ref.}} = \frac{A_{specific}}{A_{geometric}} \tag{5.5}$$

Surface	**Specifications**	**Roughness factor** r
Cu/SS	colaminated, annealed; **reference**	**1**
a-Carbon /Cu	50 nm sput.-depo.at CERN	10
a-Carbon /Cu	450 nm sput.-depo.at CERN	25
Laser-treat. Cu	COLDEX-type, witness	45
Laser-treat. Cu	D7-parameters	25

Table 5.2: Estimated roughness factors r of studied surfaces, as referenced to the LHC-grade beam-screen surface made of copper colaminated on stainless steel. Estimates are based on TPD analysis using a cryosorbed $^{15}N_2$ gas. Detailed description in the text.

For completeness and to avoid misinterpretation, the term *roughness factor* is not to be confused with a more traditional mechanical type of roughness - another characteristic of technical-grade surfaces. Many surface coatings, including amorphous-carbon coating, have high-aspect-ratio porosity hidden under a flat-top surface without a significant surface roughness.

The challenging part of this approximative method is pinpointing the transition between the sub-monolayer and multilayer regimes, where the 1 ML coverage lies. This task is already complex for a set of TPD curves acquired on a flat surface, as one can take different features to distinguish the transition between regimes: multilayer peak emergence, leading-edge departure, or approach to the probe-gas sublimation temperature. Here, all these indicators are combined to form an average estimate the equivalent monolayer-like coverage.

5.6 SEY and ESD of cryosorbed gases

The electron conditioning process can electrodesorb *large* amounts of gases, up to tens of ML, as demonstrated in the previous chapters. It is therefore important to assess how this affects the SEY and ESD, shall it be readsorbed elsewhere in the cryogenic vacuum system and repeatedly exposed to electron irradiation. This indeed represents a real-life scenario, for example, of gas recycling inside conductance-limited cryogenic beam-screens. Hence, it was systematically investigated how the SEY of conditioned and as-received copper evolves with increasingly thick overlayers of cryosorbed gas. The same was done for ESD yield, ranging the coverages from deeply submonolayer to multilayer thick gas precoverage. The 50 nm thin amorphous carbon-coated copper and laser-treated copper were equally studied since they are to be used in a cryogenic environment.

Coverages from 0.1 ML up to ∼30 ML quench-condensed atop of a sample held at 10–15 K were deemed suitable for the following studies. Particular focus was placed on 10 ML thick ices because of experimental constraints outlined in Chapter 4. A coverage of 10 ML is sufficiently thick to be substrate-agnostic to a large extent and fairly representative of semi-infinite bulk ice. Still, charging issues are mostly avoided at this coverage, with Ar as the sole exception. The results indeed connect onto the previously published article [A4] that focuses on thick cryosorbed gases, so called *ices*. The experimental findings shown here were also partially presented at [A5, A7].

5.6.1 SEY of cryosorbed gases on flat surfaces

As already discussed and reminded in Fig. 5.49, an SEY curve can be captured by a few signature parameters. This mainly includes the peak value δ_{max} and its position E_{max}. Then it is the fine structure in the low-energy 0–40 eV range, captured for simplicity at 5 eV as δ_{5eV}. And finally the ESD yield decay rate at higher energy of 300–1.5 keV that asymptotically follows the E^{-n} dependence.

As the precoverage of cryosorbed gas grows atop a substrate, the shape of the SEY curve gradually and non-monotonically transforms to a shape dictated by the cryosorbed gas itself with little to no influence of the underlying substrate. The LE-SEY region is generally the most surface-sensitive domain and changes first, already in 0–1 ML submonolayer coverages. The reflectivity increases and, as a result, the LE-SEY increases too. Here the SEY at 5 eV, marked δ_{5eV}, is selected to follow and compare the LE-SEY evolution with gas coverage, see the left side of Fig. 5.49. Meanwhile, the entire LE-SEY domain tends to develop a fine structure, as discussed below in detail. Then, around 1 ML, the δ_{max} starts changing, but whether it increases or decreases depends on the substrate δ_{max}. At last, the E_{max} starts to evolve, as it is the most bulk-dependent property, along with E^{-n} asymptotic decay. The SEY evolution with gas coverage is further discussed in Fig. 5.57 where the δ_{max} and δ_{5eV} data is overlaid for different gases cryosorbed on Cu and in Fig. 5.60 that captures multiple gases and surface treatments.

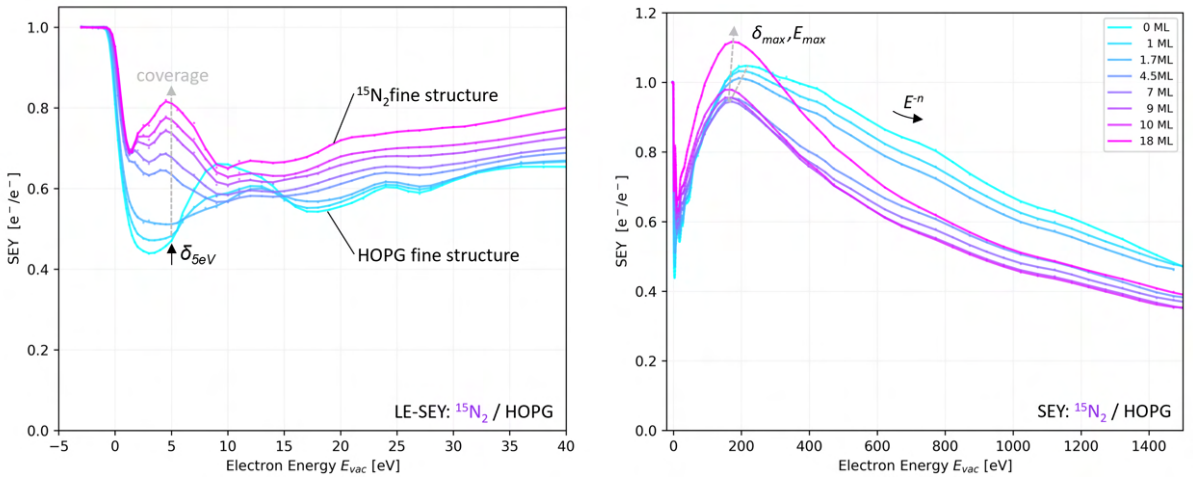

Figure 5.49: SEY curves measured at 0∼18 ML $^{15}N_2$ precoverage on a vacuum-cleaved HOPG, where a monolayer coverage is assumed to be 1 ML ≈ 10^{15} molecule.cm^{-2}. The $^{15}N_2$ was injected at ∼99% purity with about 1% of H_2 and CO pollution and quench-condensed over HOPG surface held at 12 K using direct gas injection via the collector. Note the left side zooming into the low-energy SEY region containing a fine structure that gradually changes from that of HOPG to that of $^{15}N_2$.

The HOPG is selected as a model surface to start this investigation. Although not a technical-grade metal, it is reasonably flat and atomically clean, which makes it suitable to substantiate the different points discussed. The fine structure observable in the LE-SEY for all investigated gases is likely an imprint of the electronic structure of the adsorbed gas. For instance, Fig. 5.49 shows an SEY measurement done with the $^{15}N_2$/HOPG system that clearly shows that a 1 ML already suppresses the LE-SEY fine structure of the HOPG and one corresponding to the $^{15}N_2$ starts emerging. At coverages of ∼5 ML, this LE-SEY fine structure becomes similar to that emergent in the $^{15}N_2$/Cu system in Fig. 5.50. Also note the peak SEY, characterised by δ_{max} that first decreases for a thin layer and only then starts increasing for coverages above ∼5 ML. The peak position E_{max} shifts from 230 eV to 180 eV as a consequence of changing the surface composition by adsorbing the $^{15}N_2$. The shape of the decay in the around 300 eV-1.5 keV also changes and a much faster decay appears, resulting from the ∼100 % lower density of N_2 ice compared to that of HOPG. The fact that at 18 ML the SEY curve is mostly independent of the flat surface beneath illustrates that the primary electrons at hundreds of eV penetrate about this deep into the cryosorbed overlayers. This distance gets even shorter for the slow electrons in the LE-SEY region where ∼5 ML is enough to entirely change the SEY curve shape.

A generic SEY curve of a fully conditioned Cu substrate is taken as a baseline for further studies of the effect of cryosorbed gases on the SEY of a surface. Figures 5.50 and 5.51 capture how SEY curves evolve for different $^{15}N_2$ or $^{13}CO_2$ gas coverages deposited over an electron-conditioned substrate of a bulk supplier-cleaned technical-grade Cu. The plots in Figures 5.52 then show how δ_{max} varies with the gas dose for both as-received and conditioned Cu surface. The low-energy part of SEY curves becomes agnostic to the conditioning state of the underlying substrate at around 5∼10 ML coverage. This seems to be the case regardless of the gas used, as $^{13}CO_2$ $^{15}N_2$ on Cu, as well as $^{15}N_2$ on HOPG, both exhibit the same trend. However, the peak SEY position E_{max} and magnitude δ_{max} still remains influenced by the underlying substrate even around ∼10 ML coverage, likely due to the electrons backscattered from the substrate and/or via electron scattering at the ice/metal interface. As the coverage further increases, the electron-substrate interaction subdues, and the entire SEY curve in the 0–1 keV region becomes dictated solely by the ice.

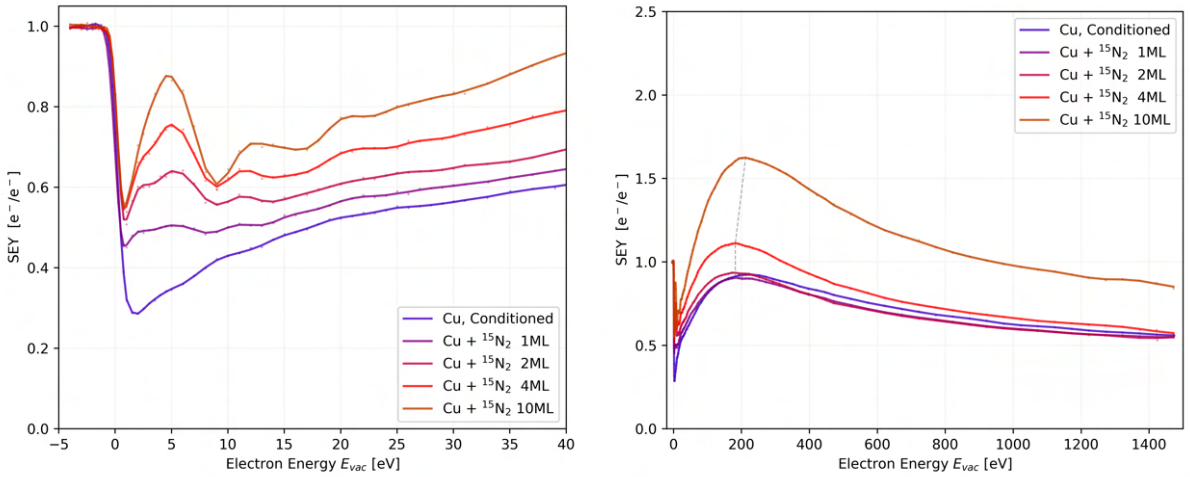

Figure 5.50: Right: SEY curves measured at 0∼10 ML $^{15}N_2$ precoverage, where a monolayer coverage is assumed to be 1 ML ≈ 10^{15} molecule.cm^{-2}. The ices were quench-condensed on a conditioned bulk Cu surface held at 15 K using direct gas injection via the collector. The CO_2 was injected at ∼99% purity with about 1% of H_2 and CO pollution. Left: Note the low-energy SEY region containing a fine structure.

Figure 5.53 schematises the secondary electrons (SE) internal reflection on the metal-ice and ice-vacuum interfaces. The electron reflection possibly explains the dip of δ_{max} observed at about 5 ML coverage of both $^{15}N_2$ and $^{13}CO_2$ deposited on an as-received bulk Cu. The same SEY suppression at ∼5 ML coverage observed in both $^{15}N_2$ and $^{13}CO_2$ on technical-grade copper, was also observed in $^{15}N_2$/HOPG adsorbate-substrate system, which is known to be atomically flat. While this effect is unsurprising on a flat HOPG surface, the technical-grade copper is indeed rough on the sub-micron scale. The SE interfacial scattering is presumably the reason for this decrease, as secondary electrons are known to scatter at interfaces, impurities, and inhomogeneities [252]. Conversely, this dip is not observed for the ice deposited on a conditioned Cu. The interface properties likely change between the metal and the ice

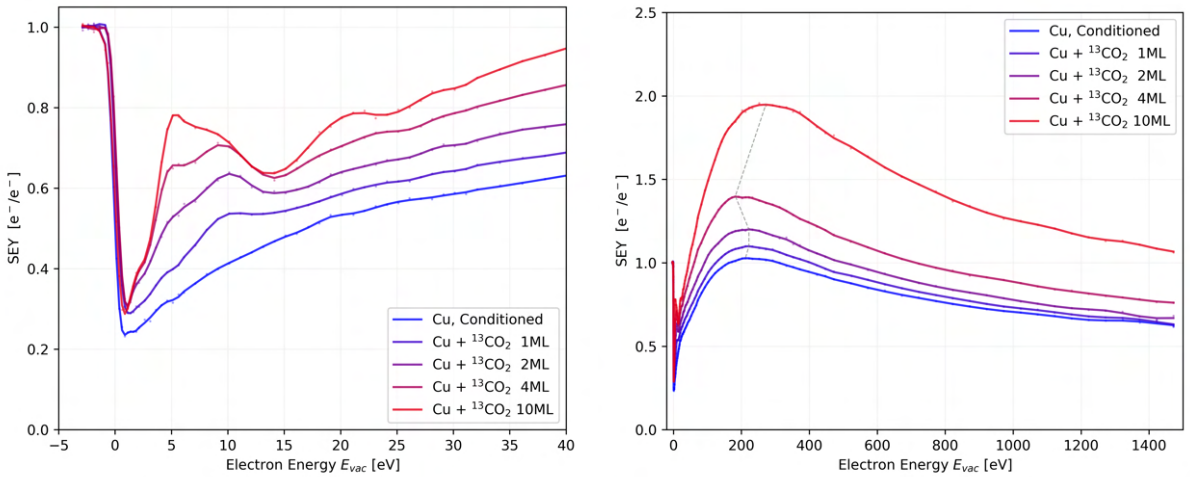

Figure 5.51: Right: SEY curves measured at 0∼10 ML $^{13}CO_2$ precoverage, where a monolayer coverage is assumed to be 1 ML ≈ 10^{15} molecule.cm^{-2}. The ices were quench-condensed on a conditioned bulk Cu surface held at 15 K using direct gas injection via the collector. The $^{13}CO_2$ was injected at ∼99% purity with about 1% of H_2 and CO pollution. Left: Note the low-energy SEY region containing a fine structure.

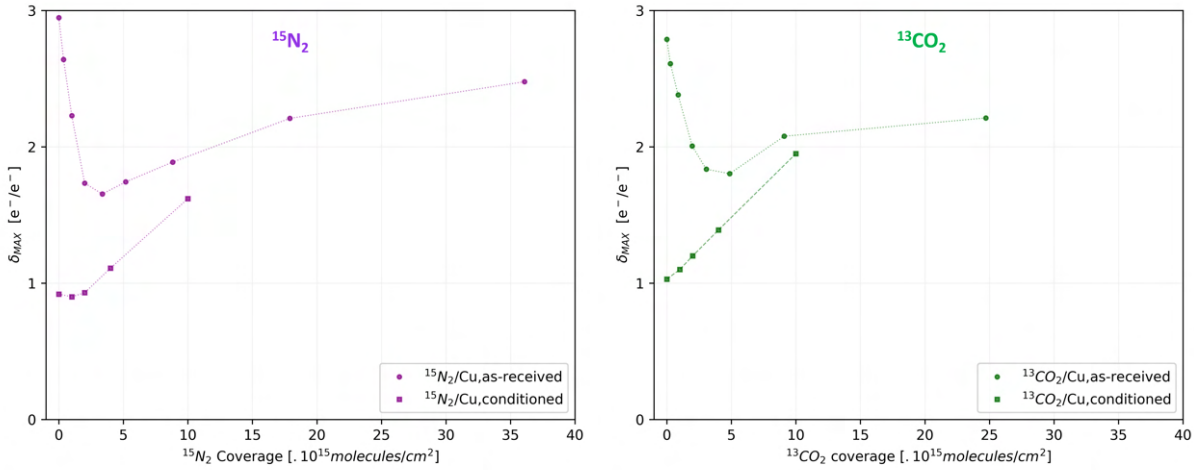

Figure 5.52: Evolution of maximum SEY δ_{max} with $^{15}N_2$ coverage (left) and CO_2 coverage (right) on as-received and conditioned bulk Cu surface. SEY curves were measured at 0∼30 ML $^{15}N_2$ precoverage, where a monolayer coverage is assumed to be 1 ML ≈ 10^{15} molecule.cm^{-2}. The ices were quench-condensed on a conditioned copper surface held at 15 K using direct gas injection via the collector. The CO_2 was injected at ∼99% purity with about 1% of H_2 and CO pollution.

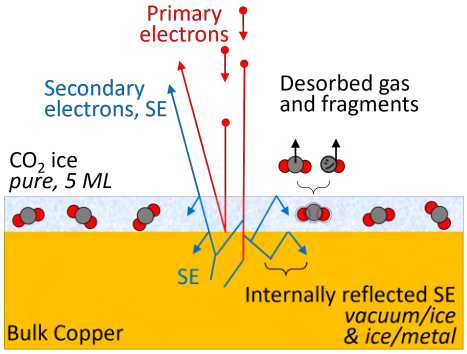

Figure 5.53: Scheme of secondary electrons internal reflection on the metal-ice and ice-vacuum interfaces. This reflection is thought to create a local δ_{max} dip at around 5 ML coverage observed for $^{15}N_2$/Cu, $^{15}N_2$/HOPG and $^{13}CO_2$/Cu systems.

and resulting in a lower potential barrier and consequently lower electron scattering on the interface. With these observations, it is possible that a suitable few-atom thin coating could be leveraged to contribute to

the suppression of secondary electron emission by utilizing interfacial scattering. A qualitatively similar decrease in δ_{max} for thin N_2 coverages was also simulated by [283] and is thought to originate in SE suppression by the adlayer and the metal-gas interface that imposes a potential barrier resisting the SE diffusion the from bulk upwards.

Figures 5.55, 5.54 and 5.56 shows a similar measurement taken for CH_4, CO and Ar gases quench-condensed at 15 K over an election-conditioned Cu surface. The SEY behaviour follows the same trend as observed in the $^{13}CO_2$/Cu and $^{15}N_2$/Cu systems discussed above in detail, mostly consisting of an SEY increase with coverage and a gradual shift towards higher energies. This evolution also includes the gas-specific fine structure in the LE-SEY region and the depth of 5∼10 ML at which the substrate and its surface state no longer matter. It remains unclear if the smooth structure observed for CH_4 is intrinsic or due to the contamination which is known to smear out the LE-SEY pattern.

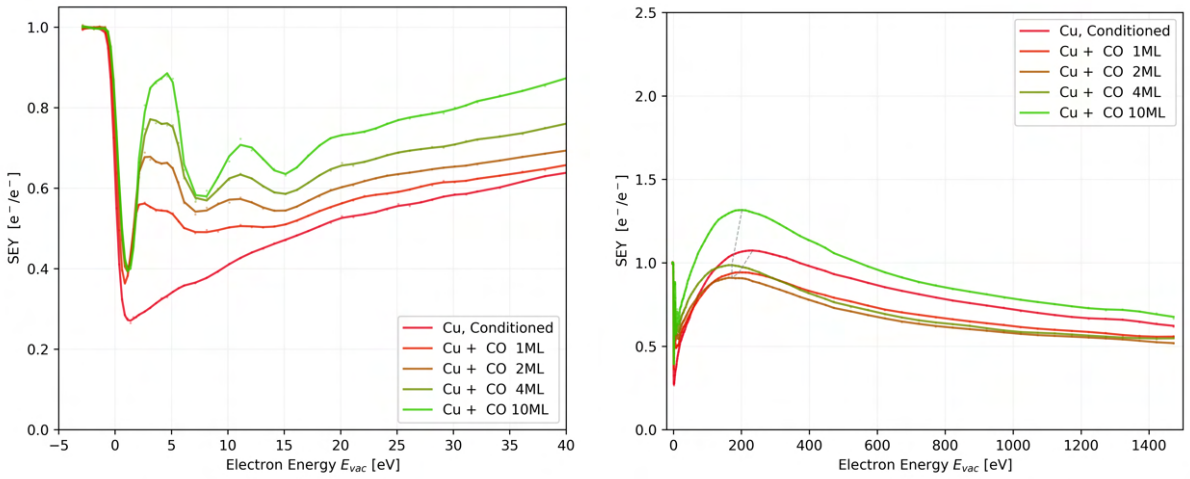

Figure 5.54: Right: SEY curves measured at 0∼10 ML CO precoverage, where a monolayer coverage is assumed to be 1 ML ≈ 10^{15} molecule.cm^{-2}. CO was injected at ∼99% purity with about 1% H_2 pollution and quench-condensed on a conditioned bulk Cu surface held at 15 K using direct gas injection via the collector. Left: Note the low-energy SEY region containing a fine structure.

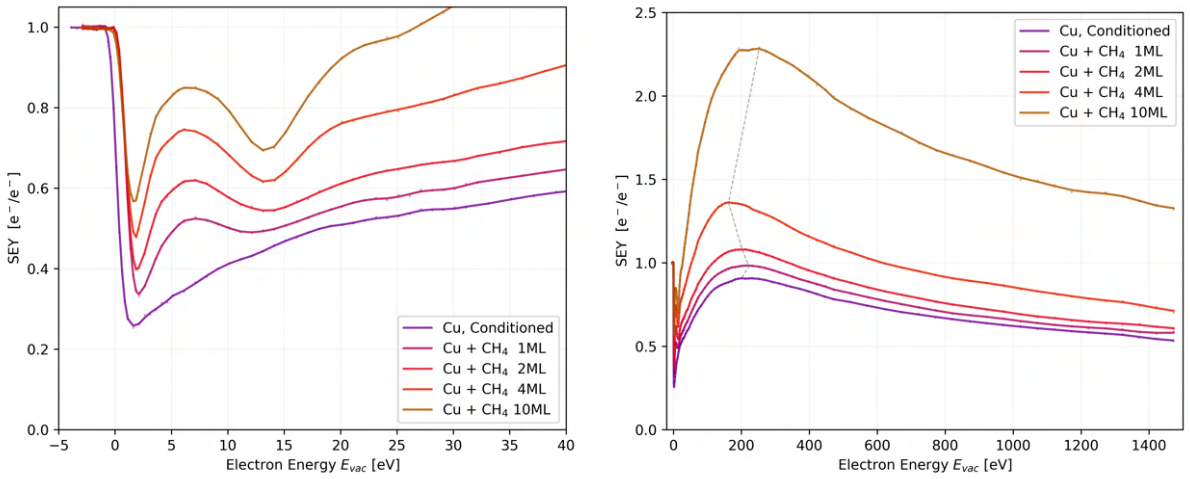

Figure 5.55: Right: SEY curves measured at 0∼10 ML CH_4 precoverage, where a monolayer coverage is assumed to be 1 ML ≈ 10^{15} molecule.cm^{-2}. CH_4 was injected at ∼91% purity with 7% CO and 1% H_2 pollution and quench-condensed on a conditioned bulk Cu surface held at 15 K using direct gas injection via the collector. Left: Note the low-energy SEY region containing a fine structure.

The quench-condensed Argon, Fig. 5.56, has a very high SEY when compared to similar coverages of other gases, which is consistent with prior measurements of Bojko et al. [284]. The peak SEY δ_{max} measured in thick cryosorbed gases tends to flatten at high coverages for all gases, which was previously shown by Kuzucan&Neupert [199]. Except for the noble gases whose SEY and ESD yields keep rising with increasing coverages. We recently discussed and demonstrated [A4] this effect to be the result of

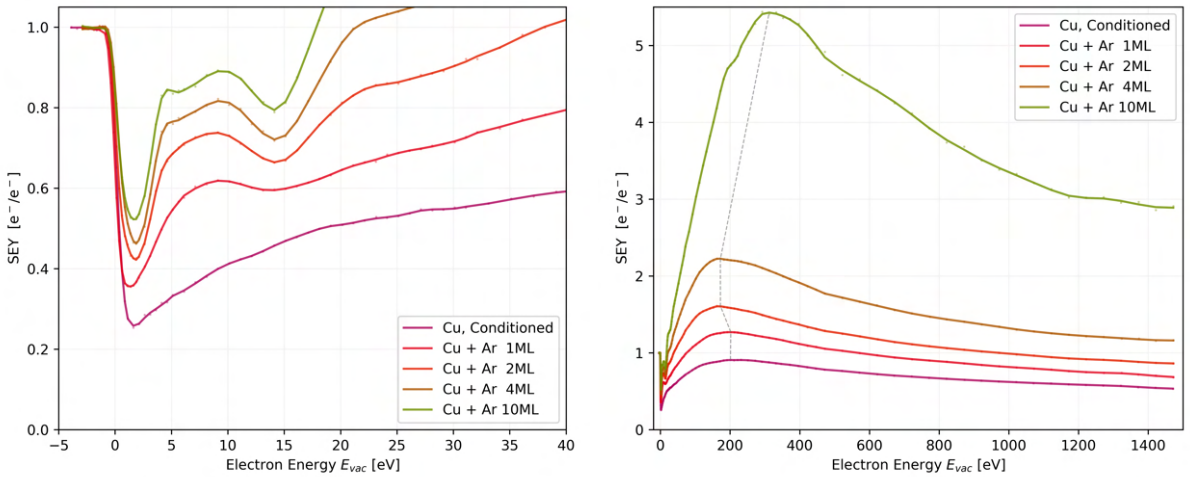

Figure 5.56: SEY curves measured at 0∼10 ML Argon precoverage, where a monolayer coverage is assumed to be 1 ML ≈ 10^{15} molecule.cm^{-2}. The ice was quench-condensed on a conditioned bulk Cu surface held at 15 K using direct gas injection via the collector. Ar was injected at ∼96% purity with some 1% H_2 and 3% CO pollution. Negative charging issues appear at 200 eV, decreasing the primary energy and hence the SEY too. Left: Note the low-energy SEY region containing a fine structure.

excitons (=bound state of electron and hole) diffusion through the condensed noble gas from its bulk towards the surface, which is normally the case for pure noble gases.

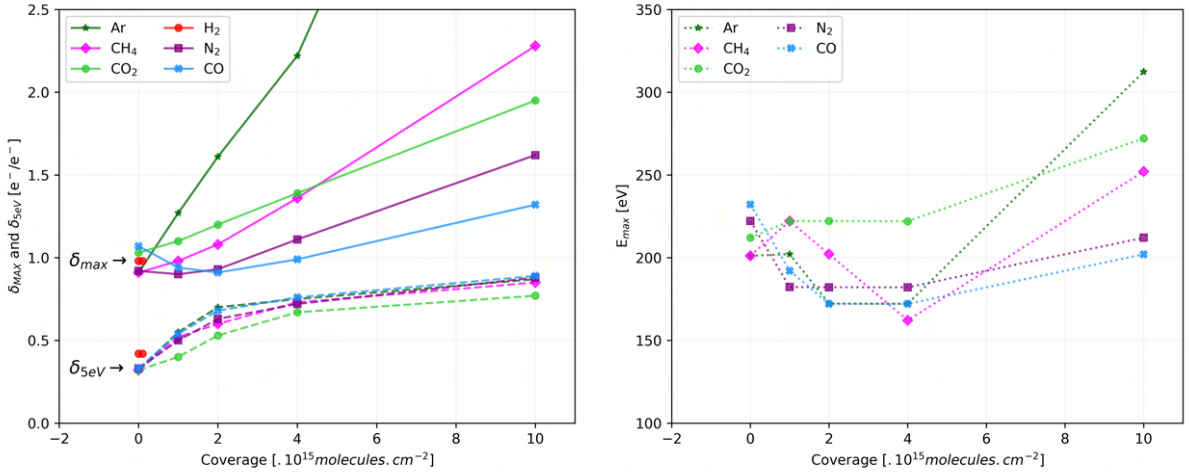

Figure 5.57: Left: Evolution of SEY at its maximum δ_{max} and at SEY at 5 eV δ_{5eV} for all investigated pure gases condensed at 0–10 ML coverages over a conditioned Cu substrate. Note the high sensitivity of δ_{5eV}, representative of the LE-SEY region, to the gas coverage. Right: Evolution of energy at maximum SEY, E_{max} as a function of gas dose.

The left side of Figure 5.57 plots the evolution of δ_{max} and δ_{5eV} measured at 5 eV for all investigated gases. The pure gas coverage varied in the 0–10 ML range and was condensed over a conditioned bulk Cu substrate. It is remarkable that the δ_{max} of all gases, aside of Argon, only starts rising around 2-4 ML coverage. The δ_{5eV} is already almost saturated at this coverage. In fact, only 1 ML seems to be enough to double δ_{5eV}, essentially doubling the 5 eV electron reflectivity for all studied condensed gases, from 0.3 to 0.6. These measurements and trends observed within allow us to infer the electron penetration and/or escape depths. For instance in the $^{15}N_2$/HOPG system, the HOPG fine structure peak at 5 eV disappears at around 5 ML coverage. Given that electrons have to make a double pass through the cryosorbed overlayer, allows us to estimate a range around 10 ML, or 3.6 nm. This can be compared to an extrapolated fit of Adams&Hansma [285], who also used this 'mirror' method and obtained a 1 nm range. However, the mismatch is not unexpected, as the sub-keV electron stopping powers are highly scattered, Fig. 2.2 and other effects can be at play, such as the wave-like nature of electrons. Mind the de Broglie wavelength at these low energies is in the nanometre range, about equal to the thin overlayer. Unfortunately, the CASINO simulation is not of help here due to being outside of its definition domain.

Some authors even use the periodically changing low-energy electron reflectivity to calculate the IMFP [286, 287] by presuming the wave-like electron interferes on the thin film deposited over an atomically clean surface.

On the other hand, the peak SEY δ_{max} and its location E_{max} are given by the balance between energy deposition depth and SE escape depth. This dynamic balance seems to equilibrate at around 200 eV and 5 ML coverage, at least for the studied $^{15}N_2$ and $^{13}CO_2$. This behaviour also indicates that the 300 eV electrons penetrate and SE escape on average a 5 ML thick ice column. This coverage amounts to around 1.7 nm when multiplied by the molecule kinetic diameter of around $\sim 3.5\mathring{A}$. The SEY position E_{max} can also in theory be used for analysis, but in practice turned out to be questionable, see right side of Fig. 5.57. The E_{max} is dictated by the substrate for thin ice coverages, whereas the peak is unreliable due to charging issues for thicker ice coverages.

The acquired experimental SEY curves characterised by the δ_{max} and E_{max} and their evolution with a surface coverage generally agree with prior measurements done at CERN by Chmielinska[200] and Kuzucan[198, 199]. This work now extends the research to the low-energy and low-coverage region that is very much relevant to technical applications and further adds ESD and TPD measurements discussed below. The measurements of Fang et al. [288] are in agreement with data presented here, Fig. 5.60, and observations reported by [198–200]. They report lower SEY for as-received Cu, Al and SS held at cryogenic temperatures, which is deemed to be due to the presence of cryosorbed residual gases. It is worth noting here that cryosorbed gases result in different SEY characteristics than the same species in chemisorbed state, as visible when compared to the studies of Zhang et al. [289]. This is due to a different electronic structure resulting from different chemical bonding state.

Further focusing on the LE-SEY region, the link between LE-SEY fine structure and the electronic bands of the target material, is not coincidental and was independently demonstrated by different groups using energy, momentum and angle-resolved electron emission. Pokorná&Frank [290] eloquently explain that: *"An electron wave impinging on the sample surface has to transform into electron waves of the crystal periodicity (Bloch states). Its surface-parallel wavevector component has to be preserved except for the addition of any surface reciprocal-lattice vector, which means that the incident electrons may only enter when suitable Bloch states are available and empty. This means that the electron reflection is inversely proportional to the local density of states coupled to the incident wave."*

Many other authors confirmed that the fine structure links to the electronic density of states (DOS) [239, 290–294]. For instance, Pokorna [239] has developed the DOS measurement using low-energy electron reflectivity measurements done in her low-energy SEM-focused dissertation [239]. After a challenging background subtraction, she achieved a significant correspondence between the LE-SEY fine structure and the DOS charts available for all the studied surfaces: HOPG, W et Al. Further taking crystalline metallic surfaces as a study case, Mikmekova measured the reflectivity of slow electrons using a low-energy SEM [292] and reported a fine structure that varied with the crystal orientation. This is indeed expected since the electronic band structure varies between crystalographic planes, and so do the electron emission properties. This generates the crystalographic type of contrast and was reported already in 1939 by Knoll&Theile [294] while setting the foundation for SEM. Regarding the N_2/Cu_{100} system, a similar observation was previously reported by Smith et al.[291] for N_2 chemisorbed onto a Cu_{100} substrate. The measured UPS photoemission spectrum correlates to the DOS calculated for the N_2/Cu_{100} system. This exercise undoubtedly illustrates the link between low-energy 0∼40 eV electron reflectivity and the target electronic structure. However, other effects intervene, such as plasmon losses, interference effects, and scattering at defects that likely alter the fine pattern observed in the LE-SEY region.

Given this evidence, the LE-SEY region of the $^{15}N_2/Cu$ system can be revisited, see Fig. 5.58. The fine structure on the left can be extracted and better visualised by subtracting the underlying SEY curve corresponding to the bare conditioned Cu surface. The resulting spectrum on the right side of Fig. 5.58 shows the electron reflectivity introduced by the gas overlayer on top of that of the substrate. It is known for a bare HOPG, Fig. 4.9, that the fine structure in the LE-SEY region corresponds to the occupancy of electronic bands. By extension, the fine structure isolated here from the LE-SEY curve should be a mirror imprint of the electronic band structure of the cryosorbed $^{15}N_2$. Unfortunately, data suitable for comparison and support of this conjecture are not known to the author.

Following the reasoning about slow electron reflectivity resulting in a fine structure representative of the electronic bands, the peak SEY δ_{max} can be plotted as a function of the LE-SEY peak. The right side of Fig. 5.59 plots the δ_{max} as a function of LE-SEY peak width measured at its FWHM, see left side of Fig. 5.58. This peak, always present around 5 eV, is thought to be formed by reflected electrons due to an electronic band gap in the target material. This was shown experimentally for the case of

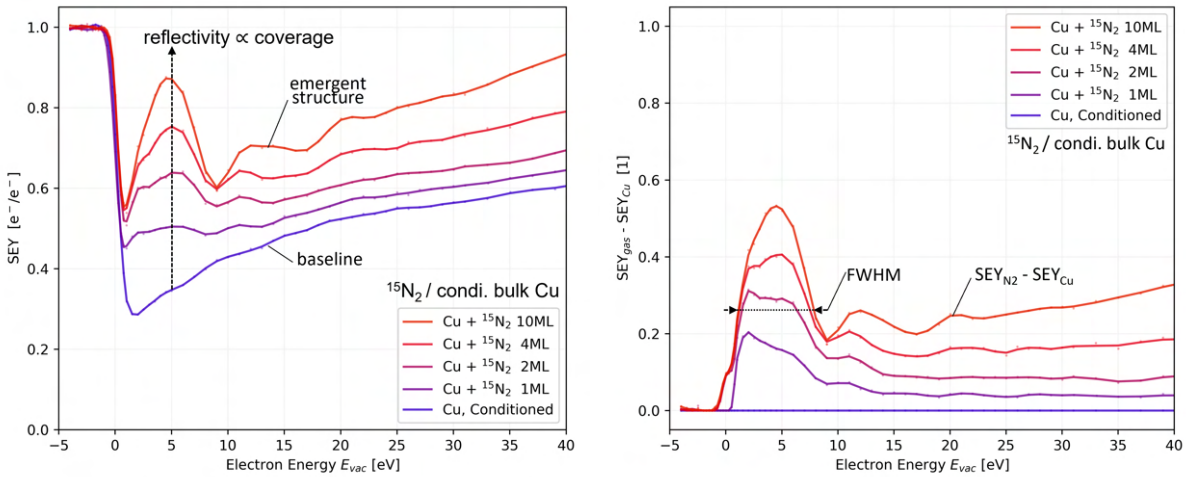

Figure 5.58: Left: Zoom on the LE-SEY area of N_2 deposited over a conditioned bulk Cu. Note the emerging fine structure as the N_2 coverage increases. Right: Cu background subtracted from the N_2 signal to obtain a Cu background-corrected fine structure emergent from a cryosorbed N_2.

HOPG [56] and also for a thin Fe layer on monocrystalline W_{110} [286]. According to the theoretical understanding, a large band gap corresponds to inefficient energy dissipation via electron scattering in the insulators, which leads to high SEY values due to a large population of hot electrons. In other words, the wider the band gap of an insulator, the more efficient secondary electron emission, owing to lower energy dissipation along the collisional cascade in the bulk material. Some authors report [295] this effect in binary systems, especially using H_2 to create either sp2-dominated or sp3-dominated carbon coating [47, 296]. They vary the composition, which increases the band gap, leading to a strong SEY variation, clearly proving a correlation, though the exact causation is still under discussion.

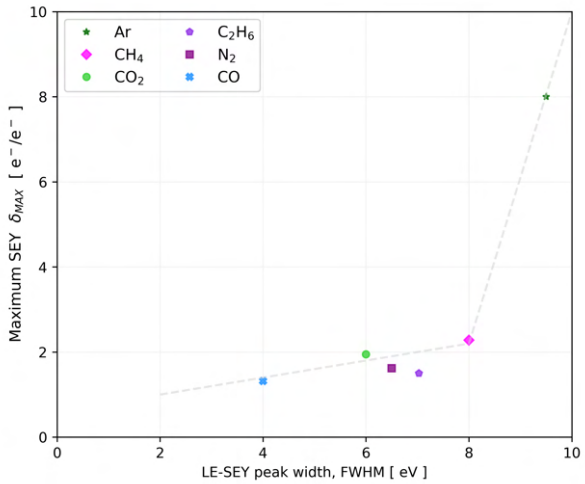

Figure 5.59: Maximum SEY δ_{max} plotted as a function of the LE-SEY 5 eV peak width at its FWHM. See text for full explanation.

5.6.2 SEY of cryosorbed gases on rough surfaces

Series of SEY, ESD and TPD measurements aimed to assess cryosorbed gases' influence when deposited over porous and rough surfaces. The TPD method was used in the previous Section 5.5 and the gas coverage corresponding to this transition in TPD curve behaviour was used to infer each studied system's specific surface relative to technical-grade Cu/SS colaminate. To estimated roughness factor r also comes into play here. The 1 ML coverage is simply assumed to be 10^{15} molecules.cm^{-2} for any surface, be it flat or porous.

Figure 5.60 shows the δ_{max} and δ_{5eV} coverage dependencies for typical gas species (left) and a range

of surfaces (right). Note the difference in SEY coverage dependence between a preconditioned bulk Cu, Fig. 5.57, and the 50 nm thin amorphous-carbon coating, left side of Fig 5.60. All studied porous surfaces (carbon-coated or laser-treated Cu) can cryosorb much higher gas coverage before δ_{max} and δ_{5eV} starts increasing. Roughly a roughness factor r-times higher coverage is necessary attain a behaviour similar to a bare Cu. This seems to apply to all studied gas species, with the sole exception of CO_2, which behaves as if it was quench-condensed on top of a *geometrical* surface and did not diffuse into the pores.

The high SEY for CO_2-covered carbon coating be explained by a high diffusion energy barrier for the CO_2 molecule on the rough surface held at low temperature of 15 K. This does not allow thermally-driven surface mobility, which prevents it from diffusing into the open pores, and so it remains on the geometrical surface and effectively increases the SEY. Annealing to a higher temperature (yet below desorption) could promote surface mobility and let the CO_2 diffuse into the pores, possibly lowering the SEY.

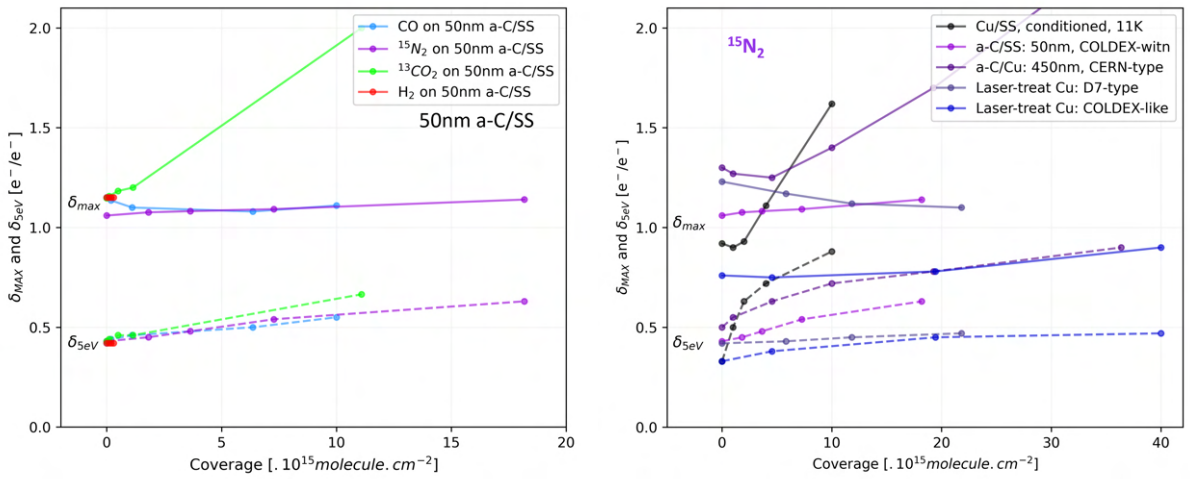

Figure 5.60: Left: Evolution of maximum SEY δ_{max} and SEY at 5 eV_{vac} δ_{5eV} for all investigated pure gases, as condensed at 0–10 ML coverages over a 50 nm a-Carbon coated stainless steel. Note the high sensitivity of LE-SEY region to the gas coverage, here represented by δ_{5eV}. Right: Series of SEY values measured for 0–40 ML coverages of $^{15}N_2$ over various surfaces. Cu/SS is also shown for reference.

5.6.3 ESD of pure cryosorbed gases

The following ESD yield energy-dependence curves were measured after acquiring the series of SEY measurements for 1-10 ML coverages discussed in the previous section. The ESD curves have several remarkable information to offer, as follows.

First, the energy threshold for electrodesorption tends to vary in the 5-12 eV range for the investigated cryosorbed gases, as shown in the insets. Thresholds for common gases, such as N_2, CO and Ar, also match the literature, e.g. Newman et al. [297], Rakhovskaia et al. [229], or Schmid et al. [36]. This coherence with other experimentalists, on both qualitative and quantitative levels, brings confidence in the novel results reported here. Furthermore, it is remarkable that CO fragmented off of the parent $^{13}CO_2$ molecule already desorbs at 6 eV, while the parent $^{13}CO_2$ has an energy threshold around 11 eV.

Figure 5.62 compares CH_4 and C_2H_6 yields as well as their H_2 fragments. There is no dehydrogenation below the parent molecule desorption energy threshold, which is an unexpected result, because it is commonly observed that organic molecules release hydrogen already at units of eV [34]. But then, bare metals commonly have the H_2 energy threshold at ~8 eV, so the presence of H_2 does not imply a low threshold. Instead, the η_{H2} yield is dictated by its chemical state, which is expected.

The inset in Figure 5.63 shows a desorption threshold for Ar at 11.7 eV, referenced to the sample's vacuum level, that is long known to exist, as reported by Lloyd et al. [298], Bass et al. [299], and Rakhovskaia et al. [229]. Aside of the threshold, the LE-ESD curve for Argon also exhibits a Feshbach resonance that is known exist at ~16 eV for Argon [129, 299, 300] and similarly for other heavier noble gases [301]. A Feshbach resonance is a short-lived electron-atom radical that releases a substantial amount of energy 0.5~1 eV upon its decay [299] that effectively boosts the desorption yield. For comparison, Argon binding energy is much lower than that, $E_{ads,Ar}$ ≈90 meV.

Since the studied thin Ar ice was accidentally deposited with CO and H_2 contamination it shows a cross-interaction of the desorption processes, i.e. mutual kick-out mechanism in the Ar↔CO system.

Despite its low concentration, CO molecule does kick-out Argon atoms in a measurable amount already at its normal 6 eV threshold. Conversely, the Feschbach resonance enhances the Argon yield at ∼16 eV, but along with it enhances the CO and H_2 yield via the knock-out mechanism. Because both CO and H_2 yields follow the same pattern, it is unlikely that this yield-enhancement effect can be assigned to de-cryotrapping (cryotrapping=condensing gas entraps more volatile species). This observed cross-interaction stimulated the research effort towards studying the cross-interaction effect in ESD of mixed gases, as is elaborated upon in Section 5.6.5. An identical effect of mutual kick-out close in the low-energy region, this time in photodesorption, was reported by Dupuy et al. [176, 302, 303].

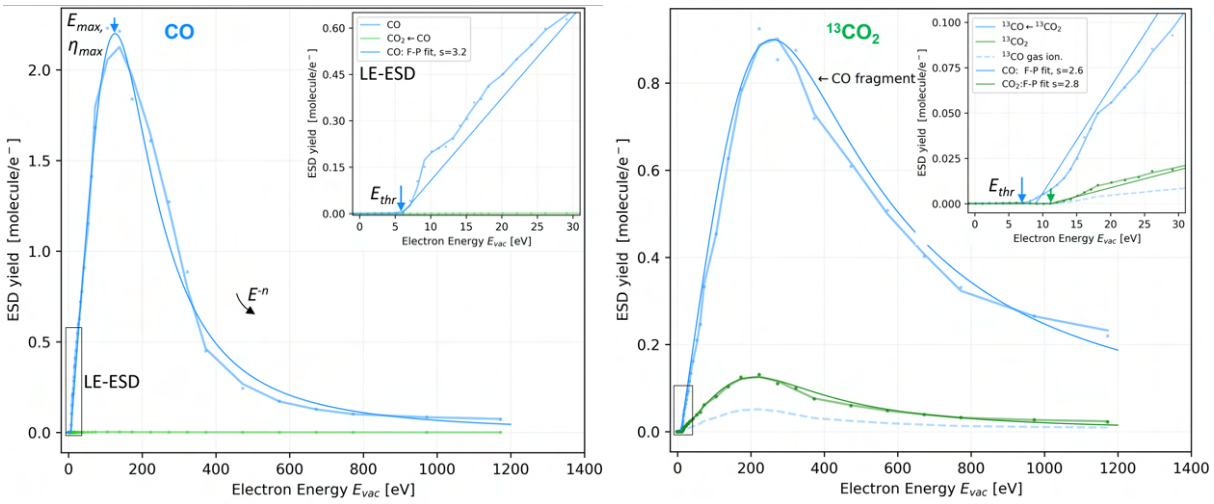

Figure 5.61: ESD yields energy dependence measured at ∼10 ML precoverage. The ices were quench-condensed on a copper substrate held at 15 K using direct injection via the collector. Both gases are injected at ∼99% purity with mostly H_2 pollution. Left: CO and CO_2 to study possible synthesis, which is not present. Note the 6 eV desorption threshold and sub-200 eV peak. Right: CO_2 and its CO fragment which dominates the desorption. The corresponding gas-phase fragmentation in the RGA ion source of CO_2 →CO only equals to 16%, so the measured CO-dominated desorption originates at the surface due to SE.

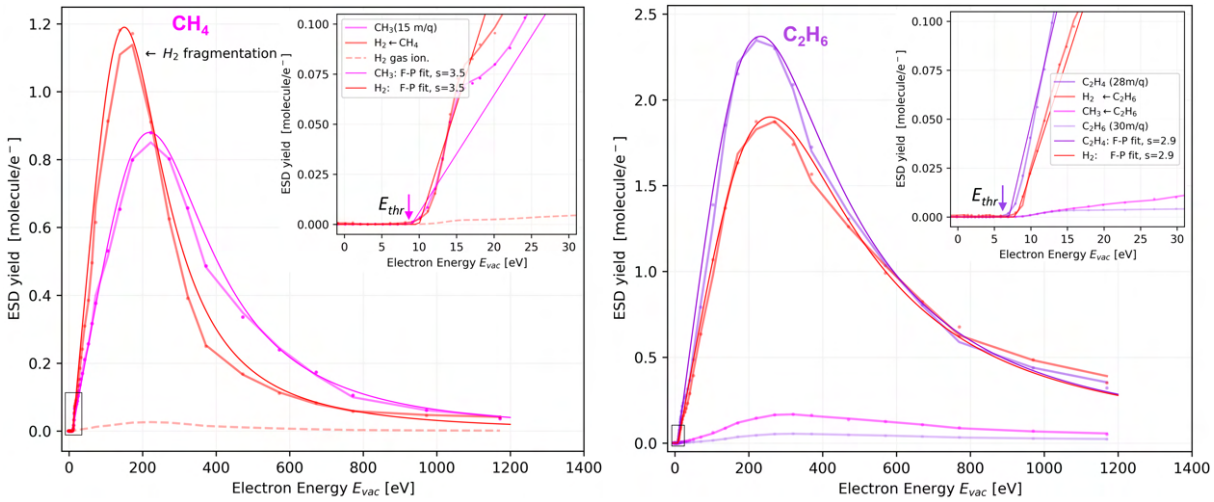

Figure 5.62: ESD yields energy dependence measured at ∼10 ML precoverage. The ices were quench-condensed on a copper substrate held at 15 K using direct injection via the collector. Left: CH_4 was injected at ∼91% purity with 7% CO and 1% H_2 contamination. Right: C_2H_6 and its fragments, mainly H_2, CH_4 and C_2H_4 dominating on the RGA. C_2H_6 was injected at ∼99% purity with 1% H_2 and CO pollution.

Second, the secondary electron-induced fragmentation pattern is very different from the gas-phase ionization, marked by a dashed lines. The gas-phase fragmentation patterns were measured during the RGA calibration via pure gas injection in the Experimental chapter 4.5.1. Hence, it is safe to state that the magnitude (and position) of the peak ESD yield of a fragment molecule is much higher than what would correspond to the gas-phase fragmentation in the RGA ionization source. The large difference in fragmentation patterns can be explained by the fact that the surface-bound gas molecules are exposed

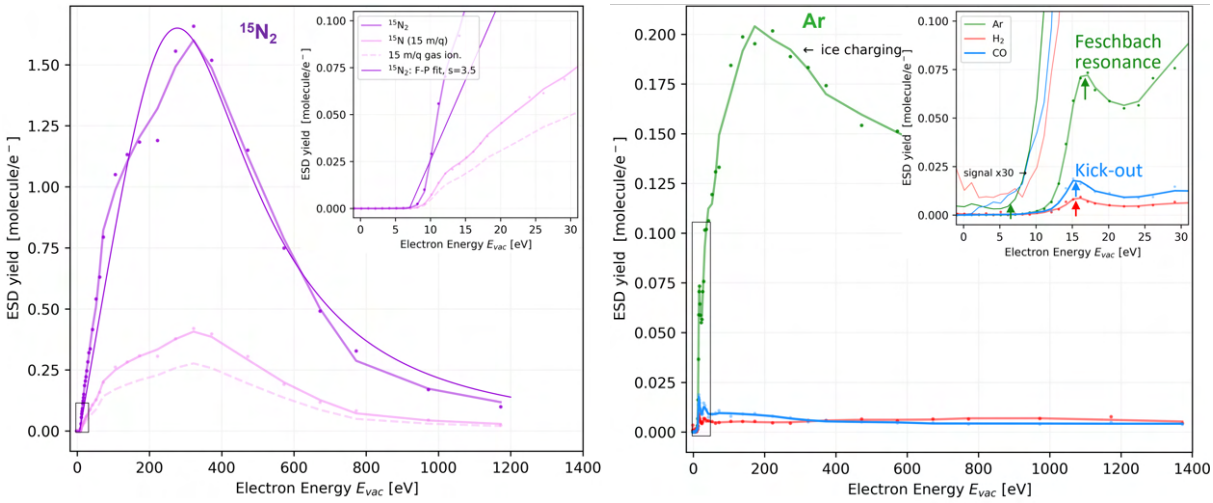

Figure 5.63: ESD yields energy dependence measured at ∼10 ML precoverage. The ices were quench-condensed on a copper substrate held at 15 K using direct injection via the collector. Left: $^{15}N_2$ was injected at ∼99% purity with 1% H_2 pollution. Right: Ar was injected at ∼96% purity with some 1% H_2 and 3% CO pollution. Negative charging issues appear at 200 eV, decreasing the primary energy and hence the ESD yield too. The inset containing the threshold, resonance and cross-kick-out between CO↔Ar is discussed in the text.

to many more secondary electrons and is consequently much more likely to fragment by those SE, than its gas phase counterpart, which is a single collision event. A factor of ∼10x of a difference between the two cracking patterns is not unusual, favouring surface-based fragment production.

The C_2H_6 electrodesorbs less H_2 than CH_4, proportionally to its stoichiometric composition. Following this trend set by two lone datapoints, it could be expected that heavier carbohydrates would leave more carbon behind, possibly already in a sp2 binding state in case of using a precursor gas with a double carbon bond C=C. The reason for $E_{max,H2}$ being much lower than the parent molecule's $E_{max,CH4}$ is unclear. Perhaps the E_{max} offset has to do with a limited bulk-to-surface diffusion length of H_2 after it was cracked from the parent CH_4.

Third, the presence of electron-induced fragmentation, but lack of electro-synthesis, means that surface-bound molecules preferentially fragment but rarely if at all synthesise under the investigated range of conditions. Moreover, taking the case of the newly fragmented CH_4 →H_2 molecule can either thermally escape or not, depending on the surface temperature of the substrate-adsorbate system. The fact that the intermediate chemical products can leave the system and therefore be unavailable for further reactions gives arise to temperature-dependent branching ratios. Note the high $^{13}CO_2$ →^{13}CO reaction. The effective reprocessing of CO_2 into CO is known and was reported by e.g. by Anashin et al. [190] for photon-induced fragmentation. Hence, there's a strong reason to believe that a radiation-exposed CO_2 is effectively reprocessed into CO, shedding off the excess oxygen atom.

Dulieu et al. [304] demonstrated that temperature can be used as a lever to prefer a certain chemical pathway by thermally desorbing the intermediate product if done at elevated temperatures, or not when cold. For instance the measurements of Baglin et al. [305] show H_2 molecule leaving during photon irradiation of CH_4, meaning that carbon-rich residue is left behind. Such reasoning also corroborates the observations of Petit et al. [245] who report different chemical pathways observed during copper conditioning at cold and ambient temperatures, at least under specific conditions. Hence, the temperature is a crucial aspect of the electron-induced chemistry that can alter the reaction products. Note that the scenario would differ shall this happen in the bulk ice, as the fragmented molecule would stay trapped in the ice and be available for further chemistry, possibly a synthesis. An efficient synthesis CO→CO_2 was observed, in much thicker cryosorbates by Huang et al. [306].

Finally, at energies above the E_{max}, the ESD yield decay rate is strictly dictated by the bulk. Along with the E_{max} position the yield decay rate is a function of the electron stopping power in the condensed gas and the diffusivity of electronic excitations. All this information can be used to infer on the underlying processes of electron, molecule and energy transport in the condensed gas. The same behaviour was reported by Ellegard et al. [307] in condensed N_2 and O_2 at energies above 1 keV, where the yield follows a generic E^{-n} decay with a best-fitted value of n =1.2. More generally, the exponent n typically varies in 0.5-2 range depending on the system. While the value $n = 2$ is a signature of electronic stopping playing the major role in the primary electron energy deposition, other diffusion-based effects can intervene (such

as bulk-to-surface exciton diffusion observed in Argon) and change the ESD yield decay rate.

Otherwise, the measured desorption yields agree overall with similar data taken on cryosorbed gases. For example Tratnik et al. report ESD data [126, 196, 197] taken at LHe temperature of 4.2 K in the same energy and coverage ranges as here and converge to similar values. The data presented here, however, extend the current knowledge towards the low-energy end of the spectrum, measure desorption thresholds and cover the SEY and TPD curves of the studied cryosorbates as well.

The experimental data are fitted with curve originally proposed by Furman&Pivi as an approximation to the SEY discussed in Section 2.2.2. Here it is offset by the energy threshold and normalised to the peak energy, as is discussed in detail in the Applications section 6.1.

Table 5.3 summarises the main characteristic features of SEY and ESD as sampled at 10 ML from the data presented above.

	SEY			**ESD**		
Species	E_{max}	δ_{max}	δ_{5eV}	E_{max}	η_{max}	η_{thr}
N_2	212	1.6	0.8	250	1.7	7
CO	202	1.3	0.8	150	2.2	6
CO_2	272	2.0	0.8	210	0.15	11
CH_4	252	2.3	0.8	220	0.85	8
C_2H_6	231	2.3	0.75	230	2.4	7
Ar	*315*	*5.4*	0.67	*320*	*0.2*	11.7

Table 5.3: Summary of characteristic SEY and ESD parameters of the investigated cryosorbed gases, as sampled at 10 ML coverage, assuming 1 ML=10^{15} molecule.cm^{-2}).

5.6.4 ESD from flat and rough surfaces

Following the SEY coverage-dependent studies, a measurement was also done for the ESD yields of cryosorbed gases in 0–10 $\cdot 10^{15}$ molecule.cm^{-2} coverage range, further denoted as 0–10 ML. The left side of Fig. 5.64 overlays ESD yields as a function of coverage for the investigated gases: $^{15}N_2$, CO, $^{13}CO_2$ and CH_4. The ESD yield coverage-dependence was measured at 300 eV, close to the peak value, except for $^{15}N_2$ measured at 100 eV. The gases were quench-condensed over a preconditioned technical-grade Cu/SS colaminate surface held below 15 K.

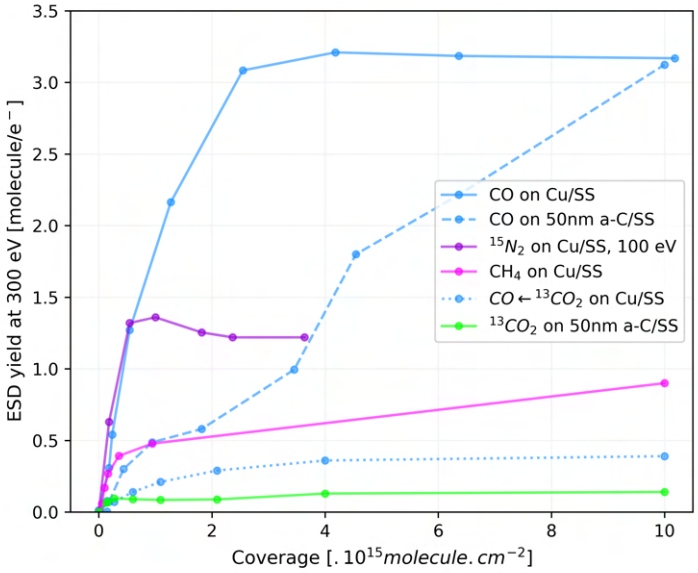

Figure 5.64: ESD measured at 300 eV (except for $^{15}N_2$ measured at 100 eV) for 0∼10 ML coverages. The gas is quench-condensed on a conditioned Cu and on a 50 nm thin carbon coating held at 12 K.

The ESD yield coverage dependence clearly has two regions. The first is the linear increase region in the 0–1 ML coverage range, where the yield of a given gas is limited by its (lack of) surface coverage.

Given the low coverage, the bonding is determined by the substrate-adsorbate interaction. Past the linear region, a saturation region is found at coverages higher than $2{\cdot}10^{15}$ molecule.cm^{-2}, where the yield is almost constant. Here, the gas desorption is no longer limited by the gas surface coverage, but by the desorption sequence quantum efficiency of a given adsorbate-adsorbate interaction. The ESD yield coverage-dependence of the ^{13}CO fragment of a parent $^{13}CO_2$ molecule follows the same trend (dotted blue line). However, it needs to be stressed that this behaviour is different from what Anashin measured on PSD, as compiled in [161], where they observe a linear increase until $\sim 10^{19}$ molecule.cm^{-2}. Also Tratnik observes a bump in ESD yields around $5{\cdot}10^{15}$ molecule.cm^{-2}, but then the ESD yields saturate at higher coverages.

A different coverage-dependence is observed for CO deposited over a 50 nm thin carbon-coated Cu and shown for comparison (dashed blue line). The CO ESD yields from carbon coating equals that of copper at ∼10x times the gas coverage. Generally, this factor of 10x is remarkably close to the roughness factor evaluated in 5.5.3, which is in fact no coincidence.

It is worth noting that the saturation of ESD (and PSD) yield when the coverage becomes *sufficiently* thick does not happen for pure noble gases until reaching thousands of monolayers. As argued by Hirayama et al. [308], this is explained by excitons' (long-lived electron-hole pair) propagation through the noble ice that transfer energy towards the surface. This behaviour however quickly disappears when introducing trace amounts of contaminants that act as sinks, quenching the diffusion process, as was shown in the data presented in Section 5.6.5, Fig. 5.66, but also by other authors [309]. Finally, the atom being ejected gains its kinetic energy from relaxation of a previously deformed lattice in a 'cavity ejection mechanism' as reported for Argon by Runne&Zimmerer [129].

5.6.5 SEY and ESD of cryosorbed gas mixtures

The data presented and discussed in the previous Section 5.6 gave hints of mutual interaction between the desorbing species. Namely, the inset of Figure 5.63 shows the LE-ESD yield measurement of Ar ice polluted with ∼3% of CO, which exhibits a mutual ESD yield enhancement observed between the CO↔Ar. Previous data acquired on pure ices also showed that the SEY and ESD yields generally tend to be anticorrelated, as illustrated in the top-left side of Figure 5.68. The SEY and ESD values acquired on pure ices show a clear negative correlation, i.e. high SEY leads to low ESD yield and vice versa - a phenomenon worth attention. It was therefore decided to explore this dependency using binary gas mixtures in proportions, ideally varying from 100 % of compound A to 100 % of component B.

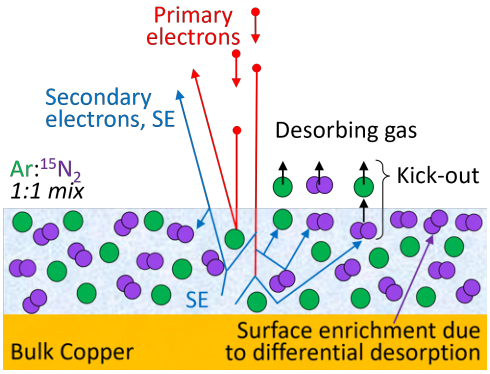

Figure 5.65: Scheme of ESD from a 1:1 mixed ice of $^{15}N_2$ and Argon at a 10 ML coverage over a Cu substrate. Besides the traditional DIET mechanism, note the kick-out mechanism, as illustrated for the $^{15}N_2$ →Ar process visible in the data, in Fig. 5.66 and right inset of Fig. 5.63.

Hence, a series of measurements were done to study the SEY and ESD evolution with the composition of binary ice cryosorbed on flat metal surfaces in the full 0–100 % composition range. The molar fraction x marks the % abundance of component B in component A. SEY and ESD yields were studied in the usual 0–1.4 keV energy range, but ultimately the maximum SEY was used for comparison and the ESD was sampled at 300 eV, being reasonably close to the maximum. Three different binary ice systems were studied ($^{13}CO_2$:$^{15}N_2$ at 30 ML, CH_4:CO and $^{15}N_2$:Ar at 10 ML), whilst continuously developing the experimental technique. Two systems are presented here, CH_4:CO and $^{15}N_2$:Ar, as they are particularly illustrative, see Fig. 5.65, and are used to derive the following narrative. To facilitate the data interpretability, the two binary mixtures were chosen such that their fragmentation patterns occupy different

channels on the RGA mass spectrum. Moreover, the components to form a binary gas mixture were intentionally selected in a way that their SEY and ESD yields are also highly dissimilar. The high scatter in the data is caused by uncertainty in mixture composition (∼2 %), pollution (<2 %) and by uncertainty in the dosed surface coverage (≈10 %). Yet, trends are still visible despite the scatter. Care was taken in this measurement not to alter the surface composition by differential desorption by extended irradiation.

First concerning the SEY and its highly nonlinear dependence, here approximated by a trendline described in Section 6.1. The higher-yielding component quickly loses the high SEY as the fraction x of the lower-yielding component increases. Taken from the opposite end, high concentrations of a high-SEY component above 50 % are necessary to significantly increase the SEY of a mixture. Here, a weighted average can lead to an SEY overestimation by about a factor of 2x. Two possibilities could explain this nonlinearity and in particular the fast SEY decrease when introducing impurities into a high-SEY compound. Either the impurities (of low-SEY components) act as exciton sinks that trap hot electrons, preventing them from being emitted. It is also possible that low electrons simply scatter more effectively in low-SEY components, bringing the SEY gradually down as the composition changes in favour of the low-SEY component.

Regarding the ESD yield, the nonlinearity is not so profound and a weighted average represents a decent estimate. Yet, accounting for nonlinear mixing effects can improve the estimate, as discussed in detail in Section 6.1. The data in Figures 5.63 and 5.66 shows that component A tends to either enhance or quench the electrodesorption of component B, depending on their relative yields. This leads to a nonlinear trend, which increases the ESD yield of the less desorbable species at the expense of the ESD yield of the more desorbable one. The yield does not even have to be the largest for a pure compound in an extreme case, visible in the 40 %CH_4 mixture (left) or for the 80 % Argon mixture (right).

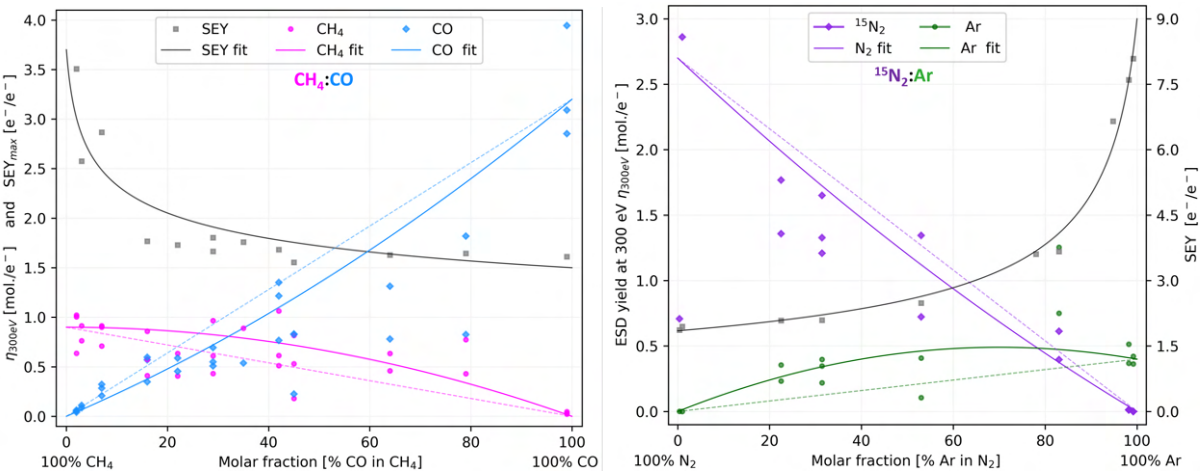

Figure 5.66: ESD and SEY measured for different compositions of binary ice systems: CH_4:CO and N_2:Ar. The SEY was taken at its maximum, whilst the ESD yield was measured at 300 eV. Precoverage of ∼10 ML of mixed ice was always pristine and cleaning TPD to a sufficiently high temperature was always performed in between measurements of different compositions. The fitted curves are discussed in the paragraphs below. The interaction coefficient is k=0.5.

It has been long observed that even trace amounts decrease the yields by effectively quenching the particle emission, be it SEY, ESD [A4] or a fluorescence yield. Brown et al. studied [309] an Ar:O_2 system and observed that a 0.1% contamination results into a 50% decrease of luminescence yield. and ∼7% decrease in ESD yield. This suppression of Argon desorption by O_2 impurities challenges the theory because O_2 reportedly, Ellegard et al. [307], has an even higher yield than N_2 and should therefore enhance the Argon ESD yield as opposed to decreasing it. A possible explanation is that Ellegard et al. measure their yield in the bulk-penetrating region as compared to the measurements done in the surface-sensitive energy region. At high energy, the bulk-deposited electronic excitations need to diffuse toward the surface before causing desorption, and if Oxygen adatoms quench this diffusion length, the ESD yield can be suppressed due to fewer excitations reaching the surface. The data previously taken on this experimental setup on around 500 ML-thick ices by Dupuy et al. [A4] also do not show such a considerable suppression of Argon ESD yield in the presence of N_2, unlike for CO, which does quench the Ar desorption. When the transition is made from contaminated ices to mixtures with equally represented constituents, the literature is even scarcer. However, a similar highly non-linear and non-monotonic behaviour of ESD yields from mixed ices was observed by Mirsaleh-Kohan et al. [310] who studied LE-

ESD of ions released from N_2O:C_2D_2 mixtures. Although other energy transfer mechanisms are discussed as responsible for the observed non-linear yields in desorbing ions, the link to our composition-dependent ESD data is undeniable. In any case, a more focused research effort is needed to sort out the discrepancies. The benefit here is that both the accelerator physics and astrophysics communities can make use of such results, as discussed in [A4, A5].

The acquired data enabled the formulation of simple parametric fit discussed in Section 6.1 that predicts SEY and ESD yields from known pure thick ice values, derived from data acquired at 10 ML coverage. The substrate properties are mostly rendered irrelevant at this coverage in the first approach and the ice almost behaves as semi-infinite with both yields defined solely by the ice properties. This reasoning can presumably be extrapolated towards thicker multilayer coverages. However, for coverages around 1 ML and below, a more linear behaviour can in theory be expected. The reasoning is that the mixed ice no longer interacts with other cryosorbed gas molecules and is instead bound directly to the metal substrate, leaving little space for a mutual interplay of the coadsorbed gas species.

5.6.6 Thermally-enhanced ESD yields

Small but measurable ESD yields temperature-dependence was observed in $^{15}N_2$ and $^{13}CO_2$ gases cryosorbed in multilayer coverages, see Fig. 5.67. The quench-condensed gases were irradiated with 100 eV and 300 eV electrons while increasing the substrate temperature. A special care was taken in these measurements to remove all types of background, which was done separately for each measured datapoint.

The ESD yield of $^{15}N_2$ and $^{13}CO_2$ is thermally enhanced just before the desorption temperature of both studied parent molecules. Contrary to that, the ESD yield of ^{13}CO fragment is suppressed past the $^{13}CO_2$ recrystallization temperature at 50 K and does not increase just under the $^{13}CO_2$ desorption temperature. The following reasoning is proposed.

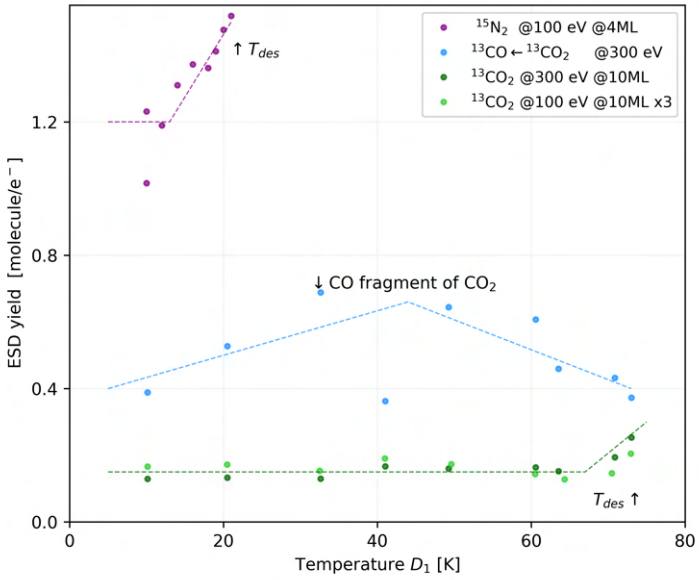

Figure 5.67: ESD yield of $^{15}N_2$ (4 ML) and $^{13}CO_2$ (10 ML) and its fragment ^{13}CO is measured at 100 eV and 300 eV. The desorption signal of each datapoint was carefully corrected for the changing background level. The yields are plotted against substrate temperature T_{D1} as measured on the sample-holder assembly, hence resulting in a 5-10 K offset from the sample surface temperature.

In contrast to $^{13}CO_2$, its ^{13}CO fragment exhibits an inverse behaviour, as its ESD yield tends to decrease before the desorption temperature. This is likely linked to the recrystallization transition and compactification of the solid $^{13}CO_2$ around 50 K, as measured by a change in optical index [311]. A more compact and crystalline structure obtained at temperatures above 50 K could lead to slower ^{13}CO diffusion towards the surface and lower ESD yields. It is arguable whether the fragmentation ratio changes with temperature at the microscopic scale. In the first approach, the fragmentation ratio is determined by electronic properties and as such should not be temperature dependent. Therefore, the different CO yield has to have a different origin, presumably at a later stage of the desorption sequence. The reason could be slower diffusion of the CO molecule towards the surface or a more effective quenching of the

excited CO species in the warm and recrystallised $^{13}CO_2$ ice.

Contrary to this observation and the reasoning, PSD measurement of H_2O and D_2O ice reported by Fillion et al. [312] also exhibits a thermal boost to the PSD yield just under the desorption temperature. However, unlike here, this also applies to the fragments: O_2 and H_2. The same effect of thermally-enhanced stimulated desorption was previously reported for much thicker cryosorbed gases by Heide [313] for ESD and Schou [127, 314] for ESD and ISD.

To conclude, this effect is only tangible so close to the desorption temperature that the pressure increase due to ESD is on par with the pressure increase due to approaching saturated vapour pressure. Moreover, a boost of a few tens of % does not present a dramatic increase compared to the normal range of ESD yields spanning across many magnitudes.

5.6.7 Exploratory data analysis

With the experimental data presented, one can explore possible correlations between parameters. Although no clear, highly correlated trends emerge from the scattered values that would unambiguously link various measured parameters, some general trends are visible, Fig. 5.68.

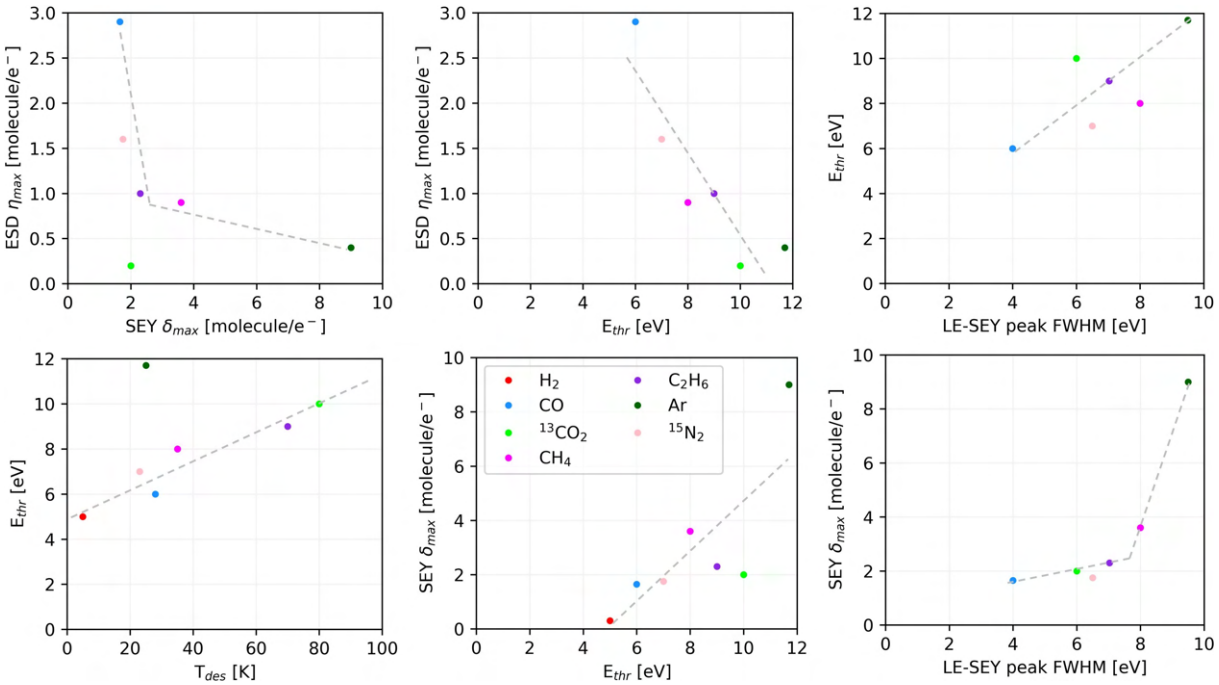

Figure 5.68: Exploratory analysis of various characteristics measured on pure (99+ %) gases quench-condensed at ∼10 ML coverages atop a technical-grade copper held at 15 K. Values for H_2 were acquired from literature, as measured by Sorensen [72] at 500 eV on condensed orto- and para-hydrogen mixtures (measurable but insignificant difference).

There is some anticorrelation of δ_{max} with η_{max} in the top-left plot. This behaviour is also observed in the binary mixtures studied below in Section 5.6.5, where it is leveraged to measure and derive combination rules for SEY and ESD of thick gas mixtures.

An anticorrelation is also found in the top-centre plot between E_{max} and E_{thr}, pointing to weakly bound (=more desorbable) gases having lower desorption thresholds and higher yields. This supports the theoretical explanation given in 2, arguing that the number of electronic excitations with energy higher than the desorption threshold is available for electrodesorption.

The top-right plot shows a correlation between δ_{max} and the LE-SEY peak FWHM width that is discussed in 5.56 of section 5.6. It is assigned to an inefficient electron scattering in the band-gap energy range resulting in correspondingly high SEY values. A similar link can be argued for the correlation in the bottom-right plot between E_{thr} and the LE-SEY peak FWHM width. The desorption threshold can only emerge once the incoming electrons have sufficient energy to pass the band gap and deposit electronic excitations into the substrate.

In the bottom-left plot, a scattered linear increase of E_{thr} with T_{des} can be observed if Argon is excluded from the datapoints. The T_{des} is measured in situ using a TPD and presented in Section 4.7. This trend points towards the weak inter-molecular forces governing the molecular interaction and

determining the energy necessary for desorption, whether delivered thermally or non-thermally. However, the dataset is scarce and noisy for a more detailed analysis, and the physical reasoning behind these trends, if any, is unclear and requires further investigation.

5.7 Chapter summary

This chapter summarises the main research results acquired from different systems of metals, non-metals and treatments with and without cryosorbed gases. Particular accent was placed on technical-grade construction materials employed in the construction of accelerator beam-vacuum systems, such as the OFE copper in bulk and colaminated form, as used in the LHC beam-screen.

First, the SEY and then the ESD were studied in various experimental settings and under various irradiation parameters like energy, dose and angle. Each influencing parameter was studied separately to decouple it from others clearly. The SEY and ESD of surfaces with cryosorbed gases, and their binary mixtures, were studied as a function of energy, temperature, composition and coverage from submonolayer to multilayer regime.

Then, using cryosorbed gases such as isotopically labelled $^{15}N_2$, the TPD method helped to characterise the studied microporous surfaces. The binding energies and specific surfaces could be measured for various gases on coatings and treatments. This includes the amorphous carbon coating frequently applied to beam tubes at CERN, laser treatments considered for the same purpose, Ti-Zr-V NEG coatings and REBCO-coated conductor tapes.

The presented results ultimately allow one to form an educated estimate in a more generic situation. Moreover, the current theoretical description, datasets and general understanding are expanded towards the cryogenic temperatures, low-energy electrons and high irradiation doses. This renders the work relevant for researchers and engineers to come, most notably in the aspects discussed in the following Application-oriented section 6.

Finally, the developed methodology and acquired data gave rise to a number of publications and conference contributions, ranging from technically-oriented [A3, A8], past data-oriented [A2, A5-A7], to future-oriented [A1].

Chapter 6
Applications of research findings

Contents

This chapter aims to demonstrate the applicability of the experimental findings and conclusions presented and discussed in the previous chapter. Firstly, the acquired experimental data is combined with the theoretical understanding, resulting in a number of semi-empirical parameterizations for SEY and ESD as a function of energy, dose, angle, composition and a combination of these. Second, the acquired data on SEY, ESD and TPD are inspected from the real-life application point of view. An emphasis is placed on the operational aspect of CERN's High-Luminosity LHC, but a significant overlap exists with other storage rings, both warm and cryogenic, and possibly other technical applications. Indeed, operation-related issues like the electron cloud and dynamic vacuum effect are strongly linked to the nature of a given beam-screen surface, which determines not only the electron cloud activity but also the dynamic vacuum effect and the scrubbing rate observed during an operation. Third, suitable temperature windows for the accelerator operation are discussed in light of TPD results acquired with gases cryosorbed on the beam-screen copper and the novel carbon coating.

6.1 SEY parametrizations

6.1.1 Energy dependence

The SEY energy dependence was discussed in detail in the theoretical Section 2.2 and is well-established, with the general tendency being modelling the SEY curve by parts. The existing description will be built upon to capture two other crucial effects. First is the parametric representation of the low-energy SEY region. Second is the evolution of the SEY curve with an electron dose, including the low-energy region. While the SEY curve is well captured by the F-P fit at higher energies, modelling the low-energy SEY below ∼50 eV, and its evolution with electron dose is seldom discussed. This is despite the fact that it has a crucial impact on the electron cloud threshold and build-up process, as discussed below in Section 6.5. Hence, it will be discussed and modelled here, at least qualitatively.

As per usual, the total SEY δ_{Total} is approximated by a composite function, eq. 6.1.

$$\delta_{Total} = \delta_{TSE} + \delta_{Inel.BSE} + \delta_{El.BSE} + \delta_{Refl.} \tag{6.1}$$

Here, the inelastically backscattered contribution $\delta_{Inel.BSE}$ is not modelled separately, hence set to zero, as it is not needed here to represent the experimental data accurately.

The Furman-Pivi [58] approximation to true secondary electrons is only briefly reminded here, as it forms the core of a SEY curve at energies above ∼50 eV. Aside from the experimentally accessible parameters δ_{max} and δ_{max}, the sole fitting parameter s was optimised to best-fit the experimental data, s =1.45.

$$\delta_{TSE,F-P} = \delta_{max} \frac{s(E/E_{max})}{s - 1 + (E/E_{max})^s} \tag{6.2}$$

The left side of Figure 6.1 plots the main constituents of a SEY curve as discussed here. True secondary electrons are modelled by the Furman-Pivi fit and are dominant at energies above 20 eV. The reflected and backscattered electrons dominate the SEY curve below ∼20 eV. The classical fit captures the backscattered part (red), attributed to Blaskiewicz [57], as follows. The value R_0=0.75 presents the SEY value at the 0 eV cross-over, i.e. the inflection point of the work-function edge. Meanwhile, the E_0=100 eV was chosen to best-fit the experimental data.

$$\delta_{El.BSE} = R_0 \left(\frac{\sqrt{E_0} - \sqrt{E_0 + E}}{\sqrt{E_0} + \sqrt{E_0 + E}} \right)^2 \tag{6.3}$$

The small low-energy peak around 5 eV and other spurious peaks in this region are characteristic of contaminated surfaces and likely originate in electrons reflected off the surface, i.e. specular elastic backscatter. These LE-SEY peaks vary from one system to another and can even exhibit a finer structure, as visible in the thin ices in Section 5.6. Hence, this region can be captured by an envelope formed by a log-normal distribution (purple curve) enclosing the fine structures in the low-energy region, forming a conservative, upper-bound estimate. The fitting parameters are the peak position E_{LE}=12 eV, the width of the σ=1 log-normal curve and its amplitude r_{LE}=0.35. This approach also seems applicable to fit the LE-SEY region of cryosorbed gases. An envelope can be fitted around the fine structure present in the LE-SEY region to approximate the behaviour.

$$\delta_{Refl.,L-N} = r_{LE} \cdot \exp(\frac{-\ln^2(E/E_{LE})}{2\sigma^2}) \tag{6.4}$$

Figure 6.1 shows an SEY curve measured on a bulk Cu sample in the initial as-received state held at 15 K. The experimental data are approximated by parametric model consisting of the above-listed components. Note that the SEY is dominated by true secondary electrons at energies above 20 eV, as modelled by the Furman-Pivi approximation. Meanwhile, the reflected and backscattered electrons prevail in the 0∼20 eV region.

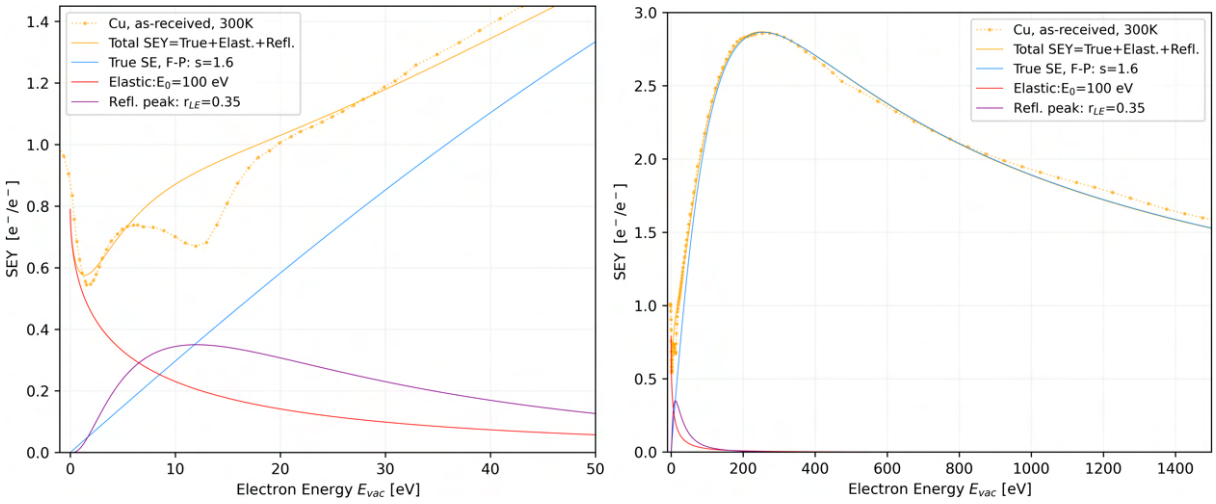

Figure 6.1: SEY curve decomposed in its main constituents and a zoom-in onto the low-energy region. Measurement done on an as-received bulk Cu sample held at 15 K serves as a baseline. A supplier cleaned the sample in an ultrasonic isopropanol bath and stored in a plastic bag. The energy is referenced to the sample vacuum level.

Figure 6.2 shows the initial, final and intermediate surface states during a 300 eV conditioning are interpolated from the known initial and final states by decreasing the δ_{max} and δ_{max} and the r_{LE} to capture the decreasing trends. The values δ_{max}, E_{max}, and the r_{LE} can be calculated, for instance, using the S-curve behaviour outlined in the paragraph below. Meanwhile, the values s, σ, R_0, E_0 can be considered dose-invariant for simplicity. The LE-SEY region is enlarged on the left. The envelope formed by the log-normal function gradually decreases and approaches that of a conditioned copper around 2 mC.mm^{-2}. Whilst this is a coarse approximation, it is a step towards a more realistic representation of the high reflectivity of low-energy electrons impinging on contaminated surfaces. Also, note the similitude to Figure 5.4, showing a series of SEY curves measured during intermittent conditioning.

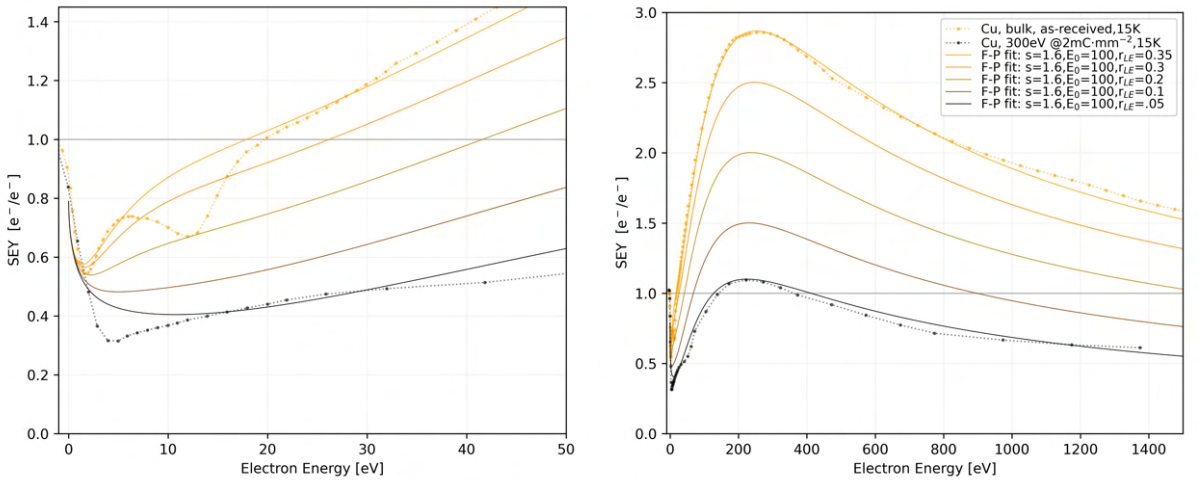

Figure 6.2: SEY curves parameterised for different stages of electron conditioning. Measurement done on an as-received bulk Cu sample held at 15 K serves as a baseline; before and after 300 eV irradiation. The supplier cleaned the sample in an ultrasonic isopropanol bath and stored it in a plastic bag. The energy is referenced to the sample vacuum level.

6.1.2 Dose dependence

Unlike the SEY energy dependence, the SEY evolution during electron conditioning is seldom modelled. Fortunately, it can be readily approximated by an equation 6.5. The SEY conditioning curves typically have a logistic S-curve profile when plotted against electron dose on a logarithmic scale, as plotted in left side of Figure 6.3. Such evolution of δ_{max} can be fairly accurately mapped between δ_{D_0} and $\delta_{D\to\infty}$ using a sigmoid function, for example. Normalising by the dose D_0, marking the inflection point, a logarithmic dose $\log D/D_0$ can be plugged as an argument into the S-curve formula. The p remains but a fitting parameter for the S-curve steepness. This equation then further simplifies as follows:

$$\delta(D) = \delta_{D_0} - (\delta_{D_0} - \delta_{D\infty}) \cdot \frac{1}{1 + exp(-p \log(\frac{D}{D_0})} = \delta_{D_0} - \cdot \frac{(\delta_{D_0} - \delta_{D\infty})}{1 + (\frac{D}{D_0})^{-p}} \tag{6.5}$$

Note the approximative dose dependence of the SEY yield at 300 eV, δ_{300eV}, fitted with 6.5 in Figure 6.3. This demonstrates that bare Cu surface and laser-treated and carbon-coated surface are all well approximated.

This method fairly accurately approximates the maximum SEY δ_{max}, or SEY at another energy close to the maximum $\delta_{E\approx E_{max}}$. Having the fit for the SEY dose-dependence, albeit approximative, adds the advantage of extrapolating from the measured data towards the ultimate SEY value $\delta_{D\infty}$ as the dose approaches ∞. The best-fit parameters converged to the inflection point located around $D_0 = 10^{-5}\sim10^{-4}$ C.mm^{-2} and steepness parameter in the range p =1∼2.

Similarly to the δ_{max}, the LE-SEY peak at 5 eV, denoted δ_{5eV} can also be modelled with the above-discussed approach. As visible in Figure 5.12, the dose-dependence of δ_{5eV} can be fitted by a sigmoid curve between the initial and final values, for example by δ_{5eV,D_0}=0.8 and δ_{5eV,D_∞}=0.3 for as-received and conditioned Cu, respectively. The highest observed was δ_{5eV,D_0}=0.9 and values above 1 are unlikely because the reflectivity can not exceed unity, because the SE generation is still inefficient below 10 eV and so the LE-SEY region is reflectivity-dominated.

Meanwhile, the LE-SEY peak shape can be conveniently approximated by a log-normal peak centred around 5∼10 eV. The inflection point p and steepness are again to be taken from the dose-dependent δ_{max} curve. The best-fit parameters for δ_{max} or δ_{300eV} dose-dependence also seem to fit the δ_{5eV} dependence, having an inflection point and steepness parameter around similar values.

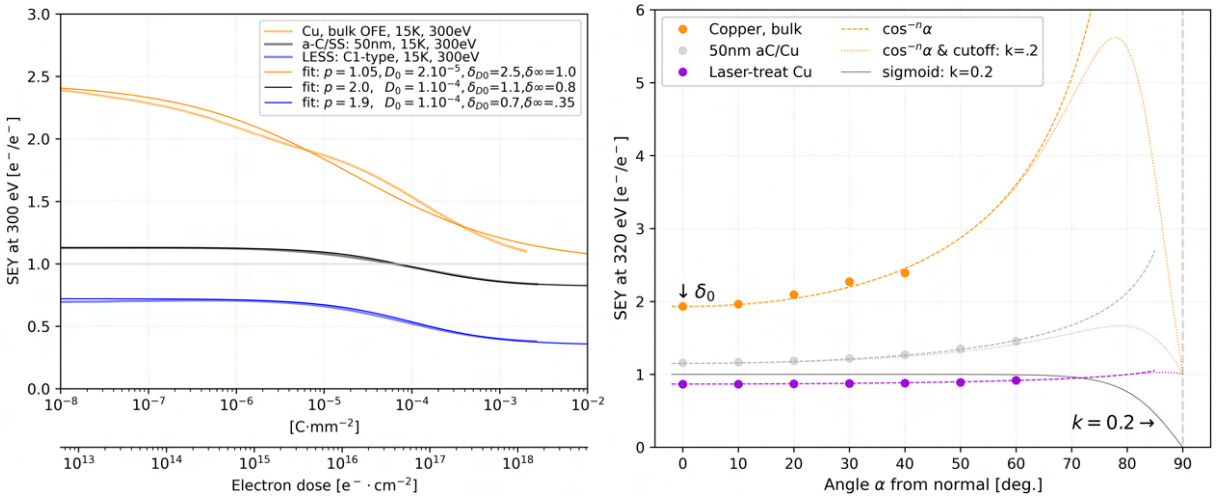

Figure 6.3: Left: SEY electron conditioning curves measured at 300 eV on varius surfaces held at 15 K. Note the approximative electron dose dependence of the SEY yield fitted with 6.5.
Right: Estimated angular dependence of a SEY yield at 320 eV plotted for different surfaces: flat copper surface, 50 nm thin carbon-coated Cu and a rough, laser-treated Cu surface.

6.1.3 Angular dependence

The SEY angular dependence was measured at the edge of experimental capabilities, which results in high uncertainties. This makes it challenging to determine which angular dependence formula best fits the acquired data. Both approximations, eqs. 6.6 and 6.7 discussed in Section 2.2.3 and 2.6.6, seem to be applicable in the 0-60° range for angle α, as measured from normal. Given the shallow energy deposition

depth at energies below ∼100 eV and the resulting angle-agnostic yields, applying these approximative formulas for energies around the peak energy and higher makes sense.

$$\delta(\alpha) = \delta_0 \cdot cos^{-n}\alpha \tag{6.6}$$

$$\delta(\alpha) = \delta_0 \cdot \exp(n.(1 - cos\alpha)) \tag{6.7}$$

Flat technical-grade metal surfaces (bulk Cu and SS) are best fitted with n =0.7-1. The rougher the surface, the less steep this dependence is and the lower exponent is appropriate. Carbon coatings is best-fitted with n =0.4 and laser treatment is approximated with n =0.1. In other words, the higher the roughness, the less sensitive the SEY is to the incidence angle and the lower the exponent n.

To extend the applicability towards higher incidence angles and all the way towards grazing incidence, one can envision adding a term to the existing relation 6.6 to bring the value back to δ =1, as $\alpha \to 90°$. In theory, many functions can serve this purpose, but a sigmoid function is used once again. Exponentiating the original relation by a sigmoid that is point-symmetric around [α =90°, 0] point and starts constant at [α =0°,1] delivers the desired behaviour, at least qualitatively. The following equation 6.8 combines the equation 6.6 and adds the half-sigmoid to the exponent. See the different fits and the sigmoid plotted in the adjacent Figure 6.3. The resulting semi-empirical formula takes into account the fact that electrons tend to reflect as the incidence angle approaches an angle parallel to the geometrical surface: $\alpha \to 90°$. The parameter k is set to k =0.2 in equation 6.8.

$$\delta(\delta_0, \alpha, n, k) = (\delta_0 \cdot cos^{-n}\alpha)^{1-2/(1+exp(k.(90-\alpha))} \tag{6.8}$$

The crucial takeaway of this exercise is that the SEY considerably increases with the incidence angle, possibly even above an application-specific threshold for electron multipacting. Regarding the energy spectrum; given the increasingly large fraction of reflected electrons, the spectrum shifts in their favour at the expense of true SE.

Quantity	**Symbol**	**Typical range**	**Unit**
maximum SEY	δ_{max}	1-3	e^-/e^-
energy at max. SEY	E_{max}	200-400	eV
skewness of SEY curve	s	1-2	1
reflectivity at 0 eV	R_0	0.5-0.8	1
reflected e^- cutoff energy	E_0	50-200	eV
low-energy reflectivity	r_{LE}	0.1-0.5	1
low-energy peak position	E_{LE}	5-15	eV
low-energy peak width	σ	1	1
as-received SEY	δ_{D0}	-	e^-/e^-
fully conditioned SEY	$\delta_{D\infty}$	-	e^-/e^-
inflection point	D_0	10^{-5}-10^{-4}	$C.mm^{-2}$
S-curve steepness	p	1-2	1
cosine exponent	n	1-2	1
high-angle cut-off parameter	k	0.1-0.3	°

Table 6.1: Parameters used as a representative estimate to model SEY energy and dose dependence in Figures 6.1 and 6.2. This table lists the typical range, while plots' legends and text show the values actually used to best represent the experimental data.

6.2 ESD parametrizations

The acquired ESD data are best fitted in this section by semi-empirical fits to approximate the underlying trends and variations with energy, dose, angle and temperature.

6.2.1 Energy dependence

The ESD energy-dependence curve can be conveniently characterised by its threshold and peak values E_{thr}, E_{max} and η_{max}. A suitable function that connects these landmark points can be either a log-normal distribution or a modified Furman&Pivi approximation, both in Sections 5.3 and 5.6 to fit the experimental data. Both the modified Furman-Pivi fit and log-normal fit have only one fitting parameter, with the rest of the variables being directly experimentally accessible. This description applies to each desorbing gas species j, but the j-index is omitted for clarity and to bring focus to the underlying equations in the following paragraphs.

As discussed in the theoretical Section 2.2, the log-normal distribution that models the true secondary electrons' energy dependence can also be used to model the ESD yield energy dependence. The sole difference is essentially the introduction of an energy offset defined by the E_{thr} to create the desired threshold behaviour, see eq. 6.9. The introduction of the dynamic background term $\eta_{dyn.BG}$ in the sub-threshold region only fits the experimental data along with these sensitivity-limiting artefacts. This term is nil for the underlying physical phenomena and should be avoided.

$$\begin{aligned} \eta(E) &= \eta_{max} \cdot \exp\left(\frac{-\ln^2((E-E_{thr})/E_{max})}{2.s^2}\right) + \eta_{BG}, \text{ for: } E \geq E_{thr} \\ \eta(E) &= 0 \qquad\qquad \text{in theory, for: } E \leq E_{thr} \\ \eta(E) &= \eta_{dyn.BG} \qquad\qquad \text{in experiment, for: } E \leq E_{thr} \end{aligned} \tag{6.9}$$

Figure 6.4 shows the log-normal model, eq. 6.9, fitted to the experimental data acquired on a bulk Cu sample. As opposed to the linear-linear projection (left), the log-log projection (right) captures interesting features on different scales, hence its systematic use. Following the equations 6.9, the η=$\eta_{dyn.BG}$ under the desorption threshold E_{thr}, as visible in the 0-10 eV region of the right plot. Above this threshold, the dependence is modelled using a log-normal distribution with only one free parameter s. The other three parameters E_{thr}, E_{max} and η_{max} are fixed by the experimental data. The square of the argument in the log-normal distribution was left to keep the E^{-2} asymptotic behaviour (characteristic to electronic stopping) at high energies, say above 1 keV. In theory, another exponent could be used as well, to model a more generic power-law decay in some special cases. This log-normal parametrization was already used in [A1, A5] to approximate the measured ESD yields' energy-dependence.

Similar reasoning and procedure was applied to the Furman-Pivi fit, originally derived for true secondary electrons, here modified to model ESD yield energy-dependence of cryosorbed gases in Section 5.6.3. The modification follows in eq. 6.10. This fit is used to approximate the ESD yield of cryosorbed gases in Section 5.6, as it better fits the low-energy region.

$$\begin{aligned} \eta(E) &= \eta_{max} \cdot \frac{s(E-E_{thr})/E_{max}}{s-1+((E-E_{thr})/E_{max})^s} + \eta_{BG}, \text{ for: } E \geq E_{thr} \\ \eta(E) &= 0 \qquad\qquad \text{in theory, for: } E \leq E_{thr} \\ \eta(E) &= \eta_{dyn.BG} \qquad\qquad \text{in experiment, for: } E \leq E_{thr} \end{aligned} \tag{6.10}$$

The best-fit to the uncertainty-weighted experimental datapoints is done in Python using a 'curve-fit' function from 'scipy.optimize' package with default parameters. Similarly to the collector conductance estimation in Section 4.14, combining an estimated physical model and a multitude of datapoints (repeated measurement) is leveraged to decrease the uncertainty interval on the combined result. The extracted best-fit parameters have lower uncertainty than a single datapoint because, to a large extent, the acquisition of nearby datapoints represents a repeated measurement. Hence, an ensemble of datapoints linked with the known model has a lower uncertainty than a single datapoint. Shown at the peak value is the combined uncertainty intervals for one datapoint is ∼30 % at 1σ, with the major driver being the systematic uncertainty of ∼28 % (a measure of absolute accuracy). Stochastic uncertainties (a measure

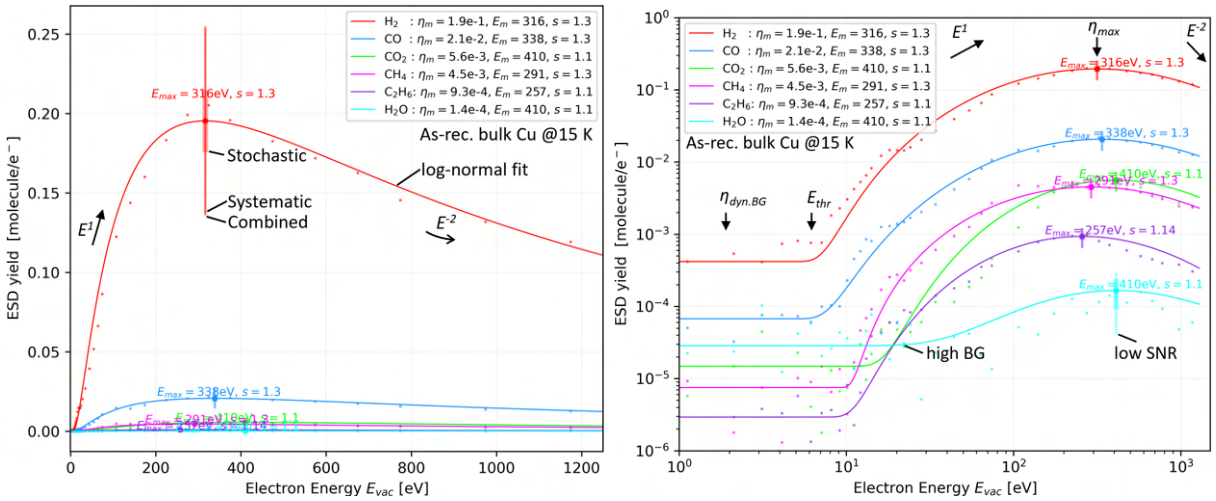

Figure 6.4: ESD energy dependence curves measured on as-received bulk Cu sample held at 15 K. The sample was UHV-cleaned at the supplier and stored in a plastic bag before analysis. The displayed uncertainty intervals are calculated at 1σ for a single datapoint at its maximum value, hence its position at E_{max}. Note the systematic and stochastic components of the combined uncertainty. The high uncertainty on water is due to a high BG and low SNR. The electron energy is referenced to the sample vacuum level. See text for more details.

of precision) on best-fit parameters are around ∼5 %, at 1σ confidence level, while isolated datapoints have a stochastic uncertainty ∼10 %. The uncertainties are derived, evaluated and further discussed in Appendix 6.8.

6.2.2 Dose dependence

The power fit introduced in the theoretical Section 2.2 well approximates at high electron doses, but fails to level off as the dose D approaches zero. This approximation presumes a high electron dose has already been achieved, such that the D_0 is above the inflection point, and the measured datapoint η_0 at dose D_0 is simply scaled according to a power law. This asymptotic behaviour is plotted as dashed line on the left side of Fig. 6.5. The exponent α determines the steepness, here referred to as the conditioning rate. The notion used here intentionally puts the variable D into the numerator, the normalising value D_0 into the denominator, and keeps the exponent negative to signify a decreasing power-law type of decay.

$$\eta(D) = \eta_{D_0} \cdot \left(\frac{D}{D_0}\right)^{-\alpha} \tag{6.11}$$

An empirical fit, originally proposed by Malyshev [161] for PSD conditioning, is used here to approximate the ESD yield dose dependence and possibly extrapolate to higher electron doses. The fit builds on a classical power law whose exponent α controls the slope in the log-log plot at high doses $D \geq 0.1\,\mathrm{mC.mm^{-2}}$. Parameters D_0 and D_1 are added to the fraction to extend the applicability towards low doses in a way that the curve asymptotically approaches the constant initial ESD yield η_0 as $D \to 0$. The parameter D_0 represents the dose imparted at the lowest measurable data point (here the first displayed data point) and can be set to 0 for simulation purposes. Parameter D_1 is solely used to position the end of the initial plateau.

$$\eta(D) = \eta_0 \cdot \left(\frac{D + D_1}{D_0 + D_1}\right)^{-\alpha} \tag{6.12}$$

This modification of the classical fit well approximates the acquired experimental data. Moreover, it is not strictly necessary to reach very high electron doses where the decay is linear (in log-log scale) to get the value for α. Instead, experimental data at electron doses at few $10^{-4}\,\mathrm{mC.mm^{-2}}$ are sufficient to best fit the formula into and extract the α without reaching fully linear decay. Similarly, it is possible to extrapolate towards D=0 $\mathrm{mC.mm^{-2}}$ to obtain the as-received yield η_0.

The utility of this fit was shown and discussed plenty throughout this manuscript, so it will not be elaborated upon here. However, the uncertainties on best-fit parameters extracted from the measurements have to be addressed. Similarly to the energy-dependence fits, the absolute uncertainty still lies in the

~30% range. Conversely, the stochastic uncertainty is in the ~10% range. When combined with the semi-empirical fit, the resulting stochastic uncertainty on the best-fit parameters is estimated to be in the sub-5% range. In other words, the shape of the conditioning curve is fairly precise (precision-limited), but the absolute accuracy (trueness; vertical offset of the conditioning curve) is the main contributor to the combined uncertainty once again. The uncertainties are derived and evaluated in Appendix 6.8.

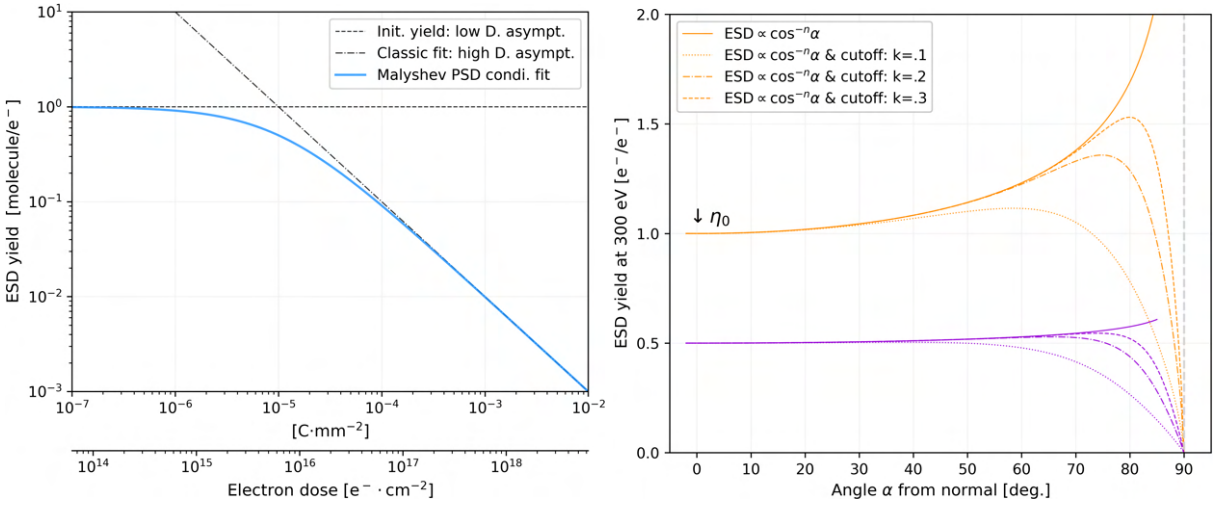

Figure 6.5: Left: Parametric fit for ESD dose dependence according to Eq. 6.12 originally proposed by Malyshev for PSD. [161]. Note the constant asymptotic behaviour at the zero dose limit and asymptotic approach to the classical power-law in the infinite dose limit, respectively.
Right: Estimated angular dependence of an ESD yield at 300 eV plotted for different surfaces: flat copper surface and rough laser-treated Cu surface. A range of cuf-off coefficients k is used to illustrate the behaviour, but the k is to be determined experimentally for each given surface.

6.2.3 Angular dependence

Considering the theoretical understanding and experimental results discussed in Section 2, and in the absence of experimental data, one can still qualitatively estimate the angular dependence of an ESD yield. It is reasonable to expect the ESD yield to abide by the same rules as the SEY angular dependence. The sole difference being that the EDS yield approaches $\eta \to 0$ as angle $\alpha \to 0$, unlike for the SEY that approaches $\delta \to 0$. Many parametrizations were proposed to capture the ESD angle-dependence, as discussed in Section 2.6.6. The simplest dependence is $\eta(\alpha) \propto cos^{-n}\alpha$, which successfully fitted the SEY data, Fig. 5.2.5. It is only reasonable to adapt this semi-empirical dependence for the ESD yield, including its n-parameter.

$$\eta(\eta_0, \alpha) = \eta_0 \cdot cos^{-n}\alpha \tag{6.13}$$

Utilising the same approach with a sigmoid function as described in 6.8, the parameter k from eq. 6.5 is varied from 0.1-0.3 to modify the cut-off energy and visualise how different electron reflectivities influence the ESD yield. Similarly to the SEY angle-dependence, identical values for n are used: n =0.3 for copper and n =0.08 for laser-treated Cu, as they best fit the experimental data taken in the α =0~60° range. The same sigmoid with k =0.2 is used as for SEY angle-dependence 6.8, except here it multiplies the ESD yield to push its value to zero. The reasoning behind is the same; reflected electrons can not excite secondary electrons and cause gas desorption via DIET. The resulting behaviour is qualitatively identical to that observed in ion stimulated desorption, Figure 2.20. The angular dependence of a plasma-etching rate [183] (also an ion-induced process) follows an equivalent trend as shown in Figure 6.5. This effect of angle-enhanced sputtering yield is well-known and often leveraged in the ion sputtering field.

$$\eta(\eta_0, \alpha, n, k) = (\eta_0 \cdot cos^{-n}\alpha) \cdot (1 - 2/(1 + exp(k.(90 - \alpha)))) \tag{6.14}$$

6.2.4 Temperature dependence

The temperature dependence of the ESD yield, measured at 300 eV, was studied in the 10–300 K region. This dependence essentially consists of a flat plateau at cryogenic 0 K limit and at ambient tempera-

ture limit. A step change occurs in between, typically around 100 K. The ESD yield reduction factor η_{300K}/η_{15K} varies between surface states and ranges from 2x to 200x, depending on the gas species, from H_2 to CO_2. As such, the ESD yield can be fitted by a modified sigmoid curve using one fitting parameter only.

$$\eta(T) = \eta_{15K} + \left(\frac{\eta_{300K} - \eta_{15K}}{1 + exp(-p.(T - T_p))} \right) \tag{6.15}$$

This approach was used in all the temperature-dependent graphs in Chapter 5. Except for p, all other used parameters are experimentally accessible observables: η_{15K} and η_{300K}, as well as the temperature T_p at the inlection point. The p parameter controls the steepness of the step-change between cryogenic regions and is best fitted to the data.

6.2.5 Combined energy and dose dependence

The equations 6.9 and 6.12 parametrizing the ESD yield as a function of energy E and dose D can be combined into a formula approximating the $\eta(E, D)$. The ESD yield energy and dose dependencies consist of an initial value, η_{max} or η_0 and a scaling function $f(E)$ or $f(D)$ that modulates the input value of η with the desired variable, as follows:

$$\begin{aligned} \eta(E) &= \eta_{max} \cdot f(E) = \eta_{max} \cdot \exp\left(\frac{-\ln^2((E - E_{thr})/E_{max})}{2s^2} \right) \\ \eta(D) &= \eta_0 \cdot f(D) \quad = \eta_0 \left(\frac{D + D_1}{D_0 + D_1} \right)^{-\alpha} \end{aligned} \tag{6.16}$$

The following approximation is derived, presuming that the influence of energy and dose are independent, i.e. the E_{thr} and E_{max}, and s do not change. Hence, the functions combine as follows:

$$\begin{aligned} \eta(E, D) &= \eta_{max,0} \cdot f(E).f(D) \\ \eta(E, D) &= \eta_{max,0} \cdot \exp\left(\frac{-\ln^2((E - E_{thr})/E_{max})}{2s^2} \right) \cdot \left(\frac{D + D_1}{D_0 + D_1} \right)^{-\alpha} \end{aligned} \tag{6.17}$$

All the parameters necessary for the fit are experimentally observable and discussed in the above-mentioned paragraphs. The background level at η_{BG} is intentionally plotted to visualise the instrumental detection limit of the used setup. Shall this background be subtracted, the surface $\eta(E, D)$ would indeed follow the power-law decay from eq. 6.12, as plotted in 6.5.

The fitting parameters used to plot the charts in Figure 6.6 are listed in Table 6.2. The parameters were used as a representative estimate to model the energy and dose dependence. Here, only the H_2 and CO ESD yields are displayed to maintain clarity of this illustration, but the general behaviour is common to other gas species. The limitation is that the conditioning energy must be chosen close to the maximum η_{max}. In the opposite case, another relation would be necessary to weight conditioning efficiencies of different primary electron energies or possibly even a continuous spectrum of energies. An equivalent exercise can be done with the modified Furman-Pivi approximation in place of the log-normal function used here to model the ESD yield energy dependence.

The following Table 6.3 lists the typical parameters that reasonably well approximate the ESD energy and dose dependence using the for baseline technical surfaces and treatments held at cryogenic temperatures. The parameters are compatible with equations from Section 6.2. While the are significant uncertainties on these best-fit parameters, the results of the dynamic vacuum effect calculations presented in Fig. 6.6 are rather robust against variation of these parameters.

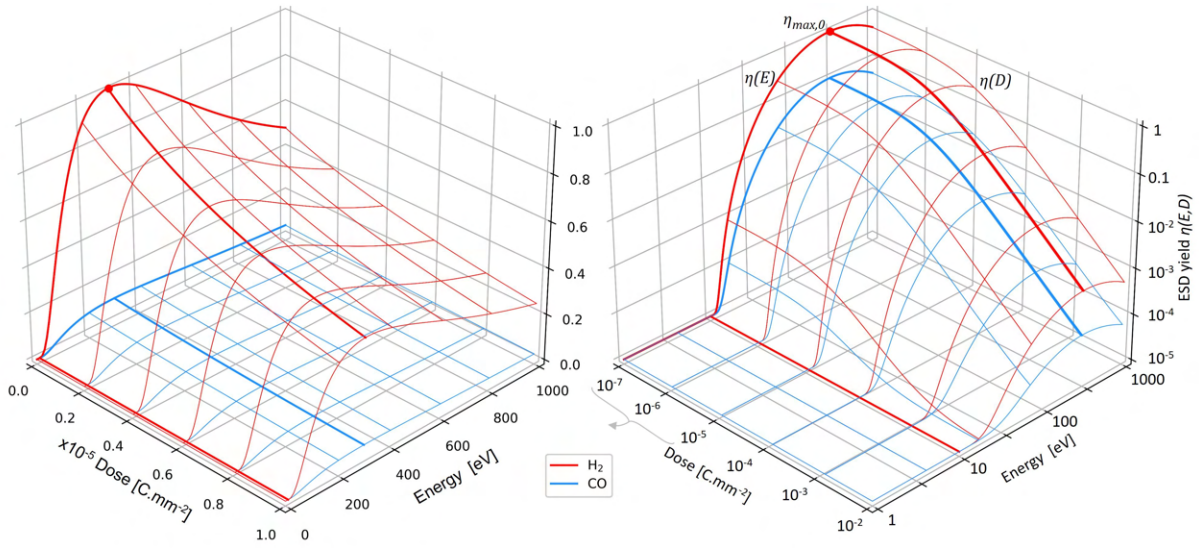

Figure 6.6: ESD yields $\eta(E, D)$ for H_2 and CO calculated as a function of energy and dose using the developed approximative model. Note the linear (left) and logarithmic (right) scales. Corresponding fitting parameters are listed in Table 6.2 and represent a typical behaviour observed in experimental data. Note the background level is intentionally plotted at η_{BG} to visualise the instrumental detection limit of the used setup.

Quantity	Quantity	Value	Unit
ESD yield maximum	$\eta_{max,0,H2}$	1	molec./e$^-$
ESD yield maximum	$\eta_{max,0,CO}$	0.1	molec./e$^-$
energy at max. ESD yield	E_{max}	300	eV
threshold energy for ESD	E_{thr}	10	eV
skewness of ESD yield curve	s	1	1
ESD yield background level	η_{BG}	10^{-5}	molec./e$^-$
dose at first datapoint	D_0	10^{-7}	C.mm^{-2}
dose at α inflection	D_1	10^{-5}	C.mm^{-2}

Table 6.2: Parameters used as a representative estimate to model the energy and dose dependence of H_2 and CO ESD yields in Figure 6.6. Parameters D_0 and η_{BG} are related and unique to the used experimental setup, while the rest has a physical origin.

Surface	E_{thr}	E_{max}	η_{H2}	η_{CO}	η_{CO2}	η_{CH4}	s	D_1	α
Cu/SS	8	320	1.9e-1	2.1e-2	5.6e-3	4.5e-3	1.2	1e-5	1.0
SS	8	280	1.6e-1	2.4e-2	4.3e-3	2.9e-3	1.1	2e-5	1.0
Al	8	320	1.9e-1	5.3e-2	3.8e-3	5.4e-3	1.2	2e-5	1.0
50 nm a-C	7	260	5.0e-2	3.0e-3	2.0e-4	4.0e-4	1.2	3e-5	0.7
450 nm a-C	7	430	5.2e-2	5.1e-3	1.0e-3	1.0e-3	1.2	3e-5	0.7
Lased Cu, COLDEX	7	700	7.0e-2	6.0e-2	1.0e-3	1.0e-3	1.2	6e-5	0.8

Table 6.3: Typical parameters to approximate the ESD energy and dose dependence for baseline surfaces and treatments at cryogenic temperatures below 20 K. Cu, SS and Al were supplier-cleaned, while the carbon-coated and COLDEX-like laser-treated Cu are of CERN origin. Mind the 30% combined uncertainty intervals (consult 6.8). Compatible with equations in Section 6.2.

6.3 SEY and ESD of cryosorbed binary mixtures

6.3.1 Combining rules derivation

A strong departure from a linearly-weighted behaviour is observed for both SEY and ESD yields from a 10 ML cryosorbed binary gas mixture, as presented in Figures 6.7, 6.8 here, and Fig. 5.66 in the previous

Chapter 5.6. In the case of binary mixtures, the molar fraction x marks the % abundance of component B in component A. The maximum SEY of a pure component A is marked as $\delta_{A,max}$, while that of a $A:B$ mixture is denoted as $\delta_{A:B,max}$. While the η_A denotes the ESD yield of a pure cryosorbed species A, the ESD yield of component A desorbing from a mixture $A:B$ is marked as $\eta_{A:B\rightarrow A}$.

SEY composition dependence

The SEY exhibits a sub-linear trend when varying the ice composition x of a binary gas mixture. Previous work on thermodynamic properties of real gas mixtures inspired me to use some existing combining (mixing) rules, possibly with a non-zero interaction coefficient. These classical combining rules, however, did not accurately approximate the high non-linearity of electronic properties of mixtures studied here. Aside of classical combining rules with non-zero interaction coefficients, other types of averages could not properly capture the dynamic evolution of SEY with composition either. Hence, a power mean (a form of a generalised average) with slight customisation had to be used with a large exponent n=-3∼-5 to approximate the dynamic sub-linear trend observed in the experimental data, see eq. 6.18. This generalised average equation reduces to a simple linear average when n =1 is used in the exponent.

$$\delta_{A:B,max}(x) = \sqrt[n]{(x-1).\delta^n_{A,max} + x.\delta^n_{B,max}} \tag{6.18}$$

This parametric fit correctly models the SEY $\delta_{A:B,max}(x)$ insensitivity to composition x when the lower-SEY compound dominates the mixture. Conversely, at the high-SEY end of the mixture composition, the $\delta_{A:B,max}(x)$ is very sensitive to the slightest impurities of the lower-SEY compound.

ESD composition dependence

The ESD yield of a species varies with its surface concentration. Hence, a specie's ESD yield at a given energy η_{300eV}, here 300 eV, could be expected to increase along with its molar fraction x. In a binary mixture described by its composition x, a linear dependence could be presumed if the cryosorbed gases were not interacting, i.e. was not mutually influencing their desorption sequences. Such a linear-weighted scenario is described by eqs. 6.19 and plotted as straight dashed lines in Figs. 5.66, 6.7 and 6.8, and is likely to happen in submonolayer coverages, where the substrate-adsorbate interaction dominates. The presumption behind this linear-weighting approach is that the mixed ice no longer interacts with other cryosorbed gas molecules and is instead bound directly to the metal substrate, leaving little space for a mutual interplay (kick-out or quenching) of the coadsorbed gas species.

$$\begin{aligned} \eta_{A:B\rightarrow A}(x) &= (x-1)\ .\eta_A \\ \eta_{A:B\rightarrow B}(x) &= x\ .\eta_B \end{aligned} \tag{6.19}$$

However, in a more general case, a mixture's ESD yields differ from a simple weighted linear average of pure compounds. This, and the fact that the molecules do interact when coadsorbed in a multilayer coverage, results in a mutually influenced desorption mechanism. The desorption of the higher-yielding component decreases in the presence of the lower-yielding one, as part of desorbing molecules quenches as they lose their kinetic energy to the lower-yielding component. Conversely, the ESD yield of the lower-yielding component is boosted by the higher-yielding component, likely via a kick-out mechanism - a direct momentum transfer from the higher-yielding molecules. Accounting for this cross-interaction translates into an improved estimate of the ESD as a function of composition x, which accounts for this quenching and boost, respectively. This cross-interaction is represented by the quadratic term $x.(x-1)$ that captures the likelihood of two atoms of the two compounds encountering one another in the mixture.

The interaction coefficient has physical meaning for values k >0, where k=0 means zero cross-interaction (no desorption boost by kick-out nor quenching). The term $k^{sign(\eta_B-\eta_A)}$ controls the sign, i.e. whether the mutual cross-interaction increases or decreases the yield by a factor k, based on the value of the other component's yield. Meanwhile, the fraction controls the intensity of this cross-interaction based on the ESD yields dissimilarity $\eta_A - \eta_B$, normalised by their average $\eta_A + \eta_B$.

The ESD yields calculated using the derived mixing rules are displayed in the following Figure 6.7. The composition x varying in the entire range of 0∼1, the interaction term k is set to either 0 or 0.5, and the ESD yields η_A and η_B are set either equal, lesser or greater. The graph in Fig. 6.7 also shows the *correct* behaviour at the boundaries and edge cases. For instance, the second term in eq. 6.20 approaches

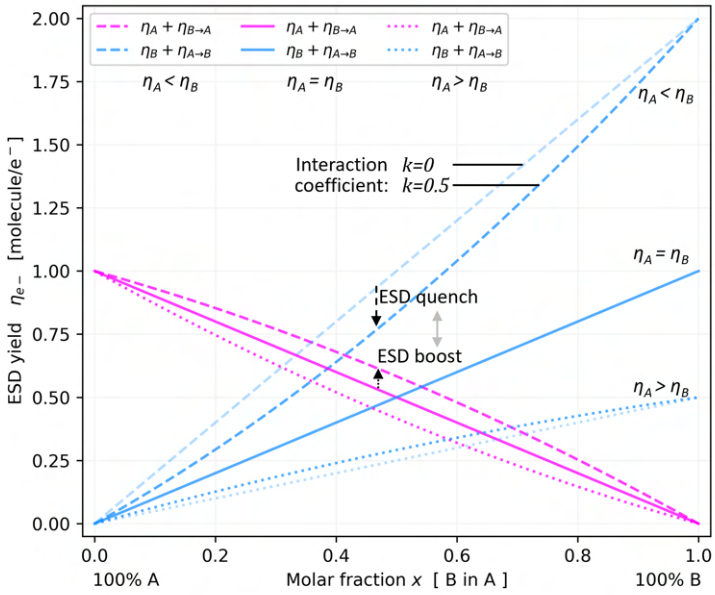

Figure 6.7: ESD yields calculated for a binary mixture with different ESD yields. Note the departure from a linear relation (sub- and super-linear) due to the cross-interaction of the co-adsorbed gas species, which is captured by the interaction coefficient k =0.5.

0 when the ESD yields are equal $\eta_A = \eta_B$, and, in such case, the equation 6.20 simplifies into the previous linear-weighted average in eq. 6.19. Similarly, the eq. 6.20 also simplifies to the previous linear case when the interaction coefficient k is 0. Finally, the yield η_B is enhanced for $\eta_A > \eta_B$, but when $\eta_A < \eta_B$, the yield η_B is diminished. Vice versa for the η_A.

$$\begin{aligned} \eta_{A:B\to A}(x) &= (x-1)\,.\eta_A \quad + \eta_B\,.x(x-1)\,.\frac{\eta_B-\eta_A}{\eta_A+\eta_B}\,.k^{sign(\eta_B-\eta_A)} \\ \eta_{A:B\to B}(x) &= x\,.\eta_B \quad + \eta_A\,.x(x-1)\,.\frac{\eta_A-\eta_B}{\eta_A+\eta_B}\,.k^{sign(\eta_A-\eta_A)} \end{aligned} \tag{6.20}$$

This treatment can presumably be extrapolated towards thicker, multilayer coverages. However, for coverages around 1 ML and below, a more linear behaviour can theoretically be expected. The reasoning is that the mixed ice no longer interacts with other cryosorbed gas molecules and is instead bound directly to the metal substrate, leaving little space for a mutual interplay of the coadsorbed gas species. Further following this reasoning, the interaction term in the equations 6.20 below could be enriched by a coverage-dependent term that would suppress this term by setting the interaction coefficient to zero $k \to 0$ as the coverage approaches zero $\theta \to 0$.

6.3.2 SEY and ESD during differential desorption

Finally, the similarity to ion sputtering of multicomponent materials [315] can be exploited. With the experimental data and newly developed models, one can also estimate the surface composition change due to differential ESD yields of multicomponent ices. This exercise applies to binary mixtures, regardless of the linearity of their SEY and ESD yields. Care was taken during the ESD yield measurement of binary ices not to alter the surface composition by unnecessarily high electron doses.

Different desorption yields will result in preferential desorption and faster depletion of the more desorbable compound off the surface, as marked by ① on the right side of Fig. 6.8. During irradiation, this differential desorption rate evolves the ratio between the constituents in favour of the less desorbable one, altering the surface composition, as marked by ②. Hence, the electron-irradiated surface potentially has a composition that differs from that of bulk by tens of %. As explained by [316], a new steady-state surface composition is gradually established during continuous irradiation, such that the lower desorption yield of one component is balanced by its increased surface concentration. Ultimately, the mass conservation law is satisfied when the surface composition changes in such a way that the desorption yield composition

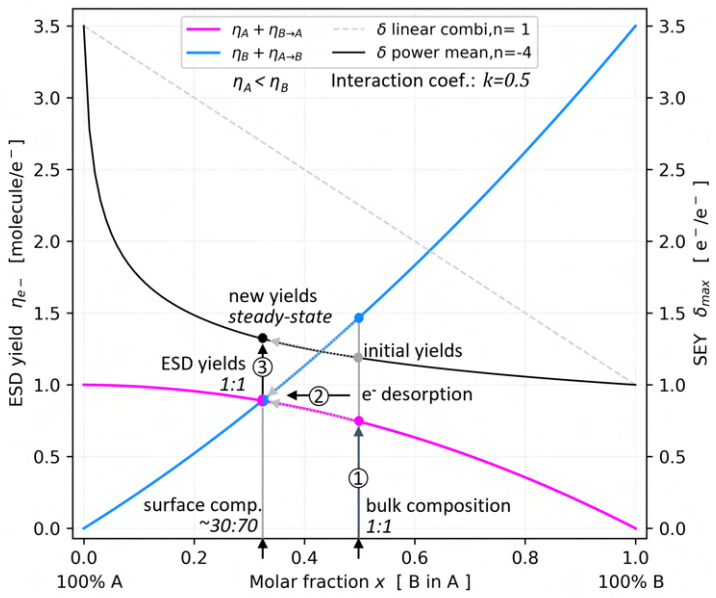

Figure 6.8: ESD and SEY composition dependence in a binary ice mixture calculated by the formulas given in 6.19 and 6.20. The strong sub-linear SEY behaviour is modelled by 6.18 with $n = -4$. Note the steady-state surface composition during irradiation, marked as 3, which is ∼20 % off from the initial, bulk composition, marked as 1.

equals that of bulk, marked as ③. This initial state and the final steady-state composition are marked in Figure 6.8 to illustrate the effect. During irradiation, the steady state yields approach a new equilibrium such that the ESD yield ratio equals the bulk composition. Note that this also means a different SEY resulting from the newly established surface composition, which is, in this case, slightly higher than in the initial state. These findings were partly presented at [A5].

6.4 Beam scrubbing of coated and treated surfaces

Both the SEY and ESD conditioning rate are important for the beam-scrubbing process. The SEY decrease with an e^- dose translates into lesser electron cloud (EC) activity, while ESD decrease diminishes the dynamic pressure rise due to EC activity. Figures 5.5 and 5.32 show that SEY reaches its minimum at few $mC.mm^{-2}$, meaning that bare metals and porous surfaces' SEY conditions similarly. Conversely, as-received initial ESD yields of coatings and treatments typically start lower than for metals, but also conditions noticeably slower, see Table 6.4. Gonzalez et al. [317] reported a qualitatively similar observation, although measured for PSD at high critical energy of few keV, substantiating the linkage between ESD and PSD.

While the conditioning rate α approaches 1 for flat clean surfaces (representative of surface-limited desorption sequence), the α tends towards $1/2$ for porous surfaces (representative of diffusion-limited desorption sequence). Though the distinction is blurry, as 50 nm thin a-C coating lies rather in between those two extremities. It is also worth noting that conditioning rates are systematically faster at cryogenic temperatures by about 0.1-0.2. This is likely due to the diffusion being ineffective at cryogenic temperatures, meaning the surface concentration is not replenished via diffusion as particles are gradually removed.

To conclude from the presented lab-produced experimental data, porous surfaces condition slower under electron irradiation, regardless of temperature. In other words, a porous beam-screen surface (carbon-coated or laser-treated) may condition at a slower rate under electron irradiation under the used laboratory conditions.

300 K / 12 K	**Cu bulk**	**Cu-SS**	**50 nm a-C**	**450 nm a-C**	**Lased Cu**
H_2	0.84/0.96	0.73/0.97	0.68/0.65	0.6/0.65	0.5/0.7
CO	0.82/0.97	0.89/1.08	0.58/0.72	0.6/0.75	0.67/0.93

Table 6.4: Conditioning rates α, as measured at 300 eV at cold and warm, representative of technical-grade OFE Cu in bulk or SS-colaminated form, carbon-coating and a laser-treated Cu. Only values for H_2 and CO are listed for clarity and for the fact they have the highest SNR.

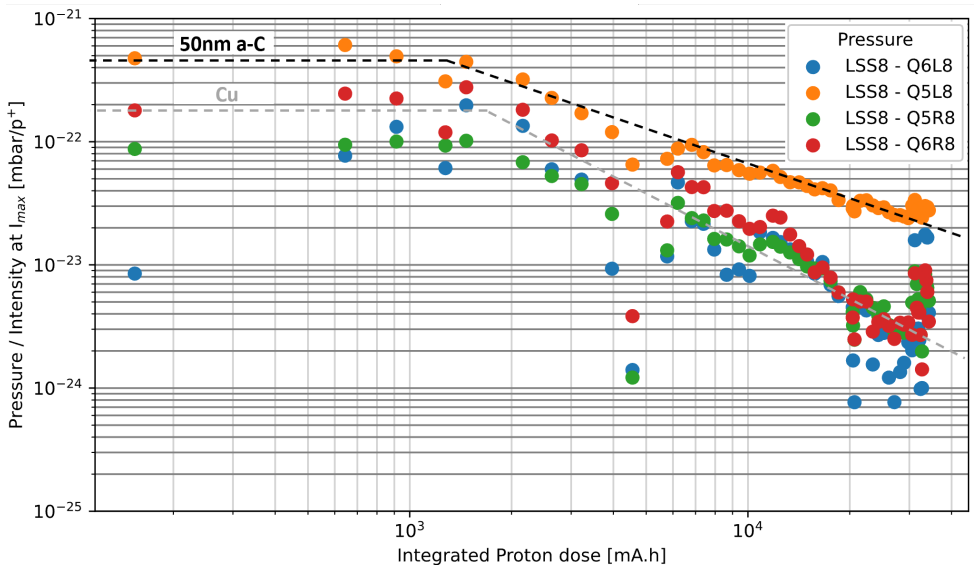

Figure 6.9: Gradual decrease of the dynamic vacuum effect during beam-scrubbing of LHC Run 3, as measured by Penning gauges located around a standalone Q5 and Q6 quadrupole cryomagnets situated at long-straight-section 8, near the LHCb experiment. The dynamic pressure rise is normalised to the proton beam current and plotted against the accumulated beam time, which is an indirect measure of the electron dose imparted onto the beam-screen during the scrubbing run. This plot was kindly provided by CERN's TE-VSC-BVO section.

Identical behaviour is also observed in the LHC during beam-scrubbing in Run 3; see Figure 6.9. Here, the standalone quadrupole Q5 magnets at point 8 serve as an example to compare the conditioning rates of different surfaces. The orange trace follows the beam-induced dynamic pressure rise measured near a magnet with its beam-screen coated with 50 nm thin carbon coating, whereas the remaining datapoints represent magnets with the original copper colaminate beam-screen surface. The orange curve clearly

has a conditioning rate α closer to 0.5, which is in agreement with the data acquired in the lab on a carbon coating held at 12 K, and is representative of a porous surface, as discussed in Section 5.4.1 and summarised in Table 6.4. Meanwhile, the copper surface exhibits a conditioning rate α approaching unity, which is representative of a bare UHV-cleaned non-porous metal surface, both warm and cold. Hence, the experimental observations shown here and presented in [A2, A6-A8] correlate well to the observations from the LHC operation shown in Fig. 6.9.

6.5 Low-energy SEY and electron cloud build-up

Early simulations done for the EC development in the LHC have suggested sensitivity of the EC to the LE-SEY region [318, 319]. It is now very clear that the high reflectivity of low-energy electrons (or the lack of) in the LE-SEY region has an important effect on the electron cloud intensity and build-up mechanism. High electron reflectivity, which is particularly profound in the low-energy range around 0-20 eV, leads to more efficient EC build-up due to the higher survival rate, which leads to more seed electrons propagating from one bunch to another. This was also clearly discussed and illustrated by Cimino et al. [57]. Iadarola has [9] investigated in his dissertation the influence of the LE-SEY parametrization on the EC simulations done in the PyECLOUD code, see Figure 6.10. The simulation results suggest that a small increase in the low-energy electron reflectivity, as modelled here by the *cos* function, leads to a significant decrease of the multipacting threshold to trigger multipacting, represented by δ_{max}, and a large increase in the heat load deposited into the BS.

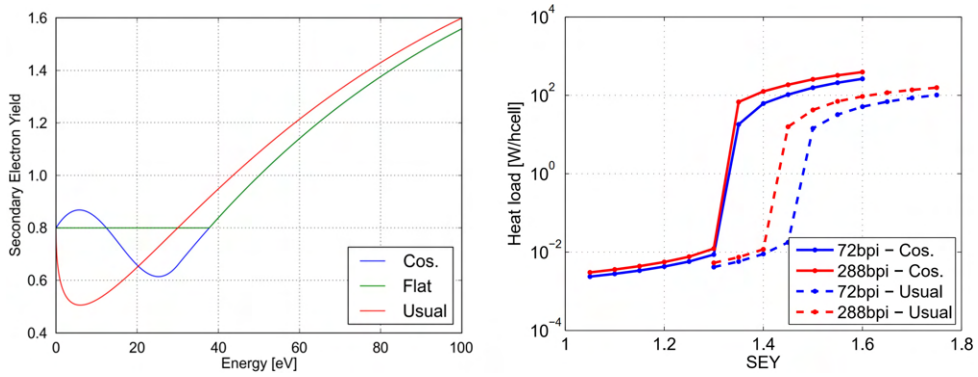

Figure 6.10: Left: Various low-energy SEY parametrizations by Iadarola [9]. Right: Resulting electron cloud-induced heat load onto the LHC beam-screen, as calculated by the PyECLOUD code [62] using the different LE-SEY parametrizations.

This effect is well-illustrated by another simulation study from the same team [320] regarding the photoelectron influence on EC. Albeit not true secondary electrons, their low-energy spectrum is very similar to true secondary electrons and, therefore, the way they contribute to the EC build-up is also similar. The study shows that a higher amount of photoelectrons acting as seeds leads to higher EC intensity and somewhat faster build-up rates. It is also remarkable that the simulation suggests that photoelectron energy distribution does not matter whatsoever.

Take Figure 5.5 to illustrate the link the above-presented experimental findings in the LE-SEY to these simulation results. The LE-SEY curves for all as-received surfaces exhibit a peak around 5 eV that is assigned to a high reflectivity of surface-bound contaminants. This peak diminishes during electron conditioning and finally disappears for a fully conditioned surface. The low-SEY coatings, be it carbon-coating or laser-treatment, exhibit a low δ_{max} but also low SEY in the low-energy region, which, in the light of the presented evidence, strongly contributes to the EC suppression. To extend this exercise closer to a real-application scenario, suppose gases are cryosorbed on the cold BS surface, be it made of copper or some low-SEY treatment. Figures 5.57 and 5.60 plot a gas coverage dependence of δ_{max} as well as that of δ_{5eV} for conditioned bulk Cu, carbon-coated Cu and laser-treated Cu. Note that it takes only 1 ML of any gas cryosorbed on copper to double the 5 eV electron reflectivity without the δ_{max} changing much. The low-SEY coatings benefit from their high porosity which delays the SEY increase with gas coverage. To significantly increase the δ_{max} and δ_{5eV}, it takes roughly 1 ML gas coverage times their roughness factor, i.e. at least 10x the gas than for bare copper.

So-called mixed filling schemes were developed for an efficient HL-LHC operation [321] that combine a standard 25 ns-spaced bunches with empty bunches in a sophisticated way to bring down the EC-induced

heat load to levels acceptable for the LHe cryogenic system, whilst maximising the luminosity. The mixed scheme leverages the relatively slow transient effects during the EC build-up and relies on a relatively fast decay during a passage of empty bunches. Having the LE-SEY region strongly influence the EC build-up and decay rates, the filling scheme is also expected to be influenced.

6.6 Energy-resolved dynamic gas load

Having the analytical expression for the measured ESD energy dependence $\eta_e(E)$, and an analytical fit to the electron cloud energy spectrum dN/dE, Fig. 6.11, the energy-resolved gas load contribution dQ/dE can be calculated for each slice of the energy spectrum dE, Fig. 6.12.

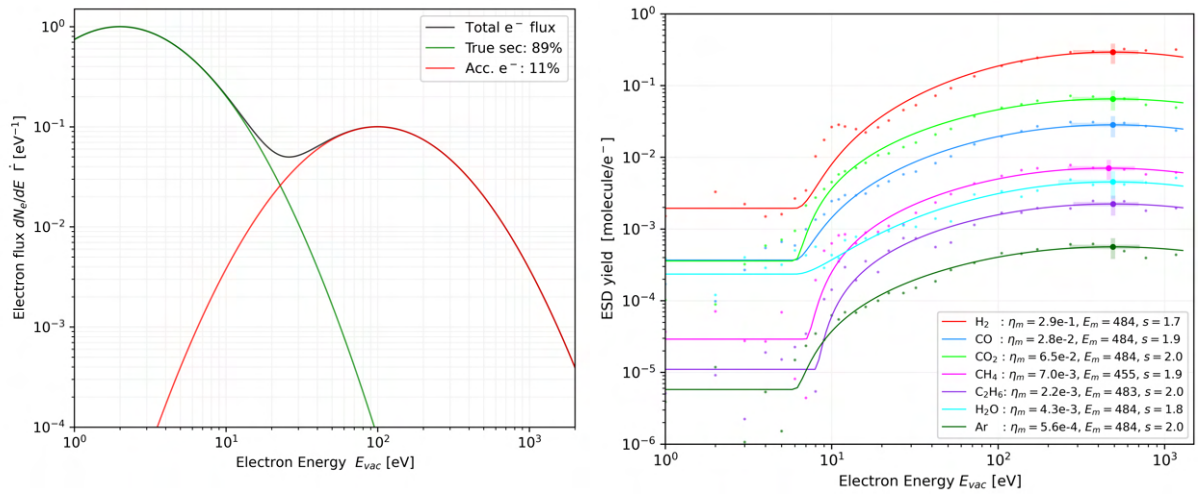

Figure 6.11: Left: Energy spectrum of an electron cloud in the LHC VPS sector modelled by two log-normal distributions, adapted from Bilgen et al. [322], based on data of E. Buratin [10]. Data were fitted to the measurements of Buratin overlaid with simulations of Iadarola [10]. Right: ESD yield at 300 eV of as-received unbaked Cu sample measured at 300 K temperature. Sample was cut&cleaned by external supplier and cleaned in warm ultrasonic isopropanol bath followed by long-term storage in plastic bag.

Figure 6.11 shows an analytical fit to the electron cloud as measured by E. Buratin [10] in the LHC's VPS sector and overlaid with simulations of Iadarola [10]. The fit developed by Bilgen et al. [322] uses a superposition of two log-normal distributions, one for the true secondary electron (SE), one for the beam-accelerated electrons.

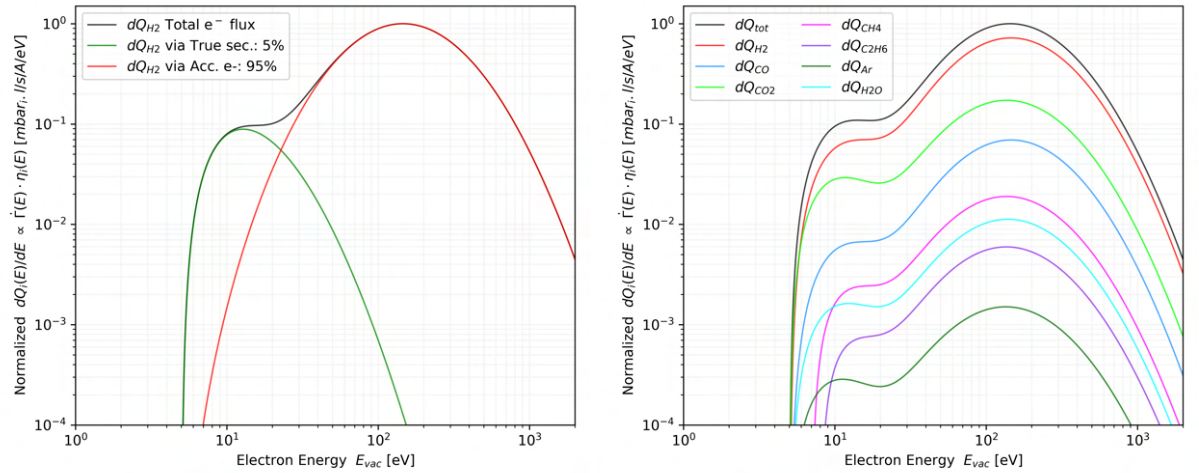

Figure 6.12: Left: Energy-resolved gas load of H_2 decomposed to contributions of true secondary electrons (green) and beam-accelerated electrons (red). Right: The energy-resolved gas load of all main gases from a warm as-received Cu sample irradiated by an electron cloud.

The graph on the left side of Fig. 6.12 shows the relative quantity of the beam-accelerated electrons

peak being 1/10 of the true secondary electrons peak. Despite this, the relative peak of gas load coming from the beam-accelerated electrons is still a factor 10x higher than the gas load coming from the true secondary electron component of the EC energy distribution, as seen on the right side. This is due to the ESD yield non-linearity and the presence of an energy threshold. Moreover, the desorption threshold also causes the gas load from sub-threshold electrons to be nil, rendering a large portion of the electron cloud harmless, which is favourable for dynamic vacuum effect mitigation. All monitored gases have a similar ESD yield energy dependence in terms of threshold energy, peak position and the curve (s-parameter) and vary only peak amplitude η_{max}. This fact also results in the gas loads following the same trend with the sole difference of a vertical offset due to the different η_{max}.

Figure 6.13 on the left shows the electron cloud energy spectrum plotted for different proportions of beam-accelerated electrons, varying from 0 to 1:10, which seems to be a realistic scenario based on prior measurements and simulations. The right side shows the corresponding differential gas loads calculated for different proportions of beam-accelerated electrons, i.e. different electron multipacting intensities. Note that for a 10:1 ratio of true secondaries vs. beam-accelerated electrons (left graph), the gas load already is 1:10 dominated by the beam-accelerated electrons (right graph). Based on these idealised calculations, the beam-accelerated electrons are by about a factor 100x more efficient in desorbing gas than the true secondary electrons. This simple exercise illustrates how important electron cloud mitigation is, especially the electron multipacting effect.

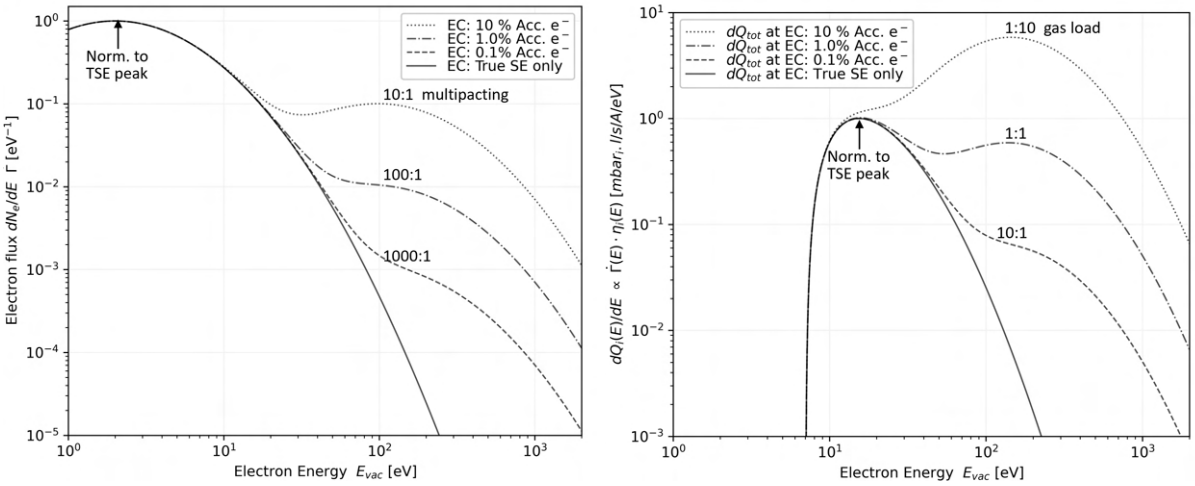

Figure 6.13: Left: Electron cloud energy spectrum plotted for different proportions of beam-accelerated electrons, ranging from 0 to 1:10. Curves are normalised to the true secondary electron peak. Right: Energy-resolved gas loads corresponding to the different proportions of beam-accelerated electrons on the left, i.e. different electron multipacting intensities.

Knowing the energy-resolved differential gas load, a few things can be done to understand better or possibly even optimise the accelerator operation. The EC can be simulated based on the beam parameters and the conditioning state of the beam-screen. By parametrizing the EC energy distribution and combining it with the energy-dependent ESD yield, the gas load due to EC can be calculated at different operating conditions. This would allow predicting the magnitude of the dynamic vacuum effect and pushing it, in an informed way, higher up towards its upper tolerable limit. With this information at hand, the beam-scrubbing could also be optimised since the beam parameters give a certain control over the EC energy distribution and, by extension, the observed dynamic vacuum effect. For example, if the gas load is to be mitigated, it is theoretically possible to choose the beam parameters such that the peak of beam-accelerated electrons offsets towards higher energies and lower amplitudes. Conversely, if the beam-screen electron conditioning is to be enhanced, the beam could be chosen such that the beam-induced electron multipacting has a large peak of beam-accelerated electrons located around 200 eV.

6.7 Considerations on beam-screen temperature windows

Figure 6.14 shows a comparative overlay of all TPD curves measured in the previous Section 5.5. The integral quantity of desorbed gas, marked as $\int Q_{des} dT$ in Section 5.5, is plotted here against the peak temperature T_{max}, i.e. the temperature of maximum desorption rate in TPD measurements. Here, the

Cu/SS surface serves as a reference baseline for the studied coatings and treatments. For completeness, the TPD measurements taken on bulk Cu resulted in the same set of TPD curves as Cu/SS.

It is worth noticing that when the same coverage is considered, gases cryosorbed on rough surfaces have systematically higher desorption temperatures than a bare Cu/SS, by about 20∼30 K. From the opposite end, at a given temperature, the rough surfaces can cryosorb higher quantities of gas than a bare Cu/SS. However, this also means that in case of a temperature excursion, rough surfaces thermally desorb a considerably larger gas quantity than a flat metal surface. The sole outlier to this general behaviour is the CO_2/Cu system, which follows n =0 kinetics and goes against all other gases that follow a classical n =1 in the sub-ML coverage range. As a result, the peak desorption temperature is ∼40 K lower for Cu than for a carbon coating. The n =1 first-order kinetics can serves a natural limit to the gas coverage by simply saturating the surface at a given temperature. Conversely, the n =0 zero order kinetics implies that *any* gas amount can be cryosorbed around this temperature, which can trigger pressure excursions in case of temperature swings. Hence, the 70–90 K temperature window should not be used in combination with high CO_2 gas loads.

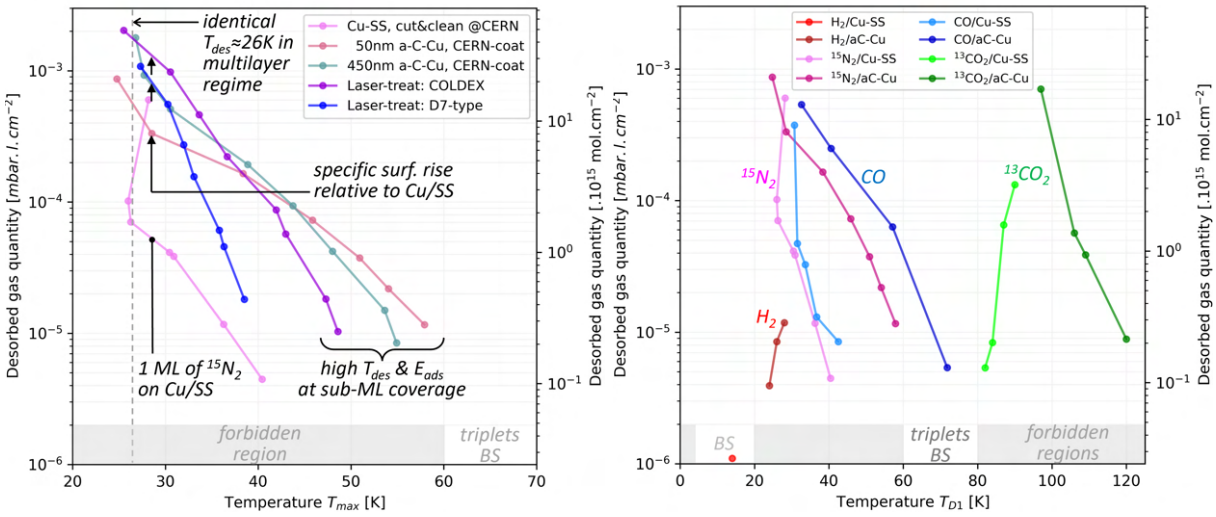

Figure 6.14: Left: Comparative temperature-dependent plot of TPD integrals varying as a function of $^{15}N_2$ coverage for different surfaces. The convergence at around 25 K corresponds to the onset of the multilayer adsorption regime (surface-agnostic desorption energy). For sub-monolayer coverages, note the high T_{max} caused by high E_{ads} of the carbon-coated and laser-treated Cu. Right: The same type of plot was made for different gases desorbing from copper colaminate (Cu/SS) and from 50 nm thin amorphous carbon (aC). Note that for sub-monolayer coverages, the carbon coating has the desorption temperatures T_{max} offset to values higher than for bare Cu. The high T_{max} results in higher binding energies E_{ads} of the carbon-coated Cu. Assumed 1 ML = 10^{15} molecule.cm^{-2}.

It is remarkable that the H_2 desorption peak for would appear around T_{max}=55 K, when the same thick carbon coating inside the COLDEX experiment [103] was dosed with submonolayer hydrogen coverages. This dissonance points to more complexity than expected, but unfortunately is outside of the experimental capabilities of the used setup.

The plots in Figures 6.14 and 6.15 also include BS temperature windows of the HL-LHC [4]. The in-arc BS is held in 5–20 K, while the newly installed inner triplet magnets are equipped with a new shielded beam-screen [30] chosen to operate in 60–80 K window. Given the presented experimental TPD data, this window is optimal for all studied surfaces and coatings, as visualised in Figure 6.14 and 6.15 as grey regions along the horizontal axis.

More generally speaking and following the beam-screen designs goals discussed and shown in Figure 1.5 of the Motivation section 1, the BS has the following functions that have to do with its surface properties:

- Maintain ultra-high vacuum, including dynamic vacuum effects and transients.
  Best in certain temperature windows.
- Reduce beam-induced cryogenic heat loads.
  Better at higher temperatures.
- Reduce resistive wall impedance.
  Better at lower temperatures.

Therefore, the challenge with a suitable beam-screen (BS) temperature is three-fold:
Low temperatures are needed for the current LHC BS design to limit the resistive wall impedance of its copper surface. The higher the surface impedance, the higher the impedance-induced beam instabilities and the higher the impedance-induced cryogenic heat load, which both worsen at higher temperatures. Hence the *soft* limit above ∼100 K for a technical-grade OFE copper. This temperature limit can be further increased by using high-temperature superconductors, for example, the REBCO coatings discussed in Sections 2.3.3 and 5.4.4. Using REBCO as a beam-screen surface coating is actively researched [122, 125, 265, 323] and this research contributes to the effort [A1].

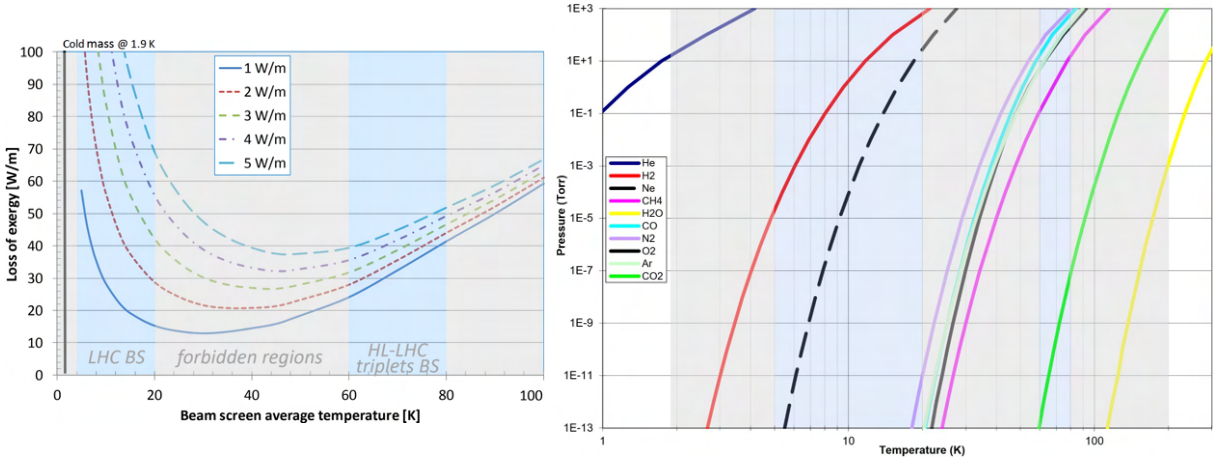

Figure 6.15: Left: Dependence of exergy on operating temperature as calculated for the LHC BS. Temperature windows for LHC-type copper-colaminated beam-screen with marked operating points for LHC. Note the forbidden temperature windows. The high impedance-induced heat load to the copper BS becomes a concern when approaching 100 K. Right: Adsorption isotherms adapted from V. Baglin [324], based on Hoonig&Hook [325].

Meanwhile, higher temperatures are beneficial for the cooling efficiency at cryogenic temperatures, as seen on the left side of Fig. 6.15. The cooling efficiency is basically dictated by the Carnot efficiency, which approaches 0 as the evaporator temperature T_{evap} approaches 0 K. Hence, the Carnot efficiency relation drives the exergy loss to unacceptably high values and a beam-screen operated around ambient temperatures would be ideal from the point of view of cooling efficiency. Therefore, unlocking a high-temperature operation window would be greatly advantageous from the cryogenics standpoint and, by extension, from the operating cost standpoint [326].

However, for the LHC BS as is, the second aspect that places a soft upper limit on the BS temperature is the heat ingress from BS (5∼20 K) to the cold bore (1.9 K) due to an imperfect thermal decoupling of the two. This effect is responsible for the exergy loss above ∼80 K, along with the impedance-induced heat load that also increases with temperature.

Finally, an appropriate window for BS operation needs to be identified, such that common residual UHV gases either do not yet cryosorb on the beam-screen and are already cryosorbed on the cold bore. As a result, small but inevitable operation-related temperature excursions will not result in the thermal desorption of significant gas quantities, translating into high-pressure excursions.

The plot in Fig. 6.14 shows BS temperature windows for the HL-LHC. The inner triplets in the 60–80 K and then the BS in the cold arcs held in 5–20 K, representing most of the machine. Note the cluster of gases in 20–40 K temperature region that forbids the BS operation here and puts an upper limit on the BS temperature. The 40–100 K window only contains the CO_2 isotherm, which does not necessarily pose a problem. Firstly because CO_2 is not abundant in high quantities, especially at cold, see Figure 5.24. Secondly, because the irradiated CO_2 is effectively reprocessed into CO. Another such window exists in the 80-100 K region, as visible in the usual Hoonig&Hook [325] saturated vapour pressure plot, right side of Fig. 6.15.

Meanwhile, the newly installed inner triplet magnets house a new (radiation) shielded beam-screen [30], which is designed to operate at higher temperatures. The 60–80 K temperature window was selected, as published in the HL-LHC design report [4]. The experimental TPD data demonstrate that the 60–80 K temperature window is feasible on all studied surfaces ranging from bare copper (LHC BS baseline) to thin and thick carbon coating. Given the presented data, this window is optimal to minimise temperature swing-induced pressure excursions for all studied surfaces and coatings, as visualised in Figure 6.14 along the horizontal axis. In this 60-80 K temperature window, all typical UHV residual gases have already been

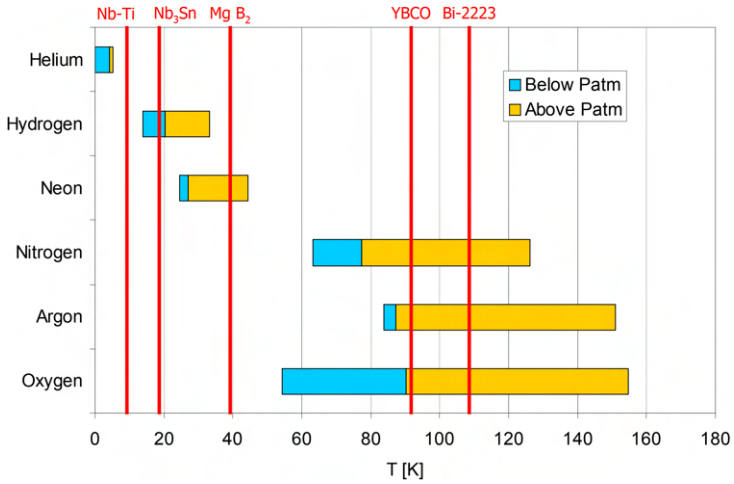

Figure 6.16: Temperature windows achievable with different refrigerant liquids, operating either above (orange) or below (blue) atmospheric pressure. The critical temperatures (at zero B-field and electric currents) are plotted as red lines for different superconductors. The HTS (YBCO) significantly overlaps with N_2 and Ar temperature windows. Image adapted from CERN-TE-CRG, based on [327]

thermally desorbed and pumped away. The CO_2 and H_2O make an exception and are still cryopumped at these temperatures.

The overall preference for higher beam-screen temperatures gave rise to studies with HTS-coated beam-screens, [125, 323]. From the beam-impedance perspective, the REBCO application to the BS opens up the feasibility of BS operation at liquid N_2 and Ar temperature windows. Note the Figure 6.16 that plots temperature windows for different cryogenic fluids. The LHC BS temperature is in fact outside of the plotted region, because the beam-screen He circuit operates in the supercritical state, as opposed to the classical liquid-vapour evaporation regime considered in the plot. Note that the HTS critical temperature (red line marked YBCO; at zero B-field and electric currents) significantly overlaps with N_2 and Ar temperature windows. This makes the HTS and nitrogen combination a promising candidate for future superconducting machines operating at elevated cryogenic temperatures.

6.8 Chapter summary

The theoretical understanding summarised in the State of the art Chapter 2 was combined with the acquired experimental data from Chapter 5 and gave rise to a number of semi-empirical parameterizations for SEY and ESD as a function of energy, dose, angle, composition and a combination of thee. In turn, this chapter demonstrates examples of the immediate applicability of the experimental findings and the derived models.

The acquired data on SEY, ESD and TPD are inspected, bearing in mind the real-life application to CERN's High-Luminosity LHC. Yet, a significant overlap exists with other warm and cryogenic storage rings. Indeed, operation-related issues like the electron cloud and dynamic vacuum effect are strongly linked to the nature of a given beam-screen surface, which determines not only the electron cloud activity but also the dynamic vacuum effect and the scrubbing rate observed during an operation. This was illustrated by modelling the ESD-induced energy-resolved gas load for different multipacting conditions. The TPD results acquired on copper and carbon coating with cryosorbed gases were discussed in terms of suitable temperature windows for the accelerator operation in terms of pressure rises during possible BS temperature excursions. Finally, the SEY and ESD studies performed on mixed cryosorbed gases offer a significant overlap with other technical disciplines and applications.

Summary and conclusions

Summary of the dissertation

This dissertation presents applied research in the vacuum science of physical phenomena relevant to the electron cloud and the dynamic pressure rise observed when circulating the bunched proton beams in the CERN's LHC. This mainly includes the secondary electron yield (SEY), the determining parameter for the electron cloud (EC) activity and possible electron multipacting. The electron stimulated desorption (ESD) yield then determines the amount of gas electrodesorbed due to the electron irradiation coming from the EC. The temperature programmed desorption (TPD) then serves to characterise the amount of cryosorbed gas, its binding energy and the specific surface of the substrate.

To begin with, Chapters 1 and 2 review the problematics underlying the electron cloud and the dynamic vacuum effects. A survey of operational observations, simulations and measurements is presented, preferably done on the LHC's cold arcs where a beam-screen protects the LHe-cooled cryogenic magnets from heat generated by the circulating proton beam. The key parameters of the LHC's beam-screen are identified to aim the research efforts better. This includes achieving low temperatures below 20 K, high imparted doses of (very) low-energy electrons, and the presence of cryosorbed gases on the studied surfaces. Contrary to the LHC, the magnetic field is omitted not to interfere with the slow electrons' trajectories.

Having set the target parameters and research objective and identifying (many) research niches, a new laboratory-based cryogenic experimental setup is conceived and optimised to reproduce the relevant parameters in a controllable manner, see Figure 6.17. Chapter 4 describes in detail the commissioning and calibration procedure of this setup, essentially to correctly count electrons and gas molecules in the setup. In this setup, the electron cloud irradiation is mimicked by an analytical-grade thermionic electron gun tuned to deliver a narrow beam with a flat-top profile of low-energy electrons in 0–1.5 keV. With high accumulated doses up to 10 $mC.mm^{-2}$, this electron source encompasses the range of beam screen-relevant conditions. A custom-made collector is then characterised to fully contain the primary electron beam, and to capture the secondary electrons and neutral gas molecules leaving the studied sample surface as a direct result of electron irradiation. An in-situ calibrated quadrupole mass spectrometer with a secondary electron multiplier measures the most subtle changes in the residual gas composition in the UHV chamber. The now-calibrated experimental setup measures the SEY and ESD at high precision and resolution in the range of energies 0–1.5 keV. Particular focus is laid on the 0-50 eV region, where the majority of EC energy spectrum resides. The SEY and ESD yields were measured as a function of environmental conditions (temperature, residual gas composition), irradiation parameters (energy, dose, angle) and the material surface state (cleaning, storage, treatments, etc.). The experimental data were acquired, analysed, discussed in detail and compared to the relevant literature. This was a key step enabling further research work at an appropriate precision, repeatability and accuracy.

A systematic approach was employed in Chapter 5 to battle the combinatorial explosion and systematically explore this large parameter space: always varying only 1 experimental variable at a time and observing how it manifests on the observable parameters. Various technical-grade metal surfaces, such as Cu, Al and SS, currently used as a baseline for construction, and functional surface coatings and treatments were studied under application-relevant conditions. The electron irradiation effect onto the SEY and ESD phenomena was investigated in unparalleled detail and hinted new insights into many technical applications. The TPD method was also developed in synergy with SEY and ESD measurements provided more holistic information. The SEY and ESD yields of cryosorbed gases and their binary mixtures were also investigated in the 0-30 ML range as they are omnipresent in devices operating under cryogenic conditions.

Finally, Chapter 6 presents an overview of semiempirical parametric models developed or modified from the existing ones to capture the SEY and ESD yields as a function of energy, dose, angle and temperature. The composition dependence of SEY and ESD was also studied in cryosorbed binary gas mixtures and enabled the formulation of combining rules for binary mixtures of real gases. Although

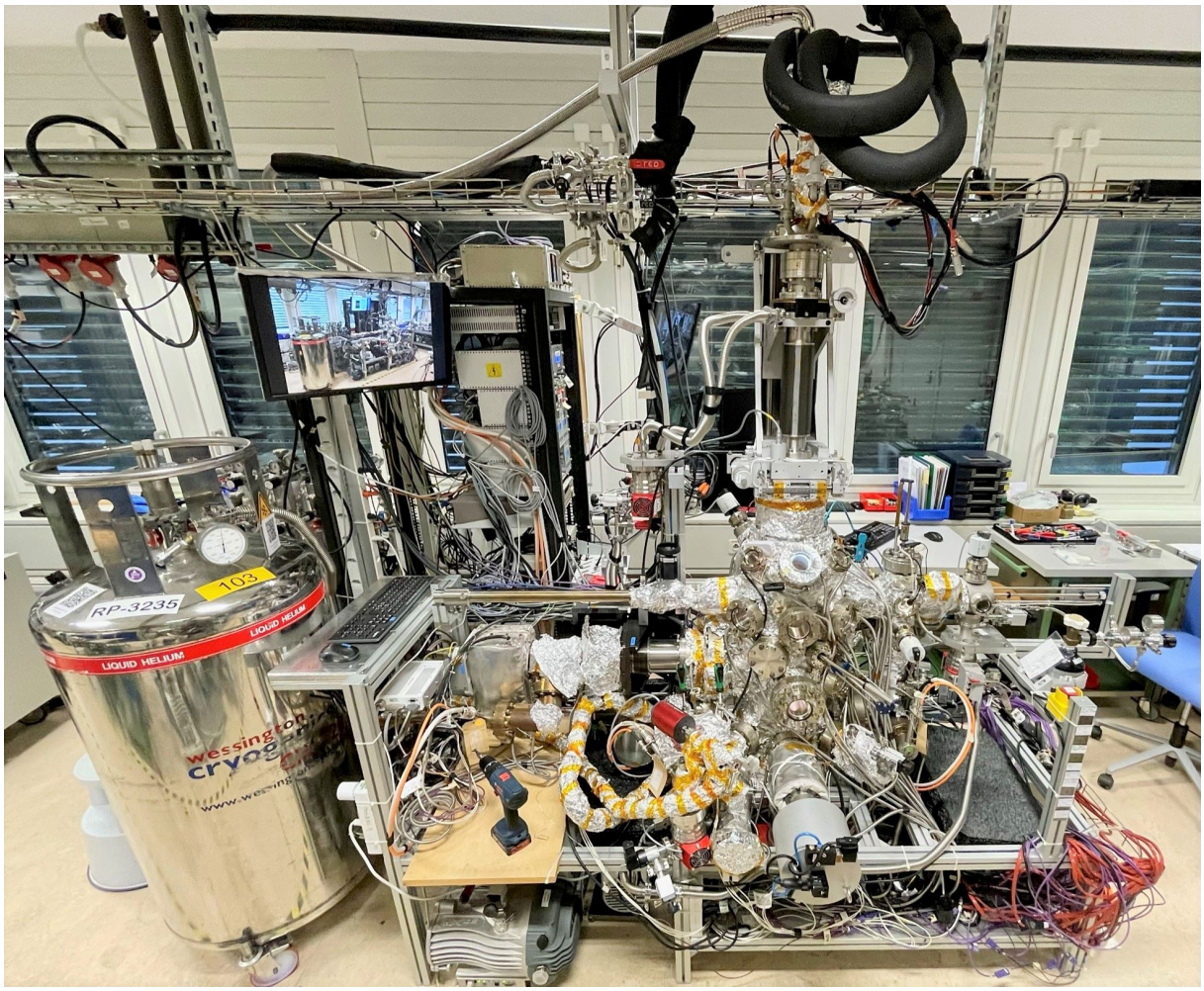

Figure 6.17: The Multisystem setup developed and commissioned for this research work, and many others to come. The photo captures the current state at the time of writing.

a particular focus is on understanding the electron cloud and dynamic vacuum phenomena in CERN's Large Hadron Collider (LHC), where possible, the research results tend to be interpreted rather generally to remain relevant to other accelerators and technical applications.

Ultimately, this dissertation presents a state-of-the-art, theory-backed, yet comprehensive understanding of the physical phenomena underlying the low-energy electron-induced emission of electrons and molecules from technical-grade metal surfaces and functional treatments.

Conclusions of the research

A particular focus is on understanding the electron cloud and dynamic vacuum phenomena in the LHC, which is characterised by cryogenic temperatures below 20 K, low electron energies in 0–1 keV range and high electron doses up to 10 mC.mm^{-2}. Moreover, additional supporting data were collected in this parameter range of energies, doses and at temperatures that directly envelope the LHC's beam screen operating conditions. Where possible and necessary, the dataset was extended to better understand the underlying behaviour and/or broaden the applicability spectrum outside the LHC scope.

The electron condition effect was studied and confirmed at cryogenic temperatures for the first time. Although the ESD yields and gas amounts differ from ambient temperatures, the SEY conditioning process led to results indistinguishable from the ones obtained at ambient temperatures. The presented data, backed by XPS analyses, clearly demonstrate that electron conditioning works equally well at cryogenic temperatures, including electron-induced graphitization of surface-bound carbon-containing contaminants. Another remarkable point is that the amount of electrodesorbed gas does not necessarily correspond to the surface roughness factor and, in fact, most of the studied surfaces electrodesorbed a

very similar gas quantity. Moreover, an intense electron-induced cracking of cryosorbed gas molecules was observed, reprocessing the parent molecules into fragments with vastly different electrochemical and vacuum dynamics behaviours.

Having studied the SEY, being at the electron cloud's origin, and the ESD, giving rise to the dynamic vacuum effect, the attention was shifted to the influence of cryosorbed gases on both SEY and ESD. The conclusion is that the SEY of metal surfaces, particularly the low-energy SEY region, change with the thinnest coverages of cryosorbed gas. Both increase and decrease in SEY are observed, depending on the particular system. This behaviour carries on to the studied porous surface treatments and coatings, albeit at much higher coverages.

By introducing the TPD method, one could quantify the amount of cryosorbed gas, the governing adsorbate-substrate interactions and corresponding binding energies, and determine specific surfaces of samples. Porous surface treatments have a higher specific surface and generally higher binding energies, which translates to delayed thermal desorption of gases and possibly even a different desorption order. The surface roughness factor was assessed via a series of TPD, and this roughness factor roughly corresponds to the amount of gas necessary to induce SEY and ESD changes similar to those on flat metal surfaces.

Finally, the SEY and ESD measured on cryosorbed binary gas mixtures exhibited a highly non-linear composition-dependent behaviour. Combining rules were developed to predict the SEY and ESD yields for a given gas composition from values of pure compounds. This presents an important step in getting realistic extrapolative predictions in real-world scenarios since, for instance, gas overlayers are typically cryosorbed from the residual gas that is a multi-compound mixture. Perhaps the data on mixed cryosorbed gases presented here can also outreach to astrophysical realms, where intense electron irradiation bombards ice grains or icy moons.

The measured SEY and ESD data were approximated by a series of semiempirical models that allow grasping the underlying trends and interpolating across the scarcely populated dataset. Generalising the experimental observations and grasping the emergent patterns is an important step in refining the understanding and generating knowledge from the acquired data. These parametric models that approximate the SEY and ESD allow further use in the field by, for instance, coupling to an electron-cloud simulation at the input and/or to vacuum dynamics calculation software on the output.

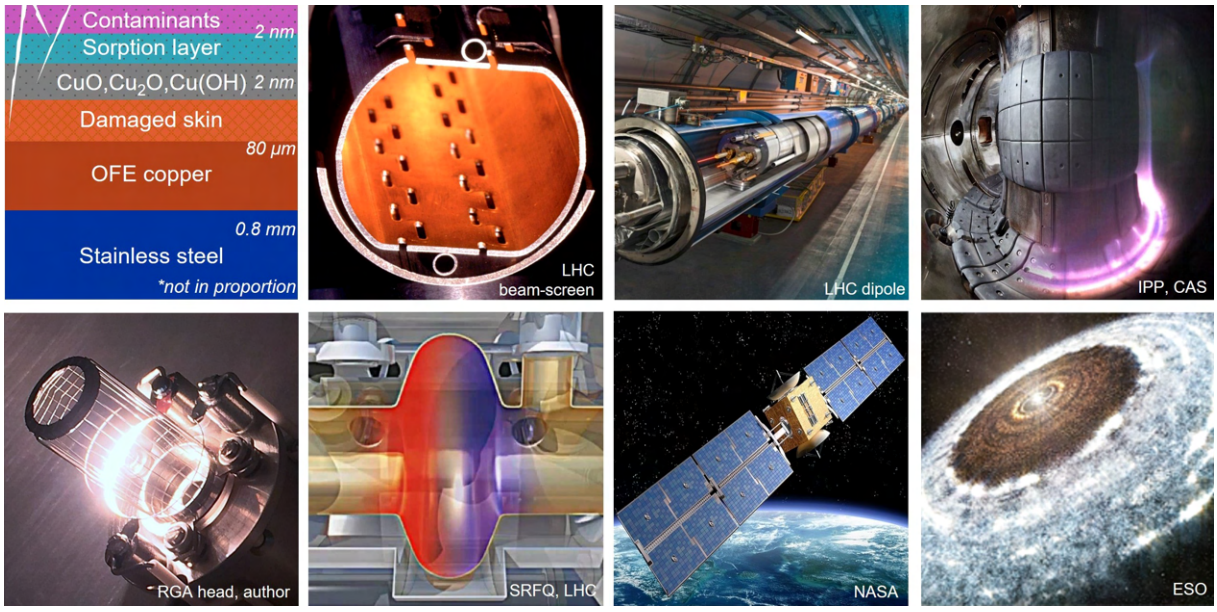

Figure 6.18: Outreach of this applied research work to other applications and domains. Ranging from engineering applications and surface analysis, past high-energy physics, to astrophysics. All these fields deal with electron irradiation of possibly cold, ill-defined surfaces.

Assessment of achieved dissertation objectives

The dissertation objectives outlined in Chapter 3 were successfully achieved on all fronts, effectively expanding the current knowledge in the field of science and engineering.

- Innovative experimental methodology was developed and enabled a detailed combined study of low-energy electron impact-induced electronic and molecular emission (SEY and ESD parameters) from technical surfaces at cryogenic temperatures and with adsorbed gases.
- Uniquely detailed study was performed for various technical-grade surfaces held at cryogenic temperatures and resulted in a detailed investigation of the electronic and molecular emission phenomena as a function of material (metals, coatings, treatments), irradiation (electron energy, dose, angle) and environmental (substrate temperature, adsorbate composition) properties.
- Large amounts of acquired data allowed the formulation of parametric models that well approximate the data (both original and external), and generalisation of the findings and observations. This includes parametric semiempirical models that capture the energy, dose, angle and composition dependence of SEY and ESD yields for various technical surfaces, and can be directly used in further research and engineering practice.
- The newly collected SEY, ESD and TPD data and the derived knowledge was immediately confronted with practical applications and scenarios. For instance, linking the electron cloud activity (its energy and dose dependence) to the dynamic vacuum effect in the LHC, or considering suitable temperature windows for a beam-screen operation.

Personal contribution and achieved scientific results

To begin the research, I elaborated an extended literature review of the studied phenomena and surveyed the diverse applications that may benefit from this research. While continuously expanding this knowledge background, I proceeded to commission the laboratory-based experiment and develop an innovative experimental methodology for the collector-based cryogenic SEY, ESD and TPD measurements. I was privileged to build, commission, calibrate, and iteratively improve the experimental setup, originally designed by V. Baglin and B. Henrist, based on their extensive prior experience. This innovative top-class analytical *Multisystem* setup is designed for a combined collector-based measurement of ESD, SEY, TPD and possibly others. The multi-domain experimental capability enables unique research and resulted in a number of articles produced in recent years.

The applied research work yielded an experimental methodology-oriented article [A3] and an article with the first results [A2], which I both wrote as the main contributing author. Still, as the main author, I led the collaborative work between three institutes on a future-focused article [A1] dealing with applying high-temperature superconductors in high-energy physics. The research work even overlapped to an astrophysics-relevant publication by R. Dupuy et al. from the Sorbonne University [A4], which I co-authored, and deals with the irradiation of thick cryosorbed ices. Given the newly available experimental data, work is underway on a follow-up article focusing on thin cryosorbed ices. I further presented the research project at a number of conferences [A5-A8], where it triggered the interest and response of the scientific community and received an IUVSTA Elsevier Student Award. This includes conferences such as the 16^{th} European Vacuum Conference [A7], the 35^{th} European Conference on Surface Science [A6], 18^{th} International Conference on Thin Films & 18^{th} Joint Vacuum Conference [A8], and the 2022 Electron Cloud workshop [A5].

Future developments and research directions

The developed experimental setup could be further improved by increasing the sensitivity and resolution of instruments or decreasing the static and dynamic backgrounds. Faster DAQ and pulsed electron-beam measurements could unlock the direction of SEY measurements in dielectrics. However, expanding the experimental capabilities would be the most beneficial to understanding the studied problems. This can be the addition of analytical instruments, such as an XPS or a Kelvin probe, or devices, such are ion and photon guns, or additional chambers for thermal or non-thermal surface treatments.

The large space of parameters influencing the SEY, ESD and TPD inherently produces many research directions. Insofar, each direction was merely probed by a simple measurement. Although this

concentrated research effort contributed much data, the parameter space is still very scarcely populated. For instance, metal surfaces and their treatments can be investigated ad libitum. The same applies to cryosorbed gases, their mixtures, sandwiches, crystallographic structures, etc. The studies on cryosorbed gases could also be enriched by TPD measurements done on binary mixtures, which would bring another window on the cryosorbate-substrate systems. Moreover, researching simple systems would build up confidence and would enable studying systems of growing complexity.

Correlation to other, possibly simpler, experimental methods could lead to developing a more accessible proxy for the SEY and ESD determination. This builds on the fact that ESD, PSD and ISD yields correlate as they all scale with the species' surface concentration. TPD to temperatures high enough to thermally desorb chemisorbed species could perhaps lead to interesting comparisons to the presented ESD data.

List of publications

The authored publications and conference participations related to this dissertation topic are marked as [A1]-[A8] in the manuscript. The first-author articles are attached in the Appendix.

First author publications

[A1] Haubner, M., Krkotić, P., Baglin, V., et al. (2023). Electron Beam Characterization of REBCO-Coated Conductors at Cryogenic Conditions. Applied Sciences. 13(5), 2765. DOI: 10.3390/app13052765

[A2] Haubner, M., Baglin, V., Henrist, B. (2022). Electron conditioning of technical surfaces at cryogenic and room temperature in the 0–1 keV energy range. Vacuum, 207, 111656.
DOI: 10.1016/j.vacuum.2022.111656

[A3] Haubner, M., Baglin, V., Henrist, B. (2022). Collector-based measurement of gas desorption and secondary electron emission induced by 0–1.4 keV electrons from LHC-grade copper at 15 K. Nuclear Instruments and Methods in Physics Research - B, 531, 34-43. DOI: 10.1016/j.nimb.2022.09.013

Co-authored publications

[A4] Dupuy, R., Haubner, M., Henrist, B., Fillion, J. H., & Baglin, V. (2020). Electron-stimulated desorption from molecular ices in the 0.15–2 keV regime. Journal of Applied Physics, 128(17), 175304.
DOI: 10.1063/5.0021832

Conferences and workshops

[A5] Haubner, M., Baglin, V., Henrist, B. (2022). SEY and ESD of ices and technical surfaces at cryogenic temperatures. Electron-cloud workshop and Vacuum for gravity wave detectors 2022, ECLOUD'22 and GWDVac'22 workshop. URL: agenda.infn.it/event/28336/contributions/177366

[A6] Haubner, M., Baglin, V., Henrist, B. (2022). Analysis and modification of technical surfaces by low-energy electron irradiation. 35th European Conference on Surface Science. Poster presentation. ECOSS-35. DOI: 10.13140/RG.2.2.30114.09927

[A7] Haubner, M., Baglin, V., Henrist, B. (2021). Electron conditioning of technical surfaces at cryogenic and room temperature in the 0–1 keV energy range. 16th European Vacuum Conference. EVC-16. URL: secure.key4events.com/key4register/images/client/1090/files/EVC-16-Programme.pdf

[A8] Haubner, M., Baglin, V., Henrist, B. (2020). Preliminary electron desorption results of selected HL–LHC technical surfaces at cryogenic temperature. 18th International Conference on Thin Films & 18th Joint Vacuum Conference. ICTF-JVC 2020.
URL: static.akcongress.com/downloads/ictf/ictf2020-book-of-abstracts.pdf

Bibliography

[1] Oliver Sim Bruning et al. *LHC Design Report*. CERN Yellow Reports: Monographs. Geneva: CERN, 2004. DOI: 10.5170/CERN-2004-003-V-1. URL: cds.cern.ch/record/782076 (cit. on p. 12).

[2] Bernhard J Holzer. *Beam optics and lattice design for particle accelerators*. en. Tech. rep. 2013. DOI: 10.5170/CERN-2013-001.171 (cit. on p. 12).

[3] V Baglin et al. *Cryogenic Beam Screens for High-Energy Particle Accelerators*. Tech. rep. Geneva: CERN, 2013. URL: cds.cern.ch/record/1507613 (cit. on pp. 12, 15, 29).

[4] Bejar Alonso I. et al. *High-Luminosity Large Hadron Collider (HL-LHC): Technical design report*. CERN Yellow Reports: Monographs. Geneva: CERN, 2020. DOI: 10.23731/CYRM-2020-0010. URL: cds.cern.ch/record/2749422 (cit. on pp. 12, 173, 174).

[5] Annalisa Romano. "Electron cloud formation in CERN particle accelerators and its impact on the beam dynamics". Presented on 2018-08-20. 2018. URL: cds.cern.ch/record/2676577 (cit. on p. 12).

[6] G. Iadarola et al. "Electron cloud in the CERN accelerators (PS, SPS, LHC)". *AIP Conf. Proc. C* 1206051 (2013). Comments: 8 pages, contribution to the Joint INFN-CERN-EuCARD-AccNet Workshop on Electron-Cloud Effects: ECLOUD'12; 5-9 Jun 2012, La Biodola, Isola d'Elba, Italy. DOI: 10.5170/CERN-2013-002.19. arXiv: 1309.6795. URL: http://cds.cern.ch/record/1603635 (cit. on p. 13).

[7] V. Baglin et al. "Synchrotron Radiation in the LHC Vacuum System" (2011). URL: cds.cern.ch/record/1407539 (cit. on p. 13).

[8] Roberto Cimino et al. "Electron cloud in accelerators". *International Journal of Modern Physics A* 29.17 (2014). DOI: 10.1142/S0217751X14300233 (cit. on pp. 13, 25, 43).

[9] Giovanni Iadarola. "Electron cloud studies for CERN particle accelerators and simulation code development". Presented 23.05.2014. 2014. URL: cds.cern.ch/record/1705520 (cit. on pp. 13, 14, 24, 25, 170).

[10] Elena Buratin. "Electron Cloud and Synchrotron Radiation characterizations of technical surfaces with the Large Hadron Collider Vacuum Pilot Sector". Presented 10 Dec 2020. Geneva: CERN, 2020. URL: cds.cern.ch/record/2746058 (cit. on pp. 13, 25, 171).

[11] Galina Skripka et al. "Beam-induced heat loads on the beam screens of the HL-LHC arcs" (2019). URL: cds.cern.ch/record/2692753 (cit. on pp. 14, 19, 29, 87).

[12] Y. Suetsugu et al. "Mitigating the electron cloud effect in the SuperKEKB positron ring". *Phys. Rev. Accel. Beams* 22 (2 2019). DOI: 10.1103/PhysRevAccelBeams.22.023201 (cit. on pp. 14, 15).

[13] W. Fischer et al. "Electron cloud observations and cures in RHIC". 2007. DOI: 10.1109/PAC.2007.4441092. URL: www.osti.gov/biblio/910401 (cit. on p. 14).

[14] S. Y. Zhang. "eRHIC Beam Scrubbing" (2017). DOI: 10.2172/1392223. URL: www.osti.gov/biblio/1392223 (cit. on p. 14).

[15] Giovanni Rumolo et al. "Vacuum and electron cloud issues at the GSI present and future facilities" (2005). DOI: 10.5170/CERN-2005-001.95. URL: cds.cern.ch/record/846639 (cit. on p. 14).

[16] Yusuke Suetsugu et al. "Achievements and problems in the first commissioning of SuperKEKB vacuum system". *Journal of Vacuum Science and Technology A* 35.3 (2017). DOI: 10.1116/1.4977764. URL: 10.1116/1.4977764 (cit. on p. 14).

[17] Y. Suetsugu et al. "First commissioning of the SuperKEKB vacuum system". *Phys. Rev. Accel. Beams* 19 (12 2016). DOI: 10.1103/PhysRevAccelBeams.19.121001 (cit. on p. 14).

[18] C.K. Chan et al. "Conditioning of the vacuum system of the TPS storage ring without baking in situ". *Nuclear Instruments and Methods in Physics Research Section A: Accelerators, Spectrometers, Detectors and Associated Equipment* 851 (2017). DOI: 10.1016/j.nima.2017.01.027 (cit. on p. 14).

[19] R S Calder. "Ion induced gas desorption problems in the ISR". *Vacuum, v. 24, no. 10, pp. 437-443* (Oct. 1974). DOI: 10.1016/0042-207X(74)90001-3. URL: www.osti.gov/biblio/4211730 (cit. on p. 14).

[20] William C. Turner. "Ion desorption stability in superconducting high energy physics proton colliders". *Journal of Vacuum Science & Technology A* 14.4 (1996). DOI: 10.1116/1.580078 (cit. on p. 15).

[21] Oleg B. Malyshev. "The energy of ions bombarding the vacuum chamber walls. Round beams". *Nuclear Instruments and Methods in Physics Research Section A: Accelerators, Spectrometers, Detectors and Associated Equipment* 993 (2021). DOI: 10.1016/j.nima.2021.165068 (cit. on p. 15).

[22] Edgar Mahner. "Review of heavy-ion induced desorption studies for particle accelerators". *Phys. Rev. ST Accel. Beams* 11 (10 2008). DOI: 10.1103/PhysRevSTAB.11.104801. URL: link.aps.org/doi/10.1103/PhysRevSTAB.11.104801 (cit. on p. 15).

[23] V. Shiltsev et al. "Modern and future colliders". *Rev. Mod. Phys.* 93 (1 2021). DOI: 10.1103/RevModPhys.93.015006 (cit. on p. 15).

[24] I Bellafont et al. "Beam induced vacuum effects in the future circular hadron collider beam vacuum chamber". *Phys. Rev. Accel. Beams* 23 (2020). DOI: 10.1103/PhysRevAccelBeams.23.043201. URL: cds.cern.ch/record/2717914 (cit. on p. 15).

[25] Michael Benedikt et al. *FCC-hh: The Hadron Collider: Future Circular Collider Conceptual Design Report Volume 3. Future Circular Collider*. Tech. rep. Geneva: CERN, 2019. DOI: 10.1140/epjst/e2019-900087-0. URL: http://cds.cern.ch/record/2651300 (cit. on pp. 15, 118).

[26] Jingyu Tang. "Design Concept for a Future Super Proton-Proton Collider". *Frontiers in Physics* (2022). DOI: 10.3389/fphy.2022.828878 (cit. on p. 15).
[27] Mingyi Dong et al. "CEPC Conceptual Design Report: Volume 2 - Physics and Detector" (2018). Ed. by Joao Barreiro Guimaraes da Costa et al. arXiv: 1811.10545 [hep-ex] (cit. on p. 15).
[28] Baglin Vincent. "The LHC vacuum system: Commissioning up to nominal luminosity". *Vacuum* 138 (2017). DOI: 10.1016/j.vacuum.2016.12.046 (cit. on p. 15).
[29] M Brugger et al. "Particle Physics Reference Library - Interactions of Beams with Surroundings". *Particle Physics Reference Library*. Springer, 2020. ISBN: 978-3-030-34245-6. DOI: 10.1007/978-3-030-34245-6 (cit. on p. 15).
[30] Marco Morrone et al. "The shielded HL-LHC beam screen: specification and design" (2022). Paper submitted in 2022 (cit. on pp. 15, 118, 173, 174).
[31] Redhead P.A. "The first 50 years of electron stimulated desorption (1918-1968)". *Vacuum* 48.6 (1997). DOI: 10.1016/S0042-207X(97)00030-4 (cit. on pp. 16, 31, 33, 44, 57, 109).
[32] JL de Segovia. "A review of electron stimulated desorption processes influencing the measurement of pressure or gas composition in ultra high vacuum systems". *Vacuum* 47.4 (1996). 1st International Workshop on Interaction of Gases with Solids Affecting Vaccum Processes. DOI: 10.1016/0042-207X(95)00247-2 (cit. on p. 16).
[33] Theodore E. Madey et al. "Electron-Stimulated Desorption as a Tool for Studies of Chemisorption: A Review". *Journal of Vacuum Science and Technology* 8.4 (1971). DOI: 10.1116/1.1315200. URL: 10.1116/1.1315200 (cit. on pp. 16, 32).
[34] Abdoul-Carime H.A. et al. "Low-Energy (5-40 eV) Electron-Stimulated Desorption of Anions from Physisorbed DNA Bases". *Radiation Research* 155.4 (2001). DOI: 10.1667/0033-7587(2001)155[0625:leeesd]2.0.co;2. URL: http://www.jstor.org/stable/3580366 (visited on 07/07/2022) (cit. on pp. 16, 147).
[35] H.F. Dylla et al. "Electron stimulated desorption from thin organic films". *Surface Science* 144.2 (1984). DOI: 10.1016/0039-6028(84)90127-4. URL: www.sciencedirect.com/science/article/pii/0039602884901274 (cit. on p. 16).
[36] Fabian Schmidt et al. "Mechanisms of Electron-Induced Chemistry in Molecular Ices". *Atoms* 10.1 (2022). DOI: 10.3390/atoms10010025 (cit. on pp. 16, 147).
[37] Christopher R. Arumainayagam et al. "Low-energy electron-induced reactions in condensed matter". *Surface Science Reports* 65.1 (2010). DOI: 10.1016/j.surfrep.2009.09.001. URL: www.sciencedirect.com/science/article/pii/S0167572909000673 (cit. on pp. 16, 37, 38).
[38] Chris R. et al. Arumainayagam. "Extraterrestrial prebiotic molecules: photochemistry vs. radiation chemistry of interstellar ices". *Chem. Soc. Rev.* 48 (8 2019). DOI: 10.1039/C7CS00443E (cit. on p. 16).
[39] HF Dylla et al. "Scanning electron-stimulated desorption microscopy of model-biological surfaces". *Nature* 291.5814 (1981). DOI: 10.1038/291401a0 (cit. on p. 16).
[40] Michael C. Boyer et al. "The role of low-energy (undefinedeV) electrons in astrochemistry". *Surface Science* 652 (2016). Insights into Surface Phenomena: In Honor of John T. Yates Jr. DOI: 10.1016/j.susc.2016.03.012. URL: www.sciencedirect.com/science/article/pii/S0039602816001084 (cit. on p. 16).
[41] M. R. S. McCoustra et al. "Laboratory studies of desorption in model astrophysical ice systems". *AIP Conference Proceedings* 1543.1 (2013). DOI: 10.1063/1.4812624. URL: aip.scitation.org/doi/abs/10.1063/1.4812624 (cit. on p. 16).
[42] Julien Hillairet et al. "Multipactor in High Power Radio-Frequency Systems for Nuclear Fusion" (2017). DOI: 10.48550/ARXIV.1710.03629. URL: arxiv.org/abs/1710.03629 (cit. on p. 16).
[43] T. P. Graves et al. "Effect of multipactor discharge on Alcator C-Mod ion cyclotron range of frequency heating". *Journal of Vacuum Science and Technology A* 24.3 (2006). DOI: 10.1116/1.2194937. URL: 10.1116/1.2194937 (cit. on p. 16).
[44] Kai Papke et al. "Design studies of a compact superconducting RF crab cavity for future colliders using Nb/Cu technology" (2019). DOI: 10.1103/PhysRevAccelBeams.22.072001. URL: cds.cern.ch/record/2683894 (cit. on p. 17).
[45] Dieter M. Gruen et al. *Plasma-materials interactions and impurity control in magnetically confined thermonuclear fusion machines*. Undetermined. DOI: 10.1007/3540098259_5 (cit. on p. 17).
[46] M. Andritschky. "Origin of gas impurities in sputtering plasmas during thin film deposition". *Vacuum* 42.12 (1991). DOI: 10.1016/0042-207X(91)90173-G (cit. on p. 17).
[47] H. Moreno Fernandez et al. "The impact of H2 and N2 on the material properties and secondary electron yield of sputtered amorphous carbon films for anti-multipacting applications". *Applied Surface Science* 542 (2021). DOI: 10.1016/j.apsusc.2020.148552 (cit. on pp. 17, 118, 146).
[48] Miria M Finckenor et al. "A Researcher's Guide to: International Space Station–Space Environmental Effects". *NASA ISS Program Science Office* (2015). URL: ntrl.ntis.gov/NTRL/dashboard/searchResults/titleDetail/PB2016104505.xhtml (cit. on p. 17).
[49] H.-J Fitting. "Six laws of low-energy electron scattering in solids". *Journal of Electron Spectroscopy and Related Phenomena* 136.3 (2004). DOI: 10.1016/j.elspec.2004.04.003 (cit. on pp. 20, 25).
[50] Neal Jay Carron. *An introduction to the passage of energetic particles through matter*. Taylor & Francis, 2006. DOI: 10.1201/9781420012378-1 (cit. on p. 20).
[51] Wolfgang Werner. "Questioning a Universal Law for Electron Attenuation". *Physics* 12 (2019). DOI: 10.1103/Physics.12.93 (cit. on pp. 20, 107).
[52] S. Tanuma et al. "Calculations of stopping powers of 100eV-30keV electrons in 31 elemental solids". *Journal of Applied Physics* 103.6 (2008). DOI: 10.1063/1.2891044 (cit. on pp. 20, 21).

[53] K. Kanaya et al. "Penetration and energy-loss theory of electrons in solid targets". *Journal of Physics D: Applied Physics* 5.1 (1972). DOI: 10.1088/0022-3727/5/1/308 (cit. on pp. 20, 25, 27).

[54] M. P. Seah et al. "Quantitative electron spectroscopy of surfaces: A standard database for electron inelastic mean free paths in solids". *Surface and Interface Analysis* 1.1 (). DOI: 10.1002/sia.740010103 (cit. on p. 20).

[55] Olga Yu. Ridzel et al. "Low energy (1-100 eV) electron inelastic mean free path (IMFP) values determined from analysis of secondary electron yields (SEY) in the incident energy range of 0.1-10 keV". *Journal of Electron Spectroscopy and Related Phenomena* 241 (2020). Sources, Interaction with Matter, Detection and Analysis of Low Energy Electrons (SIMDALEE2). DOI: 10.1016/j.elspec.2019.02.003 (cit. on p. 20).

[56] D. Geelen et al. "Nonuniversal Transverse Electron Mean Free Path through Few-layer Graphene". *Phys. Rev. Lett.* 123 (8 2019). DOI: 10.1103/PhysRevLett.123.086802 (cit. on pp. 21, 24, 73, 74, 146).

[57] R Cimino et al. "Can low energy electrons affect high energy physics accelerators?" *Phys. Rev. Lett.* 93 (2004). revised version submitted on 2004-05-24 16:09:18. DOI: 10.1103/PhysRevLett.93.014801. URL: cds.cern.ch/record/712132 (cit. on pp. 22, 23, 157, 170).

[58] M. A. Furman et al. "Probabilistic model for the simulation of secondary electron emission". *Phys. Rev. ST Accel. Beams* 5 (12 2002). DOI: 10.1103/PhysRevSTAB.5.124404. URL: link.aps.org/doi/10.1103/PhysRevSTAB.5.124404 (cit. on pp. 22, 23, 97, 108, 157).

[59] Joseph Borovsky et al. "Do Impulsive Solar-Energetic-Electron (SEE) Events Drive High-Voltage Charging Events on the Nightside of the Moon?" *Frontiers in Astronomy and Space Sciences* 8 (May 2021). DOI: 10.3389/fspas.2021.655333 (cit. on p. 23).

[60] Yinghong Lin et al. "A new examination of secondary electron yield data". *Surface and Interface Analysis* 37.11 (2005). DOI: 10.1002/sia.2107 (cit. on p. 23).

[61] J. Cazaux et al. "Electron-induced secondary electron emission yield from condensed rare gases: Ne, Ar, Kr, and Xe". *Phys. Rev. B* 71 (3 2005). DOI: 10.1103/PhysRevB.71.035419 (cit. on pp. 23, 50).

[62] Eric Wulff et al. "Implementation and benchmarking of the Furman-Pivi model for Secondary Electron Emission in the PyECLOUD simulation code" (2019). URL: cds.cern.ch/record/2683285 (cit. on pp. 24, 170).

[63] Scholtz J.J et al. "Secondary electron emission properties". *Philips Journal of Research* 50.3 (1996). New Flat, Thin Display Technology. DOI: 10.1016/S0165-5817(97)84681-5 (cit. on p. 24).

[64] J. Cazaux. "Electron back-scattering coefficient below 5keV: Analytical expressions and surface-barrier effects". *Journal of Applied Physics* 112.8 (2012). DOI: 10.1063/1.4759367 (cit. on pp. 24, 27).

[65] H. Bruining. *Physics and Applications of Secondary Electron Emission*. Electronics and waves. McGraw-Hill Book Company, 1962. ISBN: 978-0-08-009014-6. DOI: 10.1016/C2013-0-01633-7 (cit. on pp. 25, 100).

[66] H Seiler. "Secondary electron emission in the scanning electron microscope". *Journal of Applied Physics* 54.11 (1983). DOI: 10.1063/1.332840 (cit. on p. 25).

[67] Adrianus J Dekker. *Solid state physics*. Prentice-Hall, 1957. DOI: 10.1063/1.3060172 (cit. on p. 25).

[68] Kirby R.E. et al. "Secondary electron emission yields from PEP-II accelerator materials". *Nuclear Instruments and Methods in Physics Research Section A: Accelerators, Spectrometers, Detectors and Associated Equipment* 469.1 (2001). DOI: 10.1016/S0168-9002(01)00704-5 (cit. on p. 25).

[69] Bernard Henrist et al. "Secondary electron emission data for the simulation of electron cloud" (2002). DOI: 10.5170/CERN-2002-001.75. URL: cds.cern.ch/record/585565 (cit. on p. 25).

[70] S. Liu et al. "Experimental studies on secondary electron emission characteristics of accelerator chamber materials". *CERN Yellow Rep. Conf. Proc.* 7 (2020). Ed. by Roberto Cimino et al. DOI: 10.23732/CYRCP-2020-007.109 (cit. on p. 25).

[71] M. Salehi et al. "Dependence of secondary-electron emission from amorphous materials on primary angle of incidence". *Journal of Applied Physics* 52.2 (1981). DOI: 10.1063/1.328791 (cit. on p. 25).

[72] H. Sørensen. "Secondary electron emission from solid hydrogen and deuterium resulting from incidence of keV electrons and hydrogen ions". *Journal of Applied Physics* 48.6 (1977). DOI: 10.1063/1.324035 (cit. on pp. 25, 154).

[73] H. Sørensen et al. "On the emission of electrons from solid H2 and D2 by bombardment with 1–3 keV electrons up to very large angles of incidence". *Journal of Applied Physics* 53.7 (1982). DOI: 10.1063/1.331402 (cit. on p. 25).

[74] M. Salehi et al. "Dependence of secondary-electron emission from amorphous materials on primary angle of incidence". *Journal of Applied Physics* 52.2 (1981). DOI: 10.1063/1.328791 (cit. on p. 25).

[75] V Baglin et al. *A Summary of Main Experimental Results Concerning the Secondary Electron Emission of Copper*. Tech. rep. revised version number 1 submitted on 2002-06-24 11:29:13. Geneva: CERN, 2001. URL: cds.cern.ch/record/512467 (cit. on pp. 25, 46, 112).

[76] R. Cimino et al. "Nature of the Decrease of the Secondary-Electron Yield by Electron Bombardment and its Energy Dependence". *Phys. Rev. Lett.* 109 (6 2012). DOI: 10.1103/PhysRevLett.109.064801 (cit. on pp. 25, 26, 46, 97, 103, 112).

[77] Michiru Nishiwaki et al. "Graphitization of inner surface of copper beam duct of KEKB positron ring". *Vacuum* 84.5 (2009). Proceedings of the 4th Vacuum and Surface Sciences Conference of Asia and Australia (VASSCAA-4) - Sessions on Vacuum Science and its Application. DOI: 10.1016/j.vacuum.2009.06.028 (cit. on pp. 25, 103).

[78] Rosanna Larciprete et al. "Evolution of the secondary electron emission during the graphitization of thin C films". *Applied Surface Science* 328 (2015). DOI: 10.1016/j.apsusc.2014.12.046 (cit. on pp. 25, 103).

[79] C Scheuerlein et al. "An AES study of the room temperature conditioning of technological metal surfaces by electron irradiation". *Applied Surface Science* 202.1 (2002). DOI: 10.1016/S0169-4332(02)00868-1 (cit. on pp. 25, 46, 103).

[80] Valentine Petit. "Conditioning of surfaces in particle accelerators". Dissertation. Institut Superieur de l'Aeronautique et de l'Espace, 2020. URL: hal.archives-ouvertes.fr/tel-02919120 (cit. on pp. 25, 102, 106).

[81] Valentine Petit et al. "Beam-induced surface modifications as a critical source of heat loads in the Large Hadron Collider". *Communications Physics* 4.1 (2021). DOI: 10.1038/s42005-021-00698-x (cit. on pp. 26, 96, 98, 102, 103).

[82] V Petit et al. "Origin and mitigation of the beam-induced surface modifications of the LHC beam screens". *Journal of Physics: Conference Series* 2420.1 (2023). DOI: 10.1088/1742-6596/2420/1/012088 (cit. on pp. 26, 98, 103).

[83] Marcel Himmerlich et al. "Efficient Combination of Surface Texturing and Functional Coating for Very Low Secondary Electron Yield Surfaces and Rough Nonevaporable Getter Films". *Advanced Materials Interfaces* n/a.n/a (). DOI: 10.1002/admi.202201671 (cit. on p. 27).

[84] Jacques Cazaux. "Calculated effects of work function changes on the dispersion of secondary electron emission data: Application for Al and Si and related elements". *Journal of Applied Physics* 110.2 (2011). DOI: 10.1063/1.3608046 (cit. on p. 27).

[85] J. Schaefer et al. "A contribution to the dependence of secondary electron emission from the work function and fermi energy". *Thin Solid Films* 13.1 (1972). DOI: 10.1016/0040-6090(72)90158-7. URL: www.sciencedirect.com/science/article/pii/0040609072901587 (cit. on p. 27).

[86] Ming Ye et al. "The total secondary electron yield of a conductive random rough surface". *Journal of Applied Physics* 125.4 (2019). DOI: 10.1063/1.5023769 (cit. on p. 27).

[87] Ming Ye et al. "Mechanism of total electron emission yield reduction using a micro-porous surface". *Journal of Applied Physics* 121.12 (2017). DOI: 10.1063/1.4978760 (cit. on p. 27).

[88] L. Wang et al. "Suppression of secondary emission in a magnetic field using triangular and rectangular surfaces". *Nuclear Instruments and Methods in Physics Research Section A: Accelerators, Spectrometers, Detectors and Associated Equipment* 571.3 (2007). DOI: 10.1016/j.nima.2006.11.039 (cit. on p. 27).

[89] Roberto Salemme et al. "First beam test of Laser Engineered Surface Structures (LESS) at cryogenic temperature in CERN SPS accelerator". *Journal of Physics: Conference Series* 1067 (2018). DOI: 10.1088/1742-6596/1067/8/082017 (cit. on pp. 27, 28, 122).

[90] Yangming Lin et al. "Insights into surface chemistry and electronic properties of sp2 and sp3-hybridized nanocarbon materials for catalysis". *Chem. Commun.* 53 (2017). DOI: 10.1039/C7CC02354E (cit. on p. 27).

[91] H. Niedrig. "Electron backscattering from thin films". *Journal of Applied Physics* 53.4 (1982). DOI: 10.1063/1.331005 (cit. on p. 27).

[92] Abrar Hussain et al. "Determination of electron backscattering coefficient of beryllium by a high-precision Monte Carlo simulation". *Nuclear Materials and Energy* 26 (2021). DOI: 10.1016/j.nme.2020.100862 (cit. on p. 27).

[93] R. Browning et al. "Empirical forms for the electron/atom elastic scattering cross sections from 0.1 to 30 keV". *Journal of Applied Physics* 76.4 (1994). DOI: 10.1063/1.357669 (cit. on p. 27).

[94] Shinotsuka H. et al. "Calculations of electron stopping powers for 41 elemental solids over the 50eV to 30keV range with the full Penn algorithm". *Nuclear Instruments and Methods in Physics Research Section B: Beam Interactions with Materials and Atoms* 270 (2012). DOI: 10.1016/j.nimb.2011.09.016 (cit. on p. 27).

[95] Gibaru Q. et al. "Monte-Carlo simulation and analytical expressions for the extrapolated range and transmission rate of low energy electrons [10eV-10keV] in 11 monoatomic materials". *Applied Surface Science* 570 (2021). DOI: 10.1016/j.apsusc.2021.151154 (cit. on p. 27).

[96] Chuan-Jong Tung et al. "CSDA Ranges of Electrons in Metals". *Chinese Journal of Physics* 17.1 (1979). DOI: 10.6122/CJP (cit. on p. 27).

[97] M. Angelucci et al. "Minimum thickness of carbon coating for multipacting suppression". *Phys. Rev. Research* 2 (3 2020). DOI: 10.1103/PhysRevResearch.2.032030 (cit. on pp. 27, 103, 106, 118).

[98] C Yin Vallgren et al. "Performance of Carbon Coatings for Mitigation of Electron Cloud in the SPS" (2011). URL: cds.cern.ch/record/1407930 (cit. on pp. 27, 118).

[99] Matthias Van Gompel et al. "Amorphous Carbon Thin Film Coating of the SPS Beamline: Evaluation of the First Coating Implementation" (2017). DOI: 10.18429/JACoW-IPAC2017-MOOCA3 (cit. on pp. 27, 118).

[100] V Baglin. "COLDEX: a tool to study cold surfaces in accelerators". *CERN Yellow Reports: Conference Proceedings*. Vol. 7. 2020. DOI: 10.23732/CYRCP-2020-007.165 (cit. on pp. 27, 28, 118).

[101] R. Salemme et al. "Recommissioning of the COLDEX Experiment at CERN" (2015). URL: cds.cern.ch/record/2141873 (cit. on pp. 27, 118).

[102] Roberto Salemme et al. "Amorphous Carbon Coatings at Cryogenic Temperatures with LHC Type Beams: First Results with the COLDEX Experiment". 2015. URL: cds.cern.ch/record/2141874 (cit. on pp. 27, 118).

[103] Roberto Salemme et al. "Vacuum Performance of Amorphous Carbon Coating at Cryogenic Temperature with Presence of Proton Beams" (2016). DOI: 10.18429/JACoW-IPAC2016-THPMY007. URL: cds.cern.ch/record/2207466 (cit. on pp. 27, 118, 173).

[104] Jie Wang et al. "Non-Evaporable Getter Ti-V-Hf-Zr Film Coating on Laser-Treated Aluminum Alloy Substrate for Electron Cloud Mitigation". *Coatings* 9.12 (2019). DOI: 10.3390/coatings9120839 (cit. on pp. 28, 130).

[105] David Bajek et al. “Role of surface microgeometries on electron escape probability and secondary electron yield of metal surfaces”. *Scientific Reports* 10 (2020). DOI: 10.1038/s41598-019-57160-w (cit. on p. 28).
[106] Elena Bez et al. “Influence of wavelength and accumulated fluence at picosecond laser-induced surface roughening of copper on secondary electron yield”. *Journal of Applied Physics* 133.3 (2023). DOI: 10.1063/5.0131916 (cit. on p. 28).
[107] Reza Valizadeh et al. “Low secondary electron yield engineered surface for electron cloud mitigation”. *Applied Physics Letters* 105.23 (2014). DOI: 10.1063/1.4902993 (cit. on pp. 28, 103).
[108] Sergio Calatroni et al. “First accelerator test of vacuum components with laser-engineered surfaces for electron-cloud mitigation”. *Physical Review Accelerators and Beams* 20 (2017). DOI: 10.1103/PhysRevAccelBeams.20.113201 (cit. on p. 28).
[109] Lucie Baudin. “Laser treated surfaces in particle accelerators: relation between superficial topography, particle adhesion and compatibility for ultra-high vacuum applications”. Presented 12 Oct 2020. 2020. URL: cds.cern.ch/record/2774965 (cit. on pp. 28, 118, 122).
[110] I Montero et al. “Low-secondary electron yield of ferromagnetic materials and magnetized surfaces”. *Proc. IPAC* 10 (2010). URL: cds.cern.ch/record/1287861 (cit. on p. 28).
[111] I Montero et al. “Reduction of Secondary Electron Yied (SEY) Figures on Smooth Metallic Surfaces by Means of Magnetic Roughness”. *Conf. Proc.* Vol. 130512. CERN-ACC-2013-0105. 2013. URL: cds.cern.ch/record/1576066 (cit. on p. 28).
[112] Leandro Olano et al. “Dynamic secondary electron emission in rough composite materials”. *Scientific reports* 9.1 (2019). DOI: 10.1038/s41598-019-50353-3 (cit. on p. 28).
[113] Paolo Chiggiato et al. “Ti-Zr-V non-evaporable getter films: From development to large scale production for the Large Hadron Collider”. *Thin Solid Films* 515 (2006). DOI: 10.1016/j.tsf.2005.12.218 (cit. on pp. 28, 124).
[114] Frederic Le Pimpec. “Etude de la desorption moleculaire induite par transitions electroniques dans les surfaces techniques” (2022). Presented on 19 Jun 2000. URL: cds.cern.ch/record/444304 (cit. on pp. 28, 126).
[115] F. Le Pimpec et al. “Properties of TiN and TiZrV thin film as a remedy against electron cloud”. *Nuclear Instruments and Methods in Physics Research Section A: Accelerators, Spectrometers, Detectors and Associated Equipment* 551.2 (2005). DOI: 10.1016/j.nima.2005.05.048 (cit. on p. 28).
[116] F. Le Pimpec et al. “Secondary Electron Yield Measurements of TiN Coating and TiZrV Getter Film” (2003). DOI: 10.48550/ARXIV.PHYSICS/0310071 (cit. on p. 28).
[117] J.G. Bednorz et al. “Possible high T_c superconductivity in the Ba-La-Cu-O system”. *Zeitschrift fur Physik B Condensed Matter* 64 (1986). DOI: 10.1007/BF01303701 (cit. on p. 29).
[118] Annette Bussmann-Holder et al. “High-temperature superconductors: underlying physics and applications”. *Zeitschrift fur Naturforschung B* 75.1-2 (2020). DOI: doi:10.1515/znb-2019-0103 (cit. on p. 29).
[119] Lucio Rossi et al. “HTS Accelerator Magnet and Conductor Development in Europe”. *Instruments* 5.1 (2021). DOI: 10.3390/instruments5010008. URL: www.mdpi.com/2410-390X/5/1/8 (cit. on p. 29).
[120] Jeroen Van Nugteren. “High Temperature Superconductor Accelerator Magnets”. Presented 10 Nov 2016. Dissertation. 2016. URL: cds.cern.ch/record/2228249 (cit. on p. 29).
[121] Xiaorong Wang et al. “REBCO – a silver bullet for our next high-field magnet and collider budget?” (2022). DOI: 10.48550/arXiv.2203.08736. URL: www.osti.gov/biblio/1862248 (cit. on p. 29).
[122] P Krkotić et al. “Evaluation of the nonlinear surface resistance of REBCO coated conductors for their use in the FCC-hh beam screen”. *Superconductor Science and Technology* 35.2 (2022). DOI: 10.1088/1361-6668/ac4465 (cit. on pp. 29, 127, 128, 174).
[123] J. Golm et al. “Thin Film (High Temperature) Superconducting Radiofrequency Cavities for the Search of Axion Dark Matter”. *IEEE Transactions on Applied Superconductivity* 32.4 (2022). DOI: 10.1109/TASC.2022.3147741 (cit. on p. 29).
[124] E. Metral. “Wake field, impedance and collective instability”. *Journal of Instrumentation* 16.10 (2021). DOI: 10.1088/1748-0221/16/10/P10009 (cit. on p. 29).
[125] Krkotić Patrick. “Evaluation of the Surface Impedance of ReBCO Coated Conductors and Requirements for Their Use as Beam Screen Materials for the FCC-hh”. Presented 25 Nov 2022. Dissertation (cit. on pp. 29, 128, 174, 175).
[126] Schou J. et al. “Desorption of cryogenic layers of the solid hydrogens by electron bombardment: The role of the metal substrate”. *Surface Science* 602.20 (2008). Proceedings of the 11th International Workshop on Desorption Induced by Electronics Transitions (DIET-11), Berlin, Germany, March, 11-15th, 2007. DOI: 10.1016/j.susc.2007.06.081 (cit. on pp. 30, 51, 150).
[127] Schou J. “Sputtering of frozen gases”. *Nuclear Instruments and Methods in Physics Research Section B: Beam Interactions with Materials and Atoms* 27.1 (1987). DOI: 10.1016/0168-583X(87)90020-6 (cit. on pp. 30, 44, 52, 53, 154).
[128] Andersson, S. et al. “Photodesorption of water ice - A molecular dynamics study”. 491.3 (2008). DOI: 10.1051/0004-6361:200810374 (cit. on p. 30).
[129] Marion Runne et al. “Excitonic excitations and desorption from rare-gas solids”. *Nuclear Instruments and Methods in Physics Research Section B: Beam Interactions with Materials and Atoms* 101.1 (1995). Desorption Induced by. DOI: 10.1016/0168-583X(95)00073-9 (cit. on pp. 31, 147, 151).
[130] P. A. Redhead. “Interaction of slow electrons with chemisorbed oxygen.” *Canadian Journal of Physics* 42.5 (1964). DOI: 10.1139/p64-083. URL: 10.1139/p64-083 (cit. on pp. 31–33, 37–39).

[131] P Feulner. "ESD neutrals from chemisorbed and physisorbed species: angular and energy distributions". *Desorption Induced by Electronic Transitions DIET II*. Springer, 1985. DOI: 10.1007/978-3-642-82547-7_19 (cit. on pp. 31, 32).

[132] Madey Theodore E. "History of desorption induced by electronic transitions". *Surface Science* 299-300 (1994). DOI: 10.1016/0039-6028(94)90700-5 (cit. on pp. 32, 33).

[133] John T. Yates. "Electron stimulated desorption, DIET, and photochemistry at surfaces: A personal recollection". *The Journal of Chemical Physics* 137.9 (2012). DOI: 10.1063/1.4746798. URL: 10.1063/1.4746798 (cit. on pp. 32–34).

[134] Mark D. Alvey et al. "Structure and chemistry of chemisorbed phosphorus trifluoride, phosphorus difluoride and phosphorus monofluoride on nickel(111): electron stimulated desorption ion angular distribution study". *Journal of the American Chemical Society* 110.6 (1988). DOI: 10.1021/ja00214a020. URL: 10.1021/ja00214a020 (cit. on p. 32).

[135] Yosioki ISIKAWA. "The Desorption of the Adsorbed Hydrogen on a Platinum Plate by the Impact of Slow Electrons". *Proceedings of the Imperial Academy* 18.5 (1942). DOI: 10.2183/pjab1912.18.246 (cit. on pp. 33, 38).

[136] Dietrich Menzel et al. "Desorption from Metal Surfaces by Low-Energy Electrons". *The Journal of Chemical Physics* 41.11 (1964). DOI: 10.1063/1.1725730. URL: 10.1063/1.1725730 (cit. on p. 33).

[137] Dietrich Menzel. "Thirty years of MGR: How it came about, and what came of it". *Nuclear Instruments and Methods in Physics Research Section B: Beam Interactions with Materials and Atoms* 101.1 (1995). Desorption Induced by. DOI: 10.1016/0168-583X(95)00060-7. URL: www.sciencedirect.com/science/article/pii/0168583X95000607 (cit. on p. 33).

[138] Peter R. Antoniewicz. "Model for electron- and photon-stimulated desorption". *Phys. Rev. B* 21 (9 1980). DOI: 10.1103/PhysRevB.21.3811. URL: link.aps.org/doi/10.1103/PhysRevB.21.3811 (cit. on pp. 34–36, 38).

[139] M. L. Knotek et al. "Ion Desorption by Core-Hole Auger Decay". *Phys. Rev. Lett.* 40 (14 1978). DOI: 10.1103/PhysRevLett.40.964. URL: link.aps.org/doi/10.1103/PhysRevLett.40.964 (cit. on pp. 34, 36, 38).

[140] R. D. Shannon. "Revised effective ionic radii and systematic studies of interatomic distances in halides and chalcogenides". *Acta Crystallographica Section A* 32.5 (1976). DOI: 10.1107/S0567739476001551 (cit. on p. 35).

[141] Pierre-Cyrille Dugal et al. "Mechanisms for Low-Energy (0.5-30 eV) Electron-Induced Pyrimidine Ring Fragmentation within Thymine- and Halogen-Substituted Single Strands of DNA". *The Journal of Physical Chemistry B* 104.23 (2000). DOI: 10.1021/jp9938112 (cit. on p. 37).

[142] Leo Albert Sala. "Low-energy Electron Induced Chemistry in Supported Molecular Films". Theses. Université Paris Saclay (COmUE), 2018. URL: theses.hal.science/tel-02073621 (cit. on p. 37).

[143] Esther Bohler et al. "Control of Chemical Reactions and Synthesis by Low-Energy Electrons". *Chemical Society reviews* 42 (Oct. 2013). DOI: 10.1039/c3cs60180c (cit. on p. 37).

[144] Sayyid S. et al. "Threshold behaviour in the process of electron stimulated desorption". *Surface Science* 62.2 (1977). DOI: 10.1016/0039-6028(77)90094-2. URL: www.sciencedirect.com/science/article/pii/0039602877900942 (cit. on p. 37).

[145] A. D. Bass et al. "Reactions induced by low energy electrons in cryogenic films (Review)". *Low Temperature Physics* 29.3 (2003). DOI: 10.1063/1.1542441. URL: 10.1063/1.1542441 (cit. on p. 38).

[146] Norman H Tolk et al. "Desorption induced by electronic transitions". *Nuclear Instruments and Methods in Physics Research Section B: Beam Interactions with Materials and Atoms* 2.1-3 (1984). DOI: 10.1007/978-3-642-45550-6 (cit. on p. 39).

[147] Wilhelm Brenig et al. *Desorption Induced by Electronic Transitions DIET II: Proceedings of the Second International Workshop, Schloss Elmau, Bavaria, October 15–17, 1984*. Vol. 4. Springer Science and Business Media, 2012. DOI: 10.1007/978-3-642-82547-7 (cit. on pp. 39, 52).

[148] Richard H Stulen et al. *Desorption Induced by Electronic Transitions, DIET III: Proceedings of the Third International Workshop, Shelter Island, New York, May 20–22, 1987*. Vol. 13. Springer Science and Business Media, 2013. DOI: 10.1007/978-3-642-73728-2 (cit. on p. 39).

[149] Gerhard Betz et al. *Desorption Induced by Electronic Transitions DIET IV: Proceedings of the Fourth International Workshop, Gloggnitz, Austria, October 2–4, 1989*. Vol. 19. Springer Science and Business Media, 2012. DOI: 10.1007/978-3-642-84145-3 (cit. on p. 39).

[150] Alan R Burns et al. *Desorption Induced by Electronic Transitions DIET V: Proceedings of the Fifth International Workshop, Taos, NM, USA, April 1–4, 1992*. Vol. 31. Springer Science and Business Media, 2013. DOI: 10.1007/978-3-642-78080-6 (cit. on p. 39).

[151] Theodore E. Madey et al. "9. Experimental Methods in Electron- and Photon-Stimulated Desorption". *Solid State Physics: Surfaces*. Ed. by Robert L. Park et al. Vol. 22. Methods in Experimental Physics. Academic Press, 1985. DOI: 10.1016/S0076-695X(08)60323-3 (cit. on p. 39).

[152] JL De Segovia. "Electron Stimulated Desorption (ESD): Principles, Techniques and its Applications for Surface Molecules Analysis". *Trends in Quantum Electronics* (1986). DOI: 10.1007/978-3-662-10624-2_18 (cit. on p. 39).

[153] Ramsier R.D. et al. "Electron-stimulated desorption: Principles and applications". *Surface Science Reports* 12.6 (1991). DOI: 10.1016/0167-5729(91)90013-N (cit. on p. 39).

[154] Ageev V.N. "Desorption induced by electronic transitions". *Progress in Surface Science* 47.1 (1994). DOI: 10.1016/0079-6816(94)90014-0 (cit. on p. 40).

[155] Ageev V.N. et al. "Studies of adsorption by electron-stimulated desorption and flash-filament methods". *Progress in Surface Science* 5 (1974). DOI: 10.1016/0079-6816(74)90002-1 (cit. on p. 40).

[156] A G Mathewson. *The effect of cleaning and other treatments on the vacuum properties of technological materials used in ultra-high vacuum*. Tech. rep. Geneva: CERN, 1987. URL: cds.cern.ch/record/183509 (cit. on pp. 41, 115).

[157] M.-H. Achard. *Desorption des gaz induite par des electrons et des ions de l'acier inoxydable, du cuivre OFHC, du titane et de l'aluminium purs*. Tech. rep. Geneva: CERN, 1976. URL: cds.cern.ch/record/314507 (cit. on pp. 41, 43, 45, 46, 109).

[158] Afshan Ashraf et al. "Study of Ultra-High-Vacuum Properties of Carbon-Coated Stainless Steel Beam Pipes for High-Energy Particle Accelerators". *Arabian Journal for Science and Engineering* 44.7 (2019). DOI: 10.1007/s13369-019-03761-6 (cit. on pp. 41, 47).

[159] Christina Yin Vallgren et al. "Low Secondary Electron Yield Carbon Coatings for Electron-cloud Mitigation in Modern Particle Accelerators" (2010). URL: cds.cern.ch/record/1309161 (cit. on p. 41).

[160] M Andritschky et al. "Synchrotron radiation induced neutral gas desorption from samples of vacuum chambers". *Vacuum* 38.8 (1988). DOI: 10.1016/0042-207X(88)90495-2 (cit. on pp. 41, 132).

[161] O.B. Malyshev. *Vacuum in Particle Accelerators: Modelling, Design and Operation of Beam Vacuum Systems*. John Wiley and Sons, 2020. DOI: 10.1002/9783527809134 (cit. on pp. 41, 42, 47, 48, 109, 114, 115, 131, 134, 151, 162, 163).

[162] K. Kennedy. "Electron Stimulated Desorption Rates from Candidate Vacuum Chamber Surfaces" (1986). DOI: 10.2172/1872213 (cit. on pp. 41, 47, 109, 114, 115, 131).

[163] N. R. Dean et al. "Glow discharge processing versus bakeout for aluminum storage ring vacuum chambers". *Journal of Vacuum Science and Technology* 15.2 (1978). DOI: 10.1116/1.569506 (cit. on pp. 42, 47).

[164] H. Stori. "An in situ glow discharge cleaning method for the LEP vacuum system". *Vacuum* 33.3 (1983). DOI: 10.1016/0042-207X(83)90008-8 (cit. on p. 42).

[165] Malev M.D. "Gas absorption and outgassing of metals". *Vacuum* 23.2 (1973). DOI: 10.1016/0042-207X(73)91515-7 (cit. on pp. 42, 47).

[166] O. B. Malyshev et al. "Effect of surface polishing and vacuum firing on electron stimulated desorption from 316LN stainless steel". *Journal of Vacuum Science and Technology A* 32.5 (2014). DOI: 10.1116/1.4887035 (cit. on pp. 42, 47, 84).

[167] C. Scheuerlein et al. "The assessment of metal surface cleanliness by XPS". *Applied Surface Science* 252.12 (2006). DOI: 10.1016/j.apsusc.2005.07.007 (cit. on p. 42).

[168] Y. Tito Sasaki. "A survey of vacuum material cleaning procedures: A subcommittee report of the American Vacuum Society Recommended Practices Committee". *Journal of Vacuum Science and Technology A* 9.3 (1991). DOI: 10.1116/1.577449 (cit. on p. 42).

[169] O. B. Malyshev et al. "Electron stimulated desorption from bare and nonevaporable getter coated stainless steels". *Journal of Vacuum Science and Technology A* 28.5 (2010). DOI: 10.1116/1.3478672 (cit. on p. 42).

[170] Oleg B. Malyshev et al. "Pumping and electron-stimulated desorption properties of a dual-layer nonevaporable getter". *Journal of Vacuum Science and Technology A* 34.6 (2016). DOI: 10.1116/1.4964612 (cit. on p. 42).

[171] O.B. Malyshev et al. "Electron-stimulated desorption from polished and vacuum fired 316LN stainless steel coated with Ti-Zr-Hf-V". *Journal of Vacuum Science and Technology A* 32.6 (2014). DOI: 10.1116/1.4897932. URL: 10.1116/1.4897932 (cit. on pp. 42, 47).

[172] F Billard et al. *Some results on the electron induced desorption yield of OFHC copper*. Tech. rep. Geneva: CERN, 2000. DOI: 10.17181/CERN.9UX2.0KJV. URL: cds.cern.ch/record/2805442 (cit. on pp. 43–45, 86, 108, 109).

[173] I R Collins et al. "Dynamic Gas Density in the LHC Interaction Regions 1 and 5 and 2 and 8 For Optics Version 6.3" (2001). URL: cds.cern.ch/record/691797 (cit. on pp. 44, 79).

[174] Noell J.O. et al. "Mechanisms of electron-stimulated desorption of protons from water: Gas, chemisorbed and ice phases". *Surface Science* 157.1 (1985). DOI: 10.1016/0039-6028(85)90639-9 (cit. on p. 44).

[175] Ali G. M. Abdulgalil et al. "Electron-Promoted Desorption from Water Ice Surfaces: Neutral Gas-Phase Products". *ACS Earth and Space Chemistry* 1.4 (2017). DOI: 10.1021/acsearthspacechem.7b00028 (cit. on p. 44).

[176] Remi Dupuy. "Photon and electron induced desorption from molecular ices". Presented 10 Oct 2019. Theses. Sorbonne Universite, 2019. URL: tel.archives-ouvertes.fr/tel-02354689 (cit. on pp. 44, 50, 51, 148).

[177] P. Rowntree et al. "Electron Stimulated Desorption of H2 from Chemisorbed Molecular Monolayers". *The Journal of Physical Chemistry* 100.11 (1996). DOI: 10.1021/jp9521159 (cit. on p. 44).

[178] Malyshev O.B. et al. "Electron stimulated desorption from aluminium alloy and aluminium coated stainless steel". *Vacuum* 85.12 (2011). Selected Papers from the 11th European Vacuum Conference, EVC-11 8th Iberian Vacuum Meeting, IVM-8 6th European Topical Conference on Hard Coatings, ETCHC-6, 20-24 September 2010, Salamanca, Spain. DOI: 10.1016/j.vacuum.2011.01.028 (cit. on p. 44).

[179] O. B. Malyshev et al. "Electron stimulated desorption from the 316-L stainless steel as a function of impact electron energy". *Journal of Vacuum Science and Technology A* 31.3 (2013). DOI: 10.1116/1.4798256 (cit. on pp. 44, 46, 47, 79, 109).

[180] Ding M.Q. et al. "Electron stimulated desorption of gases at technological surfaces of aluminium". *Vacuum* 39.5 (1989). DOI: 10.1016/0042-207X(89)90269-8 (cit. on p. 44).

[181] Suzuki K. et al. "Cross sections of electron stimulated desorption under technical vaccum conditions and 1 to 3 keV electron energies". *Applied Surface Science* 33-34 (1988). DOI: 10.1016/0169-4332(88)90323-6 (cit. on pp. 45, 108, 109).

[182] A.W. Molvik et al. "Experimental studies of electrons in a heavy-ion beam". *Nuclear Instruments and Methods in Physics Research Section A: Accelerators, Spectrometers, Detectors and Associated Equipment* 544.1 (2005). Proceedings of the 15th International Symposium on Heavy Ion Inertial Fusion. DOI: 10.1016/j.nima.2005.01.206 (cit. on pp. 45, 46).

[183] Sotiris Mouchtouris et al. "Multiscale Modeling of Low Pressure Plasma Etching Processes: Linking the Operating Parameters of the Plasma Reactor with Surface Roughness Evolution". *Plasma Processes and Polymers* 14.4-5 (). DOI: 10.1002/ppap.201600147 (cit. on pp. 46, 163).

[184] Cimino R. et al. "SEY and low-energy SEY of conductive surfaces". *Journal of Electron Spectroscopy and Related Phenomena* 241 (2020). Sources, Interaction with Matter, Detection and Analysis of Low Energy Electrons (SIMDALEE2). DOI: 10.1016/j.elspec.2019.06.008 (cit. on pp. 46, 103).

[185] Michiru Nishiwaki et al. "Electron stimulated gas desorption from copper material and its surface analysis". *Applied Surface Science* 169-170 (2001). DOI: 10.1016/S0169-4332(00)00764-9 (cit. on pp. 46, 47, 115).

[186] Bernard Henrist et al. "The variation of the secondary electron yield and of the desorption yield of copper under electron bombardment: Origin and impact on the conditioning of the LHC" (2002). URL: cds.cern.ch/record/566863 (cit. on pp. 46, 112).

[187] Hannah A.N. et al. "Characterisation of copper and stainless steel surfaces treated with laser ablation surface engineering". *Vacuum* 189 (2021). DOI: 10.1016/j.vacuum.2021.110210 (cit. on p. 46).

[188] Achard M.-H. et al. "The effect of bakeout temperature on the electron and ion induced gas desorption coefficients of some technological materials". *Vacuum* 29.2 (1979). DOI: 10.1016/S0042-207X(79)80335-8 (cit. on p. 46).

[189] M Pivi. "Beam Induced Electron Multipacting in the CERN Large Hadron Collider accelerator LHC". Presented on 23 Jun 2000. Dissertation. 2000. URL: cds.cern.ch/record/444457 (cit. on p. 47).

[190] Anashin V.V. et al. "Photon-stimulated desorption and the effect of cracking of condensed molecules in a cryogenic vacuum system". *Vacuum* 60.1 (2001). The Sixth European Vacuum Conference. DOI: 10.1016/S0042-207X(00)00239-6 (cit. on pp. 47, 79, 149).

[191] Baglin V et al. "Molecular desorption by synchrotron radiation and sticking coefficient at cryogenic temperatures for H2, CH4, CO and CO2". *Vacuum* 67.3 (2002). 7th European Vacuum Meeting/3rd European Topical Conference on Ha rd Coatings. DOI: 10.1016/S0042-207X(02)00226-9 (cit. on pp. 48, 49, 116).

[192] Malyshev O.B. et al. "Electron stimulated desorption from stainless steel at temperatures between -15 and +70 C". *Vacuum* 86.9 (2012). 5th International Symposium on Vacuum based Science and Technology SVST5 held at Kaiserslautern, Germany, 28th to 30th September 2010. DOI: 10.1016/j.vacuum.2012.01.002 (cit. on pp. 48, 49).

[193] J. Gomez-Goni et al. "Temperature dependence of the electron induced gas desorption yields on stainless steel, copper, and aluminum". *Journal of Vacuum Science and Technology A: Vacuum, Surfaces, and Films* 15 (1997). DOI: 10.1116/1.580852 (cit. on pp. 48, 109, 114, 115, 131).

[194] Elena Bez. "Molecular Desorption under Electron Bombardment at Cryogenic Temperatures of Candidate Surface Treatments for the HL-LHC Cryogenic Vacuum System". Private communication. Tubingen University, 2020 (cit. on p. 49).

[195] Sirvinskaite R. et al. "Electron stimulated desorption from cryogenic NEG-coated surfaces". *Proc. 10th International Particle Accelerator Conference (IPAC'19), Melbourne, Australia, 19-24 May 2019* (Melbourne, Australia). International Particle Accelerator Conference 10. Geneva, Switzerland: JACoW Publishing, 2019. ISBN: 978-3-95450-208-0. DOI: 10.18429/JACoW-IPAC2019-TUPTS114 (cit. on p. 49).

[196] H Tratnik. "Electron Stimulated Desorption of Condensed Gases on Cryogenic Surfaces". Presented on 01 Sep 2005. 2005. URL: http://cds.cern.ch/record/976630 (cit. on pp. 50–52, 150).

[197] Tratnik H. et al. "The desorption of condensed noble gases and gas mixtures from cryogenic surfaces". *Vacuum* 81.6 (2007). Proceedings of the European Vacuum Conference (EVC-9). DOI: 10.1016/j.vacuum.2005.11.064 (cit. on pp. 50–52, 150).

[198] Asena Kuzucan. "Secondary Electron Yield on Cryogenic Surfaces as a Function of Physisorbed Gases". Presented 12 Oct 2011. 2011. DOI: 10.1116/1.4736552. URL: cds.cern.ch/record/1374182 (cit. on pp. 50, 52, 145).

[199] Asena Kuzucan et al. "Secondary electron yield on cryogenic surfaces as a function of physisorbed gases". *Journal of Vacuum Science and Technology A* 30.5 (2012). DOI: 10.1116/1.4736552 (cit. on pp. 50, 143, 145).

[200] Agnieszka Chmielinska. "Secondary electron yield at low temperature for selected accelerator materials". Private communication. Cracow: AGH University of Science and Technology, 2016 (cit. on pp. 50, 145).

[201] Robert G. Lye et al. "Theory of Secondary Emission". *Phys. Rev.* 107 (4 1957). DOI: 10.1103/PhysRev.107.977. URL: link.aps.org/doi/10.1103/PhysRev.107.977 (cit. on p. 50).

[202] Robyn M. Meier et al. "Sputtering of water ice by keV electrons at 60 K". *Surface Science* 691 (2020). DOI: 10.1016/j.susc.2019.121509 (cit. on p. 51).

[203] de Jong A.M. et al. "Thermal desorption analysis: Comparative test of ten commonly applied procedures". *Surface Science* 233.3 (1990). DOI: 10.1016/0039-6028(90)90649-S (cit. on p. 53).

[204] C.-M. Chan et al. "An analysis of thermal desorption mass spectra. I." *Applications of Surface Science* 1.3 (1978). DOI: 10.1016/0378-5963(78)90038-7 (cit. on p. 53).

[205] C.-M. Chan et al. "An analysis of thermal desorption mass spectra. II". *Applications of Surface Science* 1.3 (1978). DOI: 10.1016/0378-5963(78)90039-9 (cit. on p. 53).

[206] Michael Schmid et al. “Analysis of Temperature-Programmed Desorption via Equilibrium Thermodynamics”. *ACS Physical Chemistry Au* 3.1 (2023). DOI: 10.1021/acsphyschemau.2c00031 (cit. on p. 53).
[207] Wolfgang Ranke. “Modern Methods in Heterogeneous Catalysis Research - Temperature Programmed Desorption”. Lecture. 2005 (cit. on pp. 53, 137).
[208] Michael Vollmer et al. “Analysis of fractional order thermal desorption”. *Surface Science* 187.2 (1987). DOI: 10.1016/S0039-6028(87)80067-5 (cit. on p. 53).
[209] R. Scott Smith et al. “Desorption Kinetics of Ar, Kr, Xe, N2, O2, CO, Methane, Ethane, and Propane from Graphene and Amorphous Solid Water Surfaces”. *The Journal of Physical Chemistry B* 120.8 (2016). DOI: 10.1021/acs.jpcb.5b10033 (cit. on pp. 54, 55, 134).
[210] M Polanyi et al. “The breeding and breakdown of molecules”. *Zeitschrift fur Physik* 33 (1925) (cit. on p. 54).
[211] Redhead P.A. “Thermal desorption of gases”. *Vacuum* 12.4 (1962). DOI: 10.1016/0042-207X(62)90978-8 (cit. on pp. 54, 55, 135).
[212] Assaf Paldor et al. “Xe interacting with porous silicon”. *Phys. Chem. Chem. Phys.* 12 (25 2010). DOI: 10.1039/B926692E (cit. on pp. 55, 56).
[213] Bisschop, S. E. et al. “Desorption rates and sticking coefficients for CO and N2 interstellar ices”. *A and A* 449.3 (2006). DOI: 10.1051/0004-6361:20054051 (cit. on pp. 63, 66).
[214] Leonard L. Levenson. “Condensation Coefficients of Argon, Krypton, Xenon, and Carbon Dioxide Measured with a Quartz Crystal Microbalance”. *Journal of Vacuum Science and Technology* 8.5 (1971). DOI: 10.1116/1.1316378 (cit. on p. 66).
[215] R. Cimino et al. “Detailed investigation of the low energy secondary electron yield of technical Cu and its relevance for the LHC”. *Phys. Rev. ST Accel. Beams* 18 (5 2015). DOI: 10.1103/PhysRevSTAB.18.051002 (cit. on pp. 67, 74).
[216] P. Feulner et al. “Simple ways to improve ”flash desorption” measurements from single crystal surfaces”. *Journal of Vacuum Science and Technology* 17.2 (1980). DOI: 10.1116/1.570537 (cit. on p. 67).
[217] Guido Van Rossum et al. *Python 3 Reference Manual*. Scotts Valley, CA: CreateSpace, 2009. DOI: 10.5555/1593511 (cit. on p. 68).
[218] González Gómez et al. “Practical Control of Multipactor Threshold and Insertion Losses on RF Satellite Devices and Study of Secondary Electron Emission for Multipactor and Electron Cloud Mitigation”. 2015. URL: hdl.handle.net/10486/674719 (cit. on p. 68).
[219] Matthew J Vincie. “The Challenges of Low-Energy Secondary Electron Emission Measurement”. 2019. URL: scholar.afit.edu/etd/3151 (cit. on p. 68).
[220] J.M. Hurst et al. “Assessing and Mitigating Surface Contamination of Carbon Electrode Materials”. *Chemistry of Materials* 31.18 (2019). DOI: 10.1021/acs.chemmater.9b01758 (cit. on pp. 73, 90).
[221] Roberto Cimino et al. “Vacuum chamber surface electronic properties influencing electron cloud phenomena”. *Applied Surface Science* 235 (2004). DOI: 10.1016/j.apsusc.2004.05.270 (cit. on pp. 74, 103).
[222] Jacques Cazaux. “Reflectivity of very low energy electrons (¡ 10 eV) from solid surfaces: Physical and instrumental aspects”. *Journal of Applied Physics* 111.6 (2012). DOI: 10.1063/1.3691956 (cit. on p. 74).
[223] Abraham. Savitzky et al. “Smoothing and Differentiation of Data by Simplified Least Squares Procedures.” *Analytical Chemistry* 36.8 (1964). DOI: 10.1021/ac60214a047 (cit. on pp. 74, 85, 114).
[224] L. A. Gonzalez et al. “The effect of structural disorder on the secondary electron emission of graphite”. *AIP Advances* 6.9 (2016). DOI: 10.1063/1.4963644 (cit. on p. 74).
[225] AD Cutter et al. “The ’aging’ mechanism in electron multipliers and operating life”. *42nd ASMS Conference on Mass Spectroscopy and Allied Topics*. 1994. URL: www.etp-ms.com/file-repository/15 (cit. on p. 77).
[226] Vincenc Nemanic et al. “Outgassing in thin wall stainless steel cells”. *Journal of Vacuum Science and Technology A* 17.3 (1999). DOI: 10.1116/1.581680 (cit. on pp. 79, 84).
[227] Kersevan R. et al. “Recent Developments of Monte-Carlo Codes Molflow+ and Synrad+”. *Proc. 10th International Particle Accelerator Conference (IPAC’19), Melbourne, Australia, 19-24 May 2019* (Melbourne, Australia). International Particle Accelerator Conference 10. Geneva, Switzerland: JACoW Publishing, 2019. ISBN: 978-3-95450-208-0. DOI: 10.18429/JACoW-IPAC2019-TUPMP037 (cit. on pp. 79, 200).
[228] W. K. Peterson et al. “Measurements of Energy and Angular Distributions of Secondary Electrons Produced in Electron-Impact Ionization of Helium”. *Phys. Rev. A* 5 (2 1972). DOI: 10.1103/PhysRevA.5.712 (cit. on p. 84).
[229] Rakhovskaia O et al. “Thresholds for electron stimulated desorption of neutral molecules from solid N2, CO, O2 and NO”. *Nuclear Instruments and Methods in Physics Research Section B: Beam Interactions with Materials and Atoms* 101.1 (1995). Desorption Induced by. DOI: 10.1016/0168-583X(95)00296-0 (cit. on pp. 86, 147).
[230] Hendrik Ulbricht et al. “Thermal desorption of gases and solvents from graphite and carbon nanotube surfaces”. *Carbon* 44.14 (2006). DOI: 10.1016/j.carbon.2006.05.040 (cit. on pp. 89, 134).
[231] R. Scott Smith et al. “Desorption Kinetics of Methanol, Ethanol, and Water from Graphene”. *The Journal of Physical Chemistry A* 118.37 (2014). DOI: 10.1021/jp501038z (cit. on pp. 89, 134).
[232] Stefano Sgobba. “Materials for high vacuum technology, an overview” (2007). DOI: 10.5170/CERN-2007-003.117. URL: cds.cern.ch/record/983744 (cit. on p. 93).
[233] Mauro Taborelli. *Cleaning and Surface Properties*. 2020. DOI: 10.48550/ARXIV.2006.01585 (cit. on p. 94).

[234] M Malabaila. *Operating procedure for chemical degreasing of parts for high-vacuum and ultra-high-vacuum applications*. Tech. rep. 2022 (cit. on p. 94).
[235] H. E. Farnsworth. "Electronic Bombardment of Metal Surfaces". *Phys. Rev.* 25 (1 1925). DOI: 10.1103/PhysRev.25.41 (cit. on p. 95).
[236] L A Gonzalez et al. "SEY from noble metals" (2020). DOI: 10.23732/CYRCP-2020-007.115. URL: cds.cern.ch/record/2736200 (cit. on pp. 97, 99–101).
[237] Christof Neumann et al. "Low-energy electron irradiation induced synthesis of molecular nanosheets: influence of the electron beam energy". *Faraday Discuss.* 227 (0 2021). DOI: 10.1039/C9FD00119K (cit. on p. 98).
[238] A. Tebyani et al. "Low-Energy Electron Irradiation Damage in Few-Monolayer Pentacene Films". *The Journal of Physical Chemistry C* 125.47 (2021). DOI: 10.1021/acs.jpcc.1c06749 (cit. on p. 98).
[239] Zuzana Pokorna. "Imaging the local density of electronic states by very low energy electron reflectivity". Dissertation. 2012. DOI: 10.13140/RG.2.2.22337.15201 (cit. on pp. 98, 145).
[240] F. Le Pimpec et al. "Electron conditioning of technical aluminium surfaces: Effect on the secondary electron yield". *Journal of Vacuum Science and Technology A* 23.6 (2005). DOI: 10.1116/1.2049306 (cit. on p. 99).
[241] D. R. Grosso et al. "Effect of the surface processing on the secondary electron yield of Al alloy samples". *Phys. Rev. ST Accel. Beams* 16 (5 2013). DOI: 10.1103/PhysRevSTAB.16.051003 (cit. on p. 99).
[242] Jun Tao. "Surface composition and corrosion behavior of an Al-Cu alloy". Theses. Université Pierre et Marie Curie - Paris VI, 2016. URL: https://theses.hal.science/tel-01412882 (cit. on p. 99).
[243] Iouri Bojko et al. "Influence of air exposures and thermal treatments on the secondary electron yield of copper". *Journal of Vacuum Science and Technology A* 18.3 (2000). DOI: 10.1116/1.582286 (cit. on p. 101).
[244] Madeline Brown et al. "Carbon-oxygen surface formation enhances secondary electron yield in Cu, Ag and Au". *Scientific Reports* 12 (2022). DOI: 10.1038/s41598-022-19924-9 (cit. on p. 101).
[245] Petit V. et al. "Origin and Mitigation of the Beam-Induced Surface Modifications of the LHC Beam Screens". *Proc. IPAC'22* (Bangkok, Thailand). International Particle Accelerator Conference 13. JACoW Publishing, Geneva, Switzerland, 2022, TUOXSP1. DOI: 10.18429/JACoW-IPAC2022-TUOXSP1 (cit. on pp. 102, 149).
[246] Suheyla Bilgen. "Dynamic pressure in particle accelerators: experimental measurements and simulation for the LHC". Dissertation. University of Paris-Saclay, 2020. URL: www.theses.fr/2020UPASP020 (cit. on pp. 102, 106).
[247] R. Larciprete et al. "Secondary electron yield of Cu technical surfaces: Dependence on electron irradiation". *Phys. Rev. ST Accel. Beams* 16 (1 2013). DOI: 10.1103/PhysRevSTAB.16.011002 (cit. on p. 103).
[248] C. Scheuerlein et al. "Electron stimulated carbon adsorption in ultrahigh vacuum monitored by Auger electron spectroscopy". *Journal of Vacuum Science and Technology A* 20.1 (2002). DOI: 10.1116/1.1424273 (cit. on p. 105).
[249] A. Shih et al. "Secondary electron emission studies". *Applied Surface Science* 111 (1997). Proceedings of the International Vacuum Electron Sources Conference 1996. DOI: 10.1016/S0169-4332(96)00729-5 (cit. on p. 106).
[250] Inguimbert C. et al. "Modelling the impact on the secondary electron yield of carbon layers of various thicknesses on copper substrate". *Nuclear Instruments and Methods in Physics Research Section B: Beam Interactions with Materials and Atoms* 526 (2022). DOI: 10.1016/j.nimb.2022.05.006 (cit. on p. 106).
[251] Kenji Nishimura et al. "Influence of Surface Roughness on Secondary Electron Emission and Electron Backscattering from Metal Surface". *Japanese Journal of Applied Physics* 33.8R (1994). DOI: 10.1143/JJAP.33.4727 (cit. on p. 106).
[252] Qichen Song. "Phonon and electron transport through interfaces and disordered structures". Presented 2022. Dissertation. Massachusetts Institute of Technology. Department of Mechanical Engineering, 2022. URL: hdl.handle.net/1721.1/143341 (cit. on pp. 107, 141).
[253] VL Auslender et al. "Desorption of gases from metallic surfaces under electron bombardment(Gas desorption from copper and stainless steel surfaces under electron bombardment)" (1966). URL: ntrl.ntis.gov/NTRL/dashboard/searchResults/titleDetail/N6725922.xhtml (cit. on pp. 109, 132).
[254] M. Minissale et al. "Quantum Tunneling of Oxygen Atoms on Very Cold Surfaces". *Phys. Rev. Lett.* 111 (5 2013). DOI: 10.1103/PhysRevLett.111.053201 (cit. on p. 111).
[255] C. Benvenuti et al. "Surface cleaning efficiency measurements for UHV applications". *Vacuum* 53.1 (1999). DOI: h10.1016/S0042-207X(98)00364-9 (cit. on p. 115).
[256] D. Edwards. "Ion and electron desorption of neutral molecules from stainless steel (304)". *Journal of Vacuum Science and Technology* 16.2 (1979). DOI: 10.1116/1.570077 (cit. on p. 115).
[257] J. Kouptsidis et al. *Reduction of the Photoelectron Induced Gas Desorption in the PETRA Vacuum System by In-Situ Argon Glow Discharge Cleaning*. Tech. rep. DESY-76-049. 1976. DOI: 10.3204/PUBDB-2017-12683 (cit. on p. 116).
[258] V Baglin. *Measurement of the primary photodesorption yield at 4.2 K, 77 K and room temperature in a quasi-closed geometry*. Tech. rep. Geneva: CERN, 1996. URL: cds.cern.ch/record/304957 (cit. on p. 116).
[259] Daniela Torres-Diaz et al. "Cryogenic Chemistry and Quantitative Non-Thermal Desorption from Pure Methanol Ices: High-Energy Electron versus X-Ray Induced Processes". *ChemPhysChem* n/a.n/a (). DOI: 10.1002/cphc.202200912 (cit. on p. 116).
[260] Jijil JJ. Nivas et al. "Laser-induced periodic surface structuring for secondary electron yield reduction of copper: dependence on ambient gas and wavelength". *Applied Surface Science* 622 (2023). DOI: 10.1016/j.apsusc.2023.156908 (cit. on p. 123).

[261] Frantisek Sutara et al. “Surface characterization of activated Ti-Zr-V NEG coatings”. *Vacuum* 83.5 (2009). DOI: 10.1016/j.vacuum.2008.08.002 (cit. on p. 125).
[262] Y. Gao et al. “Effect of the film thickness on electron stimulated desorption yield from Ti-Zr-V coating”. *Journal of Instrumentation* 17.08 (2022). DOI: 10.1088/1748-0221/17/08/P08025 (cit. on p. 126).
[263] J Horvat. “Nanopinning in high-temperature superconductors”. *Encyclopedia of nanoscience and nanotechnology*. Vol. 7. 218. American Scientific Publishers, 2004. DOI: 10.1166/000000004323036702 (cit. on p. 127).
[264] Filip Antoncik et al. “Nanosized Pinning Centers in the Rare Earth-Barium-Copper-Oxide Thin-Film Superconductors”. *Nanomaterials* 10.8 (2020). DOI: 10.3390/nano10081429 (cit. on p. 127).
[265] T Puig et al. “Coated conductor technology for the beam screen chamber of future high energy circular colliders”. *Superconductor Science and Technology* 32.9 (2019). DOI: 10.1088/1361-6668/ab2e66 (cit. on pp. 128, 174).
[266] Alessandro et al. Leveratto. “Future Circular Collider beam screen: progress on Tl-1223 HTS coating”. *Superconductor Science and Technology* 33 (2020). DOI: 10.1088/1361-6668/ab7fbd (cit. on p. 128).
[267] N Ishikawa et al. “Defect production and recovery in high-Tc superconductors irradiated with electrons and ions at low temperature”. *Journal of Nuclear Materials* 258-263 (1998). DOI: 10.1016/S0022-3115(98)00224-4 (cit. on p. 128).
[268] B.D. Weaver et al. “Radiation effects in high temperature superconducting films and devices for the NRL high temperature superconductivity space experiment”. *IEEE Transactions on Nuclear Science* 38.6 (1991). DOI: 10.1109/23.124106 (cit. on p. 128).
[269] Aram Sahakyan et al. “Electron irradiation effects in doped high temperature superconductors YBa2Cu3-x MxOy (M = Fe, Ni; x=0; x=0:01)”. *Open Physics* 6.4 (2008). DOI: doi:10.2478/s11534-008-0123-0 (cit. on p. 128).
[270] Prashanta Mani Niraula et al. “Particle Irradiation Induced Defects in High Temperature Superconductors”. *MRS Advances* 4.2 (2019). DOI: 10.1557/adv.2019.143 (cit. on p. 128).
[271] J. Giapintzakis et al. “Production and identification of flux-pinning defects by electron irradiation in YBa2Cu3O7-x single crystals”. *Phys. Rev. B* 45 (18 1992). DOI: 10.1103/PhysRevB.45.10677 (cit. on p. 128).
[272] Rebecca Grinham et al. “A Review of Outgassing and Methods for its Reduction”. *Applied Science and Convergence Technology* 26 (2017). DOI: 10.5757/ASCT.2017.26.5.95 (cit. on p. 131).
[273] R. Ishida et al. “Application of electron stimulated desorption for hydrogen removal from graphite”. *Journal of Nuclear Materials* 307-311 (2002). DOI: 10.1016/S0022-3115(02)01267-9 (cit. on p. 132).
[274] V Baglin. “Vacuum transients during LHC operation” (2004). URL: cds.cern.ch/record/726331 (cit. on p. 134).
[275] R. Salemme et al. “Vacuum Performance of Amorphous Carbon Coating at Cryogenic Temperature with Presence of Proton Beams”. *Proc. of International Particle Accelerator Conference (IPAC'16), Busan, Korea, May 8-13, 2016* (Busan, Korea). International Particle Accelerator Conference 7. Geneva, Switzerland: JACoW, 2016. DOI: doi:10.18429/JACoW-IPAC2016-THPMY007 (cit. on p. 136).
[276] L. Spallino et al. “On the compatibility of porous surfaces with cryogenic vacuum in future high-energy particle accelerators”. *Applied Physics Letters* 114.15 (2019). DOI: 10.1063/1.5085754 (cit. on p. 136).
[277] L. Spallino et al. “Thermal desorption of cryopumped gases from laser treated copper”. *Phys. Rev. Accel. Beams* 23 (6 2020). DOI: 10.1103/PhysRevAccelBeams.23.063201 (cit. on p. 136).
[278] Maria Kulawik et al. “STM studies of ordered (31x31)R9° CO islands on Ag(111)”. *Physical Review B, v.71, 153405-1-153405-4 (2005)* 71 (2005). DOI: 10.1103/PhysRevB.71.153405 (cit. on p. 137).
[279] Jiao He et al. “Binding Energy of Molecules on Water Ice: Laboratory Measurements and Modeling”. *The Astrophysical Journal* 825 (2016). DOI: 10.3847/0004-637X/825/2/89 (cit. on p. 137).
[280] Kaori Takeuchi et al. “Adsorption of CO2 on Graphene: A Combined TPD, XPS, and vdW-DF Study”. *The Journal of Physical Chemistry C* 121.5 (2017). DOI: 10.1021/acs.jpcc.6b11373 (cit. on p. 137).
[281] Mark Collings et al. “Probing model interstellar grain surfaces with small molecules”. *Monthly Notices of the Royal Astronomical Society* 449 (2015). DOI: 10.1093/mnras/stv425 (cit. on p. 137).
[282] The International Union of Pure et al. *Roughness factor definition*. URL: goldbook.iupac.org/terms/view/R05419 (cit. on p. 139).
[283] Xiao-Chuan Hu et al. “Monte Carlo simulation of secondary electron emission from an N2-adsorbed layer on a Cu surface”. *Results in Physics* 19 (2020). DOI: 10.1016/j.rinp.2020.103475 (cit. on p. 143).
[284] Y. Bojko et al. *Measurements of the Secondary Electron Emission from Rare Gases at 4.2K*. Tech. rep. 2013. arXiv: 1302.2334. URL: cds.cern.ch/record/1514932 (cit. on p. 143).
[285] Arnold Adams et al. “Practical range and energy loss of 0.1-3 keV electrons in thin films of N2, O2, Ar, Kr, and Xe”. *Phys. Rev. B* 22 (9 1980). DOI: 10.1103/PhysRevB.22.4258 (cit. on p. 144).
[286] R. Zdyb et al. “Inelastic mean free path from reflectivity of slow electrons”. *Phys. Rev. B* 87 (7 2013). DOI: 10.1103/PhysRevB.87.075436 (cit. on pp. 145, 146).
[287] G. Perluzzo et al. “Thickness-dependent interference structure in the 0-15 eV electron transmission spectra of rare-gas films”. *Phys. Rev. B* 30 (8 1984). DOI: 10.1103/PhysRevB.30.4292. URL: link.aps.org/doi/10.1103/PhysRevB.30.4292 (cit. on p. 145).
[288] Jianwei Fang et al. “Cryogenic secondary electron yield measurements on structural materials applied in particle accelerators”. *Nuclear Instruments and Methods in Physics Research Section A: Accelerators, Spectrometers, Detectors and Associated Equipment* 1027 (2022). DOI: 10.1016/j.nima.2021.166292 (cit. on p. 145).

[289] Na Zhang et al. "Experimental research on influence of gas adsorption on secondary electron emission of copper surface". *Micron* 142 (2021). DOI: 10.1016/j.micron.2020.103009 (cit. on p. 145).
[290] Z. Pokorna et al. "Mapping the Local Density of States by Very-Low-Energy Scanning Electron Microscope". *Materials Transactions* 51.2 (2010). DOI: 10.2320/matertrans.MC200921 (cit. on p. 145).
[291] J.R. Smith et al. "Self-consistent electronic structure calculation for nitrogen chemisorbed on copper (100)". *Solid State Communications* 24.4 (1977). DOI: 10.1016/0038-1098(77)90206-X (cit. on p. 145).
[292] Sarka Mikmekova et al. "Effect of native oxide on the crystal orientation contrast in SEM micrographs obtained at hundreds, tens and units of eV". *Ultramicroscopy* 220 (2021). DOI: 10.1016/j.ultramic.2020.113144 (cit. on p. 145).
[293] Ivo Konvalina et al. "Low-Energy Electron Inelastic Mean Free Path of Graphene Measured by a Time-of-Flight Spectrometer". *Nanomaterials* 11.9 (2021). DOI: 10.3390/nano11092435 (cit. on p. 145).
[294] M Knoll et al. "Electron scanner for structure imaging of surfaces and thin layers". *journal for physics* 113.3 (1939). DOI: 10.1007/BF01341357 (cit. on p. 145).
[295] Neal Nickles. "The role of bandgap in the secondary electron emission of small bandgap semiconductors Studies of graphitic carbon" (2002). DOI: 10.26076/2f99-4acc (cit. on p. 146).
[296] Yorick Maxence Delaup. "Measurement of Deuterium in a-C coatings". Talk. 2022. URL: indico.cern.ch/event/1125379/ (cit. on p. 146).
[297] Newman D S et al. "Metastable excitation measurements in CO and N2 by high-resolution electron impact, using a low work function detector". *Journal of Physics B: Atomic and Molecular Physics* 16.12 (1983). DOI: 10.1088/0022-3700/16/12/019 (cit. on p. 147).
[298] Lloyd C R et al. "Excitation of the first excited state in argon by electron bombardment". *Journal of Physics B: Atomic and Molecular Physics* 5.2 (1972). DOI: 10.1088/0022-3700/5/2/010 (cit. on p. 147).
[299] A. D. Bass et al. "Erratum: Feshbach electron resonances in solid Ar: Opening of electronically inelastic channels [Phys. Rev. B 57, 14 914 (1998)]". *Phys. Rev. B* 60 (7 1999). DOI: 10.1103/PhysRevB.60.5078 (cit. on p. 147).
[300] Coletti, F. et al. "Electron stimulated desorption of solid argon via exciton creation". *J. Physique Lett.* 45.9 (1984). DOI: 10.1051/jphyslet:01984004509046700 (cit. on p. 147).
[301] G. Iadarola et al. "Electron cloud in the CERN accelerators (PS, SPS, LHC)". *AIP Conf. Proc. C* 1206051 (2013). Joint INFN-CERN-EuCARD-AccNet Workshop on Electron-Cloud Effects: ECLOUD'12. DOI: 10.5170/CERN-2013-002.19 (cit. on p. 147).
[302] R. Dupuy et al. "Mechanism of Indirect Photon-Induced Desorption at the Water Ice Surface". *Phys. Rev. Lett.* 126 (15 2021). DOI: 10.1103/PhysRevLett.126.156001 (cit. on p. 148).
[303] Mathieu Bertin et al. "Indirect Ultraviolet Photodesorption from CO:N2 Binary Ices - an Efficient Grain-gas Process". *The Astrophysical Journal* 779 (2013). DOI: 10.1088/0004-637X/779/2/120 (cit. on p. 148).
[304] Francois Dulieu et al. "How micron-sized dust particles determine the chemistry of our Universe". *Scientific reports* 3.1 (2013). DOI: 10.1038/srep01338 (cit. on p. 149).
[305] V. Baglin et al. "Synchrotron radiation studies of the LHC dipole beam screen with COLDEX". *8th European Particle Accelerator Conference (EPAC 2002)*. June 2002. URL: http://cds.cern.ch/record/566864 (cit. on p. 149).
[306] C.-H. Huang et al. "Effects of 150-1000 eV Electron Impacts on Pure Carbon Monoxide Ices Using the Interstellar Energetic-Process System (IEPS)". *The Astrophysical Journal* 889.1 (2020). DOI: 10.3847/1538-4357/ab5dbe (cit. on p. 149).
[307] Ole Ellegaard et al. "Electronic sputtering of solid nitrogen and oxygen by keV electrons". *Surface science* 167.2-3 (1986). DOI: 10.1016/0039-6028(86)90718-1 (cit. on pp. 149, 152).
[308] Takato Hirayama. "Electronic Excitations and Decay Processes in Condensed Rare Gases Studied by Low-energy Electron, Photon, and Ion Impact" (2016). 77th IUVSTA Workshop at Fuefuki City (cit. on p. 151).
[309] W. L. Brown et al. "Electronically Induced Desorption and Luminescence from Multilayer Argon Films". *Desorption Induced by Electronic Transitions DIET II*. Ed. by Wilhelm Brenig et al. Berlin, Heidelberg: Springer Berlin Heidelberg, 1985. ISBN: 978-3-642-82547-7. DOI: 10.1007/978-3-642-82547-7_26 (cit. on pp. 151, 152).
[310] Nasrin Mirsaleh-Kohan et al. "Chemical transformation of molecular ices containing N2O and C2D2 by low energy electrons: New chemical species of astronomical interest". *The Journal of Chemical Physics* 154.22 (2021). DOI: 10.1063/5.0040884 (cit. on p. 152).
[311] Satorre M.A. et al. "Density of CH4, N2 and CO2 ices at different temperatures of deposition". *Planetary and Space Science* 56.13 (2008). Advances in Planetary Sciences: AOGS 2007. DOI: 10.1016/j.pss.2008.07.015 (cit. on p. 153).
[312] Jean-Hugues Fillion et al. "Vacuum-UV Photodesorption from Compact Amorphous Solid Water: Photon Energy Dependence, Isotopic and Temperature Effects". *ACS Earth and Space Chemistry* 6.1 (2022). DOI: 10.1021/acsearthspacechem.1c00302 (cit. on p. 154).
[313] Heide H.-G. "Observations on ice layers". *Ultramicroscopy* 14.3 (1984). DOI: 10.1016/0304-3991(84)90095-0 (cit. on p. 154).
[314] Baragiola R.A. et al. "Sputtering of water ice". *Nuclear Instruments and Methods in Physics Research Section B: Beam Interactions with Materials and Atoms* 209 (2003). Fifth International Symposium on Swift Heavy Ions in Matter. DOI: 10.1016/S0168-583X(02)02052-9 (cit. on p. 154).
[315] Gerhard Betz et al. "Sputtering of multicomponent material". *Sputtering by Particle Bombardment II* 52 (1983). DOI: 10.1007/3-540-12593-0_2 (cit. on p. 167).

[316] Michael Anthony Nastasi et al. *Ion implantation and synthesis of materials*. Vol. 80. Springer, 2006. DOI: 10.1007/978-3-540-45298-0_12 (cit. on p. 167).
[317] et al. Luis Antonio Gonzalez Gomez. *Photodesorption Studies on FCC-hh Beam Screen Prototypes at KARA*. FCC Week 2019. 2019. URL: indico.cern.ch/event/727555/contributions/3447250 (cit. on p. 169).
[318] Frank Zimmermann. "Electron cloud effects in the LHC" (2002). DOI: 10.5170/CERN-2002-001.47. URL: cds.cern.ch/record/585562 (cit. on p. 170).
[319] G. Arduini et al. "Present understanding of electron cloud effects in the Large Hadron Collider". *Conf. Proc. C* 030512 (2003). URL: cds.cern.ch/record/620194 (cit. on p. 170).
[320] Philipp Dijkstal et al. "Simulation studies on the electron cloud build-up in the elements of the LHC Arcs at 6.5 TeV" (2017). URL: cds.cern.ch/record/2289940 (cit. on p. 170).
[321] Giovanni Iadarola et al. "MD421: Electron cloud studies on 25 ns beam variants (BCMS, 8b+4e)" (2017). URL: cds.cern.ch/record/2260998 (cit. on p. 170).
[322] S. Bilgen et al. "Dynamic pressure evolution during the LHC operation". *Phys. Rev. Accel. Beams* 25 (8 2022). DOI: 10.1103/PhysRevAccelBeams.25.083101 (cit. on p. 171).
[323] Artur Romanov. "Superconducting Coated Conductors for Proton Beam Screens in High-Energy Particle Accelerators". Presented 19 May 2022. PhD thesis. Universitat Autonoma de Barcelona, 2022. DOI: 10.17181/CERN.4W8R.NSGX. URL: hdl.handle.net/10803/675654 (cit. on pp. 174, 175).
[324] Vincent Baglin. *Cryopumping and Vacuum Systems*. 2020. DOI: 10.48550/ARXIV.2006.01574. URL: arxiv.org/abs/2006.01574 (cit. on p. 174).
[325] Richard E Honig et al. "Vapor pressure data for some common gases". *RCA review* 21.3 (1960) (cit. on p. 174).
[326] Philippe Lebrun et al. "Beyond the Large Hadron Collider: A First Look at Cryogenics for CERN Future Circular Colliders". *Physics Procedia* 67 (2015). Proceedings of the 25th International Cryogenic Engineering Conference and International Cryogenic Materials Conference 2014. DOI: 10.1016/j.phpro.2015.06.130 (cit. on p. 174).
[327] Yoseph Bar-Cohen. *High temperature materials and mechanisms*. Vol. 44. CRC Press Boca Raton, FL, USA: 2014. DOI: 10.1201/b16545-18 (cit. on p. 175).
[328] *Lab report 4: Defining accuracy, precision and Trueness*. Accessed: 2022-12-23. 2022. URL: www.artel.co/learning%5C_center/defining-accuracy-precision-and-trueness/ (cit. on p. 197).
[329] John Cunningham McLennan et al. "The luminescence of solid nitrogen under cathode ray bombardment". *Proceedings of the Royal Society of London. Series A, Containing Papers of a Mathematical and Physical Character* 116.773 (1927). URL: www.jstor.org/stable/94711 (cit. on p. 198).
[330] O. Oehler et al. "Luminescence spectra of solid nitrogen excited by electron impact". *The Journal of Chemical Physics* 66.5 (1977). DOI: 10.1063/1.434171 (cit. on p. 198).
[331] J.M. Jimenez et al. "Observations, Analysis and Mitigation of Recurrent LHC Beam Dumps Caused by Fast Losses in Arc Half-Cell 16L2". *Proc. 9th International Particle Accelerator Conference (IPAC'18), Vancouver, BC, Canada, April 29-May 4, 2018*. International Particle Accelerator Conference 9. Geneva, Switzerland: JACoW Publishing, 2018. DOI: 10.18429/JACoW-IPAC2018-MOPMF053 (cit. on p. 198).
[332] L Mether et al. "16L2: Operation, Observations and Physics Aspects" (2019). URL: cds.cern.ch/record/2813522 (cit. on p. 198).

Appendix

Uncertainty analysis

The uncertainty analysis was performed for all the measured quantities: SEY, ESD yield, electron dose and electrodesorbed gas quantity. The approach is equivalent for all these quantities, so it only will be illustrated on the ESD yield uncertainty analysis and the remaining quantities are summarised in Table 6.5.

Starting with the expression to calculate the ESD yield η, as derived in the Experimental section 4 and used throughout the manuscript:

$$\eta = \frac{C(i - i_{BG})}{k_B T k} \Big/ \frac{I_C + I_S}{q_e} \tag{6.21}$$

The common approach to uncertainty propagation uses partial derivatives as sensitivity factors to weight the partial uncertainties according to their actual influence on the output value, here the ESD yield η_j. Hence, the uncertainty derivation starts by taking partial derivatives $\partial\eta/\partial x_i$ of the calculated quantity η_j with respect to all the input quantities generalised as x_j, but is in practice the currents on sample I_S and collector I_S, RGA currents (prop. to partial pressure) i_j and $i_{j,BG}$, temperature T, RGA absolute sensitivity k_j and collector conductance C_j. Indeed, the calculation is to be done for each given gas j, but the gas index j is omitted here for clarity in order to bring focus on the uncertainty calculation. The partial derivatives of η with respect to all the input variables derive as follows:

$$\begin{aligned}
\frac{\partial\eta}{\partial C} &= \frac{(i - i_{BG})}{k_B T k} \Big/ \frac{I_C + I_S}{q_e} \\
\frac{\partial\eta}{\partial i} &= \frac{C}{k_B T k} \Big/ \frac{I_C + I_S}{q_e} \\
\frac{\partial\eta}{\partial i_{BG}} &= \frac{-C}{k_B T k} \Big/ \frac{I_C + I_S}{q_e} \\
\frac{\partial\eta}{\partial T} &= \frac{-C(i - i_{BG})}{k_B T^2 k} \Big/ \frac{I_C + I_S}{q_e} \\
\frac{\partial\eta}{\partial k} &= \frac{-C(i - i_{BG})}{k_B T k^2} \Big/ \frac{I_C + I_S}{q_e} \\
\frac{\partial\eta}{\partial I_S} &= \frac{-C(i - i_{BG})}{k_B T k} \Big/ \frac{(I_C + I_S)^2}{q_e} \\
\frac{\partial\eta}{\partial I_C} &= \frac{-C(i - i_{BG})}{k_B T k} \Big/ \frac{(I_C + I_S)^2}{q_e}
\end{aligned} \tag{6.22}$$

Systematic and stochastic uncertainties of each measured value are calculated separately and then added into the combined uncertainty. The square summation formula 6.23 applies to summations when calculating both systematic and stochastic uncertainties. For completeness, linear summation leads to overestimating the uncertainty.

$$s^2_{\eta,comb.} = s^2_{\eta,syst.} + s^2_{\eta,stoch.} \tag{6.23}$$

The systematic and stochastic uncertainties, $s_{\eta,syst.}$ and $s_{\eta,stoch.}$ are calculated separately, but in exactly the same manner. The uncertainty s_{x_i} of each input variable x_i is weighted by the square of its partial derivative $\partial\eta/\partial x_i$, listed amongst eqs. 6.22, evaluated at the working point, i.e. around the typical value, as listed in 6.5. The contributions of all uncertainties are weighted by their partial derivatives squared and added using the square sum, as in eq. 6.24:

$$s_\eta^2 = \sum_{i=1}^{N} (\frac{\partial \eta}{\partial x_i})^2 s_{x_i}^2 \tag{6.24}$$

Having the analytical solution, the following information is necessary to evaluate combined uncertainty on the η. First, the typical value of each variable is needed, along with systematic and stochastic uncertainty representative of this input variable. Second, the partial derivatives to take into account the weight of each variable's contribution to the final uncertainty.

Table 6.5 lists values of each input variable that are typical for an ESD measurement. The listed are used to calculate the numerical value of each partial derivative around the working point. The collector conductance C_j is derived and taken from the Experimental section 4.14. The background subtraction of sample and collector currents, I_S and I_C is avoided, as it can be considered negligible in this experimental arrangement. The table lists uncertainties in % values to maintain clarity (at 1σ confidence interval) but absolute numbers are indeed used for the calculations.

Quantity		**Typical values**	**Uncert. Syst.**	**Uncert. Stoch.**	**Uncert. Comb.**	**% of** $s_{\eta_{j,comb.}}$
Temperature	T	300 K	1.5 %	1.5 %	1.5 %	0.2 %
Conductance	C_j	21.8 l/s	20 %		20 %	44.4 %
RGA current	i_j	10^{-9} A		5 %	5 %	3.4 %
RGA curr. BG	$i_{j,BG}$	10^{-10} A		5 %	5 %	0 %
RGA sensitivity	k_j	0.5 A/mbar	20 %		20 %	44.4 %
Sample current	I_S	-1.10^{-6} A	1.5 %	5 %	5 %	0.8 %
Collector curr.	I_C	2.10^{-6} A	1.5 %	5 %	5 %	6.8 %
Diameter	d	3 mm	7 %	7 %	10 %	
ESD yield	η_j	0.1 molecule/e^-	28 %	10 %	30 %	
SEY	δ	2 e^-/e^-	3 %	3 %	5 %	
e^- dose	D	1 mC/mm^{-2}	7 %	10 %	13 %	
Desorbed gas	$Q_{j,des}$	1.10^{15}mol./cm^{-2}	23 %	10 %	25 %	

Table 6.5: Typical values of variables in an ESD measurement. Uncertainties are listed in rounded % values for clarity and taken at 1σ confidence interval, i.e. at 68 %. See text for a detailed discussion.

The resulting notion of ESD yield η_j of a gas species j, along with the corresponding uncertainties is written in the following way, see eq. 6.25. The bracket contains the stochastic and systematic uncertainty interval evaluated at 1σ (68 %), while the combined uncertainty is refactored in front of the bracket. The 3 significant figures are only kept to illustrate the finesse of the calculation, but 1 significant figure suffices when dealing with such large uncertainty levels.

$$\eta_j = 0.100 \quad \pm 0.030 \quad (\pm 0.010, \quad \pm 0.029) \quad molecule/e^- \tag{6.25}$$

The uncertainties calculated here for the ESD yield are for a single measurement under nominal conditions. The main uncertainty driver is the desorbing gas flux measurement $Q_{des,j} = C_j(i_j - i_{j,BG})/k_j$. More precisely, the systematic uncertainty is driven by the RGA absolute sensitivity k_j and the collector conductance C_j. A signal-to-background ratio of 1:10 was chosen for illustration, but in practice, all ratios appear from the 0∼100 range. The uncertainty increases as the SNR diminishes. Hence, this fact is accounted for during data evaluation, and the plotted errorbars are proportionally increased when the SNR is low, as is typically visible on the infamous H_2O yield. The stochastic error, originating in the RGA's i_j and $i_{j,BG}$, increases in importance at low SNR, especially as it is amplified by a factor of 2x due to the (noisy) background subtraction. Conversely, the systematic error, represented by the collector conductance C_j and RGA absolute sensitivity k_j, is noise-independent and cancels out in a background subtraction, so zero is taken for the systematic error on C_j and k_j.

The chart in Figure 6.19 interprets the uncertainty analysis in a visual way, as it plots a precision versus trueness and shows how both combine into accuracy. The stochastic uncertainty, as a measure of precision, was calculated to be ∼10 % at 1σ confidence level. The systematic uncertainty, as a measure of absolute trueness, was evaluated as ∼28 % at 1σ. Minding the necessity of quadratic summation , the quadratic sum of these values is a combined uncertainty of ∼30 % at 1σ, which is equivalent to 68 % probability of having the true value within the confidence interval. The uncertainty is clearly dominated by the systematic uncertainty and not by the instrumental precision or repeatability. Shall an absolute reference be available, the DAQ chain could be calibrated accordingly against this standard, which would reduce ESD yield uncertainty to a ∼10 % level.

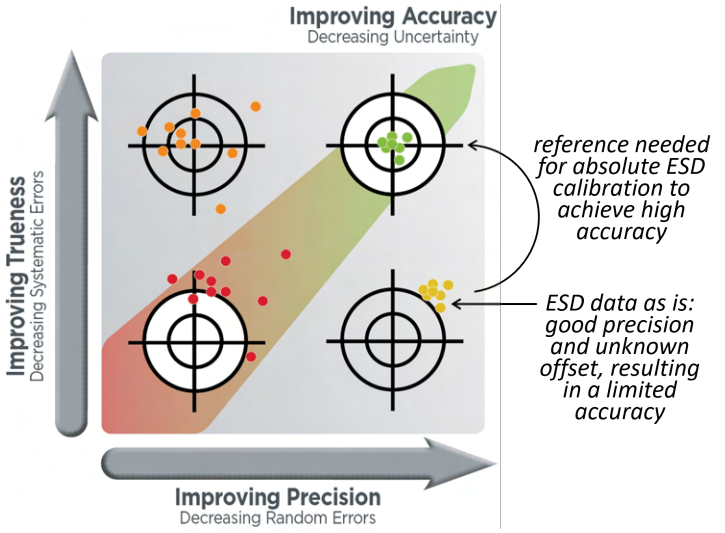

Figure 6.19: Interpretation of the uncertainty analysis on the precision versus accuracy chart. Terminology according to Joint Committee for Guides in Metrology. Scheme adapted from [328].

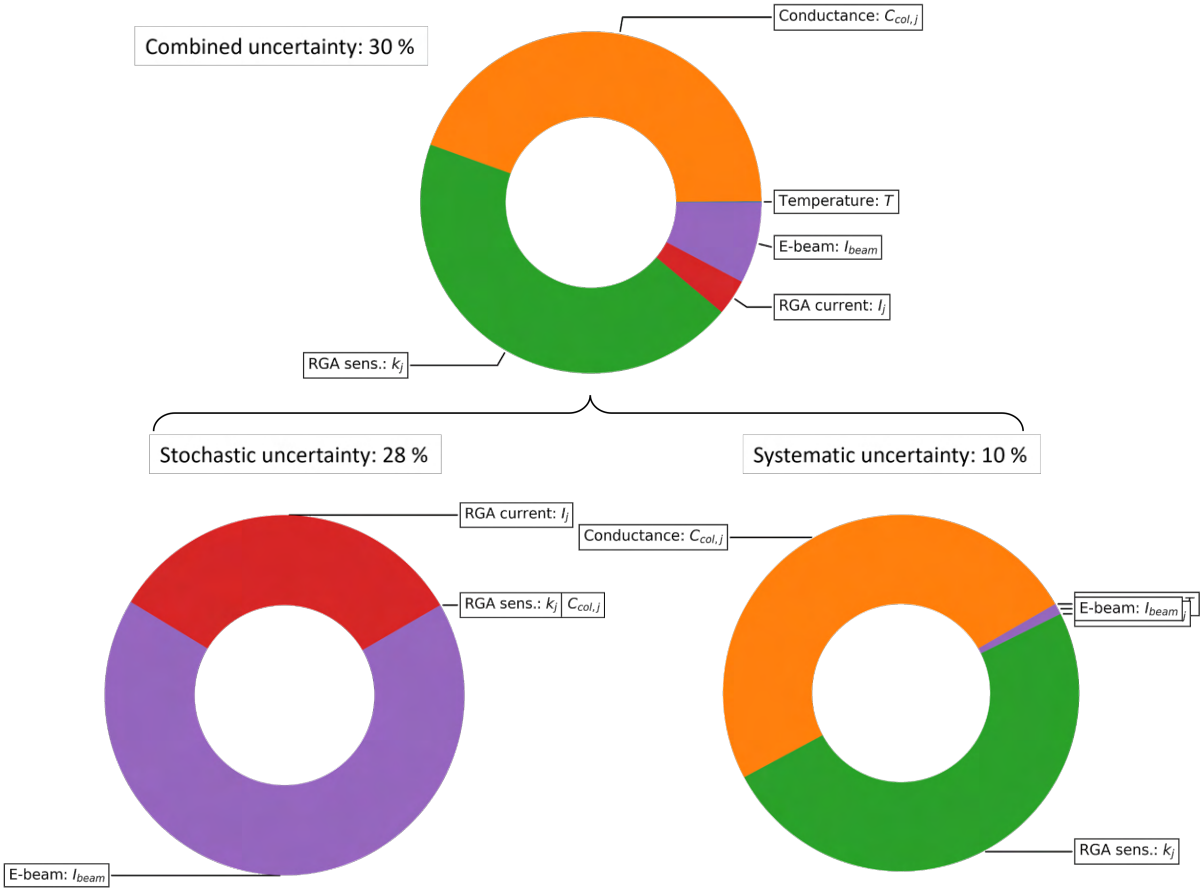

Figure 6.20: Relative contributions of measured quantities to the combined uncertainty on the measured ESD yield.

Overflow of experimental dataset

Electron-induced phosphorescence

High energy (hundreds eV) and intensity electron beam irradiation of thick layers (100+ ML) of quench-condensed N_2 gas resulted in electron-induced luminescence, see left side of Fig. 6.21. The luminescence persists for seconds after the beam is cut off, which more precisely is a sign of phosphorescence, i.e. electron relaxation via a 'forbidden transition' through an intermediate electronic state. The green colour observed in the experiment most likely corresponds to Nitrogen lines cluster around 523 nm. This effect has been long known since its discovery in 1927 [329] and well-described, including the assignment of wavelengths to the corresponding electronic transitions [330]. For a possible reference, this large surface coverages of quench-condensed N_2 gas is an amount comparable to the one suspected to be the cause of fast UFO-induced beam losses in 16L2 [331, 332].

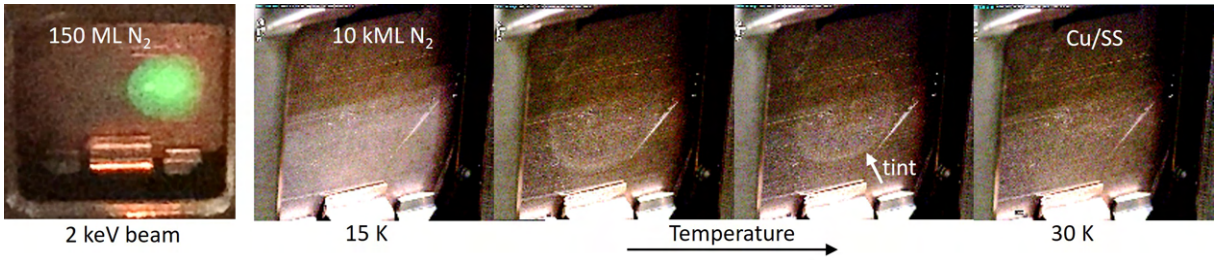

Figure 6.21: Left: Nitrogen (150 ML on Cu/SS) electron-induced phosphorescence under 2 keV electron irradiation. Right: 10^4 ML of N_2 condensed on Cu/SS create a barely visible opaque tint.

Further measurements with extremely thick N_2 ices also demonstrated that it takes about 10^4 ML of N_2 quench-condensed over Cu/SS to create a barely visible opaque tint. This tint is visible in the series of photographs taken during a TPD of the 10^4 ML thick N_2 coverage. The opaque tint gradually disappears as the coverage decreases.

ESD of technical-grade titanium

ESD energy dependence curves in linear and logarithmic scale, as measured on as-received Ti sample held at 265 K. The Ti sample was UHV-cleaned at CERN and stored in aluminium foil prior to analysis. The displayed uncertainty intervals are calculated at at 1σ for a single datapoint at its maximum value, hence its position at E_{max}. Note the systematic and stochastic components of the combined uncertainty. The high uncertainty on water is due to a high background and low SNR. The electron energy is referenced to the sample vacuum level. See text for more details.

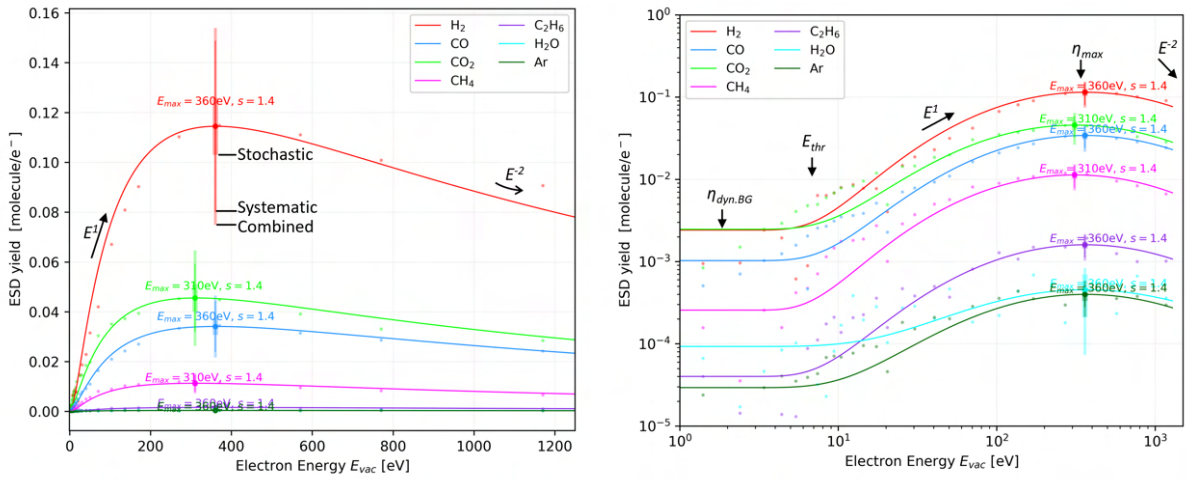

Figure 6.22: ESD energy dependence curves measured on as-received Ti sample held at 265 K.

Additional experimental details

System bakeout

Pressure and temperature profiles measured during the maiden bakeout lasting 1.5 days brought a factor of 150x improvement of the base pressure, as compared to the pre-bakeout state. The bakeout was later optimised to avoid cold-spots, and the time increased to 3 days. The NEG cartridge activation and conditioning was introduced at the end of the bakeout plateau. The NEG is kept in a conditioning mode until after all the gauges were degassed. Then, the entire system is brought back to ambient temperatures and pressures in the low 10^{-10} $\text{mbar}_{N2eq.}$ range.

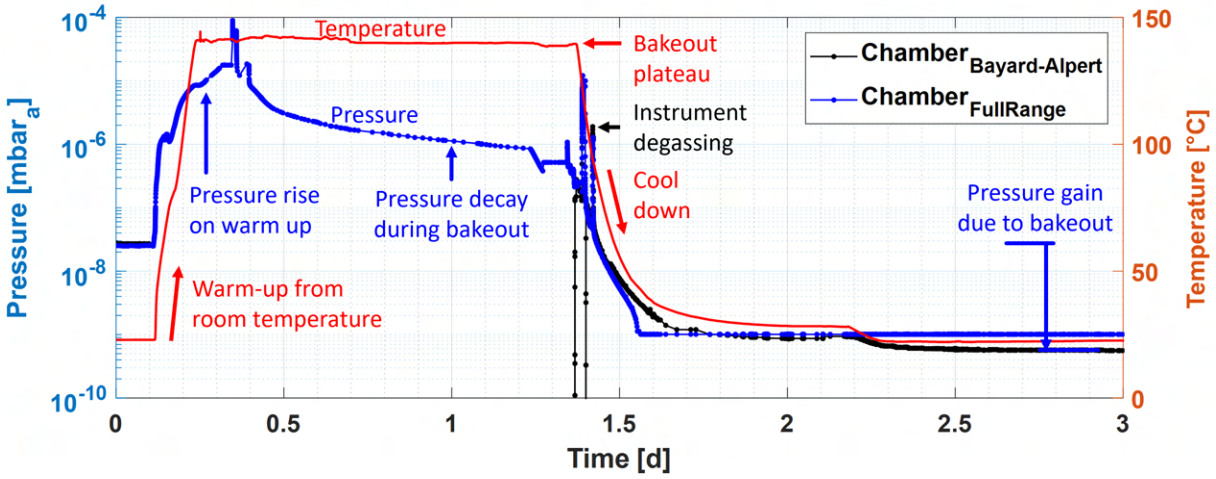

Figure 6.23: Pressure and temperature profile measured during the maiden bakeout lasting 1.5 days.

SEY measurement robustness against collector misalignment

The following measurements in Figure 6.24 were performed to verify that the used experimental arrangement is robust when subjected to small variations to the experimental parameters. Imposing a small biasing voltage on the collector had little effect on the measured SEY and, by extension, on the ESD. The same observation applies when increasing the gap between the sample and collector and introducing angular misalignment (not shown).

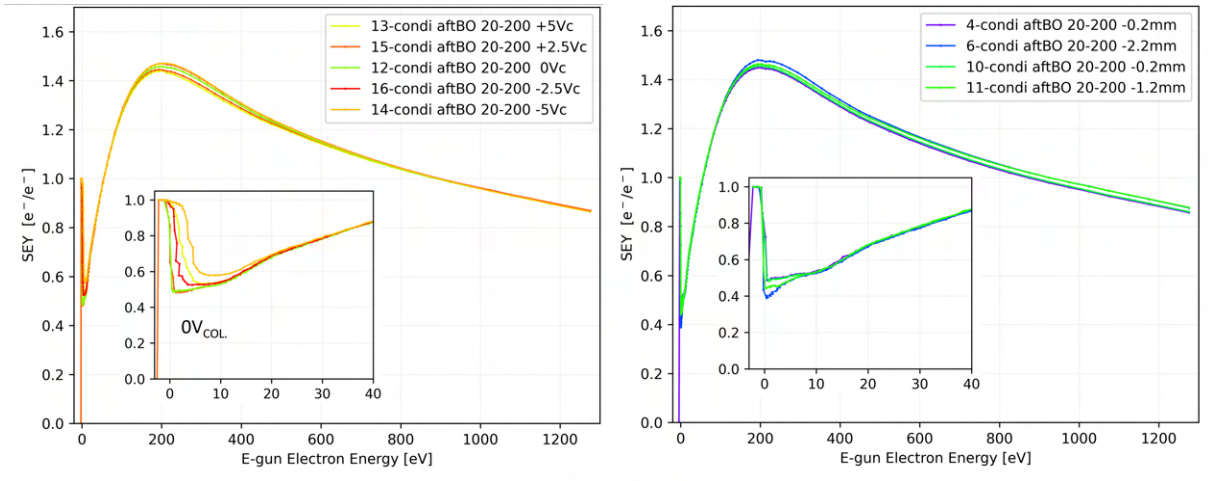

Figure 6.24: Left: SEY measurement performed on the same target but with small variations to the collector bias voltage. Right: SEY measurement performed on the same target but with variable distance between the sample and collector.

Collector Molflow+ simulation

Monte-Carlo particle tracing numerical simulation in Molflow+ [227] of gas propagation inside the collector. A simplified geometry is used without sacrificing the accuracy. The gas desorbing from the studied sample is set to be the only gas source in the system. This is a reasonable simplification, since pressure profiles in an UHV system abide by the law of superposition, i.e. a linear combination of solutions.

The simulation results indicate that the pressure profile is uniform across the entire inner volume of the collector, the tube and the endcap included.

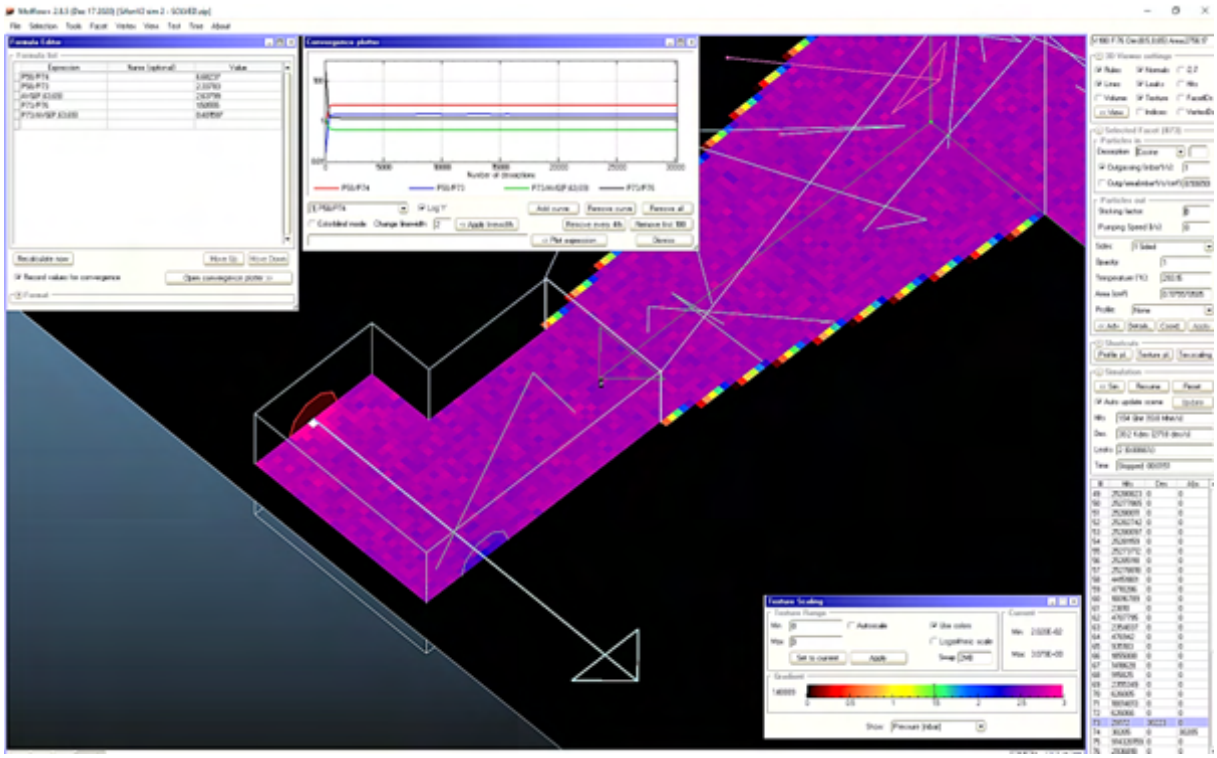

Figure 6.25: The GUI of Molflow+ Monte-Carlo simulation software package [227]. Note the wireframe of the collector and the colormap corresponding the particle density, as calculated from the green particle trajectories intercepting the mid-plane.

Curriculum Vitae

In the following pages.

First-author articles

In the following pages.

Michal HAUBNER

Czech Republic
mhaubner@cern.ch
Michal-Haubner-2
michalhaubner
CERN, Geneva, CH

Physical and instrumentation engineer with a broad skill set and demonstrated experience on interdisciplinary R&D projects. Analytical, systematic, and goal-oriented multi-domain researcher. Skilled, inventive, and resourceful laboratory experimentalist. Self-motivated and proactive, outgoing and conscientious team player who enjoys collaborative work and international setting.

Competences

Ultra-high vacuum science & technology	Electron-stimulated and temperature-programmed desorption, Secondary electron emission studies, electron gun tuning, mass spectrometer and gas flux calibration Low-energy electron beam optimization and characterization, UHV modelling
Instrumentation & Control	Sensors and DAQ system integration, calibration, signal processing and analysis System identification, controller design and implementation
Thermodynamics Fluid mechanics	Speed of sound and two-phase heat transfer measurements in real fluids Cryogenics, refrigeration, measurements and calculations of heat and mass transport
Applied research	Development and optimization of experimental methodology Data acquisition and interpretation, results presentation, and journal publication
Hands-on experience	Liquid Helium handling, fluid systems operation, laboratory and clean-room work UHV systems integration, operation, bake-out and helium leak-detection

Experience

2017 – 2022	***CERN - TE dept. – Vacuum, Surfaces and Coatings - Vacuum Studies and Measurements***
2019 – 2022 *4 years*	*Doctoral student, final year – Applied research in vacuum physics and surface science* Secondary electron emission and low-energy electron stimulated desorption measurements and modelling on metals, coatings, adsorbates and gas mixtures at 10-300K. Temperature programmed desorption studies. Innovative upgrades, calibration, troubleshooting, operation, methodology development, results interpretation, collaborative study publication
2017 – 2018 *1 year*	*Technical student – Master thesis in instrumentation engineering* Cryogenic vacuum system commissioning for electron emission and gas desorption studies
2014 – 2017 *1 month*	***CERN – EP department – Internships and collaborations at physics experiments*** Assembly of ATLAS Inner Detector cooling mock-up, SCADA system integration, tests, calibration, two-phase binary refrigerant heat transfer studies, analysis and publication
1 month	Cooling system development for Roman Pots detectors at ATLAS Forward Physics, commissioning and vacuum tests, hands-on LHC installation, on-schedule
2 months	TOTEM Roman Pots detectors' refrigeration and vacuum tests prior to LHC deployment
2016 – 2019 *4 years* *3 months*	***Physics Department – Faculty of Mechanical Engineering – Czech Technical University*** Hands-on work, research and development in students' laboratory Teaching practical physics laboratory works, training and mentoring students

Trainings

Professional	LabVIEW Core 1 & 2 Python for data analysis Scientific and technical writing	LabVIEW DAQ & Signal Conditioning Introduction to particle accelerators Rarefied gas & Vacuum dynamics courses
Technical	Cryogenics handling Electrical and radiation safety	Fire extinguisher Self-rescue mask
Soft skills	Critical thinking Teaching and tutoring	Scientific presenting First aid

Software

Proficient	Python LaTeX Molflow+ NIST RefProp	*Intermediate*	NI LabView CASINO electron tracing MATLAB, Simulink Autodesk Inventor

Languages

English	Fluent and proficient	*Czech*	Native
French	Working proficiency		

Education

	Alma mater	– Czech Technical University in Prague, CZ
2018 – 2023	***Doctorate***	– ***Mathematical and physical engineering*** Solid state, surface and vacuum physics, particle-matter interactions
	Dissertation:	*Electron beam characterization of technical surfaces at cryogenic temperatures*
2015 – 2018	***Master***	– ***Instrumentation and control engineering*** – *Graduated with honours* Control theory, system identification, controller design Precise instrumentation, Integral and discrete transforms
	Thesis:	*Commissioning of a vacuum system for measurements of electron stimulated desorption at cryogenic temperatures. 2nd at the faculty*
2011 – 2015	***Bachelor***	– ***Theoretical Fundamentals of Mechanical Engineering*** Engineering design, strength of materials, CAD, technology Applied math and physics, mechanics, fluid- and thermodynamics
	Thesis:	*Prediction of thermodynamic properties of gas mixtures using the Peng-Robinson equation of state.*
2013 – 2014	*Erasmus*	– École Polytechnique de l'Université d'Orléans, FR Mechanical, material and electrical engineering, multivariate calculus
2008 – 2009	*Exchange*	– Cañon City High School, Colorado, USA

Conferences and talks

E-CLOUD & GWDvac-22	SEY and ESD of ices and technical surfaces at cryogenic temperature
ECOSS-35 *2022*	Analysis and modification of technical surfaces by low-energy electron irradiation *Poster presentation*
EVC-16 *2021*	Electron conditioning of technical surfaces at cryogenic and room temperature in the 0-1 keV energy range, *IUVSTA Elsevier award*
ICTF/JVC-18 *2020*	Preliminary electron desorption results of selected HL-LHC technical surfaces at cryogenic temperature, *online conference*
Group seminar *2022*	Electron Stimulated Desorption and Secondary Electron Yield of technical surfaces at cryogenic temperatures
Physics seminar *2022*	Engineering perspective on CERN *Invited lecture at physics seminar series for public outreach, in Czech*
Student conf. *2016*	Experimental measurement of heat transfer coefficient in two phase flow of binary zeotropic mixture in a horizontal tube, *1st place award*

Publications

MDPI, Applied Sciences	Electron beam characterization of REBCO Coated Conductors at cryogenic conditions. 2023. Haubner, M., Krkotić, P., Baglin, V., et al.
Vacuum Journal	Electron conditioning of technical surfaces at cryogenic and room temperature in the 0-1 keV energy range. 2022. Haubner, M., Baglin, V., Henrist, B.
Nucl. Instrum. & Met. in Phys. Res.	Collector-based measurement of gas desorption and secondary electron emission induced by 0-1.4 keV electrons from LHC copper at 15 K. 2022. Haubner, M., Baglin, V., Henrist, B.
Journal of App. Physics	Electron-stimulated desorption from molecular ices in the 0.15–2 keV regime. 2020. Dupuy, R., Haubner, M., Henrist, B., Fillion, J. H., & Baglin, V.
Int. J. of Heat and Mass Transfer	Measurement of heat transfer coefficient in two phase flows of radiation-resistant zeotropic C_2F_6/C_3F_8 blends. 2017. Doubek, M., Haubner, M., … & Robinson, D.
HEFAT'17 proceedings	Experimental investigation and modelling of flow boiling heat transfer of C_3F_8/C_2F_6 blends. 2017. Doubek, M., Haubner, M., ... & Robinson, D.

Interests

Ice hockey, mountaineering, long-distance trails, glider pilot
Scientific literacy, aero- & astronautics, science fiction
Astronomy and astronautics summer camp instructor

applied sciences

MDPI

Article

Electron Beam Characterization of REBCO-Coated Conductors at Cryogenic Conditions

Michal Haubner [1,2,*], Patrick Krkotić [1], Catarina Serafim [1,3], Valentine Petit [1], Vincent Baglin [1], Sergio Calatroni [1], Bernard Henrist [1], Artur Romanov [4], Teresa Puig [4] and Joffre Gutierrez [4]

1 European Organization for Nuclear Research (CERN), 1211 Geneva, Switzerland
2 Department of Physics, Faculty of Mechanical Engineering, Czech Technical University in Prague, 166 07 Prague, Czech Republic
3 Department of Physics, University of Helsinki, FI-00014 Helsinki, Finland
4 Institute of Materials Science of Barcelona, CSIC, 08193 Madrid, Spain
* Correspondence: michal.haubner@cern.ch

Abstract: Particle accelerators with superconducting magnets operating at cryogenic temperatures use a beam screen (BS) liner that extracts heat generated by the circulating bunched charge particle beam before it can reach the magnets. The BS surface, commonly made of high–conductivity copper, provides a low impedance for beam stability reasons, low secondary electron yield (SEY) to mitigate the electron–cloud (EC) effect, and low electron–stimulated desorption yield (ESD) to limit the dynamic pressure rise due to EC. Rare–earth barium copper oxide (REBCO) high–temperature superconductors (HTSs) recently reached technical maturity, are produced as coated conductor tapes (REBCO–CCs), and will be considered for application in future colliders to decrease the BS impedance and enable operation at around 50 K, consequently relaxing the cryogenic requirements. Aside from HTS properties, industry–grade REBCO–CCs also need qualification for EC and dynamic vacuum compatibility under accelerator–like conditions. Hence, we report the SEY and ESD measured at cryogenic temperatures of 12 K under low–energy electron irradiation of 0–1.4 keV. We also verify the sample compositions and morphologies using the XPS, SEM, and EDS methods. The energy and dose dependencies of ESD are comparable to those of technical–grade metals and one sample reached SEY_{MAX} = 1.2 after electron conditioning.

Keywords: REBCO; HTS; SEY; ESD; SEM; EDS; XPS; cryogenic temperatures; electron conditioning

Citation: Haubner, M.; Krkotić, P.; Serafim, C.; Petit, V.; Baglin, V.; Calatroni, S.; Henrist, B.; Romanov, A.; Puig, T.; Gutierrez, J. Electron Beam Characterization of REBCO-Coated Conductors at Cryogenic Conditions. *Appl. Sci.* **2023**, *13*, 2765. https://doi.org/10.3390/app13052765

Academic Editor: Chao Li

Received: 30 January 2023
Revised: 15 February 2023
Accepted: 18 February 2023
Published: 21 February 2023

1. Introduction

High–temperature superconductors (HTSs) constitute a class of highly correlated anisotropic systems that theoretically have proven to be extremely difficult to address. Since their discovery in 1986 [1], numerous studies have been conducted to describe these materials, as well as to produce them at a scale suitable for large–scale technical applications. The general interest lies in the fact that the critical surface of HTS is significantly higher than that of low–temperature superconductors (LTSs), as visible in Figure 1a. Consequently, work gradually proceeded on technical applications, leading to large–scale HTS–based prototype devices over the years, and demonstrating the possible performance advantages over devices based on conventional LTS [2] or even normal–conducting technology.

The most promising industry-grade method available for a large–scale HTS application is by coating a thin layer of rare–earth barium copper oxide (REBCO) material on flexible metal tapes, in a complex–layered structure containing buffering metal oxide underlayers and stabilizing and protecting Cu and Ag overlayers. This technology is known as a second-generation coated conductor (CC), as depicted in Figure 1b, and is already commercially available in kilometer–lengths from several manufacturers. These second–generation REBCO–CC tapes promise high–performance properties, such as high current densities

and compatibility with high magnetic field applications, and their matured technology and mass production make them an affordable and viable engineering solution.

Aside from the imminent application in high–temperature superconducting magnets, in the next–generation, particle accelerators [3,4], passive microwave devices (not generating power) will be equally strong candidates for eventual HTS–coating commercialization. A HTS can have lower microwave surface impedance compared to pure metal [5]. Subsequently, this could allow the design of high–performance RF devices, such as high–quality factor (Q–factor) resonators, narrow–band filters, and antennas with improved functioning over conventional normal–conducting devices. Additionally, such complex microwave signal transmission and signal–processing systems could be designed to be more compact and more efficient [2,6]. For instance, a potential application lies within future space–based communication systems with a more effective strategy by producing fewer and lighter high-performance satellites with the reduced weight of cavities and filters. Furthermore, the feasibility of coating curved walls with REBCO–CCs enables manufacturing high Q–factor RF cavities, such as the one developed within the relic axion detector exploratory setup (RADES) [7]. Here, the detector sensitivity scales linearly with the Q–factor of the 9 GHz resonant cavity held at 4.2 K, and REBCO is the essential technology enabling operation in a strong magnetic field of 11 T while maintaining a high Q–factor.

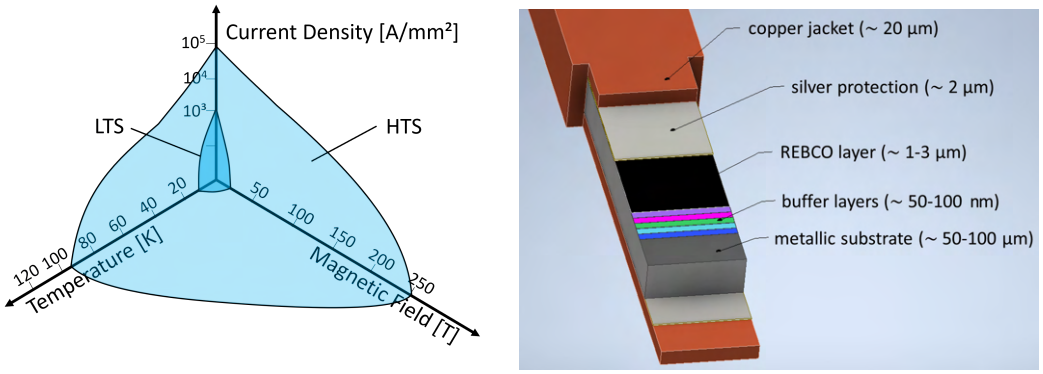

(**a**) Critical surface of LTS and HTS. (**b**) Layers of the REBCO–coated conductor tape.

Figure 1. (**a**) Comparison of the critical surface phase space for LTS and HTS formed by the three interdependent characteristic parameters of a superconductor, i.e., the critical temperature, critical magnetic field, and critical current density. Superconductivity can only occur below the critical surfaces, which are unique for each material. The figure is inspired by [8]. (**b**) Structure of a complex–layered REBCO HTS–coated conductor tape. Note the substrate and buffer layers residing under the REBCO coating, the silver and copper stabilizing, and protecting overlayers.

In particle accelerators with magnets operating at cryogenic temperatures, a beam screen (BS) inserted into the cryomagnet apertures is used to intercept the heat and radiation generated by the circulating particle beam before it can reach the superconducting magnets. The BS can equally be considered an RF device due to the time–variant electric field induced by the passing bunched charged particle beam. Taking the BS in the Large Hadron Collider (LHC) as an example, its steel structure is co–laminated with Cu to reduce the surface impedance at its operating temperatures of 5–20 K [9]. The flat geometry makes REBCO–CC a feasible alternative coating material for BS to potentially reduce the resistive-wall impedance at operating temperatures of ∼50 K [10]. Decreasing the impedance reduces the beam instabilities [11] and heat load to the BS [12].

Electron multipacting can occur inside the BS when certain resonant operating conditions are met [13]. The electric field wake created by passing bunches repeatedly accelerates electrons and results in avalanche–like electron multiplication and the formation of a stable and self–sustaining electron cloud (EC). The precondition for EC emergence in a BS, or another RF device, is a sufficiently high value of a secondary electron yield (SEY), defined as the number of secondary electrons leaving a surface after the incoming primary electron

impact. If this ratio is above unity, the electrons can multiply, while a surface with a SEY below unity acts as an electron absorber, therefore, hindering EC build–up. The EC is a phenomenon commonly observed during the operation of storage rings [14–17] and RF devices [18,19] and is detrimental to the accelerator operation in many regards, such as EC–induced beam instabilities, leading to emittance growth [14], EC–induced heat–load deposited into the cryogenically cooled BS [12], and electron–induced gas desorption [20] that deteriorates the ultra–high vacuum (UHV) conditions in the BS. The EC–induced gas load is characterized by the electron–stimulated desorption (ESD) yield. The EC has a characteristic energy spectrum known from calculations, in situ measurements, and simulations [13,15,18,21,22], mostly consisting of low–energy electrons below 20 eV, and a smaller population of electrons accelerated by the electric field to hundreds of electron volts. Fortunately, both SEY and ESD yields decrease during electron irradiation to acceptable levels. This effect is leveraged in so–called beam–scrubbing [17,23], i.e., in situ electron and photon conditioning by circulating a beam when gradual decreases in EC activity and the dynamic vacuum effect are observed during the accelerator operation. These effects mainly pertain to accelerator storage rings, which aim to circulate bunched, positively charged beams at high intensity and high energy while maintaining a low emittance to generate high luminosity for physics research [24], such as the Future Circular Hadron Collider (FCC–hh) led by CERN [10] and the Super Proton–Proton Collider (SPPC) led by IHEP and CAS in China [25].

Previous studies [26–29] done on REBCO–CC samples (of the same type and provider studied here) produced experimental evidence for compatibility from the RF and superconducting perspectives across the necessary temperatures, fields, and current densities. This makes them potential candidates that are currently being investigated for BS construction to be used in future accelerators [27].

Hence, this manuscript investigates the compatibility of REBCO–CC surface properties linked to the dynamic vacuum effect and electron cloud at conditions representative of an accelerator application. This includes cryogenic temperatures and electron irradiation similar to that of an actual EC, i.e., with a focus on the entire 0–1 keV energy region. The following measurements use various electron beam–based methods to infer the sample's response to electron irradiation. First, the surface morphology and composition were investigated to verify that the REBCO coating was actually exposed and matched the manufacturer's specifications. The analytical methods we used were X-ray photoelectron spectroscopy (XPS) and scanning electron microscopy (SEM), conducted on a device equipped with an energy–dispersive X-ray spectroscopy (EDS) function. Second, the SEY was investigated as the main EC–driving property. SEY is a strongly surface–dependent property mostly derived from surface electronic properties that unwind from the chemical composition and surface state. Third, the ESD yield was measured as a function of energy and dose to estimate how the REBCO–CCs would react to an EC irradiation in an accelerator. The ESD yield is proportional to the amount of desorbable surface–bound contaminants that are normally present, even on UHV–grade cleaned surfaces.

2. Material and Methods

2.1. Samples Preparation

The two investigated samples of REBCO–coated conductors came from two different manufacturers, SuNAM and SuperOx. The samples were stored in a plastic box filled with air dehumidified by silica beads. Prior to measurements, the REBCO tapes were scissor–cut into 1 cm^2 large pieces, glued to flag–style copper sample holders with a silver–filled epoxy, and cured to 80 °C under a high vacuum.

The tapes have a layered structure deposited over a Hastelloy C276 used as a substrate, as visualized in Figure 1 on the right. There is a range of deposition methods [30], from which SuNAM uses RCE–DR (reactive co–evaporation by deposition and reaction) [31] and SuperOx uses PLD (pulsed laser deposition) [32]. Hence, the samples will be referred to as PLD–deposited and RCE–deposited to best represent the surface. The REBCO layer itself,

i.e., the Gd–Ba–Cu–O, was deposited with 1600 nm and 900 nm thickness for RCE and PLD, respectively, and was grown on buffer underlayers [27]. Moreover, these studied samples were not the typical off–the–shelf REBCO tapes because they lacked the micrometer–sized protective overlayers typically present on industry-grade tapes. Indeed, this is done because the application in RF requires the HTS coating to be exposed, minding the small micrometer–sized skin depth. The RCE–deposited sample had its usual Ag overlayer removed by the manufacturer so effectively that it lacked Ag traces in the XPS spectrum, unlike the PLD–deposited sample. The protective micrometer–thick Ag overlayer had to be etched away from the PLD–deposited sample using a solution of NH_3:H_2O_2:CH_3OH in 1:1:5 proportions, as detailed in [28], which inevitably affected its surface chemical state.

2.2. Sample Analysis

The SEM imaging, EDS analysis, and XPS analysis were acquired in this order after the SEY and ESD measurements were taken (in order to not interfere with the SEY and ESD results, which are both highly surface–sensitive).

2.2.1. Surface Morphology Imaging via SEM

Figure 2 presents the SEM images of the two different REBCO tape samples, PLD–deposited (left) and RCE–deposited (right). The apparent surface texture and morphology differences can be attributed to the different deposition methods. The high contrast of nanocrystals against the Gd–Ba–Cu–O substrate in the background is likely due to a combination of relatively higher atomic mass (higher Ba and Gd content) and a localized charging effect due to the dielectric nature of the oxide nanocrystals.

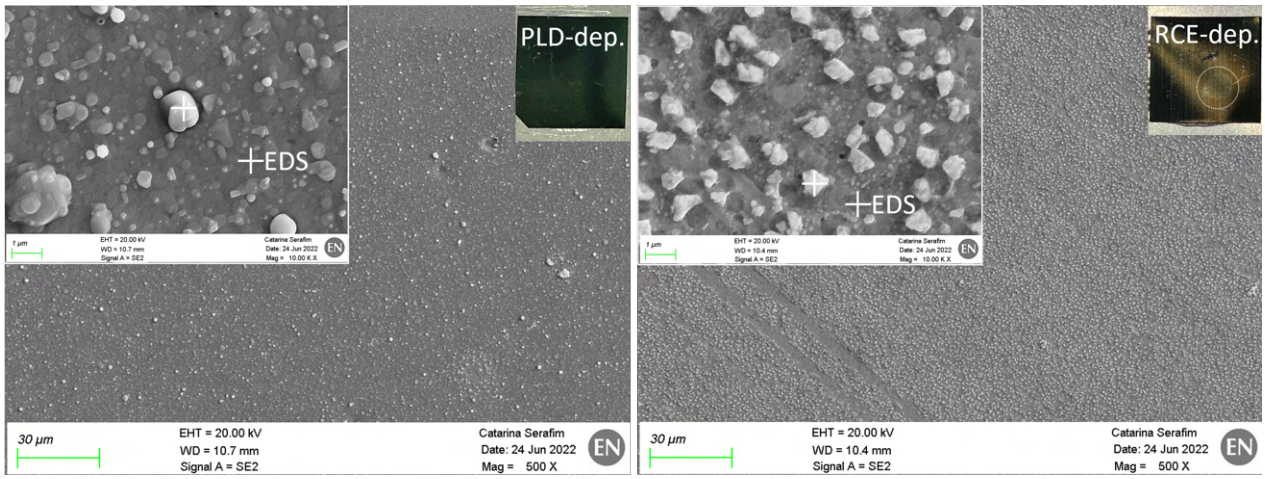

Figure 2. SEM images of REBCO samples with the well–visible nanocrystal–covered surface. Crosses represent the EDS measurement positions. **Left**: PLD–deposited, a wide range of crystal sizes. **Right**: RCE–deposited coating, uniformly sized crystals. Details in the text. The SEM images were taken on FE–SEM Zeiss Sigma.

The RCE coating process produces sharp uniformly sized and spaced nanocrystals, while the PLD coating process gives a wide range of oval–shaped nanocrystal sizes spaced at irregular intervals. These nanocrystals uniformly cover the entire surfaces of both samples.

2.2.2. Composition Analysis via EDS

The energy dispersive X-ray spectrometry analysis was performed on both studied samples to verify the surface chemical composition. EDS utilizes the X-ray spectrum emitted by a solid sample bombarded with a focused electron beam to obtain a localized chemical analysis. We identified the specific energy of the X-ray peaks characteristic for each element. The relative intensity of an X-ray line is approximately proportional to the mass concentration of an element. In a quantitative analysis, the concentrations of the

elements present are determined by measuring the relative intensities for the lines identified in the spectrum for each element. The resulting concentrations of the identified elements are compiled in Table 1. However, the EDS analysis depth of ∼5 µm also incorporates all buffer layers and part of the Hastelloy substrate, which offsets the composition measurement.

For the RCE–deposited sample, the EDS spectrum was measured in an area with a nanocrystal and an area without, i.e., the substrate. The locations analyzed by EDS are marked by crosses in the insets of Figure 2. The precipitates segregated at the RCE–deposited surface may be Cu–O or Cu–Ba–O, resulting from the liquid process of RCE–DR to grow the Gd–Ba–Cu–O [31]. The PLD–deposited sample was analyzed in the same way, and the measured compositions derived from EDS spectra are listed in Table 1. Given the PLD growth method, the segregated precipitates at the surface are droplets of the same composition as the REBCO layer [32].

Table 1. Weight concentrations in percentage (%) of elements detected by the EDS method on the surface of PLD-deposited and RCE-deposited samples, at spots indicated in Figure 2. Analysis depth in ∼5 µm range.

Sample	C	O	Cu	Ba	Gd
PLD–deposited: precipitate	4.5	13.0	21.0	33.5	28.0
PLD–deposited: Gd–Ba–Cu–O film	5.7	13.2	21.0	33.3	26.8
RCE–deposited: precipitate	6.6	17.4	62.0	9.4	4.6
RCE–deposited: Gd–Ba-Cu–O film	4.4	13.1	19.1	29.2	34.2

2.2.3. Composition Analysis via XPS

The surface chemical analysis by XPS was performed in a room temperature UHV system equipped with a monochromated Al K_α X-ray source and a hemispherical electron energy analyzer collecting photoelectrons at normal emission angles. The energy scale was calibrated by setting the Cu $2p_{3/2}$ and the Au $4f_{7/2}$ states of sputter–cleaned metals to 932.6 and 84.0 eV, respectively. A mild charging effect was observed (deformed C 1s line) for the RCE–deposited sample. No charge compensation was applied. The atomic concentrations of the present elements were obtained assuming a uniform material and weighting the respective peak area of the XPS spectrum after background subtraction by the corresponding sensitivity factors. Table 2 lists the main elements found on the surface of the two REBCO samples. Elements such as Cl, P, F, Zn, and Ca were also detected, amounting to less than 10 atomic % in total. These elements likely come from post–production sample handling; for instance, Cl is introduced by epoxy–gluing. Meanwhile, the carbon, also observed in EDS spectra, is a common and dominant surface contaminant that has a naturally low SEY value if present in the sp2 state.

Table 2. Atomic concentrations in % of elements detected on the surface of as–received PLD–deposited and RCE–deposited samples by the XPS method. Analysis depth in the ∼nm range.

Sample	C	O	Cu	Ba	Gd	N	Ag	Si
PLD–deposited:	33.2	42.7	2.8	8.0	0.9	2.1	1.2	0.0
RCE–deposited:	49.3	36.3	1.7	1.9	0.4	1.4	0.0	5.3

The analysis depth in the nanometer range renders the XPS highly sensitive to the oxidized surface layer, making it challenging to infer the bulk REBCO composition. Still, the XPS surface chemical composition analysis, such as the EDS, could identify the main chemical constituents of the Gd-Ba-Cu-O coating. The chemical states of the different elements are known to greatly influence the SEY of a surface [33,34]. This is particularly the case for barium, which shows a maximum SEY below unity for the pure metallic state, while BaO displays a maximum SEY beyond 2 [33]. From the XPS spectra, the position of the Ba $3d_{5/2}$ core level at a binding energy of 780.1 eV for the PLD–deposited sample

is compatible with the presence of BaO oxide [35]. The additional shift of the Ba $3d_{5/2}$ line to 780.4 eV for the RCE–deposited sample can be explained by a mild charging effect. Hence, in the presence of BaO with intrinsically high SEY, it is likely the elevated carbon surface concentration on the RCE–deposited sample that is responsible for the low SEY reported below.

2.3. Experimental Techniques

2.3.1. Experimental Setup

A newly developed analytical system was used to acquire the SEY and ESD data. The corresponding methodology for cryogenic measurements was described in detail in preceding articles [36,37].

The studied sample was mounted on a cryogenic manipulator installed in a baked UHV μ–metal chamber held at room temperature, with a base pressure in the 10^{-10} mbar range. A Kimball ELG–2 electron gun irradiated the sample at normal incidence with a focused beam of 0–1.4 keV electrons at sub–nA to a few µA beam currents and a 2–3 mm wide flat–top beam profile. A custom–designed collector held at 300 K formed closed geometry over the studied cold sample and captured the emitted secondary electrons and neutral gas species.

The sample was biased to −28 V to impose a retarding potential that slowed the primary electron beam down to 0 eV. By doing so, both SEY and ESD energy dependence measurements started from 0 eV, as referenced in the sample vacuum level. Conversely, the electron conditioning was performed at a +46 V sample bias to minimize the gas desorption caused by the secondary electrons. Indeed, the electron energy was always corrected for the used bias.

2.3.2. SEY Measurement

The SEY, denoted as δ, is defined as the ratio between the primary electrons impinging the sample and the secondary electrons leaving the sample, irrespective of their physical origins. The collector current I_C and the sample drain current I_S were directly measured in our experiment. The beam current was recollected as a sum of the sample drain current and the collector current $I_B = I_S + I_C$. Then, the SEY was directly calculated from the observables.

$$\delta = \frac{I_{Secondary}}{I_{Primary}} = \frac{I_C}{I_B} = \frac{I_C}{I_C + I_S} \tag{1}$$

The SEY and ESD energy dependencies were measured point–wise, starting from 0 eV. The SEY data points were spaced 0.25 eV apart at low energy and up to 50 eV apart around 1.4 keV. The beam current of ∼0.5 nA preserved a signal–to–noise ratio (SNR) of ∼50 on the measured currents, while avoiding a significant conditioning effect during the measurement.

2.3.3. ESD Measurement

The same collector also captures the electro-desorbed gas and directs it toward a calibrated quadrupolar mass spectrometer (QMS). The QMS absolute sensitivity k_j [$A_j/mbar_j$] is known for each gas species j of interest by an in situ calibration, so the partial pressure can be measured as $\Delta p_j = k_j \cdot \Delta i_j$. Knowing the pressure differential Δp_j and the geometrically fixed collector conductance C_j allows measuring the electro-desorbing gas flux of each monitored species. Finally, the ESD yield [molecule/e^-−] is given by the ratio of gas molecules, leaving the sample to the impinging primary electrons.

$$\eta_j = \frac{C_j \cdot \Delta p_j}{k_B \cdot T} \Big/ \frac{I_B}{q_e} \tag{2}$$

In an ESD energy dependence measurement, the data points are spaced at 1 eV in the low–energy region and up to 300 eV around 0–1 keV. The beam current of ∼2 µA is sufficient

to create a measurable pressure rise on the QMS, but low enough not to significantly damage the sample, as discussed in [36].

2.4. Measurement Procedure

The SEY and ESD analyses were performed first, as they were the most sensitive to the sample surface state. All SEY and ESD measurements were taken at cryogenic temperatures below 20 K and were done on intact as–received spots of the same REBCO sample. An XPS analysis subsequently followed the SEY and ESD measurements to investigate the surface chemical composition of the studied samples. An intact spot was chosen to capture the as–received surface state. Finally, the SEM and EDS analyses were done to study the sample surface morphology and localize in–depth bulk chemical composition. The XPS, SEM, and EDS were performed ex situ at ambient temperatures, as they were temperature–independent in this case.

The two REBCO samples mounted on a flag–type sample holder were inserted into the UHV system via a load lock. Once the system was cold, the sample was rapidly heated to ∼100 K to desorb gases that could cryosorb from the background during the cool–down. Care was taken during the second and final cool–down from 100 K back to 12 K to ensure that the sample cooled down as the last, once again, mitigating the possibility of residual gas cryosorption. The sample was then ready for data–taking after the final cool–down when the system stabilized around T_S = 12 K. Multiple SEY curves were acquired at different locations on the as–received sample to study variability within the sample itself. Measuring the SEY at the same locations at ambient temperatures prior to cool–down showed no tangible difference, as discussed below. Following the non–destructive SEY measurements, the ESD energy and dose dependencies were measured on two separate as–received spots of the same sample. The ESD energy dependence was measured first and was followed by a dose–dependent measurement at 300 eV to acquire a so–called conditioning curve. The SEY and ESD energy scans took about 5 min to finish, and the electron conditioning measurement took about 90 min. Once the ESD conditioning measurement was done, the SEY curve was acquired once again to capture the conditioned sample surface.

3. Results and Discussion

3.1. Secondary Electron Yield

The secondary electron yield measurements reported in Figure 3 provide a few important findings. First, there are no charging effects, even at ambient temperatures, despite the thick REBCO layer. This is essential since charging effects (often on dielectric surfaces) are detrimental in many technical applications, including applications in beam screens or RF devices.

Secondly, similar to technical–grade metals, the SEY of a REBCO-CC sample decreases under 300 eV of electron irradiation, a phenomenon known as electron conditioning. As most UHV–cleaned metal surfaces exhibit high SEY in their as–received air–exposed states [36,37], they typically condition during electron irradiation to reach SEY values at around 1, which are low enough to prevent electron multipacting.

The first stage of the SEY decrease is dominated by the ESD process, while graphitization of carbon-containing surface–bound contaminants dominates in the later stages, as proven independently by Cimino [38], Nishiwaki [39], and Scheuerlein [40], who linked the SEY decrease to graphitization. The conditioning process is mostly done at a dose of a few mC·mm^{-2} and further electron irradiation at 300 eV does not lead to a significant SEY decrease. The SEY of the RCE–deposited sample conditions to an acceptable value of δ_{max} = 1.2 at 1 mC·mm^{-2} dose. Conversely, the PLD-deposited sample only conditions to around δ_{max} = 2. The XPS analysis reveals two factors that explain the significant difference in SEY. Firstly, barium, which is present in BaO oxide form, is known to have a high SEY. Secondly, carbon contamination, when graphitized under electron irradiation, can reduce the SEY of surfaces close to unity. The RCE–deposited sample showed a higher atomic concentration ratio of carbon to barium than the PLD–deposited sample. This may partially

account for the lower SEY observed after irradiation of the RCE–deposited sample. However, even after conditioning, the SEY of the PLD–deposited sample is too high for technical applications, and further SEY–reducing treatment is necessary to prevent multipacting.

Puig and Krkotić et al. [26] and Leveratto et al. [41] also reported high as–received SEY values of $\delta_{max} \approx 2.9$, as measured at ambient temperatures.

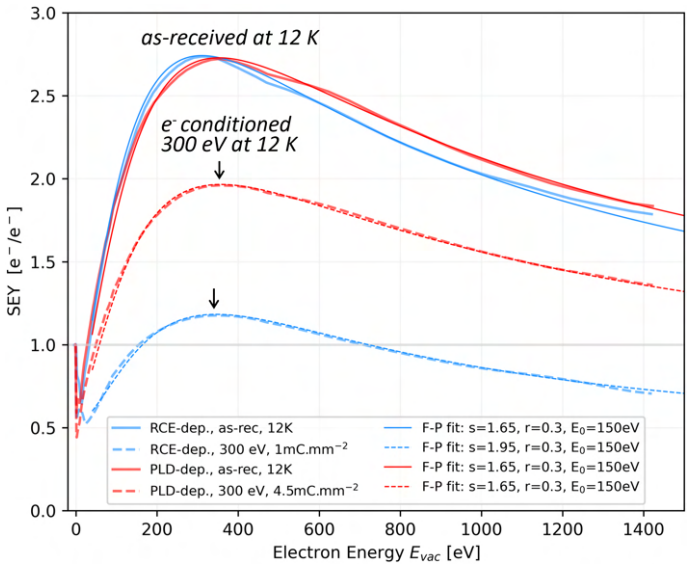

Figure 3. SEY energy dependence of REBCO samples held at 12 K measured in as–received and electron–conditioned states using 300 eV electrons at a few mC·mm^{-2} doses, as indicated in the legend. The measured data points (not shown) are smoothed with a Savitzky–Golay filter [42] and plotted as a thick line, while the Furman–Pivi approximation [43] is the thin line.

The shapes of the SEY curves also closely resemble classical technical metals, as described by the E_{max} and δ_{max} values. This is somewhat unexpected given the surface roughness observed in the SEM images that could point toward a more flat energy dependence that is typical for rough surfaces. The energy of maximum SEY δ_{max}, the E_{max}, is important for the following reason. The typical energy spectrum of an electron cloud developed in an RF device consists of a high–energy peak at hundreds to thousands of eV [15,18,21,22]. The multipacting conditions can be better mitigated if the high–energy peak of EC is offset from the SEY peak position E_{max}, as is visible in the simulations done in [21].

Similar to the other technical–grade metals characterized in this setup, such as Cu, Al, and steel, the SEY of the studied REBCO coatings is temperature–invariant within the experimental precision and conditions in the investigated 12–300 K temperature and 0–1.4 keV energy ranges. Hence, the secondary electron emission seems to be agnostic to cryogenic temperatures, including around the superconducting transition around 90 K. The tentative explanation for the SEY stability in HTS under electron irradiation lies in the fact that electronic excitations have an energy range of units to tens of eV, while the binding energy of superconducting pairs is on the order of tens of meV, as theoretically calculated for HTS cuprates [44]. Recent measurements conducted at cryogenic temperatures [28] and further reasoning in [45] show that high–energy synchrotron radiation does not impair the superconducting properties in any way. This suggests that electron irradiation, which also decays into electronic excitations, is unlikely to impair the HTS performance. Therefore, the SEY can also be expected to remain unaffected by the conducting state of the HTS.

The experimental SEY curves can be fitted using a multi–component semi–empirical model, given in Equation (3), as implemented in PyECLOUD code [46] to facilitate further application. The three main components to fit the entire SEY curve, marked here as δ_{TOT}, are the following: The true secondary electrons (TSE) part δ_{TSE} that dominate at primary energies above ∼20 eV and are fitted with a classical Furman–Pivi fit [43]. The elastically

backscattered (EBS) part δ_{EBS} that dominates at sub ~20 eV energies is approximated by a fit reportedly derived by Blaskiewicz [47]. Meanwhile, the inelastic backscattered (IBS) part δ_{IBS} starts at 0, but swiftly increases to the r value, reaching 63% at 10 eV. An exponential function was chosen here for simplicity, but the low–energy SEY region generally deserves greater care given its crucial role in EC build–up.

$$\begin{aligned} \delta_{TOT} &= \delta_{TSE} + \delta_{EBS} + \delta_{IBS} \\ \delta_{TSE} &= (\delta_{max} - r_{BSE}) \cdot \frac{s(E/E_{max})}{s - 1 + (E/E_{max})^s} \\ \delta_{EBS} &= r_0 \cdot \left(\frac{\sqrt{E_0} - \sqrt{E_0 + E}}{\sqrt{E_0} + \sqrt{E_0 + E}} \right)^2 \\ \delta_{IBS} &= r_{BSE} \cdot (1 - e^{-E/10}) \end{aligned} \tag{3}$$

The parameters that best approximate the measured data are listed in the legend of Figure 3 and correspond to those suitable for technical metals. The following parameters were used here to accurately represent the measured SEY curves: reflectivity at 0 eV r_0 = 0.75, EBS cutoff at E_0 = 150 eV, skewness parameter s = 1.65, and IBS fraction r = 0.3. Lastly, the values of δ_{max} and E_{max} of the fitted curve have to match the measured values.

3.2. Electron Stimulated Desorption

3.2.1. Energy Dependence

ESD measurements were performed on both investigated samples at 12 K in an intact as–received state. Similarly to the SEY, the ESD curves acquired here for the two REBCO–CCs, displayed in Figure 4, also resemble regular metal surfaces. This applies to comparing the electro-desorbed gas composition, desorption thresholds, and nominal ESD yields and their maximum to technical–grade UHV–cleaned metals, such as Cu previously studied on this cryogenic setup [36,37] and other technical metals studied by other authors at ambient temperatures [48–53]. The energy thresholds for desorption are in the typical 5–10 eV region characteristic of technical–grade metals, such as Cu measured on the same setup [36], or extrapolated by Billard et al. [50]. The energy E_{max} of the peak desorption yield η_{max} of both samples lies in the 300–500 eV region. H_2 has the maximum yield and is followed by CO, CO_2, CH_4, and other UHV–typical (but less abundant) species. A sample storage more suitable for UHV components would likely lead to significantly lower ESD yields but similar energy and dose dependencies.

A semi-empirical fit was used to approximate the acquired experimental data for ESD yields and energy dependencies. The fit consisted of a log-normal distribution with an energy offset and cutoff at the desorption energy threshold E_{thr}, as described by the following equation.

$$\eta(E) = \eta_{max} \cdot \exp\left(\frac{-\ln^2((E - E_{thr})/E_{max})}{2\sigma^2} \right) \quad \text{, for} \quad E \geq E_{thr} \tag{4}$$

The peak ESD value η_{max} at energy E_{max} was used to normalize the energy distribution, whilst the σ parameter determined its width. The legend in Figure 4 lists (for all measured gases) the relevant parameters necessary to reconstruct the energy dependence in the studied 0.1 keV region: E_{thr}, η_{max}, E_{max}, and σ. In practice, a constant was added to the parametric fit to model the non–zero background, which represents the detection limit of the used experimental setup.

The uncertainties were evaluated for η_{max}, as well as E_{max} values, and are plotted in Figure 4 at the ESD yield peak value η_{max}. The bars represent a combined uncertainty of ~30% at 1 σ confidence interval, corresponding to 68% probability of containing the true value.

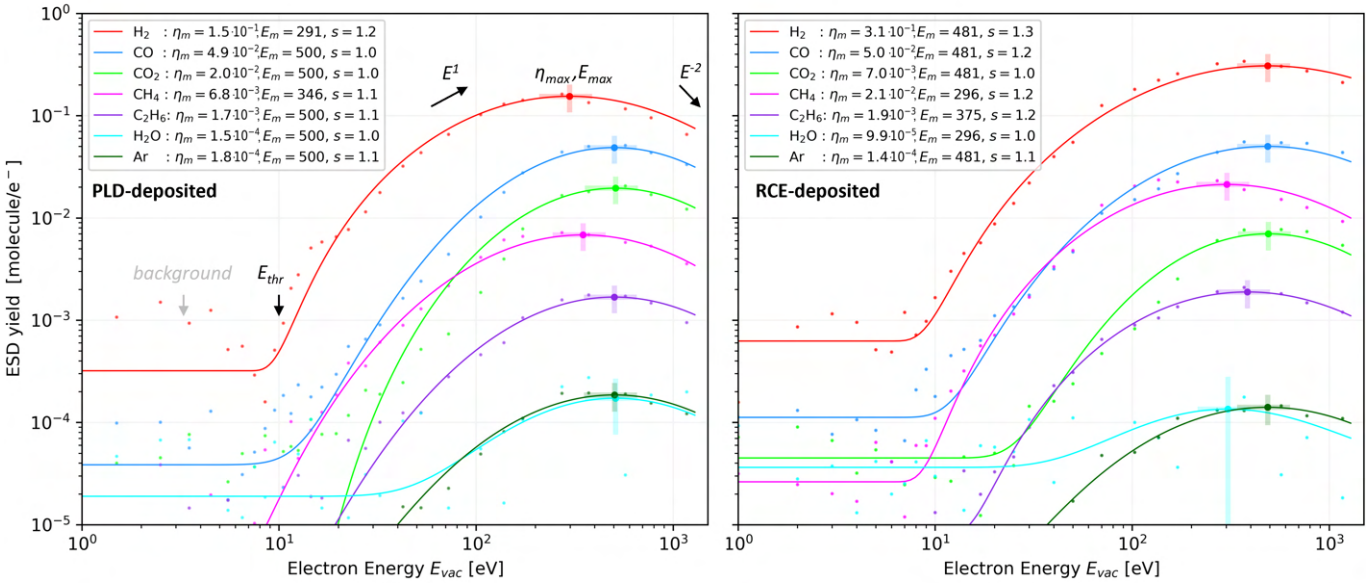

Figure 4. ESD energy dependence of as–received REBCO samples. The RCE–deposited sample (**right**) is characterized at 12 K and PLD–deposited at 19 K (**left**). Note the high uncertainty for water on the right plot, partially due to the high background and partially due to the low signal–to–noise ratio. The best–fit parameters for Equation (4) are listed in the legend. More details are in the text.

3.2.2. Dose Dependence

The conditioning curves, i.e., the ESD yield decreases with the electron doses, were acquired during a 300 eV electron irradiation performed at 12 K and are reported in Figure 5. The initial yields η_0, although slightly higher for the RCE–deposited sample, are characteristic of UHV–cleaned metal surfaces. The conditioning rates are just as rapid as for bare technical–grade metal surfaces and represent gas desorption from a non–porous surface. The slope of 0.3∼0.4 is typical for water electrodesorption from technical–grade metals. It is most likely the reason for a dynamic balance between electron stimulated water desorption and electron irradiation–induced synthesis. This is commonly observed in water electrodesorption because the H_2O molecule is known to act as a chemical attractor [54] due to its high binding energy.

The irradiated RCE–deposited surface showed discoloration following the 300 eV electron conditioning at 12 K, as seen in the inset of Figure 2. Going from a dark to a light shade is unusual and the opposite of what happens to metals due to electron–induced surface graphitization. Instead, this bleaching effect could indicate a reduction of surface oxides and hydroxides.

The ESD conditioning curves measured here for the studied REBCO coatings also reveal no significant departure from the expected behavior when compared to the technical–grade Cu, Al, and steel previously measured using the same methods [36,37]. The data equally well compare to data from other authors who conditioned metals held at ambient temperatures in terms of the electro–desorbed gas composition, initial ESD yields η_0, inflection point location D_1, and conditioning rates α. This includes work by Gomez–Goñi and Mathewson [52], Billard et al. [50], Achard [53] from CERN, Suzuki et al. [51], Kennedy [48], and Malyshev [49].

The fact that both the SEY and ESD decrease during electron irradiation has severe implications for applicability. As outlined in Section 1, the electron conditioning is leveraged in accelerators during beam–scrubbing [17,23] to bring down the EC activity by decreasing the SEY and mitigating the dynamic vacuum effect by conditioning the desorption yields.

An empirical fit, initially proposed by Malyshev [49] for photodesorption, was used here to approximate the ESD yield dose dependence and possibly extrapolate to higher

electron doses. The fit builds on a classical power law whose exponent α controls the slope in the log–log plot at high doses $D \geq 0.1\,\mathrm{mC{\cdot}mm^{-2}}$. Parameters D_0 and D_1 are added to the fraction to extend the applicability toward low doses in a way that the curve asymptotically approaches the constant initial ESD yield η_0 as $D \to 0$. The parameter D_0 represents the dose imparted at the lowest measurable data point (here, it is the first displayed data point). Parameter D_1 is solely used to position the end of the initial plateau.

$$\eta(D) = \eta_0 \cdot \left(\frac{D + D_1}{D_0 + D_1} \right)^{-\alpha} \tag{5}$$

Values for η_0, D_1, and α parameters in Equation (5) can be read directly from the legends in Figure 5 and plugged into the presented parametric fits for the ESD yield dose dependence. The same uncertainty analysis leading to ∼30 % at 1 σ confidence interval applies to the ESD yield values presented here too, although not plotted.

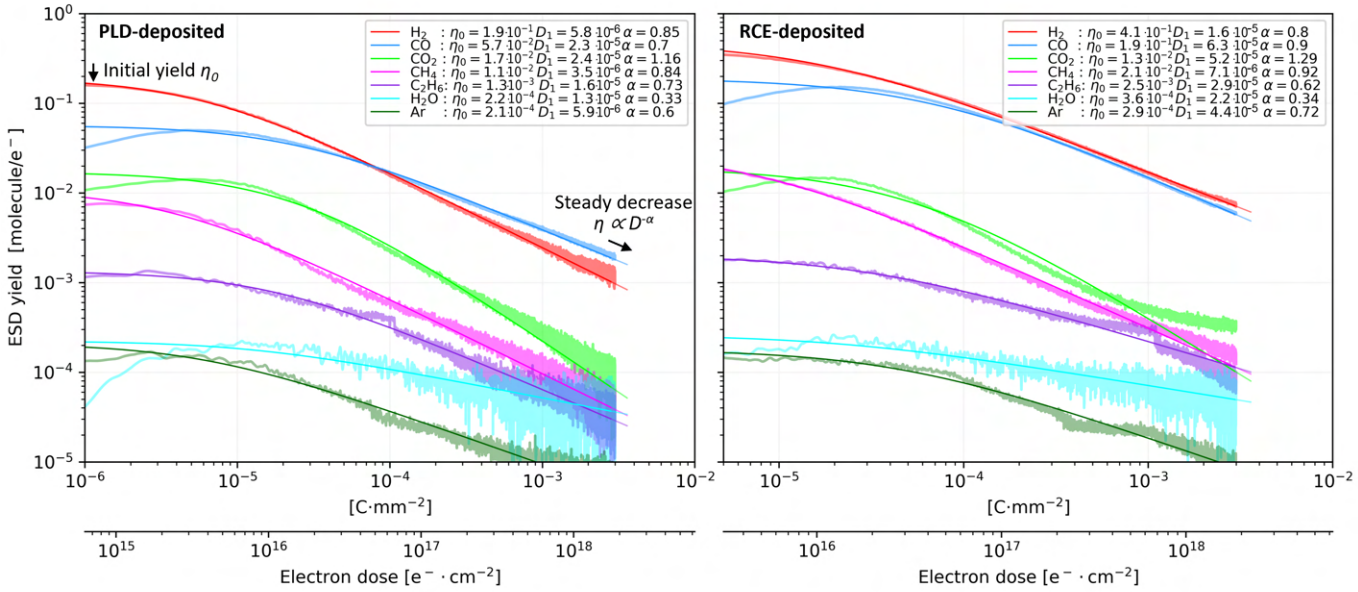

Figure 5. ESD dose dependence measured at 300 eV for PLD–deposited (**left**) and RCE–deposited (**right**) REBCO samples held at 12 K starting from an as–received state. Best–fit parameters for Equation (5) from [49] is listed in the legend. More details are in the text.

4. Summary and Conclusions

This electron beam–based laboratory investigation of REBCO–CCs aims to characterize surface properties related to electron clouds in accelerators, including the secondary electron yield (SEY), which is a determining factor for electron multipacting, and electron stimulated desorption (ESD), which links dynamic pressure rise to EC activity during operation. The presented results are applicable to other types of RF devices that use HTS, such as radio–frequency waveguides and cavities, which may also suffer from electron cloud or multipacting effects.

We first identified the surface morphology and composition using SEM imaging with an EDS capability. SEM imaging showed a flat surface structure covered with segregated nanocrystalline precipitates with characteristic sizes in the micrometer range. The ESD conditioning rate and the shape of measured SEY curves generally resemble those of bare technical–grade metals, which supports the SEM observation of a flat, non–porous, surface structure covered with micrometer–sized precipitates. The EDS measurement is bulk–sensitive at the micrometer range, and considering the characteristic micrometer–sized skin depths, the EDS results are relevant to the HTS properties. Meanwhile, the XPS measurement with a probe–depth in the nanometer range makes it highly surface sensitive,

rendering the XPS results relevant to the SEY properties. Both EDS and XPS analyses could identify the main chemical constituents at the surface of the Gd–Ba–Cu–O film.

Knowing the morphology and composition of the samples and that the REBCO was directly exposed on the surface, we held the samples at 12 K and studied their response to electron irradiation. The energy range of 0–1.4 keV was chosen to cover the entire relevant EC spectrum [13,15,21]. Meanwhile, 300 eV irradiation was selected for electron conditioning studies, as it represents the high–energy part of the EC, which is responsible for the conditioning effect [38], i.e., the decrease of SEY and ESD yields during electron irradiation commonly observed during beam–scrubbing of an accelerator [20,23]. We measured the SEY energy dependence in the 0–1.4 keV range both before and after the 300 eV irradiation with a clear conclusion that the SEY decreases in the entire studied range. The SEY of the RCE–deposited sample decreased to a value of δ_{max} = 1.2 at 1 mC·mm^{-2} electron dose, which is a value acceptable for many applications. Conversely, the PLD–deposited sample SEY only conditioned to $\delta_{max} \approx 2$ at a 4.5 mC·mm^{-2} dose. The reason for this is unclear, but based on the XPS analysis, it can be hypothesized that the etched PLD–deposited sample lacks surface–bound carbon contaminants that would graphitize into a sufficiently thick graphitic overlayer with intrinsically low SEY values. The XPS spectrum seconds this hypothesis since the RCE–deposited sample had 49% carbon content whilst the PLD–deposited sample only had 33%, resulting in a smaller SEY reduction.

The electron conditioning was studied up to a few mC·mm^{-2}, which is an electron dose rapidly achievable during an accelerator operation. The RCE-deposited case represents a proof-of-concept capability of REBCO-type coatings to electron condition to SEY values sufficiently low not to trigger electron multipacting, resulting in EC build-up in the beam screen. Parallel studies by Puig et al. [26] also consider depositing a thin, anti-multipacting, low-SEY layer of amorphous carbon coating atop the REBCO-CCs to alleviate the need for beam scrubbing. Therefore, future SEY and ESD studies could focus on characterizing carbon-coated REBCO-CCs at cryogenic conditions.

The acquired ESD data represent a link between the EC and the dynamic vacuum effect caused by EC electron-desorbing gases from the cryogenic BS wall. Hence, the ESD yield measurements also covered the energy and dose dependencies similar to the SEY. Irradiation with 300 eV electrons at a dose of a few mC·mm^{-2} resulted in a decrease in all measured ESD yields by about 2 orders of magnitude for both studied REBCO-CCs held at 12 K. The ESD yields were also measured for the two samples as functions of energy in the 0–1 keV range. The acquired ESD results are similar to the usual technical-grade UHV-cleaned metals previously studied in this setup [36,37] and by other authors under similar conditions [48–53], in terms of desorption thresholds, nominal ESD yields, and conditioning rates of all UHV–typical gases. Hence, the dynamics of the beam–induced gas desorption from REBCO–CCs can be expected to be very similar to the technical-grade metals currently used as the baseline [55]. Moreover, the ESD yield reported here can be considered as a proxy for photon– and ion–stimulated desorption yields that are known to correlate with the ESD [36,56–58].

Author Contributions: M.H., V.B. and S.C. conceived and designed the study. V.B. and B.H. designed the SEY and ESD measurement apparatus. M.H. commissioned the apparatus, performed the SEY and ESD measurements, and analyzed the data. C.S. and V.P. conducted the XPS and SEM and EDS analyses and interpreted the data. P.K., S.C., T.P. and J.G. provided valuable feedback on REBCO superconductivity and edited the manuscript. M.H., P.K., V.B. and S.C. interpreted the results. A.R. and M.H. prepared the samples. M.H. wrote and edited the manuscript with contributions from all authors. All authors have read and agreed to the published version of the manuscript.

Funding: The authors acknowledge the support from the HL–LHC project and CERN funding FCCGOV–CC-0208 (KE4947/ATS). The authors acknowledge the support and samples provided by Superox and SuNAM. M. Haubner acknowledges partial support from the Czech Technical University in Prague, grant number: SGS21/149/OHK2/3T/12. A. Romanov acknowledges MSCA-COFUND-2016-754397 for the PhD grant. A. Romanov, T. Puig, J. Gutierrez acknowledge funding from PID2021-127297OB-C21 and CEX2019-000917-S.

Data Availability Statement: Data are available upon reasonable request.

Acknowledgments: The authors would like to acknowledge the support and samples provided by SuperOx and SuNAM. The authors acknowledge the support from the EN-MME group for providing the tools for SEM and EDS analysis.

Conflicts of Interest: The authors declare no conflict of interest.

Abbreviations

The following abbreviations are used in this manuscript:

BS	Beam Screen
CC	Coated Conductor
EC	Electron Cloud
EDS	Energy Dispersive X-ray Spectroscopy
ESD	Electron Stimulated Desorption
FE-SEM	Field-Emission SEM
HTS	High Temperature Superconductor
LTS	Low Temperature Superconductor
LHC	Large Hadron Collider
PLD	Pulsed Laser Deposition
QMS	Quadrupolar Mass Spectrometer
RCE-DR	Reactive Co-Evaporation by Deposition and Reaction
REBCO	Rare-Earth Barium Copper Oxide
RF	Radio Frequency
SEM	Secondary Electron Microscope
SEY	Secondary Electron Yield
SNR	Signal to Noise Ratio
UHV	Ultra-High Vacuum
XPS	X-ray Photoelectron Spectroscopy

References

1. Bednorz, J.; Müller, K. Possible high T_c superconductivity in the Ba-La-Cu-O system. *Z. Phys. B Condens. Matter* **1986**, *64*, 189–193. [CrossRef]
2. Newman, N.; Lyons, W. High-temperature superconducting microwave devices: Fundamental issues in materials, physics, and engineering. *J. Supercond.* **1993**, *6*, 119–160. [CrossRef]
3. Rossi, L.; Senatore, C. HTS Accelerator Magnet and Conductor Development in Europe. *Instruments* **2021**, *5*, 8. [CrossRef]
4. Wang, X.; Yahia, A.; Bosque, E.; Ferracin, P.; Gourlay, S.; Gupta, R.; Higley, H.; Kashikhin, V.; Kumar, M.; Lombardo, V.; et al. REBCO–A Silver Bullet for Our Next High-Field Magnet and Collider Budget? *arXiv* **2022**, arXiv:2203.08736.
5. Hein, M. *High-Temperature-Superconductor Thin Films at Microwave Frequencies*; Wiley-VCH Verlag GmbH & Co. KGaA: Weinheim, Germany, 1999. [CrossRef]
6. Larbalestier, D.; Gurevich, A.; Feldmann, D.M.; Polyanskii, A. High-T_C superconducting materials for electric power applications. *Nature* **2001**, *414*, 368?377. [CrossRef]
7. Golm, J.; Arguedas Cuendis, S.; Calatroni, S.; Cogollos, C.; Döbrich, B.; Gallego, J.; García Barceló, J.; Granados, X.; Gutierrez, J.; Irastorza, I.; et al. Thin Film (High Temperature) Superconducting Radiofrequency Cavities for the Search of Axion Dark Matter. *IEEE Trans. Appl. Supercond.* **2022**, *32*, 1–5. [CrossRef]
8. Van Nugteren, J. High Temperature Superconductor Accelerator Magnets. Ph.D. Thesis, University of Twente, Enschede, The Netherlands, 2016.
9. Metral, E. Beam Screen Issues. *arXiv* **2011**, arXiv:1108.1643. Comments: 7 pages, Contribution to the EuCARD-AccNet-EuroLumi Workshop: The High-Energy Large Hadron Collider, Malta, 14–16 October 2010; CERN Yellow Report CERN-2011-003, pp. 83–89.
10. Benedikt, M.; Khachatryan, V.; Sirunyan, A.; Tumasyan, A.; Adam, W.; Aguilo, E.; Bergauer, T.; Dragicevic, M.; Erö, J.; Fabjan, C.; et al. FCC-hh: The Hadron Collider. *Eur. Phys. J. Spec. Top.* **2019**, *228*, 755–1107. [CrossRef]
11. Metral, E. Wake field, impedance and collective instability. *J. Instrum.* **2021**, *16*, P10009. [CrossRef]
12. Skripka, G.; Iadarola, G. Beam-Induced Heat Loads on the Beam Screens of the HL-LHC Arcs. 2019. Available online: https://cds.cern.ch/record/2692753/files/CERN-ACC-2019-0041.pdf (accessed on 17 February 2023).
13. Cimino, R.; Demma, T. Electron cloud in accelerators. *Int. J. Mod. Phys. A* **2014**, *29*. [CrossRef]
14. Romano, A.; Boine-Frankenheim, O.; Buffat, X.; Iadarola, G.; Rumolo, G. Electron cloud buildup driving spontaneous vertical instabilities of stored beams in the Large Hadron Collider. *Phys. Rev. Accel. Beams* **2018**, *21*, 061002. [CrossRef]

15. Buratin, E. Electron Cloud and Synchrotron Radiation Characterizations of Technical Surfaces with the Large Hadron Collider Vacuum Pilot Sector. Ph.D. Thesis, École Polytechnique Fédérale de Lausanne, Lausanne, Switzerland, 2020.
16. Iadarola, G.; Rumolo, G. Electron cloud in the CERN accelerators (PS, SPS, LHC). *AIP Conf. Proc. C* **2013**, *1206051*, 19–26. [CrossRef]
17. Zhang, S.Y. *eRHIC Beam Scrubbing*; Brookhaven National Lab. (BNL): Long Island, NY, USA, 2017. [CrossRef]
18. Graves, T.P.; Wukitch, S.J.; LaBombard, B.; Hutchinson, I.H. Effect of multipactor discharge on Alcator C-Mod ion cyclotron range of frequency heating. *J. Vac. Sci. Technol. A* **2006**, *24*, 512–516. [CrossRef]
19. Hillairet, J.; Goniche, M.; Fil, N.; Belhaj, M.; Puech, J. Multipactor in High Power Radio-Frequency Systems for Nuclear Fusion. *arXiv* **2017**, arXiv:1710.03629.
20. Vincent, B. The LHC vacuum system: Commissioning up to nominal luminosity. *Vacuum* **2017**, *138*, 112–119. [CrossRef]
21. Iadarola, G. Electron Cloud Studies for CERN Particle Accelerators and Simulation Code Development. Ph.D. Thesis, Universita degli Studi di Napoli Federico II, Naples, Italy, 2014.
22. Papke, K.; Carvalho, A.A.; Zanoni, C.; Grudiev, A. Design studies of a compact superconducting RF crab cavity for future colliders using Nb/Cu technology. *Phys. Rev. Accel. Beams* **2019**, *22*, 072001. [CrossRef]
23. Bruning, O.; Caspers, F.; Collins, I.; Grobner, O.; Henrist, B.; Hilleret, N.; Laurent, J.M.; Morvillo, M.; Pivi, M.; Ruggiero, F.; et al. Electron Cloud and Beam Scrubbing in the LHC. In Proceedings of the 1999 Particle Accelerator Conference (Cat. No.99CH36366), New York, NY, USA, 27 March–2 April 1999; Volume 4, pp. 2629–2631. [CrossRef]
24. Shiltsev, V.; Zimmermann, F. Modern and future colliders. *Rev. Mod. Phys.* **2021**, *93*, 015006. [CrossRef]
25. Tang, J. Design Concept for a Future Super Proton-Proton Collider. *Front. Phys.* **2022**, *10*, 828878. [CrossRef]
26. Puig, T.; Krkotić, P.; Romanov, A.; O'Callaghan, J.; Zanin, D.A.; Neupert, H.; Pinto, P.C.; Demolon, P.; Costa, A.G.; Taborelli, M.; et al. Coated conductor technology for the beamscreen chamber of future high energy circular colliders. *Supercond. Sci. Technol.* **2019**, *32*, 094006. [CrossRef]
27. Romanov, A.; Krkotić, P.; Telles, G.e.a. High frequency response of thick REBCO coated conductors in the framework of the FCC study. *Sci. Rep.* **2020**, *10*, 12325. [CrossRef] [PubMed]
28. Krkotić, P.; Romanov, A.; Tagdulang, N.; Telles, G.; Puig, T.; Gutierrez, J.; Granados, X.; Calatroni, S.; Perez, F.; Pont, M.; et al. Evaluation of the nonlinear surface resistance of REBCO coated conductors for their use in the FCC-hh beam screen. *Supercond. Sci. Technol.* **2022**, *35*, 025015. [CrossRef]
29. Krkotić, P.; Tagdulang, N.D.; Calatroni, S.; O'Callaghan, J.M.; Pont, M. Potential impedance reduction by REBCO-coated conductors as beam screen coating for the Future Circular Hadron Collider. *Europhys. Lett.* **2022**, *140*, 64001. [CrossRef]
30. MacManus-Driscoll, J.L.; Wimbush, S.C. Processing and application of high-temperature superconducting coated conductors. *Nat. Rev. Mater.* **2021**, *6*, 587–604. [CrossRef]
31. Lee, J.H.; Lee, H.; Lee, J.W.; Choi, S.M.; Yoo, S.I.; Moon, S.H. RCE-DR, a novel process for coated conductor fabrication with high performance. *Supercond. Sci. Technol.* **2014**, *27*, 044018. [CrossRef]
32. Samoilenkov, S.; Molodyk, A.; Lee, S.; Petrykin, V.; Kalitka, V.; Martynova, I.; Makarevich, A.; Markelov, A.; Moyzykh, M.; Blednov, A. Customised 2G HTS wire for applications. *Supercond. Sci. Technol.* **2015**, *29*, 024001. [CrossRef]
33. Seiler, H. Secondary electron emission in the scanning electron microscope. *J. Appl. Phys.* **1983**, *54*, R1–R18. [CrossRef]
34. Petit, V.; Taborelli, M.; Zanin, D.A.; Himmerlich, M.; Neupert, H.; Chiggiato, P.; Iadarola, G. Beam-induced surface modifications as a critical source of heat loads in the Large Hadron Collider. *Commun. Phys.* **2021**, *4*, 1–10. [CrossRef]
35. Koenig, M.; Grant, J. XPS studies of the chemical state of Ba on the surface of impregnated tungsten dispenser cathodes. *Appl. Surf. Sci.* **1985**, *20*, 481–496. [CrossRef]
36. Haubner, M.; Baglin, V.; Henrist, B. Collector-based measurement of gas desorption and secondary electron emission induced by 0?1.4 keV electrons from LHC-grade copper at 15 K. *Nucl. Instrum. Methods Phys. Res. Sect. B Beam Interact. Mater. Atoms* **2022**, *531*, 34–43. [CrossRef]
37. Haubner, M.; Baglin, V.; Henrist, B. Electron conditioning of technical surfaces at cryogenic and room temperature in the 0–1 keV energy range. *Vacuum* **2023**, *207*, 111656. [CrossRef]
38. Cimino, R.; Commisso, M.; Grosso, D.R.; Demma, T.; Baglin, V.; Flammini, R.; Larciprete, R. Nature of the Decrease of the Secondary-Electron Yield by Electron Bombardment and its Energy Dependence. *Phys. Rev. Lett.* **2012**, *109*, 064801. [CrossRef] [PubMed]
39. Nishiwaki, M.; Kato, S. Electron stimulated gas desorption from copper material and its surface analysis. *Appl. Surf. Sci.* **2001**, *169–170*, 700–705. [CrossRef]
40. Scheuerlein, C.; Taborelli, M.; Hilleret, N.; Brown, A.; Baker, M. An AES study of the room temperature conditioning of technological metal surfaces by electron irradiation. *Appl. Surf. Sci.* **2002**, *202*, 57–67. [CrossRef]
41. Leveratto, A.; Saba, A.; Kagerbauer, S.; Himmerlich, M.; Henrist, B.; Fernandez-Pena, S.; Moros, A.; Bernardi, J.; Eisterer, M.; Bernini, C.; et al. Future Circular Collider beam screen: Progress on Tl-1223 HTS coating. *Supercond. Sci. Technol.* **2020**, *33*, 054004. [CrossRef]
42. Savitzky, A.; Golay, M.J.E. Smoothing and Differentiation of Data by Simplified Least Squares Procedures. *Anal. Chem.* **1964**, *36*, 1627–1639. [CrossRef]
43. Furman, M.A.; Pivi, M.T.F. Probabilistic model for the simulation of secondary electron emission. *Phys. Rev. ST Accel. Beams* **2002**, *5*, 124404. [CrossRef]
44. Tavkhelidze, A. Possible mechanism of Cooper pairing in HTS cuprates. *arXiv* **2008**, arXiv:0807.0889.

45. Krkotić, P. Evaluation of the Surface Impedance of ReBCO Coated Conductors and Requirements for Their Use as Beam Screen Materials for the FCC-hh. Ph.D. Thesis, Universitat Politecnica de Catalunya, Barcelona, Spain, 2022. [CrossRef]
46. Wulff, E.; Iadarola, G. *Implementation and Benchmarking of the Furman-Pivi Model for Secondary Electron Emission in the PyECLOUD Simulation Code*; Technical report; CERN: Geneva, Switzerland, 2019.
47. Cimino, R.; Collins, I.R.; Furman, M.A.; Pivi, M.; Ruggiero, F.; Rumolo, G.; Zimmermann, F. Can low energy electrons affect high energy physics accelerators? *Phys. Rev. Lett.* **2004**, *93*, 014801. [CrossRef]
48. Kennedy, K. *Electron Stimulated Desorption Rates from Candidate Vacuum Chamber Surfaces*; Lawrence Berkeley National Lab. (LBNL): Berkeley, CA, USA, 1986. [CrossRef]
49. Malyshev, O. *Vacuum in Particle Accelerators: Modelling, Design and Operation of Beam Vacuum Systems*; John Wiley and Sons: Hoboken, NJ, USA, 2020. [CrossRef]
50. Billard, F.; Hilleret, N.; Vorlaufer, G. *Some Results on the Electron Induced Desorption Yield of OFHC Copper*; Technical report; CERN: Geneva, Switzerland, 2000. [CrossRef]
51. Suzuki, K.; Kobayashi, S.; Katsube, T. Cross sections of electron stimulated desorption under technical vaccum conditions and 1 to 3 keV electron energies. *Appl. Surf. Sci.* **1988**, *33–34* 325–334. [CrossRef]
52. Gomez-Goni, J.; Mathewson, A. Temperature dependence of the electron induced gas desorption yields on stainless steel, copper, and aluminum. *J. Vac. Sci. Technol. Vacuum Surfaces Film.* **1997**, *15*, 3093. [CrossRef]
53. Achard, M.H. *Desorption des Gaz Induite par des Electrons et des Ions de l'Acier Inoxydable, du Cuivre OFHC, du Titane et de l'Aluminium Purs*; Technical report; CERN: Geneva, Switzerland, 1976.
54. Dulieu, F. Physical and chemical processes at Cryogenic Surfaces: A lesson from the Space. In Proceedings of the ECLOUD'22 and GWDVAC'22 Workshops, Portoferraio, Italy, 25–30 September 2022.
55. Baglin, V.; Lebrun, P.; Tavian, L.; van Weelderen, R. *Cryogenic Beam Screens for High-Energy Particle Accelerators*; Technical report; CERN: Geneva, Switzerland, 2013.
56. Collins, I.R.; Malyshev, O.B. *Dynamic Gas Density in the LHC Interaction Regions 1 and 5 and 2 and 8 for Optics Version 6.3*; Technical report; CERN: Geneva, Switzerland, 2001.
57. Baglin, V.; Collins, I.R.; Grobner, O.; Grunhagel, C.; Jenninger, B. Molecular desorption by synchrotron radiation and sticking coefficient at cryogenic temperatures for H_2, CH_4, CO and CO_2. *Vacuum* **2002**, *67*, 421–428. [CrossRef]
58. Andritschky, M.; Grobner, O.; Mathewson, A.; Schumann, F.; Strubin, P.; Souchet, R. Synchrotron radiation induced neutral gas desorption from samples of vacuum chambers. *Vacuum* **1988**, *38*, 933–936. [CrossRef]

Nuclear Instruments and Methods in Physics Research B 531 (2022) 34–43

Contents lists available at ScienceDirect

Nuclear Inst. and Methods in Physics Research, B

journal homepage: www.elsevier.com/locate/nimb

Collector-based measurement of gas desorption and secondary electron emission induced by 0–1.4 keV electrons from LHC-grade copper at 15 K

Michal Haubner [a,b,*], Vincent Baglin [b], Bernard Henrist [b]

[a] Department of Physics, Faculty of Mechanical Engineering, Czech Technical University in Prague, Czech Republic
[b] European Organization for Nuclear Research (CERN), Geneva, Switzerland

ARTICLE INFO

Keywords:
Electron stimulated desorption
Secondary electron yield
Electron conditioning
Technical surface
Cryogenic temperatures
Feulner cap

ABSTRACT

CERN's Large Hadron Collider cryomagnets embed a 1.9 K UHV chamber lined with a 5–20 K beam-screen (BS) that intercepts the synchrotron radiation and electron cloud (EC). The low–energy EC irradiates the BS and desorbs gas, creating a dynamic vacuum effect. A novel setup controllably reproduces this by irradiating an unbaked as-received BS copper sample at 15 K with 0–1.4 keV electrons, representing a slice of the EC spectrum. This collector-based setup is qualified using a HOPG reference for secondary electron yield (SEY) and $^{15}N_2$ as a tracer in low-energy electron stimulated desorption (ESD) measurements. Measurement at 15 K revealed sub-10 eV ESD thresholds and a maximum around 300 eV of 0.18 H_2/e^- and 0.13 CO/e^-. Irradiation with 300 eV and 1 keV electrons at $\sim 8.10^{-4}$ C.mm^{-2} conditioned ESD and SEY alike. Similar dose at 17 eV only caused minor SEY reduction and no ESD decline. The as-received H_2 and CO_2 yields at 300 eV decreased 5-150x between 15 and 265 K, respectively..

1. Introduction

In storage rings, accelerators and light sources, the circulating charged particle beam may provoke a large pressure increase by up to five orders in magnitude above the base pressure. This dynamic pressure rise, potentially limiting the machine's performance, has been long observed in room temperature machines but only recently at cryogenic temperatures in the CERN's Large Hadron Collider (LHC) [1], or the Relativistic Heavy Ion Collider, RHIC in the USA [2]. Large accelerators are designed considering the dynamic vacuum effect. This includes machines currently under construction, such are the electron–ion collider, eRHIC [3] or the heavy ion synchrotron SIS100 in Germany [4], as well as the next large colliders such as Future Circulars Colliders (FCC-ee and FCC-hh) in Europe [5,6] and the Circular Electron Positron Collider, CEPC, or Super Proton-Proton Collider, SPPC in China [7]. This effect is mainly attributed to non-thermal gas desorption stimulated by particles, such as photons, electrons, ions and beam-loss particles, impinging on the inner surface of a vacuum vessel. In particular, the electron stimulated desorption (ESD) is of major importance for modern machines that exhibit electron cloud (EC), a phenomenon originating from closely spaced dense bunched beams.

The LHC is a proton storage ring of 27 km circumference designed to collide proton beams at 14 TeV in the centre of mass [8]. It consists of superconducting magnets with a 1.9 K cold bore. A beam–screen (BS) cooled to 5–20 K, is inserted into the cold bore to extract the heat generated by the circulating beam via resistive wall heating, synchrotron radiation (SR) and by electron cloud (EC) [9,10]. At the nominal beam energy of 7 TeV, the relativistic proton beam emits synchrotron radiation of 44 eV critical energy that is intercepted by the BS. As observed during the beam energy ramp-up above 2 TeV [1], the energy of the emitted SR photons surpasses the ~4 eV work function of the copper surface to extracts photoelectrons. Slow photoelectrons are then accelerated by the electric field of the passing proton bunches [11], impinge on the beam-screen surface again, multipact and form an EC [12]. Under the conditions when the EC prevails, a self-sustaining electron population continuously irradiates the BS surface, desorbing gas. The closed geometry of the beam tube inherently limits the pumping speed and makes the gas sources mitigation even more important. Similar to room temperature machines, while operating the LHC, the electron-cloud activity and the dynamic vacuum diminish [1], a phenomenon systematically observed during LHC's Run 1 [13–17] and Run 2 [18,19]. This is due to the decrease of the secondary electron yield (SEY) and the surface conditioning (decrease of ESD) under electron bombardment. As a result, the dynamic vacuum effect gradually

* Corresponding author at: European Organization for Nuclear Research (CERN), Geneva, Switzerland.
E-mail address: michal.haubner@cern.ch (M. Haubner).

https://doi.org/10.1016/j.nimb.2022.09.013
Received 7 July 2022; Received in revised form 7 September 2022; Accepted 14 September 2022
Available online 30 September 2022

attenuates with operation time to an acceptable level but remains a concern when pushing up the accelerators' performance [20]. During the LHC commissioning, this non-thermal electron desorption mechanism was confirmed as the predominant gas source. Hence, the relationship between EC and the dynamic pressure rise calls for a systematic investigation, as it plays a crucial role in an effective operation of the LHC and its upcoming high-luminosity upgrade, the HL–LHC [21].

Available problematics overviews [22], including simulations [23] and even recent measurements [24] taken on the LHC's long straight sections, have shown that the electrons energy distribution of an EC resides mainly in the low energy, with a major peak below 10 eV and half of the population below ~20 eV. When the EC establishes a stable population, the major peak of secondary electrons is followed by a minor peak of beam-accelerated electrons at hundreds of eV. This electron energy distribution indeed varies with the actual beam parameters and the geometry, magnetic fields and surface state of the beam-screen. Therefore, we have designed an experimental setup to investigate material samples representative of the LHC's beam screen under the conditions it experiences in LHC cryomagnets. The setup controllably reproduces the relevant conditions in terms of: cryogenic temperatures under 20 K, ultrahigh vacuum in the 10^{-11} mbar range and low-energy and high-dose electron irradiation. Our present research focuses on developing a new measurement procedure to study the ESD and SEY in the sub-keV energy region at cryogenic temperatures, which is particularly relevant for the dynamic vacuum effect, but equally experimentally challenging.

Technical-grade metal surfaces are prevalent in industrial-scale installations, such as particle accelerators and impose a technical challenge due to their ill-defined surface state. Indeed, the employed UHV-grade cleaning procedures effectively reduce outgassing, both thermal and stimulated, as demonstrated by Mathewson [25]. Still, a technical surface exhibits statistical nature in terms of crystal orientation, chemical composition, oxide layer thickness, micro-porosity and texture, due to various air–exposure times, contamination, stains and batch-to-batch variation, differences in machining, cleaning and storage. The hereafter investigated surface was sampled from an LHC-grade metal sheet; an industrially produced technical-grade polycrystalline oxygen-free electronic "OFE" copper colaminated onto a stainless-steel sheet and thermally treated to 900 °C in a H_2 atmosphere. After cutting, the copper sample was cleaned for UHV in a warm ultrasonically agitated isopropanol bath, packaged in a plastic foil and then briefly exposed to an atmospheric air prior to insertion into the UHV chamber via a load-lock system. Hence, we study copper sample in an unbaked as–received surface state, as it is in the LHC cryomagnets.

2. Material and methods

2.1. Setup description

The experimental setup developed to study the ESD and SEY at cryogenic temperatures mainly consists of a μ–metal vacuum chamber, a 4-axis cryomanipulator, a low-energy electron gun and a quadrupolar mass spectrometer (QMS) fitted inside a collector. The setup is further equipped with a storage chamber and a load-lock chamber to introduce unbaked samples into the baked experimental chamber, allowing us to study the LHC BS in its actual as received unbaked surface state.

The vacuum chamber is constructed of μ–metal that shields off stray magnetic fields by a factor of 100, preventing deviation of the primary electron beam and altering trajectories of low-energy secondary electrons. A base pressure in the ultra-high vacuum (UHV) range of 10^{-11} mbar is achieved by a combination of turbomolecular, getter-cartridge vacuum pumps, cryo-pumping and a bakeout to 150 °C for 3 days. This ensures a monolayer (ML) formation time in the range of hours, such that the studied cold surface is not altered during a measurement, e.g. not altered following cryosorption of residual gas from the background.

The studied flag-type sample is inserted into the cryomanipulator which uses an open-cycle liquid He circuit that is vibration-free and capable of approaching a temperature of 10 K, as measured by a diode sensor mounted directly inside the sample holder. The sample holder is mounted onto the cryostat via a sapphire plate for a good thermal contact but electrical insulation, allowing the sample biasing and current measurement. The cryostat itself goes below 5 K, generating a strong cryopumping effect that reduces the base pressure from 10^{-10} to 10^{-11} mbar range.

A Kimball ELG-2 electron gun is used to imitate a monoenergetic slice of the energy spectrum of the LHC's electron cloud, allowing us to decouple contributions of different primary electron energies. According to specifications, the gun provides a stable, focused (<1 mm^2), monoenergetic ($\Delta E < 1$ eV), low energy (2 eV – 2 keV) and low intensity (0.1 nA – 10 μA) analytical beam. The electron gun is equipped with a Faraday cup (FC) for a direct current measurement of the emitted electrons. The focused beam irradiates the studied sample with perpendicular incidence from a focal distance of ~ 5 cm through circular openings in the collector.

As schematized in Fig. 1, the setup features a collector tube made of 0.1 mm thick stainless-steel sheet custom-designed to contain the secondary electrons and desorbed gas species. The collector geometry composes of a 75 mm wide and 750 mm long tube with an QMS on one side and an endcap on the opposite side. The endcap has two concentric 4 mm diameter openings that are in a line of sight with the e^- gun nozzle, allowing the primary electron beam to reach the studied sample. The closed geometry formed by the collector positioned 0.25 mm from the sample effectively captures most of the emitted and backscattered secondary electrons, which we have evidenced experimentally and by simulation. Both the sample and collector are electrically insulated from the ground (>100 GΩ at 500 V_{DC}), by a sapphire plate and a ceramic interpiece, to allow biasing and net current measurement of electrons arriving and leaving the system. Electric battery cells are used to bias the sample, chosen for their long-term stability and low intrinsic dark current. The collector is held at the ground potential for all experiments, whereas the sample bias V_S is set at −28 V for all energy-dependent SEY & ESD measurements and at +46 V for electron conditioning measurements using monoenergetic beams. The sole exception is conditioning using low-energy electrons, where a retarding bias set at −28 V is required to reach such low energies. For electron energies above 70 eV, the +46 V bias has the advantage of smaller dynamic background at the expense of no simultaneous SEY measurement.

The SEY is measured solely via the electron currents captured on the sample and collector. However, the ESD yield measurement can be subdivided into the current measurement of the primary electron beam and the measurement of the desorbing gases. For clarity, these will be treated separately, starting with the beam current measurement followed by a SEY measurement of Highly Oriented Pyrolytic Graphite (HOPG) reference sample.

2.2. Beam current measurement

The closed geometry of the sample–collector system effectively forms a Faraday cup, so that the sample current I_S and the collector current I_C sum up to the primary electron beam current I_B that interacts with the studied surface. The nozzle of the electron gun is also equipped with a rotating Faraday cup, whose reading equals to the net current gathered by the sample–collector system across the investigated energy range. The data acquisition (DAQ) chain consists of two Keithley 428 ammeters that typically provide a gain of 10^6 V/A and 10^9 V/A for ESD and SEY measurements, respectively. We use a built-in function of 100 ms integration time to suppress noise before directing the amplified signal into a DAQ card with a 16-bit wide A/D converter. The proper calibration and the nominal current reading are regularly verified across the DAQ chain. Coherent current reading across our system, from the e-gun Faraday cup to the sample–collector system, is also checked regularly

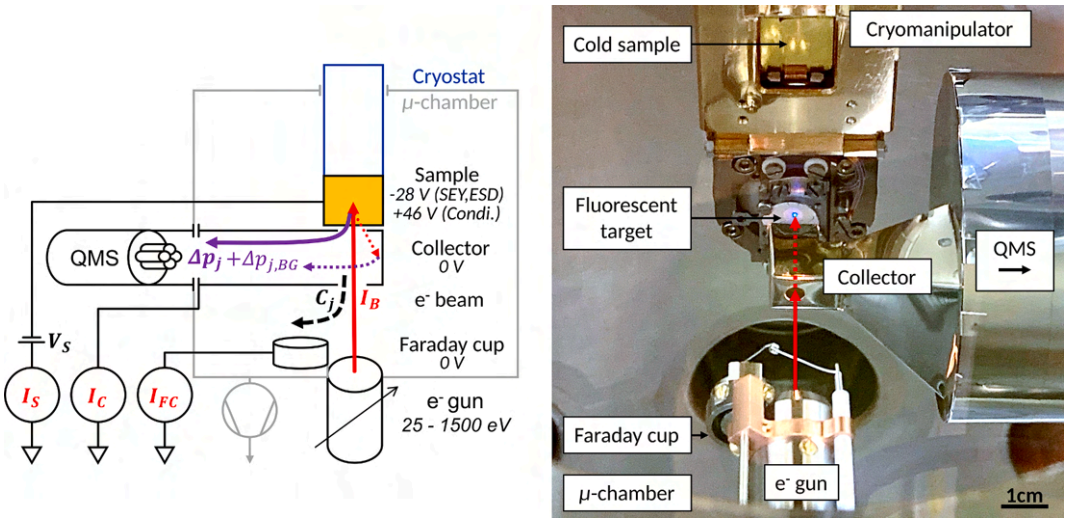

Fig. 1. Schematized arrangement for SEY and ESD yield measurements in the sub-keV region. See the text for detailed description.

and brings confidence in our electron current measurements.

The negative bias of $V_S = -28$ V imposed on the sample creates a retarding potential that decelerates the primary electron beam before impact. The potential gradient also repels the emerging secondary electrons away from the negatively biased sample towards the grounded collector, where they are measured as the collector current I_c. The scan across the energy spectrum is realized by incrementally ramping up the electron gun energy from 25 eV up to 1.4 keV, being the energy interval feasible in our arrangement. Doing so, the measurement of both SEY and ESD effectively starts from 0 eV electron kinetic energy as referenced to the vacuum level E_{vac} of the biased sample. When the kinetic energy of primary electrons lies below the electrostatic potential of the sample, the entire beam is reflected towards the collector, as measured in our setup and illustrated in Fig. 4. Once the kinetic energy surpasses the retarding potential, the primary electron beam begins interacting with the sample in various ways and all secondaries are recollected and sum up to the collector current I_C.

To obtain a uniform electron dose across the irradiated spot, we under-focused the electron beam from an originally Gaussian transverse profile (≈Ø1 mm) to a circular shape with an approximately flat-top profile. We first visually tuned the beam profile at different energies using a fluorescent target and then verified the transverse profile by cross–scanning it in two directions using a Ø 10 mm Faraday cup mounted on the cryomanipulator's rear side. To ensure that the probe beam fits into the conditioned spot, we used a Ø 3 mm wide beam spot (7.1 mm^2) for conditioning, but only Ø 2 mm wide beam (3.1 mm^2) to probe the ESD and SEY energy dependence. We also verified the spot size post-mortem by measuring the diameter of the discolored spot that appeared on the conditioned sample. The Fig. 2 schematizes the use of the knife edge scan technique for an e^- beam profile measurement of a 260 eV beam spot. The FC current I_{FC} increases, as the beam gradually crosses the edge and enters the FC. Finally, the width of the ramp determines the beam size to be Ø 3 mm (6.5–3.5 mm) wide, as marked in the plot. The same result is obtained in both horizontal and vertical directions, marked X and Z.

Table 1 lists the typical electron beam parameters used in our measurements. The beam current used for a SEY measurement is about 0.5 nA and surpasses by a factor of 50 the dark current of the data acquisition electronics. A SEY measurement is considered non-destructive, as it does not desorb gas from the sample, nor does it chemically alter the surface. Conversely, an ESD scan over the feasible energy range (0–1.1 keV) is by definition destructive as the surface gas coverage is depleted.

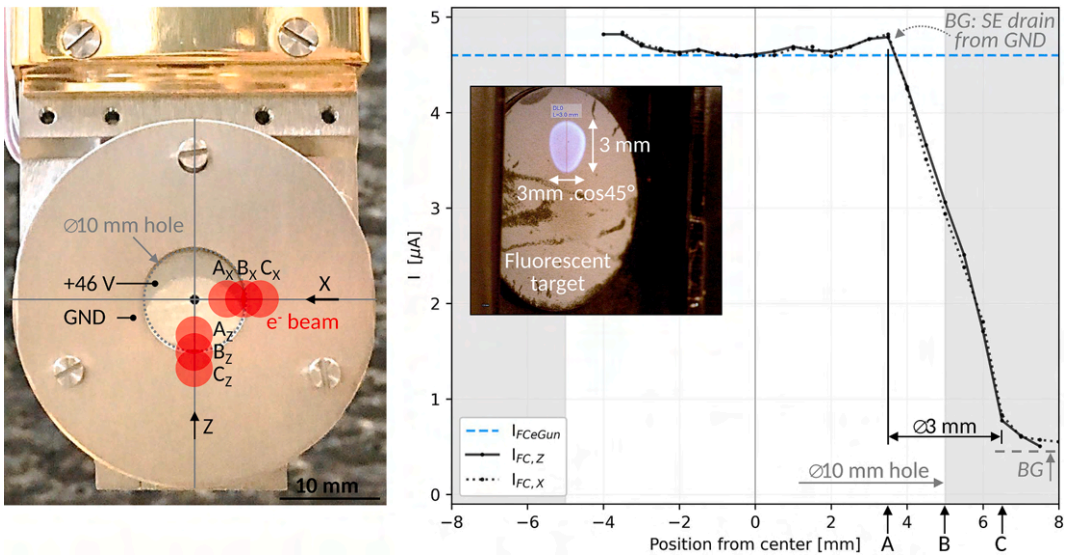

Fig. 2. Left: Cryomanipulator far side with concentric Faraday cups and annotations. Right: Scan of e^- beam transverse profile in X and Z directions using a knife edge scan technique on the Ø 10 mm wide Faraday cup.

Table 1
Typical electron beam parameters used to measure the SEY and ESD energy dependence and for electron conditioning.

	I_B [A]	Spot diameter [mm]	Dose per measurement [C.mm^{-2}]	Dose per datapoint [C.mm^{-2}]	Time per measurement [min]
SEY energy scan	0.5nA	2	2.10^{-8}	2.10^{-10}	5
ESD energy scan	2 μA	2	7.10^{-5}	2.10^{-6}	5
Conditioning	~2μA	3	5.10^{-3}	–	90

Typically, a beam current in the μA range is necessary to generate a significant change in partial pressure of the studied gas species. In an effort to minimize the conditioning effect, i.e. electron dose per area imparted by an energy scan for ESD measurement, we minimize the irradiation time, the beam current and the number of datapoints. We also under-focus the beam to Ø 2 mm to increase the spot diameter, as compared to the focused ≈Ø 1 mm Gaussian profile. Besides that, most measured datapoints reside below 20 eV, as the datapoints are dense in this dynamic low-energy region and sparse above that. As a result, an ESD measurement with a dose in the mid 10^{-5} C.mm^{-2} range has a minor conditioning effect, which is limited, in the worst-case scenario, to some tens of % on an as-received surface. We verified that the curve preserves its shape when doing the energy scan in a reverse direction, hence ruling out a possible conditioning effect. We also obtain the same shape on a conditioned surface, where electron dose imparted by the energy scan can be neglected. Finally, we calculated a combined uncertainty of 10 % on the imparted dose per unit area. Indeed, the combined uncertainty is evaluated via the square sum of uncertainties weighted by the respective partial derivatives squared.

2.3. SEY measurement

In engineering practice, the SEY is defined as the average number of electrons emitted from the sample per incoming primary electron, regardless of the scattering mechanism. In our setup, the SEY can be directly evaluated from the currents measured on the collector and sample, which allows the acquisition of a full SEY curve during a single routine. This helps in avoiding uncertainties linked to the e- gun stability when the SEY is acquired in a two-step mode (e.g. when modifying the sample bias or inserting a Faraday cup to measure the primary electron beam). We estimate a combined uncertainty of about 5 % on the SEY value across the studied range.

The sample current I_S is a sum of arriving primaries and escaping secondaries. The SEY of the surface renders this net current either positive or negative. The collector current I_C contains all secondaries and is always positive. Normalizing the collector current I_C by the beam current I_B allows us to calculate the SEY, denoted δ, as follows in eq. (1):

$$\delta = I_{SE}/I_B = I_C/(I_S + I_C) \quad (1)$$

The SEY evolves with the primary energy and so do the relative proportions of reflected, backscattered and secondary electrons. The incoming electrons can either be elastically backscattered at the original energy, inelastically backscattered at an intermediate energy, or create true low-energy secondary electrons. The electron energy distribution of secondaries was calculated [26] and also measured [27] for the exact same technical-grade polycrystalline copper as in our present investigation. Reflected electrons, i.e. elastically backscattered, are predominant for primary energies below ~ 20 eV, and true secondary electrons dominate above.

We used a HOPG as a calibration reference to validate our current measurement method, which is crucial for SEY and ESD measurements. The HOPG sample with a 0.8° mosaic spread was air–cleaved and load–locked into the UHV, where it was conditioned by 300 eV electrons to remove the surface contaminant overlayer. The HOPG sample was not baked nor high temperature annealed. Fig. 2 shows the SEY curve measured on the HOPG sample and its inset zooms into the low-energy region.

The inset clearly shows the work function edge of the SEY curve, where the primary electrons just make it over the potential barrier of the studied surface. The sample current is nil below and non-zero above this value [28]. We used this edge as a reference to calibrate the energy scale and set the vacuum energy level $E_{vac} = 0$ eV, thereby excluding the work function and its possible changes from our studies. The exact position of 0 eV is verified for each sample in each run and used as a reference also for the ESD energy scans.

Above this edge, the SEY curve exhibits a fine structure across the studied energy range but is especially visible at energies below 40 eV. The ability to detect this fine structure substantiates the energy resolution we achieve with this setup. These findings, along with the peak value δ_{max} are in excellent agreement with the HOPG SEY measurements of Gonzalez, Cimino et al. [29,30] and Bellissimo et al. [31].

2.4. Desorbing gas flux measurement

When positioned at only 0.25 mm away from the studied sample, the collector also acts as a Feulner cap [32], directing the desorbed gas species towards the QMS positioned inside the collector. Hence, the desorbed species are analyzed before being pumped from the collector's inner volume through the geometry-restricted opening that is the only pumping port, i.e. with no additional pumping on the collector. The collector's closed geometry creates a conductance-limited system, which restricts the pumping speed, decouples the collector's inner volume from the heavily cryo-pumped chamber and invariably defines the pumping speed across all experiments and irrespective of possible variations. The differential pumping also rules out possible sample contamination by electron source degassing. Aside from the QMS, the collector houses a Bayard-Alpert Gauge (BAG) that only serves the described calibration purposes and is switched off during regular operation to reduce outgassing and prevent possible gas fragmentation, pumping, and a memory effect. A bakeout combined with electron conditioning of the inner surfaces ensures low thermal outgassing [33] and low stimulated gas desorption of the collector [34], further minimizing the residual gas background, as detailed in the next section. For completeness, the collector used here was recently redesigned towards the current Feulner cap style since our last publication [35]. This upgraded design enhanced the sensitivity of desorption measurements, for both ESD and Temperature Programmed Desorption (TPD), by more than 2 orders of magnitude by reducing the cryopumping of desorbed molecules onto the cryostat. Given the collector's geometrical proportions, cryopumping on the cold sample can only lead to an underestimation of the measured ESD yield by a factor of 2 in the upper limit. This factor is given by the ratio of pumping to cryopumping speeds, both given by the two 4 mm holes. We indeed observe this transient effect in the early stage of electron conditioning, and it is in line with the observations made by Anashin [36] and Malyshev [37].

The gas load Q_j [mbar.l.s^{-1}] of a species j desorbed in the collector is calculated from the known pumping speed of the collector C_j [l.s^{-1}], from the measured change in the QMS current Δi_j [A] and QMS absolute sensitivity k_j, [A.mbar^{-1}] to a gas j. Both the conductance and the QMS sensitivity are calibrated in-situ by a gas injection at room temperature, as follows.

To determine the collector conductance C_j, a constant flux Q_j of a single gas species is injected alternately through the collector conductance C_j or through a reference conductance $C_{j,ref}$ (not shown ins Fig. 1).

This reference conductance is calculated analytically, corrected for the Clausius factor and the result checked against a simulation. Since the flux Q_j is kept constant, the resulting pressure differences Δp_j and $\Delta p_{j,ref}$ are in the same proportion as the conductances C_j and $C_{j,ref}$. The H_2, CH_4, N_2 and Ar gases are injected to measure the conductance C_j as a function of molar mass M_j, uniformly covering the relevant mass/charge range from 2 m/q to 40 m/q. The measured conductances C_j are then fitted with a scaling factor inversely proportional to the molar mass $(1/M_j)^{1/2}$ to obtain a function of $C_j = f(M_j)$ used for gas load calculation. This calibration procedure for $C_j = f(M_j)$ results into a pumping speed of 21.8 ℓ/s for H_2 with a systematic uncertainty of ~20 % for all masses. Such approach provides a more robust estimate of the collector conductance than one would achieve by simply measuring and scaling the H_2 conductance by $(2/M)^{1/2}$ for heavier gases.

Since the QMS calibration is essential for partial pressure measurement of individual gas species present in the collector, we performed an in-situ calibration by injecting gases of interest, i.e. dominant residual gases: H_2, CO, and CH_4, C_2H_6 as well as N_2 and Ar. The absolute sensitivities for CO_2 and H_2O were adopted from ex-situ measurements due to their challenging nature. An ex–situ calibrated BAG served as an absolute pressure reference to determine the absolute sensitivity k_j of the Pfeiffer QMG700 QMS to a partial pressure of a gas species j. A gas injection creates a single gas-dominated atmosphere, that allows us to reference the QMS current reading at the corresponding mass/charge to the pressure read by the BAG, corrected for the relative sensitivity to N_2. The QMS sensitivity k_j is referenced to an ex-situ calibrated BAG (SVT type) that has an estimated 10 % uncertainty on the absolute pressure reading. We calculated a systematic uncertainty of QMS partial pressure p_j measurement of 20 %, induced by long-term variations, but considered constant throughout a run. The noise-induced statistical uncertainty is measured around 10 % for the partial pressure change Δp_j.

2.5. ESD yield derivation

The measured ESD yield $\eta_{e,j}$ of a given gas species j is calculated by dividing the gas flux of each desorbed gas species Q_j by the total electron flux impinging on the sample surface I_B/q_e, as seen in eq. (2). The flux of desorbing gas is calculated knowing the gas-dependent pumping speed $Q_j(M_j)$ and the partial pressure rise Δp_j measured by a calibrated QMS. The change in a partial pressure Δp_j is calculated as the change in QMS current Δi_j divided by the absolute sensitivity $k_j[A.mbar^{-1}]$ of the QMS to a given gas species j. The temperature T is estimated to be 300 K, as any desorbing gas quickly thermalizes in the room-temperature collector before reaching the QMS, hence no need to correct for thermal transpiration. The electron flux is obtained from the total current of the primary electron beam $I_B = I_C + I_S$ divided by the electron charge q_e. The input variables uncertainties propagate to about 30 % combined uncertainty at 1 σ confidence level for the calculated ESD yields across all relevant conditions. The statistical uncertainty contributes with about 10 % and leads to a repeatability and precision of the same magnitude.

$$\eta_{e,j} = \frac{C_j.\Delta i_j/k_j}{k_B.T} \Big/ \frac{I_B}{q_e} + \frac{C_j.\Delta i_{j,BG}/k_j}{k_B.T} \Big/ \frac{I_C}{q_e} \simeq \frac{C_j.\Delta i_j/k_j}{k_B.T} \Big/ \frac{I_B}{q_e} \quad (2)$$

The second term in the eq. (2) stands for the parasitic gas desorption originating from the collector's inner surface, which recollects reflected, backscattered, and true secondary electrons emitted by the sample. This irradiation creates a so-called 'dynamic background' that manifests as a non-zero value of ESD yield around 0 eV energy and below, where the molecular desorption threshold from the sample itself is nil (see Fig. 4). Since the dynamic background intensity scales linearly with the primary beam current I_B, it cannot be avoided by optimizing the beam current. Instead, we reduced this dynamic background by about one order of magnitude by electron conditioning the collector's inner surface. This was done by holding a dummy sample at –200 V with respect to the grounded collector and irradiating it with a high current and high energy primary beam. The reflected and secondary electrons escaping from the dummy sample effectively conditioned the stainless-steel surface of the collector in direct view of the sample. Following this procedure, the dynamic background is conditioned and currently limits our instrumental sensitivity to about 10^{-3} H_2 /e^- and 10^{-4} CO/e^-, depending on the biasing scheme. However, it is only a limiting factor for measuring highly conditioned metal surfaces with low ESD yields, typically around threshold energy and at high electron doses. In all other cases, i.e. above the threshold energy and at moderate electron doses, the strong signal from the high-yielding sample dominates over the dynamic background signal. The true ESD yield is then measured, as represented by the right term of eq. (2).

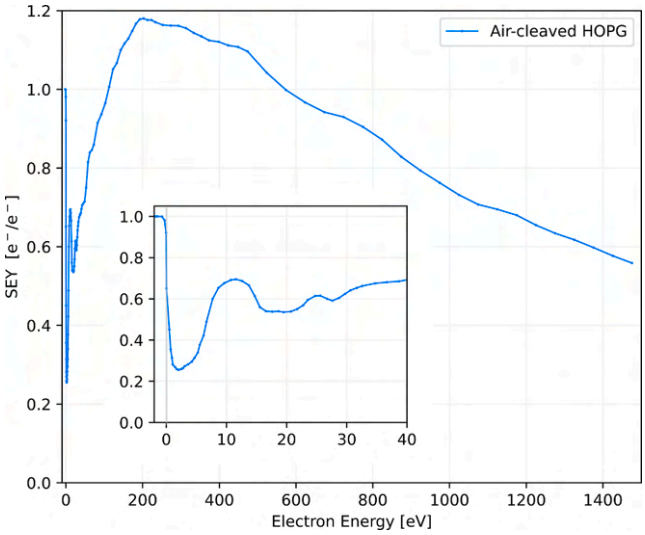

Fig. 3. SEY measured as a function of primary electron kinetic energy on an air-cleaved HOPG reference sample held at ambient temperature. The inset zooms into the low-energy region. The energy is referenced to the vacuum level.

2.6. ESD threshold derivation

The ESD yield energy dependence can be measured point-by-point at discrete values of primary electron energies. The top-left side in Fig. 4 plots a time series of square wave modulation of the beam current, as measured in the sample-collector system. Each peak is measured with incrementally larger primary electron energy. For this ESD measurement, the datapoints are spaced by 1 eV below 16 eV and progressively more above this low-energy region. The bottom-left side shows the QMS readout, which is also modulated in direct response to the electron beam. Each displayed datapoint is sampled during a 5 s long irradiation interval, allowing a stable QMS reading interleaved with a 5 s long idle time with no e^- beam to recover the background pressure and retune the e^- gun. We began with the QMS sampling through all channels at 1 Hz rate and later increased it to 10 Hz for higher temporal resolution at the cost of marginal noise increase. To speed up the acquisition time of an ESD energy scan, as well as to minimize the imparted electron dose, we later decreased the modulation period to 4 s and tuned down the beam current to units of μA. This optimized measurement routine is now automated in LabVIEW with postprocessing in Python to ensure reproducibility. As denoted for the QMS channel at 2 m/q, corresponding to H_2, the signal consists of a static background (1 nA) coming from the residual gas, then a dynamic background (0.25 nA) originating from the electron-irradiated collector, and finally, the signal from the sample itself that interests us.

To calculate the ESD yield, the static background is subtracted from all measured datapoints, as denoted by the Δi_j in Eq. (2). Only the dynamic component is kept, illustrating the detection limit imposed by the dynamic background. Hence, the right side of Fig. 4 plots the 'uncorrected' ESD yield is for $^{15}N_2$, H_2 and CO as a function of the primary

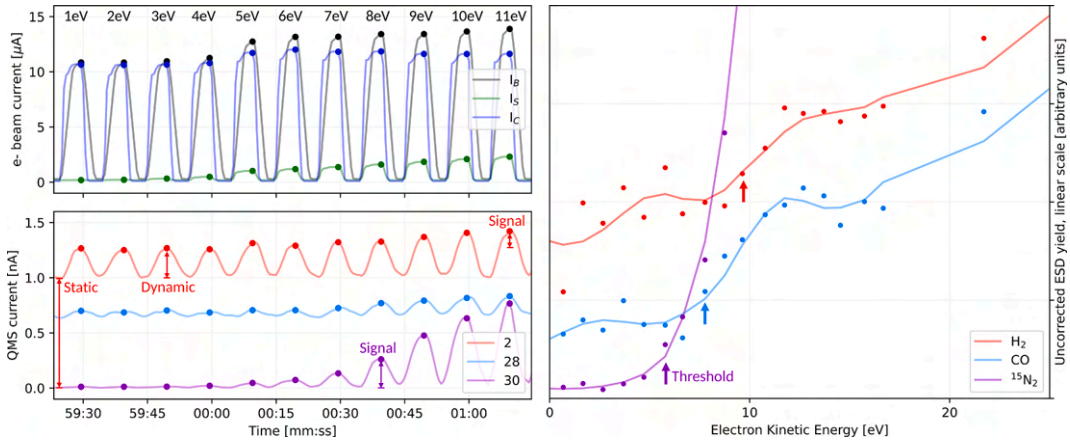

Fig. 4. Low-energy ESD yield measurement of partly conditioned copper surface held at 15 K with a 1 ML precoverage of $^{15}N_2$ used as a tracer. Top-left: Time series of e^- beam, sample and collector currents, all modulated to a square wave. The kinetic energy is incremented by 1 eV each cycle. Bottom-left: QMS currents for 2, 28 and 30 m/q modulated in response to the e^- beam current. Right: Datapoints and S-G smoothed trendlines for H_2, CO and $^{15}N_2$ yields as a function of primary e^- kinetic energy. Arrows mark the desorption threshold energies for each gas. Note the noise and dynamic background levels of $^{15}N_2$ compared to H_2 and CO.

electron kinetic energy referenced to the sample. To capture the approximative trendline behind the scattered datapoints, we used a Savitzky-Golay (S-G) smoothing filter [38], that effectively removes noise while preserving detail of the dynamics behind it.

We used an isotopically labelled $^{15}N_2$ as a tracer gas to commission this measurement method by obtaining an easily and unambiguously interpretable data. A thin pre-coverage of $^{15}N_2$ (1 monolayer, ML) was quench–condensed over the semi-conditioned copper substrate held at 15 K. The gas dose equivalent to a 1ML coverage was determined by analysing a series of TPD curves, a method described earlier[35]. The sample is then irradiated with electrons of increasing energy that would eventually surpass the energy threshold and start desorbing the cryosorbed $^{15}N_2$. As opposed to the $^{14}N_2$ that resides at a highly polluted peak 28 *m/q* of a residual gas spectrum, the $^{15}N_2$ isotope resides at a peak 30 *m/q*, which is a clean channel with little natural background. This makes our $^{15}N_2$ signal clearly distinguishable from the static and dynamic backgrounds, so the desorption threshold can be clearly identified. We measured the threshold energy for the $^{15}N_2$ desorption to be around 6 eV. This corresponds to Rakhovskaia's [39] measurement for a 50 ML thick N_2 coverage that gives 7.6 eV, referenced to the vacuum level. This is reasonably close to our result and the observed difference can be either a sensitivity limitation imposed by the dynamic background or a substrate-related effect linked to a single- versus multilayer coverage regime.

Despite the 1 ML-thick adsorbate overlayer, the electron beam interacts with the copper substrate, desorbing the hereafter studied H_2 and CO. The noisy and elevated background renders it difficult to identify the signal coming from the copper sample, but, knowing what to look for, the same threshold behaviour can also be identified for H_2 and CO. The dynamic background maintains a quasi-constant value across this low-energy region. Once the primary electron energy surpasses the desorption threshold, the ESD yield rises about linearly with energy and ultimately the signal of the high-yielding sample rapidly dwarves the background. To locate the threshold energy, one can characterize the dynamic background by its mean value and standard deviation. The threshold can be defined as the first datapoint that surpasses the background's mean value and standard deviation. Indeed, this experimental approach works well for relatively high-yielding samples but cannot detect energy thresholds below this noisy background. Following this method, one can estimate the energy threshold for H_2 to be around 9 eV and 8 eV for CO, as indicated in Fig. 4 and discussed in detail in Section 3.2.

We carried out a series of complementary measurements to support the correctness of our threshold identification from our experimental data. First, we tested the energy threshold moves accordingly when imposing a small variation to the sample's retarding bias. Second, we dosed multilayer pre-coverages of other gases, such as $^{15}N_2$, CH_4 and Ar over Cu and Au substrates, to verify that these cryosorbed gases exhibit similarly high yields and low energy thresholds around 10 eV and irrespective of the used substrate. Further tests performed with as-received copper samples held at ambient temperatures did not show any measurable difference in the energy thresholds as compared to the cryogenic conditions. These experiments unambiguously link the desorbing $^{15}N_2$ gas, and by extension other gases, to the source at the cold sample, demonstrating that the chosen experimental approach is correct and provides valid and reproducible data in agreement with the literature.

3. Results and discussion

With the presented experimental methods, we obtained the following results for an unbaked as-received OFE copper surface held at 15 K, sampled from an industrially produced LHC sheet. All measurements, i.e. electron conditioning, ESD and SEY energy scans, were performed at 15 K. Each electron conditioning and subsequent ESD and SEY energy scan was measured on a previously intact spot of the same copper sample. The sample was heated to 100 K and cooled back down to 15 K before each ESD measurement to desorb gases that could cryosorb from the residual gas background. For clarity, we commence with measurements of SEY energy dependence and its dependence on electron irradiation. We then add energy scans of ESD yields for the same conditioning states. Finally, we investigate the influence of temperature on ESD yields when going from ambient to cryogenic temperatures.

3.1. SEY measurement

We measured the SEY curves of each surface state before and after each electron irradiation, see Fig. 5 The as-received surface state of the LHC-grade copper again serves as the baseline, having a high $\delta_{max} = 2.9$ located at $E_{max} = 250$ eV.

First, we measured that 300 eV electron irradiation most effectively decreases the SEY curve across the entire studied energy range. Electron dose of $8.4 \cdot 10^{-4}$ C.mm^{-2} conditions the SEY to a peak value $\delta_{max} = 1.1$, a value below the multipacting threshold in dipoles, quadrupoles and field-free regions in the LHC that have thresholds of 1.3, 1.1 and 1.5, respectively. A similar dose of 1 keV electrons only conditioned the SEY to $\delta_{max} = 1.25$, but further irradiation proved that 1 keV can also decrease the SEY to $\delta_{max} = 1.1$. Furthermore, 1 keV irradiation does not

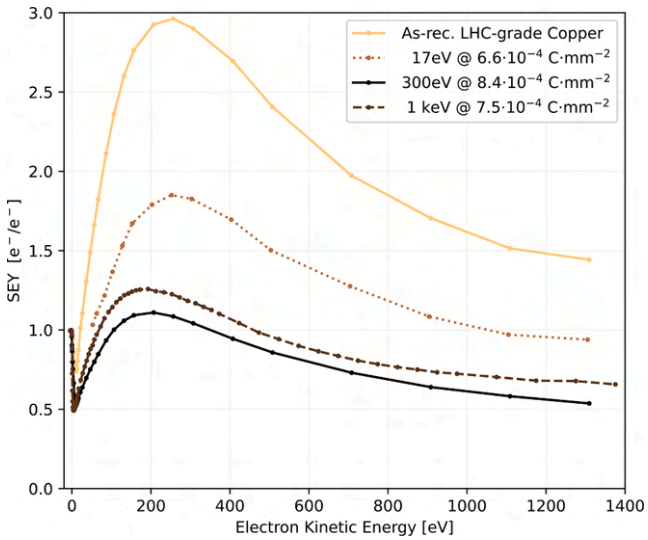

Fig. 5. SEY of a Cu surface held at 15 K as a function of primary electron kinetic energy and surface state. Note that the effective SEY decreases when conditioned with 300 eV and 1 keV instead of a limited conditioning effect of 17 eV electron irradiation.

condition proportionally faster than 300 eV, but is less performant instead. This, along with the general shape of SEY curve, suggest that it is the near-surface true secondary electrons responsible for the conditioning effect.

Irradiation with 17 eV electrons at this moderate dose manifested as a limited decrease of SEY to $\delta_{max} = 1.8$. The slight decrease seems to be linked to a limited removal of contaminants. As for the peak position E_{max} on the energy axis is shifted from 250 eV to about 200 eV when conditioned with 300 eV and 1 keV, but remains unchanged after the 17 eV irradiation. Note that the HOPG from Fig. 3, representing a graphitic surface, peaks out around $E_{max} = 200$ eV. The inability to approach $\delta_{max} = 1.1$ and no E_{max} decrease both point to the lack of graphitization of surface contaminants when irradiated with 17 eV electrons. Increasing the 17 eV electron dose up to a 5 mC.mm^{-2} does bring a more tangible conditioning effect, achieving $\delta_{max} \approx 1.5$, but never reaches the ultimate efficacy of higher energy electron irradiation.

Our SEY measurements taken at cryogenic temperatures correspond with the results presented in literature, typically taken at ambient temperature. We observe the same effect as, Nishiwaki [40], or Scheuerlein [41], who linked the SEY decrease to surface graphitization and Cimino et al. [42,43], who demonstrated the limited conditioning effect of low-energy electrons. Our experimental observations agree with the general understanding of SEY conditioning developed at ambient temperatures and seen as well at cryogenic conditions by Cimino et al. [27]. More SEY curves taken at ambient and cryogenic temperature were published for technical-grade Cu, Al and SS [44], which exhibit similarly positioned E_{max} but different δ_{max}. Though these results are inconclusive due to an unspecified surface state in terms of e$^-$ conditioning and cryosorbate precoverage.

3.2. ESD yield energy dependence

We then studied the energy dependence of H_2 and CO ESD yields in the 0–1.1 keV energy range using the measurement procedure and data analysis detailed above. Similarly to SEY scrubbing, the primary electron energy plays a major role in the ESD conditioning. Fig. 6 shows H_2 and CO yields measured as a function of primary electron energy for an unbaked LHC–grade copper in several conditioning states. Other gases, such as CO_2 and CH_4 were also measured and exhibit the same general behaviour but are not depicted for simplicity. The ESD curves were first measured for an as-received surface state and then again after irradiation with an electron dose of ~7.10^{-4} C.mm^{-2} at energies of 17 eV, 300 eV and 1 keV. The discrete scattered datapoints are smoothed with an S-G filter to facilitate reading the general trend. To illustrate the statistical uncertainty of the measurement, we plot the raw datapoints around the smoothed curve of the as–received state.

This investigated energy range contains the following regions of interest for H_2 and CO. We will discuss these regions separately and also interpret the acquired data in the framework of the IMGR model [45–47] as Desorption Induced by Electronic Transitions (DIET).

First, it is the desorption threshold, where the ESD yield of each gas rises significantly above the dynamic background once the primary electron energy surpasses the threshold energy necessary to trigger the desorption. As the initial step of the gas desorption process, the electronic transition brings about a threshold behaviour that we observed for both physisorbed and chemisorbed gas species. We measured the threshold energies around 6 eV for cryosorbed $^{15}N_2$, and higher for chemisorbed gases: 8 eV for CO and 9 eV for H_2. This indeed agrees with the theoretical framework, as stronger-bound species should have higher thresholds and lower yields. The threshold energy lies just under 10 eV, remarkably close to the anecdotal '10-Volt effect' from Redhead's memoirs [48]. Besides this, the only closest dataset is that of Billard et al. [49], who measured desorption from a technical-grade copper surface at ambient temperature and only extrapolated towards the low energy. Their extrapolated energy threshold lies in the 10 eV region for both H_2

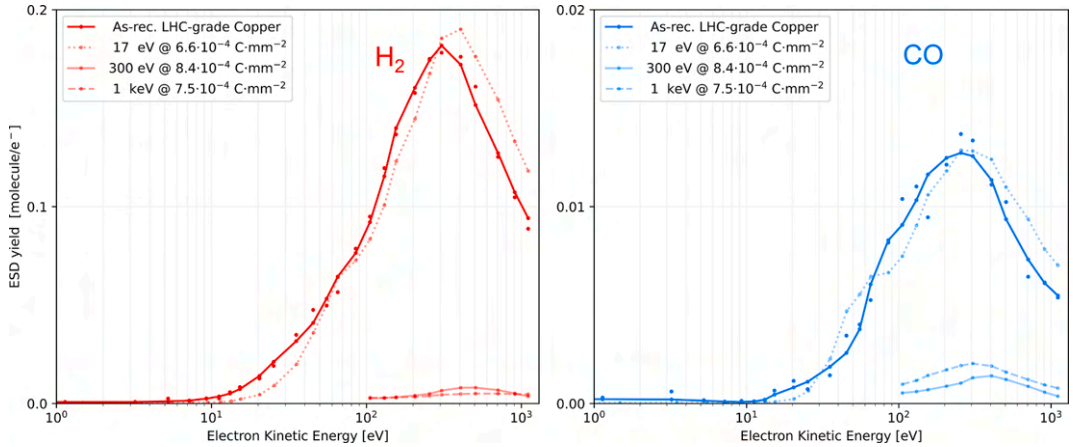

Fig. 6. H_2 (left) and CO ESD yields for LHC-grade copper surface held at 15 K at different conditioning states measured as a function of primary electron energy. Datapoints measured on an as-received Cu are scatter-plotted around the smoothed curve to illustrate the statistical uncertainty. Mind the log x-scale to capture the low energy region and different vertical scales for H_2 and CO.

and CO, which compares well to our values. There is no other available data regarding the low-energy ESD from unbaked technical-grade metals, especially at cryogenic temperatures.

Beyond the energy threshold, the ESD yield increases monotonically until about 300 eV, where the ESD yield peaks out. In this energy region, the ESD yield is proportional to the net energy deposited by the primary electrons within the electron escape depth, i.e. 'close' to the surface and therefore available to stimulate desorption. The primary electron energy is deposited in electronic excitations that may further dissipate by triggering either electron or molecular emission, manifesting as SEY or ESD phenomena. This common origin places the peaks at about the same energy for both ESD and SEY curves. Once more, the experimental observations support the DIET interpretation.

As the primary electron energy increases, the energy deposition depth also increases, and fewer electronic excitations reach the surface to promote gas desorption (or secondary electron emission). We have recently illustrated this argument in detail for the case of thick adsorbate layers [35]. Consequently, the ESD yield either levels off or even peaks out at few hundreds of eV.

When further increasing the primary energy, the peak is followed by a slow decay with a generic $1/E^n$ energy dependence, as the energy deposition depth penetrates deeper into the bulk [50], below the escape depth of electronic excitations [51]. Such general behaviour was also measured for technical copper by Achard [52] in an open–geometry experimental arrangement similar to ours. By contrast, Malyshev devised a closed-geometry experiment [53], more similar to an actual beam–screen, and measures a knee, where others detect a peak, followed by only a less steep increase at few hundreds of eV. This dissonance of results taken in different experimental arrangements is to be better understood.

As for the electron conditioning effect, i.e. ESD decrease during extended electron irradiation, the exposure to 300 eV and 1 keV electrons efficiently scrubs off gas prone to desorption and gradually decreases the ESD yield across the investigated energy range. The result of conditioning strongly varies when comparing the conditioning effect of 17 eV, 300 eV and 1 keV electron irradiation. A moderate dose of 300 eV and 1 keV electron effectively reduced the yield across the investigated energy range by a factor of 20 for H_2 yield and the CO yield by about a factor of 5. It is worth noting here that 1 keV irradiation does not condition proportionally faster when compared to 300 eV, similarly to what is observed for SEY. As opposed to 300 eV and 1 keV, irradiation with 17 eV electrons had no measurable effect on the ESD yield at this moderate electron dose and needs to be further investigated at much higher doses. The limited conditioning effect of low-energy electrons was indeed observed for ESD yield of stainless steel at ambient temperatures by Malyshev et al. [53] and is in line with observations made on SEY of copper by Cimino et al. Hence, the primary electron energy significantly influences the electron conditioning efficiency.

3.3. ESD yield temperature dependence

Since the cryomanipulator allows active control of the sample temperature, we also investigated the ESD yield temperature dependence between 15 K and 265 K, see Fig. 7 The transition to cryogenic temperatures strongly influences the ESD yield as measured on another as-received copper sample irradiated by 300 eV electrons. Notably, ESD yields of all followed gasses decreased at cold on average by a factor of 10, with the sole exception of CO_2 yield which plummeted by 2 decades. No hysteresis or conditioning was observed, as the same ESD yields were measured during a cool-down and warm-up phase. When decreasing the temperature, the ESD yield drops first for heavier molecules, such as H_2O, and at lower temperatures for lighter ones, such as H_2. However, the molar mass alone does not explain all the variability.

This measurement suggests that the ESD yield's limiting step is the recombination rate and/or surface mobility, which are both strongly temperature-dependent. This phenomenon is to be studied better to understand the origin of this decrease at low temperatures. A similar trend was observed by Baglin and Jenninger in COLDEX [54], when exposing a semi-conditioned copper BS to a synchrotron radiation of 194 eV critical energy while varying the temperature from ambient down to 5 K. The PSD yield from the studied technical-grade copper had notably similar behaviour, i.e. also dropped at cryogenic temperatures by a similar factor as we observed here for the ESD. This is no coincidence, as the DIET theory also encompasses the PSD, as practically illustrated by Schumann et al. [55].

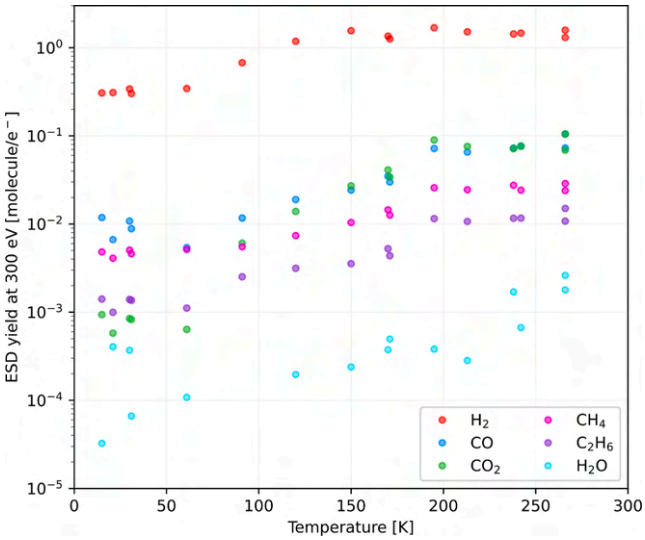

Fig. 7. Temperature dependence of ESD yield as measured at 300 eV energy on an as-received LHC-grade copper surface.

4. Summary and conclusions

We have designed and commissioned an experimental approach to measure the SEY and ESD yield of metal surfaces held at cryogenic conditions, in order to investigate the low-energy electron irradiation of LHC-grade copper beam screen material held at cryogenic temperatures. This includes the ESD yield evolution with energy and temperature, measurement of the desorption threshold energy, and assessing the scrubbing efficiency of different electron energies.

To reach this objective, we use a combination of a low-energy monochromatic electron source and a retarding sample bias, which enables the study of the 0–1.4 keV energy range. In combination with electron conditioning of the dynamic background, a newly designed molecular collector in a Feulner cap style [31] increased our experimental sensitivity to 10^{-3} H_2/e^- range. We used a Highly Oriented Pyrolytic Graphite as a reference sample to validate the SEY measurement against existing data. We then used an isotopically labelled $^{15}N_2$ cryosorbed onto the copper sample, which enabled us to discriminate the signal from static and dynamic backgrounds, thus validating the low-energy ESD measurement. The newly commissioned setup delivers reproducible results in agreement with the general understanding of the problematics and comparable data, whether for SEY [27,43] or ESD yields, thresholds and conditioning [52,49,56].

With this new instrument at hand, we present the first direct laboratory measurement of ESD yield in the sub–keV energy range of LHC-grade copper held at a temperature of 15 K. We demonstrated that the post-irradiation ESD yield and SEY both strongly depend on the primary electron energy used for irradiation, as shown for 17 eV, 300 eV and 1 keV at doses around 7.10^{-4} C.mm^{-2}. The presented data further demonstrates that the electron conditioning equally works at cryogenic temperatures in a manner similar to ambient temperatures and drives the SEY below the multipacting limit of LHC quadrupoles $\delta_{max} < 1.1$. We then substantiate the importance that surface temperature has on the

ESD yield by varying temperatures between from 265 K to 15 K and back.

Our experimental results are particularly relevant for understanding the relation between the electron cloud activity and the dynamic vacuum effect systematically observed in LHC's cryogenic beam tube during Run 1 [1,10,13–17] and Run 2 [18,19], or other accelerators operating at cryogenic temperature [57], including the future ones [3,4,6,7]. Considering that the energy spectrum of an electron cloud lies mostly below the desorption threshold [24], the data we present can be used to better understand the dynamic vacuum effect or optimize the beam-scrubbing strategy toward faster conditioning rates [58]. Insofar, our experimental data indicate that the beam scrubbing effect can be partly attributed to the decrease of SEY and partly to the ESD yield decrease, also in the cryogenic temperature region that was previously uncharted. We also demonstrated that the primary electron energy is of major importance in this low-energy region and needs further investigation. Therefore, we intend to continue the research to refine the understanding of ESD problematics for various technical-grade metal surfaces taken under a range of environmental and irradiation conditions.

CRediT authorship contribution statement

Michal Haubner: Data curation, Formal analysis, Investigation, Methodology, Software, Visualization, Writing – original draft, Writing – review & editing. **Vincent Baglin:** Conceptualization, Funding acquisition, Methodology, Project administration, Writing – review & editing. **Bernard Henrist:** Conceptualization, Methodology, Resources.

Declaration of Competing Interest

The authors declare that they have no known competing financial interests or personal relationships that could have appeared to influence the work reported in this paper.

Data availability

Data will be made available on request.

Acknowledgements

The authors thankfully acknowledge the support of CERN's TE-VSC group, its workshop, and N. Kos for providing the LHC-grade samples.

The corresponding author's work was partly supported by the Ministry of Education, Youth and Sports of the Czech Republic [Czech Technical University in Prague project SGS21/149/OHK2/3T/12] and by the HL-LHC Project.

References

[1] V. Baglin, G. Bregliozzi, G. Lanza, J.M. Jimenez. Synchrotron radiation in the LHC vacuum system (No. CERN-ATS-2011-245). URL: epaper.kek.jp/IPAC2011/papers/tups019.pdf. 2011.

[2] W. Fischer, M. Blaskiewicz, M. Brennan, H. Huang, H.C. Hseuh, V. Ptitsyn, ... U. Iriso. Electron cloud observations and cures in RHIC. In 2007 IEEE Particle Accelerator Conference (PAC) (pp. 759-763). IEEE. https://doi.org/10.1103/PhysRevSTAB.11.041002. 2007.

[3] S.Y. Zhang. eRHIC Beam Scrubbing, BNL-114220-2017-IR, June 2017, Brookhaven National Laboratory, Upton, NY, United States. https://doi.org/10.2172/1392223.

[4] G. Rumolo, I. Hofmann, E. Mustafin, O. Boine-Frankenheim. Vacuum and electron cloud issues at the GSI present and future facilities. Proc. of ECLOUD'04: 31st advanced ICFA beam dynamics workshop on electron-cloud effect,. 2005, Napa, CA, USA, (pp. 95-101). https://doi.org/10.5170/CERN-2005-001.95.

[5] M. Benedikt, et al., FCC-ee: the lepton collider, Eur. Phys. J. Special Top. 228 (2) (2019) 261–623, https://doi.org/10.1140/epjst/e2019-900045-4.

[6] M. Benedikt, et al., FCC-hh: the hadron collider, Eur. Phys. J. Special Top. 228 (4) (2019) 755–1107, https://doi.org/10.1140/epjst/e2019-900087-0.

[7] The CEPC-SPPC Study Group, CEPC-SppC Preliminary Conceptual Design Report, Vol II: Accelerator, IHEP-CEPC-DR-2015-01, March 2015. URL: https://cepc.ihep.ac.cn/preCDR/Pre-CDR_final_20150317.pdf.

[8] O. Brüning, et al. LHC Design Report. CERN-2004-003, June 2004, Geneva, Switzerland. https://doi.org/10.5170/CERN-2004-003-V-1.

[9] O. Gröbner, Overview of the LHC vacuum system, Vacuum 60 (1–2) (2001) 25–34, https://doi.org/10.1016/S0042-207X(00)00240-2.

[10] F. Zimmermann (2002). Electron cloud effects in the LHC. https://doi.org/10.5170/CERN-2002-001.47.

[11] S. Berg. Energy gain in an electron cloud during the passage of a bunch (No. LHC-Project-Note-97). CERN-LHC-Project-Note-97. URL: https://cds.cern.ch/record/692004.

[12] G. Arduini, V. Baglin, E. Benedetto, R. Cimino, P. Collier, I. Collins, ... & F. Zimmermann. Present understanding of electron cloud effects in the Large Hadron Collider. In Proceedings of the 2003 Particle Accelerator Conference (Vol. 3, pp. 1727-17s29). IEEE. URL: https://cds.cern.ch/record/620194. 2003.

[13] G. Rumolo, N. Mounet, C. Zannini, Arduini, et al. Electron cloud observations in LHC (No. CONF, pp. 2862-2864), Proc. of IPAC'11, Sept 2011, San Sebastian, Spain. URL: https://jacow.org/IPAC2011/papers/THOBA01.pdf. 2011.

[14] G. Bregliozzi, V. Baglin, P. Chiggiato, P. Cruikshank et al. Observations of electron cloud effects with the LHC vacuum system, Proc. of IPAC'11, September 2011, San Sebastian, Spain. paper TUPS018, pp. 1560-1562. URL: https://jacow.org/IPAC2011/papers/TUPS018.pdf.

[15] G. Lanza, V. Baglin, G. Bregliozzi, J. M. Jimenez. LHC Beam vacuum during 2011 machine operation, Proc. of IPAC'12, May 2012, New Orleans, Louisiana, USA. URL: https://jacow.org/IPAC2012/papers/WEPPD018.pdf.

[16] G. Lanza, V. Baglin, G. Bregliozzi, J.M. Jimenez. LHC vacuum system: 2012 review and 2014 outlook, Proc. of LHC beam operation workshop - Evian 2012, December 2012, CERN-ATS-2013-045, Geneva, Switzerland. URL: https://cds.cern.ch/record/2302432.

[17] V. Baglin, G. Bregliozzi, G. Lanza, J.M. Jimenez. Vacuum performance and lessons for 2012, Proc. of Chamonix 2012 workshop on LHC performance, CERN-2012-006, Geneva, Switzerland. https://doi.org/10.5170/CERN-2012-006.74.

[18] E. Buratin, V. Baglin, B. Henrist, P. Chiggiato, A. Fasoli, Electron flux and pressure dynamic in the LHC vacuum pilot sector as a function of beam parameters and beam pipe properties, Phys. Rev. Accelerators Beams 23 (11) (2020), 114802, https://doi.org/10.1103/PhysRevAccelBeams.23.114802.

[19] C.Y. Vallgren, P.R. Metidieri, G. Bregliozzi. Beam induced dynamic pressure during Run 2 (2015-2018): Machine operation in the LHC. In CERN Yellow Reports: Conference Proceedings (Vol. 7, pp. 65-65). https://doi.org/10.23732/CYRCP-2020-007.65. 2020.

[20] V. Baglin, The LHC vacuum system: commissioning up to nominal luminosity, Vacuum 138 (2017) 112–119, https://doi.org/10.1016/j.vacuum.2016.12.046.

[21] High-Luminosity Large Hadron Collider (HL-LHC): Technical Design Report Ed. by I. Bejar Alonso, O. Brüning, P. Fessia, M. Lamont, L. Rossi, L. Tavian, M. Zerlauth. CERN 2020-10, CERN, Geneva, Switzerland. https://doi.org/10.23731/CYRM-2020-0010.

[22] R. Cimino, T. Demma, Electron cloud in accelerators, Int. J. Modern Phys. A 29 (17) (2014) 1430023.

[23] G. Iadarola. Electron cloud studies for CERN particle accelerators and simulation code development (Doctoral dissertation, CERN). URL: https://cds.cern.ch/record/1705520/. 2014.

[24] E. Buratin. Electron Cloud and Synchrotron Radiation characterization of technical surfaces with the Large Hadron Collider Vacuum Pilot Sector (Doctoral dissertation, CERN). EPFL. URL: https://cds.cern.ch/record/2746058. 2020.

[25] A.G. Mathewson. The effects of cleaning and other treatments on the vacuum properties of technological materials used in ultra high vacuum. Vuoto, Scienza e Tecnologia, 17(3) 1987 102-116. URL: https://cds.cern.ch/record/183509.

[26] J. Cazaux, Reflectivity of very low energy electrons (<10 eV) from solid surfaces: physical and instrumental aspects, J. Appl. Phys. 111 (6) (2012), 064903, https://doi.org/10.1063/1.3691956.

[27] R. Cimino, I.R. Collins, Vacuum chamber surface electronic properties influencing electron cloud phenomena, Appl. Surface Sci. 235 (1–2) (2004) 231–235, https://doi.org/10.1016/j.apsusc.2004.05.270.

[28] R. Cimino, L.A. Gonzalez, R. Larciprete, A. Di Gaspare, G. Iadarola, G. Rumolo, Detailed investigation of the low energy secondary electron yield of technical Cu and its relevance for the LHC, Phys. Rev. ST Accel. Beams 18 (5) (2015), 051002, https://doi.org/10.1103/PhysRevSTAB.18.051002.

[29] L.A. Gonzalez, R. Larciprete, R. Cimino, The effect of structural disorder on the secondary electron emission of graphite, AIP Adv. 6 (9) (2016), 095117, https://doi.org/10.1063/1.4963644.

[30] R. Cimino, M. Angelucci, L.A. Gonzalez, R. Larciprete, SEY and low-energy SEY of conductive surfaces, J. Electron Spectrosc. Relat. Phenomena 241 (2020), 146876, https://doi.org/10.1016/j.elspec.2019.06.008.

[31] Bellissimo, Alessandra, et al. Secondary electron generation mechanisms in carbon allotropes at low impact electron energies. J. Electron Spectrosc. Relat. Phenomena 241 (2020): 146883. https://doi.org/10.1016/j.elspec.2019.07.004.

[32] P. Feulner, D. Menzel, Simple ways to improve ''flash desorption'' measurements from single crystal surfaces, J. Vacuum Sci. Technol. 17 (2) (1980) 662–663.

[33] V. Nemanič, J. Setina, Outgassing in thin wall stainless steel cells, J. Vacuum Sci. Technol. A: Vacuum, Surfaces, Films 17 (3) (1999) 1040–1046, https://doi.org/10.1116/1.581680.

[34] O.B. Malyshev, B.T. Hogan, M. Pendleton. Effect of surface polishing and vacuum firing on electron stimulated desorption from 316LN stainless steel. J. Vacuum Sci. Technol. A: Vacuum, Surfaces, Films, 32(5) 2014 051601. DOI: https://doi.org/10.1116/1.4887035.

[35] R. Dupuy, M. Haubner, B. Henrist, J.H. Fillion, V. Baglin, Electron-stimulated desorption from molecular ices in the 0.15–2 keV regime, J. Appl. Phys. 128 (17) (2020), 175304, https://doi.org/10.1063/5.0021832.

[36] V.V. Anashin, O.B. Malyshev, I.R. Collins, O. Gröbner. Photon-stimulated desorption and the effect of cracking of condensed molecules in a cryogenic vacuum system. Vacuum, 60(1-2) 2001 15-24. https://doi.org/10.1016/S0042-207X(00)00239-6.
[37] O.B. Malyshev. Vacuum in Particle Accelerators: Modelling, Design and Operation of Beam Vacuum Systems. John Wiley & Sons. 2020. https://doi.org/10.1002/9783527809134.
[38] A. Savitzky, M.J. Golay, Smoothing and differentiation of data by simplified least squares zprocedures, Analyt. Chem. 36 (8) (1964) 1627–1639, https://doi.org/10.1021/ac60214a047.
[39] O. Rakhovskaia, P. Wiethoff, P. Feulner, Thresholds for electron stimulated desorption of neutral molecules from solid N_2, CO, O_2 and NO, Nucl. Instrum. Methods Phys. Res. B Nucl. Instrum. Meth. B 101 (1–2) (1995) 169–173, https://doi.org/10.1016/0168-583X(95)00296-0.
[40] M. Nishiwaki, S. Kato, Graphitization of inner surface of copper beam duct of KEKB positron ring, Vacuum 84 (5) (2009) 743–746, https://doi.org/10.1016/j.vacuum.2009.06.028.
[41] C. Scheuerlsein, M. Taborelli, N. Hilleret, A. Brown, M.A. Baker, An AES study of the room temperature conditioning of technological metal surfaces by electron irradiation, Appl. Surf. Sci. 202 (1–2) (2002) 57–67, https://doi.org/10.1016/j.vacuum.2009.06.028.
[42] R. Larciprete, D.R. Grosso, M. Commisso, R. Flammini, et al., Secondary electron yield of Cu technical surfaces: dependence on electron irradiation, Phys. Rev. Special Top.-Accelerators Beams 16 (1) (2013), 011002, https://doi.org/10.1103/PhysRevSTAB.16.011002.
[43] R. Cimino, M. Commisso, D.R. Grosso, T. Demma, V. Baglin, R. Flammini, R. Larciprete, Nature of the decrease of the secondary-electron yield by electron bombardment and its energy dependence, Phys. Rev. Lett. 109 (6) (2012), 064801, https://doi.org/10.1103/PhysRevLett.109.064801.
[44] J. Fang, Y. Hong, S. Wang, Y. Wang, B. Zhu, W. Zhang, B. Bian, Y. Wang, Cryogenic secondary electron yield measurements on structural materials applied in particle accelerators, Nucl. Instrum. Methods Phys. Res. Sect. A: Accelerators, Spectrometers, Detectors and Associated Equipment 1027 (2022) 166292, https://doi.org/10.1016/j.nima.2021.166292.
[45] Y. Isikawa, 51. The desorption of the adsorbed hydrogen on a platinum plate by the impact of slow electrons, Proc. Imperial Acad. 18 (5) (1942) 246–250, https://doi.org/10.2183/pjab1912.18.246.
[46] D. Menzel, R. Gomer, Desorption from metal surfaces by low-energy electrons, J. Chem. Phys. 41 (11) (1964) 3311–3328, https://doi.org/10.1063/1.1725730.
[47] P.A. Redhead, Interaction of slow electrons with chemisorbed oxygen, Can. J. Phys. 42 (5) (1964) 886–905, https://doi.org/10.1139/p64-083.
[48] P.A. Redhead, The first 50 years of electron stimulated desorption (1918–1968), Vacuum 48 (6) (1997) 585–596, https://doi.org/10.1016/S0042-207X(97)00030-4.
[49] F. Billard, N. Hilleret, G. Vorlaufer. Some results on the electron induced desorption yield of OFHC copper. Vacuum Technical Note 00-32, CERN. https://doi.org/10.17181/CERN.9UX2.OKJV. 2000.
[50] K.A. Kanaya, S. Okayama, Penetration and energy-loss theory of electrons in solid targets, J. Phys. D: Appl. Phys. 5 (1) (1972) 43, https://doi.org/10.1088/0022-3727/5/1/308.
[51] Q. Gibaru, C. Inguimbert, M. Belhaj, M. Raine, D. Lambert, Monte-Carlo simulation and analytical expressions for the extrapolated range and transmission rate of low energy electrons [10 eV–10 keV] in 11 monoatomic materials, Appl. Surf. Sci. 570 (2021), 151154, https://doi.org/10.1016/j.apsusc.2021.151154.
[52] M.H. Achard (1976). Desorption des gaz induite par des electrons et des ions de l'acier inoxydable, du cuivre OFHC, du titane et de l'aluminium purs, CERN-ISR-VA-76-34, CERN, Geneva, Switzerland. CM-P00064839. URL: https://cds.cern.ch/record/314507.
[53] O.B. Malyshev, et al., Electron stimulated desorption from the 316 L stainless steel as a function of impact electron energy, J. Vacuum Sci. Technol. A: Vacuum, Surfaces, Films 31 (3) (2013), 031601, https://doi.org/10.1116/1.4798256.
[54] V. Baglin, I.R. Collins, O. Gröbner, C. Grünhagel, B. Jenninger, Molecular desorption by synchrotron radiation and sticking coefficient at cryogenic temperatures for H_2, CH_4, CO and CO_2, Vacuum 67 (3–4) (2002) 421–428, https://doi.org/10.1016/S0042-207X(02)00226-9.
[55] M. Andritschky, O. Gröbner, A.G. Mathewson, F. Schumann, P. Strubin, R. Souchet, Synchrotron radiation induced neutral gas desorption from samples of vacuum chambers, Vacuum 38 (8–10) (1988) 933–936, https://doi.org/10.1016/0042-207X(88)90495-2.
[56] K. Kennedy. Electron stimulated desorption rates from candidate vacuum chamber surfaces. LBL, Berkeley, July 1986. DOI: 10.2172/1872213 URL: https://www.osti.gov/biblio/1872213/.
[57] S.Y. Zhang, L. Ahrens, J. Alessi, M. Bai, et al. Experience in reducing electron cloud and dynamic pressure rise in warm and cold regions in RHIC, Proc. of EPAC 2006, June 2006, Edinburgh, Scotland. URL: https://www.osti.gov/biblio/885019.
[58] O. Bruning, F. Caspers, I.R. Collins, O. Grobner, B. Henrist, N. Hilleret, ... X. Zhang. Electron cloud and beam scrubbing in the LHC. In Proceedings of the 1999 Particle Accelerator Conference (Cat. No. 99CH36366) (Vol. 4, pp. 2629-2631). IEEE. URL: https://cds.cern.ch/record/386682. 1999.

Contents lists available at ScienceDirect

Vacuum

journal homepage: www.elsevier.com/locate/vacuum

Electron conditioning of technical surfaces at cryogenic and room temperature in the 0–1 keV energy range

Michal Haubner [a,b,*], Vincent Baglin [b], Bernard Henrist [b]

[a] Department of Physics, Faculty of Mechanical Engineering, Czech Technical University in Prague, Czech Republic
[b] European Organization for Nuclear Research (CERN), Geneva, Switzerland

ARTICLE INFO

Keywords:
Electron conditioning
Electron-stimulated desorption
Secondary electron yield
Dynamic vacuum effect
Technical surface
Cryogenic temperatures

ABSTRACT

In the superconducting magnets of the Large Hadron Collider (LHC) at CERN, most of the beam-induced heat load is intercepted by a beam-screen (BS) cryogenically cooled to 5–20 K. When circulating the bunched proton beam, an electron cloud (EC) can form and bombard the BS copper surface with high doses of predominantly low-energy electrons, which desorb gas and consequently increase the pressure. The beam-induced pressure rise decreases during operation as the electron irradiation diminishes the secondary electron yield (SEY) and the electron-stimulated desorption (ESD) yield, a phenomenon referred to as 'beam conditioning'. Low ESD and SEY values achieved rapidly are requisite to mitigate EC and maintain UHV in storage rings. We report data on ESD and SEY electron conditioning completed at cryogenic temperature with 0–1 keV electrons up to an electron dose of 5.10^{-3} C mm^{-2}. Our results show that SEY conditioning depends on the primary electron energy and also that ESD yield significantly decreases with temperature. At 15 K, the amorphous-carbon coating and laser-treated copper present SEY below 1.1 and have initial ESD yields 3–6 times lower than OFE copper. Our results conform to the SEY and ESD's general understanding and extend it towards cryogenic temperatures.

1. Introduction

The CERN's Large Hadron Collider (LHC) and other present or future cryogenic storage rings [1–6] develop an electron cloud (EC) when circulating a bunched particle beam. Inside the LHC beam-screen (BS) the circulating 7 TeV proton beam emits synchrotron radiation (SR) at critical energy of 44.1 eV [7], which irradiates the technical-grade copper surface of the BS and extracts photoelectrons [8,9]. These mostly low-energy electrons gain more energy from the electric wake-field behind passing proton bunches and impinge on the BS surface again while extracting secondary electrons. If the secondary electron yield (SEY) is sufficiently high, a positive feedback loop can form that is known as electron multipacting. The EC activity also leads to a pressure rise via electron stimulated desorption (ESD). High EC activity triggered by high SEY values imposes additional heat load on the BS cryogenic cooling, while high ESD yield values ultimately lead to a large dynamic pressure rise when circulating the proton beam. Hence, low values of ESD and SEY achieved in a short time of operation, are an imperative to maintain UHV conditions, to mitigate EC and to limit the heat load on cryogenics of storage ring. As a remedy, both the SEY and the ESD yield of the BS decrease to sufficiently low values when subjected to extended electron irradiation, which is a commonly observed effect in LHC [10–13] and other accelerators [3,14–16]. In fact, dedicated beam-scrubbing runs were performed in the LHC to quickly reach high electron doses on the BS, leading to low SEY and ESD values that enable operating the machine at its full performance [17]. In-situ measurements performed at the LHC Vacuum Pilot Sector (VPS) by E. Buratin [18], as well as EC simulations by G. Iadarola [19], and other investigations [20], demonstrated that low-energy electrons below 20 eV dominate the EC energy spectrum with a minor peak of beam-accelerated electrons at few hundreds of eV. New accelerators operating at cryogenic temperature are designed with techniques in mind to mitigate the EC and the dynamic vacuum effect [21–23]. For the High-Luminosity LHC (HL-LHC) upgrade, novel low-SEY surface treatments are developed to effectively suppress electron multipacting leading to an EC formation and doing so also suppress the dynamic pressure rise caused by the ESD [24].

We present new ESD and SEY data measured at room and cryogenic temperatures for a technical-grade OFE copper in an as-received unbaked state cleaned for UHV by a warm ultrasonic isopropanol bath. The copper we used in this study closely represents the current state of the LHC beam-screen surface [8,9], which is made of an OFE

* Corresponding author. Department of Physics, Faculty of Mechanical Engineering, Czech Technical University in Prague, Czech Republic.
E-mail address: michal.haubner@cern.ch (M. Haubner).

https://doi.org/10.1016/j.vacuum.2022.111656
Received 6 January 2022; Received in revised form 1 July 2022; Accepted 1 November 2022

copper, colaminated onto a stainless-steel sheet and heat-treated under H_2 atmosphere. We didn't measure a notable difference between these two within our instrumental precision. This OFE copper surface serves as a baseline for comparing the two new low-SEY surface treatments studied for the HL-LHC: amorphous-carbon (a-C) coating [25] and laser-treated copper [26].

The amorphous-carbon was proven to lower the SEY below the EC multipacting limit, even at remarkably thin coverages [27]. We investigate the same 50 nm thin a-C coating that was recently deployed in one LHC quadrupole magnet during Long Shutdown 2. This is not to be confused with a much thicker version of 400 nm that was tested with LHC-type proton beams at CERN's SPS machine [28,29] and at cryogenic conditions inside the COLDEX experiment [30,31] and recently deployed in the CERN's SPS [32]. The samples tested here were created as witness samples when coating the COLDEX BS with a 50 nm a-C prior to installation for future tests in the framework of the HL-LHC upgrade.

The laser-treated surface was also successfully tested at cryogenic temperatures with LHC-type proton beams in the COLDEX [33,34]. The OFE copper samples investigated here were laser-treated with the following COLDEX-like parameters: 532 nm wavelength, 5 μJ pulse energy, 10 ps pulse duration, 240 pulses. s^{-1}, 200 kHz repetition rate, 13 μm beam width, 24 μm hatch distance, 10 mm s^{-1} scanning speed and under N_2 atmosphere. The laser settings indeed influence the resulting SEY, as reported [35], and presumably also the ESD. The same laser treatment also generates equally low SEY for stainless-steel and aluminium [26].

2. Material and methods

The experimental setup aims to reproduce in a controlled way the relevant HL-LHC conditions (UHV, temperature below 20 K, unbaked sample) of its cryogenic system and to study the ESD and SEY. Detailed technical description is given in a dedicated paper [63], so only briefly (see Fig. 1). At cryogenic temperatures, residual gases cryosorb on the cold surfaces, including the studied sample. Hence, the UHV is a must, corresponding to a Langmuir monolayer formation time in the order of few hours, giving enough time to study the intact surface. The pressure range of 10^{-10} mbar is achieved by a combination of a turbomolecular pump, a non-evaporable getter pump and a bakeout at 150 °C during 72 h. The μ-metal chamber houses a 4-axis cryomanipulator capable of cooling the studied flag-type sample down to 15 K by an open-cycle LHe cooling. Samples are inserted via a Load-lock, hence unbaked samples can be studied.

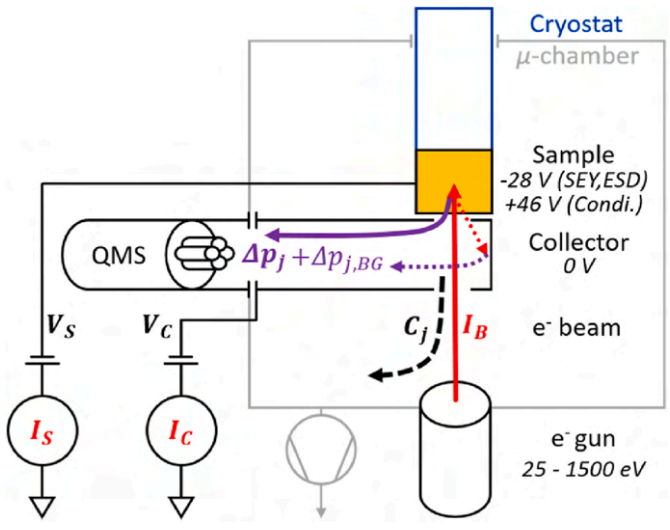

Fig. 1. Schematized arrangement for SEY and electron desorption measurements in the 0–1 keV region. See the text and Ref. [63]

Yet another experimental target is to reproduce the low-energy electron irradiation in the form of a monoenergetic slice of the electron cloud energy spectrum. This implies high accumulated doses, up to few mC.mm^{-2}, of low-energy electrons in the sub-keV range. A Kimball ELG-2 electron gun irradiates at a normal incidence the studied sample surface in a way that the EC in an accelerator would. The gun generates an electron beam with a low-energy (0–1.5 keV), low-intensity (0.1 nA - 10 μA), small spot size (3–7 mm^2) and with a flat-top profile, as measured by a Faraday-cup. A custom-designed collector is positioned 0.25 mm away from the sample and creates a closed geometry that captures the electrons and molecules that escape the studied sample as a result of the primary electron bombardment. The collector is spot-welded from stainless steel sheets, forming a geometry essentially consisting of a 75 mm wide and 750 mm long tube extending toward the QMS and an endcap with two 4 mm circular holes left for the primary electron beam to pass through the collector to the sample. Both the sample and collector are electrically floating, insulated by a sapphire plate and a ceramic interpiece, respectively, which allows measuring the electron currents and imposing a retarding sample bias. In addition, the collector acts as a Feulner cap [36] that protects the sample from any parasitic contamination originating from the setup and restricts the pumping speed to guide the desorbed gas molecules towards the quadrupole mass spectrometer (QMS) prior to being pumped. The conductance-limited pumping speed on the collector's inner volume, where the QMS is located, is invariably fixed by the geometry and does not change with the pumping speed inside the μ-chamber, that can vary. The pumping speed of the collector, with one hole covered by the sample, was calibrated against a known reference conductance by injecting gases alternately through this known conductance and into the collector. The measured conductance is 21.8 ℓ/s for H_2, with an uncertainty of 20%, and scales proportionally to $(2/M)^{1/2}$ for other gases of molecular mass M. This conductance is higher than expected for a 4 mm hole alone, because of gaps in the welded sheets. The collector is held at an ambient temperature, so the desorbing gases readily thermalize to 300 K, ruling out the need to correct for cryopumping and thermal transpiration. Meanwhile, the cryostat reaches ~5 K during a cooldown and the sample temperature remains around 15 K. The collector was redesigned since our last publication [37] towards a Feulner cap design, to mitigate gas recycling on the cold cryostat. Using this new experimental arrangement and methods, we measure the SEY and ESD yield of material surfaces as a function of energy and dose, at ambient and cryogenic temperatures, as follows.

Firstly, the Sample-Collector system acts as a Faraday cup that geometrically captures all the incoming electrons, as we have experimentally verified. The sum of collected currents equals the beam current $I_B = I_S + I_C$. This beam current I_B is then taken to calculate the SEY and ESD yield, as all these primary electrons do interact with the sample in some way. We set the sample bias to −28 V to measure the SEY and ESD as a function of primary electron energy. The low-energy electron beam in combination with the repulsive bias enables the energy sweep to start at 0 eV, as referenced to the sample. In this setting, the secondary electrons produced at the sample are repelled towards the grounded collector, where they form the collector current I_C. Dividing the collector current I_C by the beam current I_B gives the SEY, denoted δ, as follows:

$$\delta = I_{SE} / I_B = I_C / (I_S + I_C) \quad (1)$$

Secondly, the differentially pumped collector enables measuring the ESD yield $\eta_{e,j}$ of a gas species j as a result of primary electron irradiation of the studied sample. The yield is calculated from the calibrated vacuum conductance C_j of the collector and the pressure rise Δp_j, as measured by the in-situ calibrated QMS.

$$\eta_{e,j} = \frac{C_j.\Delta p_j}{k_B.T} \Big/ \frac{I_B}{q_e} + \frac{C_j.\Delta p_{j,BG}}{k_B.T} \Big/ \frac{I_C}{q_e} \approx \frac{C_j.\Delta p_j}{k_B.T} \Big/ \frac{I_B}{q_e} \quad (2)$$

The measured ESD yield of a gas species $\eta_{e,j}$ has two terms. The first

term corresponds to the gas desorption from the studied sample stimulated by the primary electron beam I_B. The second term represents the dynamic background stimulated by electron current I_C impinging on the molecular collector which itself is a source of electrodesorbed gas. The collector is made of a 0.1 mm stainless-steel sheet that was UHV-cleaned and baked to achieve low degassing [38], followed by an in-situ electron conditioning. Hence, this dynamic background, captured by the second term, is generally much lower than the first term that comes from the high-yielding as-received sample under investigation. The static background from the residual gas is subtracted, as expressed by the Δp_j term in Equation (2). However, the dynamic background is not subtracted and its level is visible in the 0–10 eV range of Fig. 4. When measuring the ESD yield conditioning in Figs. 5 and 6, we use a +46 V sample bias to further minimize the dynamic background by attracting the secondary electrons back to the sample (in this case, the beam current I_B is still calculated as a sum of $I_S + I_C$, but SEY cannot be measured). The dynamic background level measured in Fig. 4 is used to remove the dynamic background from the data in Figs. 5 and 6.

The ESD yield is monitored for H_2, CO, CO_2, CH_4, C_2H_6, which are the main gases desorbing as a direct result of electron irradiation. The energy dependence is measured on the same spot and acquired point by point, increasing the primary electron energy, as seen in Figs. 2 and 3 for the SEY and Fig. 4 for the ESD yield. The energy step is set to 1 eV and 0.25 eV for ESD and SEY energy sweep, respectively, to capture the detailed dynamics of the low-energy region. This energy step is then spaced further apart, to minimize the electron dose imposed on the studied surface. In an SEY energy sweep, the beam current of 0.3 nA integrates to a dose of 10^{-8} C mm^{-2}, making the SEY measurement a non-destructive routine. For an ESD curve, a similar energy sweep is done with a μA beam current that integrates to a few 10^{-5} C mm^{-2}. Although this current is received mostly at low energy, measuring ESD is destructive by definition, as some molecules are removed from the studied surface. Indeed during an ESD energy sweep, we observe a conditioning effect of a few tens of percent. A smoothed curve is fitted into the data to guide the eye by capturing the trend behind the scattered datapoints.

The conditioning effect achieved by extended electron irradiation can be measured at room and cryogenic temperature, as shown in Fig. 5, which plots the ESD yield against the accumulated electron dose. The same irradiation with 300 eV primary electrons is done at 260 K and 15 K for comparison. Fig. 6 shows the ESD yield conditioning curves of low-SEY surface treatments under 300 eV electron irradiation at 15 K.

The setup enables the study of SEY and ESD yields of material samples as a function of energy and dose. We typically measure the SEY and ESD energy dependence of an as-received surface state of each studied sample. Then, another intact spot is chosen on the same sample that is irradiated with electrons at a given energy. We chose the 300 eV primary energy as a baseline as it provides the most effective conditioning effect. During this irradiation, the ESD yield of the main gas species is measured and plotted as a function of the impinging electron dose. At last, another SEY curve is measured on the conditioned surface to describe the final surface state. The SEY measurement is also used to reference the primary electron energy scale with respect to the sample. Thereby, all electron energies are taken with respect to this vacuum level E_{vac}, as localized by the inflection point of the work function edge of the sample.

3. Results and discussion

3.1. SEY measurements

Using this experimental method, we have measured the effect of SEY conditioning for various surfaces held at 15 K. The effect of varying primary electron energy is illustrated on an OFE copper. The surface state of an as-received unbaked OFE copper that we studied featured a maximum SEY, $\delta_{max} = 2.8$, peaking around 300 eV. The presence of contaminants on the intact surface not only manifests by a large δ_{max}, but is also evidenced by the presence of ~7 eV peak visible in the inset of the left graph on Fig. 2. Electron conditioning was then done for three different primary electron energies. The 300 eV electrons at a dose of 2.3 mC mm^{-2} condition the δ_{max} to 1.1 and shift the peak towards 200 eV. Conditioning with 1 keV electrons at the same dose achieves almost the same conditioning effect. This conditioning process is well understood and described at ambient temperatures [39–41]. The low SEY and peak around 200 eV is assigned to precipitation of graphitic carbon overlayer on the copper surface. Conversely, 23 eV electrons do not condition the SEY nearly as well as, not even at twice the dose. The δ_{max} does not decrease below 1.45 and the peak does not shift towards 200 eV. Such limited conditioning effect that low-energy electrons have on copper was also measured by Refs. [39,42], in these cases at room temperature, and was linked to the lack of surface carbonization.

The right graph in Fig. 3 shows the SEY conditioning effect measured for the case of 50 nm thick a-C coating and for laser-treated copper

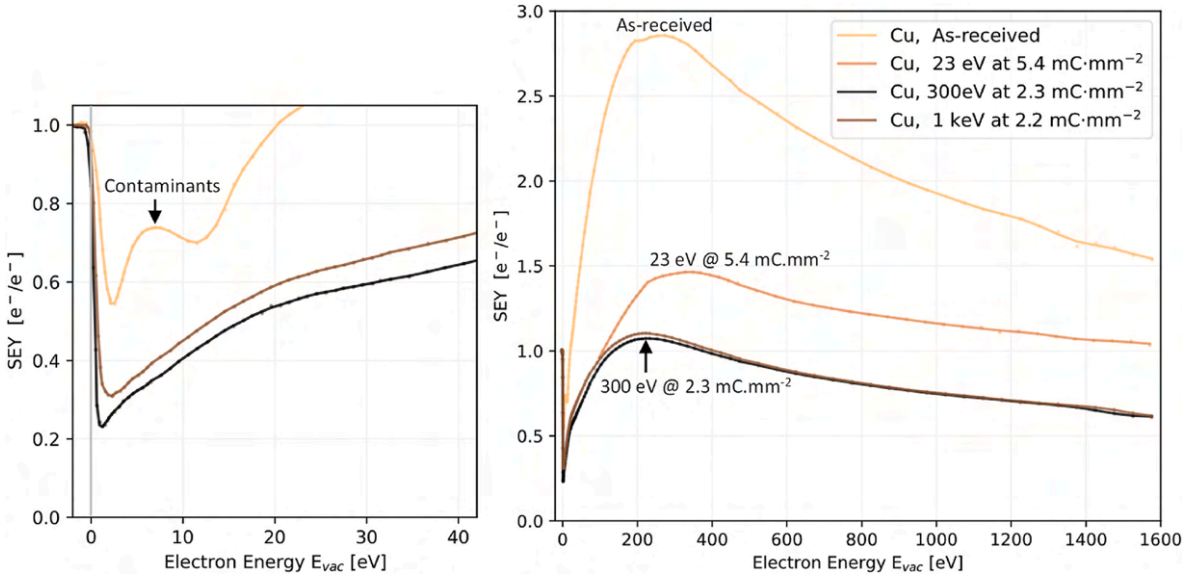

Fig. 2. SEY curves of OFE Cu measured at 15 K as a function of primary electron kinetic energy, which is referenced to the vacuum level of the sample. Left graph zooms into the low-energy region and shows the contaminant removal and surface graphitization.

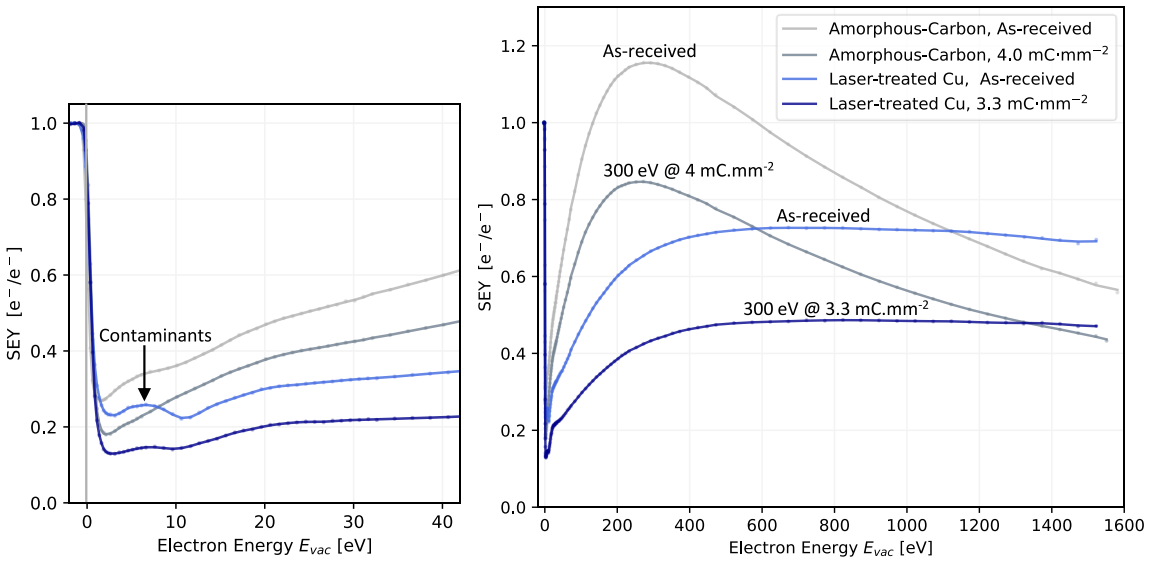

Fig. 3. SEY curves measured at 15 K as a function of primary electron kinetic energy, referenced to the sample vacuum level. The SEY curves for 50 nm amorphous-carbon and laser-treated copper show the as-received and conditioned states.

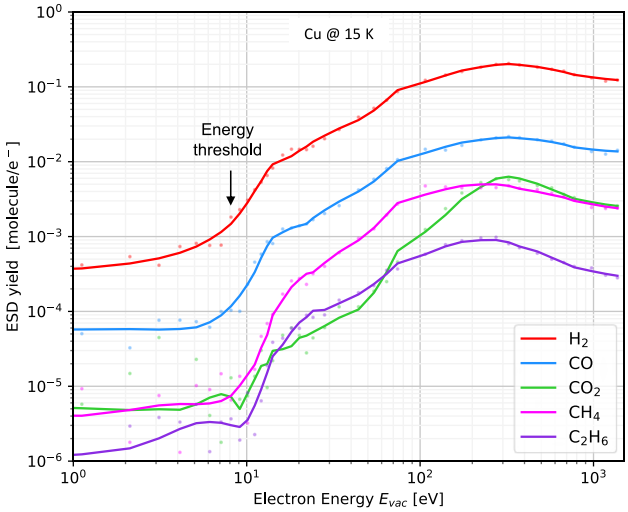

Fig. 4. ESD yield as a function of primary electron energy, as measured for an unbaked as-received OFE copper at 15K. The energy threshold is marked by an arrow around 10 eV and is similar for all chemisorbed gases. Below this threshold lies the collector's dynamic background signal, which is highest for H_2 and CO.

surface, both of which are in an as-received unbaked state and held at 15 K. Both surface treatments are designed to have intrinsically low SEY [25,26] well below the LHC multipacting limit of $\delta_{max} = 1.35$ in dipoles (or 1.1 in quadrupoles) for 6.5 TeV protons beams [43].

The data show that the SEY is further reduced by 300 eV electron irradiation. When exposed to an electron dose of 4 mC mm^{-2}, the δ_{max} of a-C drops from 1.15 to 0.85 and the peak shifts closer towards 200 eV, corresponding to the lack of contaminants on the graphitic surface. This corresponds to results obtained for amorphous-carbon in an as-received state with the δ_{max} in the 1.15 to 0.85 range. The obtained δ_{max} was demonstrated to vary with the surface state, achieved by specific coating process parameters, storage methods and thermal treatments [25, 44–46].

Owing to its microgeometry, the laser-treated copper surface exhibits a characteristically flat SEY curve with only a flat peak and intrinsically low δ_{max} [35,47–49]. We measured that the δ_{max} further decreases, from 0.73 to 0.5, when irradiated with 300 eV electrons at a dose of 3.3 mC mm^{-2}. The overall decrease can again be ascribed to the electron-stimulated removal of surface contaminants, as evidenced by the reduction of the 7 eV peak. Likewise the bare copper and a-C coating, the general shape of the SEY curve does not evolve during an e$^-$ conditioning, but only scales down towards lower SEY values.

It is remarkable to note that cooling down both studied low-SEY treatments to a cryogenic temperature does not strongly modify the δ_{max} as compared to room temperature studies [25,50]. Our data for laser-treated copper agree with SEY measurements done at cryogenic temperatures [51].

3.2. ESD yield as a function of primary electron energy

Similarly to the SEY, the ESD yield can also be measured as a function of energy, as illustrated in Fig. 4. The ESD signal only consists of the dynamic background in the 1–10 eV energy region. As the primary energy ramps up, the signal from the studied sample eventually surpasses the dynamic background level and rapidly becomes the predominant gas source. We interpret this discontinuity to be the desorption energy threshold, as described in the framework of the classical IMGR model, developed independently by Ishikawa [52], Menzel & Gomer [53] and Redhead [54]. This is remarkably close to the 10 eV effect mentioned in Redhead's memoirs [55] and the values extrapolated by Billard et al. for room temperature OFHC copper [56]. As much as the data scatter and dynamic background allows us to draw conclusions, the energy threshold is similar for all monitored gases and lies below 10 eV. Beyond this energy threshold, the ESD yield increases linearly due to the primary electron energy being deposited within the secondary electrons (SE) escape depth. The yield reaches a flat peak at a few hundreds of eV and is followed by a slow decrease. This decrease at higher energies is partly due to electron conditioning done during the energy sweep itself and partly due to the primary e$^-$ depositing energy deeper within the bulk, in a depth comparable to the SE escape depth. The ESD yield of all monitored gases follows a similar trend across the entire energy range.

3.3. ESD conditioning

Extended electron irradiation decreases the ESD yield of all desorbing gas species, i.e. H_2, CO, CO_2, CH_4, C_2H_6, in an effect called

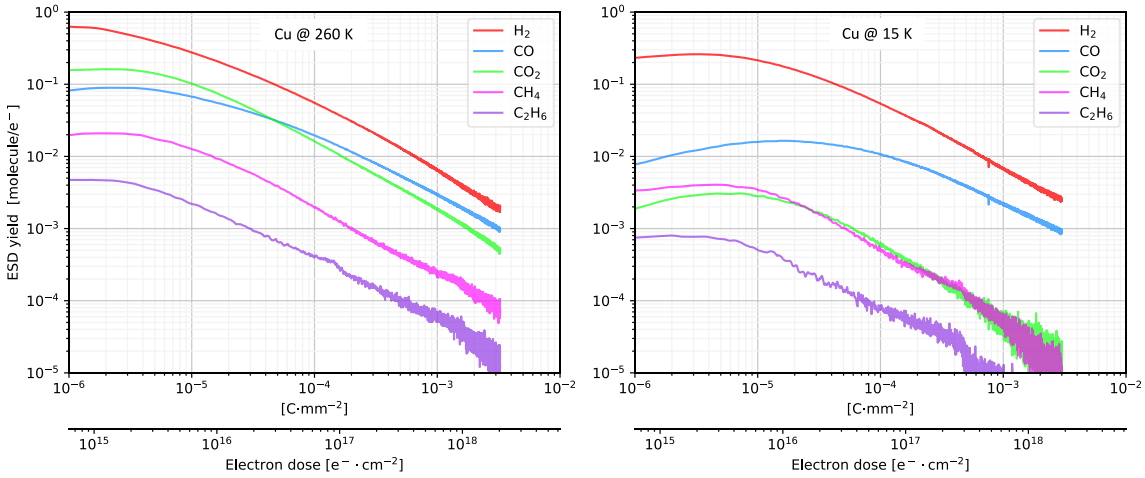

Fig. 5. ESD conditioning curves measured for OFE copper held at 260 K (left) and 15 K (right). The copper surface in an unbaked as-received surface state was irradiated with 300 eV electrons.

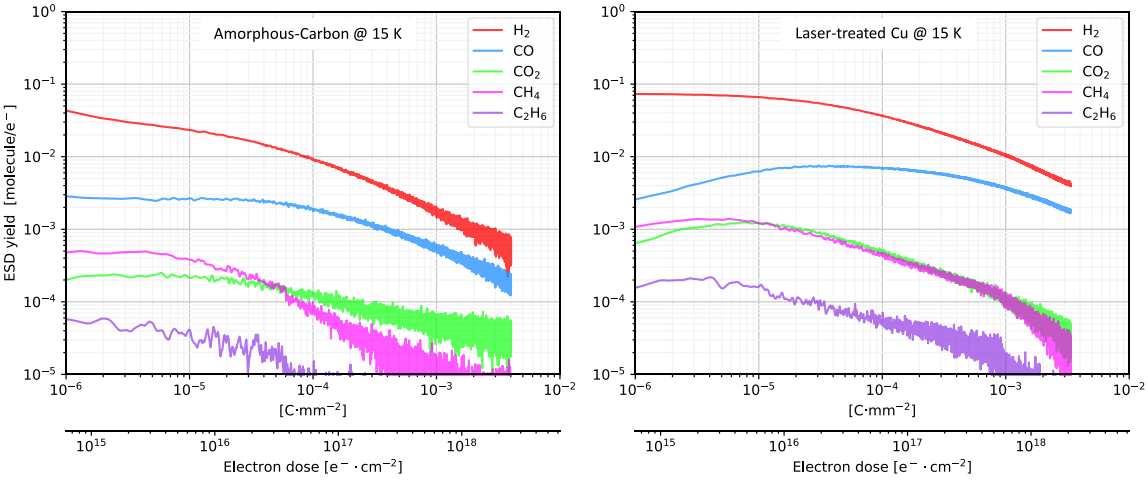

Fig. 6. ESD conditioning curves measured for 50 nm amorphous-carbon (left) and laser-treated (right) copper surface. The studied surfaces are unbaked, as-received, held at 15K and conditioned with 300 eV electrons.

conditioning. Subjecting a surface to a continuous 300 eV electron irradiation desorbs molecules, depletes their surface coverage and decreases the ESD yield. The ESD yield can be plotted as a function of accumulated e^- dose, as illustrated in Fig. 5 for unbaked copper at 260 K and 15 K. Fig. 6 shows 300 eV conditioning for amorphous carbon and laser-treated copper both unbaked and held at 15 K.

In the ambient temperature case, the conditioning curve of an ESD yield for all species typically starts with a plateau which holds the initial ESD yield for about a decade of electron dose until a few 10^{15} $e^-.cm^{-2}$. A steady decrease then follows at higher doses. The conditioning rate asymptotically approaches a constant decline that can be fitted by an inverse power law with an exponent typically in the 0.5–1 range. The conditioning rate approaches a slope of 1 for copper at ambient and cryogenic temperature. The ESD yields of CH_4, C_2H_6 and CO_2 and by extension their conditioning rates are less conclusive at high electron doses, as we are approaching the sensitivity limit of the experimental setup.

The ESD yield of all monitored gas species behaves differently, when comparing the ambient temperature to the copper at 15 K. The cryogenic temperature causes the initial yield to decrease, presumably due to lower recombination rate/mobility on the surface or diffusion in the bulk. The initial H_2 yield is the least affected and drops only by a factor of 4. The initial yield of CH_4, C_2H_6 and CO decreases by a decade, whilst the CO_2 yield drops by almost two decades. The formation of CO_2 on the surface and a subsequent desorption seems very ineffective at 15 K for all the studied surfaces. By contrast, the H_2 and CO yields, approach their room temperature counterpart at high electron doses.

The CO and CO_2 yields exhibit a transient maximum before starting a steady decrease. We ascribe this maximum to the fact that at 15 K, we measure a recycling ESD yield in our conductance-limited collector. Hence, the measured signal is a superposition of the primary desorption and secondary desorption of gases cryosorbed into a sub-monolayer coverage, similarly to the case studied in Refs. [57,58]. Indeed, we observe vacuum transients similar to the above references where the upper-limit of the recycling yield is given by the quasi-static gas density in the collector, that is determined by the ratio of the collector conductance to the cryo-sample pumping speed. In our case, this upper limit value equals 2. Hence, the initial ESD yield we measure in our experimental arrangement can only be underestimated by a factor of 2.

The same measurement of ESD yield conditioning was performed on a 50 nm amorphous-carbon and the laser-treated copper, both held at 15 K while irradiated with 300 eV electrons. The a-C exhibits an initial

Table 1
Comparison of H_2 and CO yields of the studied surfaces as sampled at the initial as-received surface state and at doses of 10^{17} $e^-.cm^{-2}$ and 10^{18} $e^-.cm^{-2}$ during the 300 eV conditioning.

	OFE Cu at 260 K		OFE Cu at 15 K		50 nm a-C/Cu at 15 K		Laser-treated Cu at 15 K	
	H_2	**CO**	**H_2**	**CO**	**H_2**	**CO**	**H_2**	**CO**
Initial Yield [molecule/e^-]	6.2E-1	8.3E-2	2.3E-1	7.9E-3	4.1E-2	2.8E-3	7.4E-2	2.7E-3
Yield at 10^{17} $e^-.cm^{-2}$ [molecule/e^-]	3.7E-2	1.4E-2	3.7E-2	8.4E-3	7.0E-3	1.5E-3	3.0E-2	6.5E-3
Yield at 10^{18} $e^-.cm^{-2}$ [molecule/e^-]	3.8E-3	1.9E-3	4.4E-3	1.5E-3	1.1E-3	4.0E-4	7.4E-3	2.9E-3
Reduction factor in 10^{17}-10^{18} $e^-.cm^{-2}$ [-]	9.8	7.1	8.4	5.6	6.6	3.8	4.0	2.3
Desorbed gas at 10^{17} $e^-.cm^{-2}$ [mbar.l.cm^{-2}]	4.5E-4	1.2E-4	3.7E-4	5.1E-5	5.7E-5	9.1E-6	1.9E-4	3.0E-5

ESD yield lower by a factor of 3–6, as compared to copper at 15 K. There is no transient maximum and after the initial plateau, the ESD yield declines for all gas species. Similarly to the a-C, the laser-treated copper exhibits lower initial ESD yields. However, a transient maximum is observed, especially for CO and CO_2, this time at a higher electron dose than for copper, which can be linked to the large specific surface.

Table 1 gives the ESD yields for different stages of the conditioning process and serves to compare the a-C and laser-treated sample against bare OFE copper at 15 K. For clarity, we focus on H_2 and CO as the predominant desorbing gases. The copper at 260 K is used to substantiate the different behaviour of ESD yield evolution with electron dose at ambient and cryogenic temperatures.

When comparing the a-C and laser-treated samples against the bare copper at 15 K, they exhibit overall lower initial ESD yields. In fact, the as-received copper at 15 K requires a dose of 10^{17} $e^-.cm^{-2}$ to reach the same H_2 yield as amorphous-carbon has ab-initio. At a dose of 10^{18} $e^-.cm^{-2}$, the copper conditions to similar ESD yields as the laser-treated surface, but the a-C already has by almost a decade lower ESD yields. The reduction of H_2 and CO yields can be calculated between doses of 10^{17} and 10^{18} $e^-.cm^{-2}$. The copper surface, regardless of the temperature, reduces its ESD yields by a factor of 5.5–10 per decade of electron dose. This is a characteristic observation for a clean metal surface, where the decrease approaches a factor of 10. By contrast, both surface treatments reduce their ESD yield at about half the rate, even at high e^- doses. Hence the electron conditioning seems less effective here and is likely linked to the surface porosity.

The integral amount of gas desorbed during a conditioning can also be evaluated. For an electron dose of 10^{17} $e^-.cm^{-2}$, there are only marginal differences in the H_2 and CO desorbed from copper, regardless of temperature, and including the laser-treated copper. The desorbed gas corresponds to 5–11 $.10^{15}$ molecules. cm^{-2} for H_2 and 0.7–3 $.10^{15}$ molecules. cm^{-2} for CO. At the same electron dose, the amorphous-carbon desorbs about 6 times less H_2 and CO than bare copper at 15 K.

4. Conclusions

We have developed and validated a methodology for measuring SEY and ESD yield at cryogenic temperatures and in the low-energy range of 0–1 keV. The new setup produces data in excellent agreement with values found in literature taken under similar parameters. This includes the SEY measured at ambient [40] and cryogenic temperatures [59] and of ESD yields and conditioning rates measured at ambient temperature [56,60,61] as well as the effect that varying primary electron energy has on the SEY conditioning process [39]. We first studied an OFE copper representing the LHC beam-screen to establish a reference at both ambient and cryogenic temperatures. We then proceeded with studies of novel low-SEY surface treatments to directly compare their SEY, ESD yields and electron conditioning effects.

We report the first laboratory measurements of electron conditioning of both SEY and ESD yield performed at a cryogenic temperature of 15 K. We showed that the primary electron energy has a major influence on the SEY conditioning efficiency. We evidence this by incomplete SEY conditioning when irradiating the OFE copper with 5.4 mC mm^{-2} of 23 eV electrons that only resulted in $\delta_{max} = 1.45$. This is to be compared to the full conditioning effect, i.e. $\delta_{max} = 1.1$, achieved by exposing copper to 300 eV electrons at a dose of 2.3 mC mm^{-2}. The lack of conditioning efficiency of low-energy e^- was previously demonstrated for copper at room temperature [39], and we evidence this effect at cryogenic conditions. Our results complement the existing data on SEY conditioning measured in the cryogenic temperature region by Cimino & Collins [59]. Here we further investigate the effect of primary electron energy on the OFE copper conditioning.

The ESD yield from OFE copper at 15 K was also studied as a function of primary e^- energy, revealing a ~10 eV threshold, below which the electron-stimulated desorption yield is nil. This observation compares well to the values extrapolated by Billard et al. [56] for as-received OFHC copper at ambient temperature. The energy dependence of ESD is linear for all monitored gases until reaching a flat peak at a few hundreds of eV. Unlike for the SEY conditioning which is rather temperature-independent, the ESD yields are substantially lower for copper at 15 K. The cryogenic conditions lead to about a decade lower initial ESD yield for CH_4, C_2H_6 and CO, whilst the initial H_2 yield drops by a factor of ~3 and the initial CO_2 yield decreases by 2 decades. The ESD conditioning curves also exhibit a very different behaviour at cryogenic temperatures, when compared to copper ambient temperatures. The CH_4, C_2H_6 and CO_2 yields remain lower at high electron doses. By contrast, the H_2 and CO yields ultimately converge to the values obtained for a room temperature copper. The conditioning rate at high electron doses remains unchanged at 15 K and approaches a slope of 1 for copper and about half of that for the studied low-SEY treatments.

We also report the first results taken at cryogenic temperatures on electron conditioning of HL-LHC-relevant low-SEY surface treatments. We demonstrate across the studied energy range that both surface treatments preserve their low δ_{max} even at cryogenic temperatures. Indeed, the SEY of as-received unbaked amorphous-carbon (50 nm) and laser-treated copper do remain well below the multipacting threshold for LHC cryodipole, i.e. $\delta_{max} < 1.3$. The SEY further decreases when exposed to 300 eV electron irradiation at 15 K. The δ_{max} of amorphous-carbon conditions from 1.15 to 0.85 at a dose of 4 mC mm^{-2}, whilst δ_{max} of laser-treated copper conditions from 0.73 to 0.5 at a dose of 3.3 mC mm^{-2}.

The initial ESD yields of both low-SEY surface treatments are lower than of an as-received unbaked OFE copper. The ESD yield of copper only conditions to comparable ESD values at an electron dose of few 10^{-4} C mm^{-2}. Compared to the copper, the amorphous-carbon coating lower by almost a decade at an electron dose of few mC.mm^{-2}. Contrary to the copper surface, both amorphous-carbon and laser-treated copper exhibit a slower ESD conditioning rates that approach a slope of 0.5 rather than 1. The conditioning curves produced at a cryogenic temperature do complement the observations made by Hannah et al. for a laser-treated copper at ambient temperature [62]. The conditioning rates at high electron doses are similar to Hannah's, but the initial yields are overall lower at 15 K, which is expected knowing the substantial decrease of copper ESD yields in Fig. 5.

The presented experimental results link the e^- cloud activity, the dynamic vacuum effect and the beam conditioning, all observed in the LHC's cold arcs. These new insights into the LHC vacuum system are especially relevant with the HL-LHC upgrade under way [24]. The data

can also serve other cryogenic machines [3] and provide an input for design and simulations of new accelerators, such as the FCC-hh [5,23].

CRediT authorship contribution statement

Michal Haubner: Writing – review & editing, Writing – original draft, Visualization, Software, Methodology, Investigation, Data curation. **Vincent Baglin:** Writing – review & editing, Supervision, Resources, Project administration, Funding acquisition, Formal analysis. **Bernard Henrist:** Supervision, Methodology, Formal analysis, Data curation, Conceptualization.

Declaration of competing interest

The authors declare that they have no known competing financial interests or personal relationships that could have appeared to influence the work reported in this paper.

Data availability

Data will be made available on request.

Acknowledgements

The work and material for this research was supported by the HL-LHC project. The authors also thankfully acknowledge the support of CERN's TE-VSC group. The corresponding author's participation conference was supported by the Ministry of Education, Youth and Sports of the Czech Republic [Czech Technical University in Prague project SGS21/149/OHK2/3T/12].

References

[1] G. Rumolo, N. Mounet, C. Zannini, Arduini, et al., Electron cloud observations in LHC (No. CONF, in: Proc. of IPAC'11, Sept 2011, San Sebastian, Spain, 2011, pp. 2862–2864. URL: jacow.org/IPAC2011/papers/THOBA01.pdf.
[2] G. Iadarola, G. Rumolo, G. Arduini, H. Bartosik, et al., Electron Cloud and Scrubbing Studies for the LHC (No. CERN-ACC-2013-0054), in: Proc. Of IPAC'13, May 2013, Shanghai, China, 2013. URL: cds.cern.ch/record/1572988.
[3] W. Fischer, M. Blaskiewicz, M. Brennan, H. Huang, et al., Electron cloud observations and cures in the relativistic heavy ion collider, Phys. Rev. ST Accel. & Beams 11 (2008), 041002, https://doi.org/10.1103/PhysRevSTAB.11.041002.
[4] C. Montag, V. Ptitsyn, eRHIC in ICFA Beam Dynamics Newsletter No. 74, E Gianfelice-Wendt, August 2018.
[5] M. Benedikt, et al., FCC-Hh: the hadron collider, Eur. Phys. J. Spec. Top. 228 (4) (2019) 755–1107, https://doi.org/10.1140/epjst/e2019-900087-0.
[6] The CEPC-SPPC Study Group, CEPC-SppC Preliminary Conceptual Design Report, Vol vol. II: Accelerator, IHEP-CEPC-DR-2015-01, March 2015. URL: cepc.ihep.ac.cn/preCDR/Pre-CDR_final_20150317.pdf.
[7] Baglin, V., Bregliozzi, G., Lanza, G., Jimenez, J. M. Synchrotron radiation in the LHC vacuum system, Proc. Of IPAC'11, September 2011, San Sebastian, Spain. URL: cds.cern.ch/record/1407539.
[8] O. Brüning, et al., LHC Design Report, CERN-2004-003, Geneva, Switzerland, June 2004, https://doi.org/10.5170/CERN-2004-003-V-2.
[9] O. Gröbner, Overview of the LHC vacuum system, Vacuum 60 (1–2) (2001) 25–34, https://doi.org/10.1016/S0042-207X(00)00240-2.
[10] G. Bregliozzi, V. Baglin, P. Chiggiato, P. Cruikshank et al. Observations of electron cloud effects with the LHC vacuum system, Proc. of IPAC'11, September 2011, San Sebastian, Spain. paper TUPS018, pp. 1560-1562. URL: jacow.org/IPAC2011/papers/TUPS018.pdf.
[11] G. Lanza, V. Baglin, G. Bregliozzi, J. M. Jimenez. LHC Beam vacuum during 2011 machine operation, Proc. Of IPAC'12, May 2012, New Orleans, Louisiana, USA. URL: jacow.org/IPAC2012/papers/WEPPD018.pdf.
[12] G. Lanza, V. Baglin, G. Bregliozzi, J. M. Jimenez. LHC vacuum system: 2012 review and 2014 outlook, Proc. Of LHC Beam Operation Workshop - Evian 2012, December 2012, CERN-ATS-2013-045, Geneva, Switzerland. URL: cds.cern.ch/record/2302432.
[13] Baglin, V., Bregliozzi, G., Lanza, G., & Jimenez, J. M. Vacuum performance and lessons for 2012, Proc. Of Chamonix 2012 Workshop on LHC Performance, CERN-2012-006, Geneva, Switzerland. DOI: 10.5170/CERN-2012-006.74.
[14] S.Y. Zhang, L. Ahrens, J. Alessi, M. Bai, et al., Experience in reducing electron cloud and dynamic pressure rise in warm and cold regions in RHIC, in: Proc. Of EPAC 2006, June 2006. Edinburgh, Scotland. URL: www.osti.gov/biblio/885019.
[15] Y. Suetsugu, K. Kanazawa, S. Kato, et al., Present status of the KEK B-factory vacuum system, J. Vac. Sci. Technol., A 21 (2003) 1436, https://doi.org/10.1116/1.1577129.
[16] Y. Suetsugu, K. Shibata, T. Ishibashi, et al., Achievements and problems in the first commissioning of superKEKB vacuum system, J. Vac. Sci. Technol., A 35 (2017), 03E103, https://doi.org/10.1116/1.4977764.
[17] V. Baglin, The LHC vacuum system: commissioning up to nominal luminosity, Vacuum 138 (2017) 112–119, https://doi.org/10.1016/j.vacuum.2016.12.046.
[18] E. Buratin, Electron Cloud and Synchrotron Radiation Characterization of Technical Surfaces with the Large Hadron Collider Vacuum Pilot Sector (Doctoral dissertation, CERN), 2020. EPFL. URL: cds.cern.ch/record/2746058.
[19] G. Iadarola, Electron Cloud Studies for CERN Particle Accelerators and Simulation Code Development, Doctoral dissertation, CERN, 2014. URL: cds.cern.ch/record/1705520.
[20] R. Cimino, T. Demma, Electron cloud in accelerators, Int. J. Mod. Phys. 29 (No.17) (2014), 1430023, https://doi.org/10.1142/S0217751X14300233.
[21] S.Y. Zhang, eRHIC Beam Scrubbing, BNL-114220-2017-IR, Brookhaven National Laboratory, Upton, NY, United States, June 2017, https://doi.org/10.2172/1392223.
[22] G. Rumolo, I. Hofmann, E. Mustafin, O. Boine-Frankenheim, Vacuum and electron cloud issues at the GSI present and future facilities, in: Proc. Of ECLOUD'04: 31st Advanced ICFA Beam Dynamics Workshop on Electron-Cloud Effect, 2005, pp. 95–101, https://doi.org/10.5170/CERN-2005-001.95. Napa, CA, USA.
[23] I. Bellafont, M. Morrone, L. Mether, J. Fernández, et al., Design of the future circular hadron collider beam vacuum chamber, Physical Review Accelerators and Beams 23 (3) (2020), 033201, https://doi.org/10.1103/PhysRevAccelBeams.23.033201.
[24] High-Luminosity Large Hadron Collider (HL-LHC): Technical Design Report Ed. by I. Bejar Alonso, O. Brüning, P. Fessia, M. Lamont, L. Rossi, L. Tavian, M. Zerlauth. CERN 2020-10, CERN, Geneva, Switzerland. DOI: 10.23731/CYRM-2020-0010.
[25] P.C. Pinto, S. Calatroni, H. Neupert, D. Letant-Delrieux, et al., Carbon coatings with low secondary electron yield, Vacuum 98 (2013) 29–36, https://doi.org/10.1016/j.vacuum.2013.03.001.
[26] R. Valizadeh, O.B. Malyshev, S. Wang, Zolotovskaya, et al., Low secondary electron yield engineered surface for electron cloud mitigation, Appl. Phys. Lett. 105 (23) (2014), 231605, https://doi.org/10.1063/1.4902993.
[27] M. Angelucci, A. Novelli, L. Spallino, Liedl, et al., Minimum thickness of carbon coating for multipacting suppression, Physical Review Research 2 (3) (2020), 032030.
[28] C.Y. Vallgren, P. Chiggiato, P.C. Pinto, H. Neupert, et al., Performance of carbon coating for mitigation of electron cloud in the SPS, in: Proc. 2nd Int. Particle Accelerator Conf.(IPAC'11), 2011, pp. 1590–1592, https://doi.org/10.1103/PhysRevResearch.2.032030.
[29] M. Van Gompel, P. Chiggiato, P.C. Pinto, P. Cruikshank, et al., Amorphous carbon thin film coating of the SPS beamline: evaluation of the first coating implementation, in: 8th Int. Particle Accelerator Conf. (IPAC'17), May 2017, Copenhagen, Denmark, 2017, May, https://doi.org/10.18429/JACoW-IPAC2017-MOOCA3.
[30] Salemme, R., Baglin, V., Bregliozzi, G., Chiggiato, P et al. Amorphous carbon coatings at cryogenic temperatures with LHC type beams: first results with the COLDEX experiment, Proc. Of IPAC'15, May 2015, Richmond, Va, USA. URL: cds.cern.ch/record/2141874.
[31] R. Salemme, V. Baglin, G. Bregliozzi, P. Chiggiato, Vacuum performance of amorphous carbon coating at cryogenic temperature with presence of proton beams, in: Proc. Of IPAC'16, May 2016, https://doi.org/10.18429/JACoW-IPAC2016-THPMY007. Busan, Korea.
[32] Amorphous carbon coating in SPS, W. Vollenberg, et al., Proc. Of IPAC'21, virtual ed, September 2021, https://doi.org/10.18429/JACoW-IPAC2021-WEPAB338. Campinas, Brazil.
[33] R. Salemme, V. Baglin, S. Calatroni, P. Chiggiato, et al., First beam test of Laser Engineered Surface Structures (LESS) at cryogenic temperature in CERN SPS accelerator, in: Journal of Physics: Conference Series, vol. 1067, IOP Publishing, 2018, September, 082017, https://doi.org/10.18429/JACoW-IPAC2018-WEPMG005, 8.
[34] Baglin, V. COLDEX: a tool to study cold surfaces in accelerators, Proceedings of ECLOUD'18, June 2018, Isola d'Elba, Italy. CERN-2020-09-19, Geneva, Switzerland. DOI: 10.23732/CYRCP-2020-007.165.
[35] D. Bajek, S. Wackerow, D.A. Zanin, L. Baudin, et al., Role of surface microgeometries on electron escape probability and secondary electron yield of metal surfaces, Sci. Rep. 10 (1) (2020) 1–8, https://doi.org/10.1038/s41598-019-57160-w.
[36] P. Feulner, D. Menzel, Simple ways to improve" flash desorption" measurements from single crystal surfaces, 1980, https://doi.org/10.1116/1.570537.
[37] R. Dupuy, M. Haubner, B. Henrist, J.H. Fillion, V. Baglin, Electron-stimulated desorption from molecular ices in the 0.15-2 keV regime, J. Appl. Phys. 128 (17) (2020), 175304, https://doi.org/10.1063/5.0021832.
[38] V. Nemanič, J. Šetina, Outgassing in thin wall stainless steel cells, J. Vac. Sci. Technol.: Vacuum, Surfaces, and Films 17 (3) (1999) 1040–1046, https://doi.org/10.1116/1.581680.
[39] R. Cimino, M. Commisso, D.R. Grosso, T. Demma, et al., Nature of the decrease of the secondary-electron yield by electron bombardment and its energy dependence, Phys. Rev. Lett. 109 (6) (2012), 064801, https://doi.org/10.1103/PhysRevLett.109.064801.
[40] M. Nishiwaki, S. Kato, Graphitization of inner surface of copper beam duct of KEKB positron ring, Vacuum 84 (5) (2009) 743–746, https://doi.org/10.1016/j.vacuum.2009.06.028.
[41] C. Scheuerlein, M. Taborelli, N. Hilleret, A. Brown, M.A. Baker, An AES study of the room temperature conditioning of technological metal surfaces by electron

irradiation, Appl. Surf. Sci. 202 (1–2) (2002) 57–67, https://doi.org/10.1016/S0169-4332(02)00868-1.
[42] R. Larciprete, D.R. Grosso, M. Commisso, R. Flammini, et al., Secondary electron yield of Cu technical surfaces: dependence on electron irradiation, Phys. Rev. Spec. Top. Accel. Beams 16 (1) (2013), 011002, https://doi.org/10.1103/PhysRevSTAB.16.011002.
[43] G. Iadarola, A.P. Axford, G. Rumolo, H. Bartosik, K. Li, Effect of Electron Cloud in Quadrupoles on Beam Instability, Proc. of. IPAC'15, Richmond, VA, USA, May 2015, https://doi.org/10.18429/JACoW-IPAC2015-MOPJE051.
[44] C.Y. Vallgren, A. Ashraf, S. Calatroni, P. Chiggiato, et al., Low secondary electron yield carbon coatings for electron cloud mitigation in modern particle accelerators, in: Proc. Of IPAC'10, May 2010, Kyoto, Japan., 2011 cds.cern.ch/record/1309161.
[45] A. Ashraf, M. Mehmood, S.A. Janjua, Study of ultra-high-vacuum properties of carbon-coated stainless steel beam pipes for high-energy particle accelerators, Arabian J. Sci. Eng. 44 (7) (2019) 6593–6600, https://doi.org/10.1007/s13369-019-03761-6.
[46] H.M. Fernández, M. Himmerlich, P.C. Pinto, J. Coroa, Sousa, et al., The impact of H_2 and N_2 on the material properties and secondary electron yield of sputtered amorphous carbon films for anti-multipacting applications, Appl. Surf. Sci. 542 (2021), 148552, https://doi.org/10.1016/j.apsusc.2020.148552.
[47] M. Pivi, F.K. King, R.E. Kirby, T. Raubenheimer, et al., Sharp reduction of the secondary electron emission yield from grooved surfaces, J. Appl. Phys. 104 (10) (2008), 104904, https://doi.org/10.1063/1.3021149.
[48] Y. Wang, W. Zhang, S. Wang, W. Wei, et al., Influence of primary electron incident angle and electron bombardment on the secondary electron yield of laser-treated copper, Journal of Vacuum Science & Technology B, Nanotechnology and Microelectronics: Materials, Processing, Measurement, and Phenomena 39 (3) (2021), 034201, https://doi.org/10.1116/6.0000952.
[49] M. Ye, P. Feng, Y. Li, D. Wang, et al., The total secondary electron yield of a conductive random rough surface, J. Appl. Phys. 125 (4) (2019), 043301, https://doi.org/10.1063/1.5023769.
[50] R. Valizadeh, O.B. Malyshev, S. Wang, T. Sian, et al., Reduction of secondary electron yield for E-cloud mitigation by laser ablation surface engineering, Appl. Surf. Sci. 404 (2017) 370–379, https://doi.org/10.1016/j.apsusc.2017.02.013.
[51] S. Calatroni, E.G.T. Valdivieso, A.T.P. Fontenla, Taborelli, et al., Optimization of the secondary electron yield of laser-structured copper surfaces at room and cryogenic temperature, Physical Review Accelerators and Beams 23 (3) (2020), 033101, https://doi.org/10.1103/PhysRevAccelBeams.23.033101.
[52] K. Mase, A. Nambu, Pioneers of study on desorption induced by electronic transitions; achievements by dr. Yoshioki Ishikawa and dr. Yoshio ohta, Journal of the Vacuum Society of Japan 49 (10) (2007) 610–617, https://doi.org/10.3131/jvsj.49.610.
[53] D. Menzel, R. Gomer, Desorption from metal surfaces by low-energy electrons, J. Chem. Phys. 41 (11) (1964) 3311–3328, https://doi.org/10.1063/1.1725730.
[54] P.A. Redhead, Interaction of slow electrons with chemisorbed oxygen, Can. J. Phys. 42 (5) (1964) 886–905, https://doi.org/10.1139/p64-083.
[55] P.A. Redhead, The first 50 years of electron stimulated desorption (1918-1968), Vacuum 48 (6) (1997) 585–596, https://doi.org/10.1016/S0042-207X(97)00030-4.
[56] F. Billard, N. Hilleret, G. Vorlaufer, Some results on the electron induced desorption yield of OFHC copper. Vacuum Technical Note 00-32, CERN, 2000.
[57] O.B. Malyshev, Vacuum in Particle Accelerators: Modelling, Design and Operation of Beam Vacuum Systems, John Wiley & Sons, 2020, https://doi.org/10.1002/9783527809134.
[58] V.V. Anashin, O.B. Malyshev, I.R. Collins, O. Gröbner, Photon-stimulated desorption and the effect of cracking of condensed molecules in a cryogenic vacuum system, Vacuum 60 (1–2) (2001) 15–24, https://doi.org/10.1016/S0042-207X(00)00239-6.
[59] R. Cimino, I.R. Collins, Vacuum chamber surface electronic properties influencing electron cloud phenomena, Appl. Surf. Sci. 235 (1–2) (2004) 231–235, https://doi.org/10.1016/j.apsusc.2004.05.270.
[60] M.H. Achard, Desorption des gaz induite par des electrons et des ions de l'acier inoxydable, du cuivre OFHC, du titane et de l'aluminium purs, CERN-ISR-VA-76-34, CERN, Geneva, Switzerland, 1976. CM-P00064839. URL: cds.cern.ch/record/314507.
[61] K. Kennedy, Electron Stimulated Desorption Rates from Candidate Vacuum Chamber Surfaces, LBL, Berkeley, July 1986.
[62] A.N. Hannah, P. Krkotič, R. Valizadeh, O.B. Malyshev, et al., Characterisation of copper and stainless steel surfaces treated with laser ablation surface engineering, Vacuum 189 (2021), 110210, https://doi.org/10.1016/j.vacuum.2021.110210.
[63] M. Haubner, V. Baglin, B. Henrist, Collector-based measurement of gas desorption and secondary electron emission induced by 0–1.4 keV electrons from LHC-grade copper at 15 K, Nucl. Instrum. Methods Phys. Res. Sect. B Beam Interact. Mater. Atoms 531 (2022) 34–43, https://doi.org/10.1016/j.nimb.2022.09.013. In press.